



ISSN 1580-3155

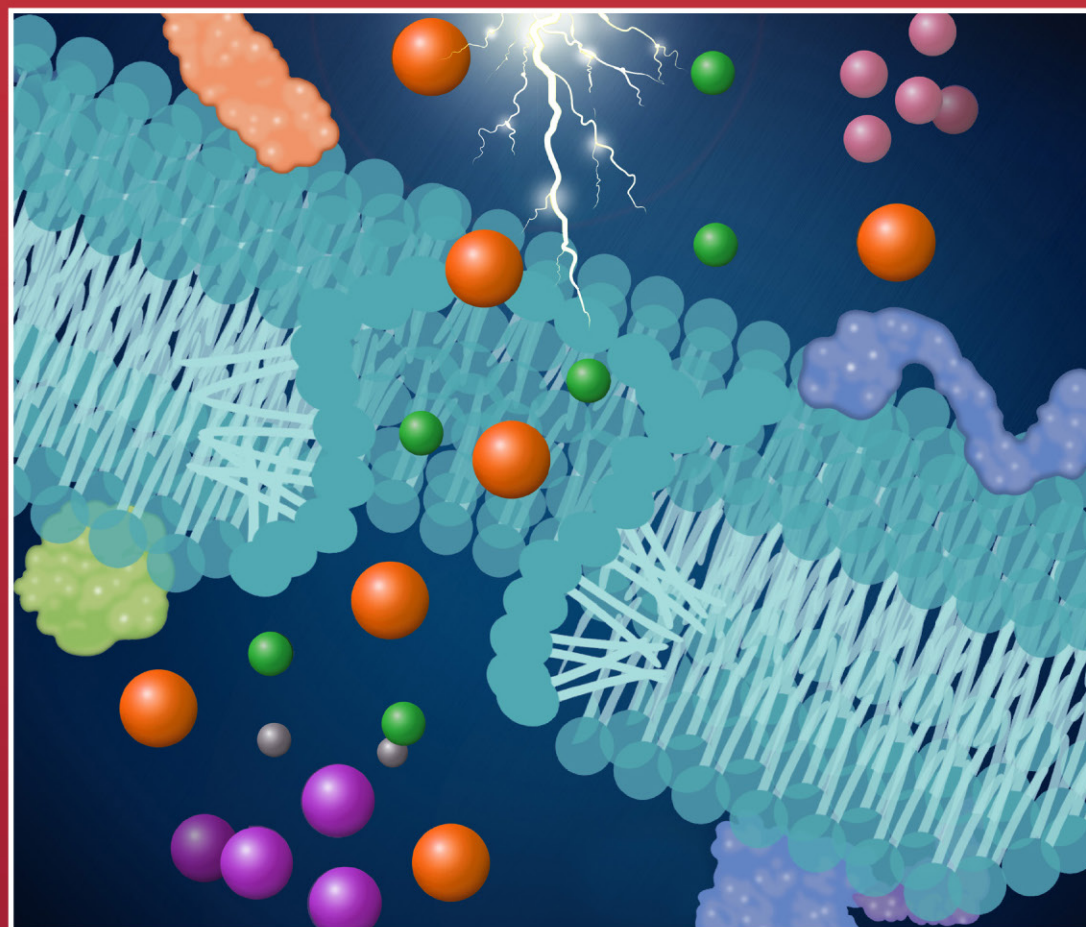
Pages 753–1038 ■ Year 2021, Vol. 68, No. 4

Slovensko kemijsko društvo
Slovenian Chemical Society



Acta Chimica Slo Acta Chimica Slo Slovenica Acta C

4



68/2021

EDITOR-IN-CHIEF

KSENIJA KOGEJ

University of Ljubljana, Faculty of Chemistry and Chemical Technology, Večna pot 113, SI-1000 Ljubljana, Slovenija
E-mail: ACSi@fkk.uni-lj.si, Telephone: (+386)-1-479-8538

ASSOCIATE EDITORS

Alen Albreht, National Institute of Chemistry, Slovenia
Aleš Berlec, Jožef Stefan Institute, Slovenia
Janez Cerkovnik, University of Ljubljana, Slovenia
Mirela Dragomir, Jožef Stefan Institute, Slovenia
Ksenija Kogej, University of Ljubljana, Slovenia
Krištof Kranjc, University of Ljubljana, Slovenia
Matjaž Kristl, University of Maribor, Slovenia

Franc Perdih, University of Ljubljana, Slovenia
Aleš Podgornik, University of Ljubljana, Slovenia
Helena Prosen, University of Ljubljana, Slovenia
Irena Vovk, National Institute of Chemistry, Slovenia

ADMINISTRATIVE ASSISTANT

Marjana Gantar Albreht, National Institute of Chemistry, Slovenia

EDITORIAL BOARD

Wolfgang Buchberger, Johannes Kepler University, Austria
Alojz Demšar, University of Ljubljana, Slovenia
Stanislav Gobec, University of Ljubljana, Slovenia
Marko Goličnik, University of Ljubljana, Slovenia
Günter Grampp, Graz University of Technology, Austria
Wojciech Grochala, University of Warsaw, Poland
Danijel Kikelj, University of Ljubljana
Janez Košmrlj, University of Ljubljana, Slovenia
Blaž Likozar, National Institute of Chemistry, Slovenia

Mahesh K. Lakshman, The City College and
The City University of New York, USA
Janez Mavri, National Institute of Chemistry, Slovenia
Friedrich Sreinc, University of Minnesota, USA
Walter Steiner, Graz University of Technology, Austria
Jurij Svete, University of Ljubljana, Slovenia
Ivan Švancara, University of Pardubice, Czech Republic
Jiri Pinkas, Masaryk University Brno, Czech Republic
Gašper Tavčar, Jožef Stefan Institute, Slovenia
Ennio Zangrando, University of Trieste, Italy

ADVISORY EDITORIAL BOARD

Chairman

Branko Stanovnik, Slovenia

Members

Udo A. Th. Brinkman, The Netherlands
Attilio Cesaro, Italy
Vida Hudnik, Slovenia
Venčeslav Kaučič, Slovenia

Željko Knez, Slovenia
Radovan Komel, Slovenia
Stane Pejovnik, Slovenia
Anton Perdih, Slovenia
Slavko Pečar, Slovenia
Andrej Petrič, Slovenia
Boris Pihlar, Slovenia
Milan Randić, Des Moines, USA

Jože Škerjanc, Slovenia
Đurđa Vasić-Rački, Croatia
Marjan Veber, Slovenia
Gorazd Vesnaver, Slovenia
Jure Zupan, Slovenia
Boris Žemva, Slovenia
Majda Žigon, Slovenia

Acta Chimica Slovenica is indexed in: *Academic Search Complete*, *Central & Eastern European Academic Source*, *Chemical Abstracts Plus*, *Chemical Engineering Collection (India)*, *Chemistry Citation Index Expanded*, *Current Contents (Physical, Chemical and Earth Sciences)*, *Digitalna knjižnica Slovenije (dLib.si)*, *DOAJ*, *ISI Alerting Services*, *PubMed*, *Science Citation Index Expanded*, *SciFinder (CAS)*, *Scopus* and *Web of Science*. Impact factor for 2020 is IF = 1.735.



Articles in this journal are published under the
Creative Commons Attribution 4.0 International License

Izdaja – Published by:

SLOVENSKO KEMIJSKO DRUŠTVO – SLOVENIAN CHEMICAL SOCIETY
Naslov redakcije in uprave – Address of the Editorial Board and Administration
Hajdrihova 19, SI-1000 Ljubljana, Slovenija
Tel.: (+386)-1-476-0252; Fax: (+386)-1-476-0300; E-mail: chem.soc@ki.si

Izdajanje sofinancirajo – Financially supported by:

National Institute of Chemistry, Ljubljana, Slovenia
Jožef Stefan Institute, Ljubljana, Slovenia
Faculty of Chemistry and Chemical Technology, University of Ljubljana, Slovenia
Faculty of Chemistry and Chemical Engineering, University of Maribor, Slovenia

Slovensko kemijsko društvo
Slovenian Chemical Society



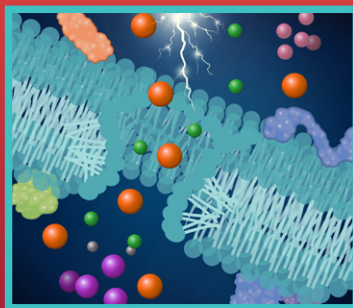
Acta Chimica Slovenica izhaja štirikrat letno v elektronski obliki na spletni strani <http://acta.chem-soc.si>. V primeru posvečenih številk izhaja revija tudi v tiskani obliki v omejenem številu izvodov.

Acta Chimica Slovenica appears quarterly in electronic form on the web site <http://acta.chem-soc.si>. In case of dedicated issues, a limited number of printed copies are issued as well.

Transakcijski račun: 02053-0013322846 Bank Account No.: SI56020530013322846-Nova Ljubljanska banka d. d., Trg republike 2, SI-1520 Ljubljana, Slovenia, SWIFT Code: LJBA SI 2X

Oblikovanje ovitka – Design cover: KULT, oblikovalski studio, Simon KAJTNA, s. p. Grafična priprava za tisk: OSITO, Laura Jankovič, s.p.

Graphical Contents



Acta Chimica Slovenica Acta Chimica Slovenica Slovenica Acta Chimica Slovenica

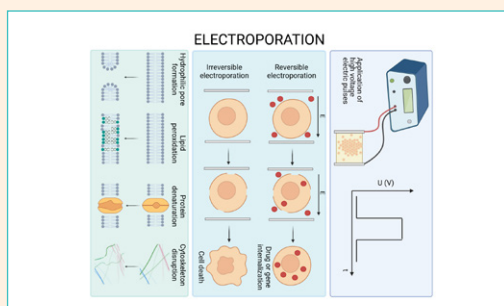
Year 2021, Vol. 68, No. 4

FEATURE ARTICLE

753–764 Feature Article

The good and the bad of cell membrane electroporation

Katja Balantič, Damijan Miklavčič, Igor Križaj and Peter Kramar



SCIENTIFIC PAPER

765–772 Analytical chemistry

Identification of Phytochemicals from the Water Extract of *Eurycoma longifolia* Roots using Solid-Liquid and Liquid-Liquid Extraction Based Fractionation Techniques

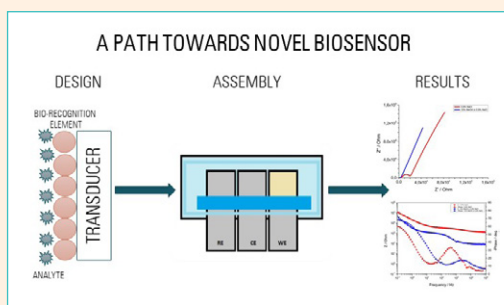
Lee Suan Chua, Abirame Segaran and Hoi Jin Wong



773–780 Analytical chemistry

Model Electrochemical Biosensor for the Detection of Methanol in Aqueous Solutions with Yeast Cells

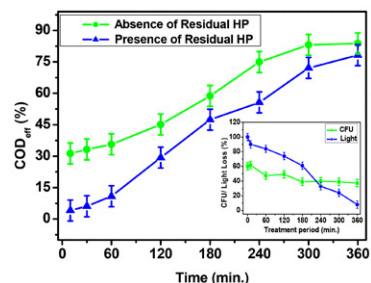
Zala Štukovnik, Urban Bren and Martin Rozman



833–848 Chemical, biochemical and environmental engineering

The Removal of Binary Mixture of Dyes by Heterogeneous Fenton Oxidation: Kinetics, Product Identification and Toxicity Assessment

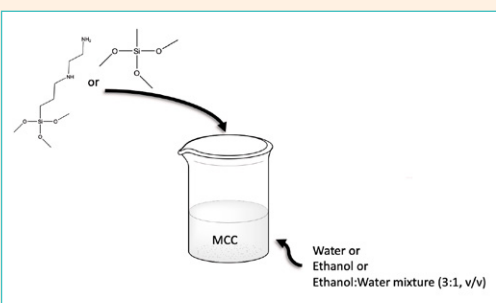
John Elisa Kumar, Tsungom Mulai, Wanshanlang Kharmawphlang, Rajeshwar Nath Sharan and Mihir Kumar Sahoo



849–860 General chemistry

Reactivity of Microcrystalline Cellulose with Methyltrimethoxysilane and 3-(2-Aminoethylamino)propyltrimethoxysilanes

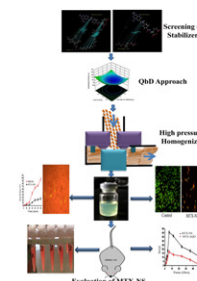
Przemysław Pietras, Hieronim Maciejewski and Bartłomiej Mazela



861–881 Biomedical applications

Development and Evaluation of Lyophilized Methotrexate Nanosuspension using Quality by Design Approach

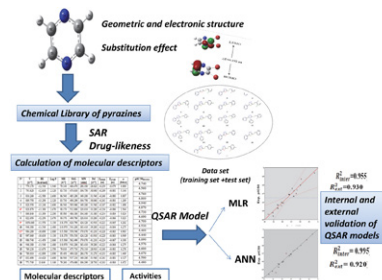
Trupti Powar, Ashok Hajare, Ravindra Jarag and Sopan Nangare



882–895 Chemical, biochemical and environmental engineering

QSAR Studies and Structure Property/Activity Relationships Applied in Pyrazine Derivatives as Antiproliferative Agents Against the BGC823

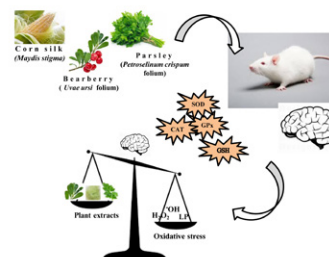
Fatima Soualmia, Salah Belaidi, Noureddine Tchouar, Touhami Lanez and Samia Boudergua



896–903 Applied chemistry

Medicinal Plants Extracts Impact on Oxidative Stress in Mice Brain under the Physiological Conditions: the Effects of Corn Silk, Parsley and Bearberry

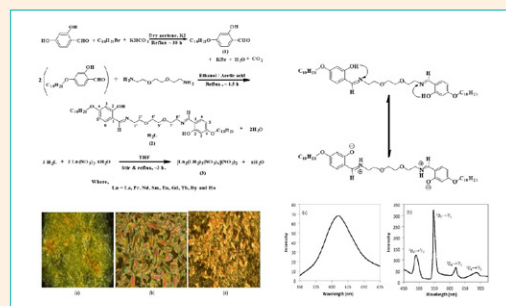
Marijana Vranješ, Dubravka Štajner, Dejan Vranješ, Bojana Blagojević, Ksenija Pavlović, Dubravka Milanov and Boris M. Popović



904–912 Inorganic chemistry

Synthesis and Spectral Studies of Some Homo Dinuclear Lanthanide(III) Complexes of a Mesogenic Schiff Base

Prem Kumar Shrestha and Pawan Raj Shakya



913–920 Applied chemistry

Determination of Some Elements in Legumes Using ICP-MS and EDXRF Methodology Applications

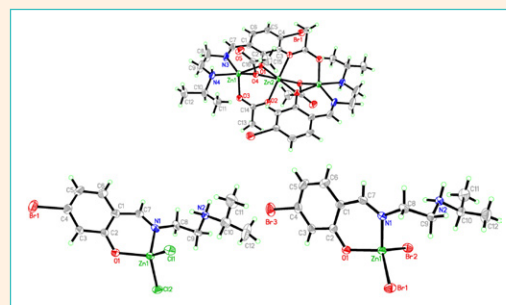
Lovro Sinkovič, Marijan Nečemer, Barbara Pipan and Vladimir Meglič



921–929 Inorganic chemistry

Zinc Complexes Derived from 5-Bromo-2-(((2-isopropylamino)ethyl)imino)methyl)phenol: Microwave-Assisted Synthesis, Characterization, Crystal Structures and Antibacterial Activities

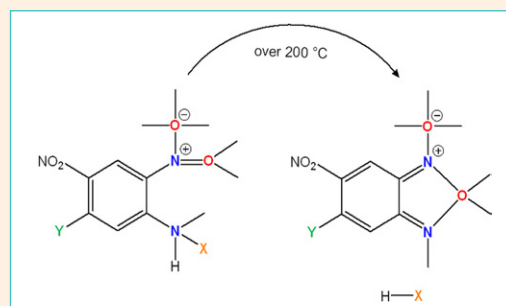
Wei-Guang Zhang and Ji-Hong Liang



930–944 Organic chemistry

Some Nitrogen Rich Energetic Material Synthesis by Nucleophilic Substitution Reaction from Polynitro Aromatic Compounds

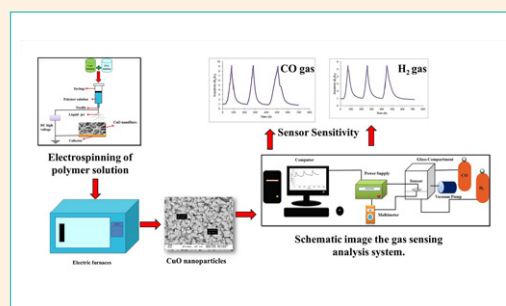
Kübra Gürpınar, Yaprak Gürsoy Tuncer, Ş. Betül Sopacı, M. Abdulkadir Akay, Hasan Nazır, Ingrid Svoboda, Orhan Atakol and Emine Kübra İnal



945–954 Inorganic chemistry

Synthesis of CuO by Electrospinning Method for Sensing of Hydrogen and Carbon Monoxide Gases

Abdollah Fallah Shojaei and Parisa Fallah Komsari

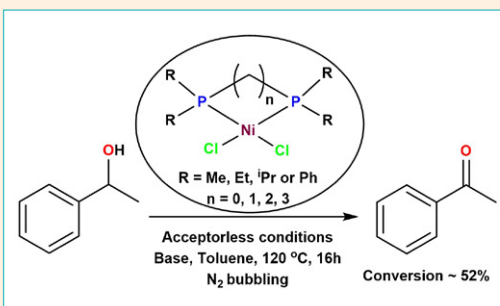


955–960

Inorganic chemistry

Dehydrogenation of 1-Phenylethanol Catalyzed by Nickel(II)diphosphine Complexes

Reshma Geetha, Meenu Kumar, Naveen V. Kulkarni and William D. Jones

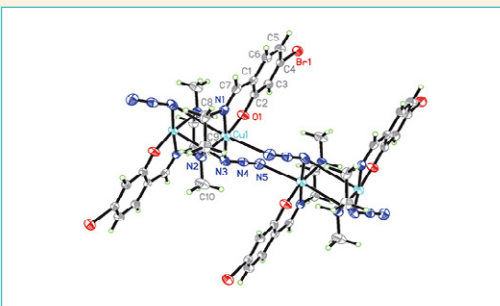


961–969

Inorganic chemistry

Synthesis, Characterization and Crystal Structures of Schiff Base Copper Complexes with Urease Inhibitory Activity

Shuang Han and Yuan Wang

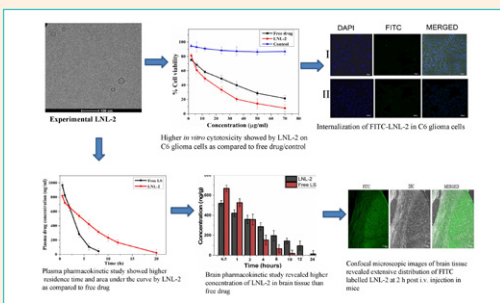


970–982

Biomedical applications

Lomustine Incorporated Lipid Nanostructures Demonstrated Preferential Anticancer Properties in C6 Glioma Cell Lines with Enhanced Pharmacokinetic Profile in Mice

Bhabani Sankar Satapathy, Ladi Alik Kumar, Gurudutta Pattnaik and Binapani Barik

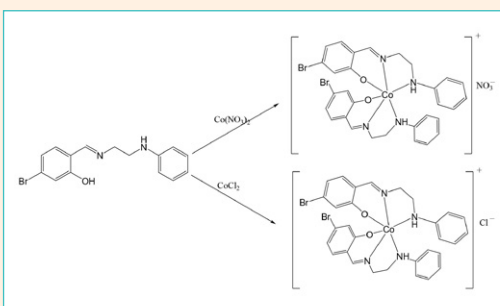


983–989

Inorganic chemistry

Synthesis, Characterization, X-Ray Crystal Structures and Antibacterial Activity of Cobalt(III) Complexes Derived from 5-Bromo-2-((2-(phenylamino)ethylimino)methyl)phenol

Cheng Liu

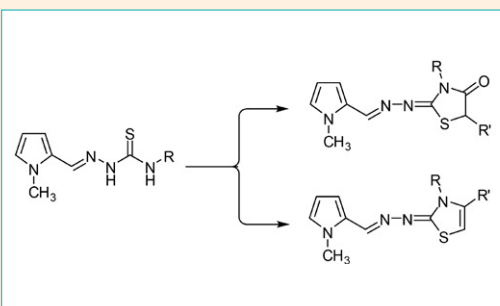


990–996

Organic chemistry

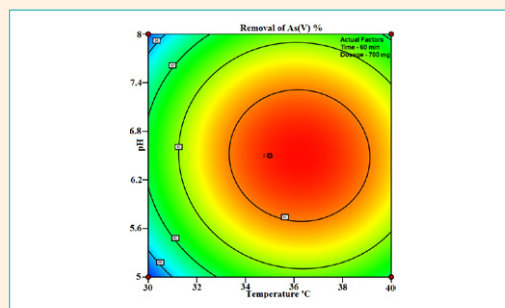
Novel Structural Hybrids of Pyrrole and Thiazole Moieties: Synthesis and Evaluation of Antibacterial and Antifungal Activities

Mohamed A. Salem, Samir Y. Abbas, Marwa A. M. Sh. El-Sharief, Mohamed H. Helal, Moustafa A. Gouda, Mohammed A. Assiri and Tarik E. Ali



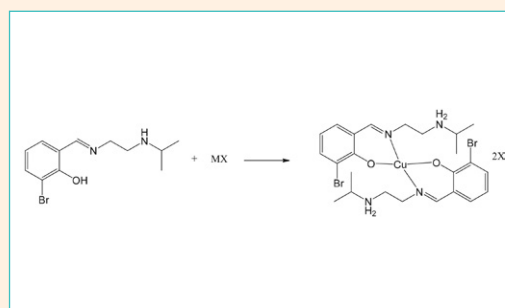
997–1007 Chemical, biochemical and environmental engineering
Statistical Optimization of As(V) Adsorption Parameters onto Epichlorohydrin/Fe₃O₄ Crosslinked Chitosan Derivative Nanocomposite using Box-Behnken Design

Vijayanand Nagarajan, Raja Ganesan, Srinivasan Govindan and Prabha Govind



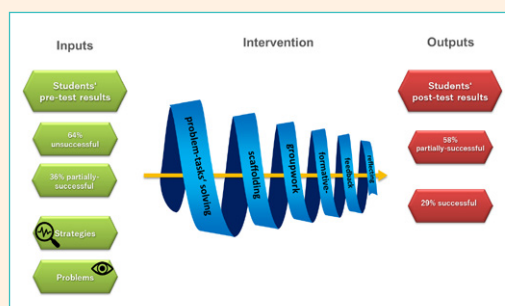
1008–1015 Inorganic chemistry
Syntheses, Characterization, Crystal Structures and Antimicrobial Activity of Schiff Base Copper(II) Complexes Derived from 2-Bromo-6-((2-(isopropylamino)ethylimino)methyl)phenol

Yong Yuan, Xi-Kun Lu, Gao-Qi Zhou and Xiao-Yang Qiu



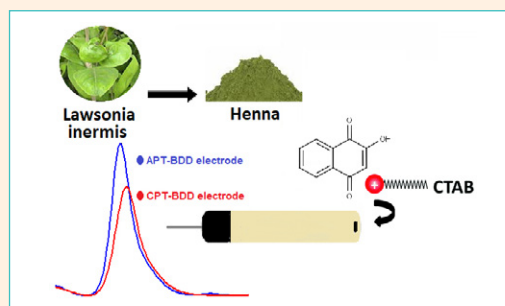
1016–1026 Chemical education
Developing Students' Problem-Solving Skills Using Learning Tasks: an Action Research Project in Secondary School

Martina Tóthová and Martin Rusek



1026–1032 Analytical chemistry
Square-Wave Voltammetric Sensing of Lawsone (2-Hydroxy-1,4-Naphthoquinone) Based on the Enhancement Effect of Cationic Surfactant on Anodically Pretreated Boron-Doped Diamond Electrode

Pınar Talay Pınar, Yavuz Yardım and Zühre Şentür



Feature article

The Good and the Bad of Cell Membrane Electroporation

Katja Balantič,^{1,2} Damijan Miklavčič,¹ Igor Križaj^{3,*} and Peter Kramar^{1,*}¹ University of Ljubljana, Faculty of Electrical Engineering, Tržaška cesta 25, Ljubljana, Slovenia² University of Ljubljana, Medical Faculty, Vrazov trg 2, Ljubljana, Slovenia³ Jožef Stefan Institute, Department of Molecular and Biomedical Sciences, Jamova cesta 39, Ljubljana, Slovenia* Corresponding author: E-mail: igor.krizaj@ijs.si (I. Križaj);
peter.kramar@fe.uni-lj.si (P. Kramar)

Received: 10-11-2021

Abstract

Electroporation is used to increase the permeability of the cell membrane through high-voltage electric pulses. Nowadays, it is widely used in different areas, such as medicine, biotechnology, and the food industry. Electroporation induces the formation of hydrophilic pores in the lipid bilayer of cell membranes, to allow the entry or exit of molecules that cannot otherwise cross this hydrophobic barrier. In this article, we critically review the basic principles of electroporation, along with the advantages and drawbacks of this method. We discuss the effects of electroporation on the key components of biological membranes, as well as the main applications of this procedure in medicine, such as electrochemotherapy, gene electrotransfer, and tissue ablation. Finally, we define the most relevant challenges of this promising area of research.

Keywords: Electroporation; cell membrane; electrochemotherapy; gene electrotransfer; tissue ablation; nanotechnology

1. Introduction

Cell membrane electroporation, also known as electroporabilization,¹ is an effective method for internalization of various molecules into biological cells, with increasing number of applications in oncology,^{2,3} gene therapy,^{4–6} tissue ablation,^{7–9} food technology^{10,11} and nanotechnology.¹²

Electroporation depends on the nature of the molecular constituents of biological membranes and their behavior in electric field. The first part of this article thus dissects out the structure of the cell membrane and describes the main transport mechanisms across this barrier. In the second part, the mechanistic principles of electroporation are presented, followed by a description of the influence of an externally applied electric field on specific cell-membrane components, such as lipids and proteins, as well as the cytoskeleton. Finally, the advantages, disadvantages, and remaining challenges of electroporation are critically discussed.

1.1. Structure of the Cell Plasma Membrane

The plasma membrane is basically a 6–10 nm-thick biological structure that surrounds every living cell, and it

provides a selective barrier between the intracellular and extracellular environments.¹³ Plasma membrane thickness of some cells can however be much larger than this basic value, for example due to glycocalyx, a highly charged layer of membrane-bound biological macromolecules attached to the membrane (e.g., endothelial and epithelial cells), or the membrane skeleton, a specialized part of the cytoskeleton closely coupled to the plasma membrane. The main function of the plasma membrane is to keep the constituents of the cell inside, while preventing unwanted substance to enter the cell. At the same time, it mediates the selective transport of essential nutrients into the cell, and of waste products in the opposite direction.¹⁴

The cell membrane provides a selective barrier due to its unique structure, which consists mainly of amphiphilic phospholipid molecules. These form a continuous double layer (the ‘phospholipid bilayer’) that has a profoundly hydrophobic core. The proteins embedded in or associated with this structure endow it with specific functions, such as the selective passage of molecules and ions. Cell shape is primarily determined by interactions between the cell-membrane components, the cytoskeleton, and the extracellular matrix,^{14,15} however factors contributing to the cell shape are much more complex.^{16–19}

As well as the major lipid constituents of the plasma membrane, the phospholipids, there are two other lipid species that are very important: sterols and glycolipids.²⁰ Cholesterol is the main sterol-based lipid molecule in the plasma membrane. It is intercalated between the lipid tails of the adjacent phospholipid molecules in the phospholipid bilayer thus increasing their ordering. In this way, it reduces membrane fluidity.^{15,21} Glycolipids (e.g., gangliosides) are very important cell-surface markers that serve as specific determinants for cellular recognition and cell-to-cell communication, and as receptors for different biomolecules. The fatty acid chains in the phospholipids and glycolipids usually contain an even number of carbon atoms, and can be saturated or unsaturated, i.e., they can contain one or more double bonds. The length of a fatty-acid chain and the number of double bonds that it contains have profound effects on the internal energy of the cell membrane; i.e., on its order and fluidity.¹³

1. 2. Molecular Transport Through the Plasma Membrane

The cell plasma membrane is selectively permeable, whereby the passage into the cell of molecules needed for its survival is highly regulated. The transport of molecules through the plasma membrane can be passive or active. Passive transport does not require energy, and its rate is governed by the physicochemical properties of the cell membrane, visco-elastic properties on both sides of the membrane, physicochemical and electrical properties of the media on both sides of the membrane, and the molecules to be transported.^{22–24} Small hydrophobic and uncharged molecules, and also gasses, are termed as permeant molecules²⁵, as these can diffuse through biological membranes freely down their electrochemical gradient.²⁶ Charged molecules, such as amino acids, nucleosides, carbohydrates, and ions, can be driven by difference in electric potential or their concentration differences to move through the membrane when assisted by specific transporter proteins, or channels, in the process known as ‘facilitated diffusion’. On the other hand, the transport of molecules and ions across biological membranes against

their electrochemical gradient requires the input of energy, and is therefore referred to as active transport.¹³ The build-up of concentration gradients of molecules and ions across biological membranes proceeds exclusively through transmembrane protein systems, such as ion pumps and the ATP-binding cassette (ABC) transporters, which are usually powered by ATP hydrolysis.²⁷ Large and charged molecules, such as proteins, nucleic acids (e.g., DNA, RNA), and diverse synthetic drugs, cannot cross cell membranes *per se* at all. Numerous therapeutic molecules are of this nature, and therefore to get them into cells, where they function, different techniques have been developed to increase the plasma membrane permeability.

1. 3. Ways to Increase the Permeability of the Plasma Membrane

The main physiological role of the cell plasma membrane is to control and regulate the flux of molecules or ions into and out of the cell. The selectivity of the plasma membrane for the passage of molecules or ions is very high, and therefore for therapeutic or biotechnological reasons, the aim is to create procedures that enable the manipulation of transmembrane transport, ideally in a relatively controlled fashion. Caution is however needed, as treatments to increase the permeability of the plasma membrane can also result in increased molecular efflux, which can then induce cell death. On the other hand, the efflux of molecules from cells can also be exploited under certain conditions in biotechnology, to extract bioproducts.²⁸

Several methods to increase the permeability of biological membranes have been described. Table 1 gives the main characteristics and applications of the main biochemical (lipid and polymer particles, microbubbles), biological (viral), and physical (ultrasound, electroporation) methods for plasma-membrane permeabilization.

In this article, the focus is on electroporation, as the alteration of the cell membrane permeability induced by exposure to an externally applied electric field. Due to the membrane exposure to pulsed electric field, pores are formed in the cell membrane and increase its conductance for various hydrophilic molecules, such as peptides, nu-

Table 1. Different methods used to manipulate cell-membrane permeability.

Method	Main characteristics	Applications	References
Sonoporation mediated by microbubbles	Transient perforation of the plasma membrane; noninvasive	Drug and gene delivery	29–31
Lipid or lipid-like vesicle fusion	Oral delivery; protects a loaded drug; release of a drug in a controlled way	Drug delivery	32,33
Virus fusion	Injection; can trigger an immune response	Gene delivery	34
Cytolytic toxins	Bacterial cytotoxic proteins	Virulence-targeted therapies	35
Ultrasound	High intensity focused ultrasound; generation of cavities due to ultrasound oscillation	Drug and gene delivery; tissue ablation	36–38
Electroporation	High voltage electric pulses; formation of hydrophilic pores in the plasma membrane	Drug and gene delivery; tissue ablation	2,7,39

leic acids, and drug molecules. Electroporation is used in medicine and biotechnology for the delivery of drugs or genes into cells, for tissue ablation, for extraction of bio-products from cells, and for microbial inactivation in food preservation.^{3,40–42}

2. Principles of Plasma-Membrane Electroporation

Electroporation leads to increased permeability of the cell membrane as a consequence of the application of electric pulses. The term electroporation was coined by Neumann and colleagues in 1982.⁴³ It originally described the process of electrically induced hydrophilic pore formation in the lipid bilayer (Figure 1).

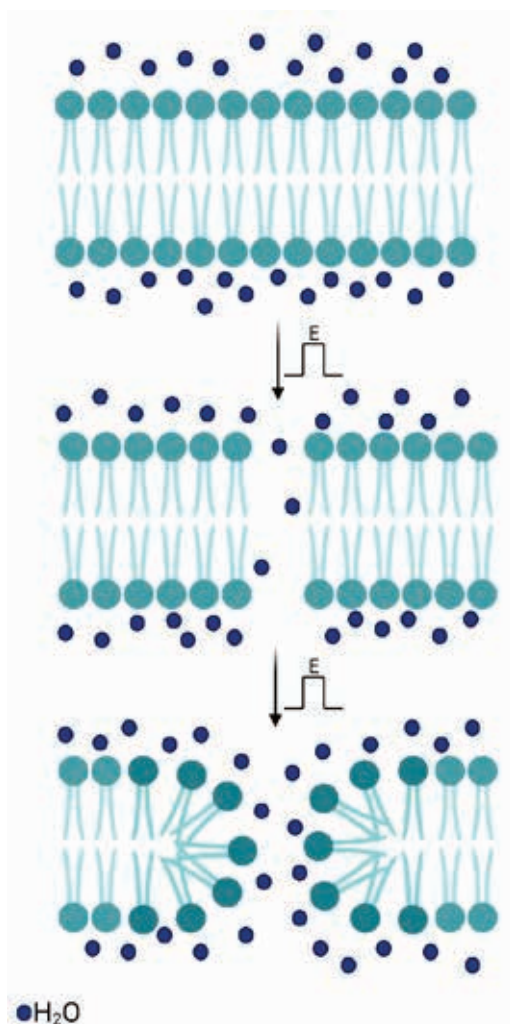


Figure 1. Formation of a hydrophilic pore in the membrane lipid bilayer. Exposure of the membrane to the electric field (E) allows the penetration of water molecules into the lipid bilayer. This induces reorientation of the polar headgroups of the lipids towards the penetrating water molecules, which ultimately leads to the formation of a hydrophilic pore, i.e. electroporation.

From the electrical point of view, the cell membrane can be regarded as a thin insulation sheet that is surrounded on both sides by an electrolyte. The transmembrane voltage is the difference in the electric potentials between outside and inside of the cell, which is due to the difference between the intracellular and extracellular ion concentrations. Specifically, different ions are present on either side of the membrane plane and have a concentration gradient across it, which results in formation of the transmembrane voltage. An electrical double layer is formed when a charged membrane plane is in contact with an electrolyte solution consisting of charged ions and oriented dipoles, resulting in accumulation of oppositely charged ions (counter-ions) and depletion of ions with the same charge (co-ions).^{44–46} Membrane itself has a net charge, which is dependent on the lipid composition, due to charged lipid head groups. The hydrophobic region of the membrane has a zero net charge. When the membrane is surrounded by an electrolyte, an interface forms, due to the separation of charged ions on either side of the membrane causing the formation of electrical double layer and consequently the transmembrane voltage.^{47–49} In the resting state, the cell membrane acquires the so called ‘resting (trans)membrane voltage, which is typically between -40 mV and -70 mV.¹

Due to the opening or closing of ion channels in the cell membrane, the resting voltage can shift to more negative or more positive values, i.e., the membrane becomes hyperpolarized or depolarized.¹³ When a cell is exposed to an external electric field, an induced transmembrane voltage is superimposed on the existing resting transmembrane voltage. The resting transmembrane voltage is always different from zero, and is equal all around the cell since the membrane is an isotropic dielectric medium with constant dielectric permittivity. On the other hand, the induced transmembrane voltage is present only for the duration of the external electric pulse, and it is anisotropic, or dependent on the position on the cell membrane.⁵⁰ Due to this induced transmembrane voltage, the structure and function of the cell membrane is locally modified.¹ The membrane undergoes electrical breakdown, which results in increased permeability for virtually all molecules. As the cell membrane behaves as a two-dimensional liquid, it can return to its pre-breakdown state, and thus the cell can survive. In such a case, we talk about reversible electroporation. However, when the exposure of the cell membrane to an electric field is very intensive, the cell will die, even if the membrane manages to reseal. This type of electroporation is referred to as irreversible (IRE).^{40,51}

In electroporation, three general levels have been defined: (1) no detectable electroporation; (2) reversible electroporation; and (3) IRE. The range over which each of these occur is characterized by the strength of the external electric field applied (V/cm) and the duration of exposure (seconds) to it. To achieve electroporation, longer pulse durations require lower electric field strengths. For example, for a pulse of 1 millisecond, no detectable elec-

roporation is seen from 0 V/cm to 250 V/cm, reversible electroporation occurs between 250 V/cm and 1750 V/cm, and IRE occurs above 1750 V/cm.⁵² In the first range for no detectable electroporation, if pores are formed, they are too small and/or too unstable to be detected. For reversible electroporation, the pores can provide a temporary pathway for molecular transport across the membrane, although once the electric pulse ceases, the membrane gradually reseals, the induced transport stops and most of these cells will survive and remain viable. For IRE, the membrane may not reseal or will reseal too slowly for cell to maintain its viability. These cells then lose their integrity, with the release of their contents, and ultimately die.^{51,53}

From a mechanistic point of view, electroporation is best described by the theory of hydrophilic pore formation. The external electric field induces a drop in the electric potential across the lipid bilayer, which leads to the formation of hydrophilic pores in the bilayer.⁴³ Both, theoretical considerations and molecular dynamics simulations suggest that electroporation is initiated by the penetration of water molecules into the hydrophobic core domain of the lipid bilayer, which then causes a re-orientation of the adjacent lipid molecules, whereby their polar headgroups will follow the direction of the invading water molecules (Figure 1).⁵⁴ First, single water molecules penetrate the hydrophobic core of the bilayer due to local defects in the lipid headgroup region. Then, these so-called water fingers expand into the hydrophobic core of the bilayer, and firstly form a hydrophobic pore.^{1,54,55} Subsequently, these pores are stabilized by reorientation of the lipid headgroups adjacent to the water molecules, thus stabilizing the pore into its hydrophilic state and allowing more water, as well as other polar molecules and ions, to enter.^{40,55,56} After the electric field is eliminated, the pores that are formed and stabilized have lifetimes from milliseconds to minutes (Table 2).¹ As indicated experimentally and theoretically, stability of the pores can be increased by intercalation of different molecules in the lipid bilayer.^{57–59}

Furthermore, membrane tension and mechanical stress can also play a role in formation of hydrophilic pores in the lipid bilayer.^{60–62} Applied electric field can cause lateral stress to the membrane influencing interfacial tension and pore formation.⁵⁵ With a reduction in membrane tension in the lateral plane a decrease in the interaction be-

tween the phospholipid molecules occurs and with it an increase in ion permeability.⁶³

3. Effects of an Electric Field on Cellular Structures

Cells consist of many different components, and an external electric field can affect these in different ways. Some of these alterations are necessary for the cell membrane electroporation to occur. However, others are not wanted, as they can induce cell death. Thus, attempts are made to reduce the unwanted effects as much as possible. We are focusing here on the effects of an external electric field on three main cellular structures: the lipids that form the plasma membrane; the proteins associated with the plasma membrane; and the cytoskeleton that lies under the plasma membrane and imposes shape to the cell (Figure 2).

3. 1. Effects of an Electric Field on the Lipid Bilayer

Application of electric pulses induces the formation of transient hydrophilic transmembrane pores in lipid bilayers. However, this does not fully describe the sustained increased permeability of the lipid bilayer, which can last long after the electric field has been removed. One possibility to explain such effects is peroxidation of lipids during the electroporation, which changes the chemical structure of the membrane to remain permeable.^{64,65}

Lipid peroxidation is a chemical reaction between lipid molecules and oxygen that results in the formation of unstable lipid peroxides. This can occur for lipid structures under stress, such as in the presence of reactive oxygen species (ROS). Lipid peroxidation is a free-radical chain reaction that can generate various products, most of which are harmful for the cell.^{66,67} The unsaturated fatty acid chains of the lipid molecules are the main targets of the peroxidation. Oxidized lipid tails become more polar and can also shorten in length. These changes can disrupt the structure of the lipid bilayer, to thus alter its fluidity, and consequently increase the permeability of the cell membrane.⁶⁸ The membrane becomes thinner, less densely

Table 2. Steps in the formation of hydrophilic pores during electroporation of a lipid bilayer.¹

Step	Main characteristics	Duration
Initiation	Membrane electrical conductivity and permeability start to increase	Nanoseconds (conductivity for electric current); microseconds (permeability for ions and molecules)
Expansion	Conductivity and permeability persist and intensify	Until the end of the pulse (up to milliseconds)
Partial recovery	After the external voltage ceases, membrane conductivity and permeability decrease rapidly, but not to zero (i.e. not to the pre-poration state)	Microseconds (conductivity for electric current); milliseconds (permeability for ions and molecules)
Resealing	The membrane recovers to its physiological state of impermeability	Seconds to minutes
Memory	The cell can show alterations to stressors before finally returning to its normal state	Hours

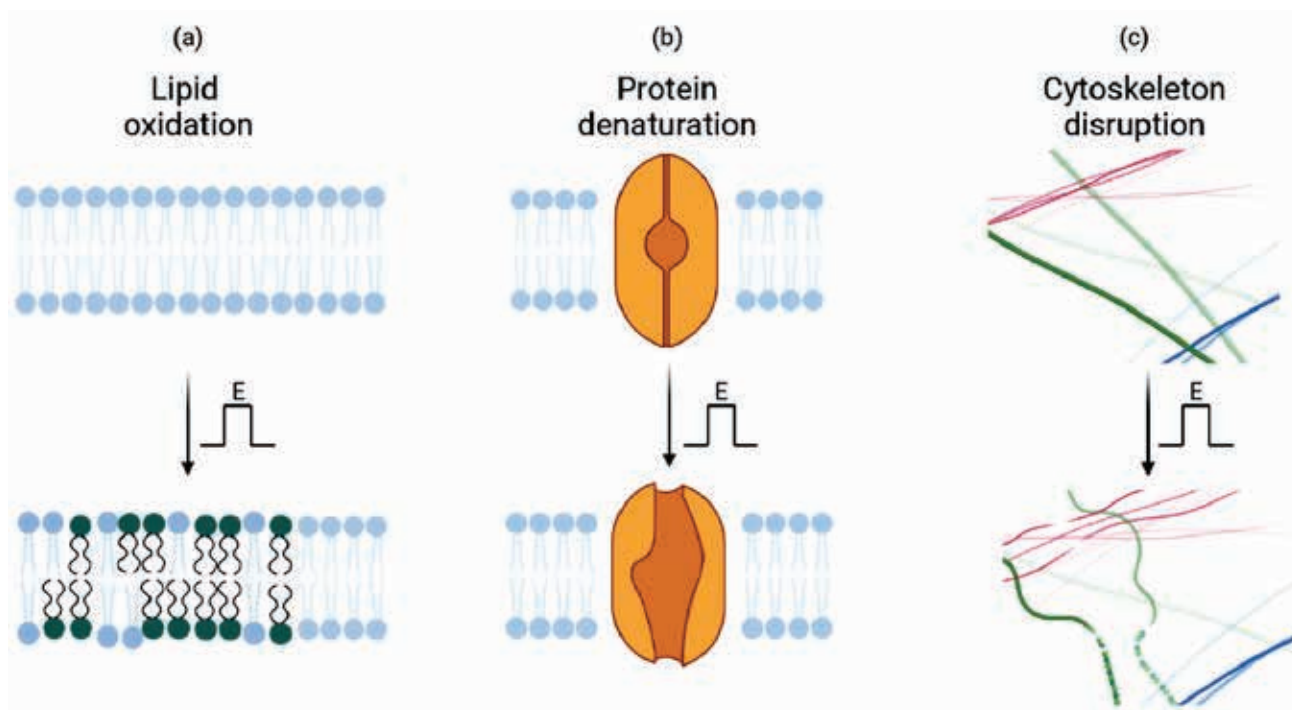


Figure 2. The effects of electric field (E) on the main cellular components. (a) The process of electroporation can induce oxidation of the lipids in the cell membrane. (b) An external electric field can induce localized heating in membrane proteins, which can lead to their reversible or irreversible denaturation, with a temporary or permanent loss of their function, respectively. (c) During electroporation, the cytoskeleton often depolymerizes and detaches from the plasma membrane (Figure adapted from reference 1).

packed, and with lower internal order. Such lipid bilayers are no longer stable and are prone to undergo lateral phase separation. The cumulative result here is that the physiological functions of the cell membrane are altered, which can lead to cell damage, and even to cell death.^{69–71}

It has been reported that electroporation induces lipid peroxidation in bacteria, plant cells, and mammalian cells, as well as in liposomes made from polyunsaturated phospholipids.¹ The origins of ROS are diverse. It has been suggested that electric pulses can generate ROS by triggering redox reactions in the water medium, on the membrane surface, and at the electrode–electrolyte interface.^{72,73} However, electric pulses initiate creation of ROS also inside the lipid bilayer and in the cell. In addition, there are always some ROS already present in the system.^{74,75} All ROS, no matter their origin, can result in peroxidation of lipids during electroporation; however, as ROS are short-lived, only those generated in close proximity to the cell membrane will cause lipid damage. It has been demonstrated that ROS peroxidize only the parts of the membrane that are electroporated. These reactions reach their peak a few seconds after application of electric pulses, and then gradually diminish.⁷⁶

3. 2. Effects of an Electric Field on the Membrane Proteins

Membrane proteins are molecules associated with (i.e., peripheral) or embedded in (i.e., integral) the lipid

bilayer of the cell membrane, and they are mainly responsible for all of the specific functions of the biological membranes.

Cell membrane electroporation affects membrane proteins to different extents, where the worst case scenario leads to their inactivation by denaturation, due to the local increase in temperature induced by the electric pulses.⁷⁷ For example, it was shown that exposure of cells to electric pulses increased the conductivity of transmembrane Na^+/K^+ -ATPases¹ and decreased transmembrane ionic currents through voltage-gated ion channels.⁷⁸ Gating potentials of voltage-gated ion channels are in the range of 50 mV. Therefore, when electric pulses are applied, these channels will open and can experience very large ion currents. This can also inflict irreversible damage to the channel proteins as a result of the local Joule heating or chemical modifications.⁷⁹ The recovery of damaged membrane proteins is much slower than their opening and closing. While channel closing occurs in microseconds, their opening can take even tens of minutes.⁷⁹ The consequences for the cell can therefore be serious, and even fatal.

3. 3. Effects of an Electric Field on the Cytoskeleton

The cytoskeleton is a cytoplasmic protein structure that is attached under the cell plasma membrane. As it is attached to the plasma membrane, it shapes the cell and has important roles in cell adhesion and migration. The

main components of the cytoskeleton are microfilaments, intermediate filaments, and microtubules.¹³

The application of electric pulses can affect the integrity of the cytoskeleton. Exposure of cells to electric pulses can disrupt the network of microfilaments and microtubules. These effects are voltage-dependent and reversible, as the cytoskeleton can fully recover within hours without significant loss of cell viability.^{1,80} The disruption of microfilaments was shown to even protect the cell from being killed by external electric pulses.⁸¹ Electroporation of vesicles with actin filaments showed that membrane rigidification occurs, which blocks any large deformation of the vesicles, and prevents the formation of large membrane pores.⁸² The mechanism of cytoskeleton disruption includes conformational changes and electromechanical processes, although it remains not entirely clear to date.^{83,84} Atomic force microscopy has revealed a decrease in membrane stiffness, leading to the rippling and destabilization of microfilaments. The main reason for the morphological changes observed was shown to be the impaired attachment of the cytoskeleton to the cell membrane. Electroporation often results in cell swelling due to the induced osmotic imbalance, and the resulting swelling force is an important factor in the dislocation of the cytoskeleton from the membrane.¹

4. Advantages and Disadvantages of Cell Electroporation

Electroporation is an efficient method for the manipulation of cell membrane permeability. It can be applied to all types of cells, and no matter which stage of the cell cycle they are in. Its efficiency depends on the size of the cell, as stronger electric fields are required for induction of pore formation in smaller cells than in larger cells. Moreover, the electrical properties of the tissue also greatly influence the electroporation process, such as its conductivity.⁸⁵ As the transport of materials into and out of electroporated cells is not specific, an ionic imbalance can occur, which can be harmful for the cell. Thus, for each specific application of electroporation, the electric pulse parameters need to be appropriately adjusted to minimize unwanted cell damage, or even cell death.⁵³

The most widely used applications of electroporation in medicine, electrochemotherapy (ECT), electro-transfer of genes (GET), and irreversible electroporation (IRE) for tissue ablation are illustrated in Figure 3.

4.1. Electrochemotherapy

Electrochemotherapy (ECT) is a local treatment that includes chemotherapy followed by tumor-directed elec-

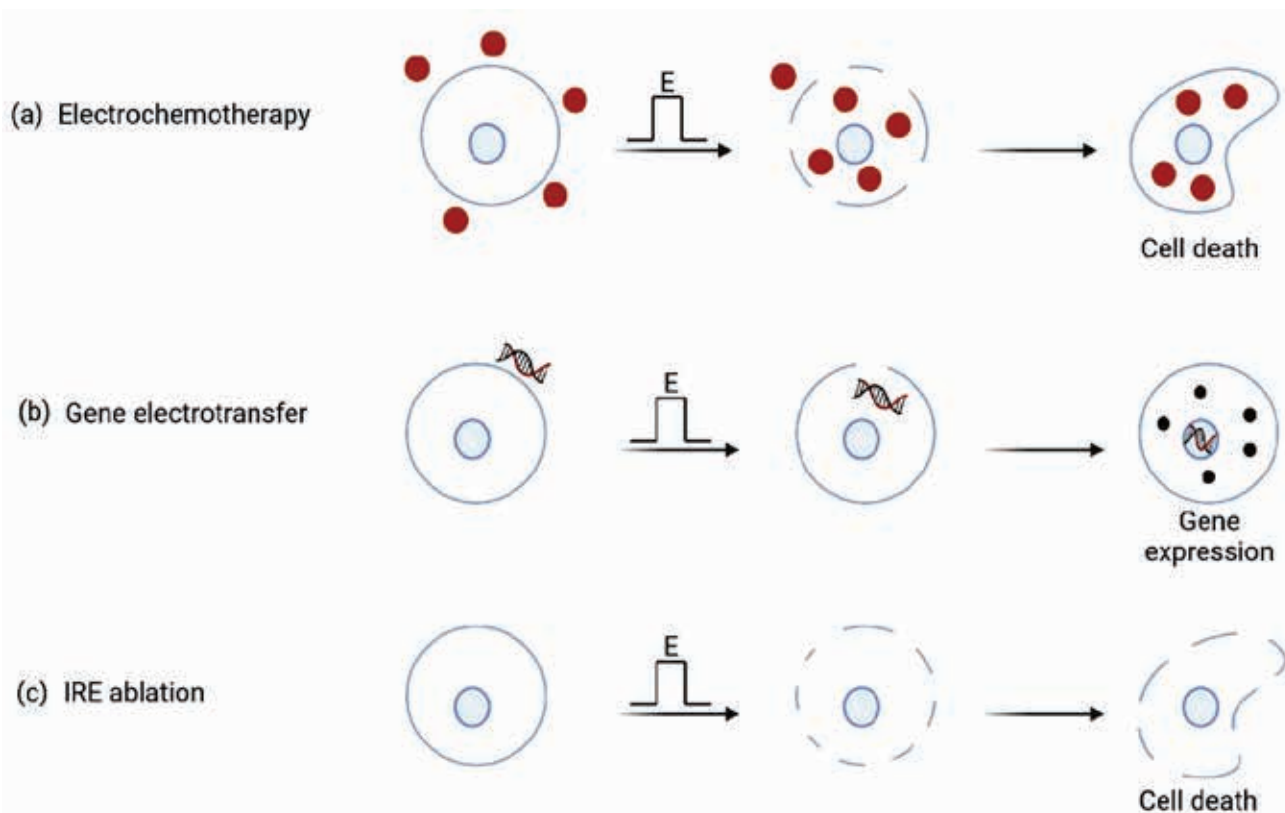


Figure 3. The main applications of electroporation in medicine. (a) Electrochemotherapy uses electroporation to increase the uptake of chemotherapeutic drugs into cells, thus boosting their cytotoxic effects. (b) Gene electrotransfer uses electroporation to transfer DNA or RNA molecules into cells, to induce expression of the desired proteins. (c) Irreversible electroporation (IRE) causes cell death and is used to nonthermally ablate tissue (Figure adapted from reference 86).

tric pulses, to increase the drug delivery into the malignant cells. Electric pulses are applied through metal plate or needle electrodes, to permeabilize the membranes of the cells, and hence to increase the uptake and effectiveness of the drug that was injected prior to the application of the electric pulses.⁸⁷

Electrochemotherapy is simple and easy to perform. It is also a relatively inexpensive treatment. To perform ECT, we need an electric pulse generator (i.e., an electroporator) and suitable electrodes. The treatment can be performed on practically any part of the body. After the treatment, patients do not require special care, nor post-treatment medication. The main advantage of ECT when compared to other techniques is that it combines chemotherapy and the application of electric pulses. The targeted cells die in a more controlled manner, which results in slower shrinkage of the tumor, without development of massive necrosis that represents a major burden for patients and is accompanied by the risk of complications, such as infections.⁸⁸

As well as these advantages, ECT also has some disadvantages. One of these is the pain that patients can experience during the application of the electric pulses as well as muscle contraction.⁸⁵ The factors that can limit the use of ECT include the size of the tumor⁸⁹ and difficult accessibility of a tumor by electrodes. For safety reasons, ECT is currently contraindicated for patients with cardiac pacemakers and patients on anticoagulant therapy.^{3,90}

4. 2. Gene Electrotransfer

Gene electrotransfer (GET) uses high-voltage electric pulses to deliver DNA or RNA molecules into cells. In oncology, this is used to induce anticancer effects in tumor cells.^{4,6} GET can also be used for DNA or RNA vaccination, or for gene therapy, as it improves the expression of pertinent proteins.⁹¹ GET can be used to treat cardiovascular, autoimmune, and infectious diseases. Two specific benefits of GET are that it does not induce unwanted specific immunity, and that it lowers the risk of integration of therapeutic nucleic acids into the host genome, or their environmental spread.⁶ Nowadays GET is among the most promising nonviral methods for gene delivery to cells, due to its safety, efficacy, flexibility, ease of application, and relatively low cost.^{4,92}

The main obstacle against the more widespread use of GET, particularly in human medicine², is that when applied *in vivo*, there can be substantial increases in the local temperature and large changes in the pH close to the electrodes, both of which reduce the efficacy of the therapy.^{4,92}

4. 3. Irreversible Electroporation Ablation

Electroporation, as IRE, is used as a minimally invasive surgical technique for tissue ablation.⁷ With this procedure, it is possible to ablate undesirable tissue in a

controlled and precise manner, without damaging the surrounding critical structures.⁹³

There are different minimally invasive methods for tissue ablation, but IRE has certain advantages over these. IRE is not temperature based, and therefore the target tissue can be destroyed without overheating of the tissue. IRE is easy to apply, the local blood flow does not influence its efficacy, and it does not require the use of supportive drugs. It affects only the membranes of living cells, while the extracellular structures remain intact. The result is less scarring and faster healing of the treated tissue.^{94–96} One of the most promising applications of IRE in medicine is for cardiac ablation after atrial fibrillation.^{97,98} This is a catheter-based ablation, and due to its advantages over the contemporary ablation procedures, it has also been recently transferred to human cardiology.^{99,100}

On the other hand, IRE can damage the entire tissue that is exposed to the electric pulses if the operating parameters are not correctly selected. Therefore, meticulous treatment planning and setting of the correct electroporation parameters are important, to avoid such damage.¹⁰¹

5. The Challenges Ahead

Electroporation of biomembranes has been studied and developed over the past 40 years; nevertheless, there remain some challenges for further improvement of this methodology.

One fundamental challenge that remains to be resolved for biomembrane electroporation is to identify the underlying molecular mechanisms. Only full understanding of the phenomenon at molecular level will allow unraveling its full potential and its reliable control. For example, the contribution of electric pulses to increased cell membrane permeability due to lipid peroxidation and protein modifications are far from being well understood today.

Preclinical and clinical trials have confirmed the great potential for electroporation-based treatments for cancer and gene therapy, as well as in tissue ablation. However, it is evident that there remains room for further technical improvements to increase the precision and specificity of these treatments, one of the possibilities is through the use of nanoparticles for enhanced electroporation efficiency.¹⁰² Furthermore, the reduction or elimination of the serious side effects that sometimes occur is of great importance.^{6,85,103} In this context, the processes that occur directly at the electrodes inserted into the tissue during pulse applications need to be better controlled, such as the electrochemical reactions, bubble formation, and local large changes in pH.

Last, but not least, a major problem for the use of electroporation in medicine that awaits resolution is reduction of the intensity and the extent of muscle contraction during the treatments. This would attenuate or even

eliminate the pain that treated patients experience today, without the need for muscle relaxants.⁸⁷ In this respect, trials that are investigating high-frequency bipolar electroporation pulses appear to be very promising.^{104–107}

Acknowledgments

This work was funded by the Slovenian Research Agency grants P1-0207 (to I.K.), P2-0249 (to D.M. and P.K.) and junior researcher funding grant P2-0249 (to K.B.).

6. References

- Kotnik, T.; Rems, L.; Tarek, M.; Miklavčič, D. Membrane Electroporation and Electroporation: Mechanisms and Models. *Annu. Rev. Biophys.* **2019**, *48* (1), 63–91. DOI:10.1146/annurev-biophys-052118-115451
- Geboers, B.; Scheffer, H. J.; Graybill, P. M.; Ruarus, A. H.; Nieuwenhuizen, S.; Puijk, R. S.; van den Tol, P. M.; Davalos, R. V.; Rubinsky, B.; de Gruijl, T. D.; Miklavčič, D.; Meijerink, M. R. High-Voltage Electrical Pulses in Oncology: Irreversible Electroporation, Electrochemotherapy, Gene Electroporation, Electrofusion, and Electroimmunotherapy. *Radiology* **2020**, *295* (2), 254–272. DOI:10.1148/radiol.2020192190
- Serša, G.; Miklavčič, D.; Čemažar, M.; Rudolf, Z.; Pucihar, G.; Snoj, M. Electrochemotherapy in Treatment of Tumours. *Eur. J. Surg. Oncol. EJSO* **2008**, *34* (2), 232–240. DOI:10.1016/j.ejso.2007.05.016
- Rosazza, C.; Haberk Meglič, S.; Zumbusch, A.; Rols, M.-P.; Miklavčič, D. Gene Electroporation: A Mechanistic Perspective. *Curr. Gene Ther.* **2016**, *16* (2), 98–129. DOI:10.2174/1566523216666160331130040
- Rols, M.-P. Electroporation, a Physical Method for the Delivery of Therapeutic Molecules into Cells. *Biochim. Biophys. Acta BBA - Biomembr.* **2006**, *1758* (3), 423–428. DOI:10.1016/j.bbamem.2006.01.005
- Lambricht, L.; Lopes, A.; Kos, S.; Serša, G.; Prát, V.; Vandermeulen, G. Clinical Potential of Electroporation for Gene Therapy and DNA Vaccine Delivery. *Expert Opin. Drug Deliv.* **2016**, *13* (2), 295–310. DOI:10.1517/17425247.2016.1121990
- Davalos, R. V.; Mir, I. L. M.; Rubinsky, B. Tissue Ablation with Irreversible Electroporation. *Ann. Biomed. Eng.* **2005**, *33* (2), 223–231. DOI:10.1007/s10439-005-8981-8
- van Es, R.; Konings, M. K.; Du Pré, B. C.; Neven, K.; van Wesel, H.; van Driel, V. J. H. M.; Westra, A. H.; Doevendans, P. A. F.; Wittkamp, F. H. M. High-Frequency Irreversible Electroporation for Cardiac Ablation Using an Asymmetrical Waveform. *Biomed. Eng. OnLine* **2019**, *18* (1), 75. DOI:10.1186/s12938-019-0693-7
- McBride, S.; Avazzadeh, S.; Wheatley, A. M.; O'Brien, B.; Coffey, K.; Elahi, A.; O'Halloran, M.; Quinlan, L. R. Ablation Modalities for Therapeutic Intervention in Arrhythmia-Related Cardiovascular Disease: Focus on Electroporation. *J. Clin. Med.* **2021**, *10* (12), 2657. DOI:10.3390/jcm10122657
- Mahnič-Kalamiza, S.; Vorobiev, E.; Miklavčič, D. Electroporation in Food Processing and Biorefinery. *J. Membr. Biol.* **2014**, *247*. DOI:10.1007/s00232-014-9737-x
- Genovese, J.; Kranjc, M.; Serša, I.; Petracchi, M.; Rocculi, P.; Miklavčič, D.; Mahnič-Kalamiza, S. PEF-Treated Plant and Animal Tissues: Insights by Approaching with Different Electroporation Assessment Methods. *Innov. Food Sci. Emerg. Technol.* **2021**, *74*, 102872. DOI:10.1016/j.ifset.2021.102872
- Kim, K.; Lee, W. G. Electroporation for Nanomedicine: A Review. *J. Mater. Chem. B* **2017**, *5* (15), 2726–2738. DOI:10.1039/C7TB00038C
- Alberts, B.; Johnson, A.; Lewis, J.; Raff, M.; Roberts, K.; Walter, P. The Lipid Bilayer. *Mol. Biol. Cell 4th Ed.* **2002**.
- Lodish, H.; Berk, A.; Zipursky, S. L.; Matsudaira, P.; Baltimore, D.; Darnell, J. Biomembranes: Structural Organization and Basic Functions. *Mol. Cell Biol. 4th Ed.* **2000**.
- Cooper, G. M. Structure of the Plasma Membrane. *Cell Mol. Approach 2nd Ed.* **2000**.
- Gov, N. S. Guided by Curvature: Shaping Cells by Coupling Curved Membrane Proteins and Cytoskeletal Forces. *Philos. Trans. R. Soc. Lond. B. Biol. Sci.* **2018**, *373* (1747), 20170115. DOI:10.1098/rstb.2017.0115
- Alimohamadi, H.; Smith, A. S.; Nowak, R. B.; Fowler, V. M.; Rangamani, P. Non-Uniform Distribution of Myosin-Mediated Forces Governs Red Blood Cell Membrane Curvature through Tension Modulation. *PLOS Comput. Biol.* **2020**, *16* (5), e1007890. DOI:10.1371/journal.pcbi.1007890
- Mahapatra, A.; Uysale, C.; Rangamani, P. The Mechanics and Thermodynamics of Tubule Formation in Biological Membranes. *J. Membr. Biol.* **2021**, *254* (3), 273–291. DOI:10.1007/s00232-020-00164-9
- Mesarec, L.; Drab, M.; Penič, S.; Kralj-Iglič, V.; Iglič, A. On the Role of Curved Membrane Nanodomains and Passive and Active Skeleton Forces in the Determination of Cell Shape and Membrane Budding. *Int. J. Mol. Sci.* **2021**, *22* (5), 2348. DOI:10.3390/ijms22052348
- Berg, J. M.; Tymoczko, J. L.; Stryer, L. There Are Three Common Types of Membrane Lipids. *Biochem. 5th Ed.* **2002**.
- Marquardt, D.; Heberle, F. A.; Nickels, J. D.; Pabst, G.; Katsaras, J. On Scattered Waves and Lipid Domains: Detecting Membrane Rafts with X-Rays and Neutrons. *Soft Matter* **2015**, *11* (47), 9055–9072. DOI:10.1039/C5SM01807B
- Przybyło, M.; Drabik, D.; Dosekocz, J.; Iglič, A.; Langner, M. The Effect of the Osmotically Active Compound Concentration Difference on the Passive Water and Proton Fluxes across a Lipid Bilayer. *Int. J. Mol. Sci.* **2021**, *22* (20), 11099. DOI:10.3390/ijms222011099
- Hanneschlaeger, C.; Horner, A.; Pohl, P. Intrinsic Membrane Permeability to Small Molecules. *Chem. Rev.* **2019**, *119* (9), 5922–5953. DOI:10.1021/acs.chemrev.8b00560
- Martínez-Balbuena, L.; Hernández-Zapata, E.; Santamaría-Holek, I. Onsager's Irreversible Thermodynamics of the Dynamics of Transient Pores in Spherical Lipid Vesicles. *Eur. Biophys. J.* **2015**, *44* (6), 473–481.

- DOI:10.1007/s00249-015-1051-8
25. Yang, N. J.; Hinner, M. J. Getting Across the Cell Membrane: An Overview for Small Molecules, Peptides, and Proteins. *Methods Mol. Biol. Clifton NJ* **2015**, 1266, 29–53. DOI:10.1007/978-1-4939-2272-7_3
 26. Cooper, G. M. Cell Membranes. *Cell Mol. Approach 2nd Ed.* **2000**.
 27. Cooper, G. M. Transport of Small Molecules. *Cell Mol. Approach 2nd Ed.* **2000**.
 28. Martínez, J. M.; Delso, C.; Álvarez, I.; Raso, J. Pulsed Electric Field-Assisted Extraction of Valuable Compounds from Microorganisms. *Compr. Rev. Food Sci. Food Saf.* **2020**, 19 (2), 530–552. DOI:10.1111/1541-4337.12512
 29. Wang, M.; Zhang, Y.; Cai, C.; Tu, J.; Guo, X.; Zhang, D. Sonoporation-Induced Cell Membrane Permeabilization and Cytoskeleton Disassembly at Varied Acoustic and Microbubble-Cell Parameters. *Sci. Rep.* **2018**, 8 (1), 3885. DOI:10.1038/s41598-018-22056-8
 30. He, C.; Gu, Q.; Zeng, H.; Zhang, H.; Huang, M.; Yang, X.; Xing, J.; Chen, J. Microbubble-Enhanced Cell Membrane Permeability in High Gravity Field. *Cell. Mol. Bioeng.* **2013**, 6 (3), 266–278. DOI:10.1007/s12195-013-0279-6
 31. Barak, M.; Katz, Y. Microbubbles: Pathophysiology and Clinical Implications. *Chest* **2005**, 128 (4), 2918–2932. DOI:10.1378/chest.128.4.2918
 32. Xu, W.; Ling, P.; Zhang, T. Polymeric Micelles, a Promising Drug Delivery System to Enhance Bioavailability of Poorly Water-Soluble Drugs. *J. Drug Deliv.* **2013**, 2013, 340315. DOI:10.1155/2013/340315
 33. Guimarães, D.; Cavaco-Paulo, A.; Nogueira, E. Design of Liposomes as Drug Delivery System for Therapeutic Applications. *Int. J. Pharm.* **2021**, 601, 120571. DOI:10.1016/j.ijpharm.2021.120571
 34. Cevher, E.; Sezer, A. D.; Çağlar, E. Ş. *Gene Delivery Systems: Recent Progress in Viral and Non-Viral Therapy*; IntechOpen, 2012. DOI:10.5772/53392
 35. Anderluh, G.; Sepčić, K.; Turk, T.; Maček, P. Cytolytic Proteins from Cnidarians - an Overview. *Acta Chim. Slov.* **2011**, 58 (4), 724–729.
 36. Frenkel, V. Ultrasound Mediated Delivery of Drugs and Genes to Solid Tumors. *Adv. Drug Deliv. Rev.* **2008**, 60 (10), 1193–1208. DOI:10.1016/j.addr.2008.03.007
 37. Lawrie, A.; Brisken, A. F.; Francis, S. E.; Tayler, D. I.; Chamberlain, J.; Crossman, D. C.; Cumberland, D. C.; Newman, C. M. Ultrasound Enhances Reporter Gene Expression After Transfection of Vascular Cells In Vitro. *Circulation* **1999**, 99 (20), 2617–2620. DOI:10.1161/01.CIR.99.20.2617
 38. Liang, H.-D.; Tang, J.; Halliwell, M. Sonoporation, Drug Delivery, and Gene Therapy. *Proc. Inst. Mech. Eng. [H]* **2010**, 224 (2), 343–361. DOI:10.1243/09544119JEIM565
 39. Cukjati, D.; Batuskaite, D.; André, F.; Miklavčič, D.; Mir, L. M. Real Time Electroporation Control for Accurate and Safe in Vivo Non-Viral Gene Therapy. *Bioelectrochemistry* **2007**, 70 (2), 501–507. DOI:10.1016/j.bioelechem.2006.11.001
 40. Kotnik, T.; Kramar, P.; Pucihar, G.; Miklavčič, D.; Tarek, M. Cell Membrane Electroporation- Part 1: The Phenomenon. *IEEE Electr. Insul. Mag.* **2012**, 28 (5), 14–23. DOI:10.1109/MEI.2012.6268438
 41. Kotnik, T.; Frey, W.; Sack, M.; Haberl Meglič, S.; Peterka, M.; Miklavčič, D. Electroporation-Based Applications in Biotechnology. *Trends Biotechnol.* **2015**, 33 (8), 480–488. DOI:10.1016/j.tibtech.2015.06.002
 42. Muramatsu, T.; Nakamura, A.; Park, H. M. In Vivo Electroporation: A Powerful and Convenient Means of Nonviral Gene Transfer to Tissues of Living Animals (Review). *Int. J. Mol. Med.* **1998**, 1 (1), 55–117. DOI:10.3892/ijmm.1.1.55
 43. Neumann, E.; Schaefer-Ridder, M.; Wang, Y.; Hofschneider, P. H. Gene Transfer into Mouse Lyoma Cells by Electroporation in High Electric Fields. *EMBO J.* **1982**, 1 (7), 841–845. DOI:10.1002/j.1460-2075.1982.tb01257.x
 44. Franklin, J. C.; Cafiso, D. S.; Flewelling, R. F.; Hubbell, W. L. Probes of Membrane Electrostatics: Synthesis and Voltage-Dependent Partitioning of Negative Hydrophobic Ion Spin Labels in Lipid Vesicles. *Biophys. J.* **1993**, 64 (3), 642–653. DOI:10.1016/S0006-3495(93)81423-1
 45. Bohinc, K.; Kralj-Iglič, V.; Iglič, A. Thickness of Electrical Double Layer. Effect of Ion Size. *Electrochimica Acta* **2001**, 46 (19), 3033–3040. DOI:10.1016/S0013-4686(01)00525-4
 46. Gongadze, E.; Iglič, A. Relative Permittivity in Stern and Diffuse Layers. *Acta Chim. Slov.* **2014**, 61 (2), 241–245.
 47. Lebar, A. M.; Velikonja, A.; Kramar, P.; Iglič, A. Internal Configuration and Electric Potential in Planar Negatively Charged Lipid Head Group Region in Contact with Ionic Solution. *Bioelectrochemistry Amst. Neth.* **2016**, 111, 49–56. DOI:10.1016/j.bioelechem.2016.04.006
 48. Heinrich, R.; Gaestel, M.; Glaser, R. The Electric Potential Profile across the Erythrocyte Membrane. *J. Theor. Biol.* **1982**, 96 (2), 211–231. DOI:10.1016/0022-5193(82)90222-3
 49. Iglič, A.; Gongadze, E.; Kralj-Iglič, V. Differential Capacitance of Electric Double Layer - Influence of Asymmetric Size of Ions, Thickness of Stern Layer and Orientational Ordering of Water Dipoles. *Acta Chim. Slov.* **2019**, 66 (3), 534–541. DOI:10.17344/acsi.2019.5495
 50. Kotnik, T.; Pucihar, G.; Miklavčič, D. The Cell in the Electric Field; 2011; pp 19–29. DOI:10.1007/978-1-4419-8363-3_3
 51. Batista Napotnik, T.; Polajžer, T.; Miklavčič, D. Cell Death Due to Electroporation – A Review. *Bioelectrochemistry* **2021**, 141, 107871. DOI:10.1016/j.bioelechem.2021.107871
 52. Yarmush, M. L.; Golberg, A.; Serša, G.; Kotnik, T.; Miklavčič, D. Electroporation-Based Technologies for Medicine: Principles, Applications, and Challenges. *Annu. Rev. Biomed. Eng.* **2014**, 16 (1), 295–320. DOI:10.1146/annurev-bioeng-071813-104622
 53. Polajžer, T.; Jarm, T.; Miklavčič, D. Analysis of Damage-Associated Molecular Pattern Molecules Due to Electroporation of Cells in Vitro. *Radiol. Oncol.* **2020**, 54 (3), 317–328. DOI:10.2478/raon-2020-0047
 54. Rems, L. Lipid Pores: Molecular and Continuum Models. In *Handbook of Electroporation*; Springer International Publishing: Cham, **2016**; pp 1–21. DOI:10.1007/978-3-319-26779-1_76-1
 55. Tarek, M. Membrane Electroporation: A Molecular Dynam-

- ics Simulation. *Biophys. J.* **2005**, *88* (6), 4045–4053. DOI:10.1529/biophysj.104.050617
56. Dehez, F.; Delemotte, L.; Kramar, P.; Miklavčič, D.; Tarek, M. Evidence of Conducting Hydrophobic Nanopores Across Membranes in Response to an Electric Field. *J. Phys. Chem. C* **2014**, *118* (13), 6752–6757. DOI:10.1021/jp4114865
57. Karatekin, E.; Sandre, O.; Guitouni, H.; Borghi, N.; Puech, P.-H.; Brochard-Wyart, F. Cascades of Transient Pores in Giant Vesicles: Line Tension and Transport. *Biophys. J.* **2003**, *84* (3), 1734–1749. DOI:10.1016/S0006-3495(03)74981-9
58. Fošnarič, M.; Kralj-Iglič, V.; Bohinc, K.; Iglič, A.; May, S. Stabilization of Pores in Lipid Bilayers by Anisotropic Inclusions. *J. Phys. Chem. B* **2003**, *107* (45), 12519–12526. DOI:10.1021/jp035035a
59. Kandušer, M.; Fošnarič, M.; Šentjurc, M.; Kralj-Iglič, V.; Hägerstrand, H.; Iglič, A.; Miklavčič, D. Effect of Surfactant Polyoxyethylene Glycol (C12E8) on Electroporation of Cell Line DC3F. *Colloids Surf. -Physicochem. Eng. Asp. - A* **2003**, *214*. DOI:10.1016/S0927-7757(02)00410-7
60. Bennett, W. F. D.; Sapay, N.; Tieleman, D. P. Atomistic Simulations of Pore Formation and Closure in Lipid Bilayers. *Biophys. J.* **2014**, *106* (1), 210–219. DOI:10.1016/j.bpj.2013.11.4486
61. Sandre, O.; Moreaux, L.; Brochard-Wyart, F. Dynamics of Transient Pores in Stretched Vesicles. *Proc. Natl. Acad. Sci.* **1999**, *96* (19), 10591–10596. DOI:10.1073/pnas.96.19.10591
62. Brochard-Wyart, F.; de Gennes, P. G.; Sandre, O. Transient Pores in Stretched Vesicles: Role of Leak-Out. In *Simple Views on Condensed Matter*; Series in Modern Condensed Matter Physics; WORLD SCIENTIFIC, 2003; Vol. Volume 12, pp 327–346. DOI:10.1142/9789812564849_0038
63. Lewis, T. J. A Model for Bilayer Membrane Electroporation Based on Resultant Electromechanical Stress. *IEEE Trans. Dielectr. Electr. Insul.* **2003**, *10* (5), 769–777. DOI:10.1109/TDEI.2003.1237326
64. Rems, L.; Viano, M.; Kasimova, M. A.; Miklavčič, D.; Tarek, M. The Contribution of Lipid Peroxidation to Membrane Permeability in Electroporation: A Molecular Dynamics Study. *Bioelectrochemistry* **2019**, *125*, 46–57. DOI:10.1016/j.bioelechem.2018.07.018
65. Wiczew, D.; Szulc, N.; Tarek, M. Molecular Dynamics Simulations of the Effects of Lipid Oxidation on the Permeability of Cell Membranes. *Bioelectrochemistry* **2021**, *141*, 107869. DOI:10.1016/j.bioelechem.2021.107869
66. Frankel, E. N. Free Radical Oxidation. In *Lipid Oxidation*; Elsevier, **2012**; pp 15–24. DOI:10.1533/9780857097927.15
67. Girotti, A. W. Mechanisms of Lipid Peroxidation. *J. Free Radic. Biol. Med.* **1985**, *1* (2), 87–95. DOI:10.1016/0748-5514(85)90011-X
68. Yusupov, M.; Wende, K.; Kupsch, S.; Neyts, E. C.; Reuter, S.; Bogaerts, A. Effect of Head Group and Lipid Tail Oxidation in the Cell Membrane Revealed through Integrated Simulations and Experiments. *Sci. Rep.* **2017**, *7* (1), 5761. DOI:10.1038/s41598-017-06412-8
69. Parra-Ortiz, E.; Browning, K. L.; Damgaard, L. S. E.; Nordström, R.; Micciulla, S.; Bucciarelli, S.; Malmsten, M. Effects of Oxidation on the Physicochemical Properties of Polyunsaturated Lipid Membranes. *J. Colloid Interface Sci.* **2019**, *538*, 404–419. DOI:10.1016/j.jcis.2018.12.007
70. Van der Paal, J.; Neyts, E. C.; Verlaack, C. C. W.; Bogaerts, A. Effect of Lipid Peroxidation on Membrane Permeability of Cancer and Normal Cells Subjected to Oxidative Stress. *Chem. Sci.* **2016**, *7* (1), 489–498. DOI:10.1039/C5SC02311D
71. Neto, A. J. P.; Cordeiro, R. M. Molecular Simulations of the Effects of Phospholipid and Cholesterol Peroxidation on Lipid Membrane Properties. *Biochim. Biophys. Acta BBA - Biomembr.* **2016**, *1858* (9), 2191–2198. DOI:10.1016/j.bbamem.2016.06.018
72. Chang, D. C.; Reese, T. S. Changes in Membrane Structure Induced by Electroporation as Revealed by Rapid-Freezing Electron Microscopy. *Biophys. J.* **1990**, *58* (1), 1–12. DOI:10.1016/S0006-3495(90)82348-1
73. Gabriel, B.; Teissie, J. Generation of Reactive-Oxygen Species Induced by Electroporation of Chinese Hamster Ovary Cells and Their Consequence on Cell Viability. *Eur. J. Biochem.* **1994**, *223* (1), 25–33. DOI:10.1111/j.1432-1033.1994.tb18962.x
74. Breton, M.; Delemotte, L.; Silve, A.; Mir, L. M.; Tarek, M. Transport of siRNA through Lipid Membranes Driven by Nanosecond Electric Pulses: An Experimental and Computational Study. *J. Am. Chem. Soc.* **2012**, *134* (34), 13938–13941. DOI:10.1021/ja3052365
75. Benov, L. C.; Antonov, P. A.; Ribarov, S. R. Oxidative Damage of the Membrane Lipids after Electroporation. *Gen. Physiol. Biophys.* **1994**, *13* (2), 85–97.
76. Teissie, J.; Eynard, N.; Gabriel, B.; Rols, M. P. Electroporation of Cell Membranes. *Adv. Drug Deliv. Rev.* **1999**, *35* (1), 3–19. DOI:10.1016/S0169-409X(98)00060-X
77. Tsong, T. Y. On Electroporation of Cell Membranes and Some Related Phenomena. *Bioelectrochem. Bioenerg.* **1990**, *24* (3), 271–295. DOI:10.1016/0302-4598(90)80028-H
78. Rems, L.; Kasimova, M. A.; Testa, I.; Delemotte, L. Pulsed Electric Fields Can Create Pores in the Voltage Sensors of Voltage-Gated Ion Channels. *Biophys. J.* **2020**, *119* (1), 190–205. DOI:10.1016/j.bpj.2020.05.030
79. Tsong, T. Y. Electroporation of Cell Membranes. *Biophys. J.* **1991**, *60* (2), 297–306. DOI:10.1016/S0006-3495(91)82054-9
80. Kanthou, C.; Kranjc, S.; Serša, G.; Tozer, G.; Zupanič, A.; Čemažar, M. The Endothelial Cytoskeleton as a Target of Electroporation-Based Therapies. *Mol. Cancer Ther.* **2006**, *5* (12), 3145–3152. DOI:10.1158/1535-7163.MCT-06-0410
81. Xiao, D.; Tang, L.; Zeng, C.; Wang, J.; Luo, X.; Yao, C.; Sun, C. Effect of Actin Cytoskeleton Disruption on Electric Pulse-Induced Apoptosis and Electroporation in Tumour Cells. *Cell Biol. Int.* **2011**, *35* (2), 99–104. DOI:10.1042/CBI20100464
82. Perrier, D. L.; Vahid, A.; Kathavi, V.; Stam, L.; Rems, L.; Mulla, Y.; Muralidharan, A.; Koenderink, G. H.; Kreutzer, M. T.; Boukany, P. E. Response of an Actin Network in Vesicles under Electric Pulses. *Sci. Rep.* **2019**, *9* (1), 8151. DOI:10.1038/s41598-019-44613-5
83. Graybill, P. M.; Davalos, R. V. Cytoskeletal Disruption after

- Electroporation and Its Significance to Pulsed Electric Field Therapies. *Cancers* **2020**, *12* (5), 1132.
DOI:10.3390/cancers12051132
84. Kim, H. B.; Lee, S.; Chung, J. H.; Kim, S. N.; Sung, C. K.; Baik, K. Y. Effects of Actin Cytoskeleton Disruption on Electroporation In Vitro. *Appl. Biochem. Biotechnol.* **2020**, *191* (4), 1545–1561. DOI:10.1007/s12010-020-03271-4
 85. Bolhassani, A.; Khavari, A.; Orafa, Z. Electroporation – Advantages and Drawbacks for Delivery of Drug, Gene and Vaccine; **2014**. DOI:10.5772/58376
 86. Calvet, C.; Mir, L. The Promising Alliance of Anti-Cancer Electrochemotherapy with Immunotherapy. *Cancer Metastasis Rev.* **2016**, *35*. DOI:10.1007/s10555-016-9615-3
 87. Miklavčič, D.; Mali, B.; Kos, B.; Heller, R.; Serša, G. Electrochemotherapy: From the Drawing Board into Medical Practice. *Biomed. Eng. OnLine* **2014**, *13* (1), 29. DOI:10.1186/1475-925X-13-29
 88. Čemažar, M.; Serša, G. Recent Advances in Electrochemotherapy. *Bioelectricity* **2019**, *1* (4), 204–213. DOI:10.1089/bioe.2019.0028
 89. Serša, G.; Čemažar, M.; Rudolf, Z. Electrochemotherapy: Advantages and Drawbacks in Treatment of Cancer Patients. *Cancer Therapy* **2003**, Vol 1, 133–142.
 90. Jarm, T.; Krmac, T.; Magjarević, R.; Kos, B.; Cindrič, H.; Miklavčič, D. Investigation of Safety for Electrochemotherapy and Irreversible Electroporation Ablation Therapies in Patients with Cardiac Pacemakers. *Biomed. Eng. OnLine* **2020**, *19* (1), 85. DOI:10.1186/s12938-020-00827-7
 91. Broderick, K. E.; Humeau, L. M. Enhanced Delivery of DNA or RNA Vaccines by Electroporation. In *RNA Vaccines*; Kramps, T., Elbers, K., Eds.; Methods in Molecular Biology; **2017**; Vol. 1499, pp 193–200. DOI:10.1007/978-1-4939-6481-9_12
 92. Potočnik, T.; Miklavčič, D.; Maček Lebar, A. Gene Transfer by Electroporation with High Frequency Bipolar Pulses in Vitro. *Bioelectrochemistry* **2021**, *140*, 107803. DOI:10.1016/j.bioelechem.2021.107803
 93. Rubinsky, B. Irreversible Electroporation in Medicine. *Technol. Cancer Res. Treat.* **2007**, *6* (4), 255–259. DOI:10.1177/153303460700600401
 94. Cindrič, H.; Kos, B.; Miklavčič, D. Ireverzibilna Elektroporacija Kot Metoda Ablacije Mehkih Tkiv: Pregled in Izzivi Pri Uporabi v Kliničnem Okolju. *Slov. Med. J.* **2021**, *90* (1–2), 38–53. DOI:10.6016/ZdravVestn.2954
 95. Howard, B.; Haines, D. E.; Verma, A.; Packer, D.; Kirchhof, N.; Barka, N.; Onal, B.; Fraasch, S.; Miklavčič, D.; Stewart, M. T. Reduction in Pulmonary Vein Stenosis and Collateral Damage With Pulsed Field Ablation Compared With Radiofrequency Ablation in a Canine Model. *Circ. Arrhythm. Electrophysiol.* **2020**, *13* (9). DOI:10.1161/CIRCEP.120.008337
 96. Bradley, C. J.; Haines, D. E. Pulsed Field Ablation for Pulmonary Vein Isolation in the Treatment of Atrial Fibrillation. *J. Cardiovasc. Electrophysiol.* **2020**, *31* (8), 2136–2147. DOI:10.1111/jce.14414
 97. Sugrue, A.; Vaidya, V.; Witt, C.; DeSimone, C. V.; Yasin, O.; Maor, E.; Killu, A. M.; Kapa, S.; McLeod, C. J.; Miklavčič, D.; Asirvatham, S. J. Irreversible Electroporation for Catheter-Based Cardiac Ablation: A Systematic Review of the Pre-clinical Experience. *J. Interv. Card. Electrophysiol.* **2019**, *55* (3), 251–265. DOI:10.1007/s10840-019-00574-3
 98. Štublar, J.; Žižek, D.; Jan, M.; Jarm, T.; Miklavčič, D. Zdravljenje atrijske fibrilacije s katetsko ablacijo. *Slov. Med. J.* **2021**, *1–10*. DOI:10.6016/ZdravVestn.3078
 99. Reddy, V. Y.; Koruth, J.; Jais, P.; Petru, J.; Timko, F.; Skalsky, I.; Hebel, R.; Labrousse, L.; Barandon, L.; Kralovec, S.; Funosako, M.; Mannuva, B. B.; Sediva, L.; Neuzil, P. Ablation of Atrial Fibrillation With Pulsed Electric Fields: An Ultra-Rapid, Tissue-Selective Modality for Cardiac Ablation. *JACC Clin. Electrophysiol.* **2018**, *4* (8), 987–995. DOI:10.1016/j.jacep.2018.04.005
 100. Loh, P.; van Es, R.; Groen, M. H. A.; Neven, K.; Kassenberg, W.; Wittkamp, F. H. M.; Doevendans, P. A. Pulmonary Vein Isolation With Single Pulse Irreversible Electroporation. *Circ. Arrhythm. Electrophysiol.* **2020**, *13* (10), e008192. DOI:10.1161/CIRCEP.119.008192
 101. Silk, M.; Tahour, D.; Srimathveeravalli, G.; Solomon, S. B.; Thornton, R. H. The State of Irreversible Electroporation in Interventional Oncology. *Semin. Interv. Radiol.* **2014**, *31* (02), 111–117. DOI:10.1055/s-0034-1373785
 102. Zu, Y.; Huang, S.; Liao, W.-C.; Lu, Y.; Wang, S. Gold Nanoparticles Enhanced Electroporation for Mammalian Cell Transfection. *J. Biomed. Nanotechnol.* **2014**, *10*, 982–992. DOI:10.1166/jbn.2014.1797
 103. Campana, L. G.; Edhemovic, I.; Soden, D.; Perrone, A. M.; Scarpa, M.; Campanacci, L.; Cemazar, M.; Valpione, S.; Miklavčič, D.; Mocellin, S.; Sieni, E.; Serša, G. Electrochemotherapy – Emerging Applications Technical Advances, New Indications, Combined Approaches, and Multi-Institutional Collaboration. *Eur. J. Surg. Oncol.* **2019**, *45* (2), 92–102. DOI:10.1016/j.ejso.2018.11.023
 104. Mahnič-Kalamiza, S.; Miklavčič, D. Scratching the Electrode Surface: Insights into a High-Voltage Pulsed-Field Application from in Vitro & in Silico Studies in Indifferent Fluid. *Electrochimica Acta* **2020**, *363*, 137187. DOI:10.1016/j.electacta.2020.137187
 105. Sweeney, D.; Reberšek, M.; Dermol-Černe, J.; Rems, L.; Miklavčič, D.; Davalos, R. Quantification of Cell Membrane Permeability Induced by Monopolar and High Frequency Bipolar Bursts of Electrical Pulses. *Biochim. Biophys. Acta BBA - Biomembr.* **2016**, *1858*. DOI:10.1016/j.bbamem.2016.06.024
 106. Scuderi, M.; Reberšek, M.; Miklavčič, D.; Dermol-Černe, J. The Use of High-Frequency Short Bipolar Pulses in Cisplatin Electrochemotherapy in Vitro. *Radiol. Oncol.* **2019**, *53* (2), 194–205. DOI:10.2478/raon-2019-0025
 107. Dong, S.; Wang, H.; Zhao, Y.; Sun, Y.; Yao, C. First Human Trial of High-Frequency Irreversible Electroporation Therapy for Prostate Cancer. *Technol. Cancer Res. Treat.* **2018**, *17*, 1533033818789692. DOI:10.1177/1533033818789692

Povzetek

Elektroporacija je metoda, s katero povečamo prepustnost celične membrane z uporabo visokonapetostnih električnih pulzov. Metodo uporabljamo na različnih področjih: v medicini, biotehnologiji in v živilski industriji. Visokonapetostni električni pulzi izzovejo nastanek hidrofilnih por v lipidnem dvosloju celične membrane, ki omogočijo prehajanje molekul, ki sicer membrane ne prehajajo. V članku podajamo pregled osnovnih principov electroporacije ter kritično spregovorimo o prednostih in slabostih te metode. Razpravljamo o učinkih electroporacije na ključne komponente bioloških membran, kot tudi o glavnih uporabah te metode v medicini, o elektrokemoterapiji, vnosu genov v celice in odstranjevanju tkiv. V zaključku predstavimo še najbolj relevantne izzive tega obetavnega področja raziskav.



Except when otherwise noted, articles in this journal are published under the terms and conditions of the Creative Commons Attribution 4.0 International License

Scientific paper

Identification of Phytochemicals from the Water Extract of *Eurycoma longifolia* Roots using Solid-Liquid and Liquid-Liquid Extraction Based Fractionation Techniques

Lee Suan Chua,^{1,2,*} Abirame Segaran^{1,2} and Hoi Jin Wong³¹ Institute of Bioproduct Development, Universiti Teknologi Malaysia, 81310 UTM Skudai, Johor Bahru, Johor, Malaysia.² Department of Bioprocess and Polymer Engineering, School of Chemical and Energy Engineering, Faculty of Engineering, Universiti Teknologi Malaysia, 81310 UTM Skudai, Johor Bahru, Johor, Malaysia.³ Biotropics Malaysia Berhad, Lot 21, Jalan U1/19, Section U1, Hicom Glenmarie Industrial Park, 40150 Shah Alam, Selangor.* Corresponding author: E-mail: lschua@ibd.utm.my; chualeesuan@utm.my
Tel.: +6019-7214378, fax: +607-5569706

Received: 05-29-2020

Abstract

Phytochemicals in the water extract of *Eurycoma longifolia* roots were identified using both solid-liquid and liquid-liquid extraction based fractionation techniques. A reversed phase C18 solid phase extraction (SPE) was used as solid-liquid extraction, whereas solvent partition was applied as liquid-liquid extraction. Total saponin was increased after fractionation. A few known quassinoids; eurycomanone, 13 α (21)-epoxyeurycomanone, pasakbumin D, 13 β ,18-dihydroeurycomanol and 13 β ,21-dihydroxyeurycomanol were identified from the 40% and 60% methanol fractions of SPE. Solvent partition extract using ethyl acetate was found to have the highest saponin content compared to butanol and chloroform fractions. Subsequent acetone precipitation of the organic fractions recovered a formylated hexose trimer and other saccharide-containing compounds. Ethyl acetate effectively recovered saponins from *E. longifolia* water extract using liquid-liquid extraction followed by acetone precipitation.

Keywords: Eurycomanone; *Eurycoma longifolia*; quassinoids; solid phase extraction; solvent partition; saponins

1. Introduction

Natural products are very complex in chemical composition. A wide range of phytochemicals with diverse properties tends to complicate the study of profiling. However, the demand of phytochemical profiling is getting increasingly necessary for plant authentication, identification and standardization. This is because the presence of phytochemicals will influence the quality of herbs, and subsequently affect the efficacy and safety of herbal products. Phytochemical profiling is an unbiased and comprehensive technique for quality control and standardization of herbal materials. Different high throughput and sensitivity techniques have been applied for phytochemical profiling. This includes LC-MS/MS,¹ GC-MS,² FTIR and 2D-IR,³ NMR,⁴ HPTLC⁵ and so on with minimal sample preparation and treatment requirements.

Eurycoma longifolia Jack (Simaroubaceae) which is locally known as Tongkat Ali has been popularly called as Malaysian Ginseng. The roots of the herb are commonly prepared as ethnomedicine by indigenous people in the form of decoction to strengthen stamina and treat many diseases such as sexual dysfunction, malaria, cancer and androgen deficient osteoporosis.^{6–8} The application of the herbal decoction is still practiced till to date. Recent scientific findings have revealed that quassinoids are the major phytochemicals of *E. longifolia*. Quassinoids are the degraded triterpene lactones consisting of C-18, C-19, C-20, C-22, and C-25 types of compounds.⁹ Their derivatives usually present in the form of methylated, methoxylated, oxygenated, epoxyated and glycosylated quassinoids. In particular, triterpenoidal or steroidal saponins are abundant in the plant extract. Zaini et al.¹⁰ and Mutschlechner et al.¹¹ developed and validated liquid chromatographic

methods to identify quassinoids. In addition to quassinoids, there were also phenolics and alkaloids detected from the plant roots.^{12,13} Although total saponin has been estimated to be > 40% in the plant extract according to the Malaysian Standard, MS 2409:2011,¹⁴ the identification of individual saponins is relatively limited in literature. This could be due to the complexity of the chemical structure of saponins and the limitations of analytical instrumentation.

In the present study, fractionation technique was introduced in order to minimize the complexity of compounds in *E. longifolia* water extract. Both fractionation techniques; solid-liquid and liquid-liquid extractions were applied to separate the complex phytochemicals into few sub-clusters according to the polarity of solvents. Solid phase extraction (SPE) was applied as the solid-liquid extraction based fractionation technique using C18 reversed phase cartridge as absorbent. While, solvent partition was chosen as liquid-liquid extraction based fractionation technique. Three organic solvents; ethyl acetate, butanol and chloroform were chosen to partition phytochemicals. Previous studies reported that those solvents were suitable to partition saponins from ethanolic plant extracts, but were yet to be applied in SPE based fractionation.¹⁵ It is also known that saponins possess a wide range of polarity and solubility depending on the structural diversity of aglycone and sugar moieties. Often, saponins are reported to be abundant in plant roots rather than plant leaves and flowers.^{15,16} Therefore, it is also important to investigate phytochemicals in the water extract of *E. longifolia* roots since water extract is widely consumed in the form of decoction with ethnopharmacological importance.

2. Experimental

2.1. Plant Material and Chemicals

Physta[®] (registration number, 2011000601) which is the proprietary standardized extract powder of *Eurycoma longifolia* roots was provided by Biotropics Malaysia Berhad (Shah Alam, Selangor, Malaysia). The plant extract was prepared at the stipulated temperature and pressure in water. Analytical grade of ethanol, ethyl acetate, chloroform, butanol, acetone and sulfuric acid (98%) were purchased from Merck (Darmstadt, Germany). The LC grade of acetonitrile was sourced from Fisher Scientific (Chino, California, USA). Standard chemicals of vanillin ($\geq 97\%$), escin ($\geq 95\%$) and oleanolic acid ($\geq 97\%$) were obtained from Sigma-Aldrich (St. Louis, MO, USA). C-18ec solid phase extraction (SPE) cartridges (6 mL, 500 mg) were purchased from Macherey-Nagel (Duren, Germany).

2.2. Solid-Liquid Extraction using C18ec SPE Cartridge

Solid phase extraction was carried out to fractionate Physta into individual fractions using C18ec cartridges.

The mobile phase was methanol at different concentrations ranged from 0-100%v/v. The cartridges were activated using 100% methanol and followed by 100% water before use. Physta (25 mg) was reconstituted in water (0.5 mL) and loaded onto the cartridge. Elution was carried out and 3 mL was collected for each fraction.

2.3. Solvent Partition by Liquid-Liquid Extraction

Phytochemicals in Physta were also partitioned into different organic solvents such as ethyl acetate, butanol and chloroform using liquid-liquid extraction. Physta (0.5 g) was dissolved in water (10 mL) and extracted with 10 mL ethyl acetate vigorously in a 50 mL separating funnel. The top layer of organic phase was withdrawn and another fresh portion of ethyl acetate (10 mL) was added into the remaining aqueous phase for further extraction. The process was repeated for three times and the collected ethyl acetate fraction (30 mL) was combined for vacuum drying. Subsequently, the other two fractions, namely butanol and chloroform fractions were prepared using fresh Physta in separate experiments according to the above-mentioned procedures.

2.4. Acetone Precipitation

The organic fractions obtained from liquid-liquid extraction were reconstituted (1 mg/mL) in their respective solvents and slowly added into chilled acetone (20 mL) in dropwise manner. Precipitate was formed and harvested by centrifugation. The precipitate and the filtrate were then dried in an oven prior to LC-MS/MS analysis.

2.5. Total Saponin Content

The total saponin content was carried out according to the procedures described by Makkar et al.¹⁷ Samples were dissolved in 50% methanol and prepared by serial dilution. A 250 μ L sample (1 mg/mL) was mixed with 250 μ L vanillin (8 g/100 mL ethanol), and topped up with 2.5 mL sulfuric acid (72%). The mixture was heated for 10 min at 60 °C, and then cooled in an ice-water bath for 5 min. The absorbance of the mixture was recorded by a UV-vis spectrophotometer (UV-1800, Shimadzu, Japan) at 544 nm. Escin and oleanolic acid were used as the standard chemicals for calibration. The results are expressed as milligram escin equivalent per milligram sample (mg EE/mg) or milligram oleanolic acid equivalent per milligram sample (mg OAE/mg).

2.6. LC-PDA-MS/MS for Phytochemical Screening

A hyphenated LC-MS/MS system was used to detect and identify compounds in samples. The system consisted of liquid chromatograph (Dionex Corporation Ultimate

3000; Sunnyvale, CA) coupled to a diode array detector (Dionex Ultimate 3000) and a quadrupole – time-of-flight, QTOF mass spectrometer (AB SCIEX QSTAR Elite; Foster City, CA). All samples were prepared in 2 mg/L in the mixture of methanol and water (50:50) and then filtered through 0.2 µm nylon membrane before injection into a C18 reversed phase XSelect HSS T3 column (2.1 × 100 mm, 2.5 µm). The injection volume was 5 µL and the detection was performed at the wavelength of 254 nm. The mobile phase was composed of solvent A (water with 0.1% formic acid) and solvent B (acetonitrile) and was programmed as: 0–10 min, 5% B; 10–20 min, 5–90% B; 20–25 min, 90% B; 25–25.1 min, 90–5% B; 25.1–30 min, 5% B. The flow rate of mobile phase was set at 0.15 mL/min.

The mass range of m/z 120–2000 was set for mass spectrometer in phytochemical screening. The TOF MS scan was acquired with two dependent product ion scans using rolling collision energy. Nitrogen gas was used as nebulizing (40 psi) and curtain (20 psi) gas. The voltage of ion spray was set at –4500 V and 5500 V for negative and positive ion modes, respectively. The declustering potential and the focusing potential was set at 40 V and 300 V, respectively.

3. Results and Discussion

3.1. Phytochemical Screening of *Eurycoma longifolia* Extract

Physta which is consisted of a complex mixture of phytochemicals was extracted from the raw material of *E. longifolia* roots. A fast screening process for phytochemicals in Physta was carried out using LC-PDA-MS/MS. The detected compounds based on their fragment ions are listed in Suppl. Mat. Table S1 for both positive and negative ion modes. The results revealed that they were mostly from the group of quassinoids which are also known as degraded triterpenes with all-chair cyclic and highly oxygenated squalene. This also explains the bitter principle of the plant extract.

3.2. Solid Phase Extraction Based Fractionation

The principle of solid-liquid extraction was used to separate phytochemicals in Physta into individual fractions using aqueous methanol as the mobile phase and C18ec cartridge as the adsorbent. The total saponins of fractions are presented in Figure 1. The 40% methanol fraction shows to have the highest total saponins. The results expressed in escin equivalent were about 2 times higher than those results expressed in oleanolic acid equivalent. Escin is a saponin with larger molecular size (1131.269 g/mol) compared to oleanolic acid (456.711 g/mol). The presence of 3 sugar moieties in the molecular structure of escin may hinder its hydroxyl group at C-3 and double bond at C-12 to react with vanillin in order to form a red coloured complex for measurement. The hindrance can be seen from the lower slope of calibration curve exhibited by escin, and therefore higher total saponins expressed in escin equivalent.

The chromatogram shows an intense peak at 12.5 min for the 40% methanol fraction (Figure 2). The chromatogram of 100% methanol fraction shows no peak, but

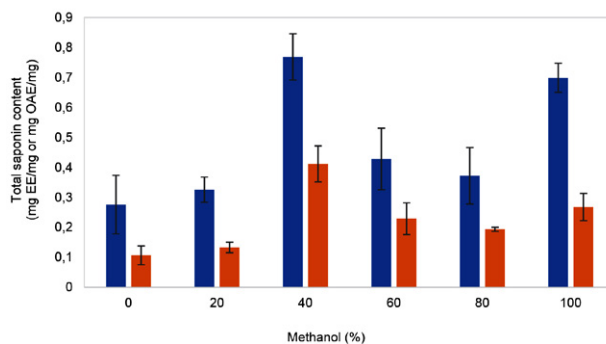


Figure 1. Total saponin content of *Eurycoma longifolia* fractions collected from solid phase extraction where blue bars are total saponin content expressed in milligram escin equivalent per milligram sample (mg EE/mg) and orange bars are total saponin content expressed in milligram oleanolic acid equivalent per milligram sample (mg OAE/mg).

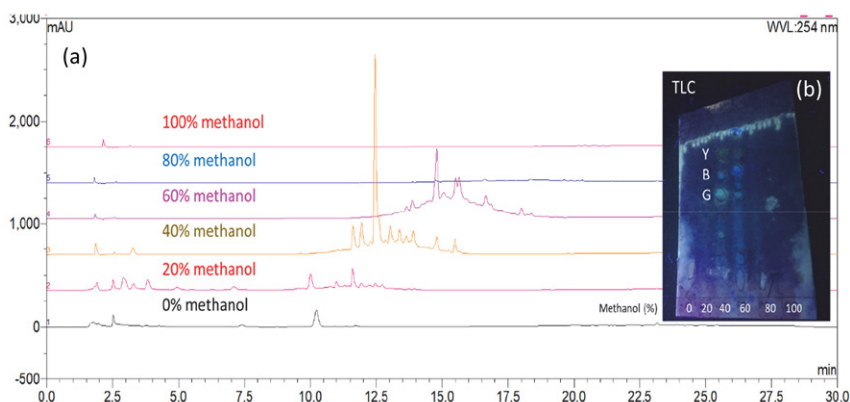


Figure 2. Chromatograms of methanol fractions collected from the elution of *Eurycoma longifolia* water extract using C18ec cartridges. The compound detection was performed using (a) liquid chromatography and (b) thin layer chromatography.

its total saponin content was the second highest among the fractions. Saponins in that fraction could have non-UV-absorbing property for detection. The 40% methanol fraction was also spotted on thin layer chromatographic plate. Interestingly, the plate displayed 3 intense spots with the retention factors of 0.62 (green), 0.74 (blue) and 0.88 (yellow) on the plate eluted by the solvent system consisting of chloroform: methanol: water (32:8:1). Saponins usually produce yellowish up to blue or violet blue spots after spraying with vanillin-sulfuric acid reagent and heating until dryness prior to visualization under UV light at 254 nm.¹⁸ The colour was attributed to the formation of complex compound from the reaction of vanillin with tri-

terpenoidal or steroidal aglycone in the presence of sulfuric acid as a strong oxidizing agent.¹⁹

The 40% methanol fraction was further purified using another new C18ec SPE cartridge into a few sub-fractions. The gradient of methanol was slowly increased from 5, 7, 10, 15, and 20% and 3 mL was also collected for each fraction. It was found that peak 3 could be retained longer in the cartridge for better separation from peak 1 and 2 (Figure 3). The peaks were tentatively identified as eurycomanone (peak 3) and its derivatives (peak 1 and 2) as presented in Table 1. This is also the first report to isolate eurycomanone using SPE assisted by analytical techniques of thin layer chromatography and LC-PDA-MS/MS. Euryco-

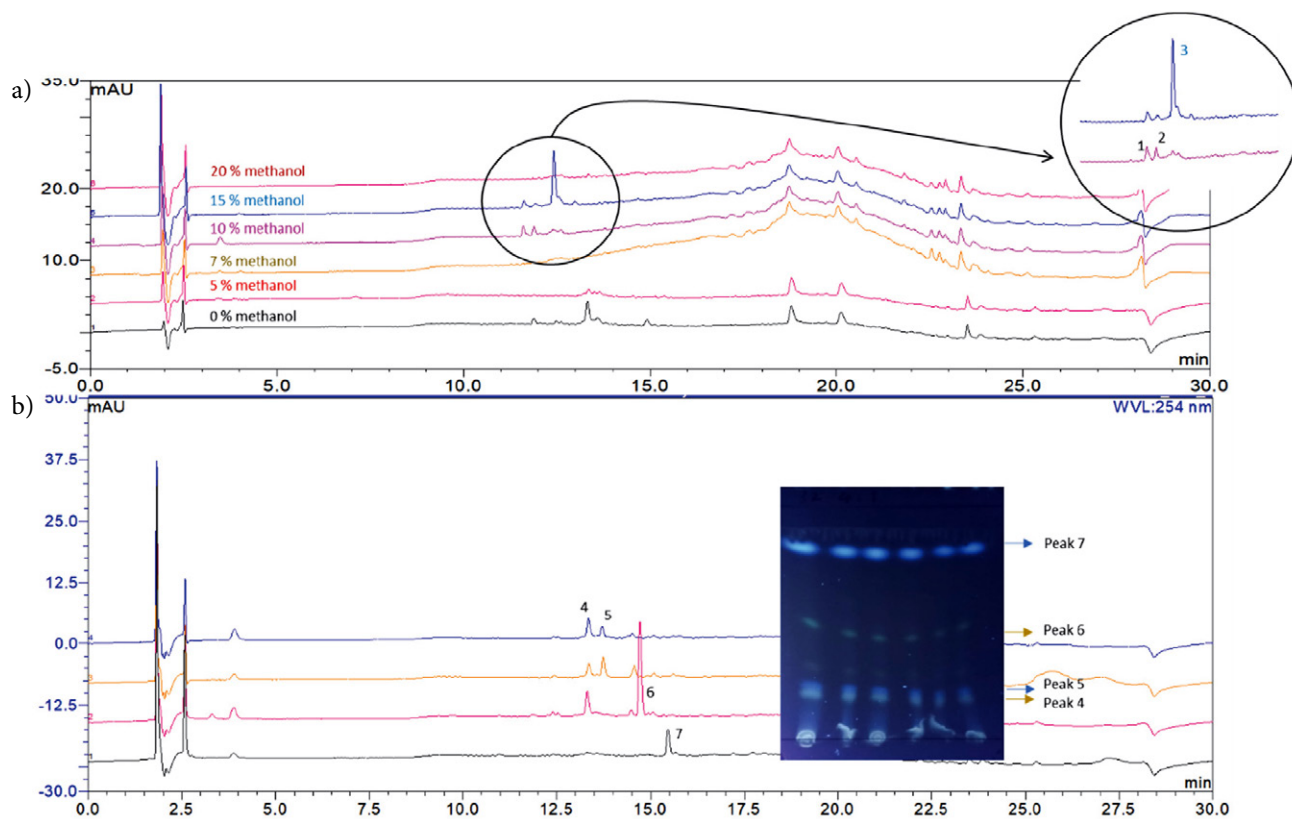


Figure 3. (a) Chromatograms of sub-fractions collected from the 40% methanol fraction using C18ec cartridge in solid phase extraction, (b) chromatograms of 4 intense spots collected from thin layer chromatographic plate using 60% methanol fraction.

Table 1. Putative compounds detected from 40 % and 60 % methanol fractions spotted on the plates of thin layer chromatography.

Peak	Retention time (min)	Retention factor	Positive ion (m/z)	Negative ion (m/z)	Putative compound on TLC plate	Spot colour
1	11.3	0.88	443/425/407/389/359/267	441/331/301/285	Pasakbumin D	Yellow
2	11.6	0.74	425/407/397/389/377/361/343/267	423/301	13 α (21)-epoxyeurycomanone (Pasakbumin B)	Blue
3	12.5	0.62	409/391/373	407/299/287	Eurycomanone (Pasakbumin A)	Green
4	13.5	0.47	413/395/377/359/285	411/291	13 β ,18-dihydroeurycomanol	yellow
5	13.7	0.50	445/429/415/405/397/343	443/379/317	13 β , 21-dihydroxyeurycomanol	Blue
6	14.7	0.67	na	441/395/377	unknown	Yellow
7	15.4	0.97	193/178	191/176	Scopoletin*	Violet blue

*Refer to reference [5] and <https://massbank.eu/MassBank/Search> (BML00378)

manone belongs to the C20 quassinoid which is well known as the biomarker of *E. longifolia* with pharmacological activities such as enhancing testosterone steroidogenesis,²⁰ antimalarial activity against *Plasmodium falciparum* William H. Welch (Plasmodiidae) strains,²¹ suppressing the expression of lung cancer cell tumour markers²² and regulating signaling pathways of cell proliferation, cell death and inflammation.²³

The second dimension of SPE did not improve the separation of peaks in 60% methanol fraction. Hence, 60% methanol was also spotted on the TLC plate and observed under UV light at 254 nm. There were 4 intense spots with the retention factors of 0.47 (yellow), 0.5 (blue), 0.67 (yellow) and 0.97 (violet blue) using the solvent system of chloroform:methanol:water (32:4:1). Four intense spots were scratched from the TLC plate, collected in tubes and extracted with methanol. The methanol solution was filtered and injected for LC-PDA-MS/MS analysis. The chromatograms of the four intense spots are presented in Figure 3 and their putative compounds (peak 4–7) are also tabulated in Table 1. Scopoletin (peak 7) is a plant growth regulator which is also a derivative of coumarin.

3. 3. Solvent Partition of *Eurycoma longifolia* Extract

In another fractionation technique, *E. longifolia* extract was reconstituted in water and partitioned using different organic solvents, namely ethyl acetate, butanol and chloroform. The results showed that ethyl acetate could recover a wide range of phytochemicals with the retention

time ranged from 12–19 min, especially peak 7 and 8 as presented in Figure 4. The phytochemicals were mostly partitioned in ethyl acetate because of high dipole moment (1.78) of the solvent. However, butanol was likely to extract more polar phytochemicals such as peak 1 and 2. On the other hand, chloroform preferred to partition less polar phytochemicals (peak 7 and 8). The chromatographic profile of chloroform fraction was close to the profile of ethyl acetate fraction. Chloroform and ethyl acetate could recover peak 7 significantly compared to peak 2 which could be recovered more by butanol. Peak 8 was another intense peak recovered by ethyl acetate. The putative compounds of the assigned peaks are listed in Suppl. Mat. Table S1. In line with the chromatograms (Figure 4), total saponin content of ethyl acetate fraction was found to be the highest in escin or oleanolic acid equivalent per milligram sample (Table 2). The results showed to have similar descending trend of total saponins in the fractions of ethyl acetate, chloroform and butanol partitioned from ethanolic extract in previous studies.¹⁵ The total saponin in butanol fraction was lower than chloroform fraction. However, butanol fraction showed to have a significant increment of saponins after acetone precipitation. Another observation was that total saponins of the organic fractions were inversely related to their recovered amount. Although butanol fraction had the lowest total saponins, the fraction was shown to have the highest weight (17%). The weight of chloroform and ethyl acetate fractions was 9.3% and 4.7%, respectively. This indicates that other compounds rather than saponins could be partitioned in butanol.

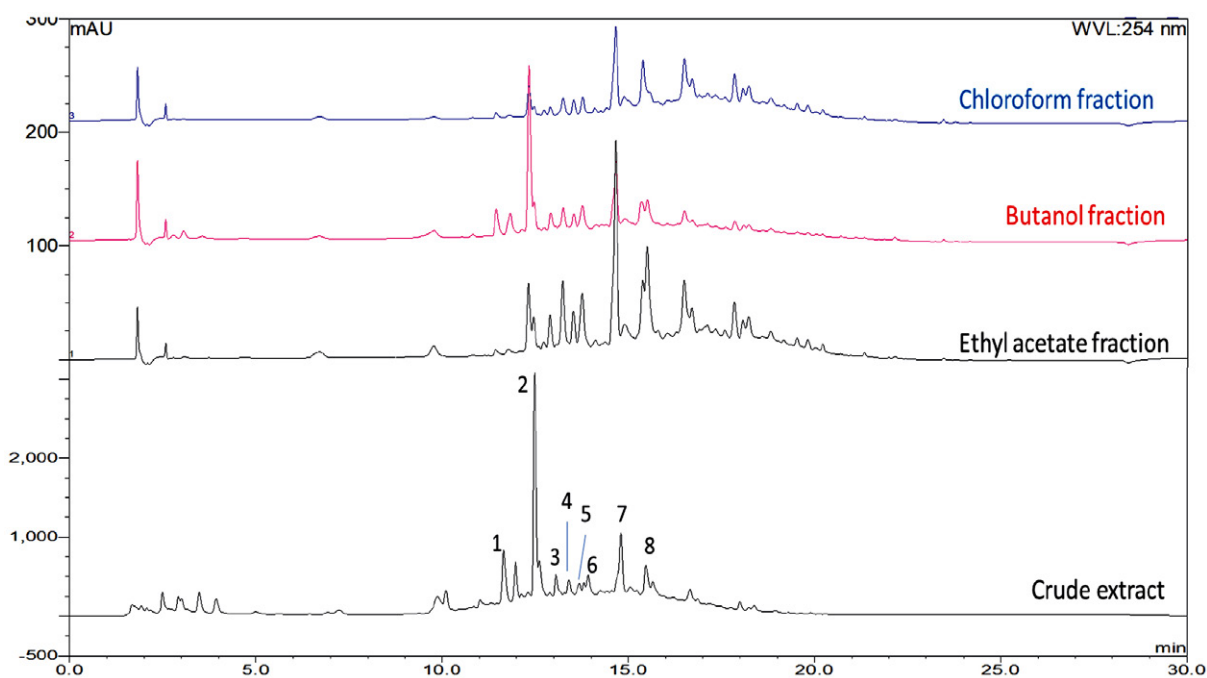


Figure 4. Chromatograms of *Eurycoma longifolia* extract and its organic fractions; ethyl acetate, butanol and chloroform. Peak 1-8 have been assigned in Suppl. Mat. Table S1.

Table 2. Total saponin content of organic fractions and their aqueous counterparts after solvent partition, and precipitates and its filtrates after acetone precipitation

Total saponin content of solvent partition			
	Sample	mg EE/mg	mg OAE/mg
Organic fraction	Extract	0.10 ± 0.03	0.05 ± 0.02
	Ethyl acetate	0.68 ± 0.03	0.34 ± 0.01
	Butanol	0.36 ± 0.05	0.19 ± 0.01
	Chloroform	0.53 ± 0.03	0.23 ± 0.02
Aqueous fraction	Ethyl acetate	0.22 ± 0.05	0.09 ± 0.02
	Butanol	0.28 ± 0.04	0.07 ± 0.02
	Chloroform	0.33 ± 0.02	0.13 ± 0.02
Total saponin content of acetone precipitate			
	Sample	mg EE/mg	mg OAE/mg
Precipitate	Extract	0.29 ± 0.08	0.04 ± 0.01
	Ethyl acetate	1.43 ± 0.14	0.83 ± 0.15
	Butanol	0.62 ± 0.18	0.20 ± 0.06
	Chloroform	0.52 ± 0.17	0.22 ± 0.06
Filtrate	Extract	0.59 ± 0.19	0.27 ± 0.11
	Ethyl acetate	1.09 ± 0.21	0.66 ± 0.13
	Butanol	0.64 ± 0.16	0.32 ± 0.03
	Chloroform	0.98 ± 0.20	0.58 ± 0.07

mg EE/mg denotes milligram escin equivalent per milligram sample
mg OAE/mg denotes oleanolic acid equivalent per milligram sample

Subsequently, the organic fractions were slowly precipitated in cold acetone. The results found that acetone precipitation improved the total saponin content of precipitates (Table 2). In particular, the precipitate of ethyl acetate fraction showed to have an increment in total saponins from its fraction. The fraction also shows to have slightly higher total saponins than its filtrate as shown in Table 2. The observation explains that saponins in *E. longifolia* are favourable to stay in ethyl acetate than acetone. The solvation of saponins was limited and precipitate was rapidly formed when ethyl acetate fraction was slowly dropped into the large volume of cold acetone. Therefore, saponins in *E. longifolia* could be recovered by ethyl acetate > butanol > chloroform in descending order. Again, total saponins recovered from the precipitation method were not in line with the harvested amount of precipitates.

Chloroform precipitate achieved the highest amount, 47%, followed by ethyl acetate precipitate (12%) and butanol precipitate (8%).

Direct precipitation of *E. longifolia* extract in cold acetone without the process of solvent partition produced a sticky precipitate. This sticky precipitate is believed to be mostly polysaccharides. Polysaccharides are soluble in water and they immediately formed a precipitate in acetone. The attractive hydrogen bonding forces within the polysaccharide chain become more prevalent in acetone. Their polysaccharide chains tend to bond within and between themselves rather than with the solvent. These intra- and intermolecular hydrogen bonds lead to agglomeration and precipitation as solvation decreases. This approach appeared to be effective to recover polysaccharides. Approximately half of the *E. longifolia* extract could be precipitated in cold acetone (51%).

The chromatograms of organic fractions and their precipitates are illustrated in Suppl. Mat. Figure S1. Almost no peak could be detected in the precipitates by UV detector of liquid chromatography. The compounds in precipitates could have non-UV-absorbing property. The total ion chromatogram (TIC) of mass analyzer shows to have an intense peak for the precipitates. The intense peak was found to have m/z 723/677(-46)/593/451(-226)/431 and m/z 792/679/661/565/548/453/435/341/228/116 for negative and positive ion modes, respectively. The presence of m/z 723 was also detected in previous studies of similar group of researchers.¹⁵ The compound was tentatively identified as [3M+HCOOH], namely 3 monomers of formylated hexoses with formate adduct ion. The other detected saccharide-containing compounds are tabulated in Table 3. The detection was performed at the negative ion mode as previous studies reported that saccharide-containing compounds were more ionizable in the negative ion mode.¹⁰ The result showed to have more saccharide-containing compounds detected from the chloroform precipitate in this study. Although many studies had been conducted for *E. longifolia* roots, most of the studies were focused on the quassinoids and biological properties of the plant crude extract. There were limited studies on the application of fractionation techniques to recover saponins

Table 3. Detected saccharide-containing compounds from the precipitates of organic fractions

t_R (min)	Negative ion (m/z)	Precipitates		
		Ethyl acetate	Butanol	Chloroform
12.5	407/299(-108)/287(-120)/283/271(-136)		√	√
12.6	575(-46)/529/395/367(-162)/349/331	√		√
13.5	557/349(-208)/313		√	√
14.0	695/449(-246)/253(-196)		√	√
15.0	587/541(-46)/407/343/333(-162)/179			√
15.5	723/677(-46)/593/451(-226)/387/341/225/179	√	√	√
17.4	819/657(-162)/476		√	
19.8	401/357/313/225(-176)/181/121		√	√

from *E. longifolia*. Elhag et al.²⁴ applied the sequential extraction just to optimize the yield of saponins using ultrasound assisted extraction followed by water extraction. However, this study applied solvent partition to increase saponin content, and consequently identify mass fragmentation patterns of saccharide-containing compounds which could be saponins in the organic fractions.

4. Conclusions

The phytochemical profile of *E. longifolia* extract had been investigated using the fractionation techniques of solid-liquid and liquid-liquid extraction. Both techniques could increase total saponin content of samples. The technique of solid-liquid extraction was found to identify few previously reported quassinoids including the marker compound, eurycomanone in the 40% methanol fraction. While the technique of liquid-liquid extraction followed by acetone precipitation could increase the total saponin content of ethyl acetate fraction. Precipitates of chloroform fractions did not show significant increment of saponin content. Nevertheless, formylated hexose trimer was found to be the most significant saccharide-containing compound in the precipitates. The detection of *m/z* and their fragment ions could be further studied to elucidate the structural diversity of saponins in *E. longifolia* roots.

Acknowledgement

The authors would like to thank the internship students; Ms Lee Yik Sin (Universiti Malaysia Kelantan), Ms. Nor Hanani Ab Halim (Universiti Malaysia Terengganu) and Ms. Norfarahin Hamzah (Universiti Malaysia Pahang) for their efforts to prepare samples for experiments. High appreciation is also given to Ministry of Higher Education, Malaysia (HICoE 4J263) and Biotropics Malaysia Berhad (4C177) for giving research grants.

5. References

1. L. S. Chua, N. A. Amin, J. C. Neo, T. H. Lee, C. T. Lee, M. R. Sarmidi, R. A. Aziz, *J. Chromatogr. B Analyt. Technol. Biomed. Life Sci.* **2011**, 879, 3909–3919. DOI:10.1016/j.jchromb.2011.11.002
2. A. K. M. S. Islam, Z. Ismail, B. Saad, A. R. Othman, M. N. Ahmad, A.Y.M. Shakaf, *Sensor Actuators B: Chem.* **2006**, 120, 245–251. DOI:10.1016/j.snb.2006.02.020
3. A. M. Adib, Z. Abdullah, *Vib. Spectrosc.* **2018**, 96, 1–9. DOI:10.1016/j.vibspec.2018.02.003
4. F. Ebrahimi, B. Ibrahim, C. H. Teh, V. Murugaiyah, C. K. Lam, *Planta Med.* **2017**, 83, 172–182. DOI:10.1055/s-0042-110857
5. N. Zakaria, K. S. Mohd, M. S. R. Hamil, A. H. Memon, A. Z. Asmawi, Z. Ismail, *J. Fundam. Appl. Sci.* **2017**, 9, 661–679. DOI:10.4314/jfas.v9i2s.41
6. M. Tambi, A. Kadir, *Asian J. Androl.* **2006**, 8, 49–50.
7. P. C. Kuo, A. G. Damu, K. H. Lee, T. S. Wu, *Biorg. Med. Chem.* **2004**, 12, 537–544. DOI:10.1016/j.bmc.2003.11.017
8. G. Fiaschetti, M. Grotzer, T. Shalaby, D. Castelletti, A. Arcaro, *Curr. Med. Chem.* **2010**, 18, 316–328. DOI:10.2174/092986711794839205
9. S. Park, N. X. Nhiem, P. V. Kiem, C. V. Minh, B. H. Tai, N. Kim, H. H. Yoo, J. H. Song, H. J. Ko, S. H. Kim, *Bioorg. Med. Chem. Lett.* **2014**, 24, 3835–3840. DOI:10.1016/j.bmcl.2014.06.058
10. N. N. Zaini, O. Rozita, J. Hafizan, S. Norashikin, *Molecules*, **2016**, 21, 583. DOI:10.3390/molecules21050583
11. B. Mutschlechner, S. Schwaiger, T. V. A. Tran, H. Stuppner, *Fitoterapia*, **2018**, 124, 188–192. DOI:10.1016/j.fitote.2017.11.015
12. P. B. Ngoc, T. B. Pham, H. D. Nguyen, T. T. Tran, H. H. Chu, V. M. Chau, J. H. Lee, T. D. Nguyen, *Nat. Prod Res.* **2016**, 30, 1360–1365. DOI:10.1080/14786419.2015.1056187
13. J. Ruan, Z. Li, Y. Zhang, Y. Chen, M. Liu, L. Han, Y. Zhang, T. Wang, *Molecules*, **2019**, 24, 3157. DOI:10.3390/molecules24173157
14. Malaysian Standard, MS 2409, Department of Standards Malaysia: Cyberjaya, SGR, Malaysia, **2011**.
15. L. S. Chua, C. H. Lau, C. Y. Chew, D.A.S. Dawood, *Molecules* **2019**, 24, 1416. DOI:10.3390/molecules24071416
16. N. Husain, A. Kumar, *Int. J. Sci. Res.* **2016**, 5, 1613–1615.
17. H. P. S. Makkar, P. Siddhuraju, K. Becker, in: *Methods in Molecular Biology* 393. New Jersey, Humana Press, Clifton, **2007**, p. 93–100. DOI:10.1007/978-1-59745-425-4_16
18. W. Oleszek, I. Kapusta, A. Stochmal, in: *Waksmundzka-Hajnos M, Sherma J, Kowalska T (Eds): Thin Layer Chromatography in Phytochemistry*. 1st ed. New York, CRC Press, Taylor & Francis Group, **2008**, p. 519–41.
19. A. V. Le, S. E. Parks, M. H. Nguyen, P. D. Roach, *Technologies* **2018**, 6, 84. DOI:10.3390/technologies6030084
20. B. S. Low, S. B. Choi, H. Abdul Wahab, P. K. Das, K. L. Chan, *J. Ethnopharmacol.* **2013**, 149, 201–207. DOI:10.1016/j.jep.2013.06.023
21. K. L. Chan, C. Y. Choo, N. R. Abdullah, Z. Ismail, *J. Ethnopharmacol.* **2014**, 92, 223–227. DOI:10.1016/j.jep.2004.02.025
22. P. F. Wong, W.F. Cheong, M. H. Shu, C. H. Teh, K. L. Chan, S. Abu Bakar, *Phytomed.* **2012**, 19, 138–144. DOI:10.1016/j.phymed.2011.07.001
23. S. Hajjouli, S. Chateavieux, M. H. Teiten, B. Orlikova, M. Schumacher, M. Dicato, C.Y. Choo, M. Diederich, *Molecules* **2014**, 19, 14649–66. DOI:10.3390/molecules190914649
24. H. E. E. A. Elhag, A. Naila, A. Ajit, B. A. Aziz, A. Z. Sulaiman, *Materials Today: Proceedings*, **2018**, 5, 21672–21681. DOI:10.1016/j.matpr.2018.07.018

Povzetek

V vodnem ekstraktu korenin rastline *Eurycoma longifolia* smo identificirali fitokemikalije s tehnikami frakcionacije trdno-tekoče in tekoče-tekoče. Kot ekstrakcijo trdno-tekoče smo uporabili reverzno-fazno C18 ekstrakcijo na trdno fazo (SPE), medtem ko smo kot ekstrakcijo tekoče-tekoče uporabili porazdeljevanje med topila. Po frakcionaciji se je povečala vsebnost skupnih saponinov. V 40 % in 60 % metanolni frakciji SPE smo identificirali nekaj poznanih kasi-noidov: eurikomanon, 13 α (21)-epoksieurikomanon, pasakbumin D, 13 β ,18-dihidroeurikomanol in 13 β ,21-dihidrok-sieurikomanol. Ugotovili smo, da ima največjo vsebnost saponinov ekstrakt po porazdeljevanju v etil acetat, v primerjavi z butanolno in kloroformno frakcijo. Z nadaljnjim obarjanjem organskih frakcij z acetonom smo pridobili formilirani heksozni trimer in druge saharide vsebujoče spojine. Z ekstrakcijo tekoče-tekoče z etil acetatom, ki ji je sledilo obarjanje z acetonom, smo učinkovito izolirali saponine iz vodnega ekstrakta rastline *E. longifolia*.



Except when otherwise noted, articles in this journal are published under the terms and conditions of the Creative Commons Attribution 4.0 International License

Scientific paper

Model Electrochemical Biosensor for the Detection of Methanol in Aqueous Solutions with Yeast Cells

Zala Štukovnik,¹ Urban Bren^{1,2} and Martin Rozman^{1,*}¹ University of Maribor, Faculty of Chemistry and Chemical Engineering, Smetanova ulica 17, 2000 Maribor, Slovenia² University of Primorska, Faculty of mathematics, Natural sciences and information technologies, Glagoljaška Ulica 8, 6000 Koper, Slovenia

* Corresponding author: E-mail: martin0rozman@gmail.com

Received: 11-27-2020

Abstract

An electrochemical device that serves as a model biosensor and contains yeast *Saccharomyces cerevisiae* as the active biological element was developed. Different configurations of the electrochemical cells were assembled and tested. Stainless steel was used in the electrochemical cell composition process and the surface of this metal electrode was modified with a thin layer of WO₃ if necessary. The yeast *Saccharomyces cerevisiae* was adhered to the working electrode. The resulting model biosensor was then used to monitor the response to a 10% CH₃OH. For detection of biological activity, the electrochemical impedance spectroscopy (EIS) method was applied with a portable potentiostat/galvanostat, where the Bode and the Nyquist plots were interpreted. The stability of the device was beforehand determined by measuring the open circuit potential (OCP). The topography of the electrodes was inspected using the techniques of scanning electron microscopy and optical microscopy. The investigated model biosensor serves as a case study for the development of more complex biosensors that utilize living cells as the active layer.

Keywords: Biosensor, electrochemistry, electrochemical impedance spectroscopy, yeast *Saccharomyces cerevisiae*

1. Introduction

A biosensor represents an analytical device that combines a biological element and a physical transmitter to generate a measurable signal proportional to the concentration of the analyte.^{1,2,3} The quality of the information provided by the biosensor depends on the type of analyte solution, the active biological component, the design of the biosensor and the properties of the physical transducer.³ Biosensors can be classified according to the method of physico-chemical conversion or according to the type of biologically active element. Based on the transducer, biosensors are classified into electrochemical, optical and mechanical biosensors.⁴ Active biological components can generally include unicellular organisms, enzymes, antibodies, cells, organelles or tissues.⁵

The aim of this study was to develop an electrochemical cell that is transferable and connectable to smartphones, computers, servers, etc., while remaining highly specific, responsive and repeatable.

The presented electrochemical cell is a part of a biosensor and it is designed as a three-electrode electrochemical system. At the working electrode (WE) the process is

monitored, the reference electrode (RE) has a constant potential that does not change during the process while the counter electrode (CE) provides the current required to detect the electrochemical cell response.^{6,7}

In an electrochemical cell intended for use in biosensors, a biological component capable of recognizing and quantifying specific stimuli or pulses is applied to the working electrode.⁸ Electrodes for biosensors can be reused from other electrochemical systems and can incorporate different materials, with focus on non-toxic metals and metal oxides.^{9,10} As a biological component, the *Saccharomyces cerevisiae* yeast was used, which has many advantageous properties that make it useful for biosensing: the robustness of the cells, the ease of maintenance, and the rate of the cell production.^{11,12} Yeast *Saccharomyces cerevisiae* represents a single-celled eukaryotic organism used primarily in the food industry in the preparation of bakery products and alcoholic beverages.¹³ Yeast *Saccharomyces cerevisiae* are chemoorganotrophic and anaerobic organisms classified in the kingdom of fungi, the phylum Ascomycota, the class Saccharomycetes, the order Saccharomycetales and the family Saccharomycetaceae.¹⁴ *Saccharomyces cerevisiae* can exist in two different forms, the hap-

loid or the diploid form.¹⁵ A yeast cell possesses typical properties of a single-nucleus eukaryotic cell and characteristic organelles such as vacuoles and lipid droplets.¹⁶ Yeast cells are usually spherical to slightly spherical and occasionally ellipsoidal to cylindrical in shape.¹⁷ Yeasts, unlike certain other biological components, do not require sophisticated sterile techniques or complex media and are also economically advantageous.¹²

The electrochemical impedance spectroscopy (EIS) method was used for detection. With the EIS technique the frequency response of the electric current was measured and thus provided data on the yeast adhesive layer on the electrode surfaces. EIS represents a non-destructive method with which one can quantify certain parameters and simultaneously trace several electrochemical processes.¹⁸ The measurement comprises the real (electric resistance) and the imaginary (capacitance) component of the impedance response of an electrochemical system.¹⁹ Electrochemical impedance spectroscopy has been widely used in the production and optimization of biosensors,^{20,21} as this method allows characterization of the biological component attached to the sensor and the analyte present in the sample. Because biosensors generate a rapid response, they can be used to monitor molecular events in real time.²²

To determine cell mortality, the method of staining cells with methylene blue was applied. When cells are stained with methylene blue, dead cells remain blue while living cells reduce methylene blue and become colorless due to the reaction.²³ In the current study a model biosensor containing yeast *Saccharomyces cerevisiae* as the active biological element was developed and tested using electrochemical impedance spectroscopy as well as scanning electron microscopy and optical microscopy.

2. Experimental

Various procedures for composition of electrochemical cells have been tested. In the process of assembling the electrochemical cell, stainless steel type SS316 (manufacturer TBJ Industries, Germany) was used and in some experiments, the surface of the metal electrode was modified with a thin layer of WO_3 . Yeasts *Saccharomyces cerevisiae* were applied to the working electrode as a biological component. Using a model biosensor, the yeasts response to a 10% CH_3OH solution when changing various parameters was monitored.

Model electrochemical devices that used different working electrodes and utilized different dimensions were assembled and tested. The electrodes were manufactured in two different dimensions (figure 1): dimension of electrode 20 mm × 2 mm where the active component was applied to 5 mm × 2 mm (figure 1a) and dimension of electrode 20 mm × 5 mm where the active component was applied to 5 mm × 5 mm (figure 1b). The position of electrodes was al-

ways side-by-side and from left to right placing the reference (RE), the counter (CE) and finally the working electrode (WE) which we marked the RCW configuration. 0.050 mm thick stainless steel and stainless steel covered with a thin layer of WO_3 was used. The electrochemical cell consisted of three electrodes, where the biological component or yeast *Saccharomyces cerevisiae* was applied to the working electrode (WE). Electrodes were insulated on fixation side. The system was closed with glass.

Biosensor device manufacturing process:

- Production of electrodes with dimension 20 mm × 2 mm for small electrochemical cell and dimension 20 mm × 5 mm for large electrochemical cell. Electrodes were cut from a 0.050 mm thick stainless steel foil and from a 0.050 mm thick stainless steel foil covered with a thin layer of WO_3 .
- Application of a biological component on the working electrode (WE) by spin coater at the coating speed of 2000 rpm for 10 s.
- Placement and fixation of electrodes on the glass support in the RCW configuration described previously.
- System closure with small glass slide.

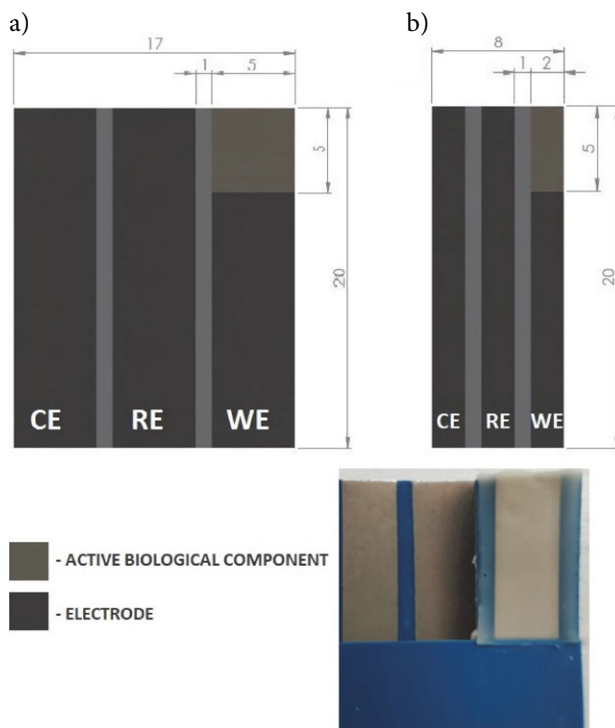


Figure 1: In figure 1a, large electrochemical cell with three electrodes in reference-counter-working (RCW) side-by-side configuration is presented. Dimension of electrode is 20 mm × 5 mm, where the active biological component is applied to 5 mm × 5 mm. In figure 1b a small electrochemical cell with three electrodes in RCW side-by-side configuration is depicted. Dimension of electrode is 20 mm × 2 mm, where the active biological component is applied to 5 mm × 2 mm. An actual assembled device, with biological component is presented on lower right part of the figure, with active surface area of each individual electrode being 5 mm × 2 mm.

Two solutions were prepared for the measurements: 0.9% NaCl solution (saline) and 10% CH₃OH in 0.9% NaCl solution. The solution was injected into the system. For evaluation of electrochemical cells electrochemical impedance spectroscopy method (EIS) was used.

The measurements were carried out with a PalmSens4 potentiostat/galvanostat. The frequency range for EIS tests was 10 mHz to 100 kHz, the recording range of the electrical current measurement range was between 1 nA and 10 mA, the amplitude potential was 20 mV, and the number of measured frequency points was 61 = 10/dec.

Electrochemical impedance spectroscopy was used to obtain the data on the events on the surface of the electrode and the applied layers, and the Bode and Nyquist plots were interpreted as a result.

The stability of the device and the prepared layers was previously determined by measuring the potential of the open circuit (OCP), in which the potential difference between the reference electrode (RE) and the working electrode (WE) is measured.

Biosensor device connection and testing procedure:

- Connection of the biosensor device to the potentiostat/galvanostat.
- Addition of 0.9% NaCl solution. The solution was applied with syringe onto top of the open device, after which the device was sealed with clamps to prevent movement of individual components. After addition of solution, the device was for approximately 5 min to ensure that all of the electrodes were sufficiently soaked.
- Open Circuit Potential measurement (OCP). The time of the measurement was 30 s.
- Measurement of electrochemical impedance spectroscopy (EIS). The expected duration of the measurement was 2 min and 12 s, and the time was commonly prolonged up to 3 min.
- Addition of 0.9% NaCl solution with 10% CH₃OH. The measurements were carried out after exposure to methanol as a toxic component. A paper tissue was placed under electrochemical cell and a 1 mL syringe fitted with needle that was filled with investigating solution was carefully stuck onto side of device in such way, that it did not touch biological component. After positioning of the needle, the content of the syringe was dumped into the electrochemical cell, ensuring that the device was excessively soaked with new solution. This rinsing process was repeated at least three times. Electrochemical cells were rinsed with 0.9% NaCl core solution with added CH₃OH to prevent loss of electrolyte and change of conductive properties.
- Excess liquid was removed with paper tissue and device was then left connected to potentiostat/galvanostat in idle mode for 60–90 s for the methanol to have effect on the cells before open circuit potential (OCP) measurement was carried out.

- Open circuit potential measurement (OCP). The time of the measurement was 30 s.
- Measurement of electrochemical impedance spectroscopy (EIS). The expected duration of the measurement was 2 min and 12 s, where the time was commonly prolonged to up to 3 min to enable assembled cell to achieve stable open circuit potential equilibrium, with potential drift being less than 0.2 mV/s.

The morphology of the electrodes was additionally verified by the technique of scanning electron microscopy (SEM) and by classical microscopy, where the number of living yeast cells of the species *Saccharomyces cerevisiae* on the surface of the electrodes was examined. To determine cell mortality, the method of staining cells with methylene blue was used. When cells are stained with methylene blue, dead cells remain blue stained and living cells reduce methylene blue and become colorless due to the reaction.²³ For methylene blue dye testing, 50 mL of both original 0.9% NaCl blank solution and 50 mL of 0.9 % NaCl and 10 % CH₃OH solution were modified by adding 0.5 mL of methylene blue dye solution that was prepared from 0.1 g of powdered methylene blue in 50 mL of demineralized water. Cells were first exposed to the dyed saline and afterwards to the dyed 10% CH₃OH solution. The duration of exposure to dyed saline and in dyed methanol was approximately 60–90 s, similar to the undyed devices that were used in electrochemical measurements (OCP, EIS). For technique of scanning electron microscopy (SEM), Zeiss ULTRA plus field emission microscope (accelerating voltage 0.02 to 30 kV and 100,000x magnification) was used. The configuration of the microscope enables quality analysis of practically all solid nonvolatile samples. For optical microscopy Olympus SZX16 microscope and 120x magnification was used.

3. Results and Discussion

Model electrochemical cells of different dimensions described previously in experimental section were assembled and tested.

3. 1. Electrochemical Impedance Spectroscopy (EIS)

a) Biosensor with stainless steel working electrode

The impedance response of the biosensor with yeast cells attached to stainless steel in the absence and presence of CH₃OH as a toxic component was measured.

In the graphs, EIS Nyquist plots (Figures 2a and 2b), representing the response in complex units are represented. A 0.9% sodium chloride (NaCl) solution was first added to the system followed by a solution consisting of 0.9% sodium chloride (NaCl) and 10% methanol (CH₃OH). With the addition of NaCl solution to the system, the charge transfer and then the diffusion process are shown

on the plots. The capacitance (imaginary part of impedance) and the resistance (real part of impedance) increased with the frequency drop.

In the Nyquist diagram of the large electrochemical cell (Figure 2a), the solution resistance (R_s), the capacitance of the electric double layer (C_{dl}), and the charge transfer resistance (R_{ct}) are detected in kinetic controlled process of the EIS spectrum and are displayed as semi-circle pattern. Mass transfer-controlled process of the EIS spectrum describes the diffusion as a linear behavior.

In the Nyquist diagram of the small electrochemical cell (Figure 2b), the solution resistance (R_s), the capacitance of the electric double layer (C_{dl}), the charge transfer resistance (R_{ct}) and the Warburg impedance (Z_w), which describes the process of transferring ions through layers and is presented in the Nyquist diagram as a linear behavior with a gradient of 45° are detected. The semi-circle is smaller, confirming a higher conductivity and a smaller charge transfer resistance (R_{ct}).

The Bode plots presented in the supplementary information (Figures 1S and 2S) consist of two spectra simultaneously (impedance spectrum and phase spectrum), where the dependence of impedance (Z) and phase angle on frequency is shown. In the impedance spectrum, the activity on the working electrode is determined according to the slopes of the line, and on the phase spectrum the activity is determined according to a phase angle. In the Bode plot, as in the Nyquist plot, it appears that the resistance and capacitance decreased with the addition of 10% CH_3OH solution.

In the Bode diagram of large electrochemical cell (Figure 1S), with the addition of NaCl solution, the solution resistance (R_s) with gradient of 0 in impedance spectrum, then the capacitance of the electric double layer (C_{dl}) with gradient of -1 , which occurs at the phase boundary between the electrode and the electrolyte, the charge transfer resistance with gradient of 0 (R_{ct}), which occurs due to the electrochemical reaction or charge transfer between the electrolyte and the metal, and the diffusion with gradient of -0.5 (Warburg impedance) were detected. With the addition of 10% CH_3OH solution, a similar solution resistance (R_s), lower capacitance of the electric double layer (C_{dl}) and more pronounced diffusion were observed. Negative phases are lower than usual, it can be concluded that the charge transfer resistance (R_{ct}) is high.

The Bode plot of the small electrochemical cell is represented in the supplementary information as Figure 2S. With the impedance spectrum curve in the direction of frequency decay, „non-ideal“ capacitor (CPU) which describes the capacitance of the electric double layer (C_{dl}) and has a gradient of about -1 is represented. In the phase spectrum, negative phase angle of 80° corresponds to a capacitance of the electric double layer. At lower frequencies, diffusion (Z_w) is observed, which is shown in the impedance spectrum with a gradient of -0.5 and in the phase spectrum with a negative phase angle of 45° .

Nyquist plots and Bode plots show that the addition of 10% CH_3OH solution decreased the resistance and capacitance in comparison to addition of NaCl solution to the system, indicating that the electrode surface was released and, consequently, that CH_3OH caused the death of *Saccharomyces cerevisiae* cells.

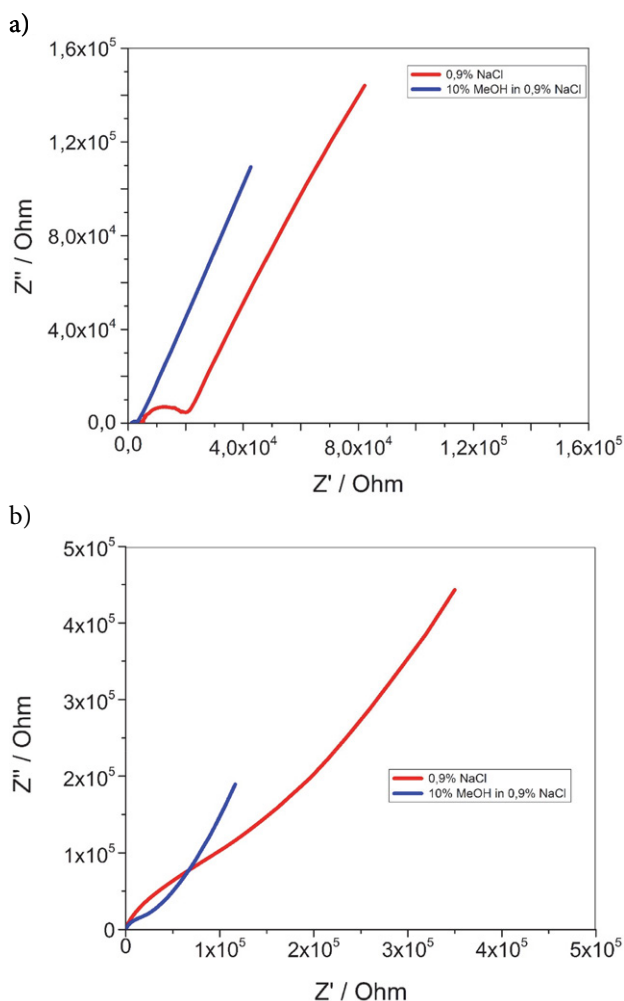


Figure 2: Nyquist diagrams of the EIS measurement on a larger biosensor (Figure 2a) and on a smaller biosensor (Figure 2b) using a working electrode of stainless steel are depicted, where the red curve shows the measurement of a 0.9% NaCl solution added to the system and the blue curve shows the measurement of a 0.9% NaCl solution with 10% CH_3OH added to the system.

b) Biosensor with stainless steel coated with thin layer of trioxotungsten working electrode

As with the stainless steel working electrode biosensor, the EIS measurements were repeated for the WO_3 -coated stainless steel working electrode biosensor of various sizes. 0.9% sodium chloride (NaCl) solution was injected to the system first, followed by 10% methanol (CH_3OH) solution. The capacitance (imaginary part of impedance) and the resistance (real part of impedance) increased with frequency drop.

The diagram shows resistance response due to process of the charge transfer in the electrolyte and then the additional resistance response due to the diffusion layer. With the addition of 10% CH₃OH solution, the resistance and the capacitance response are both decreased, suggesting a change on the electrode surface.

In the case of the biosensor with a larger working electrode dimension (20 mm × 5 mm) represented in Figure 3a, the Nyquist plot shows a decrease in the resistance and the capacitance with the addition of CH₃OH compared to the measurement where NaCl solution was added. Kinetic controlled process describes the solution resistance (R_s), and the charge transfer resistance (R_{ct}), where the charge transfer resistance (R_{ct}) is more profound in comparison to electrochemical cells without WO₃ coat. Mass transfer-controlled process of the EIS spectrum describes diffusion (Z_w) as linear behavior. In the case of the biosensor with a smaller working electrode dimension

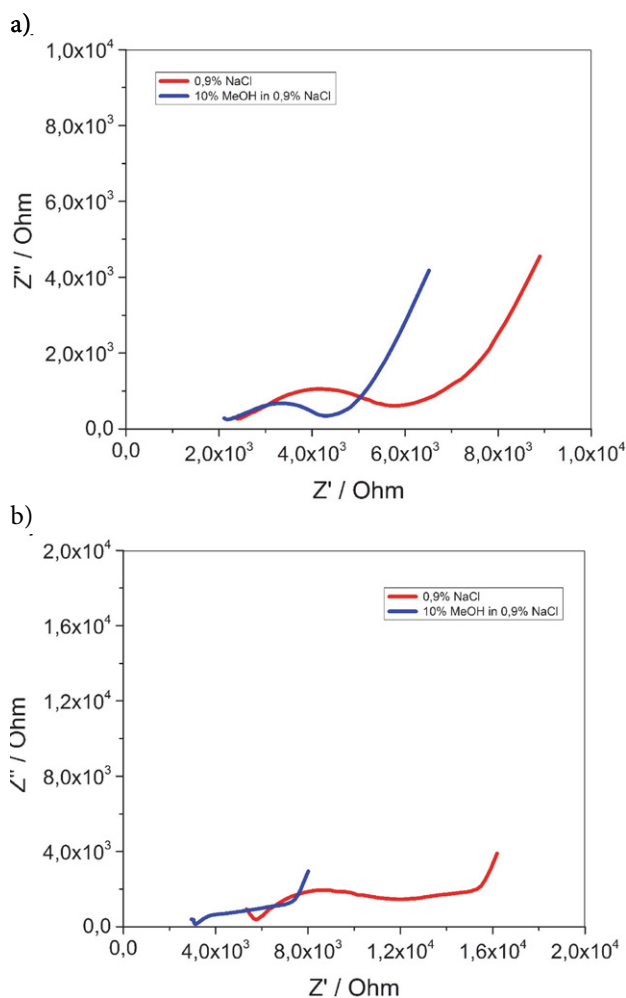


Figure 3: Nyquist diagram of the EIS measurement of a larger (Figure 3a) and smaller (Figure 3b) biosensor using a working electrode of stainless steel coated with a thin layer of WO₃, where the red curve represents the measurement of 0.9% NaCl solution added to the system and the blue curve represent the measurement of 0.9% NaCl solution with 10% CH₃OH added to the system.

(5 mm × 2 mm), the Nyquist diagram (Figure 3b) shows a decrease in resistance with the addition of CH₃OH enriched solution compared to the measurement where only NaCl solution was added. The capacitance (imaginary part of the impedance) did not change significantly in the Nyquist plot, but the change is visible in the Bode diagram, where it is slightly lower with the addition of CH₃OH solution than with the addition of NaCl solution.

In the Bode plot of the biosensor with larger electrodes dimension (20 mm × 5 mm), as in the Nyquist diagram, it is seen that the resistance and capacitance decreased with the addition of 10% CH₃OH solution. In the Bode diagram (Figure 3S) with the addition of NaCl solution and then the addition of CH₃OH solution, at higher frequencies the solution resistance (R_s), the charge transfer resistance (R_{ct}) and the capacitance of the electric double layer (C_{dl}) formed at the phase boundary between the electrode are represented. At lower frequencies Warburg impedance (Z_w) is shown.

In the Bode diagram of the biosensor with smaller electrodes dimension (20 mm × 2 mm) (Figure 4S), the solution resistance, then the capacitance of the electric double layer (C_{dl}) and the charge transfer resistance (R_{ct}), and diffusion as Warburg impedance (Z_w) are observed at higher frequencies with the addition of NaCl solution and with addition of CH₃OH solution. The charge transfer resistance is more pronounced in regular NaCl solution compared to the addition of CH₃OH enriched solution, again most likely due to the cells fully blocking the electrode surface when no methanol is present. Additionally, resistance in general due to electron transfer is higher compared to electrodes that are not coated with the WO₃ layer.

The electric equivalent circuit and the fitted impedance spectrum of the large electrochemical cell with the stainless steel working electrode is presented in the supplementary information as Figure 5S and Figure 6S, and the electric equivalent circuit and the fitted impedance spectrum of the large electrochemical cell with the stainless steel covered with WO₃ working electrode is presented in the supplementary information as Figure 7S and Figure 8S.

The limit of detection (LOD) for each electrochemical cell was estimated by performing measurements at the six different concentrations of the CH₃OH: 0.0%, 0.1%, 0.5%, 1.0%, 5.0% and 10.0% of percent by volume and then comparing obtained data. The blank solution consisted of 0.9% NaCl solution (saline). The minimum reference total impedance (Z) value for LOD was established at approximately $\Delta = 3 \text{ k}\Omega$ for 2 measurements at selected concentration and at lowest frequency ($10^{0.9} \text{ Hz}$). This is a value that can be determined with sufficient repeatability and represent 30 % error at lower impedance ($10^4 \Omega$) and 3 % error at higher impedance ($10^5 \Omega$). In order to accurately determine measurement during individual error, 5 measurement points, closest to lowest frequency were taken for sta-

tistical comparison. The LOD for stainless steel working electrode was estimated at about 5.0%v/v CH₃OH for small surface and 1.0%v/v CH₃OH for large surface. The LOD electrochemical cells with stainless steel covered with thin layer of WO₃ working electrode was determined as low as 1.0%v/v CH₃OH for small device and as low as 0.5%v/v CH₃OH for large device. It must be noted, that for large electrode covered with WO₃ there were minor issues in detecting signals at higher concentrations, suggesting that there is a limit in concentration response. This suggests that it might be possible to increase LOD on the expense of range of concentrations. The data presented in Table 1 was recorded at the frequency of 10^{-0.9} Hz, while the graphs for estimate of LOD (Figures 9S-12S) along with Nyquist diagrams of LOD estimate measurements (Figures 13S-16S) are presented in supplementary information.

Table 1: Impedance of the large electrochemical cell with the stainless steel working electrode (S1), the small electrochemical cell with stainless steel working electrode (S2), the large electrochemical cell with the stainless steel electrode covered with WO₃ working electrode (W1) and the small electrochemical cell with the stainless steel electrode covered with WO₃ working electrode (W2) measured at percent by volume concentrations: 0.0, 0.1, 0.5, 1.0, 5.0, 10.0.

	S1	S2	W1	W2
Concentration (%)	Impedance (Ω)			
0.0	10 ^{4.95}	10 ^{5.31}	10 ^{4.60}	10 ^{4.48}
0.1	10 ^{4.97}	10 ^{5.32}	10 ^{4.52}	10 ^{4.45}
0.5	10 ^{4.98}	10 ^{5.31}	10^{4.43}	10 ^{4.42}
1.0	10^{4.74}	10 ^{5.30}	10 ^{4.36}	10^{4.39}
5.0	10 ^{4.71}	10^{5.17}	10 ^{4.28}	10 ^{4.31}
10.0	10 ^{4.42}	10 ^{5.16}	10 ^{4.27}	10 ^{4.26}

3. 2. SEM Analysis

The morphology of steel electrodes (Figure 4a) and steel electrodes coated with a layer of WO₃ (Figure 4b) was

observed by the scanning electron microscopy (SEM) technique at 100,000x magnification. On uncoated stainless steel surface shown in Figure 4a, it can be seen small crystals and slightly uneven surface, which is due to steel being prepared as 'hot-rolled' steel along with possible artefacts that could be made during production or handling of steel foil. This type of steel foil is known for its defects on surface compared to 'cold-rolled' steel and defects in form of crystals can be observed on photomicrography. As shown in Figure 4b, the stainless steel electrodes coated with a thin layer of WO₃ are more porous than stainless steel electrodes (Figure 4a). This mesoporous surface is formed during sintering process of WO₃ thin film preparation, and is due to fast heating and drying of thin film sol-gel WO₃ precursor. This phenomena is well investigated and has been described in different literature.⁹ Due to porous structure of WO₃ thin film, it has much higher roughness compared non-coated steel foil and because of this, yeast can more easily adhere onto surface. This data is in accordance with observations during preparation of devices, where WO₃ coated steel foil had better adhesion of yeast compared to non-coated steel foil.

3. 3. Optical Microscopy

The number of living cells of the yeast *Saccharomyces cerevisiae* on the surface of the electrodes was observed by optical microscopy. Methylene blue was used to check cell mortality, where dead cells remain blue stained and living cells reduce methylene blue and become colorless due to the reaction. With the addition of 0.9% NaCl solution, yeast cells remained colorless (Figure 5a). With the addition of 10% CH₃OH solution, the cells were blue stained (Figure 5b). By staining the cells with methylene blue dye it was additionally proven, that methanol causes the death of *Saccharomyces cerevisiae* yeast cells. It can be noticed that with a larger group of yeasts (top left in figure 5b),

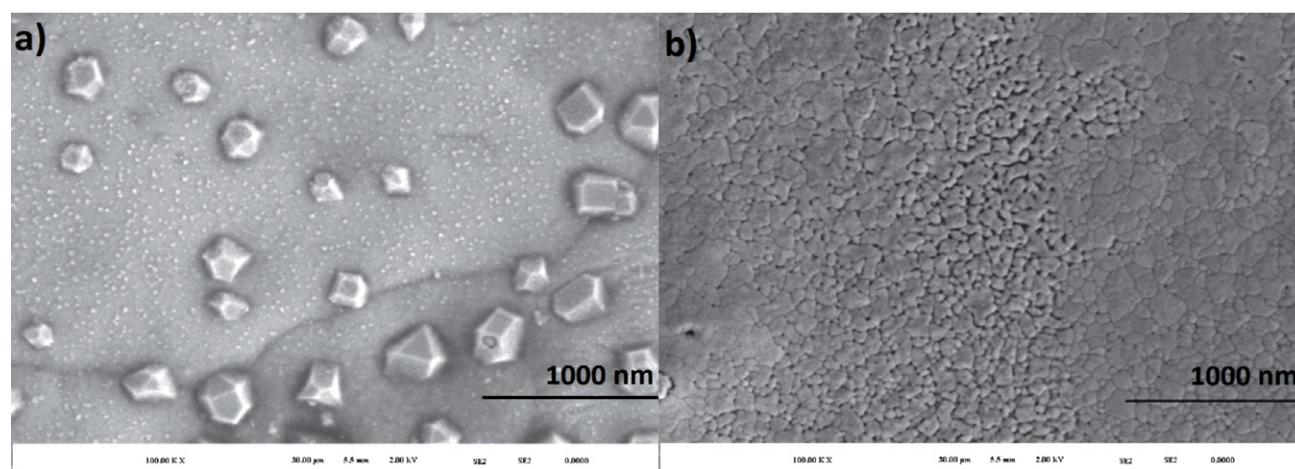


Figure 4: a) the SEM analysis (morphology) of stainless steel is presented. b) the SEM analysis (morphology) of stainless steel covered with a thin film of WO₃ is presented.

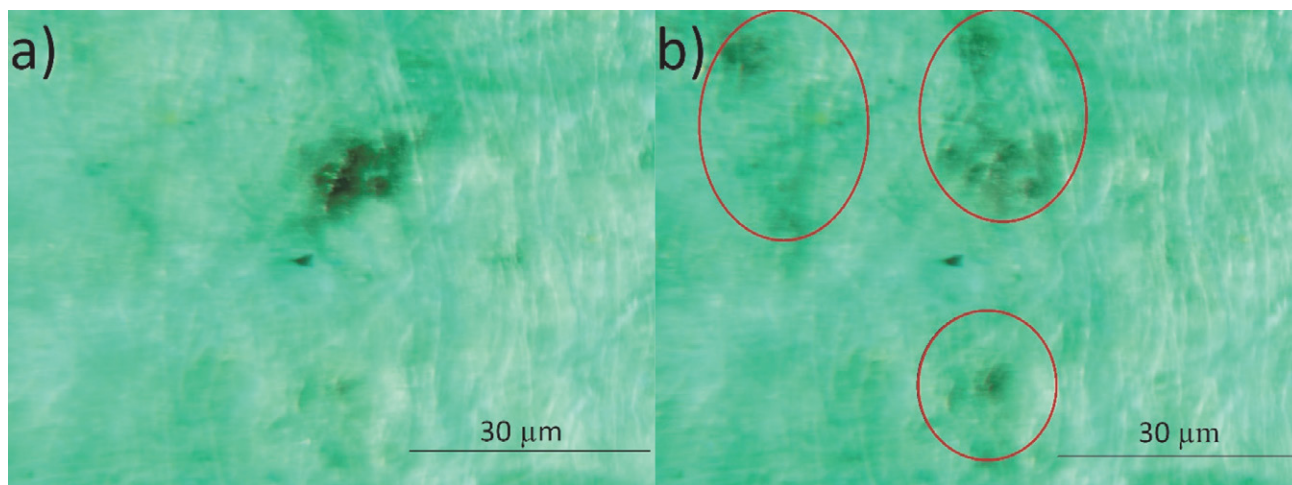


Figure 5: Microphotographs of the steel working electrode with adhered yeasts on covered with electrolyte carrier with methylene blue dye added along with 0.9% NaCl (a) and along with 10% CH₃OH and 0.9% NaCl (b). Both microphotographs are shown using 120x magnification

staining can be observed after the addition of 10% CH₃OH solution.

4. Conclusions

Electrochemical impedance spectroscopy (EIS) was used to obtain data on the yeast layer of *Saccharomyces cerevisiae* adhered on the electrode surface. The Nyquist diagrams of the investigated electrochemical cells show that the addition of 0.9% NaCl solution with 10% CH₃OH decreased both the resistance and capacitance, suggesting that the electrode surface is released, and consequently it can be concluded, that methanol causes the death and desorption of yeast cells *Saccharomyces cerevisiae*. It was shown that all investigated electrochemical cells are effective in the detection of methanol in aqueous solutions. Large electrochemical cells where the active component is applied to a greater surface area (5 mm × 5 mm) and stainless steel electrochemical cells coated with a layer of WO₃ were found more effective. In the case of 0.050 mm thick electrochemical cells covered with a layer of WO₃, several times lower capacitance and resistance was observed than in the case of stainless steel electrochemical cells. Moreover WO₃ coated electrodes have lower conductivity compared to plain stainless steel electrodes and the yeast cells are better adhered onto the surface of the electrodes coated with WO₃ due to greater porosity of surface. Using the method of staining cells with methylene blue it was shown that methanol causes the death of yeast cells *Saccharomyces cerevisiae*.

It was demonstrated that all investigated electrochemical biosensors are effective in detecting methanol in aqueous solutions and that they are applicable using less expensive portable potentiostat/galvanostat instruments. Therefore, this opens a new approach in the biosensors development where the key is to assemble an inexpensive

and disposable electrochemical system, which can be used to detect harmful compounds. In the future, certain other toxins could be detected with yeast cells using our model of electrochemical biosensor assembly. Additionally, other biologically active components, such as enzymes, antibodies, or organ cells could be applied. Last but not least, low cost biosensors based on the presented approach, that would use simplified potentiostat/galvanostat, could be applied on large scale for environmental monitoring or even for medical diagnostics.

Acknowledgments

Financial support of the Slovenian Research Agency through programme (P2-0046, and P1-0403) as well as project (J1-2471) grants is gratefully acknowledged.

6. References

1. S. Singh, V. Kumar, D. S. Dhanjal, S. Datta, R. Prasad and J. Singh, *Microbial Biotechnology: Basic Research and Applications* **2020**, 317–335. DOI:10.1007/978-981-15-2817-0_14
2. B. Caballero, L. C. Trugo and P. M. Finglas, *Book Encyclopedia of food sciences and nutrition*, Academic, **2003**.
3. N. Bhalla, P. Jolly, N. Formisano and P. Estrela, *Essays Biochem* **2016**, 60, 1–8. DOI:10.1042/EBC20150001
4. S. Kamel and T. A. Khattab, *Biosensors (Basel)* **2020**, 10, 67. DOI:10.3390/bios10060067
5. F. Karim and A. N. M. Fakhruddin, *Reviews in Environmental Science and Bio/Technology* **2012**, 11, 261–274. DOI:10.1007/s11157-012-9268-9
6. K. Dziąbowska, E. Czaczyk and D. Nidzworski: *Biosensing Technologies for the Detection of Pathogens – A Prospective Way for Rapid Analysis*, **2018**. DOI:10.5772/intechopen.72175

7. T. Hoshikawa, M. Yamada, R. Kikuchi and K. Eguchi, *Journal of Electroanalytical Chemistry* **2005**, 577, 339–348. DOI:10.1016/j.jelechem.2004.11.040
8. R. Monošik, M. Stred'anský and E. Šturdík, *J Clin Lab Anal* **2012**, 26, 22–34. DOI:10.1002/jcla.20500
9. M. Rozman, B. Žener, L. Matoh, R. F. Godec, A. Mourtziou, E. Stathatos, U. Bren and M. Lukšič, *Electrochimica Acta* **2020**, 330, 135329. DOI:10.1016/j.electacta.2019.135329
10. N. Cotoalan, M. Rak, M. Bele, A. Cör, L. M. Muresan and I. Milošev, *Surface and Coatings Technology* **2016**, 307, 790–799. DOI:10.1016/j.surfcoat.2016.09.082
11. H. Martin-Yken, *Biosensors (Basel)* **2020**, 10, 51. DOI:10.3390/bios10050051
12. G. G. Stewart, **2014**, pp. 309–315. DOI:10.1016/B978-0-12-384730-0.00292-5
13. F. Farid, O. Sideeq, F. Khan and K. Niaz, **2019**, pp. 501–508. DOI:10.1016/B978-0-12-812491-8.00066-7
14. S.-O. Suh, M. Blackwell, C. P. Kurtzman and M.-A. Lachance, *Mycologia* **2006**, 98, 1006–1017. DOI:10.1080/15572536.2006.11832629
15. C. R. Landry, J. P. Townsend, D. L. Hartl and D. Cavalieri, *Molecular Ecology* **2006**, 15, 575–591. DOI:10.1111/j.1365-294X.2006.02778.x
16. J. Deacon, **2013**, pp. 142–157. DOI:10.1002/9781118685068
17. F. Sherman, in: C. Guthrie and G. R. Fink (Eds.): *Methods in Enzymology*, Academic Press, **2002**, pp. 3–41. DOI:10.1016/S0076-6879(02)50954-X
18. N. Meddings, M. Heinrich, F. Overney, J.-S. Lee, V. Ruiz, E. Napolitano, S. Seitz, G. Hinds, R. Raccichini, M. Gaberscek and J. Park, *Journal of Power Sources* **2020**, 480, 228742. DOI:10.1016/j.jpowsour.2020.228742
19. N. Jaffrezic-Renault, in: K. Wandelt (Ed.): *Encyclopedia of Interfacial Chemistry*, Elsevier, Oxford, **2018**, pp. 241–247. DOI:10.1016/B978-0-12-409547-2.13489-4
20. X. Fan, Z. Li, S. Wang, L. Liu, P. Liu, F. Chen and X. Zheng, *Journal of the Brazilian Chemical Society* **2019**, 30, 1762–1768. DOI:10.21577/0103-5053.20190081
21. E. Randviir and C. Banks, *Analytical methods* **2013**, 5, 1098–1115. DOI:10.1039/c3ay26476a
22. K. Kivirand, M. Min and T. Rinken: *Environmental Biosensors*, IntechOpen, **2019**. DOI:0.5772/intechopen.89334
23. K. Painting and B. Kirsop, *World J Microbiol Biotechnol* **1990**, 6, 346–7. DOI:10.1007/BF01201311

Povzetek

Razvili smo elektrokemijsko celico, ki služi kot modelni biosenzor, ter kot aktivno biološko komponento vsebuje glive kvasovke *Saccharomyces cerevisiae*. Testirali smo različne postopke sestave elektrokemijskih celic, kjer smo uporabili nerjavno jeklo, površina kovinske elektrode pa je bila po potrebi modificirana s tanko plastjo volframovega trioksida (WO_3). Na delovno elektrodo smo adherirali kvasovke *Saccharomyces cerevisiae*. Z modelnim biosenzorjem smo nato spremljali odziv na 10 % raztopino metanola pri različnih dimenzijah elektrod in modifikacijah površine. Za detekcijo smo uporabili metodo elektrokemijske impedančne spektroskopije (EIS), s katero smo merili frekvenčno odzivnost električnega toka in s tem pridobili podatke o adherirani plasti kvasovk na površinah elektrod, kot rezultat pa smo interpretirali Bodejeve in Nyquistove diagrame. Topografijo in sestavo elektrod smo dodatno preverjali s tehnikami vrstične elektronske mikroskopije in klasične optične mikroskopije. Predstavljeni biosenzor služi kot vzorčni primer za razvoj kompleksnejših biosenzorjev, ki kot aktivno plast uporabljajo žive celice.



Scientific paper

Synthesis of Adenine-based Fluorescent and Naked-eye Chemosensors: Specific DNA Probes for the Detection of Bacterial Pathogens

Burak Şener,¹ Ömür Baysal,^{1,*} Said Nadeem² and Ragıp Soner Silme³

¹ Department of Molecular Biology and Genetics, Faculty of Science, Muğla Sıtkı Koçman University, Menteşe-Muğla, 48121, Turkey

² Adnan Menderes Technology Development Incorporation (ADU Technopark), Aydın Adnan Menderes University, 80b, Efeler-Aydın, Turkey

³ Center for Research and Practice in Biotechnology and Genetic Engineering, Istanbul University, Istanbul, Turkey

* Corresponding author: E-mail: omurbaysal@mu.edu.tr
Tel. +90 252 2113240; Fax. +90 252 2111472

Received: 02-12-2021

Abstract

A rapid and confident tool to identify and diagnose bacterial pathogens with more accuracy using DNA as fingerprints is necessary. Herein, we report a smart chemosensor having a terminal adenine sticking to the thymine of single-stranded DNA (ssDNA) through supramolecular interactions and, which leaves ssDNA when the same ssDNA matches with the targeting desired DNA. We have synthesized a naked-eye coloured chemosensor with carbazole. As a model genetic material, DNA of *Clavibacter michiganensis* subsp. *michiganensis* was hybridized to ssDNA and immobilized over nitrocellulose membrane. The prepared adenine-chemosensor, by passing through the nitrocellulose-ssDNA membrane caused the formation of ssDNA nitrocellulose-ssDNA-adenine-chemosensor. FTIR results of the immobilized ssDNAs showed that the matching of same ssDNA releases the adenine-chemosensor from the surface of nitrocellulose-ssDNA that results in formation of the double stranded DNA. The selectivity of chemosensor was also confirmed with different bacterial DNA (*Bacillus subtilis*) as control. These data highlights accurate and reliable results of a new diagnostic kit prototype promising for further studies, which is able to diagnose DNA quickly and precisely.

Keywords: Bacterial pathogens; detection; DNA probe; kit designing; naked-eye chemosensor; nanotechnology

1. Introduction

Biosensors have recently become efficient analytical tools attracting the attention of researchers due to their easy, convenient and specific diagnosis potential compared to traditional methods. DNA-based method “DNA sensors or gene sensors” are specifically used for diagnosis and the detection of the targeted region.^{1–3} These biosensors usually relies on detecting the hybridization of the target ssDNA strand, which are complementary strands.^{1,2,4} The advances in molecular biology have become the reason for increasing the interest in the design of DNA hybridization-based biosensors.^{5–9} DNA-based biosensors can be used in many areas such as clinical, environmental and food safety issues. The principle of nucleic acid tests is

based on targeted DNA-primer or probe hybridization. Nucleotide sequences called primers or probes are compatible with bacterial DNA and hybrid molecules formed after adaptation. The diagnosis is made with the direct or indirect detection of the hybrid formation. In direct detection, the hybrid detected with the presence of a reporter molecule provides signal amplification, while the product resulting from enzymatic amplification of the hybrid is detected indirectly.¹⁰

Our study aims the synthesizing analytes binding to the ssDNA which acts as a biosensor, when the same strand meets the complementary DNA strand. This hybridized complex is used to identify the target DNA with the signal to be received depending on the separation of

the sensor. The originality of our study is using the chain of the whole target DNA as a probe. Diagnosis has been made by measuring the hybridization involving complementary and/or high similarity to the target DNA.

Many different methods can be used for the measurement of hybridization.¹ In recent years, new synthesised fluorescent materials such as quantum dots (QDs), up conversion nanoparticles and nano-clusters (NCs) have been extensively investigated.^{11–13} As reported in a previous study, modified biosensors based on electrochemical impedance spectroscopy, gold nanoparticles (AuNPs) have also been used in diagnosis of a toxin producer bacteria *Bacillus cereus*.¹⁴ Another diagnosis method relies on measuring the Fourier-transform infrared spectroscopy (FTIR) spectrum. As known, there are many studies on DNA-dependent diagnosis using FTIR and Raman spectra.^{15–17} In FTIR analysis, samples are exposed to infrared radiation. Infrared radiation activates the atomic vibrations in molecules and, specific absorption or transmission peaks are formed. This makes the FTIR technique very useful for molecular diagnostics cause of rapidly characterization with sensitivity and accuracy.^{18,19} Infrared spectra (IR) are divided into three spectra according to their wavelengths. These are far-IR ($<400\text{ cm}^{-1}$), mid-IR ($400\text{--}4000\text{ cm}^{-1}$) and near-IR ($4000\text{--}13000\text{ cm}^{-1}$) spectra. The most commonly used spectrum is the mid-IR spectrum consisting of four different parts; single bond region ($2500\text{--}4000\text{ cm}^{-1}$), triple bond region ($2000\text{--}2500\text{ cm}^{-1}$), double bond region ($1500\text{--}2000\text{ cm}^{-1}$), fingerprint region ($600\text{--}1500\text{ cm}^{-1}$).^{20,21}

The aim of our study is to synthesize molecules that can act as sensors binding to single-stranded DNA, and to make fast and sensitive DNA diagnosis with the help of FTIR spectra to be obtained based on the hybridization of these molecules with target DNA. As a result of our preliminary studies, we distinguished the same/different species on the basis of DNA matching.

2. Experimental

2. 1. Synthesis of Fluorescent Chemosensor

The fluorescence-based chemosensor was synthesized in three steps; alkylation of dihydroxybenzophenone, McMurry reaction and alkylation of adenine.

2. 1. 1. Alkylation of 4,4-dihydroxybenzophenone (1)

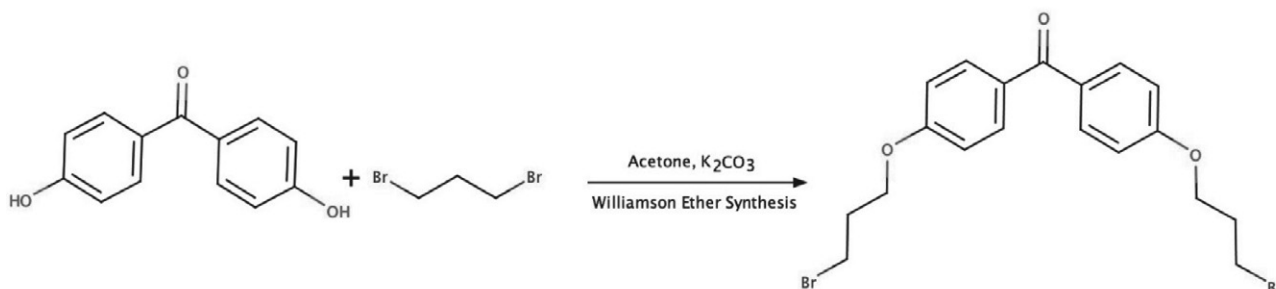
4,4-dihydroxybenzophenone (DBP) was chosen as the starting material for the synthesis of the Burak Synthesis Product (BSP-3) chemosensor. DBP was alkylated using Williamson ether synthesis (WES). For this purpose, 20 mL acetone, 0.43 g dihydroxybenzophenone, 700 μL dibromopropane and 1.38 g potassium carbonate were mixed as shown in Scheme 1. The reaction was followed by Thin-layer chromatography (TLC). After 2 hours stirring at 60°C , reaction mixture was extracted with chloroform, dried with sodium sulphate and evaporated using rotary evaporator. The crude extract was subjected to column chromatography using hexane and ethyl acetate (1:1, v/v). Pure alkylated DBP paste was dried and subjected to hydrogen-1 NMR (HNMR) (Bruker Ultrashield Plus Biospin- Avance III 400 MHz NaNoBay FT-NMR).

2. 1. 2. McMurry Reaction (2)

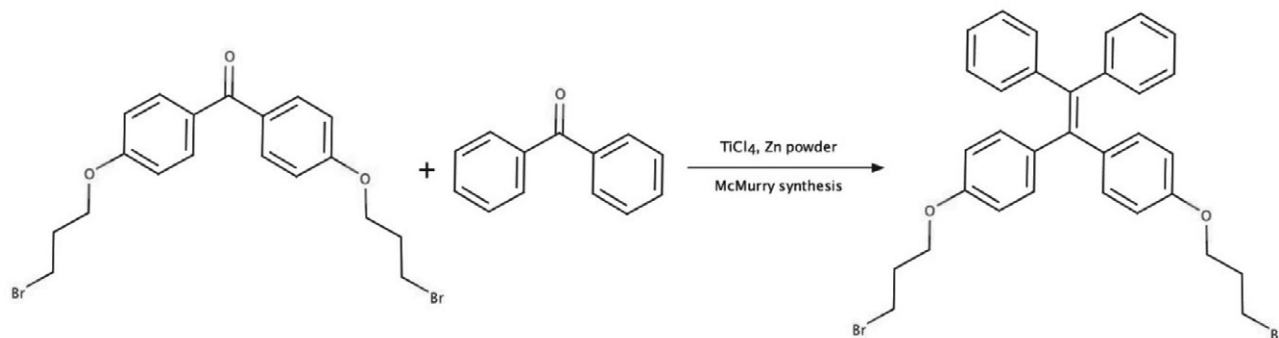
Alkylated DBP (1) was forwarded to McMurry reaction to put fluorescence properties into the molecule. For this purpose, 0.566 g of zinc powder, 10 mL of Tetrahydrofuran (THF), and 0.476 mL of TiCl_4 were added into a dried flask and mixed on a magnetic stirrer as shown in Scheme 2. The mixture was refluxed at 90°C for two hours. 0.2 g of diphenylketone was transferred into the flask and refluxed further for 4 hours. The mixture obtained was poured into 10% 30 mL K_2CO_3 and vortexed for five minutes. It was left to dry after filtering and washing processes. The mixture obtained was separated by column chromatography and visualized under UV on the TLC layer. The photophysical properties of the product were determined by Perkin Elmer LS 55 fluorescence spectroscopy. The molecular structure of the product was checked by HNMR analysis.

2. 1. 3. Alkylation of adenine using the McMurry product (3)

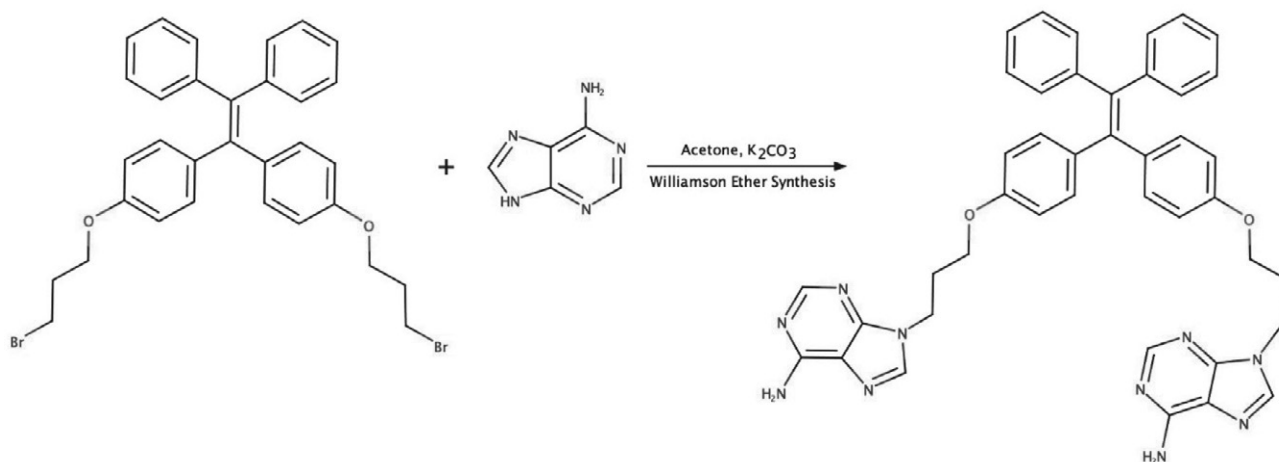
Adenine was attached to the McMurry product to obtain the final DNA-based chemosensor. After the necessary calculations, 0.076 g of adenine base was added to the dissolved (0.5g) McMurry product with acetone and mixed in a magnetic stirrer for 24 hours at 60°C as shown



Scheme 1. Alkylation of 4,4-dihydroxybenzophenone using Williamson ether synthesis.



Scheme 2. McMurry reaction of alkylated benzophenone.



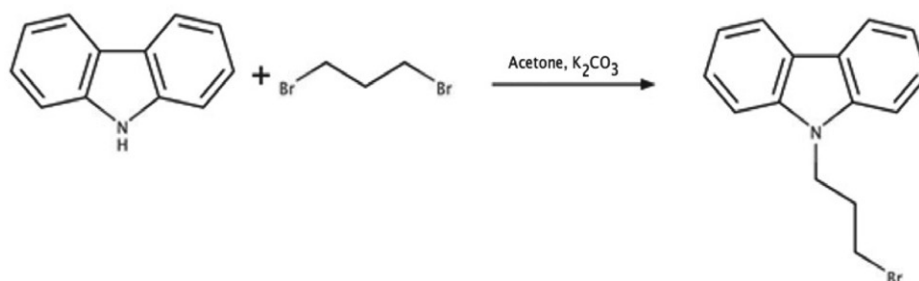
Scheme 3. Alkylation of adenine to get the final fluorescent chemosensor.

in Scheme 3. Various combinations of heptane, chloroform and ethanol were used to check the TLC.

2. 2. Synthesis of Naked-eye Chemosensor

2. 2. 1. Alkylation of Carbazole (4)

To produce a naked-eye chemosensor, 9H-carbazole was also passed through all the steps mentioned above, except the McMurry reaction, used for the alkylation of DBP. Commercially purchased 9H-carbazole compound (Sigma Aldrich) 167 mg, 0.612 mL of 1,3-dibromopropane, 200 mg of potassium carbonate and 10 mL acetone were mixed on magnetic stirrer for 24 hours at room temperature to obtain the alkylated carbazole as shown in Scheme 4.

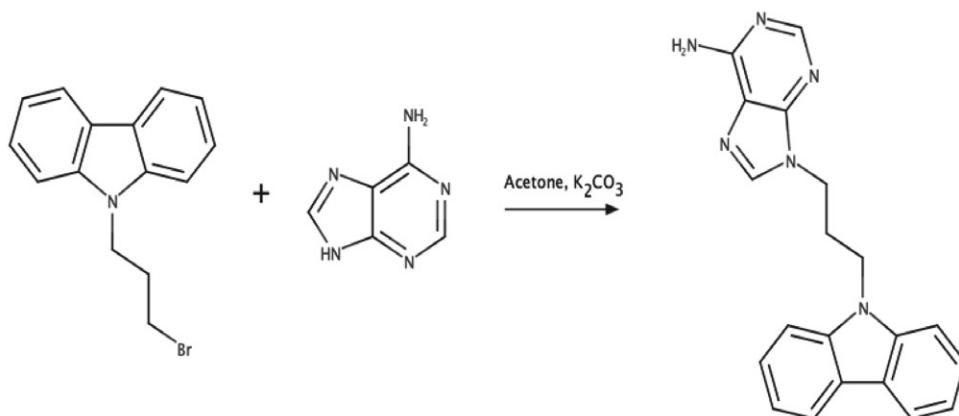


Scheme 4. Alkylation of Carbazole compound.

The crude mixture was poured in distilled water to dilute produced salts. The organic phase was extracted using ethyl acetate and further dried over sodium sulphate and evaporated using rotary evaporator. The extract was forwarded to purification by column chromatography. The purified product did not need any additional purification process.

2. 2. 2. Alkylation of Adenine (5)

Of adenine base 1 mol, 2 moles of potassium carbonate and 15 mL of acetone were added to 1 mol of the alkylated-carbazole. The reaction mixture was stirred at room temperature on magnetic stirrer for 1 day as shown in Scheme 5.



Scheme 5. Williamson ether synthesis of adenine.

2. 3. Preparation and Fixation of DNA

DNA of *Clavibacter michiganensis* subsp. *michiganensis* (Cmm) and *Bacillus thuringiensis* (Bt) were used to test the supramolecular interactions of synthesized chemosensors. The Cmm isolate was grown in shaking liquid nutrient broth medium and incubated at 27 °C with 120 rpm for 72 h.²² Stock Bt culture was also inoculated into same liquid medium and grown as Cmm culture. After incubation, DNA was isolated from the performed cultures using the Gene JET Genomic DNA Purification Kit. All

Cmm and Bt DNAs were denatured by diluting 1:10 in distilled water, then kept in a 95°C water bath for 30 minutes and chilled in ice for 15 minutes. Denatured Cmm and Bt ssDNAs (~ 20 ng /μL) were separately fixed by dripping them onto nitrocellulose membranes.

2. 4. Hybridization of ssDNAs with Biosensors

The fixed Cmm and Bt ssDNAs were dried, 10 μL of chemosensors (3 and 5) were dripped separately on each

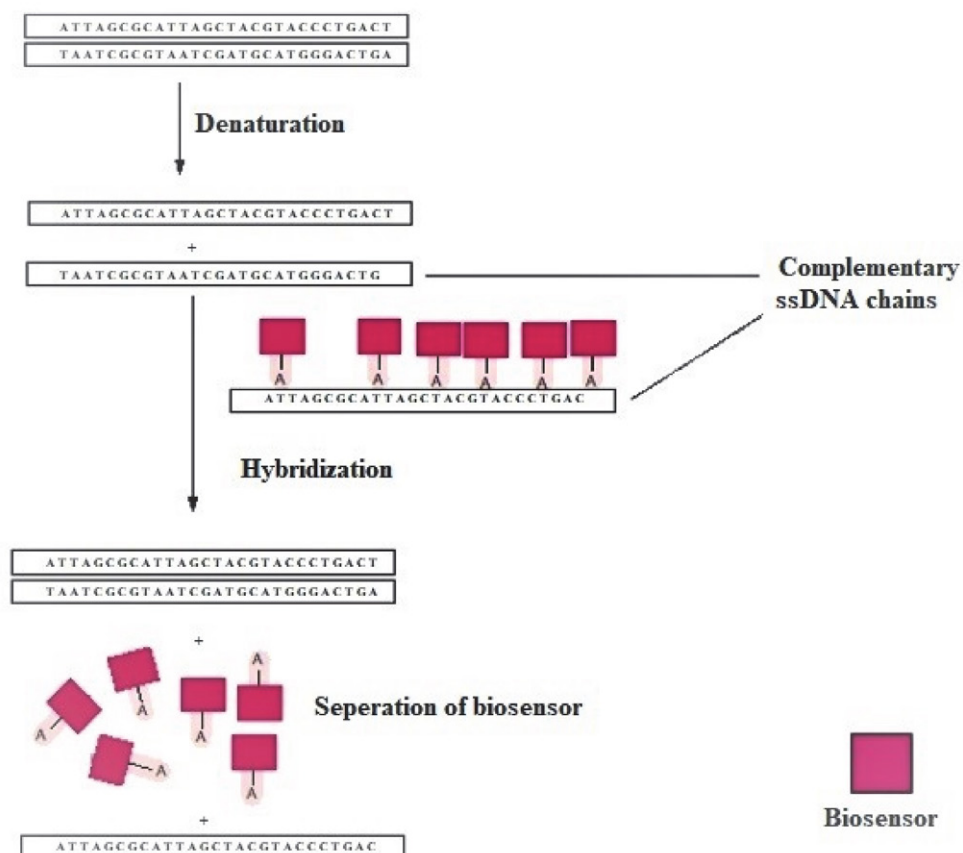


Figure 1. Separation of the biosensor from the hybrid complex with the matching of complementary ssDNAs.

membrane. After the membranes were dried, some membranes were washed with distilled water to eliminate non-specific binding. Then, during the drying process, other Cmm and Bt ssDNAs (~ 20 ng/ μ L) were dripped onto the membrane to fix DNAs of the same species. Once complementary ssDNAs had been fixed, the connection of the biosensor was established with the DNA on the fixed surface and weak adenines were washed off (Figure 1). As negative control, ssDNAs of different species were compiled together to see whether the biosensor was separated from the reaction surface. At all stages, analysis was performed by FTIR-ATR (Attenuated total reflectance) transmittance spectra.

2. 5. FTIR Analysis and Data Processing

ACD/ Spectrus Processor program was used to process the raw FTIR data. Correction procedures involving auto baseline correction, smoothing and auto threshold resolution procedures were applied to all data, respectively. Transmittance peak values were recorded from all data. The noise factor was set to 3 and the minimum peak intensity was set to 10%. Thus, very weak bands were eliminated. IRPal 2.0 and IR Wizard 2019 beta programs were used to observe functional groups and bonds in the samples.

3. Results

The peaks of the methylene ($-\text{CH}_2-$) groups in the structure of the synthesized BSP-3 chemosensor were determined by HNMR analysis (Figure 2a). As a result of HNMR, three methylene ($-\text{CH}_2-$) groups should be observed in aromatic and aliphatic regions. Hydroxybenzophenone and benzophenone peaks were observed in the aromatic region of the HNMR spectrum at 7.02, 6.97 and 6.65 ppm. In addition, peaks were at 4.01, 3.60 and 2.27

ppm in the aliphatic methylene ($-\text{CH}_2-$) region. The data showed that the chemosensor was synthesized purely.

BSP-3 chemosensor known to be fluorescent emitted high fluorescence as expected when viewed under UV. Chloroform, acetone and dimethylformamide were used as mobile phase in TLC, but the chemosensor did not work with a solvent except for acetone (Figure 2b).

FTIR measurement was recorded from the empty nitrocellulose membrane as a blank (Figure 3a). Figure 3b shows the FTIR analysis result recorded after Cmm ssDNA addition onto the nitrocellulose membrane. The band at 3331 cm^{-1} are hydrogen bonds that displays stretching movements such as O-H and N-H in the DNA structure. The band in 1105 cm^{-1} shows carbon bond stretching movements such as C-N, C-C and C-O, and band C-O and P-O stretches observed in 1029 cm^{-1} . Phosphate group bonds are important for the proving of DNA hybridized onto the membrane.

The graphic formed after adding BSP-3 chemosensor to the membrane is shown with line in Figure 3a. Particularly, the new band at 1509 cm^{-1} is important to represent the C = C double bond contained in BSP-3, on account of there is no aliphatic C = C bond in the DNA structure. This band proved the hybridization of chemosensor onto the membrane.

In another experiment, once Cmm ssDNA has introduced onto the membrane, the OH and NH bands stretch at 3330 cm^{-1} , P = O bonds stretch at 1314 cm^{-1} and 1157 cm^{-1} , CO, CN and CC stretches in 1106 cm^{-1} , PO stretches in 1053 cm^{-1} , as in the previous results (yellow line spectrum) (Figure 4a). In FTIR results obtained after BSP-3 treatment, C = C double bond at 1622 cm^{-1} was detected as a sharp band (black line spectrum) (Figure 4b).

When a different Cmm ssDNA was dripped on the membrane, the C = C sharp band disappeared as expected (blue line spectrum) (Figure 5). As we stated in our hypothesis, the chemosensor was separated from the DNA hybrid with matching the complementary DNA. With the

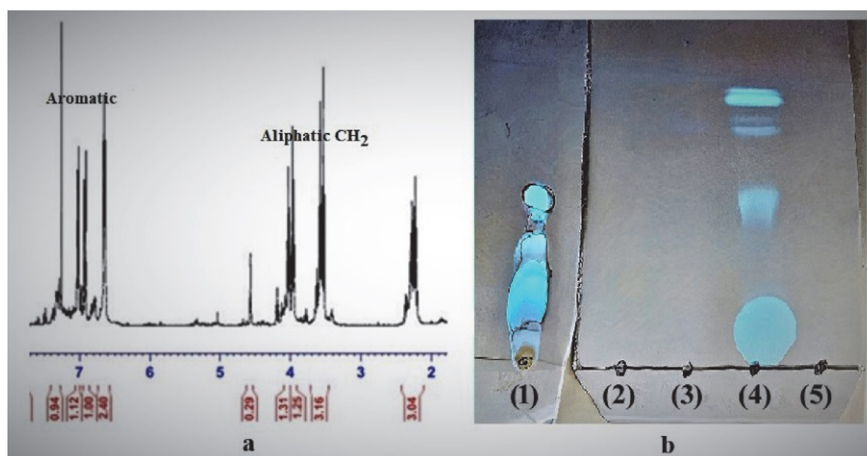


Figure 2.a. HNMR analysis of chemosensor 3; **b.** (1) The appearance of fluorescence BSP-3 (2) DMF, (3) Chloroform, (4) Acetone and (5) H₂O under UV light on TLC.

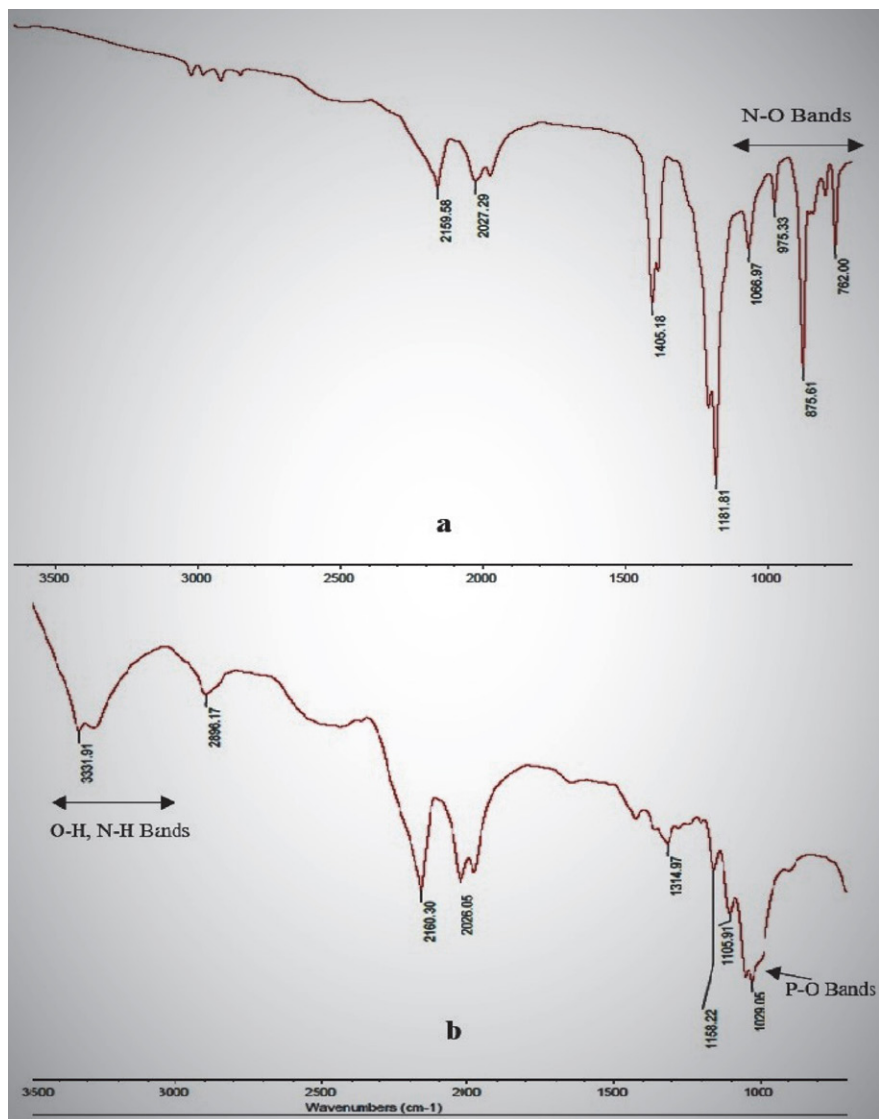


Figure 3. a. Nitrocellulose membrane (Blank) FTIR Transmittance Image, b. Membrane + Cmm ssDNA FTIR Transmittance Image.

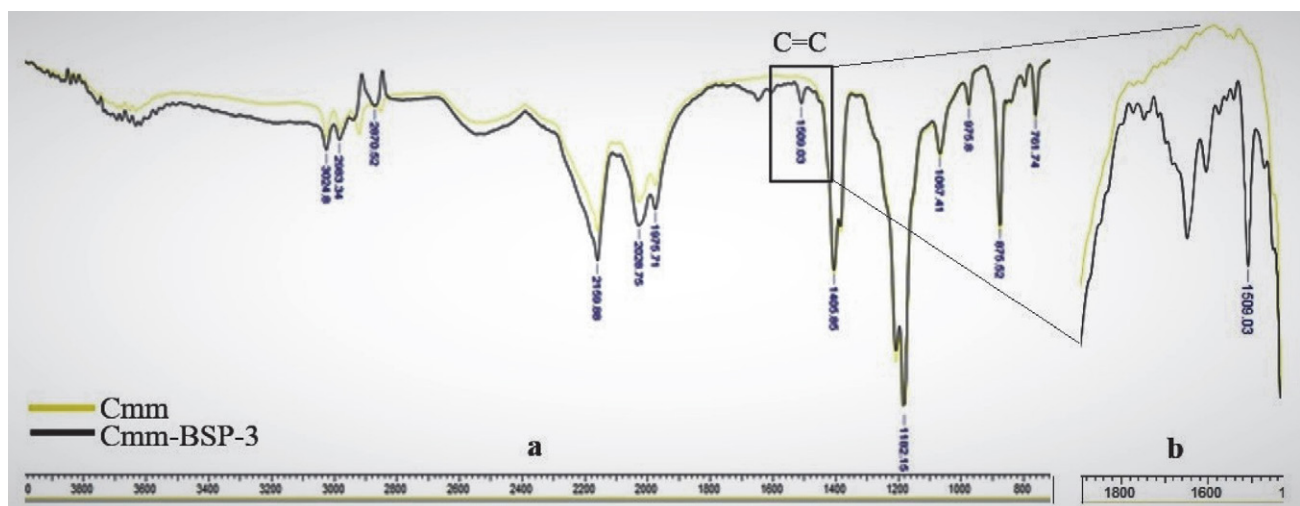


Figure 4 a. FTIR Image after BSP-3 addition b. Zoomed FTIR image of C = C band showing BSP-3.

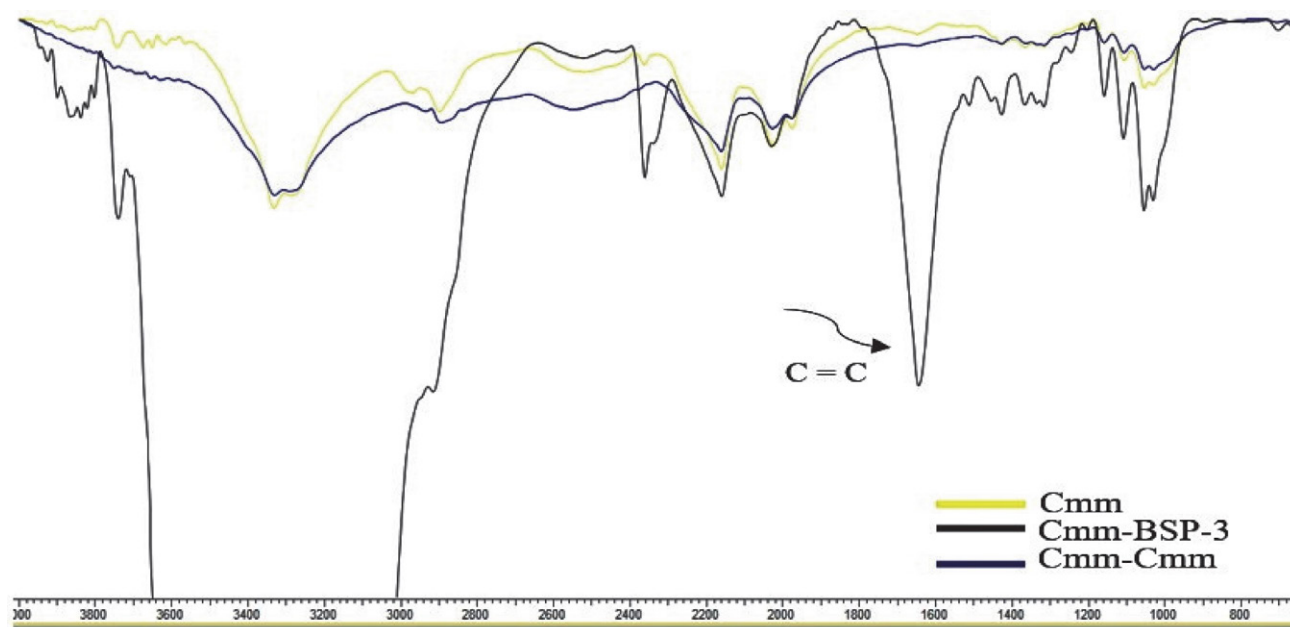


Figure 5. Band recorded by BSP-3 disappears with Cmm-Cmm hybrid.

separation of the chemosensor from the surface, it is concluded that the DNA belongs to the same species.

Different bacterial DNAs were used as negative control. As a result, to eliminate non-specific binding after BSP-3 treatment, the membrane washed off with distilled water. After rinsing, Bt ssDNA was dripped onto the membrane. In further step, it is expected that the BSP-3 chemosensor will not release from the hybrid and the C = C bond will continue to appear as a result of FTIR cause of non-complementary ssDNAs. In fact, our hypothesis was

confirmed in FTIR analysis. In Figure 6, the presence of the band recorded by BSP-3 at 1648 cm^{-1} after rinsing and Bt ssDNA treatment is shown as vertical and horizontally zoomed.

Bt-Bt hybrid was used with carbazole in the experiment. Peak was observed at 1652 cm^{-1} after the carbazole treatment. These observed peaks are much sharper after rinsing. When the second Bt ssDNA was added, these peaks became very weak. This means that the signal observed by the chemosensor becomes weaker (Figure 7).

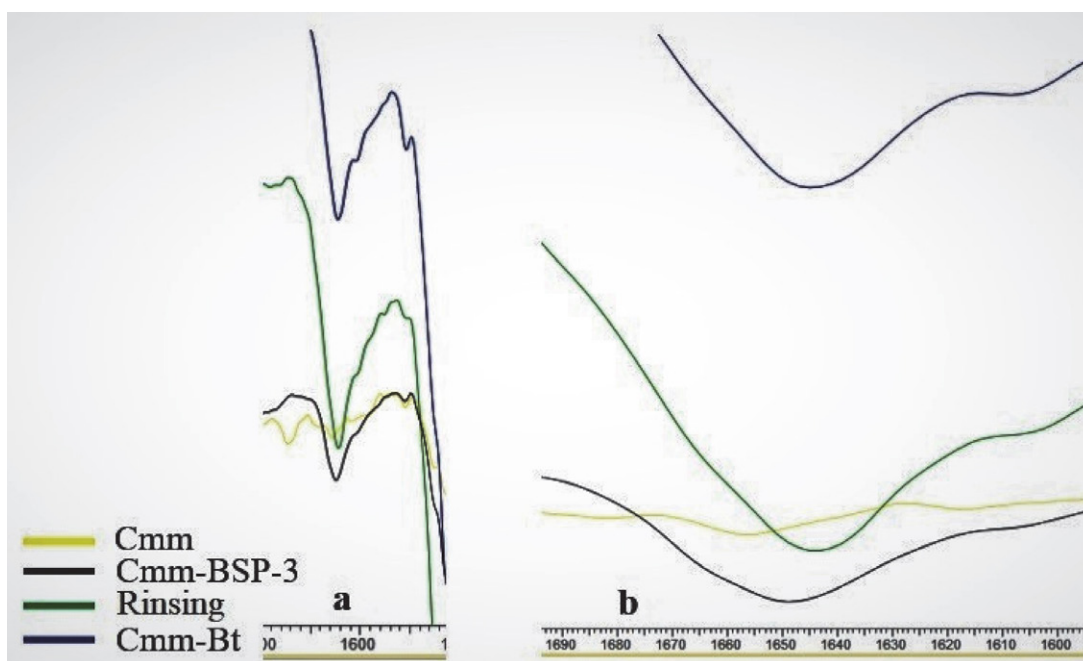


Figure 6. a. Vertical zoomed FTIR bands, b. horizontal zoomed FTIR bands. BSP-3 chemosensor emits the signal due to non-complementary ssDNAs.

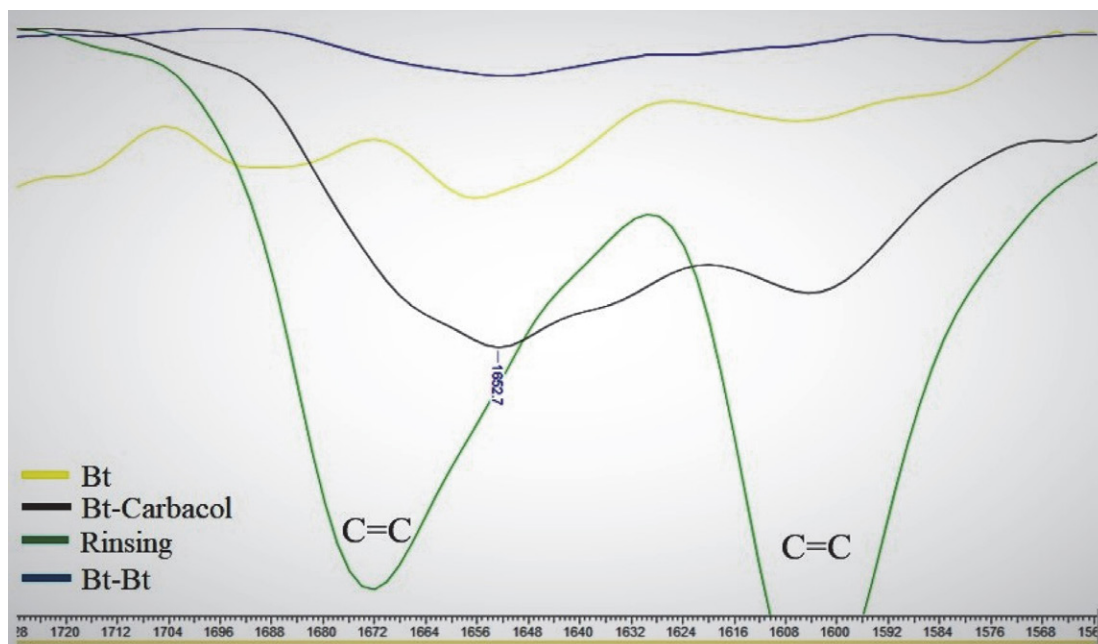


Figure 7. The peaks of carbazole disappear after the Bt-Bt matching at 1600 and 1672 cm^{-1} .

4. Discussion

In our study, we have developed a diagnostic method that relies on DNA-based ssDNA chain and chemosensor hybridization. Our method involves a different and novel version of the chemosensor used by Arulraj et al. 2015, which changes its fluorescence due to the presence of Ag^+ in the environment.²³ Our synthesized chemosensor enables us to diagnose based on DNA replacing Ag^+ and depending on the changes with IR spectrum. The synthesized chemosensors have fluorescent properties and they can be detected under UV lamp after synthesis cause of its emitting fluorescence. We have examined in detail whether the product obtained at every step of the synthesis is pure as a targeted molecule. Benzophenone and hydroxybenzophenone peaks in the chemosensor were detected by NMR analysis. In addition, the aliphatic methylene ($-\text{CH}_2-$) peaks showed that synthesis was completed.

The rapid diagnosis with high accuracy using FTIR analysis can be suggested by BSP-3. Due to bands of BSP-3 with densities varying between 6–10%, the desired difference could not be achieved in some trials. By keeping the noise factor high, we minimized the bands which may cause the deceptive measurements.

Another compound used as a chemosensor was carbazole. It has been stated that carbazole can bind to human telomeric G-quadruple DNA and stabilizes and the previous studies indicated it as an anti-carcinogenic agent.^{24,25} As a pioneer study, we showed the carbazole as a chemosensor that could also bind to microbial DNA. In the diagnosis with carbazole, the actions of aromatic C = C bonds were used by BSP-3. Although the presence of aromatic C = C bonds in DNA bases causes a problem, the carbazole

separation was followed from the hybrid-formation depending on the band density. In the experiment with carbazole, rinsing with water increased the severity of the peak recorded by the carbazole.

Diagnostic methods using chemosensors seem a good alternative to conventional methods such as PCR.²⁶ Most DNA chemosensor techniques are based on hybridization techniques in which DNA is detected by electroluminescence, fluorescence or calorimetric methods.²⁶ The diagnostic method based on chemosensor as a prototype kit designed in our study mimics other methods in terms of fixing the DNA to a surface and measurements relied on hybridization. The most prominent aspect that distinguish our diagnostic kit of other suggested methods is the use of whole DNA as a template and the measurement of its hybridization. In other tested methods, while the measurement is performed in the form of detecting the DNA bound to the chemosensor, in our study it works with the detection of the chemosensor separated from the environment which resulted the binding of the complementary ssDNA.²⁶ Since the method detects indirectly, its sensitivity and accuracy ratio could be relatively lower than other methods relied on direct hybridization. In addition, the method has advantages, it does not require expensive equipment and can be applied practically compared to other detection methods.

The accurate and reliable results of the developed diagnostic kit are promising for future studies. It is possible that this kit, which can diagnose DNA quickly and precisely with a new technique, will become even more comprehensive by further studies. For example, the use of a triple hydrogen bonding guanine or cytosine base instead of the

adenine base is another option. There are many variables such as concentrations of DNA, additional chemosensors, hybridization temperatures and drying times of membranes. These factors can be considered as the primary actions for the diagnosis to work with an accuracy of almost 100% by setting them according to optimum standards. Moreover, it seems possible to convert the bacterial DNA diagnostic kit, which we have presented as a prototype, into a commercial product.

5. Conclusion

A hydroxybenzophenone-based fluorescence chemosensor and a carbazole-based naked-eye chemosensor were both prepared separately. The idea was to utilize the supramolecular interactions of adenine with thymine in the identification of DNA-based pathogens. Adenine was chemically binded to the both chemosensors and settled over the ssDNA, thereby the adenine of the chemosensor would bind to the thymine of the ssDNA. As ssDNA binds with the same exact ssDNA more strongly, it was supposed that the presence of the same ssDNA would remove the adenine of chemosensor from the immobilized ssDNA. Supramolecular interactions of the adenine-chemosensor with the ssDNA were analyzed using FTIR spectra that clearly showed the tested ssDNA removes the adenine-chemosensor from the immobilized ssDNA when both ssDNA were the same. However, sophisticated techniques are necessary to obtain optimum conditions affecting different parameters such as pH, solvent, temperature and buffer required for kit manufacturing in commercialization process. Our method will provide rapid and most accurate fingerprint to identify any kind of pathogen with further studies.

Acknowledgement

The authors wish to thank Scientific Research Projects Department of Muğla Sıtkı Koçman University for financial support with projects Nr.17/090 and Nr.19/082/03/1/2 and to Merve Çolak, Suna Savran for technical assistance concerning chemosensor synthesis process.

6. References

1. Y. Du, S. Dong, *Anal. Chem.* **2017**, *89*, 189–215. DOI:10.1021/acs.analchem.6b04190
2. F. Teles, L. P. Fonseca, *Talanta*. **2008**, *77*, 606–623. DOI:10.1016/j.talanta.2008.07.024
3. T. G. Drummond, M. G. Hill, J. K. Barton, *Nat. Biotechnol.* **2003**, *21*, 1192–1199. DOI:10.1038/nbt873
4. A. Sassolas, B. D. Leca-Bouvier, L. J. Blum, *Chem. Rev.* **2008**, *108*, 109–139. DOI:10.1021/cr0684467
5. B. Şener, Rapid Diagnostic Kit Design for Bacterial Cancer Diagnosis. Master Thesis. Thesis Nr. 650831, Muğla Sıtkı Koçman University, Muğla, **2020**, 96 p. (In Turkish).
6. K. J., Odenthal, J. J. Gooding, *Analyst*. **2007**, *132*, 603–610. DOI:10.1039/b701816a
7. M. Minunni, S. Tombelli, E. Mariotti, M. Mascini, M. Mascini, *Fresenius J. Anal. Chem.* **2001**, *369*, 589–593. DOI:10.1007/s002160100761
8. S. Hahn, S. Mergenthaler, B. Zimmermann, W. Holzgreve, *Bioelectrochemistry*, **2005**, *67*, 151–154. DOI:10.1016/j.bioelechem.2004.07.006
9. H. Nakamura, I. Karube, *Anal. Bioanal. Chem.* **2003**, *377*, 446–468. DOI:10.1007/s00216-003-1947-5
10. A. Muthukumar, N. L. Zitterkopf, D. Payne, *Lab. Med.* **2008**, *39*, 430–436 DOI:10.1309/M6MBU1KGP0FF1C00
11. X. Chu, X. Dou, R. Liang, M. Li, W. Kong, X. Yang, J. Luo, M. Yang, M. Zhao, *Nanoscale*, **2016**, *8*, 4127–4133. DOI:10.1039/C5NR08284F
12. S. Dai, S. Wu, N. Duan, Z. Wang, *Talanta*. **2016**, *158*, 246–253. DOI:10.1016/j.talanta.2016.05.063
13. Y. Teng, X. Jia, S. Zhang, J. Zhu, E. Wang, *Chem. Commun.* **2016**, *52*, 1721–1724. DOI:10.1039/C5CC09138A
14. Z. Izadi, M. Sheikh-Zeinoddin, A. A. Ensafi, S. Soleimani-Zad, *Biosens. Bioelectron.* **2016**, *80*, 582–589. DOI:10.1016/j.bios.2016.02.032
15. L. Potocki, J. Depciuch, E. Kuna, M. Worek, A. Lewinska, M. Wnuk, *Int. J. Mol. Sci.* **2019**, *20*, 988. DOI:10.3390/ijms20040988
16. A. M. Hamad, H. M. Fahmy, W. M. Elshemey, *Radiat. Phys. Chem.* **2020**, *166*, 108522, DOI:10.1016/j.radphyschem.2019.108522
17. J. D. Fredericks, P. Bennett, A. Williams, K. D. Rogers, *Genetics*. **2012**, *6*, 375–380. DOI:10.1016/j.fsigen.2011.07.014
18. R. E. Kirk, D. F. Othmer, *Encyclopedia of Chemical Technology*, 5th edition, Wiley, New York, **2004**, 864 p.
19. N. Jaggi, D. Vij, in: D. Vij (Ed.), *Handbook of Applied Solid State Spectroscopy*, Springer, Boston, **2006**, pp. 411–450.
20. J. Coates, in: R. A. Meyers (Ed.), *Encyclopedia of Analytical Chemistry*, John Wiley & Sons Ltd, Chichester, **2000**, pp. 10815–10837.
21. A. B. D. Nandiyanto, R. Oktiani, R. Ragadhita, *Indones. J. Sci. Technol.* **2019**, *4*, 97–118. DOI:10.17509/ijost.v4i1.15806
22. Ö. Baysal, F. Mercati, H. İkten, R. Ç. Yıldız, F. Carimi, Y. Aysan, J. A. Teixeira da Silva, *Physiol. Mol. Plant Pathol.* **2011**, *75*, 113–119. DOI:10.1016/j.pmpp.2010.10.002
23. A. D. Arulraj, R. Devasenathipathy, S-M. Chen, V. S. Vasantha, S-F. Wang, *Sens. Biosensing Res.* **2015**, *6*, 19–24. DOI:10.1016/j.sbsr.2015.10.004
24. A. Gluszyńska, B. Juskowiak, B. Rubiś, *Molecules* (Basel, Switzerland), **2018**, *23*, 3154. DOI:10.3390/molecules23123154
25. C. C. Chang, J. Y. Wu, C. W. Chien, W. S. Wu, H. Liu, C. C. Kang, L. J. Yu, T. C. Chang, *Anal. Chem.* **2003**, *75*, 6177–6183. DOI:10.1021/ac034789i
26. M. Khater, A. de la Escosura-Muñiz, A. Merkoçi, *Biosens. Bioelectron.* **2017**, *93*, 72–86. DOI:10.1016/j.bios.2016.09.091

Povzetek

Detekcija in identifikacija patogenih bakterij zahteva razvoj hitrih in zanesljivih metod temelječih na značilnem DNA odtisu. V tem delu poročamo o razvoju inteligentnega kemosenzorja s terminalnim adeninom, ki se poveže s timinom enovijačne DNA (ssDNA) preko supramolekularnih interakcij ter se sprosti z enovijačne DNA v prisotnosti ujemajoče DNA. Pripravili smo kemosenzor osnovi karbazola, katerega obarvanost je mogoče zaznati s prostim očesom. Kot modelni genski material smo uporabili enovijačno DNA *Clavibacter michiganensis* podvrste *michiganensis*, ki smo jo imobilizirali na nitrocelulozno membrano. Sintetiziran adeninski kemosenzor smo prečrpali skozi membrano z imobilizirano enovijačno DNA pri čemer se je nanjo vezal in tvoril ssDNA nitrocelulozni-ssDNA-adeninski-kemosenzor. FTIR analiza imobilizirane enovijačne DNA je pokazala, da prisotnost ujemajoče enovijačne DNA povzroča sproščanje adeninske kemosenzorja in tvorbo dvovijačne DNA. Selektivnost kemosenzorja je bila potrjena z uporabe kontrolne DNA *Bacillus subtilis*. Podatki kažejo, da je metoda točna in zanesljiva ter predstavlja prototip diagnostičnega kita za hitro in natančno določanje DNA.



Except when otherwise noted, articles in this journal are published under the terms and conditions of the Creative Commons Attribution 4.0 International License

Scientific paper

Selective Removal of Sodium Ions from Aqueous Media Using Effective Adsorbents: Optimization by RSM and Genetic Algorithm

Lei Yao,^{1,*} Chao Hong,² Hani Dashtifard³ and Hossein Esmaeili⁴¹ College of Civil and Architecture Engineering, Chuzhou University, Chuzhou 239000, Anhui, China² Nanjing Siweipu Environmental Protection Technology Co., Ltd., Nanjing 210000, Jiangsu, China³ Department of Chemical Engineering, Bushehr Branch, Islamic Azad University, Bushehr, Iran

* Corresponding author: E-mail: yaolei@chzu.edu.cn

Received: 02-19-2021

Abstract

This study aimed to determine the best adsorbent among *Moringa oleifera*-derived activated carbon (AC), eggshell-derived CaO nanoparticles and CaO/Fe₃O₄ for sodium (Na⁺) removal from aqueous media. In the first step, the appropriate adsorbent for sodium adsorption was determined among the three adsorbents, which the results showed that the AC had the highest sorption efficiency. Then, response surface methodology (RSM) was used to evaluate the impact of different factors on the Na⁺ ion sorption efficiency using the AC. The highest removal efficiency was obtained to be 95.91% at optimum conditions such as pH of 11, contact time of 45 min, temperature of 25 °C, sodium ion concentration of 900 mg/L, and adsorbent dosage of 5 g/L. Also, the best conditions using the genetic algorithm was obtained at contact time of 94.97 min, adsorbent dosage of 3.52 g/L, Na⁺ ion concentration of 939.92 mg/L and pH value of 10.92. Moreover, the maximum sorption capacity using the Langmuir model was obtained to be 249.67 mg/g, which was a significant value. Besides, the equilibrium and kinetic studies indicated that the experimental data of sodium adsorption process were fitted well with the Langmuir isotherm model and the pseudo-second-order kinetic model, respectively. Furthermore, the thermodynamic study indicated that the sorption process was endothermic. Generally, among the three adsorbents used, activated carbon with a high removal efficiency and significant sorption capacity can be considered as a promising adsorbent for the removal of sodium from wastewater on an industrial scale.

Keywords: Adsorption, sodium, *Moringa oleifera*, Response surface methodology (RSM), Genetic algorithm

1. Introduction

For the past several decades, there has been a growing concern about water pollution, which affects animals, plants, and humans.^{1,2} Sea water is a good source of sodium ion, the salinity which does not allow humans to consume it. Sodium ion is a major component in the sea water, where its weight percent is about 16 times higher than magnesium ions, about 22 times higher than sulfur ions and about 48 times higher than bromine and potassium ions.³ The shortage of water resources and the risk of water crisis in the world as well as the pollution of surface and underground water resources with sodium ion and other pollutants from industrial and municipal sewage has made

it necessary to find environmentally acceptable solutions for the elimination of these contaminants from water.⁴ The main sources of water pollution with sodium are human activities. Excessive consumption of sodium over the standard level causes various sicknesses like high blood pressure, the risk of cardiovascular illnesses, heart attack, and damages to kidneys.⁵

There are various methods to eliminate pollutants from wastewater, including ion exchange, reverse osmosis, biological process, electro dialysis, distillation, and chemical precipitation.⁶ The reverse osmosis and ion exchange processes can't selectively eliminate sodium ion and require continuous regeneration; these two processes do not make any chemical changes in sodium and result in pollut-

ed wastewater.^{7,8} The biological process is mainly applied to wastewater and is not preferred for water treatment processes due to the application of organic materials and the need for maintenance. Furthermore, the resultant biological sludge needs to be treated before disposal.⁹

Adsorption process is more effective than other techniques in the elimination of pollutants, even at low concentrations (1 mg/L).¹⁰ Depending on the type of the adsorbent, this simple and applicable method is superior from the aspects of capital cost, reuse of wastewater, simplicity, and flexibility of design, easy operation, and insensitivity to toxic compounds and pollutants.^{11,12}

One of the main adsorbents used in this field is activated carbon (AC), which is made from various herbal resources. Activated carbon can be used to remove metal ions from water and wastewater due to many advantages such as the simplicity in its synthesis, high specific surface area, high sorption performance, low-cost, and ability to remove low concentrations of heavy metal ions.^{13–15}

Iron oxide nanoparticles are also known to be an available, cheap, and environmentally friendly material for effective sorption of pollutants due to their easy synthesis process. The magnetic nature of these nanoparticles allows their easy separation from pollutants through an external magnetic field. Considering some properties like the area to volume ratio, easy separation, recovery of nanoparticles by using an external magnetic field, low toxicity, and possibility of surface modification of nanoparticle resulted in their high efficiency of sorption. Also, the surface of magnetic materials can be modified by other materials such as CaO to increase their adsorption capacity.^{16–18}

Moreover, the eggshell is an important adsorbent for the elimination of dyes and heavy metals from wastewater and has been applied several times in previous studies.¹⁹

Different adsorbents have been used so far for removal of sodium ions from aqueous solutions, which some of them are included zeolites,⁴ chitosan,²⁰ activated carbon made from rice husk²¹ and polyantimonic acid.²²

This study aims to compare the ability of cheap adsorbents like AC made from *Moringa oleifera* leaf, eggshell-derived CaO nanoparticles, and CaO/Fe₃O₄ composite in the removal of sodium ion from synthetic wastewater, which these adsorbents have not been used to remove sodium ions in previous studies. Different analyses such as X-ray diffraction (XRD), scanning electron microscope (SEM), Brunauer–Emmett–Teller (BET), and Fourier-transform infrared spectroscopy (FTIR) were used to determine the surface properties of the activated carbon. Also, different parameters such as temperature, contact time, pH, and sorbent dosage were studied on the Na⁺ ion removal, and the best conditions were obtained using the response surface method (RSM). Also, the equilibrium, kinetic, and thermodynamic behaviors of the sorption process were studied. Moreover, genetic algorithm method was applied to optimize the best conditions for Na⁺ removal using the AC, which is another innovation of this research.

2. Materials and Methods

2.1. Chemicals

In this work, FeCl₂·4H₂O and FeCl₃·6H₂O were purchased from Merck Co. (Germany, purity>99%) and were used for preparing iron oxide. Sodium chloride (NaCl, purity>99%), sodium hydroxide (NaOH, purity>99%) and hydrochloric acid (HCl, purity=37%) were all supplied from Merck Co. (Germany). For the preparation of stock solution with 1000 ppm concentration, 2.543 g NaCl was dissolved in 1000 ml double distilled water. For preparing other solutions with lower concentrations, the stock solution was diluted with double distilled water.

2.2. Preparation of Activated Carbon from *Moringa Oleifera* Plant

The *Moringa oleifera* is a native plant of Bushehr province (Iran), which was utilized to produce AC. To do this, the *Moringa oleifera* leaves were placed in a furnace at 650 °C for 4 hours and then was pulverized and sieved by a 25-mesh size sieve. Then, the resultant powder was kept in glass bottles for uptake tests. To determine surface characteristics of the AC, XRD, SEM, BET, and FTIR analyses were carried out. The XRD analysis was used to determine the crystalline phases of the AC. Additionally, SEM and FTIR analyses were done to determine the morphology and functional groups in the AC structure, respectively. Also, BET analysis was applied to determine the specific surface area of the adsorbent.

2.3. Preparation of CaO and CaO/Fe₃O₄ from Eggshell Waste

To prepare CaO, eggshell wastes were first washed for several times with tap water and then was placed in an oven at 105 °C to be dried completely. After being dried, the eggshells were placed in a furnace at 800 °C for 4 hours. After this time, the eggshells were cooled down at room temperature. The calcined eggshells were pulverized in a mill and then stored in plastic bottles.¹³ To support Fe₃O₄ nanoparticles on the CaO structure obtained from eggshells, a solution containing Fe⁺³ and Fe⁺² with a 2:1 molar ratio was prepared. Then, about 1 g of CaO was added to the solution and it was blended for 20 min with mixing rate of 400 rpm. Then, sodium hydroxide with 3 M concentration was added dropwise to this solution, and the oxidation process progressed. The addition of sodium hydroxide was continued until a black colored solution was obtained. Afterwards, the prepared adsorbent was separated from the solution and washed with distilled water several times to be neutralized. After that, the adsorbent was placed in an oven at 105 °C for 24 hours to be completely dried. The dried adsorbent was then pulverized to be used in the uptake of sodium ion.

2. 4. Adsorption Test

The experiments were performed in a 200 ml Erlenmeyer, which were filled with 100 ml of sodium solution. Then, the impact of various factors like sodium concentration (300–1500 ppm), contact time (15–75 min), pH (3–11) and sorbent dosage (1–9 g/l) were studied on the Na⁺ ion removal, and the best operating conditions for the removal of Na⁺ ion were determined using Design Expert 10 and Central Composite Design (CCD) method.

Then, the solution was filtered using a fiber glass filter for elimination of solid particles. The filtered solution was analyzed to determine the residual Na⁺. The pH of each sample was adjusted by hydrochloric acid (0.1 M) and sodium hydroxide (0.1 M). A flame atomic absorption spectroscopy (model Varian AA240, Australia) was applied to specify the residual Na⁺ ion in the samples. In all samples, the Na⁺ ion sorption percentage (R%) and sorption capacity (q) were determined using equations 1 and 2, respectively.

$$R(\%) = \frac{C_0 - C_e}{C_0} \times 100 \quad (1)$$

$$q = (C_0 - C_e) \times \frac{V}{M} \quad (2)$$

where, C₀ is the initial sodium concentration and C_e is the equilibrium sodium concentration after uptake process, R is the removal efficiency of Na⁺, M is the weight of adsorbent in the solution (g) and V is the volume of the solution (L).

3. Results and discussion

3. 1. Determination of the Primary Efficiency of the Three Utilized Adsorbents

To evaluate the initial performance of the adsorbents, their adsorption efficiency in the removal of sodium ions was studied. To this end, experiments were performed at different contact times. Other conditions were kept constant, including pH of 7, temperature of 25 °C, Na⁺ ion concentration of 900 mg/L, and adsorbent dosage of 5 g/L. Since these conditions have been used in most previous work to perform the sodium adsorption process, the adsorption experiments were performed under these conditions to compare the three adsorbents. Figure 1 indicates the sodium uptake efficiency from aqueous solution using the eggshell derived CaO, CaO/Fe₃O₄ composite, and AC prepared by *Moringa oleifera* plant leaves. As can be seen, the AC with an uptake efficiency of 79% has the maximum uptake efficiency compared to the other two adsorbents. According to Figure 1, the removal efficiency of Na⁺ using AC is about 25% higher than CaO/Fe₃O₄ and 35% higher than eggshell derived CaO and this difference in efficiency is observed at all times. Therefore, the AC was used for further experiments and to determine the optimal conditions for Na⁺ ion removal.

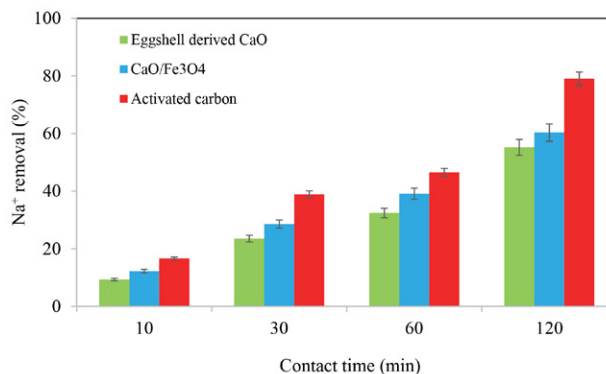


Figure 1. Primary investigations about three studied adsorbents in 10, 30, 60, and 120 min and neutral pH

3. 2. Characteristics of the Adsorbent

FTIR analysis was used to determine functional groups in the structure of *Moringa oleifera* leaves-derived AC as shown in Figure 2-a. These spectra approve the presence of many functional groups and indicate the natural complex of this material. As shown, the absorption peak at 3048 cm⁻¹ is related to the tensile vibration of OH group in proteins, fatty acids, carbohydrates, and lignin, which are due to its high contents in plant grain as well as N-H tensile bonding in amides.^{24–25} Also, the peak at 2895 cm⁻¹ is related to the =C-H bond.²³ Moreover, the peaks at 795 cm⁻¹ and 926 cm⁻¹ are attributed to the N-H and O-H functional groups, respectively. Furthermore, the peaks at 1232.8, 1396.8, 1506 and 1615.6 cm⁻¹ can be attributed to the C-O, C-H, C=C, and C=O, respectively.^{24,26–28}

Also, SEM analysis was applied to characterize the morphology of the *Moringa oleifera*-derived AC and its image is seen in Figure 2-b. It is obvious that the AC has a relatively porous structure with heterogeneous distribution. Also, some pores are observed on the surface of the adsorbent that include the accessible sites. These pores provide suitable conditions for the uptake of Na⁺ ions from aqueous solution.²⁹

Moreover, XRD analysis is used to identify and evaluate the crystalline phases in the adsorbent structure. Generally, materials are classified into different groups of amorphous, semi-crystalline, and crystalline. Figure 2-c shows the XRD pattern of the AC. According to Figure 2-c, the adsorbent shows a long peak at 2θ = 20°, which is attributed to the crystalline phase of (111) in the AC structure.^{30,31}

Besides, BET analysis showed that the specific surface area, pore volume and mean pore diameter of the activated carbon prepared from *Moringa oleifera* leaves were obtained as 136.25 m²/g, 0.158 cm³/g, and 55 °Å, respectively, which shows that the adsorbent has a significant specific surface area. Also, the mean pore size of the adsorbent indicates that the adsorbent has a mesoporous structure, because the mean pore size is between 2–50 nm.¹³

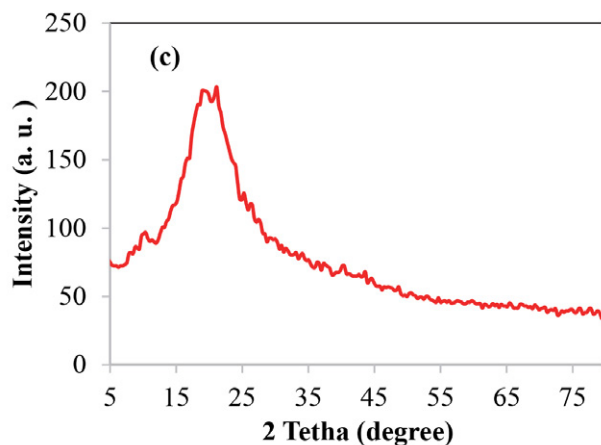
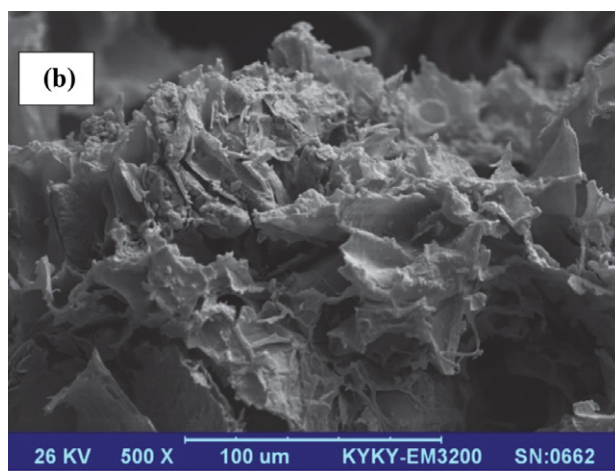
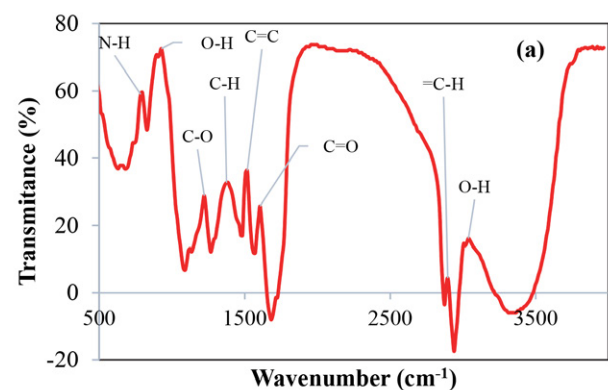


Figure 2. The characteristics of the activated carbon made from *Moringa oleifera* plant using various analyses, including FTIR (a), SEM (b), and XRD (c).

3. 3. Effective Parameters on the Sorption Process

The impact of various factors on the sodium ion sorption using the AC is demonstrated in Figure 3. As seen in this Figure, the uptake efficiency of Na^+ ion increases with increasing pH, contact time, and adsorbent dosage.

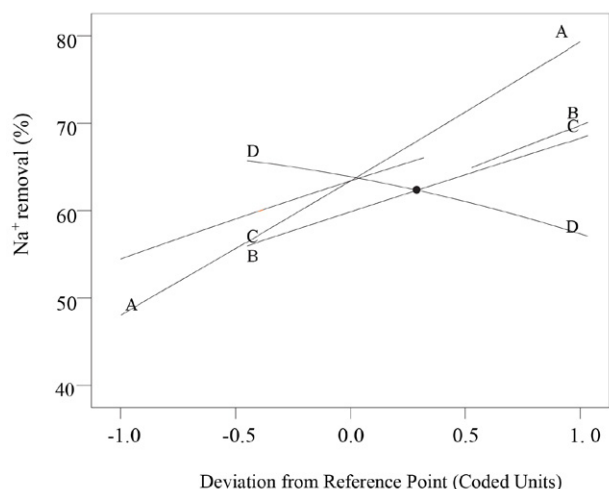


Figure 3. Effective parameters on adsorption process (separately and without any effect on each other) at pH of 7, contact time of 45 min, the adsorbent dosage of 5 g/L, and initial Na^+ concentration of 900 mg/l.

The impact of pH and Na^+ concentration on the Na^+ ion removal efficiency using the AC simultaneously is shown in Figure 4. Other experimental conditions were kept constant, including contact time of 45 min, temperature of 25 °C, and adsorbent dosage of 5 g/L. According to the results, the sorption efficiency increased with increasing the pH value from 3 to 11 and the maximum sorption efficiency was obtained at pH = 11. The formation of hydroxide ion (OH^-) and its bonding to the surface of the adsorbent makes the adsorbent surface negatively charged and the adsorbent ability increases in the sorption of cations. The reason of reduction in the adsorption efficiency in acidic pH might be that the increase in hydrogen ion production creates a positive charge on the adsorbent surface (protonation of the adsorbent).³² In other words, the pH of zero point charge (isoelectric pH) plays an important role in the adsorption process. Since this pH was obtained about 6.5 for the studied adsorbent, the *Moringa oleifera* adsorbent surface will be negatively charged in higher pH values and consequently, a strong electrostatic attraction will form between the surface groups and available cations (Na^+). Therefore, the adsorption efficiency was increased and the maximum sodium ion adsorption efficiency was obtained 95.53%, but in pH values less than the isoelectric point, the adsorbent surface is positively charged and forms a stable electrostatic repulsion force, which reduces the sorption of Na^+ ions. Another reason for the reduction in Na^+ ion adsorption in acidic conditions is the strong competition between the hydrogen ion (H^+) and positively charged sodium ions to be adsorbed on the adsorbent surface, which decreases the adsorption efficiency.

Therefore, pH = 11 was selected as the optimum pH and further adsorption experiments were carried out at

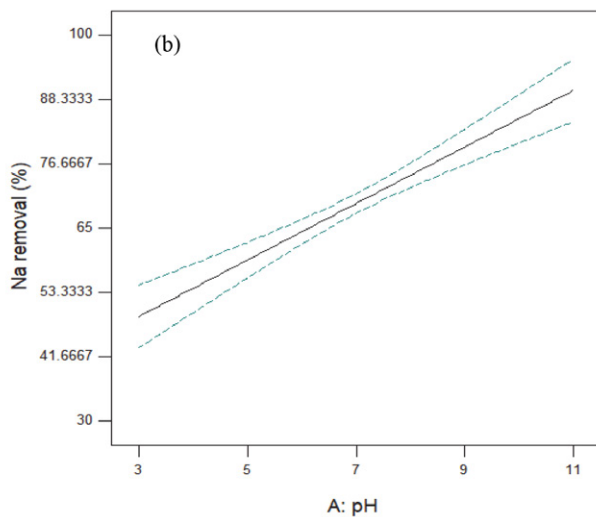
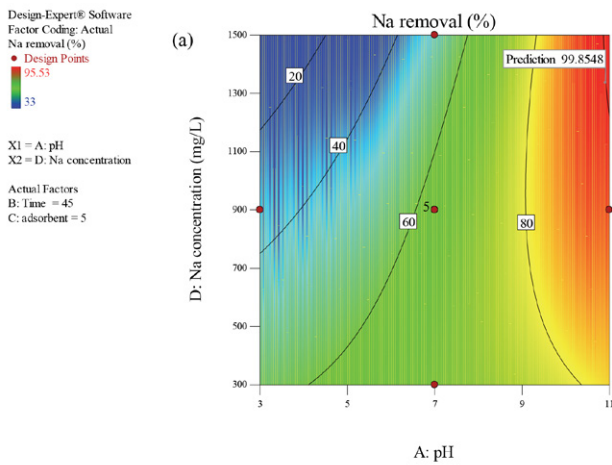


Figure 4. The effect of pH on the sodium ion adsorption from an aqueous solution using the AC in different concentrations of sodium ion

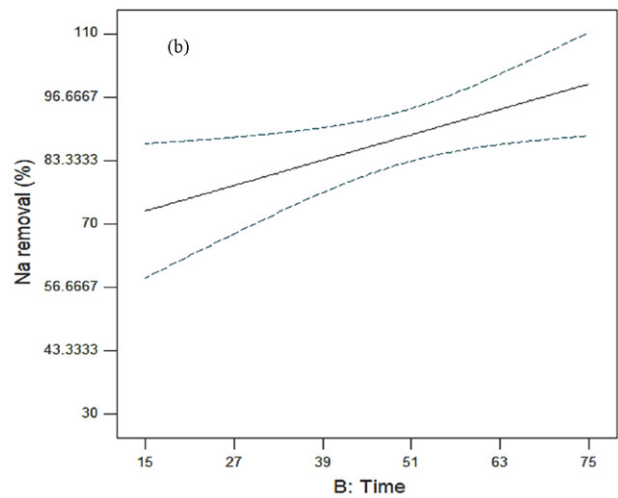
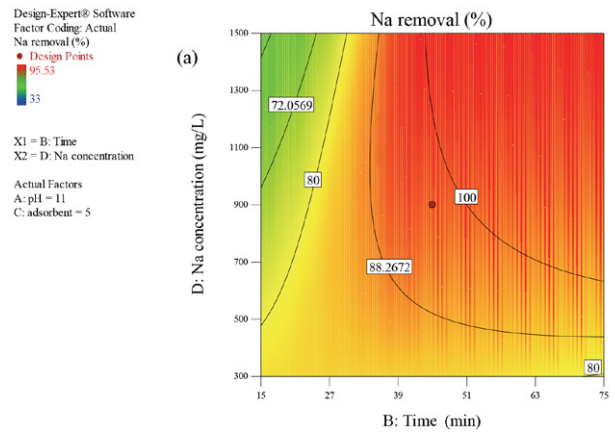


Figure 5. The effect of contact time on sodium adsorption from aqueous solution using the AC in different sodium ion concentrations

this pH value. Figure 5 shows the effect of contact time on the sorption efficiency of sodium using the activated carbon, in different sodium concentrations. Experiments were carried out at pH=11 (the optimum value) and adsorbent dosage of 3.5 g/L. As can be seen, increasing the contact time has increased sodium adsorption efficiency and then it has reached the equilibrium value. Changes in the adsorbent capacity, when contact time increases, indicated that in the first 45 min, the intensity of changes was high and then the adsorption trend became constant. Rapid enhancement of adsorption capacity in the early stages of the adsorption process was due to the high number of active sites for sodium adsorption on the adsorbent surface. When the process continued, the access of ions to the active sites was reduced, and eventually, the adsorption process reached an equilibrium at a specific time. After the equilibrium, there might be negligible changes in the adsorption capacity. Therefore, the optimum contact time was attained 47 min.

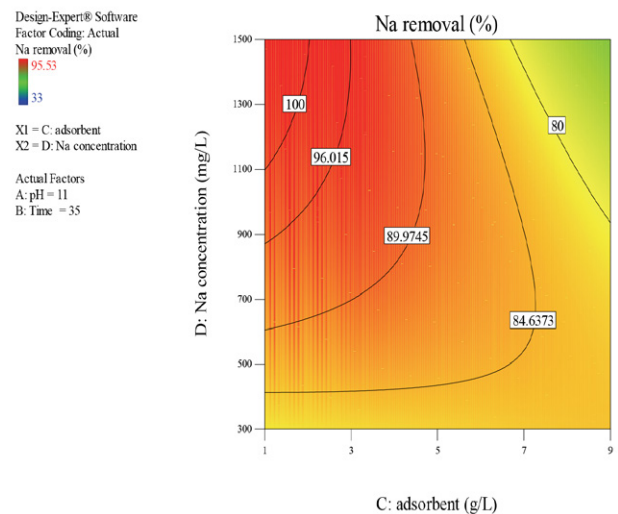


Figure 6. Effect of adsorbent dose on sodium adsorption from aqueous solutions in different concentrations of sodium ion

The effect of adsorbent dosage on sodium ion adsorption efficiency is indicated in Figure 6. According to the results, the removal efficiency increases with increasing adsorbent dosage, which is due to the enhancement of active sites on the adsorbent surface.¹⁹ The research results indicated that the enhancement of the initial concentration of sodium ion decreases the adsorption efficiency, which is due to the saturation of the adsorbent surface in high sodium concentrations.

Nowadays, using statistical design and presenting logical correlations between variables is widely used in many research fields. Using statistical methods decreases the number of experiments and as a result, the costs and manpower.^{33–34} Utilization of statistical method in this study resulted in the following equation that shows the empirical correlation between experimental variables and efficiency percentage in a coded form:

$$\begin{aligned} Na^+ \text{removal} = & 63.4 + 15.63A + 8.47B \\ & + 6.51C - 4.47D + 0.95AB - 5.45AC \\ & + 4.65AD - 0.51BC + 5.47BD - 2.3C \\ & + 0.3A^2 - 0.46B^2 - 0.07C^2 \end{aligned} \quad (3)$$

X_1 , X_2 , X_3 , and X_4 show the pH, contact time, adsorbent dosage, and pollutant concentration, respectively. The effect of studied parameters on the sorption efficiency of sodium ion was investigated by analysis of variance (ANOVA) and the outcomes are presented in Table 1.

The values of $R^2 = 0.9950$ and $\text{Adj } R^2 = 0.9834$ verifies that sodium adsorption by the activated carbon made from *Moringa oleifera* can be well explained by the de-

signed model. Also, the F-value was obtained 85.88, which shows the ability of the selected model in data analysis. The low value of CV also verifies that this model is suitable for interpretation of the studied process. Adequate precision is the parameter that indicates the ratio of signal to noise; if its value is more than 4, it shows an appropriate relation between the experimental data and the calculated values (desirability). In this study, the mentioned parameter was obtained 38.36. Then, the influence of the effective parameters on the uptake process of Na^+ was studied using the analysis of variance. The results indicated that X_1 , X_2 , X_3 , X_4 , X_1X_3 , X_1X_4 , X_2X_4 , and X_3X_4 parameters had significant effect ($P < 0.05$) on sodium adsorption.³⁴ The sequence of two parameters of the sum of squares and F-value was pollutant concentration < adsorbent dosage < contact time < pH that indicates the maximum effect of pH and the minimum effect of pollutant concentration on the Na^+ removal. Investigation of the normality of the studied data and the residuals, as two important assumptions, is essential for using this statistical model. The normal probability curve shows the normal distribution of data around a mean value and the linearity of this curve shows that experimental data are normal.

The R-squared value was obtained to be 0.942 from the normal probability curve. The test of normality of output data and residuals are shown in Figure 7.

Figure 7 shows the actual (experimental) and the predicted values of sodium adsorption by Design Expert 10 in 21 different runs. The high level of conformity of the actual value with the predicted one indicates the excellent ability of the software in the prediction of the experiment results in different runs.

Table 1. Results of the analysis of variance for the studied model

ANOVA for Response Surface Quadratic model					
Source	Sum of Squares	df	Mean Square	F Value	p-value
Model	4860.52	14	347.18	85.88	<0.0001
A-pH	1955.00	1	1955.00	483.57	<0.0001
B-Time	573.93	1	573.93	141.96	<0.0001
C-adsorbent	677.69	1	677.69	167.63	<0.0001
D- Na^+ concentration	159.85	1	159.85	0.90	<0.0008
AB	3.62	1	3.62	0.90	0.3806
AC	237.29	1	237.29	58.69	0.0003
AD	86.63	1	86.63	21.43	0.0036
BC	2.09	1	2.09	0.52	0.4991
BD	119.52	1	119.52	29.56	0.0016
CD	42.46	1	42.46	10.50	0.0177
A^2	2.47	1	2.47	0.61	0.4641
B^2	5.31	1	5.31	1.31	0.2954
C^2	0.13	1	0.13	0.032	0.8649
D^2	23.13	1	23.13	5.72	0.0539
Residual	24.26	6	4.04		
R^2	0.9950	R^2 -Adjusted	0.9834	R^2 -Predicted	0.9462

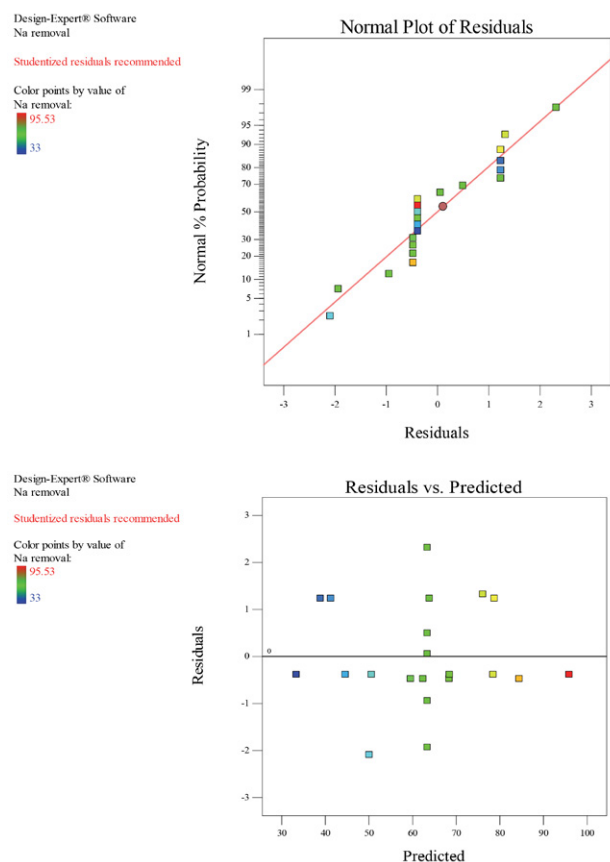


Figure 7. The normality of primary data and residuals

The very high value of R-square confirms the prediction ability of the Na^+ ion adsorption process in the studied system. Then, the real (experimental) values are plotted versus the predicted values and compared with each other. As predicted, the resulted R-square from regression was very close to 1.

3. 4. Prediction of Adsorption Process by the Software

In Table 2, independent variables and the range and levels of experimental values are presented for activated carbon as an adsorbent in the removal of Na^+ ions. In this study, the total number of experiments in the CCD design method was 21. Furthermore, the sorption efficiency of sodium ion in different experimental conditions was reported.

Figure 8(a) shows the actual and predicted values of sodium ion removal percentage using activated carbon in various experiments. The predicted values of sodium ion removal efficiency are extracted from Figure 8(a) and then reported in Table 2. As reported in Table 2, the maximum removal efficiency of N^+ ion was achieved 95.91%. Also, the value of R^2 coefficient was achieved 0.9975, which indicates a good ability of the model in the prediction of data.

Figure 8(b) also shows the experimental outcomes versus the predicted ones by Design Expert 10. As seen in this figure, the R^2 value of 0.9462 was achieved for the prediction, which verifies the results obtained in the previous stage.

Table 2. The impact of independent variables on the removal efficiency of sodium using AC. Experimental design was done by CCD method

Run	A: pH	B: Time (min)	C: adsorbent dose (g/L)	D: Na^+ conc. (mg/l)	Na^+ removal (%)	Predicted value of Na^+ removal (%)
1	5	60	7	1200	59.11	59.58
2	11	45	5	900	95.53	95.91
3	7	45	9	900	77.45	76.12
4	5	60	3	1200	42.54	41.3
5	3	45	5	900	33	33.38
6	7	45	5	900	63.45	63.39
7	9	60	7	600	84	84.47
8	7	45	5	900	65.71	63.39
9	7	75	5	900	78.11	78.49
10	7	45	5	900	63.89	63.39
11	7	45	5	1500	50.23	50.61
12	9	30	7	1200	61.94	62.41
13	7	45	5	900	62.45	63.39
14	7	15	5	900	44.23	44.61
15	7	45	5	300	68.11	68.49
16	5	30	7	600	67.95	68.42
17	5	30	3	600	40.12	38.88
18	9	30	3	1200	65.11	63.87
19	7	45	5	900	61.46	63.39
20	9	60	3	600	80	78.76
21	7	45	1	900	48	50.09

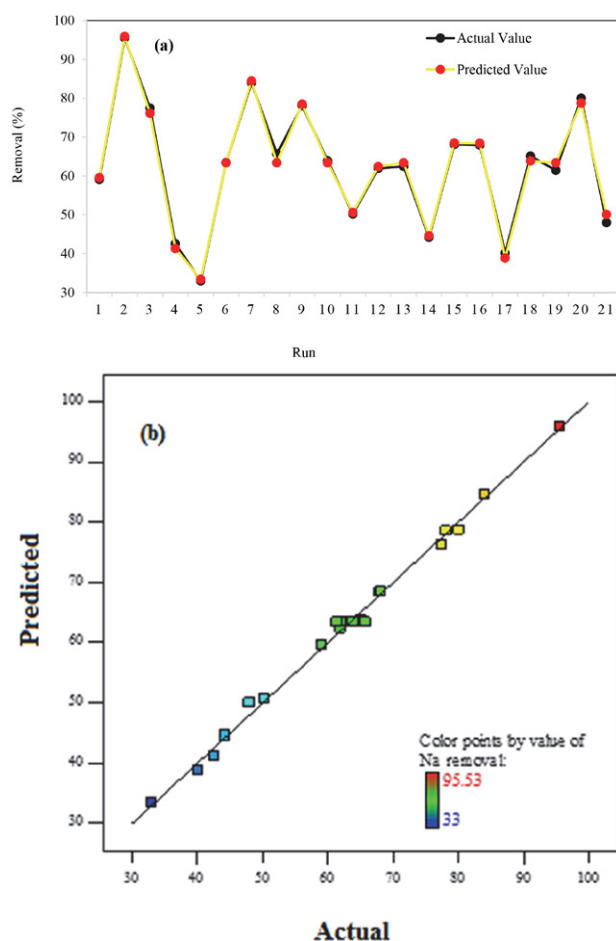


Figure 8. Predicted and real values of efficiency in different runs of the experiment (a) the experimental results versus the predicted results by the software (b)

3. 5. Optimization of Sodium Adsorption Process

Optimization of process conditions is necessary for any statistical model. To do this, Genetic Algorithm (GA) was applied for the optimization of Na⁺ uptake process. In this model, the best conditions for eliminating Na⁺ ions were determined. To optimize the uptake process, the studied parameters were selected in the range of their maximum and minimum values. In fact, the algorithm genetic method is capable of interpolating data and can optimize results. Therefore, interpolation between data is a prominent feature of the genetic algorithm method compared to the CCD method. The target variable (Na⁺ removal efficiency (%)) was considered in the maximum value. The purpose of using the GA method was to determine the best conditions of the Na⁺ removal and uses the results of the CCD method. After determining the optimal conditions by the CCD method, the data were entered into the software to optimize the parameters and to do this, Na⁺ removal efficiency was considered as the response

(target function).³⁵ It should be noted that before optimizing the effective parameters in the adsorption process, the studied algorithm has determined some points (Generation) in the first step, and then, in the next step, it looks for the generation that has the minimum error. Eventually, it optimizes the parameters of the generation with the minimum possible error. The response of the genetic algorithm with the best efficiency and the mean efficiency of sodium removal in different generations are presented in Figure 9. As can be seen, when generations increase, the conformity of these two figures increases as well, so that in the generation =135, the best and the mean efficiencies are matched and there will be no mutation or sudden change on it. Figure 9 is plotted to ensure more reliability of the first stage which is to find the most accurate generation. Here, the distances between all individual generations are presented. As it was expected, when the number of generations increases, the mean distance between them decreases, and in generation=135, this distance is almost zero. After determining the best generation, the optimum effective factors were determined in the sodium adsorption process. According to Figure 9, the optimum values of pH, contact time, adsorbent dosage, and Na⁺ ion concentration were obtained 10.918, 46.967 min, 3.516 g/L, and 939.921 mg/L, respectively. Then, to check the accuracy of the genetic algorithm in the optimization of the conditions, all the results obtained in the laboratory (real conditions) were repeated and similar results were obtained. In the optimum conditions, the removal efficiency of Na⁺ ion was obtained 94.23% by the genetic algorithm.

3. 6. Adsorption Isotherms

Adsorption isotherms are used to describe the equilibrium relationship between adsorbent and adsorbate in an aqueous solution. Also, they are the main factors in the design of sorption systems.³⁶ The most common isotherms are Freundlich and Langmuir isotherms. The Freundlich equilibrium isotherm is based on the multilayer and heterogeneous adsorption on the adsorbent. The linear form of this equation is expressed below:³⁷

$$\ln q_e = \ln k_F + \frac{1}{n} \ln C_e \quad (4)$$

where, k_F ($\text{mg/g(L/mg)}^{1/n}$) and n are the Freundlich constants.³⁸

The Langmuir isotherm model assumes monolayer sorption on a surface containing a limited number of uniform energy adsorption sites.³⁶ This model also states that adsorption only occurs on homogeneous sites, without any action between the adsorbate and adsorbent molecules.³⁹ The linear form of the Langmuir model is expressed as follows:

$$\frac{C_e}{q_e} = \frac{C_e}{q_o} + \frac{1}{k_L q_o} \quad (5)$$

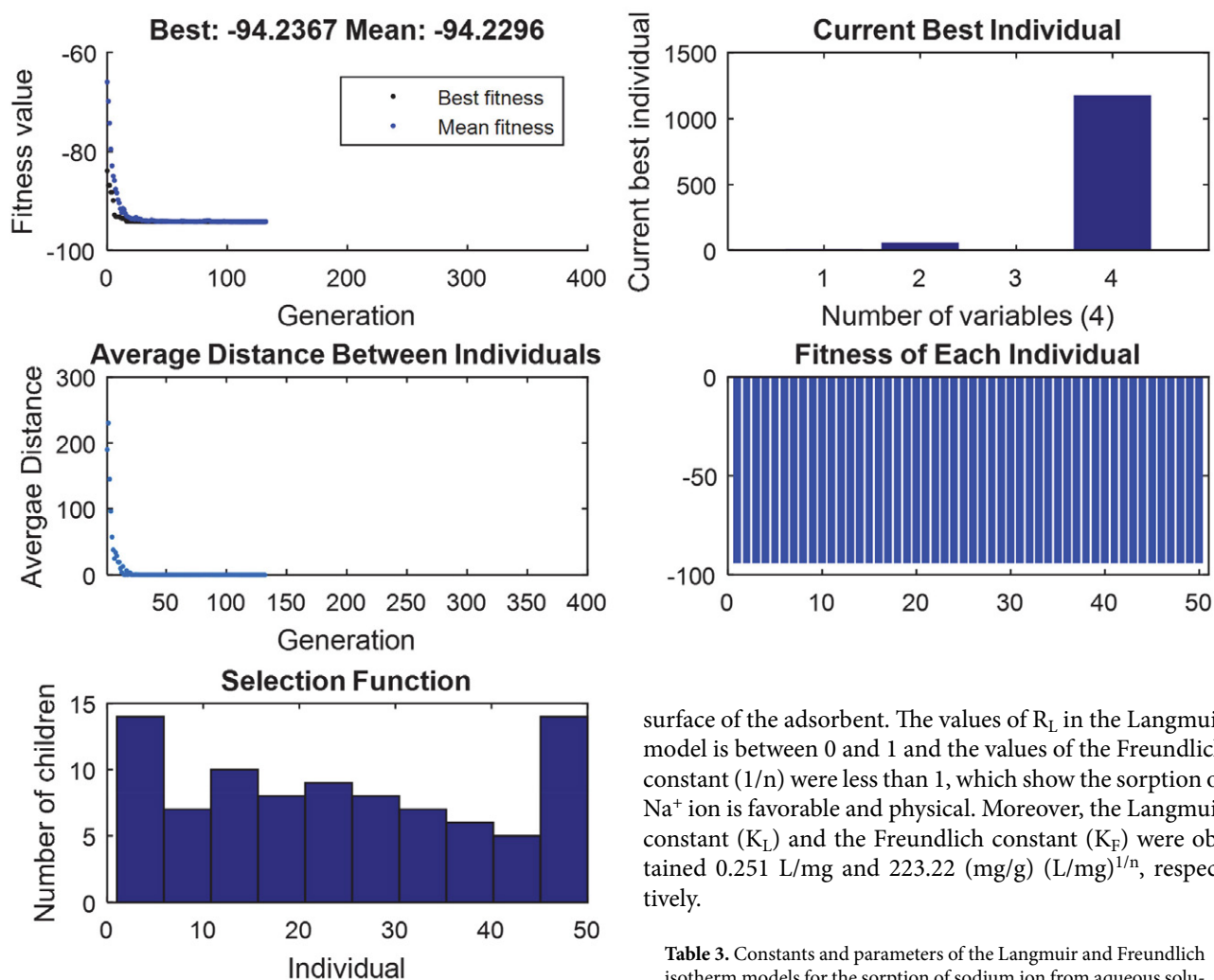


Figure 9. The optimization steps of adsorption parameters using genetic algorithm

where, k_L is the Langmuir constant (L/mg) and q_0 is the maximum adsorbed amount per gram of the adsorbent (mg/g), C_e is the equilibrium concentration of the adsorbate (mg/L), and q_e is the initial amount of adsorbate at equilibrium (mg/g).

The value of the parameters of Langmuir and Freundlich models are presented in Table 3. Also, the plots of the Langmuir and Freundlich models for the sodium sorption process are shown in Figure 10. Considering the results, the maximum uptake capacity by the Langmuir model was determined 249.67 mg/g, which was a significant value. Also, the correlation coefficient for the Langmuir model ($R^2 = 1$) was greater than the Freundlich model ($R^2 = 0.993$). Therefore, in all three studied temperatures, the Langmuir model could better describe the equilibrium behavior of the sorption process, and the sorption process of sodium ion took place as monolayer on the homogeneous

surface of the adsorbent. The values of R_L in the Langmuir model is between 0 and 1 and the values of the Freundlich constant ($1/n$) were less than 1, which show the sorption of Na^+ ion is favorable and physical. Moreover, the Langmuir constant (K_L) and the Freundlich constant (K_F) were obtained 0.251 L/mg and 223.22 (mg/g) (L/mg) $^{1/n}$, respectively.

Table 3. Constants and parameters of the Langmuir and Freundlich isotherm models for the sorption of sodium ion from aqueous solution using activated carbon

Isotherm	parameter	value
Langmuir	q_0 (mg/g)	249.67
	K_L (L/mg)	0.251
	R^2	1
Freundlich	K_F (mg/g)(L/mg) $^{1/n}$	223.22
	n	59.95
	R^2	0.993

3. 7. Adsorption Process Kinetics

It is necessary to study the process kinetics for the investigation of the effective parameters on the sorption rate. The sorption process may occur in several stages with different rates. Here, we just discuss the two main and common kinetic models that are quasi-first-order (QFO) and quasi-second-order (QSO) kinetic models.¹⁹

The QFO kinetic model is based on the sorption capacity in adsorption of a pollutant and is used when the

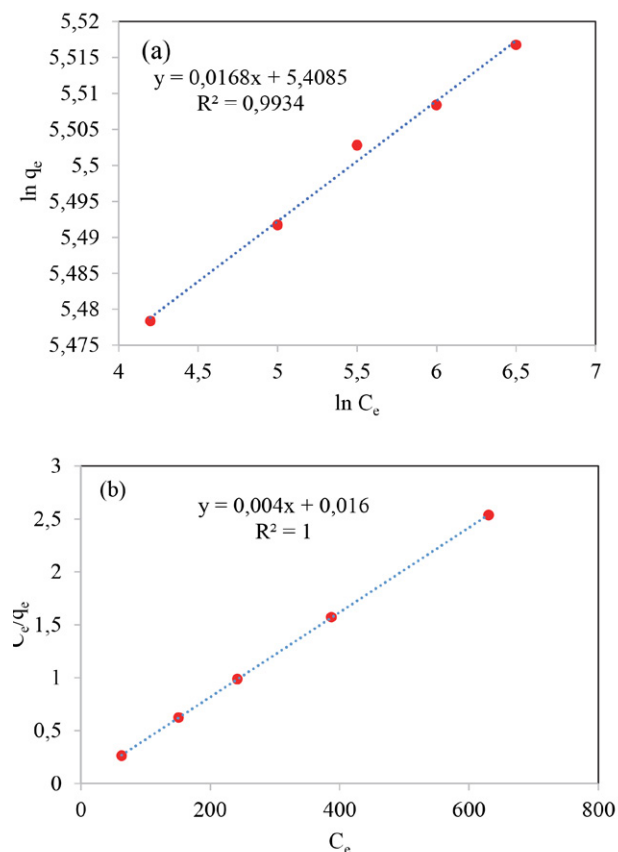


Figure 10. The Freundlich (a) and Langmuir (b) equilibrium isotherms

adsorption follows the diffusion mechanism through a boundary layer. The QFO model is described as follows:¹⁷

$$\ln(q_e - q_t) = \ln q_e - k_1 t \quad (6)$$

Where, q_e and q_t are the uptake capacity at equilibrium and at time t in terms of mg/g and k_1 is the QFO kinetic constant (min^{-1}).

Also, the linear form of the QSO kinetic model is define below:¹⁷

$$\frac{t}{q_t} = \frac{1}{k_2 q_e^2} + \frac{1}{q_e} t \quad (7)$$

The values obtained from the kinetic parameters of sodium adsorption on *Moringa oleifera*-derived AC are listed in Table 4. The results of kinetic models are also displayed in Figure 11. It can be seen that the correlation coefficient (R^2) for the QSO kinetic model is higher than the QFO kinetic model and is around 1, therefore sodium sorption by the AC follows the QSO kinetic model. Furthermore, the calculated values of uptake capacity ($q_{e, \text{cal}}$) follows the QSO kinetic model.¹⁷ Therefore, the QSO kinetic model was better fitted with the experimental data. Also, the constant values of the QFO and QSO models were determined 0.128 L/mg and 0.000463 L/mg, respectively.

Table 4. Constants and parameters of the QFO and QSO kinetic models for the sorption of sodium ion from aqueous solution using activated carbon

model	parameter	value
QFO	$q_{e, \text{cal}}$ (mg/g)	559.6
	K_1 (L/mg)	0.128
	R^2	0.8797
QSO	$q_{e, \text{cal}}$ (mg/g)	286.98
	K_2 (L/mg)	0.000463
	R^2	0.9959

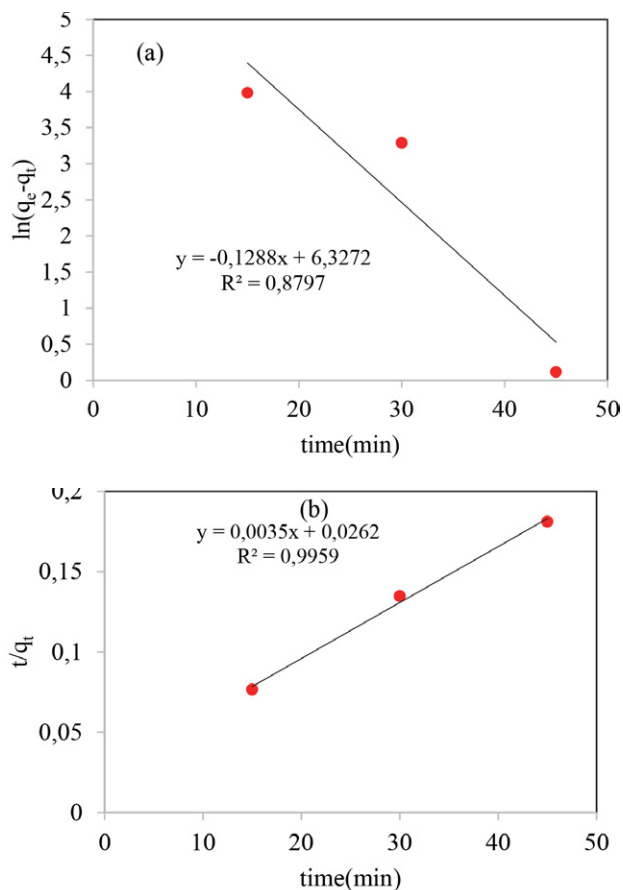


Figure 11. QFO (a) and QSO (b) kinetic models

3. 8. Thermodynamic Study

The thermodynamic parameters provide information about the spontaneity of the sorption process and an increase or decrease of randomness at the interface of solid-liquid. Also, they determine whether a sorption process is exothermic or endothermic.^{40,41} Three main thermodynamic parameters should be determined to study the thermodynamics of the uptake process. These three parameters are changes of enthalpy (ΔH°), Gibbs free energy (ΔG°), and entropy (ΔS°). The values of ΔH° and ΔS° are obtained from the slope and intercept of the following equation:^{42,43}

$$\ln k_c = \frac{\Delta S^\circ}{R} - \frac{\Delta H^\circ}{RT} \quad (8)$$

$$K_c = \frac{q_e}{C_e} \quad (9)$$

Where, R is the global gas constant (8.314 J/mol K) and K_c (L/g) is the ratio of the adsorbed material on the adsorbate (mg/g) to the residual material in the solution (mg/L). The values of ΔG° is calculated from the following equation:

$$\Delta G^\circ = -RT \ln K_c \quad (10)$$

Generally, the negative values of ΔG° show that the sorption process is spontaneous. The negative values of ΔH° show that the sorption process is exothermic and also it is favorable at lower temperatures.

The negative values of ΔS° indicate that the efficiency decreases as the temperature increases at the solid-liquid interface during the sorption process and it is vice versa for positive values.^{44,45}

The values of thermodynamic parameters for the sodium ion adsorption using the AC are presented in Table 5. The experiments were done in the initial sodium concentration of 100 mg/L and temperatures of 20–50 °C. It is observed in Table 5 that the values of ΔH° and ΔS° are both negative and are –147 and –0.455 (kJ/mol), respectively. Also, the values of ΔG° for temperatures of 20, 35, and 50 °C are –16.208, –4.849, and –2.67 (kJ/mol), respectively. Moreover, the study of the thermodynamic parameters for the sodium ion adsorption using the AC showed that ΔH° had a negative value, which shows the Na^+ uptake process is exothermic, it also implies that the uptake process is more favorable in lower temperatures. Furthermore, the negative value of ΔS° is an indication of the reduction in efficiency and degree of freedom at the solid-liquid interface during the uptake process. Besides, the negative values of ΔG° indicate that the Na^+ uptake process is spontaneous.³⁹

Table 5. Thermodynamic parameters for the sorption process of sodium ion from aqueous solution using activated carbon

Temperature (°C)	– ΔG° (kJ/mol)	ΔH° (kJ/mol)	ΔS° (kJ/mol K)
293	–16.208	–147	–0.455
308	–4.849		
323	–2.67		

3. 9. Final Comparison of the Adsorbents

After determining the optimal conditions for the removal of Na^+ from aqueous solution using AC, a comparison was done between AC and other adsorbents such as eggshell derived CaO and CaO/ Fe_3O_4 composite and the

results are shown in Figure 12. The experiments were done under optimal conditions such as pH of 11, contact time of 45 min, adsorbent dosage of 5 g/L, temperature of 25 °C and sodium ion concentration of 900 mg/L. As shown, the removal efficiency of Na^+ using AC (95.91%) is higher than CaO (83.45%) and CaO/ Fe_3O_4 (89.2%), indicating the high performance of AC compared to the other two adsorbents.

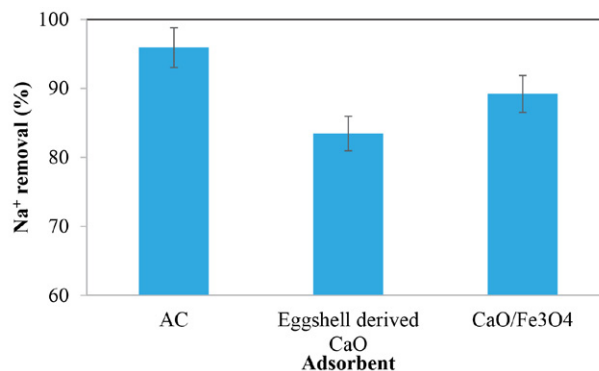


Figure 12. The removal efficiency of the adsorbents at optimal conditions (pH=11, time= 45 min, adsorbent dosage= 5 g/L, temperature =25 °C and initial sodium concentration= 900 mg/L)

4. Conclusion

The obtained results indicated that the AC made from *Moringa oleifera* plant is an effective adsorbent for the removal of sodium ion from aqueous solutions. Based on the present study, removal of sodium ion increases with increasing contact time and pH at room temperature however, it has an opposite relationship with the enhancement of sodium ion concentration. Furthermore, the studies indicated that the maximum sodium ion removal efficiency of 95.91% was achieved at contact time of 45 min, adsorbent dosage of 5 g/L, and pH of 11. Also, the equilibrium and kinetic studies indicated that the equilibrium data were better explained by the Langmuir isotherm than the Freundlich isotherm and the best kinetic correlation for sodium adsorption by the adsorbent in laboratory conditions follows the QSO kinetic model. Furthermore, the thermodynamic behavior of the Na^+ ion process indicated that the sodium ion sorption by the AC is spontaneous, exothermic, and possible. Moreover, the maximum uptake capacity of Na^+ ion was obtained 249.67 mg/g, which was a significant amount. Generally, *Moringa oleifera* can be used as an effective adsorbent for the removal of Na^+ ion from water and wastewater due to its benefits such as cheapness, nativity, and availability.

Disclosure statement

No potential conflict of interest was reported by the authors.

5. Reference

1. L. He, M. X. Li, F. Chen, S.S. Yang, J. Ding, L. Ding, N.Q. Ren, *J. Hazard. Mater.* **2021**, *417*, 126113. DOI:10.1016/j.jhazmat.2021.126113
2. S. Yang, Z. Li, K. Yan, X. Zhang, Z. Xu, W. Liu, Z. Liu, H. Liu, *J. Environ. Sci.* **2021**, *103*, 59–68. DOI:10.1016/j.jes.2020.10.013
3. M. Fathy, M. A. Mousa, T. A. Moghny, A. E. Awadallah, *Appl. Water Sci.* **2017**, *7*, 4427–4435. DOI:10.1007/s13201-017-0588-3
4. A. M. Siemens, J. J. Dynes, W. Chang, *Environ. Technol.* **2020**. DOI: 10.1080/09593330.2020.1721567
5. L. He, Y. Chen, J. Li, *Resour. Conserv. Recycl.*, **2018**, *133*, 206–228. DOI:10.1016/j.resconrec.2018.02.015
6. K. C. Khulbe, T. Matsuura, *Appl. Water Sci.* **2018**, *8*, 19. DOI:10.1007/s13201-018-0661-6
7. Q. Guan, G. Zeng, J. Song, C. Liu, Z. Wang, S. Wu, *J. Environ. Manage.* **2021**, *293*, 112961. DOI:10.1016/j.jenvman.2021.112961
8. J. S. George, A. Ramos, H. J. Shipley, *J. Environ. Chem. Eng.* **2015**, *3*, 969–976. DOI:10.1016/j.jece.2015.03.011
9. S. Ren, B. Ye, S. Li, L. Pang, Y. Pan, H. Tang, *Nano Res.* **2021**. DOI:10.1007/s12274-021-3694-3
10. A. Garg, M. Mainrai, V. K. Bulasara, S. Barman, *Chem. Eng. Commun.* **2015**, *202*, 123–130. DOI:10.1080/00986445.2013.836636
11. T. Jesionowski, J. Zdarta, B. Krajewska, *Adsorption*, **2014**, *20*, 801–821. DOI:10.1007/s10450-014-9623-y
12. X. Cheng, L. He, H. Lu, Y. Chen, L. Ren, *J. Hydrol.*, **2016**, *540*, 412–422. DOI:10.1016/j.jhydrol.2016.06.041
13. S. Abbasi, R. Foroutan, H. Esmaeili, F. Esmaeilzadeh, *Desalin. Water Treat.* **2019**, *141*, 269. DOI:10.5004/dwt.2019.23569
14. R. Salahshour, M. Shanbedi, H. Esmaeili, *Acta Chim. Slov.* **2021**, *68*, 363–373. DOI:10.17344/acsi.2020.6311
15. A. R. Lucaci, D. Bulgariu, I. Ahmad, G. Lisă, A. M. Mocanu, L. Bulgariu, *Water*, **2019**, *11*, 1565. DOI:10.3390/w11081565
16. A. Attarad, Z. Hira, Z. Muhammad, H. Ihsanul, P. Abdul Rehman, S. Joham, H. Altaf, *Nanotechnol. Sci. Appl.* **2016**, *9*, 49–67. DOI:10.2147/NSA.S99986
17. S. M. Mousavi, S. A. Hashemi, H. Esmaeili, A. M. Amani, F. Mojoudi, *Acta Chim. Slov.* **2018**, *65*, 750–756. DOI:10.17344/acsi.2018.4536
18. A. A. Alqadami, M. Naushad, Z. A. Allothman, M. Alsuhybani, M. Algamdi, *J. Hazard. Mater.* **2020**, *389*, 121896. DOI:10.1016/j.jhazmat.2019.121896
19. R. Foroutan, R. Mohammadi, S. Farjadfard, H. Esmaeili, B. Ramavandi, G.A. Sorial, *Adv. Powder Technol.* **2019**, *30*, 2188–2199. DOI:10.1016/j.apt.2019.06.034
20. S. M. Jamil, M. W., Ali, A. Ripin, A. Ahmad, *J. Appl. Sci.* **2015**, *15*, 516–523. DOI:10.3923/jas.2015.516.523
21. R. Rostamian, M. Heidarpour, S. F. Mousavi, M. Afyuni, *J. Agr. Sci. Tech.* **2018**, *17*, 1057–1069.
22. R. Caletka, C. Konečný, M. Šimková, *J. Radioanal. Chem.* **1972**, *10*, 5–15. DOI:10.1007/BF02518760
23. S. Yang, X. Wan, K. Wei, W. Ma, Z. Wang, *Miner. Eng.* **2021**, *169*, 106966. DOI:10.1016/j.mineng.2021.106966
24. Z. Wang, Q. Lei, Z. Wang, H. Yuan, L. Cao, N. Qin, Z. Lu, J. Xiao, J. Liu, *Chem. Eng. J.* **2020**, *395*, 125180. DOI:10.1016/j.cej.2020.125180
25. K. Zhang, L. Qiu, J. Tao, X. Zhong, Z. Lin, R. Wang, Z. Liu, *Hydrometallurgy* **2021**, *205*, 105722. DOI:10.1016/j.hydromet.2021.105722
26. Z. Fan, P. P. Ji, J. Zhang, D. Segets, D. R. Chen, S. C. Chen, *J. Membr. Sci.* **2021**, *635*, 119503. DOI:10.1016/j.memsci.2021.119503
27. Q. Pan, Y. Zheng, Z. Tong, L. Shi, Y. Tang, *Angew. Chem. Int. Ed.* **2021**, *60*, 11835–11840. DOI:10.1002/anie.202103052
28. R. Chen, Y. Cheng, P. Wang, Y. Wang, Q. Wang, Z. Yang, C. Tang, S. Xiang, S. Luo, S. Huang, C. Su, *Chem. Eng. J.* **2021**, *421*, 129682. DOI:10.1016/j.cej.2021.129682
29. X. Li, T. Shi, B. Li, X. Chen, C. Zhang, Z. Guo, Q. Zhang, *Mater. Des.* **2019**, *183*, 108152. DOI:10.1016/j.matdes.2019.108152
30. R. Wang, Y. Yuan, J. Zhang, X. Zhong, J. Liu, Y. Xie, S. Zhong, Z. Xu, *J. Power Sources* **2021**, *501*, 230006. DOI:10.1016/j.jpowsour.2021.230006
31. S. Yang, X. Wan, K. Wei, W. Ma, Z. Wang, *Waste Manage.* **2021**, *120*, 820–827. DOI:10.1016/j.wasman.2020.11.005
32. R. Chen, Y. Cheng, P. Wang, Q. Wang, S. Wan, S. Huang, R. Su, Y. Song, Y. Wang, *Sci. Total Environ.* **2021**, *756*, 143871. DOI:10.1016/j.scitotenv.2020.143871
33. H. Yin, C. Han, Q. Liu, F. Wu, F. Zhang, Y. Tang, *Small* **2021**, *17*, 2006627. DOI:10.1002/smll.202006627
34. R. Foroutan, R. Mohammadi, H. Esmaeili, F.M. Bektashi, S. Tamjidi, *Waste Manage.* **2020**, *105*, 373–383. DOI:10.1016/j.wasman.2020.02.032
35. H. Li, B. Xu, G. Lu, C. Du, N. Huang, *Energy Convers. Manag.* **2021**, *236*, 114063. DOI:10.1016/j.enconman.2021.114063
36. G. Abbas, I. Javed, M. Iqbal, R. Haider, F. Hussain, N. Qureshi, *Desalin. Water Treat.* **2017**, *95*, 274–285. DOI:10.5004/dwt.2017.21465
37. I. Khoshkerdar, H. Esmaeili, *Acta Chim. Slov.* **2019**, *66*, 208–216. DOI:10.17344/acsi.2018.4795
38. L. P. Lingamdinne, J. S. Choi, J. K. Yang, Y. Y. Chang, J. R. Koduru, J. Singh, *Acta Chim. Slov.* **2018**, *65*, 599–610. DOI:10.17344/acsi.2018.4254
39. D. Humelnicu, M. Ignat, M. Sucheai, *Acta Chim. Slov.* **2015**, *62*, 947–957. **2016**, *107*, 012067. DOI:10.17344/acsi.2014.1825
40. W. Y. Huang, G. Q. Wang, W. H. Li, T. T. Li, G. J. Ji, S. C. Ren, M. Jiang, L. Yan, H. T. Tang, Y. M. Pan, Y. J. Ding, *Chem* **2020**, *6*, 2300–2313. DOI:10.1016/j.chempr.2020.06.020
41. A. Awwad, M. Amer, M. Al-aqarbeh, *Chem. Int.* **2020**.
42. W. Y. Huang, D. Li, Z. Q. Liu, Q. Tao, Y. Zhu, J. Yang, Y. M. Zhang, *Chem. Eng. J.* **2014**, *236*, 191–201. DOI:10.1016/j.cej.2013.09.077
43. F. Takmil, H. Esmaeili, S.M. Mousavi, S.A. Hashemi, *Adv. Powder Technol.* **2020**, *31*, 3236–3245. DOI:10.1016/j.apt.2020.06.015
44. J. Fu, Z. Chen, M. Wang, S. Liu, J. Zhang, J. Zhang, Q. Xu, *Chem. Eng. J.* **2015**, *259*, 53–61. DOI:10.1016/j.cej.2014.07.101
45. Z. Li, M. Peng, X. Zhou, K. Shin, S. Tunmee, X. Zhang, C. Xie, H. Saitoh, Y. Zheng, Z. Zhou, Y. Tang, *Adv. Mater.* **2021**, *2100793*. DOI:10.1002/adma.202100793

Povzetek

Namen študije je bil določiti optimalni adsorbent izmed aktivnega oglja na osnovi *Moringa oleifera* (AC), CaO nanodelcev pridobljenih in jajčnih lupin in CaO/Fe₃O₄ za odstranjevanje natrijevih (Na⁺) ionov iz vodnih raztopin. V prvem koraku smo določili njihovo adsorpcijsko učinkovitost, pri čemer se je AC adsorbent izkazal kot najboljši. Z metodologijo odzivnih ploskev (ang. response surface methodology – RSM) smo ovrednotili vpliv različnih parametrov na učinkovitost adsorpcije (Na⁺) ionov AC adsorbenta. Najvišja učinkovitost odstranjevanja pod optimalnimi pogoji je znašala 95.91 %, pri pH vrednosti 11, kontaktnem času 45 min, temperaturi 25 °C, koncentraciji natrijevih ionov 900 mg/L in količini adsorbenta 5 g/L. Optimalni pogoji določeni z uporabo genetskih algoritmov pa so bili pri kontaktnem času 94.97 min, količini adsorbenta 3.52 g/L, koncentraciji natrijevih ionov 939.92 mg/L in pH vrednosti 10.92. Maksimalna adsorpcijska kapaciteta določena z Langmuirjevim modelom je bila ocenjena na 249.67 mg/g, kar je znatna količina. Poleg tega smo pokazali, da lahko eksperimentalne podatke ravnotežja in kinetike adsorpcije natrijevih ionov dobro opišemo z Langmuirjevo izotermo in kinetiko adsorpcije psevdodrugega reda. Termodinamična analiza je pokazala, da je adsorpcija endotermen proces. Zaključimo lahko, da je predstavlja aktivno oglje, z visoko učinkovitostjo odstranjevanja in visoko adsorpcijsko kapaciteto, obetajoč adsorbent za odstranjevanje natrija iz onesnaženih voda na industrijskem nivoju.



Except when otherwise noted, articles in this journal are published under the terms and conditions of the Creative Commons Attribution 4.0 International License

Synthesis, Crystal Structures and Urease Inhibition of 4-Bromo-*N*'-(1-(pyridin-2-yl)ethylidene)benzohydrazide and Its Dinuclear Copper(II) Complex

Hui Zhao,^{1,2} Xiu-Rui Liu,^{1,2} Xue Wang,^{1,2} Jing Hu,³ Ya-Jun Cai^{1,2} and Qi-An Peng^{1,2,*}

¹ School of Environmental Engineering, Wuhan Textile University, Wuhan 430073, P. R. China

² Engineering Research Center for Clean Production of Textile Printing, Ministry of Education, Wuhan 430073, P. R. China

³ Center for Evaluation and Inspection, Hubei Drug Administration, Wuhan 430073, P. R. China

* Corresponding author: E-mail: Cyjxy227@163.com

Received: 02-27-2021

Abstract

A new dinuclear copper(II) complex $[\text{Cu}_2(\mu\text{-Br})_2\text{L}_2] \cdot 0.5\text{MeOH}$ with the benzohydrazone ligand 4-bromo-*N*'-(1-(pyridin-2-yl)ethylidene)benzohydrazide (HL) has been synthesized and characterized by elemental analysis, IR and UV-Vis spectroscopic studies. Single crystal structures of the complex and the benzohydrazone compound were studied. The Cu atoms in the complex are coordinated by two benzohydrazone ligands and two Br bridging groups, forming square pyramidal coordination. The complex has good inhibitory activity on *Jack bean* urease, with IC_{50} value of $1.38 \mu\text{mol} \cdot \text{L}^{-1}$.

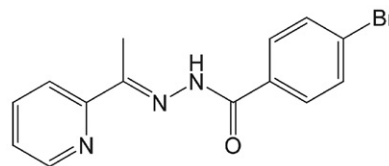
Keywords: Benzohydrazone; copper complex; crystal structure; urease inhibitory activity

1. Introduction

Urease (urea amidohydrolase; E.C.3.5.1.5) is a nickel-containing enzyme that catalyzes the rapid hydrolysis of urea to form ammonia.¹ It is harmful for environment, agriculture and human health. In the last few years, urease inhibitors have attracted much attention and numerous urease inhibitors have been reported.² Among the known urease inhibitors, hydroxamic acids, phosphoramides and thiols are the best recognized species. Because the low efficiency and negative side effect of the present urease inhibitors, the discovery of new and more efficient urease inhibitors is of high urgency.

Hydrazones constitute a class of famous ligands that have attracted much attention for their versatile coordination behavior toward various metal ions,³ and wide applications especially in biological fields such as antibacterial,⁴ antitumor,⁵ anti-inflammatory⁶ and cytotoxic,⁷ etc. Interestingly, hydrazone compounds have been reported to have urease inhibitory activities.⁸ Some vanadium complexes with hydrazone ligands also show effective biological activities, like antibacterial and urease inhibitory aspects.⁹ In the last few years, a number of Schiff bases and their com-

plexes have shown effective urease inhibitory activities.¹⁰ Among the complexes, those with copper atoms are of particular attention due to their high activities on urease.¹¹ In continuation of our work,¹² and aiming at obtaining new copper based urease inhibitors, in this work, a new benzohydrazone compound 4-bromo-*N*'-(1-(pyridin-2-yl)ethylidene)benzohydrazide (HL, Scheme 1), and its copper(II) complex, $[\text{Cu}_2(\mu\text{-Br})_2\text{L}_2] \cdot 0.5\text{MeOH}$, are presented.



Scheme 1. The hydrazone HL

2. Experimental

2.1. Materials and Methods

2-Acetylpyridine and 4-bromobenzohydrazide with analytical grade were purchased from TCI. All other chemicals were obtained from Xiya Chemical Co. Ltd. All

the starting materials were used as received. Elemental analyses (CHN) were performed on a Perkin-Elmer 240 C elemental analyzer. Infrared spectra were recorded on a Jasco FT/IR-4000 spectrophotometer in the region 4000–400 cm^{-1} using KBr pellets. Electronic absorption spectra were recorded with a Lambda 35 spectrophotometer. ^1H NMR and ^{13}C NMR spectra for the benzohydrazone compound were recorded on a Bruker 500 MHz spectrometer. Single crystal X-ray diffraction was carried out with a Bruker SMART 1000 CCD diffractometer.

2. 2. Synthesis of 4-Bromo- N^2 -(1-(pyridin-2-yl)ethylidene)benzohydrazide (HL)

2-Acetylpyridine (1.21 g, 0.01 mol) was dissolved in 50 mL methanol, to which was added 50 mL methanol solution of 4-bromobenzohydrazide (0.21 g, 0.01 mol). The mixture was stirred and refluxed for 1 h. Then, the solvent was removed by distillation under reduced pressure. The white solid residue was re-crystallized from methanol to obtain colorless single crystals. Yield 2.9 g (76%).

Anal. Calcd for $\text{C}_{14}\text{H}_{12}\text{BrN}_3\text{O}$: C, 52.8; H, 3.8; N, 13.2%. Found: C, 53.0; H, 3.9; N, 13.0%. FT-IR data (KBr, cm^{-1}): $\nu(\text{NH})$ 3283, $\nu(\text{C}=\text{O})$ 1659, $\nu(\text{C}=\text{N})$ 1587. UV data [10^{-3} mol L^{-1} in methanol, λ/nm ($\epsilon/\text{L mol}^{-1} \text{cm}^{-1}$): 245 (15,300), 298 (18,100), 365 (7,600). ^1H NMR (500 MHz,

d^6 -DMSO, ppm) δ 10.92 (s, 1H, NH), 8.61 (d, 1H, PyH), 8.11 (d, 1H, PyH), 7.84–7.71 (m, 6H, PyH + ArH), 2.46 s (3H, CH_3). ^{13}C NMR (126 MHz, d^6 -DMSO, ppm) δ 163.19, 154.98, 148.56, 147.71, 136.54, 132.04, 130.11, 129.58, 125.22, 124.81, 120.36, 12.63.

2. 3. Synthesis of $[\text{Cu}_2(\mu\text{-Br})_2\text{L}_2] \cdot 0.5\text{MeOH}$

The benzohydrazone HL (0.32 g, 1.0 mmol) was dissolved in methanol (30 mL), to which was added solid CuBr_2 (0.22 g, 1.0 mmol). The mixture was stirred at room temperature for 30 min. The solution was filtered to remove minor unresolved residues. The filtrate was kept in air for several days to give blue block-shaped single crystals of the complex. Yield: 183 mg (40%).

Anal. Calcd for $\text{C}_{28.5}\text{H}_{24}\text{Br}_4\text{Cu}_2\text{N}_6\text{O}_{2.5}$: C, 36.5; H, 2.6; N, 9.0. Found: C, 36.3; H, 2.5; N, 9.2%. FT-IR data (KBr, cm^{-1}): $\nu(\text{C}=\text{O})$ 1648; $\nu(\text{C}=\text{N})$ 1591; 1446, 1373, 1160, 1077, 947, 855, 543, 522. UV data [10^{-3} mol L^{-1} in methanol, λ/nm ($\epsilon/\text{L mol}^{-1} \text{cm}^{-1}$): 272 (12,300), 380 (13,100). Λ_{M} (10^{-3} M in methanol): $25 \Omega^{-1} \text{cm}^2 \text{mol}^{-1}$.

2. 4. X-Ray Crystallography

The X-ray data of the benzohydrazone compound and the copper complex were collected at 298(2) K on a

Table 1. Crystal data for the benzohydrazone compound (HL) and the copper complex

	HL	$[\text{Cu}_2(\mu\text{-Br})_2\text{L}_2] \cdot 0.5\text{MeOH}$
Formula	$\text{C}_{14}\text{H}_{12}\text{BrN}_3\text{O}$	$\text{C}_{28.5}\text{H}_{24}\text{Br}_4\text{Cu}_2\text{N}_6\text{O}_{2.5}$
FW	318.2	937.2
Crystal shape/color	block/colorless	block/blue
Crystal size /mm	$0.10 \times 0.07 \times 0.06$	$0.20 \times 0.20 \times 0.15$
Crystal system	Triclinic	Triclinic
Space group	<i>P1</i>	<i>P1</i>
<i>a</i> (Å)	4.0153(15)	8.7406(11)
<i>b</i> (Å)	11.0020(19)	9.3175(13)
<i>c</i> (Å)	15.6170(15)	11.5701(15)
α (°)	85.102(2)	75.321(2)
β (°)	87.249(2)	80.994(2)
γ (°)	89.880(2)	64.845(2)
<i>V</i> (Å ³)	686.6(3)	823.79(19)
<i>Z</i>	2	1
λ (MoK α) (Å)	0.71073	0.71073
<i>T</i> (K)	298(2)	298(2)
μ (MoK α) (cm^{-1})	2.989	6.176
<i>T</i> _{min}	0.7543	0.3714
<i>T</i> _{max}	0.8410	0.4199
<i>R</i> _{int}	0.0482	0.0184
Reflections/parameters	4028/176	4423/209
Unique reflections	2527	3057
Observed reflections [$I \geq 2\sigma(I)$]	1332	2227
Restraints	1	13
Goodness of fit on <i>F</i> ²	0.974	1.053
<i>R</i> ₁ , <i>wR</i> ₂ [$I \geq 2\sigma(I)$]	0.0660, 0.1656	0.0427, 0.1014
<i>R</i> ₁ , <i>wR</i> ₂ (all data)	0.1324, 0.2132	0.0710, 0.1155

Table 2. Selected bond lengths (Å) and angles (°) for the copper complex

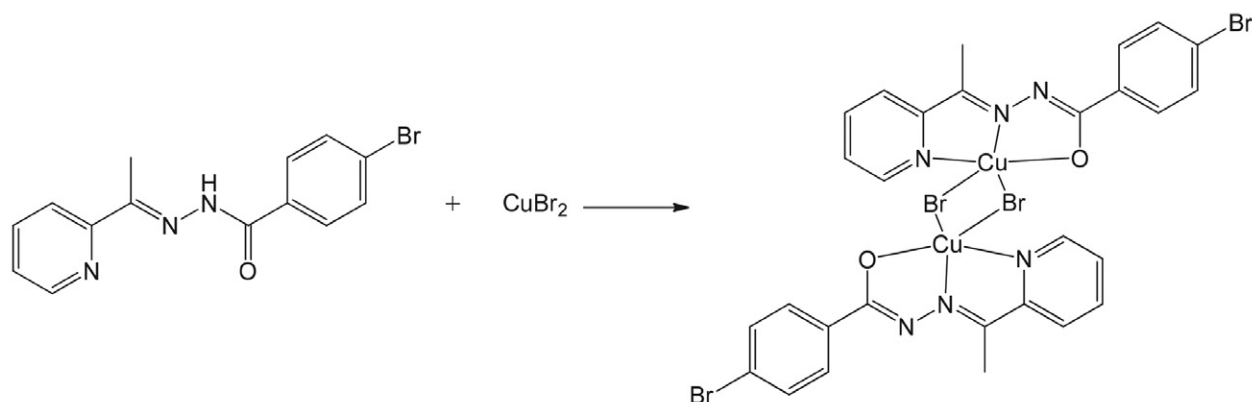
Cu1-N2	1.928(4)	Cu1-O1	1.950(4)
Cu1-N1	2.001(4)	Cu1-Br1A	2.3966(9)
Cu1-Br1	2.8263(10)		
N2-Cu1-O1	79.9(2)	N2-Cu1-N1	80.4(2)
O1-Cu1-N1	160.3(2)	N2-Cu1-Br1A	157.5(2)
O1-Cu1-Br1A	98.6(1)	N1-Cu1-Br1A	100.0(1)
N2-Cu1-Br1	107.1(1)	O1-Cu1-Br1	94.7(1)
N1-Cu1-Br1	90.1(1)	Br1-Cu1-Br1A	95.4(1)

Bruker SMART 1000 CCD diffractometer with graphite-monochromated Mo K α radiation (0.71073 Å) from a classical sealed tube. The intensity data were reduced with SAINT.¹³ The multi-scan absorption correction was performed with SADABS.¹⁴ Structures of the benzohydrazone compound and the copper complex were solved with SHELXTL by direct methods and refined against F^2 by full-matrix least-squares method.¹⁵ All non-hydrogen atoms of the compounds were refined anisotropically. The hydrogen atoms were placed in calculated positions and constrained to ride on their parent atoms. Crystallographic data for the benzohydrazone compound and the copper complex are summarized in Table 1. Selected bond lengths and angles are given in Table 2.

3. Results and Discussion

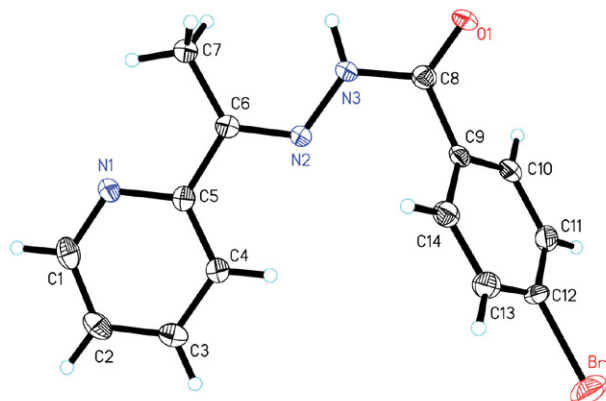
3.1. Synthesis

The benzohydrazone compound was facile synthesized by reaction of 2-acetylpyridine and 4-bromobenzohydrazide in methanol. The copper complex was readily prepared by the self-assembly reaction of the benzohydrazone compound with copper bromide in methanol. Single crystals of the ligand and the copper complex were formed by typical slow evaporation method. Molar conductivity of the copper complex in methanol with a concentration of $1.0 \times 10^{-3} \text{ mol} \cdot \text{L}^{-1}$ is $25 \Omega^{-1} \cdot \text{cm}^2 \cdot \text{mol}^{-1}$, indicating the non-electrolytic nature of the complex.¹⁶

**Scheme 2.** The synthetic procedure for the copper complex

3.2. Structure Description of the Benzohydrazone Compound (HL)

The molecular structure of the benzohydrazone compound is shown in Figure 1. The molecule shows *E* configuration with respect for the ethylidene group (C=N). The bond (C6–N2) with distance of 1.289(7) Å, confirms a typical double bond. In addition, the C8–N3 bond is shorter than usual, while the C8=O1 bond is longer than usual; suggest there are conjugation effects in the molecule. All the bond lengths are within normal values.^{9c,17} The pyridine and benzene rings form a dihedral angle of 57.5(5)°. In the crystal structure of the complex, the adjacent two

**Figure 1.** Molecular structure of the benzohydrazone compound, showing the atom-numbering scheme. Displacement ellipsoids are drawn at the 30% probability level.

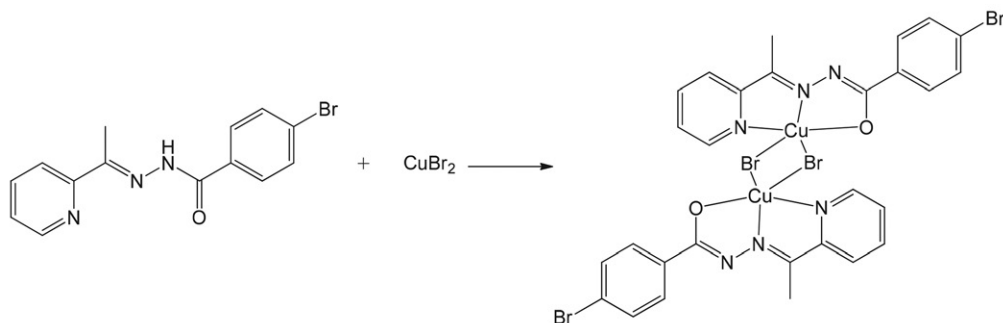


Figure 2. Molecular packing structure of the benzohydrazone compound, viewed down the *a* axis. Hydrogen bonds are drawn as dotted lines.

molecules are linked through intermolecular N–H...O hydrogen bonds (Table 3), to generate a dimeric structure (Figure 2).

3. 3. Structure Description of the Copper Complex

Molecular structure of the dinuclear copper(II) complex is shown in Figure 3. The compound contains a copper complex molecule and half of a methanol molecule. The Cu...Cu distance is 3.528(2) Å. The complex possesses crystallographic inversion center symmetry. The center is located at the central site of the two Cu atoms. The ligand coordinates to the Cu atom through the imino N, pyridine N, and enolate O atoms, generating five-membered chelate rings with bite angles of 79.9(2)° and 80.4(2)°. The Cu atom is in square pyramidal coordination, with the three donor atoms of the hydrazone ligand,

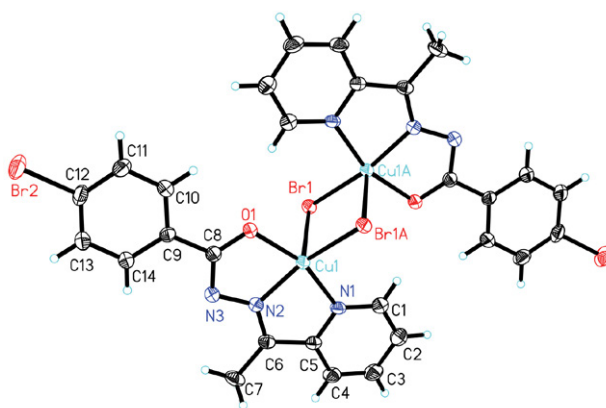


Figure 3. Molecular structure of the complex, showing the atom-numbering scheme. Displacement ellipsoids are drawn at the 30% probability level. Atoms labeled with the suffix A and unlabeled atoms are related to the symmetry operation $-x, -y, 1-z$. The methanol molecule is omitted for clarity.

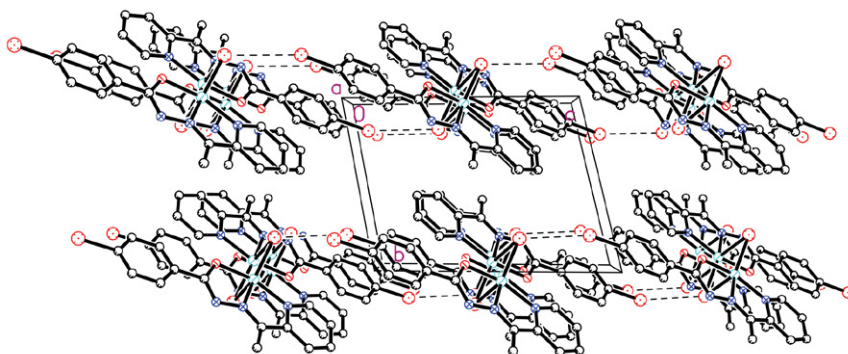


Figure 4. Molecular packing structure of the complex, viewed down the *a* axis. Hydrogen bonds are drawn as dotted lines.

Table 3. Hydrogen bond distances (Å) and bond angles (°) for HL and the complex

<i>D</i> –H... <i>A</i>	<i>d</i> (<i>D</i> –H)	<i>d</i> (H... <i>A</i>)	<i>d</i> (<i>D</i> ... <i>A</i>)	Angle (<i>D</i> –H... <i>A</i>)
HL				
N3–H3...O1 ^{#1}	0.90(1)	2.07(2)	2.963(6)	173(6)
The complex				
C1–H1...O1 ^{#2}	0.93	2.60(3)	3.400(5)	145(5)
C4–H4...Br1 ^{#3}	0.93	2.89(3)	3.778(5)	160(5)

Symmetry codes: #1: $2 - x, 1 - y, -z$; #2: $-x, -y, 1 - z$; #3: $-x, 1 - y, 1 - z$.

and one Br atom located at the basal plane, and with the other Br atom at the apical site. The Cu atom deviates by 0.237(1) Å from the basal plane. The bond lengths around the Cu atom are within normal values with the reported copper(II) complexes derived from hydrazones.¹⁸ The square pyramidal geometry is distorted, which are demonstrated from the *cis* and *trans* bond angles of 79.9(2)–107.1(2)° and 157.5(2)–160.3(2)°, respectively. The pyridine and benzene rings form dihedral angle of 6.6(5)° in the hydrazone ligand.

The neighboring molecules of the complex are connected by hydrogen bonds (Table 3), to form dimeric structure (Figure 4). There exists C–H... π interactions between C1 atom and the Br1–Cu1–Br1A–Cu1A ring, with the distance of 2.79(2) Å.

3. 4. IR and UV Spectra

The N–H and C=O absorptions of the free hydrazone HL are observed at 3283 cm^{-1} and 1659 cm^{-1} . The C=O absorption is shifted to lower wave number, *viz.* 1648 cm^{-1} for the complex, indicates it participates in coordination. The C=N absorptions of HL and the complex are located at about 1590 cm^{-1} .^{9c,19}

The UV spectra of the free hydrazone and the complex displayed strong bands in the region 270–300 nm, which are assigned to the π – π^* transition. The charge transfer LMCT bands of the complexes are located in the region 350–400 nm.²⁰

3. 5. Pharmacology Study

The assay of the urease inhibitory activity was in accordance with the literature method.²¹ The free hydrazone HL has weak activity, with inhibition rate of 13.5% at concentration of 100 $\mu\text{mol} \cdot \text{L}^{-1}$. However, the copper complex has stronger activity than HL, with inhibition rate of 93.5% at the same concentration, and with IC_{50} value of 1.38 $\mu\text{mol} \cdot \text{L}^{-1}$. The complex has even better activity than the reference drug acetohydroxamic acid ($\text{IC}_{50} = 28.1 \mu\text{mol} \cdot \text{L}^{-1}$) and the copper perchlorate ($\text{IC}_{50} = 8.8 \mu\text{mol} \cdot \text{L}^{-1}$).

3. 6. Molecular Docking Study of the Complex

The molecular docking technique was used to study the binding effects of the complex with the *Jack bean* urease. The binding models are shown in Figures 5 and 6. It is clear that the complex molecule fits very well with the urease active pocket. Detailed interactions were established in a variety of conformations of the complex molecule with the amino acid residues of the urease. The docking score is –7.13, which is lower than the reference drug acetohydroxamic acid (–5.01). There are hydrogen bonds between the complex molecule and the amino acid residue His323. Moreover, there are hydrophobic interactions between the complex molecule and the amino acid residues of the ure-

ase. The results indicate that the copper complex may be served as a potential urease inhibitor.

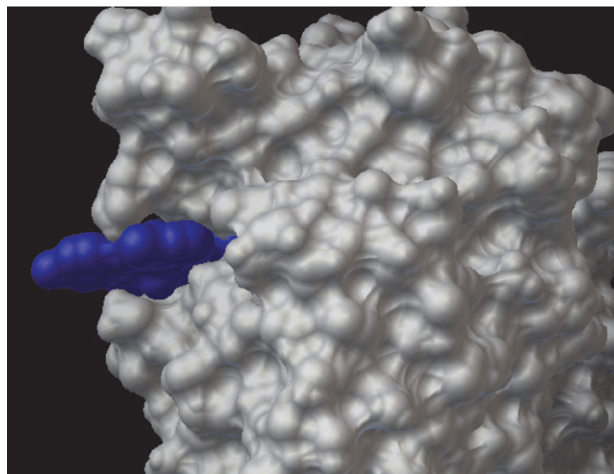


Figure 5. Binding mode of the complex with *Jack bean* urease. The enzyme is shown as surface, and the complex is shown as filling model.

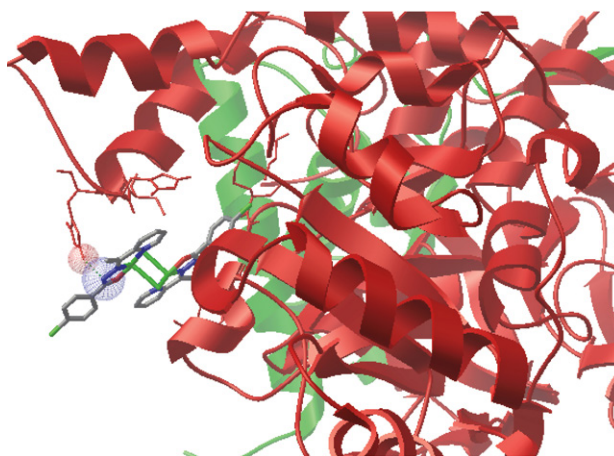


Figure 6. Binding mode of the complex with *Jack bean* urease. The enzyme is shown as ribbons, and the complex is shown as sticks.

4. Conclusion

The present study reports the synthesis, characterization and crystal structures of a hydrazone compound 4-bromo-*N*'-(1-(pyridin-2-yl)ethylidene)benzohydrazide and its dinuclear copper complex. The hydrazone compound coordinates to the Cu atoms through the pyridine nitrogen, imino nitrogen and enolate oxygen. The Cu atom in the complex is in square pyramidal coordination. The complex has interesting biological activity, with good urease inhibitory activity.

Supplementary Data

CCDC 1878329 (HL), 1874306 (the complex) contain the supplementary crystallographic data for this paper. These

data can be obtained free of charge via <http://www.ccdc.cam.ac.uk/conts/retrieving.html>, or from the Cambridge Crystallographic Data Centre, 12 Union Road, Cambridge CB2 1EZ, UK; fax: (+44) 1223-336-033; or e-mail: deposit@ccdc.cam.ac.uk.

Acknowledgments

This work was supported by the scientific research project of Hubei Provincial Department of Education, “Adsorbent prepared from agricultural and forestry waste biomass and treatment of dye wastewater with adsorbent” (Project No. B20111609).

5. References

- (a) P. A. Karplus, M. A. Pearson, R. P. Hausinger, *Acc. Chem. Res.* **1997**, *30*, 330–337; DOI:10.1021/ar960022j
- (b) Z.-P. Xiao, Z.-Y. Peng, J.-J. Dong, R.-C. Deng, X.-D. Wang, H. Ouyang, P. Yang, J. He, Y.-F. Wang, M. Zhu, X.-C. Peng, W.-X. Peng, H.-L. Zhu, *Eur. J. Med. Chem.* **2013**, *68*, 212–221; DOI:10.1016/j.ejmech.2013.07.047
- (c) Z.-P. Xiao, Z.-Y. Peng, J.-J. Dong, J. He, H. Ouyang, Y.-T. Peng, C.-L. Lu, W.-Q. Lin, J.-X. Wang, Y.-P. Xiang, H.-L. Zhu, *Eur. J. Med. Chem.* **2013**, *63*, 685–695. DOI:10.1016/j.ejmech.2013.03.016
- (a) W.-W. Ni, H.-L. Fang, Y.-X. Ye, W.-Y. Li, C.-P. Yuan, D.-D. Li, S.-J. Mao, S.-E. Li, Q.-H. Zhu, H. Ouyang, Z.-P. Xiao, H.-L. Zhu, *Future Med. Chem.* **2020**, *12*, 1633–1645; DOI:10.4155/fmc-2020-0048
- (b) Q. Liu, W.-K. Shi, S.-Z. Ren, W.-W. Ni, W.-Y. Li, H.-M. Chen, P. Liu, J. Yuan, X.-S. He, J.-J. Liu, P. Cao, P.-Z. Yang, Z.-P. Xiao, H.-L. Zhu, *Eur. J. Med. Chem.* **2018**, *156*, 126–136; DOI:10.1016/j.ejmech.2018.06.065
- (c) W.-W. Ni, Q. Liu, S.-Z. Ren, W.-Y. Li, L.-L. Yi, H. Jing, L.-X. Sheng, Q. Wan, P.-F. Zhong, H.-L. Fang, H. Ouyang, Z.-P. Xiao, H.-L. Zhu, *Bioorg. Med. Chem.* **2018**, *26*, 4145–4152; DOI:10.1016/j.bmc.2018.07.003
- (d) W.-K. Shi, R.-C. Deng, P.-F. Wang, Q.-Q. Yue, Q. Liu, K.-L. Ding, M.-H. Yang, H.-Y. Zhang, S.-H. Gong, M. Deng, W.-R. Liu, Q.-J. Feng, Z.-P. Xiao, H.-L. Zhu, *Bioorg. Med. Chem.* **2016**, *24*, 4519–4527; DOI:10.1016/j.bmc.2016.07.052
- (e) Z.-P. Xiao, W.-K. Shi, P.-F. Wang, W. Wei, X.-T. Zeng, J.-R. Zhang, N. Zhu, M. Peng, B. Peng, X.-Y. Lin, H. Ouyang, X.-C. Peng, G.-C. Wang, H.-L. Zhu, *Bioorg. Med. Chem.* **2015**, *23*, 4508–4513. DOI:10.1016/j.bmc.2015.06.014
- (a) K.-H. Yang, *Acta Chim. Slov.* **2014**, *61*, 629–636;
- (b) M. Sutradhar, E. C. B. A. Alegria, K. T. Mahmudov, M. F. C. G. da Silva, A. J. L. Pombeiro, *RSC Advances* **2016**, *6*, 8079–8088; DOI:10.1039/C5RA25774C
- (c) P. Wang, Y.-S. Wu, X.-M. Han, S.-S. Zhao, J. Qin, *Acta Chim. Slov.* **2017**, *64*, 431–437; DOI:10.17344/acsi.2017.3268
- (d) Y.-J. Cai, Y.-Y. Wu, F. Pan, Q.-A. Peng, Y.-M. Cui, *Acta Chim. Slov.* **2020**, *67*, 896–903; DOI:10.17344/acsi.2020.5895
- (e) Y. Tan, *Acta Chim. Slov.* **2020**, *67*, 1233–1238. DOI:10.17344/acsi.2020.6136
- (a) M. V. Angelusiu, S. F. Barbuceanu, C. Draghici, G. L. Almajan, *Eur. J. Med. Chem.* **2010**, *45*, 2055–2062; DOI:10.1016/j.ejmech.2010.01.033
- (b) O. O. Ajani, C. A. Obafemi, O. C. Nwinyi, D. A. Akinpelu, *Bioorg. Med. Chem.* **2010**, *18*, 214–221; DOI:10.1016/j.bmc.2009.10.064
- (c) Z.-Q. Sun, S.-F. Yu, X.-L. Xu, X.-Y. Qiu, S.-J. Qiu, *Acta Chim. Slov.* **2020**, *67*, 1281–1289; DOI:10.17344/acsi.2020.6236
- (d) Y.-L. Sang, X.-S. Lin, W.-D. Sun, *Acta Chim. Slov.* **2020**, *67*, 581–585; DOI:10.17344/acsi.2019.5595
- (e) H.-Y. Qian, *Acta Chim. Slov.* **2019**, *66*, 995–1001; DOI:10.4149/neo_2019_190112N36
- (f) L.-W. Xue, Y.-J. Han, X.-Q. Luo, *Acta Chim. Slov.* **2019**, *66*, 622–628. DOI:10.17344/acsi.2019.5039
- (a) Y. H. Zhang, L. Zhang, L. Liu, J. X. Guo, D. L. Wu, G. C. Xu, X. H. Wang, D. Z. Jia, *Inorg. Chim. Acta* **2010**, *363*, 289–293; DOI:10.1016/j.ica.2009.08.017
- (b) T. Horiuchi, J. Chiba, K. Uoto, T. Soga, *Bioorg. Med. Chem. Lett.* **2009**, *19*, 305–308. DOI:10.1016/j.bmcl.2008.11.090
- (a) M. A. A. El-Sayed, N. I. Abdel-Aziz, A. A. M. Abdel-Aziz, A. S. El-Azab, Y. A. Asiri, K. E. H. ElTahir, *Bioorg. Med. Chem.* **2011**, *19*, 3416–3424; DOI:10.1016/j.bmc.2011.04.027
- (b) S. M. Sondhi, M. Dinodia, A. Kumar, *Bioorg. Med. Chem.* **2006**, *14*, 4657–4663. DOI:10.1016/j.bmc.2006.02.014
- (a) P. Krishnamoorthy, P. Sathyadevi, A. H. Cowley, R. R. Btorac, N. Dharmaraj, *Eur. J. Med. Chem.* **2011**, *46*, 3376–3387; DOI:10.1016/j.ejmech.2011.05.001
- (b) P. G. Avaji, C. H. V. Kumar, S. A. Patil, K. N. Shivananda, C. Nagaraju, *Eur. J. Med. Chem.* **2009**, *44*, 3552–3559. DOI:10.1016/j.ejmech.2009.03.032
- K. M. Khan, F. Rahim, A. Khan, S. Ali, M. Taha, S. M. Saad, M. Khan, Najeebullah, A. Shaikh, S. Perveen, M. I. Choudhary, *J. Chem. Soc. Pak.* **2015**, *37*, 479–483.
- (a) R. Ara, U. Ashiq, M. Mahroof-Tahir, Z. T. Maqsood, K. M. Khan, M. A. Lodhi, M. I. Choudhary, *Chem. Biodiversity* **2007**, *4*, 58–71; DOI:10.1002/cbdv.200790007
- (b) H. Y. Qian, *Inorg. Nano-Met. Chem.* **2018**, *48*, 461–466; DOI:10.1080/24701556.2019.1569689
- (c) H. Y. Qian, *Russ. J. Coord. Chem.* **2017**, *43*, 780–786; DOI:10.1134/S1070328417110070
- (d) H.-Y. Qian, *Acta Chim. Slov.* **2019**, *66*, 995–1001. DOI:10.4149/neo_2019_190112N36
- (a) W. Chen, Y. G. Li, Y. M. Cui, X. A. Zhang, H.-L. Zhu, Q. F. Zeng, *Eur. J. Med. Chem.* **2010**, *45*, 4473–4478; DOI:10.1016/j.ejmech.2010.07.007
- (b) D. H. Shi, Z. L. You, *Russ. J. Coord. Chem.* **2010**, *36*, 535–540; DOI:10.1134/S1070328410070109
- (c) N. Zhang, C.-Y. Huang, D.-H. Shi, Z.-L. You, *Inorg. Chem. Commun.* **2011**, *14*, 1636–1639; DOI:10.1016/j.inoche.2011.06.027
- (d) J.-Q. Ren, Q.-Z. Jiao, Y.-N. Wang, F.-Y. Xu, X.-S. Cheng, Z.-L. You, *Chinese. J. Inorg. Chem.* **2014**, *30*, 640–648;
- (e) D.-H. Shi, L. Zhang, L.-L. Ni, S. Bai, Z.-L. You, *Synth. Re-*

- act. Inorg. Met.-Org. Nano-Met. Chem.* **2010**, *40*, 359–363;
DOI:10.1080/15533174.2010.487057
- (f) Y.-T. Li, J.-W. Dong, Y. Lu, Y.-T. Gu, C.-N. Shang, F.-Y. Liu, Y. Xin, C.-L. Jing, Z.-L. You, *Chinese J. Inorg. Chem.* **2018**, *34*, 1192–1198;
- (g) Z.-L. You, Y.-M. Cui, Y.-P. Ma, C. Wang, X.-S. Zhou, K. Li, *Inorg. Chem. Commun.* **2011**, *14*, 636–640;
DOI:10.1016/j.inoche.2011.01.038
- (h) Y.-M. Cui, W.-X. Yan, Y.-J. Cai, W. Chen, H.-L. Zhu, *J. Coord. Chem.* **2010**, *63*, 3706–3713;
DOI:10.1080/00958972.2010.517268
- (i) C. L. Jing, C. F. Wang, K. Yan, K. D. Zhao, G. H. Sheng, D. Qu, F. Niu, H. L. Zhu, Z. L. You, *Bioorg. Med. Chem.* **2016**, *24*, 270–276; DOI:10.1016/j.bmc.2015.12.013
- (j) A. de Fatima, C. D. Pereira, C. R. S. D. G. Olimpio, B. G. D. Oliveira, L. L. Franco, P. H. C. da Silva, *J. Adv. Res.* **2018**, *13*, 113–126. DOI:10.1016/j.jare.2018.03.007
11. (a) F. Niu, K.-X. Yan, L. H. Pang, D. Qu, X. L. Zhao, Z. L. You, *Inorg. Chim. Acta* **2015**, *435*, 299–304;
DOI:10.1016/j.ica.2015.07.014
- (b) Z.-L. You, L. Zhang, D.-H. Shi, X.-L. Wang, X.-F. Li, Y.-P. Ma, *Inorg. Chem. Commun.* **2010**, *13*, 996–998;
DOI:10.1016/j.inoche.2010.05.016
- (c) Z. L. You, M. Y. Liu, C. F. Wang, G. H. Sheng, X. L. Zhao, D. Qu, F. Niu, *RSC Advances* **2016**, *6*, 16679–16690.
DOI:10.1039/C6RA00500D
12. H. Zhao, X. P. Tan, Q. A. Peng, C. Z. Shi, Y. F. Zhao, Y. M. Cui, *Russ. J. Coord. Chem.* **2021**, *47*, 58–65.
DOI:10.1134/S107032842011010X
13. Bruker, SMART (Version 5.628) and SAINT (Version 6.02); Bruker AXS: Madison, Wisconsin, USA, 1998.
14. G. M. Sheldrick, SADABS Program for Empirical Absorption Correction of Area Detector, University of Göttingen, Germany, 1996.
15. G. M. Sheldrick, *Acta Crystallogr.* **2008**, *A64*, 112–122.
DOI:10.1107/S0108767307043930
16. W. J. Geary, *Coord. Chem. Rev.* **1971**, *7*, 81–120.
DOI:10.1016/S0010-8545(00)80009-0
17. A. Barakat, F. F. El-Senduny, Z. Almarhoon, H. H. Al-Rashed, F. A. Badria, A. M. Al-Majid, H. A. Ghabbour, A. El-Faham, *J. Chem.* **2019**, 9403908.
DOI:10.1155/2019/9403908
18. (a) Z. You, H. Yu, B. Zheng, C. Zhang, C. Lv, K. Li, L. Pan, *Inorg. Chim. Acta* **2018**, *469*, 44–50;
DOI:10.1016/j.ica.2017.09.011
- (b) Z. You, H. Yu, Z. Li, W. Zhai, Y. Jiang, A. Li, S. Guo, K. Li, C. Lv, C. Zhang, *Inorg. Chim. Acta* **2018**, *480*, 120–126.
DOI:10.1016/j.ica.2018.05.020
19. (a) H.-Y. Qian, *Inorg. Nano-Met. Chem.* **2018**, *48*, 615–619;
DOI:10.1080/24701556.2019.1567542
- (b) H. Y. Qian, *Russ. J. Coord. Chem.* **2018**, *44*, 32–38.
DOI:10.1134/S1070328418010074
20. H.-Y. Qian, N. Sun, *Transit. Met. Chem.* **2019**, *44*, 501–506.
DOI:10.1007/s11243-018-00296-x
21. T. Tanaka, M. Kawase, S. Tani, *Life Sci.* **2003**, *73*, 2985–2990.
DOI:10.1016/S0024-3205(03)00708-2

Povzetek

Sintetizirali smo nov dvojedrni bakrov(II) kompleks $[\text{Cu}_2(\mu\text{-Br})_2\text{L}_2] \cdot 0.5\text{MeOH}$ z benzohidrazonskim ligandom 4-bromo- N^2 -(1-(piridin-2-il)etiliden)benzohidrazid (HL) ter produkt karakterizirali z elementno analizo, IR in UV-Vis spektroskopijo. Preučevali smo monokristalne strukture kompleksa in benzohidrazonske spojine. Bakrovi atomi v kompleksu so koordinirani z dvema benzohidrazonskima ligandoma in dvema mostovnima bromidnima ligandoma v kvadratno planarni koordinaciji. Kompleks je pokazal dobro aktivnost kot inhibitor *Jack bean* ureaze, vrednost IC_{50} je znašala $1.38 \mu\text{mol} \cdot \text{L}^{-1}$.



Except when otherwise noted, articles in this journal are published under the terms and conditions of the Creative Commons Attribution 4.0 International License

Scientific paper

Electrochemical Oxidation of Different Therapeutic Classes of Pharmaceuticals Using Graphite-PVC Composite Electrode

Zainab H. Mussa,¹ Fouad F. Al-Qaim,^{2,*} Zahraa H. Alqaim³ and Jalifah Latip⁴¹ Faculty of Pharmacy, University of Al-Ameed, Karbala, Iraq² Department of Chemistry, Faculty of Science for Women, University of Babylon, PO Box 4, Hilla, Iraq³ Medical laboratories Technique Department, Al-Mustaqbal University College, Iraq⁴ School of Chemical Sciences and Food Technology, Faculty of Science and Technology, Universiti Kebangsaan Malaysia, Selangor, Malaysia

* Corresponding author: E-mail: fouadalkaim@yahoo.com

Received: 02-27-2021

Abstract

This study reports electrochemical treatment of different therapeutic classes of pharmaceuticals (caffeine, prazosin, enalapril, carbamazepine, nifedipine, levonorgestrel, and simvastatin) in a mixture. The electrochemical process was investigated using graphite-PVC anode at different applied voltages (3, 5, and 12 V), initial concentrations of studied pharmaceuticals in aqueous solution (5 and 10 mg/L), and concentrations of sodium chloride (1 and 2 g/L). The % removal of pharmaceuticals increased with the applied voltage, and was found higher than 98% after 50 min of electrolysis at 5 V. Energy consumption ranged between 0.760 and 3.300 Wh/mg using 12 V being the highest value compared to 3 and 5 V. The formation of chlorinated by-products from four selected pharmaceuticals, simvastatin (C₁₁H₁₃Cl₃O₅, and C₁₀H₁₂Cl₄O₃), prazosin (C₁₃H₁₂Cl₃N₅O₃ and C₁₀H₁₁Cl₄N₂O₂), carbamazepine and caffeine (C₁₅H₁₁N₂O₂Cl and C₈H₆N₄O₂Cl) was identified and elucidated using liquid chromatography-time of flight mass spectrometry (LC-TOF/MS).

Keywords: Pharmaceuticals; indirect electrochemical oxidation process; graphite-PVC anode; solid phase extraction; LC-TOF/MS; energy consumption

1. Introduction

Pharmaceuticals are defined as organic compounds used for the treatment of disease. They are present in prescription medicines, over-the-counter therapeutic drugs, and veterinary drugs. Different therapeutic classes of pharmaceuticals such as caffeine, prazosin, enalapril, carbamazepine, nifedipine, levonorgestrel, and simvastatin are categorized and prescribed for different treatments.

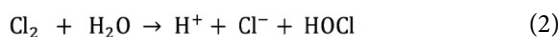
Caffeine is one of the most widely used drugs for the nervous system. It is considered a non-prescribed drug as it is available naturally in tea and coffee. Caffeine is used as a central nervous system (CNS) stimulant, mild diuretic, and respiratory stimulant (in neonates with apnea of prematurity). Caffeine is used to treat migraines and other headache types.¹ Prazosin is one of the antihypertensive compounds. It is used for the treatment of hypertension,

symptomatic benign prostatic hyperplasia, and severe congestive heart failure.¹ Enalapril is an example of renin-angiotensin system inhibitor that is used for the treatment of essential or renovascular hypertension and symptomatic congestive heart failure.¹ Carbamazepine is one of the most widely used antiepileptic drugs to treat partial seizures, tonic-clonic seizures, and the pain of neurologic origin such as trigeminal neuralgia.¹ Nifedipine is one of the calcium channel blockers (CCBs) class that is used to treat chronic stable angina, hypertension, and Raynaud's phenomenon.¹ Levonorgestrel is a progestin or a synthetic form of the naturally occurring female sex hormone, progesterone. Levonorgestrel is used for the treatment of menopausal and postmenopausal disorders alone or in combination with other hormones as an oral contraceptive.¹ Simvastatin, the methylated form of lovastatin, is a lipid-modifying agent that inhibits HMG-CoA reductase

(3-hydroxy-3-methyl-glutaryl-CoA reductase). Simvastatin is used in the treatment of primary hypercholesterolemia. It is effective in reducing total and LDL-cholesterol as well as plasma triglycerides and apolipoprotein B.¹

Pharmaceutical compounds were detected in the surface water situated near the sewage water treatment plants (STP).² The detection of pharmaceuticals in the aquatic environment at trace levels ranging from nanograms to micrograms per litre has been widely discussed and published in previous studies.^{3,4,5} In Malaysia, the studied pharmaceuticals have been analysed and frequently detected in water samples such as influent and effluent of sewage treatment plants, hospitals, and surface water.^{6,7,8,9,10} In Malaysia, the main sewage treatment plant applies a biological treatment process, which is unable to accomplish complete degradation of some pharmaceuticals. However, caffeine was found in the effluent sewage treatment plants up to 1464 ng/L, while prazosin and other pharmaceuticals were detected between 16 and 77 ng/L. Nifedipine was not detected anymore because it is light-sensitive, which causes rapid photodegradation.⁶ Biological treatment methods are extensively used for the removal of pharmaceuticals from wastewater. It was observed that the option of biological treatment may not be suitable because microbial growth could be inhibited in the presence of chloride.¹¹ Advanced oxidation process (AOP) was attempted to remove the pharmaceutical compounds but their degradation was observed to be only partial.¹² Thus, looking for an alternative treatment process is necessary to remove the pharmaceuticals from water bodies.

The electrochemical oxidation process for wastewater treatment has been widely applied due to its environmental friendliness, amenability to automation, and effectiveness to process wide variety of organic pollutants.¹³ The removal of a wide spectrum of pharmaceuticals from aqueous solution using graphite-PVC electrode was reported in our previous studies.¹⁴ The electrochemical oxidation process could be classified into indirect and direct electrochemical processes. When the organic pollutants are degraded by anodic electrodes after adsorption of these pollutants on the anode, this type is called a direct process. In contrast, an indirect electrochemical process is the elimination of compounds in bulk solution, which is accompanied by strong and active oxidizing agents such as hypochlorite/chlorine.¹⁵ The mechanism of formation of hypochlorite, chloride, and chlorine could be illustrated by these equations:



Combining ultrasonic and electrochemical oxidation as advanced oxidation process using graphite as a

cathode has been used for the degradation of malachite green wastewater. It was observed that the highest degradation of malachite green obtained was 94.24% when the voltage was 20 V, ultrasonic power was 300 W, and electrolyte solution was 15.0 g/L Na_2SO_4 .¹⁶ Treatment of domestic wastewater has been given a big attention to reduce its impact on the aquatic environment. Using iron(III) doped titanium dioxide-coated graphite electrode exhibited good potential application on the purification of domestic wastewater.¹⁷ Graphite electrode has been used as anode for electrochemical degradation of raw water and digested water. It was observed that the% removal in terms of chemical oxygen demand (COD) was 37% and 25% for raw water and digested water, respectively.¹⁸

The electrochemical oxidation process has been applied for the degradation of real biotreated petrochemical wastewater. However, different parameters have been studied such as current density, pH value, agitation rate, and anode materials on their influence on the% removal of COD of real biotreated petrochemical wastewater. It was observed that higher oxidation occurred at the current density of 10 mA/cm², a pH value of 3, and an agitation rate of 400 rpm.¹⁹ The application of indirect electrochemical process reported that diclofenac, simvastatin, and their by-products were completely removed after 140 min using graphite-PVC composite anode.^{20,21} The COD of synthetic textile effluent was removed $\geq 75\%$ using graphite rod anode for 45 min.²² It was observed that the electrochemical oxidation process has achieved more than 90% removal of COD, BOD, and colour of textile dye using Ag/C composite anode after 100 min.²³ Indirect electrochemical treatment of landfill leachate showed 87% removal of COD using graphite-PVC anode by operating at 15 V applied voltage for 105 min of electrolysis.²⁴ However, the electrochemical oxidation process was not applied yet for the removal of different therapeutic classes of pharmaceuticals mixture in one batch.

This study aims to determine the effectiveness of an electrochemical process using graphite-PVC as anode for the degradation of different therapeutic classes of pharmaceuticals in one mixture. The pharmaceuticals were further identified for the formation of their chlorinated by-products during the electrochemical treatment process using LC-TOF/MS.

2. Experimental

2.1. Materials and Methods

Pure standards ($\geq 98\%$) of nifedipine (NFD) (CAS no. 21829-25-4), enalapril maleate (ENL) (CAS no. 76095-16-4), prazosin (PRZ) (CAS no. 19237-84-4), caffeine (CAF) (CAS no. 58-08-2), levonorgestrel (LNG) (CAS no. 797-63-7), carbamazepine (CBZ) (CAS no. 298-46-4), simvastatin (SMV) (CAS no. 79902-63-9) were purchased

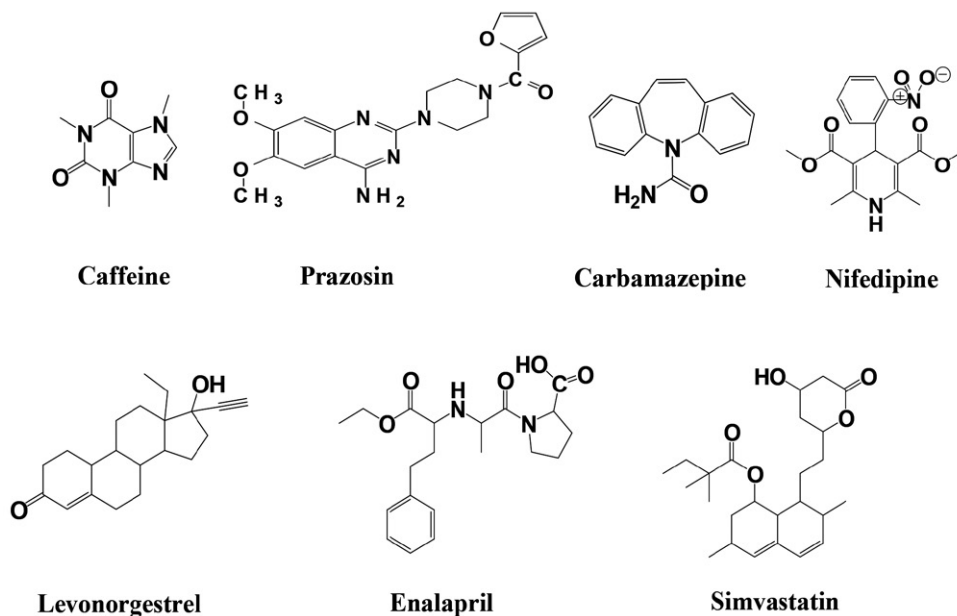


Figure 1. Chemical structures of seven pharmaceutical compounds

from Sigma-Aldrich (St. Louis, MO). Deionized water (DIW) was supplied by EASYPure RODI (Thermo Fisher Scientific, Waltham, MA). HPLC-grade methanol (MeOH), acetonitrile (ACN), acetone, and formic acid (FA) were supplied by Merck (Darmstadt, Germany). The chemical structure of all studied pharmaceuticals is presented in Figure 1.

The consumption profile of the studied pharmaceutical compounds in a particular country affects the profile of compounds found in wastewater and surface water. In Malaysia, Ministry of health publishes annually statistical report on drug consumption.²⁵ Table 1 presents the defined daily doses (DDD) of a drug per thousand inhabitants of the studied pharmaceuticals as a top 50 consumed pharmaceutical compounds over the years 2011–2014 in Malaysia. The DDD values are based on Anatomical Therapeutic Chemical (ATC) classification system by World Health Organization (WHO).²⁶ The annual consumption

(kg/y) of the pharmaceuticals can be calculated using the following formula:

$$\text{Consumption (kg/y)} = \text{DDD(g)} \times \frac{\text{DDD}}{1000\text{inh}} \times \frac{\text{Population}}{1000000} \times 366 \quad (4)$$

2. 2. Standard Preparation and Graphite-PVC Electrochemical Setup

A 1000 mg/L solutions of the standards were prepared individually using methanol as a solvent and stored at -18 . A mixture of solutions was prepared in water after an appropriate dilution of the individual standard. The conductivity of solutions was controlled by adding different amounts of NaCl (Merck, Germany). All experiments were conducted using a Pyrex glass vessel (100 mL). The

Table 1. Defined daily doses and the consumption of the selected pharmaceuticals in Malaysia 2011–2014

Compound	Classification	DDD (mg) ^a	Consumption (kg/y)			
			2011	2012	2013	2014
Caffeine ^b	Stimulant	400 (O,P)	–	–	–	–
Prazosin	Antihypertensive	5 (O)	92	88	108	122
Enalapril	Renin-angiotensin system inhibitors	10 (O,P)	597	616	564	667
Carbamazepine ^c	Anti-epileptics	1000 (O,R)	–	–	–	–
Nifedipine	Calcium channel blockers	30 (O,P)	2004	1650	1235	998
Levonorgestrel	Sex hormones	NA	–	–	–	–
Simvastatin	Lipid modifying agents	30 (O)	2044	3832	5024	5401
Population (10 ⁷ inhabitants)			2.9062	2.9510	2.9915	3.0261

^aWHO (2018), ^b over-the-counter compounds, ^ccompound not listed as top 50 consumed pharmaceuticals in Malaysia (2011–2014). O= Oral, P=Parenteral, R=Rectanal, NA: not available.

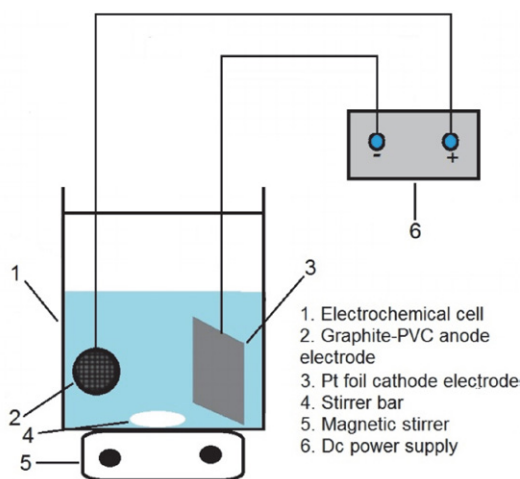


Figure 2. Electrochemical cell set up

Pyrex glass electrochemical cell (reactor) was placed on a magnetic stirring block to keep its contents well mixed during the experiment as shown in Figure 2.

Pt metal foil and graphite-PVC as cathode and anode, respectively, were prepared according to the previously reported procedure.²⁴ Graphite-PVC pellet was used as anode and prepared from the graphite powder.²⁰ The distance between two electrodes in the electrochemical cell was 2.5 cm in all experiments. The electrodes were connected to a DC power supply (CPX200 DUAL, 35V 10A PSU).

2. 3. Electrochemical Treatment Procedure

Aqueous solution of 5 and 10 mg/L of the seven compounds were prepared in deionized water. All solutions were treated electrochemically at applied voltages of 3 V, 5 V, and 12 V. The % removal was calculated according to the equation (5). Comparative electrochemical experiments of 100 mL mixture solutions of caffeine, prazosin, enalapril, carbamazepine, levonorgestrel, nifedipine and

simvastatin in deionized water were provided. The intervals were 0, 10, 20, 30, 40, and 50 min. The monitoring of the chlorinated by-products was performed after solid phase extraction for caffeine, prazosin, simvastatin and carbamazepine only at fixed conditions: 100 mL of solution, 0.5 mg/L of compound, 5 V of applied voltage and 0.2 g NaCl as supporting electrolyte.

$$R\% = \frac{A_0 - A_t}{A_0} \times 100\% \quad (5)$$

Where $R\%$ is the percentage removal of parent compound; A_0 is the initial peak area of parent compound; A_t is the residual peak area after time (t).

2. 4. Solid Phase Extraction Method

It is well known that by-products could be formed after the treatment of pharmaceuticals individually. An Oasis HLB (3 cc, 60 mg) cartridge from Waters (Milford, MA) was used for the purpose of SPE. The solid phase extraction method was conducted according to the previous study as follows: all experiments were subjected to a 10-sample GAST SPE vacuum manifold DOA-P504-BN (Büchi Labortechnik AG, Flawil, Switzerland), treated samples were loaded at a flow rate of 3 mL/min under vacuum conditions then the by-products were eluted out of sorbent using 5 mL of methanol.²⁷ Dry extracts were reconstituted with 500 μ L of solvent and filtered using 0.2 μ m Nylon syringe filters. A 30 μ L of the extract was automatically injected into the LC-ESI-TOF/MS system for analysis.

2. 5. Chemical Analysis

All pharmaceuticals and their by-products were separated on a Gemini 5 μ m NX 110Å C18 column 2 mm \times 150 mm (Phenomenex, Torrance, CA) using a Dionex UL-

Table 2. Chromatographic separation of selected pharmaceuticals and their by-products for both PI and NI ESI-TOF/MS modes

Positive ion (only selected pharmaceuticals)						
Mobile phase					A: 0.1% FA in DIW	
					B: ACN-MeOH (3:1, v/v)	
Flow rate					0.3 mL/min	
Injection volume					30 μ L	
Gradient program	Time (min)	0	3	6	11	11.1
	B%	5%	60%	97%	97%	5%
						16.1
						5%
Negative ion (by-products)						
Mobile phase					A: 0.1% FA in DIW	
					B: ACN-MeOH (2:3, v/v)	
Flow rate					0.3 mL/min	
Injection volume					30 μ L	
Gradient program	Time (min)	0	5	10	10.1	15.1
	B%	5%	95%	95%	5%	5%

timate 3000/LC 09115047 (Thermo Fisher Scientific, Waltham, MA) system equipped with a vacuum degasser, a quaternary pump, and an auto-sampler. The studied pharmaceuticals were analysed by TOF/MS in positive ESI ionization mode while the by-products were analysed in negative ESI ionization mode. The mobile phase and elution program are presented in Table 2.

3. Results and Discussion

According to our previous work, the electrochemical process was influenced by the initial concentration of the pharmaceuticals, NaCl amount, and applied voltage during the treatment of organic pollutants. Mainly, the oxidation of pollutants could take place by a strong oxidizing agent, which was chlorine/hypochlorite.^{27,28}

3. 1. Effect of Initial Concentration

A mixture of the studied pharmaceuticals solution with two different initial concentrations of 5 and 10 mg/L, was treated by indirect electrochemical oxidation process using graphite-PVC as the anode at a fixed applied voltage of 5 V and 2 g/L NaCl. The% removal was plotted against electrochemical treatment time for both initial concentrations as shown in Figure 3a. Degradation of pharmaceuticals was achieved in all cases; however, it is evident that faster elimination occurred at lower initial concentration. At 5 mg/L and 5 V, three pharmaceuticals were eliminated in a reaction time of 50 min, but at 10 mg/L and 5 V, the complete degradation may require a longer time. As the results indicated, the% removal decreased with an increase in drug concentration. Nifedipine was removed quickly; it was removed just after 10 min using 5 mg/L concentration whilst it was eliminated after 40 min with 10 mg/L of initial concentration. Only caffeine, prazosin, enalapril, and carbamazepine were still resistant using 5 mg/L, they were not completely removed after 40 min.

3. 2. Effect of Sodium Chloride Dose

Hypochlorite ions ClO^- are produced due to the presence of chloride ions (Cl^-)/free chlorine (Cl_2) in the electrolysis system and are regarded as the main oxidizing agent of the electrochemical oxidation process. The ClO^- production is higher and dominant in the presence of NaCl salt compared to the absence of NaCl.

The addition of NaCl as an electrolyte plays an important role to enhance the efficiency of electrochemical removal for the studied pharmaceuticals. Therefore, the continuous addition of sodium chloride was employed in this present study. Two different amounts of NaCl, 0.1 and 0.2 g per 100 mL, were investigated within 50 min. The applied voltage was kept at 5 V and the initial concentration was fixed at 5 mg/L. It was observed from Figure 3b,

the initial% removal increased with increasing of NaCl amount and it was reached as the highest when NaCl was 0.2 g/100 mL. It was observed that nifedipine was completely degraded after 10 min of electrolysis in the presence of 2 g/L NaCl, in which levonorgestrel and simvastatin were eliminated in the same way at the end of process. However, most of the pharmaceuticals achieved more than 50% removal after 30 min. On the other hand, all compounds were not completely removed in the presence of 1 g/L NaCl. The reason was attributed to the role of Cl^- in the electrochemical oxidation process to generate ClO^- , which was not sufficient to make the full degradation for the studied pharmaceuticals at 1 g/L NaCl.

It was observed from the LC-TOF/MS profile that most of the pharmaceuticals were eliminated in the presence of 2 g/L NaCl compared to 1 g/L NaCl under the same conditions of 5 V and 50 min treatment time (Figure S1). The indirect electrochemical oxidation mechanism for the generation of active chlorine (Cl_2 , HOCl , and ClO^-) was presented in the Introduction section.

3. 3. Effect of Applied Voltage

Anodic oxidation of pharmaceuticals generates intermediates by the electrochemical oxidation -reactions of the chloride ions in the solution as described by the equations (1-3) in the Introduction section. However, the solution contained chloride ions due to the aqueous dissociation of the NaCl into Na^+ and Cl^- . Thus, the oxidation under these conditions, usually called electrooxidation with active chlorine, is based on the direct oxidation of Cl^- at the anode to yield soluble chlorine, which diffuses away from the anode to be rapidly hydrolysed and transformed into hypochlorous acid (HOCl) and the chloride ion. Hypochlorous acid is then in equilibrium with hypochlorite ion at $\text{p}K_a = 7.55$. From the literature, it was found that the dominant species are as follows: Cl_2 until pH near 3, HClO in the pH range 3-8, and ClO^- at pH > 8. It has been reported that the oxidation treatment with active chlorine species is faster in acid than in alkaline media because of the higher standard potential of Cl_2 ($E^0 = 1.36$ V) and HClO ($E^0 = 1.49$ V) compared to ClO^- ($E^0 = 0.89$ V).²⁹

In Figure 3c, the% removal increased when applied voltage was raised from 3 to 12 V, indicating an enhancement of the oxidation rate. This was due to the higher electroregeneration of ClO^- ions from chlorine as discussed before. It was observed that at 12 V that the% removal bar curves reveal a quicker decay. Only prazosin, enalapril and carbamazepine were present after 10 min. However, after 50 min all compounds were completely removed. In the case of 5 V, the% removal was between 81 and 96% for caffeine, prazosin, enalapril, and carbamazepine. Nifedipine, levonorgestrel and simvastatin were completely removed at the end of the electrochemical treatment process. The trend was different for 3 V, it was shown that all pharmaceuticals were not removed after 50

min. The reason may be attributed to the fact that the concentration of the formed ClO^- was low. LC-TOF/MS profile for the removal of pharmaceuticals has been observed

and showed that most of the pharmaceuticals were eliminated following the increasing of applied voltage as presented in Figure S2.

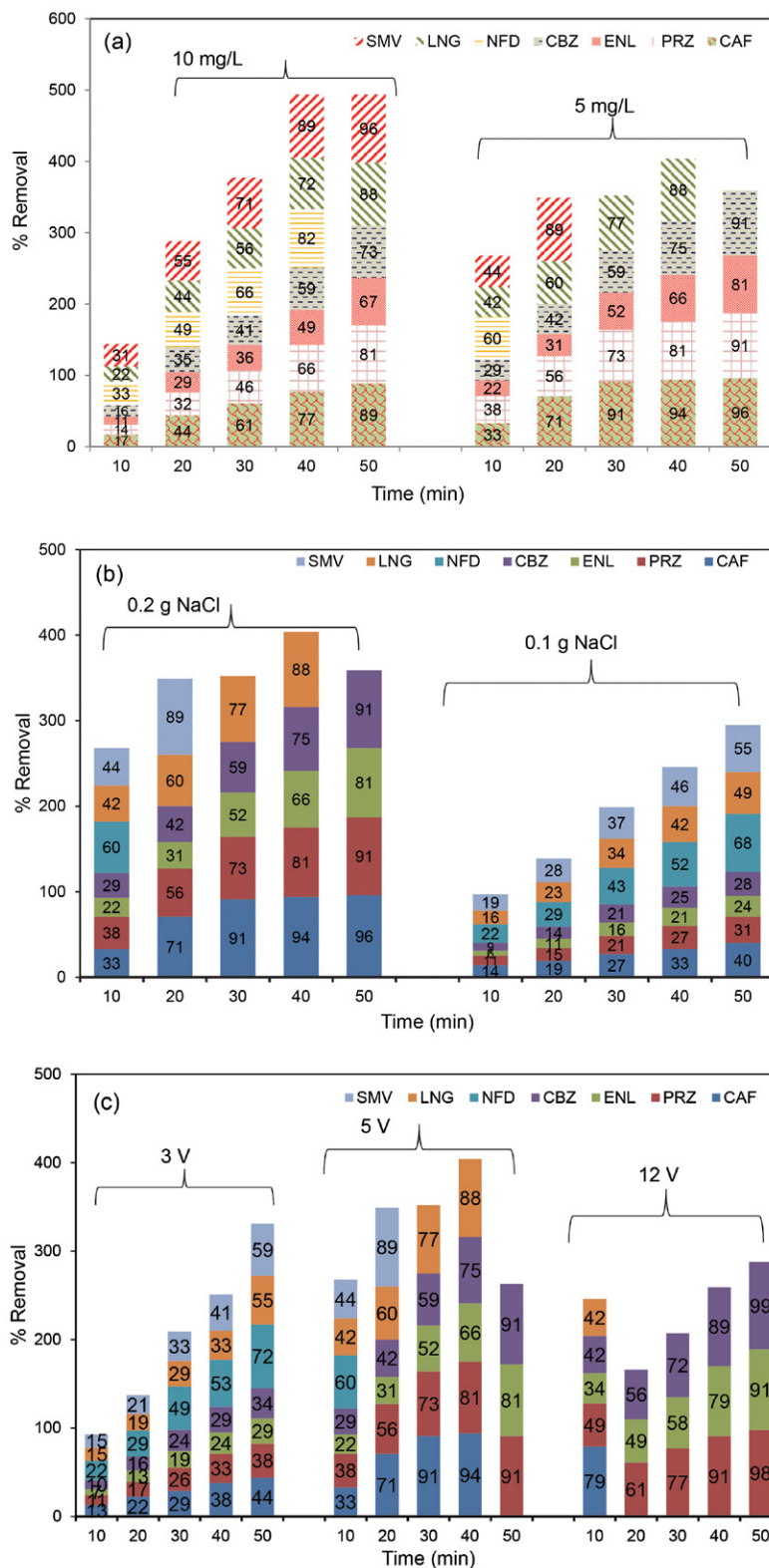


Figure 3. % Removal for all studied pharmaceuticals: (a) effect of initial concentration at 5 V and 2 g/L NaCl, (b) effect of NaCl amount at 5 V and 5 mg/L and (c) effect of applied voltage at 5 mg/L and 2 g/L NaCl.

During the electrochemical process, energy consumption was considered for four pharmaceuticals only (caffeine, prazosin, enalapril, and carbamazepine) as a model of pharmaceuticals. It was calculated using equation 6:³⁰

$$EC = \left[\frac{V I \Delta t}{\Delta m} \right] \quad (6)$$

where EC (kWh/g compound) is energy consumption for the process; V (volt) is the applied voltage, I (ampere) is the current, t (hours) is the electrolysis time and Δm (gram) is the amount of reduced compound.

From Figure 4, energy consumption exhibited the highest value at 12 V compared to 5 and 3 V. Energy consumption was almost similar at 5 and 3 V, however, it was very low compared to 12 V. On the other hand, % removal was higher at 5 V compared to 3 V as shown in Figure 3c. Consequently, 5 V was the best choice for further experiments due to its low energy consumption and good compromise % removal for most of the compounds.

3. 4. Identification of the By-products

After electrochemical degradation of the parent compounds, some new by-products were formed. However,

analysis of the by-products requires some further experiments to ensure their detection in trace amounts. LC-TOF/MS is an instrument used for this purpose. In this study, only chlorinated by-products were analysed and reported because chlorinated by-products are more common harmful compounds than other non-chlorinated by-products. Furthermore, chlorine has two isotopes ³⁵Cl and ³⁷Cl with a big difference in abundance between them so they show clear separation and are very readily seen in mass spectrometry spectra and chromatograms.

Four pharmaceutical compounds, simvastatin, prazosin, carbamazepine, and caffeine were analysed and discussed in terms of the generation of their by-products using LC-TOF/MS. Other pharmaceuticals have not presented chlorinated by-products. It was observed that chlorinated by-products could be formed due to the presence of chlorine in the solution then oxidation reaction will occur via hypochlorite ion ClO^- .³¹ During the electrochemical oxidation, several compounds were produced in the solution, however, it was very difficult to identify them because the electrochemical process was non-selective. Hence, it is very important to use an accurate instrument LC-TOF/MS for this purpose. The formation of the chlorinated by-products suggested the attack of ClO^- generated by electrochemical oxidation of Cl^- as has been discussed

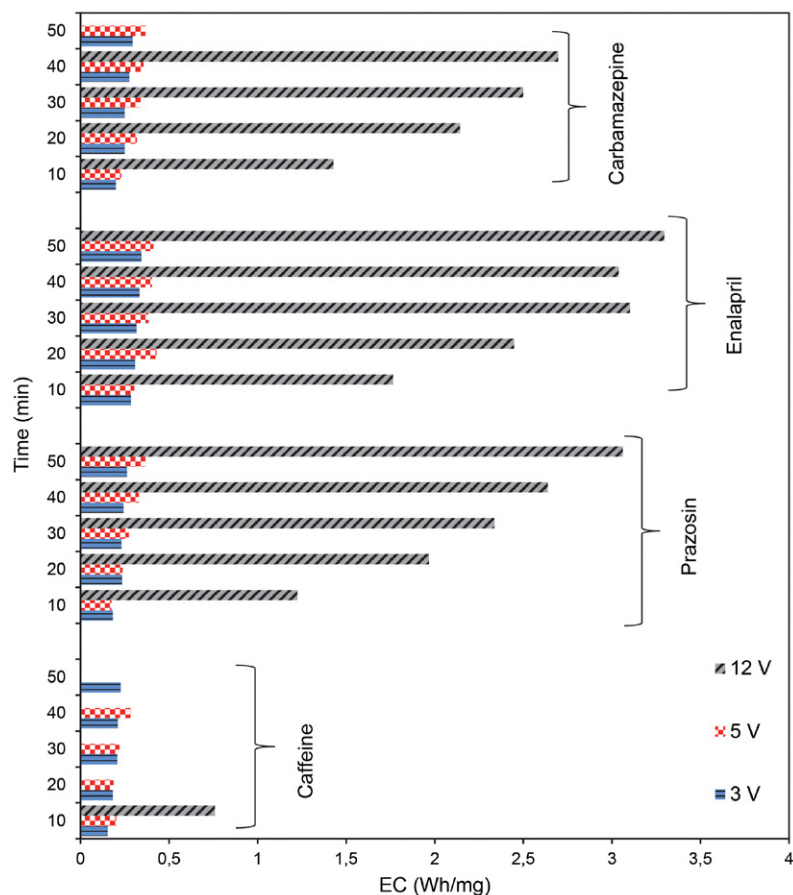


Figure 4. Effect of applied voltage on the energy consumption at 5 mg/L and 2 g/L NaCl.

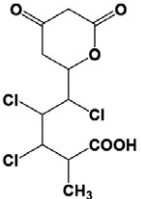
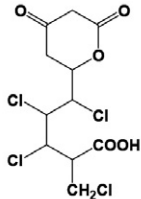
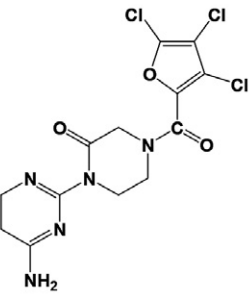
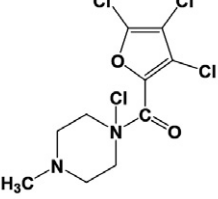
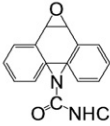
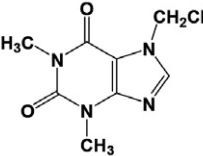
previously.^{32,33} However, two main products, $C_{11}H_{13}Cl_3O_5$, and $C_{10}H_{12}Cl_4O_3$, were produced during the electrochemical oxidation of simvastatin as presented in Table 3.

Figure 5a shows the mass spectrum of simvastatin by-product (m/z 327.9688). The most striking aspects of these spectra were the clusters of intense peaks that were separated by m/z 2 units. However, the identification of the ion cluster m/z 327.9/329.9/331.9/333.9 is explained here.

After careful examination of the ion cluster, it is evident that it should be a chlorine-containing by-product. The four peaks at m/z 327.9/329.9/331.9/333.9 display an ion cluster with an isotopic peak abundance ratio of 100%:95.6%:30.5%:3.2%, indicating that this by-product contains three chlorine atoms.

On the other hand, the by-product $C_{10}H_{12}Cl_4O_3$ (m/z 361.9310) has four chlorine atoms. However, the mass spectrum profile for this product shows five main

Table 3. Accurate mass measurement for selected pharmaceuticals and their by-products under the conditions 5 V and 5 g/L NaCl.

Parent compound/	Elemental composition /by-product	Ionization mode	Molecular structure	Mass to charge ratio (m/z)
Simvastatin	$C_{11}H_{13}O_5Cl_3$	Negative		327.9688
	$C_{11}H_{12}O_5Cl_4$	Negative		361.9310
Prazosin	$C_{13}H_{12}N_5O_3Cl_3$	Negative		389.9985
	$C_{10}H_{11}N_2O_2Cl_4$	Negative		329.9486
Carbamazepine	$C_{15}H_{11}N_2O_2Cl$	Positive		309.0248
Caffeine	$C_8H_9N_4O_2Cl$	Positive		229.0475

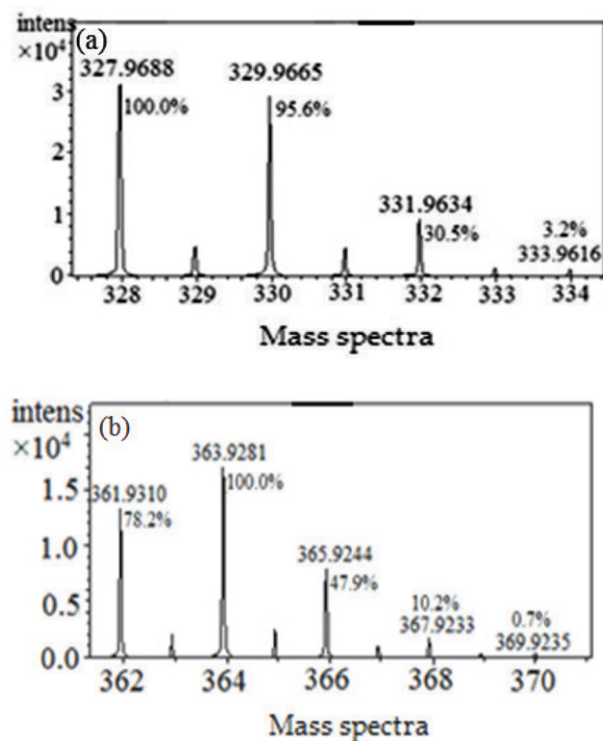


Figure 5. Mass spectra profile using LC-TOF/MS for simvastatin chlorinated by-products (a): three chlorine atoms and (b) four chlorine atoms.

peaks at m/z 361.9, 363.9, 365.9, 367.9, and 369.9, as presented in Figure 5b. The probability of appearance of these five isotopic mass peaks is arranged as 78.2%:100%:47.9%:10.2%:0.7%, respectively.

Table 3 shows an illustration of the formation of two products: $C_{13}H_{12}Cl_3N_5O_3$ and $C_{10}H_{11}Cl_4N_2O_2$. After careful examination of the ion cluster for $C_{13}H_{12}Cl_3N_5O_3$, it was evident that it should be a chlorine-containing by-product. The inset panel shows that the peak at m/z 390/392/394/396 displays an ion cluster with an isotopic peak abundance ratio of 100%:100%:33%:4%, indicating that this by-product contains three chlorine atoms. On the other hand, product $C_{10}H_{11}Cl_4N_2O_2$, m/z 329.9486, has four chlorine atoms identified as the five main peaks at m/z 329.9, 331.9, 333.9, 335.9, and 337.9, and arranged as 75%:100%:50%:11%:1%, respectively.

In case of carbamazepine and caffeine, their by-products with one chlorine atom were identified as $C_{15}H_{11}N_2O_2Cl$ and $C_8H_9N_4O_2Cl$, respectively, as shown in Table 3. The intense peaks for both compounds are presented in similar arrangement for the intense base isotope peaks as 100%:30%.

4. Conclusions

In this study, different pharmaceuticals were treated using the electrochemical oxidation process. The electrochemical process showed that caffeine, prazosin, simvas-

tatin, and levonorgestrel were eliminated within 30–50 min using graphite-PVC composite electrode at 5 and 12 V. This present study was reported for the first time explaining the treatment of the mixture of pharmaceuticals in a single reactor. The electrochemical oxidation process was investigated in the presence of NaCl as a supporting electrolyte under different applied voltages. Energy consumption was evaluated for four pharmaceuticals under different conditions. It ranged between 0.154 and 0.345 Wh/mg at 3 V, 0.175 and 0.430 Wh/mg at 5 V, and 0.760 and 3.300 Wh/mg at 12 V. The formation of chlorinated by-products was identified and elucidated strongly using LC-TOF/MS.

Conflicts of Interest: The authors declare no conflict of interest.

Acknowledgments

The authors thank Mr. Alefee who is the person-in-charge of LC-TOF/MS. The authors also would like to thank University of Babylon to make agreement with other universities for providing the facilities to conduct this study. The authors would like to thank Al-Mustaqbal University College for funding this research.

5. References

- Drugbank database. <https://go.drugbank.com> (accessed: 28 February 2020)
- L. Vergeynst, A. Haeck, P. De Wispelaere, H. Van Langenhove, K. Demeestere, *Chemosphere*, **2015**, *119*, S2–S8. DOI:10.1016/j.chemosphere.2014.03.069
- I. Ferrer, E. M. Thurman, *J. Chromatogr. A*, **2012**, *1259*, 148–157. DOI:10.1016/j.chroma.2012.03.059
- N. K. Khalid, D. Devadasan, U. K. Aravind, C. T. Aravindakumar, *Environ. Monit. Assess.* **2018**, *190*, 1–12. DOI:10.1007/s10661-018-6745-9
- R. W. Becker, M. Ibáñez, E. C. Lumbaque, M. L. Wilde, T. F. da Rosa, F. Hernández, C. Sirtori, *Sci. Total Environ.* **2020**, *699*, 134–218. DOI:10.1016/j.scitotenv.2019.134218
- F. F. Al-Qaim, M. P. Abdullah, M. R. Othman, J. Latip, Z. Zakaria, *J. Chromatogr. A*, **2014**, *1345*, 139–153. DOI:10.1016/j.chroma.2014.04.025
- F. F. Al-Qaim, M. P. Abdullah, M. R. Othman, J. Latip, W. Afiq, *J. Brazil. Chem. Soc.* **2014**, *25*, 271–281. DOI:10.5935/0103-5053.20130294
- F. F. Al-Qaim, M. P. Abdullah, M. R. Othman, Z. H. Mussa, Z. Zakaria, J. Latip, W. M. Afiq, *J. Brazil. Chem. Soc.* **2015**, *26*, 1124–1135. DOI:10.5935/0103-5053.20150075
- F. F. Al-Qaim, Z. Mussa, A. Yuzir, N. Tahrim, N. Hashim, S. Azman, *Water*, **2018**, *10*, 916. DOI:10.3390/w10070916
- F. F. Al-Qaim, Z. H. Mussa, A. Yuzir, *Anal. Bioanal. Chem.* **2018**, *410*, 4829–4846. DOI:10.1007/s00216-018-1120-9

11. C. L. Amorim, I. S. Moreira, A. R. Ribeiro, L. H. Santos, C. Delerue-Matos, M. E. Tiritan, P. M. Castro, *Int. Biodeter. Biodegr.* **2016**, *115*, 277–285. DOI:10.1016/j.ibiod.2016.09.009
12. M. Klavarioti, D. Mantzavinos, D. Kassinos, *Environ. Int.* **2009**, *35*, 402–417. DOI:10.1016/j.envint.2008.07.009
13. T. Jerič, R. J. Bisselink, W. Van Tongeren, A. M. Le Marechal, *Acta Chim. Slov.* **2013**, *60*, 666–672. <https://journals.matheo.si/index.php/ACSi/article/view/104>
14. F. F. Al-Qaim, Z. H. Mussa, M. R. Othman, M. P. Abdullah, *J. Hazard. Mater.* **2015**, *300*, 387–397. DOI:10.1016/j.jhazmat.2015.07.007
15. J. B. Parsa, M. Abbasi, *Acta Chim. Slov.* **2007**, *54*, 792.
16. Q. Ren, C. Kong, Z. Chen, J. Zhou, W. Li, D. Li, Y. Lu, *Microchem. J.* **2021**, *164*, 106059. DOI:10.1016/j.microc.2021.106059
17. I. W. Mwangi, E. M. Kinyua, R. Nthumbi, R. N. Wanjau, S. Swaleh, J. C. Ngila, *Heliyon*, **2021**, *7*, e06671. DOI:10.1016/j.heliyon.2021.e06671
18. G. Lourinho, D. M. F. Santos, P. S. D. Brito, *J. Environ. Chem. Eng.* **2021**, *9*, 104712. DOI:10.1016/j.jece.2020.104712
19. H. Li, X. Kuang, C. Qiu, X. Shen, B. Zhang, H. Li, *Water Sci. Technol.* **2020**, *82*, 773–786. DOI:10.2166/wst.2020.387
20. Z. H. Mussa, F. F. Al-Qaim, M. R. Othman, M. P. Abdullah, J. Latip, Z. Zakria, *J. Taiwan Inst. Chem. E.* **2017**, *72*, 37–44. DOI:10.1016/j.jtice.2016.12.031
21. Z. H. Mussa, F. F. Al-Qaim, M. R. Othman, M. P. Abdullah, *J. Environ. Chem. Eng.*, **2016**, *4*, 3338–3347. DOI:10.1016/j.jece.2016.07.006
22. N. Nordin, M. A. F. Pisal, N. I. H. Razman, N. F. Jaafar, *Acta Chim. Slov.* **2019**, *66*, 284–293. DOI:10.17344/acsi.2018.4705
23. N. Nordin, S. F. M. Amir, M. R. Yusop, M. R. Othman, *Acta Chim. Slov.* **2015**, *62*, 642–651. DOI:10.17344/acsi.2014.1264
24. Z. H. Mussa, M. R. Othman, M. P. Abdullah, *J. Brazil. Chem. Soc.* **2015**, *26*, 939–948. DOI:10.5935/0103-5053.20150055
25. Malaysian Statistics on Medicine, Ministry of Health Malaysia, Kuala Lumpur. **2014**. <http://apps.who.int/medicinedocs/documents/s17580en/s17580en.pdf/> (accessed: 20 February 2020).
26. World Health Organization (WHO), collaborating center for drug statistics methodology, https://www.whocc.no/atc_ddd_index/?code=C07AB02&showdescription=yes/ (accessed: 28 February 2020).
27. Z. Mussa, F. Al-Qaim, A. Yuzir, H. Hara, S. Azman, S. Chellipan, *Catalysts*, **2018**, *8*, 540. DOI:10.3390/catal8110540
28. F. F. Al-Qaim, Z. H. Mussa, A. Yuzir, J. Latip, M. R. Othman, *J. Environ. Sci.* **2018**, *74*, 134–146. DOI:10.1016/j.jes.2018.02.019
29. I. Sirés, E. Brillas, *Environ. Int.* **2012**, *40*, 212–229. DOI:10.1016/j.envint.2011.07.012
30. J. B. Parsa, M. Rezaei, A. R. Soleymani, *J. Hazard. Mater.* **2009**, *168*, 997–1003. DOI:10.1016/j.jhazmat.2009.02.134
31. M. Soufan, M. Deborde, A. Delmont, B. Legube, *Water Res.* **2013**, *47*, 5076–5087. DOI:10.1016/j.watres.2013.05.047
32. A. Sánchez-Carretero, C. Sáez, P. Cañizares, M. A. Rodrigo, *Chem. Eng. J.* **2011**, *166*, 710–714. DOI:10.1016/j.cej.2010.11.037
33. M. J. Martín de Vidales, C. Sáez, P. Cañizares, M. A. Rodrigo, *J. Chem. Technol. Biotechnol.* **2012**, *87*, 225–231. DOI:10.1002/jctb.2701

Povzetek

V tej študiji poročamo o elektrokemijski obdelavi različnih terapevtskih skupin farmacevtikov (kofein, prazosin, enalapril, karbamazepin, nifedipin, levonorgestrel in simvastatin) v mešanici. Med elektrokemijskim procesom smo raziskovali uporabo grafitne-PVC anode pri različnih potencialih (3, 5 in 12 V), različnih začetnih koncentracijah preučevanih farmacevtikov v vodni raztopini (5 in 10 mg/L) ter pri različnih koncentracijah natrijevega klorida (1 in 2 g/L). Delež odstranitve farmacevtikov se je povečeval z uporabljenim potencialom in je bil nad 98% po 50 min elektrolize pri 5 V. Poraba energije je bila med 0,760 in 3,300 Wh/mg pri 12 V, kar je bila najvišja vrednost v primerjavi s 3 ali 5 V. Nastanek kloriranih stranskih produktov smo spremljali pri štirih izbranih farmacevtikih: simvastatin ($C_{11}H_{13}Cl_3O_5$ in $C_{10}H_{12}Cl_4O_3$), prazosin ($C_{13}H_{12}Cl_3N_5O_3$ in $C_{10}H_{11}Cl_4N_2O_2$), karbamazepin in kofein ($C_{15}H_{11}N_2O_2Cl$ in $C_8H_9N_4O_2Cl$), kjer smo strukturo produktov ugotovili z uporabo tekočinske kromatografije z masno spektrometrijo na čas preleta (LC-TOF/MS).



Except when otherwise noted, articles in this journal are published under the terms and conditions of the Creative Commons Attribution 4.0 International License

Scientific paper

Experimental Studies on the Removal of Aluminium Ions from Synthetic Aqueous Solution by Hydroxyapatites

Doina Humelnicu,^{1,*} Inga Zinicovscaia,^{2,3} Ionel Humelnicu¹
and Maria Ignat¹

¹ Alexandru Ioan Cuza” University of Iasi, Faculty of Chemistry, Iasi, Romania

² Department of Nuclear Physics, Joint Institute for Nuclear Research, Dubna, Russia

³ Department of Nuclear Physics, Horia Hulubei National Institute for R&D in Physics and Nuclear Engineering, Bucharest - Magurele, Romania

* Corresponding author: E-mail: doinah@uaic.ro

Received: 03-16-2021

Abstract

In this work we have presented the results obtained in the adsorption behavior of hydroxyapatite with different treatment towards aluminium ions from synthetic wastewaters. Experiments were performed in batch technique at different pH values, temperatures, sorbent dosage, contact time and initial aluminium concentration. The thermodynamic studies on the adsorption process of aluminium onto hydroxyapatite indicated that the process is spontaneous and endothermic. The Langmuir, Freundlich, Flory-Huggins, Dubinin-Radushkevich and Temkin equilibrium models were applied to the description of experimental data. The adsorption of aluminium follows the Langmuir adsorption isotherm. The kinetics of adsorption was evaluated using the pseudo-first order, pseudo-second order and intraparticle diffusion kinetic models. The rate of aluminium adsorption was successfully described by a pseudo-second-order kinetic model. The obtained results indicated that hydroxyapatite treated with Pluronic P123 surfactant has a higher sorption capacity toward aluminium ions (117.65 mg g⁻¹) than hydroxyapatite treated with Pluronic F127 surfactant (109.89 mg g⁻¹) while untreated hydroxyapatite exhibited the lowest one (104.17 mg g⁻¹).

Keywords: Aluminium removal, adsorption, hydroxyapatite, wastewaters

1. Introduction

Wastewaters that contain metals are considered to be dangerous to both human and the environment due to their acute toxicity and non-biodegradability, even when the metals are present at very low concentrations. Metal ions are known as priority pollutants, due to their mobility and toxicity in natural water ecosystems.

Aluminium is usually present in alum treated water, effluents from aluminium based industries and also due to the salts of aluminum added to many processed foods and medicine. The main factors of the presence of aluminium in water are the industrial processes. Acid rains are the other important source for aluminium contamination of natural waters.¹⁻³

The sources of aluminium contamination is attributed to the presence of ‘residual aluminium’ present in alum

treated waters,^{4,5} effluents from aluminium based industries and also due to the salts of aluminium being to human health.¹⁻⁵ Aluminium is a neurotoxin when is added to many processed foods and medicine.⁶

Wastewaters that result from industrial activities regularly can pollute drinking water supplies as well as rivers, lakes, seawater and other aquatic ecosystems. In time, this can cause a contamination of water with aluminium and cause many medical disorders in living organisms.^{7,8}

Harmfulness of aluminium can be attributed to its accumulation in bone and central nervous system, especially in people who have kidney failure. In high doses (>110 µg L⁻¹),⁹ aluminium can cause neurotoxicity being associated with Parkinson dementia, and Alzheimer’s disease.¹⁰ Also, aluminium can reduce skeletal mineralization because it competes with calcium absorption in bones.

For the removal of aluminium from wastewaters has been proposed several methods such as ion exchange, reverse osmosis, chemical precipitation, and solvent extraction. Such methods generate toxic sludge that constitutes serious environmental and economical problems. Consequently, the adsorption has been found to be a better method for removal of metals from wastewaters due to its simplicity, efficiency and low costs.

It has been reported different type of sorbents that have the capacity to adsorb and accumulate metals from wastewaters, mainly activated carbon,^{11,12} natural zeolites,^{13,14} different algae types,^{15,16} magnetic nanoparticles,¹⁷ rice hull, polymers.^{18–21} Recently, among the widely available inorganic based adsorbents hydroxyapatite (HAP) was found to exhibit a good adsorption potential^{22,23} HAP is the most stable form of calcium phosphate with the chemical formula $\text{Ca}_{10}(\text{PO}_4)_6(\text{OH})_2$ ²⁴ being an efficient sorbent used in order to remove heavy metals from wastewaters due to its high sorption capacity²⁵ and ion exchange properties.²⁶ Different methods of synthesis influence the morphology of HAP, and, consequently cause some properties such as adsorption and mechanical strength.^{24,27,28} As a result of these properties HAP has been used as sensor, as adsorbent for dyes and heavy metals from residual waters.^{29–33}

As nanostructured HAP provide large interfaces, giving great adsorption capability in the separation field³⁰, the objective of this study was to evaluate the feasibility of using nanoporous hydroxyapatite with different available pore volumes and specific surface areas for the removal of aluminium from aqueous solution. Thus, we succeeded in synthesizing a mesoporous hydroxyapatite, using the surfactant micelle as template system in order to induce pores in HAP material. Further, the influence of experimental parameter such as contact time, sorbent dose, pH, temperature, and initial Al(III) concentration were studied in the sorption process on prepared HAP powders. The adsorption process was studied from kinetic and isotherm standpoints.

2. Material and Methods

Calcium nitrate, aluminium nitrate and phosphoric acid were purchased from Sigma Aldrich. Ethylic alcohol and liquid ammonia were purchased from Chemical Company, and surfactants (Pluronic P123 and Pluronic F127) were purchased from Sigma Aldrich. All chemicals were reagent grade and were used without further purification.

2. 1. Sorbents Synthesis

Hydroxyapatite (HAP) was prepared by coprecipitation of calcium nitrate and phosphoric acid according to the synthesis reported by Arsad and colab.³⁰ with some modifications. Aqueous solution of 0.5 M calcium nitrate was added to 50 mL ethanol and was vigorously stirred at

room temperature. Afterward few drops of 25% (v/v) ammonia solution were then added to the solution in order to adjust the pH to 10, and then a solution of 0.3 M phosphoric acid was added slowly in a dropwise manner to allow reacting with calcium nitrate. The used volumes of calcium and phosphate containing reagent solutions were calculated so as to respect the molar ratio of Ca/P equal to 1.67, as in the natural HAP. After 1 h reaction at 60 °C, the reaction mixture was allowed to age overnight at room temperature to complete the reaction. The suspension was centrifuged at 4,000 rpm for 15 min., separated and dried at room temperature. The white powder of sample was calcined for 6 hours at 550 °C and labeled as HAP.

The HAP P123 and HAP F127 samples have been obtained following the same procedure with the mention that to the reaction mixture the corresponding surfactants were added. Thus, the Pluronic P123 has been used in the synthesis of HAP P123 sample, and Pluronic F127 in the synthesis of HAP F127 sample.

The N₂ adsorption/desorption isotherms for BET specific surface area measurements were recorded on a NOVA 2200e (Quantachrome Instruments) automated gas adsorption analyzer. Before analysis the samples were outgassed at 120 °C for at least 6 h under vacuum.

2. 2. Sorption Experiments

Sorption of aluminium ions from synthetic wastewaters was carried out in batch mode to establish the sorption capacity of sorbents as function of contact time, pH, initial concentration of aluminium ions, temperature, sorbent dose.

The aluminium ion concentration in the samples collected at different contact times and at equilibrium was measured at a wavelength of 309 nm by flame atomic absorption spectroscopy (FAAS) on the continuum source atomic absorption spectrometer–contrAA® 300– equipped with an optimized high-resolution Echelle double monochromator. Infrared spectra were performed with a BRUKER ALPHA FT-IR Spectrometer between 400–4000 cm⁻¹.

Experiments were performed in triplicate and the average of measurements was used in calculation.

The amount of aluminium retained per unit mass of sorbent was calculated with Eq. (1).

$$q = \frac{(C_0 - C_e) \cdot V}{m}, \text{ (mg Al/g sorbent)} \quad (1)$$

where C₀ is initial concentration of aluminium, (mg L⁻¹), C_e is aluminium concentration in aqueous solution at equilibrium, (mg L⁻¹), V is the volume of aqueous solution (L), and m is sorbent mass (g).

3. Results and Discussion

Infrared spectra of the sorbent point out that the use of surfactants did not influence their surface chemistry,

but only changed their textural properties, meaning that the specific surface area and pores volume increased/decreased according to the used structure directing agent. The infrared spectra show broad bands characteristic to hydroxyapatite nanomaterial. The characteristic peaks attributed to PO_4^{3-} appear at 475, 570, 600, 962, 1039, and 1091 cm^{-1} , showing a distinguishable P-O stretching vibration and a triple degenerate bending vibrations of phosphate groups in hydroxyapatite.³⁴ The FTIR spectra after adsorption experiments highlight the increase in the intensity of some absorption bands.

Nitrogen adsorption-desorption analysis has been employed to characterize the porous structure of the synthesized samples.³⁵ Figure 1 shows typical isotherms char-

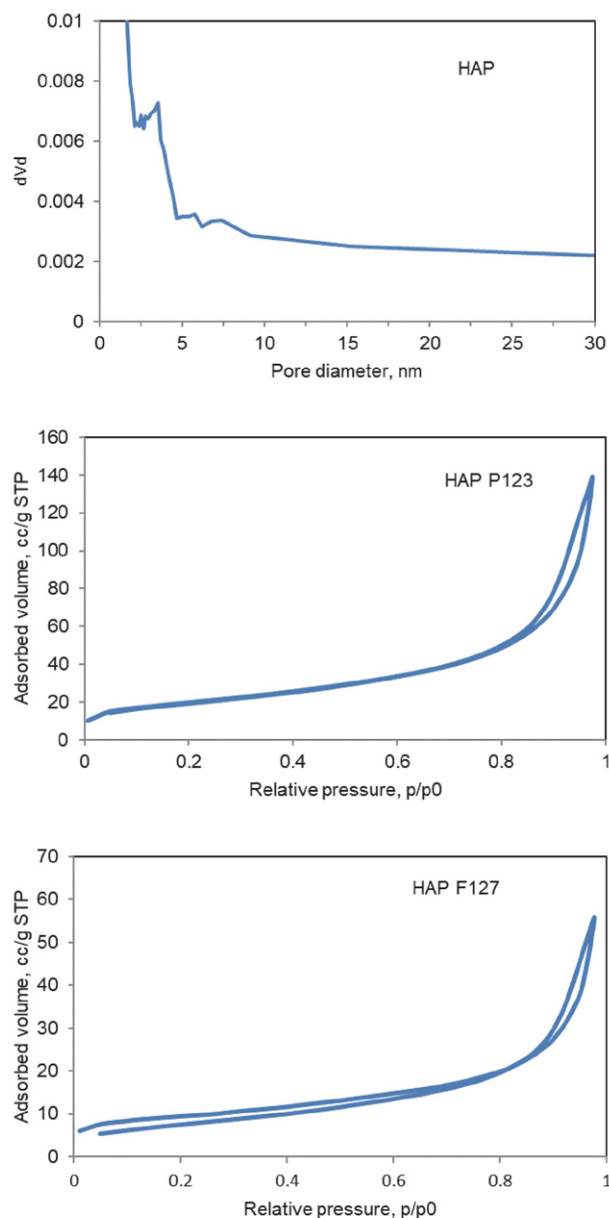


Figure 1. Nitrogen sorption isotherm and corresponding pore size distributions for the synthesized HAP samples.

acteristic to hydroxyapatite materials. All isotherms are of type IV, characterizing mesoporous materials, accompanied by a H3 type hysteresis loop, which according to IUPAC classification³⁶ is attributed to the formation of aggregated plate-like particles giving rise to pores of slit shapes.

The textural characteristics of the investigated sorbents are presented in Table 1. It can be observed that the surfactant addition during the HAP synthesis lead to the hypothesis that the abundant pore bodies of a certain size can be correlated with the abundance of pore necks that are smaller by a systematic amount.³⁷ Even more, the surfactant P123 increased considerably specific surface area and total pore volume of the hydroxyapatite material, as can be observed from the Table 1.

Table 1. Textural properties of the synthesized sorbents.

Sorbent	Specific surface, m^2/g	Pore Volume, cm^3/g	Pore diameter, nm
HAP	47.251	6.48×10^{-2}	3.12
HAP P123	69.153	1.59×10^{-1}	3.50
HAP F127	31.719	6.18×10^{-2}	4.13

Relatively large specific surface and pore volume of the synthesized HAP systems highlighted their potential application as adsorbent materials.

3. 1. Influence of Sorbent Mass on the Adsorption Process

An important factor influencing the efficiency of the adsorption process from economically point of view is the sorbent mass used to remove the pollutant. The adsorption process is not effective if it requires a large amount of sorbent.

The effect of sorbent mass variation on the adsorption process was investigated at an established metal ion

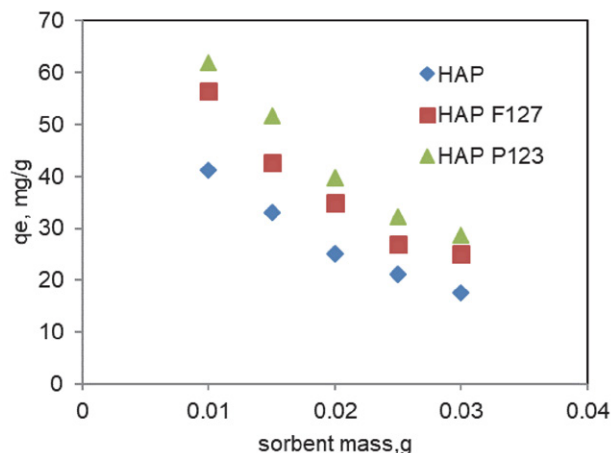


Figure 2. Dependence of adsorption process on the sorbent mass.

concentration of 50 mg L^{-1} at a temperature of $25 \text{ }^\circ\text{C}$. Figure 2 shows that with the increase of the sorbent mass from 0.01 g to 0.03 g the sorption capacity of the sorbents decreases because by increasing of the sorbent dose the number of accessible active sites increased consequently, the same amount of aluminium ions being distributed on an increasing number of binding sites. From this figure we can conclude that HAP P123 had a better sorption capacity by comparing with HAP and HAP F127, exhibiting almost similar textural properties.

3. 2. Effect of Contact Time on the Sorption Process

The influence of contact time on the adsorption of aluminium ions on the three type of hydroxyapatite was studied in a range of 0–180 minutes.

These experiments were performed at a temperature of $25 \text{ }^\circ\text{C}$ and a metal ion concentration of 50 mg L^{-1} , the sorbent mass used was 15 mg and the working volume of the solution was 20 mL . The results that were obtained are plotted in Figure 3.

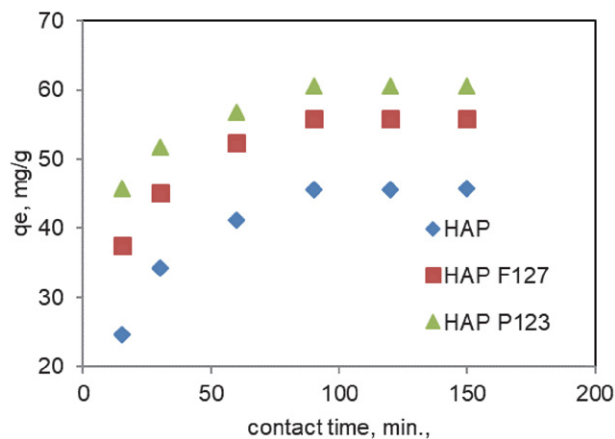


Figure 3. Dependence of adsorption process on the contact time.

It can be seen from Figure 3 that the amount of aluminium ions retained by sorbents increases with the increasing of the contact time, and equilibrium is reached after a period of 90 minutes after which the sorption remains constant. It is noted that in the case of the hydroxyapatite treated with surfactant Pluronic P123, the sorption of the aluminium ions was more efficient.

3. 3. pH Dependence of Sorption Process

pH is an important parameter that determines the ionic species in aqueous solution. The pH effect on the sorption of aluminium ions was studied by varying the solution pH in the range 2–8 with HCl and NaOH, the sorption capacity of HAPs sorbents being plotted as a function of pH in Figure 4. It is obvious that the sorption

capacity is influenced by the solution pH, the higher sorption occurring at pH 4. The value of sorption capacity of HAP was 43.21 mg g^{-1} , for HAP F127 was 52.64 mg g^{-1} and for HAP P123 was 59.85 mg g^{-1} , respectively. In aqueous solutions the solubility of aluminum increases at low pH due to the formation of ionic species: $[\text{Al}(\text{OH})]^{2+}$, $[\text{Al}(\text{OH})_2]^+$ and $[\text{Al}(\text{H}_2\text{O})_6]^{3+}$.¹⁸ At pH values ~ 4 , most Al exists as Al^{3+} .³⁸ In pH range between 5.2 and 8.8 the predominant specie is solid $\text{Al}(\text{OH})_3$, while over pH 9 the soluble $[\text{Al}(\text{OH})_4]^-$ is dominant species.

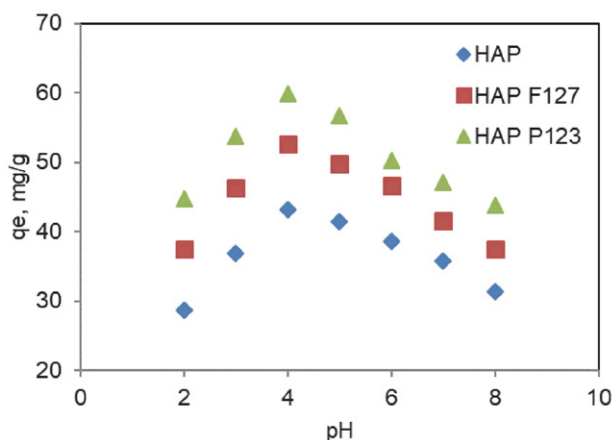
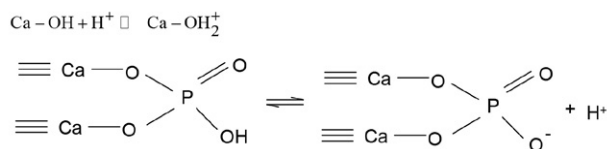


Figure 4. Influence of pH values on the adsorption process of Al(III) ions.

The increase in pH values leads to the increase of the Al(III) ions removal (Fig. 4), it reaches a maximum at pH 4 and thereafter, it decreases, probably due to the formation of the aluminum hydroxide which block the pores of the sorbent.^{39,40} It is well known that hydroxyapatite contains two different ionic Ca and P binding sites on their surface, depending on the pH values of the solution, that are able to absorb or release protons as follow:⁴¹



At low pH values the metal ions removal is weak due to the competition between the hydronium ions present in solution and the metal ions to occupy the surface-active sites. As the solution pH increases, this competition decreases and the sites from the hydroxyapatite surface become negatively charged and favors the adsorption of Al(I-II) ions by electrostatic interactions. Furthermore, some researchers have investigated the effect of pH on sorption of Al(III) using different kinds of sorbents and reported almost same pH dependent and maximum sorption was obtained at near pH values.^{9,10}

3. 4. Effect of Initial Concentration of Aluminium Ions on the Sorption Process

The effect of initial concentration on the adsorption of aluminium ions has also been investigated. Studies were performed at 25 °C, the initial concentration of aluminium ions was varied from 25 to 250 mg L⁻¹ all other parameters have been maintained at constant values (pH 4, contact time being 90 minutes and sorbent mass – 0.015 g).

From Figure 5 it can be seen that the sorption process increases with increasing the concentration of aluminium ions up to a value of 100 mg L⁻¹ after which a decrease of the adsorption process is observed. This variation can be explained by the fact that at high concentration the sorbent binding sites are saturated and other metal ions cannot be retained. Moreover, in dilute solutions the mobility of the metal ions is high and, consequently, their interaction with the sorbent is high. For an efficient removal of metal ions from wastewater, it is suggested to dilute the water containing metal ions prior to the adsorption operation.

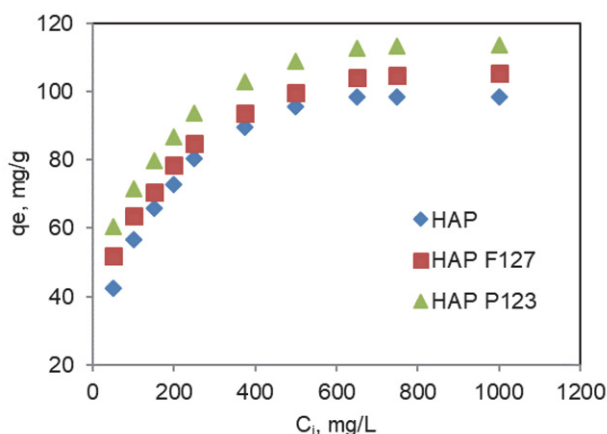


Figure 5. Influence of initial aluminium concentration on the adsorption process.

3. 5. Influence of Temperature on the Adsorption Process

The effect of the temperature on the adsorption processes of aluminium ions on the three sorbents was investigated in a temperature range of 20–40 °C while the other parameters were kept constant and the results obtained are shown in Figure 6.

Increasing the amount of adsorbed metal with increasing temperature indicates the endothermic nature of this process. This variation can be attributed either to the increase in the number of active sites on the sorbent surface available for sorption, or to the decrease in the thickness of the boundary layer surrounding the adsorbent so that the resistance of the adsorbent layer to the mass transfer decreases. Another explanation may be that with the

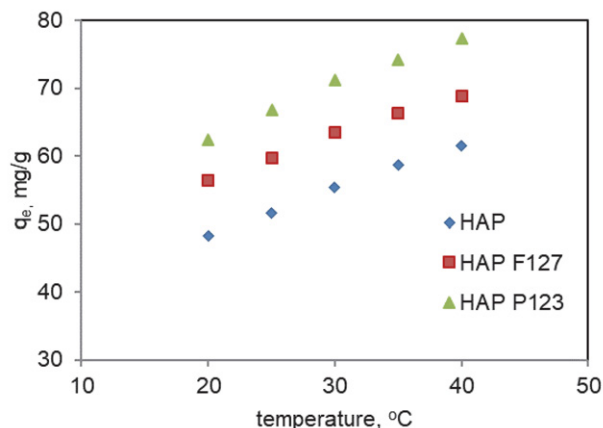


Figure 6. Dependence of adsorption process of Al(III) ions on the temperature.

increase in temperature the diffusion rate of the sorbate molecules increases along the outer layer, as well as in the internal pores of the sorbent particles.

3. 6. Thermodynamic study

The distribution coefficient, K_d , is the ratio between the concentration of the aluminium ions in the sorbent and in aqueous solution at equilibrium, and it is calculated with the Equation (3).

$$K_d = \frac{(C_0 - C_e) \cdot V}{C_e \cdot m} \text{ (mL} \cdot \text{g}^{-1}) \quad (3)$$

where C_0 is initial concentration of aluminium, (mg L⁻¹), C_e is aluminium concentration in aqueous solution at equilibrium, (mg L⁻¹), V is the volume of aqueous solution (L), and m is sorbent mass (g).

The thermodynamic parameters, such as: the standard free energy (ΔG°), enthalpy (ΔH°), and entropy of the system (ΔS°) were estimated using Eqs. (4) and (5).

$$\ln K_d = \frac{\Delta S^\circ}{R} - \frac{\Delta H^\circ}{RT} \quad (4)$$

$$\Delta G^\circ = \Delta H^\circ - T\Delta S^\circ \quad (5)$$

For the calculation of the thermodynamic parameters were used the results obtained from the study of temperature influence on the adsorption process. The values of ΔH° and ΔS° were calculated from the slope and the ordered intercept of the $1/T$ function representation of $\ln K_d$ (Figure 7). The results obtained are presented in Table 2.

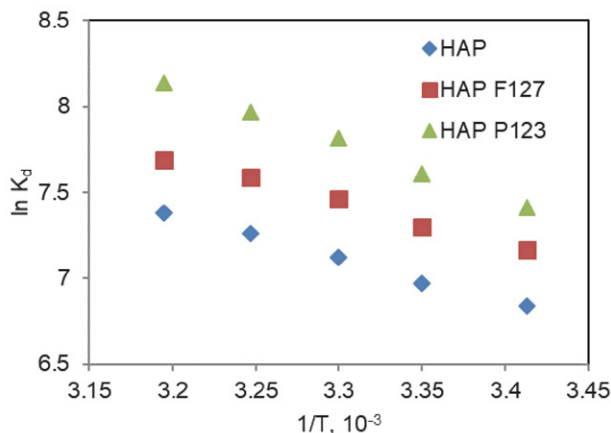
3. 7. Adsorption Isotherms Models

Adsorption isotherms are an important aspect in describing the adsorption phenomenon that occurs at different types of interfaces. Among the various isotherm models, the most common were used in this study.

Table 2. Thermodynamic parameters of the adsorption process of Al(III) ions.

Sorbent			ΔG° , kJ/mol				
	ΔH° kJ/mol K	ΔS° kJ/mol K	293	298	303	308	313
HAP	21.01	0.128	-16.49	-17.13	-17.77	-18.41	-19.05
HAP 127	20.54	0.130	-17.55	-18.2	-18.85	-19.5	-20.15
HAP 123	27.87	0.156	-17.84	-18.62	-19.40	-20.18	-20.96

The positive values obtained for ΔH° and ΔS° indicate that the adsorption process is endothermic, and the affinity of the three sorbents for the aluminium ions is high. Negative Gibbs energy values show that the adsorption process is spontaneous.

**Figure 7.** Dependence of distribution coefficient on the temperature.

Langmuir isotherm model

The Langmuir model is widely applied to the metal ion sorption processes. This model describes the quantitative adsorption of a monolayer on the external surface of the sorbent, after which no further adsorption occurs.⁴² Thus, the Langmuir isotherm is the balanced distribution of metal ions between the solid and liquid phases. The model implies uniform adsorption energy on the surface of the sorbent and no transmigration of the adsorbate in the surface plane. The Langmuir isotherm involves a surface with homogeneous binding points, equivalent sorption energies and excludes any type of interaction between the adsorbed species. The linearized mathematical expression of this isotherm is:⁴²

$$\frac{C_e}{q_e} = \frac{1}{K_L \cdot q_m} + \frac{C_e}{q_m} \quad (6)$$

where C_e is aluminium ions concentration at equilibrium (mg L^{-1}), q_e is amount of Al (III) adsorbed at equilibrium (mg/g), q_{max} is maximum adsorption capacity of the sorbent (mg/g) and K_L is Langmuir adsorption constant (L/mg). The plot of C_e/q_e in function of C_e (Figure 8a) gives a straight line with slope $1/q_{\text{max}}$ and intercept $1/q_{\text{max}} K_L$. K_L is a constant that is important in calculating the dimensional parameter (R_L) that explains the favorability of the

adsorption process; R_L is calculated using Eq. (7)

$$R_L = \frac{1}{1 + K_L C_0} \quad (7)$$

Thus, 4 situations are distinguished, namely: 1) the adsorption process is unfavorable if $R_L > 1$; 2) adsorption is linear when $R_L = 1$; 3) the adsorption process is favorable when $0 < R_L < 1$ and 4) the adsorption is irreversible if $R_L = 0$. In the studies that were performed we obtained for R_L subunit values (Table 3) which proves that the adsorption process of the aluminum ions on the three sorbents was favorable.³⁹

Freundlich isotherm model

The Freundlich isotherm is an empirical model that is not limited to monolayer adsorption, but also to the description of multilayer adsorption. The mathematical expression of the linearized form is:⁴³

$$\log q_e = \log K_F + \frac{1}{n} \log C_e \quad (8)$$

where q_e is amount of Al (III) adsorbed at equilibrium (mg/g), C_e is concentration of Al(III) in aqueous solution at equilibrium (mg/L); K_F and n are Freundlich constants that include factors that affect adsorption capacity and adsorption intensity, respectively. Graphical representation of $\log q_e$ as function of $\log C_e$ (Figure 8b) gives a linear graph with slope $1/n$ and intercept $\log K_F$ from which Freundlich constants were estimated (Table 3).

Flory-Huggins isotherm model

For a complete characterization of the adsorption process the Flory-Huggins model was used to determine the degree of sorbent surface coverage of the sorbate.⁴⁴ The linearized mathematical expression of this isotherm is:

$$\log \frac{\theta}{C_0} = \log K_{FH} + n \log(1 - \theta) \quad (9)$$

where $\theta = \left(1 - \frac{C_e}{C_0}\right)$ is the degree of coverage of the surface, and K_{FH} is the equilibrium constant of the adsorption. The parameters of Eq. (9) are calculated from the slope and

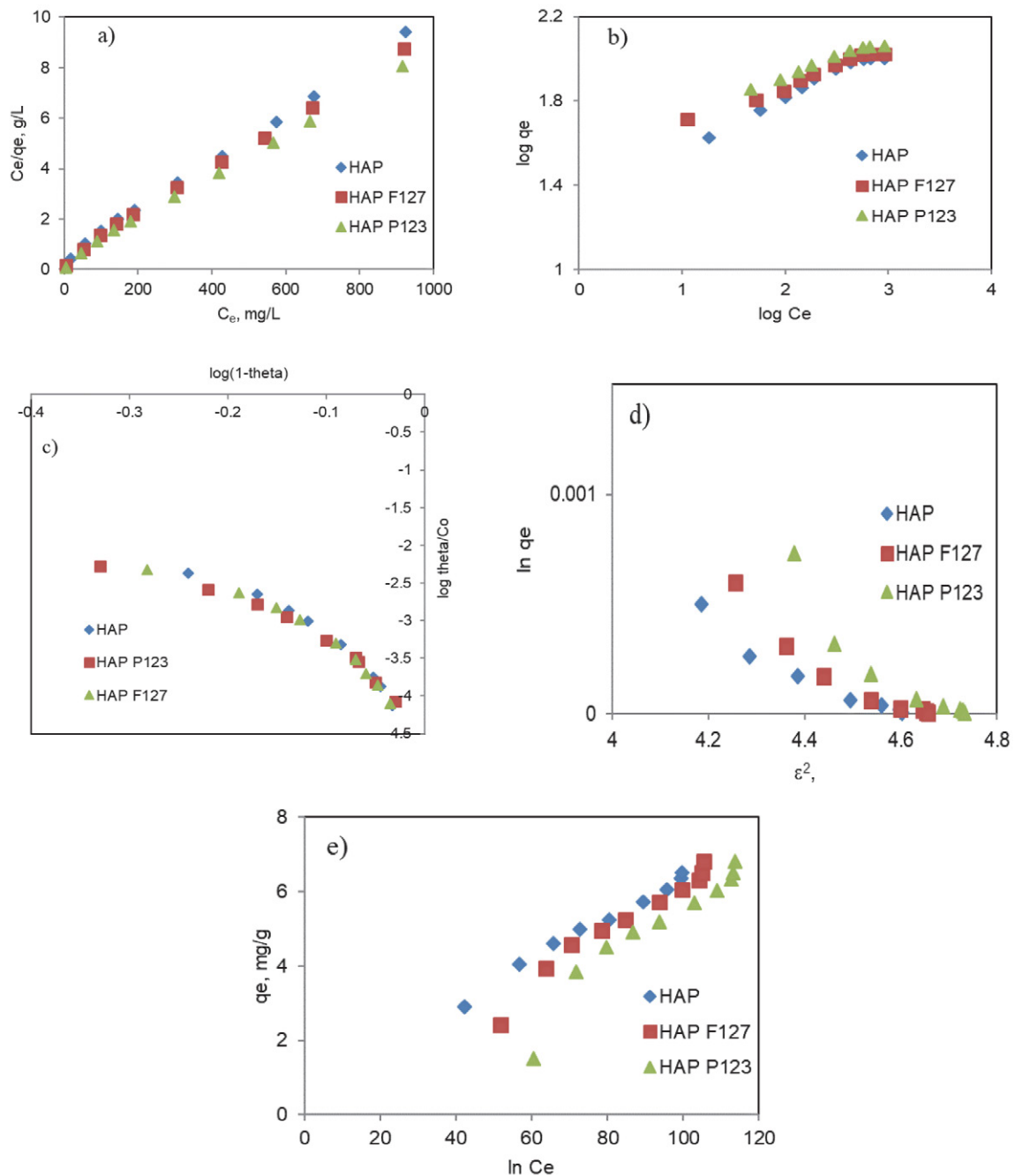


Figure 8. Langmuir (a), Freundlich (b), Flory-Huggins (c), Dubinin-Radushkevich (d) and Temkin (e) isotherms.

intercept of the graphical representation of $\log \theta / C_0$ vs $\log (1-\theta)$, (Figure 8c) and their values are given in Table 3.

Dubinin-Radushkevich isotherm model

Dubinin and Radushkevich proposed another isotherm that is applied to estimate the average free energy of adsorption. The average free adsorption energy per mole of sorbent is the energy required to transfer one mole of adsorbate from solution from infinity to the surface, and is useful in

evaluating the nature of the interaction between metal ions and binding sites.⁴⁵ If the value of E is between 8 and 16 kJ / mol, it can be assumed that the adsorption process involves chemical sorption. In contrast, values of less than 8 kJ / mol indicate that the adsorption process is physical in nature.

$$\ln q_c = \ln X_m - K_{DR} \varepsilon^2 \quad (10)$$

where K_{DR} is a constant related to adsorption energy (mol^2/kJ^2), X_m is a constant that indicates the sorption capacity of sorbent (mg/g).

Polanyi potential, ϵ , was calculated with the Eq. (11):

$$\epsilon = RT \ln \left(1 + \frac{1}{C_e} \right) \quad (11)$$

The free adsorption energy (E) was calculated using the following expression:

$$E_s = (-2K_{DR})^{-1/2} \quad (12)$$

The positive values obtained (see Table 3) indicate that the adsorption process is endothermic, being favored by high temperatures. Also, the values obtained are greater than 8 kJ/mol, indicating a chemisorption process.

Temkin isotherm model

This isotherm model considers the interactions between sorbent and adsorbate. This model assumes that the heat of adsorption process decreases linearly with the increase in coverage of sorbent, and the process is characterized by uniform distribution of the binding energies up to a maximum binding energy.⁴⁶ The linearized form of this isotherm is given by the equation (13):

$$q_e = \frac{RT}{b_T} \cdot \ln K_T + \frac{RT}{b_T} \ln C_e \quad (13)$$

$1/b_T$ indicates the sorption potential of the sorbent, and K_T is Temkin constant being calculated for each material and are given in Table 3.

Table 3. Adsorption isotherm parameters.

Model	HAP	HAP F127	HAP P123
Langmuir			
q_m , (mg g ⁻¹)	104.17	109.89	117.65
K_L , (L g ⁻¹)	0.021	0.023	0.03
R_L	0.49	0.47	0.4
R^2	0.998	0.997	0.998
Freundlich			
K_F	37.54	32.59	22.58
n	5.82	5.58	4.32
R^2	0.974	0.98	0.978
Flory-Huggins			
K_{FH}	15.28×10^3	12.07×10^3	9.18×10^3
n	8.505	7.124	5.87
R^2	0.934	0.913	0.908
Dubinin-Radushkevich			
K_{DR}	0.001	0.0013	0.0017
X_m (mol g ⁻¹)	102.48	105.61	109.48
E (kJ mol ⁻¹)	22.36	19.61	17.14
R^2	0.931	0.906	0.863
Temkin			
b_T	4.35	5.79	44.26
K_T (L g ⁻¹)	3.44	6.33	9.38
R^2	0.983	0.944	0.989

The results show that the Langmuir isotherm is the one that best describes the adsorption process of aluminium ions on the three sorbents, with a maximum adsorption capacity of 104.17 mg g⁻¹ for simple hydroxyapatite, 109.89 mg g⁻¹ for hydroxyapatite synthesized in the presence of Pluronic F127 and 117.65 mg g⁻¹ for hydroxyapatite synthesized in the presence of Pluronic P123. In all three cases, a correlation coefficient of 0.99 was obtained. The high energy adsorption value indicates a chemisorption process for the absorption of aluminium ions.

3. 8. Kinetic Studies

Kinetic studies are very important for adsorption processes because they can predict the rate at the pollutants are removed from aqueous solutions and offer some data to understand the mechanism of adsorption. In present study, three known kinetic models were used to investigate the adsorption mechanism.

Pseudo first order kinetic model

Lagergren showed that the rate of adsorption of ions on the sorbent is based on the adsorption capacity.⁴⁷ Thus, we use a pseudo-order equation for estimating the constant rate, k_1 . The nonlinear form of this equation is:

$$\frac{dq_t}{dt} = k_1(q_e - q_t) \quad (14)$$

Linearized form of this equation is:

$$\log(q_e - q_t) = \log q_e - \frac{k_1}{2.303} t \quad (15)$$

where q_e and q_t are the amounts of Al(III) (mg/g) adsorbed at equilibrium and at t (min) time, respectively, and k_1 (1/min) is the rate constant of pseudo-first order. The values of k_1 are calculated from the graphical representation of $\log(q_e - q_t)$ vs. t (Figure 9a).

Pseudo-second order kinetic model

This model is widely used for metal ion/sorbent adsorption systems. Adsorption of Al (III) ions may involve a chemical adsorption assuming a strong electrostatic interaction between the negatively charged surface of the sorbent and the metal ions.⁴⁸ The pseudo-second order kinetic equation is described in the following form:

$$\frac{dq_t}{dt} = k_2(q_e - q_t)^2 \quad (16)$$

Linearized form of this equation is:

$$\frac{1}{q_t} = \frac{1}{k_2 q_e^2} + \frac{1}{q_e} t \quad (17)$$

where k_2 (g/mg min) is the rate constant of second order. Linear form of t/q_t as function of t is shown in Figure 9b.

Intraparticle diffusion kinetic model

The kinetic model of intra-particle diffusion is based on the theory or equation proposed by Weber and Morris. It is a functional empirical relationship, common with most adsorption processes.⁴⁹ Metal ions adsorption varies almost proportionally with $t^{1/2}$ rather than with contact time, t . Weber-Morris equation is:

$$q_t = k_{id} t^{1/2} + C_i \quad (18)$$

where k_{id} is rate parameter of the i step ($\text{mg/g min}^{1/2}$), estimated from the slope of linear plot q_t as function of $t^{1/2}$. C_i is intercept of i step, giving an idea about the thickness of the boundary layer, that since the intercept is greater, the boundary layer effect is greater. For intra-particle diffusion, the plot of q_t vs. $t^{1/2}$ will be linear and if it passes through the origin, then the determinant rate process is due only to intra-particle diffusion

It can be seen from Figure 9c that the experimental data is distributed along two straight lines. The first sharpened portion is attributed to the diffusion of the ad-

sorbate by solution to the external surface of the sorbent (external diffusion), and the second portion describes the step of gradual adsorption, corresponding to the diffusion of adsorbate within the pores of the sorbent (intra-particle diffusion). It is also noted that $k_{id1} > k_{id2}$. Parameters obtained from the kinetic models are presented in Table 4.

From experimental data we can conclude that the adsorption of Al (III) ions follows the pseudo-second order kinetic model, which assumes that chemisorption can be the determining rate step.

In order to determine the effectiveness of the used sorbents, a comparison was made with the results from the literature when other sorbents were used, the results of the comparison being presented in Table 5.

Comparing the experimental data obtained in this study with those obtained by other researchers, we can see that the sorbents used have a higher sorption capacity than some sorbents reported in the literature, which recommends them to use in the removal process of aluminium ions from the waste water.

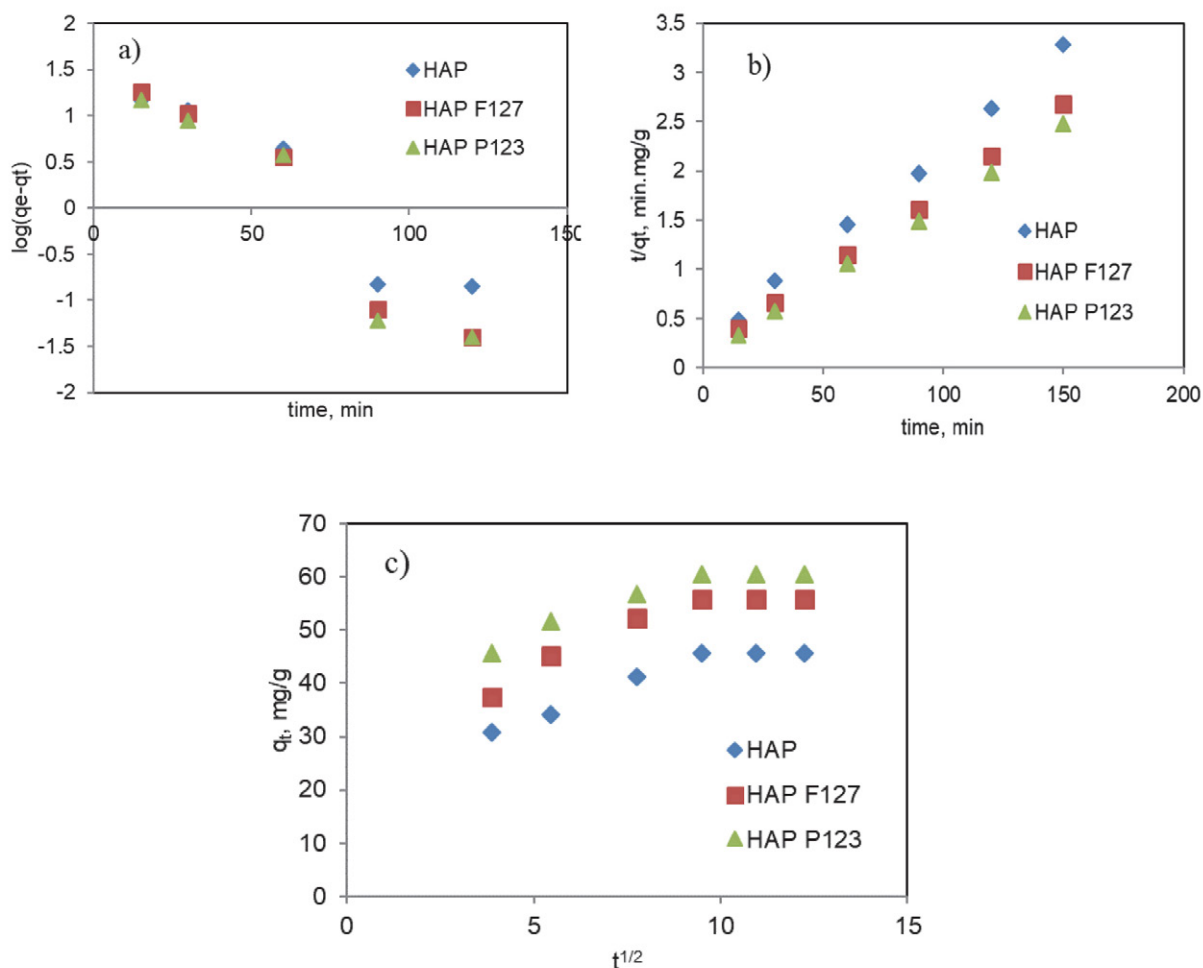


Figure 9. Pseudo-first order (a), pseudo-second order (b) and intraparticle diffusion kinetic model (c) for Al(III) adsorption onto investigated sorbents.

Table 4. Kinetic parameters of the adsorption of Al(III) ions.

Kinetic model	Sorbent		
	HAP	HAP F127	HAP P123
Pseudo first order			
$q_{e, \text{exp}}$ (mg g ⁻¹)	45.67	55.9	60.54
$q_{e, \text{calc}}$ (mg g ⁻¹)	43.61	54.60	66.91
k_1 (min ⁻¹)	0.051	0.064	0.063
R^2	0.901	0.940	0.914
Pseudo second order			
$q_{e, \text{exp}}$ (mg g ⁻¹)	45.67	55.9	60.54
$q_{e, \text{calc}}$ (mg g ⁻¹)	49.62	59.52	63.29
k_2 (g mg ⁻¹ min ⁻¹)	$1.91 \cdot 10^{-3}$	$1.97 \cdot 10^{-3}$	$1.16 \cdot 10^{-3}$
R^2	0.998	0.999	0.998
Intraparticle diffusion			
k_{id1} (mg/g min ^{1/2})	2.703	3.781	2.814
k_{id2} (mg/g min ^{1/2})	0.054	0.029	0.0216
C_1	20.024	23.476	35.378
$(R_1)^2$	0.989	0.986	0.979

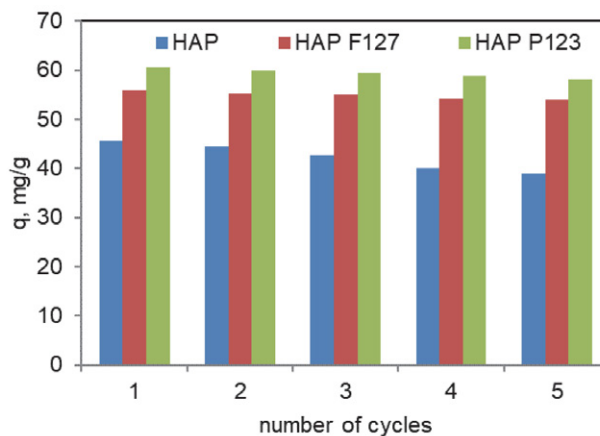
Table 5. Comparative result of adsorption efficiency of different type of sorbents towards Al(III).

Sorbent	q_e , mg/g	Reference
Beach cast seaweed	22.49	5
PAN beads	0.245	18
PAN beads thermally treated	0.154	18
Rice hull activated carbon	34.48	1
BDH activated carbon	6.56	11
<i>Rhodococcus opacus</i>	41.58	50
Granular activated carbon	106.5	12
Amberlite-IR-120H	108.7	12
Chitine	18.28	51
Chitosan	23.57	51
Hydroxyapatite	104.17	This study
Hydroxyapatite F127	109.89	This study
Hydroxyapatite P123	117.65	This study

3. 9. Regeneration and Reusability of Sorbents

The applicability of potential sorbents depends on their regeneration under convenient conditions and the possibility of their re-use in successive sorption / desorption cycles. From practical reasons, an ideal sorbent must be reused in successive sorption/desorption cycles with as less as possible loss of the initial sorption capacity. Therefore, desorption of Al (III) ions was carried out with a 0.01 M solution of HCl obtained in five successive sorption/desorption cycles as shown in Figure 10.

The results show that these sorbents could be successfully regenerated and repeatedly used in the adsorption studies of Al (III) ions without significant loss in their adsorption capacities.

**Figure 10.** Cycles of desorption-adsorption for sorbents.

4. Conclusions

The sorption of aluminium (III) ions from synthetic wastewaters onto different type of hydroxyapatite has been studied as a function of contact time, the initial metal ion concentration, sorbent mass, pH, sorbent dose and temperature. Equilibrium, kinetic and thermodynamic data were applied in order to evaluate the efficiency of the investigated sorbents for the removal of Al(III) ions from residual waters. The adsorption process of these ions on the three types of sorbents obeyed of the pseudo-second order kinetics, supporting that the chemisorption would be the rate-determining step. The equilibrium data obtained for the adsorption of aluminium ions onto investigated sorbents well fitted in the Langmuir model with a maximum theoretical adsorption capacity of 104.17 mg Al(III)/g hydroxyapatite, and 109.84 mg Al(III)/g hydroxyapatite F127, and 117.65 mg Al(III)/g hydroxyapatite P123, respectively. The sorption process is endothermic ($\Delta H^\circ > 20$ kJ/mol) and spontaneous (the increase of the negative values of ΔG° with the increase of temperature). The uptake of Al(III) by these sorbents is a reversible process and the sorbents can be used in five desorption/sorption cycles without significant loss in their adsorption capacities.

All these experimental results showed that hydroxyapatites are suitable adsorbent for removal of aluminium ions from residual waters.

Acknowledgement

This work was supported by IUCN-Dubna project, no. 03-4-1128-2017/2019, theme 100.

5. References

1. N. T. Abdel-Ghani, G. A. El-Chaghaby, E. M. Zahran, *Am. J. Anal. Chem.* **2015**, 6, 71–83. DOI:10.4236/ajac.2015.61007

2. N. T. Abdel-Ghani, A. K. Hegazy, G. A. El-Chaghaby, *Int. J. Environ. Sci. Technol.*, **2009**, *6*, 243–248. DOI:10.1007/BF03327628
3. P. T. Srinivasan, T. Viraraghavan, K. S. Subramanyam, *Water SA*, **1999**, *25*, 47–55.
4. M. E. Argun, Ş. Dursun, C. Özdemir, M. Karataş, *J. Hazard. Mater.* **2007**, *141*, 77–85. DOI:10.1016/j.jhazmat.2006.06.095
5. P. Lodeiro, A. Gudina, L. Herrero, R. Herrero, M. E. Sastre de Vicente, *J. Hazard. Mater.* **2010**, *178*, 861–866. DOI:10.1016/j.jhazmat.2010.02.017
6. S. Arendze, M. S. Sibiyi, *Water Sci. Tech. – Water Supply*, **2017**, *17*, 733–744. DOI:10.2166/ws.2016.170
7. C. N. Martyn, C. Osmond, J. A. Edwardson, D. J. Barker, E. C. Harris, J. A. Edwardson, R. F. Lacey, *The Lancet* **1989**, *333*, 59–62. DOI:10.1016/S0140-6736(89)91425-6
8. M. V. Peto, *Rejuv. Res.* **2010**, *13*, 589–598. DOI:10.1089/rej.2009.0995
9. A. Tassist, H. Lounici, N. Abdi, N. Mameri, *J. Hazard. Mater.* **2010**, *183*, 35–43. DOI:10.1016/j.jhazmat.2010.06.078
10. P. G. Pour, M. A. Takassi, T. Hamoule, *Orient. J. Chem.* **2014**, *30*, 1365–1369. DOI:10.13005/oj.300356
11. S. A. Al-Muhtaseb, M. H. El-Naas, S. Abdallah, *J. Hazard. Mater.* **2008**, *158*, 300–307. DOI:10.1016/j.jhazmat.2008.01.080
12. M. E. Goher, A. M. Hassan, I. A. Abdel-Moniem, A. H. Fahmy, M. H. Abdo, S. M. El-sayed, *Egypt. J. Aquat. Res.* **2015**, *41*, 155–164. DOI:10.1016/j.ejar.2015.04.002
13. A. M. Abdullah, *J. Pollut. Eff. Cont.* **2012**, *2*, 120–124. DOI:10.4172/2375-4397.1000120
14. F. Ji, C. Li, J. Xu, P. Liu, *Coll. Surf. A Physicochem. Eng. Asp.* **2013**, *434*, 88–94. DOI:10.1016/j.colsurfa.2013.05.045
15. D. Pitre, A. Boullemant, C. Fortin, *Chem. Cent. J.* **2014**, *8*, 8–15. doi: DOI:10.1186/1752-153X-8-8
16. A. Sari, M. Tuzen, *J. Hazard. Mater.* **2009**, *171*, 973–979. DOI:10.1016/j.jhazmat.2009.06.101
17. R. Asrarian, R. Jadidian, H. Parham, S. Haghtalab, *Adv. Mater. Res.* **2014**, *829*, 752–756. DOI:10.4028/www.scientific.net/AMR.829.752
18. Z. Aly, A. Graulet, N. Scales, T. Hanley, *Environ. Sci. Pollut. Res.* **2014**, *21*, 3972–3986. DOI:10.1007/s11356-013-2305-6
19. F. An, B. Gao, X. Huang, Y. Zhang, Y. Li, Y. Xu, Z. Zhang, J. Gao, Z. Chen, *React. Funct. Polym.* **2013**, *73*, 60–65. DOI:10.1016/j.reactfunctpolym.2012.08.022
20. A. Islam, A. Hilal, N. Zaidi, S. Yadav, *Ind. Eng. Chem. Res.* **2013**, *52*, 5213–5220. DOI:10.1021/ie303300u
21. G. N. Kousalya, G. M. Rajiv, C. Sairam Sundaram, S. Meenakshi, *Carbohydrate Polym.* **2010**, *82*, 594–599. DOI:10.1016/j.carbpol.2010.05.013
22. Duyen Thi Le, Thao Phuong Thi Le, Hai Thi Do, Hanh Thi Vo, Nam Thi Pham, Thom Thi Nguyen, Hong Thi Cao, Phuong Thu Nguyen, Thanh Mai Thi Dinh, Hai Viet Le, Dai Lam Tran, *J. Chem.*, **2019**, Article ID 8620181 DOI:10.1155/2019/8620181
23. W. Lemlikchi, P. Sharrock, M. O. Mecherri, M. Fiallo, Ange Nzihou, *Waste and Biomass Valorization*, Springer, **2012**, *3* (1), 75–79. DOI:10.1007/s12649-011-9096-0
24. A. Paz, D. Guadarrama, M. López, J. E. González, N. Brizuela, J. Aragón, *Quim. Nova* **2012**, *35*, 1724–1727. DOI:10.1590/S0100-40422012000900004
25. S. Park, A. Gomez-flores, Y. S. Chung, H. Kim, *J. Chem.* **2015**, *396290*. DOI:10.1155/2015/396290
26. G. Ciobanu, M. Harja, L. Rusu, A. M. Mocanu, C. Luca, *Korean J. Chem. Eng.* **2014**, *31*, 1021–1027. DOI:10.1007/s11814-014-0040-4
27. T. A. Salah, A. M. Mohammad, M. A. Hassan, B. E. El-Anadoul, *J. Taiwan Inst. Chem. Eng.* **2014**, *45*, 1571–1577. DOI:10.1016/j.jtice.2013.10.008
28. P. Wang, C. Li, H. Gong, X. Jiang, H. Wang, K. Li, *Powder Technol.* **2010**, *203*, 315–321. DOI:10.1016/j.powtec.2010.05.023
29. A. I. Adeogun, R. B. Babu, *Appl. Nanosci.* **2015**, *5*, 1–13. DOI:10.1007/s13204-015-0484-9
30. M. S. M. Arsad, P. M. Lee, L. K. Hung, 2nd International Conference on Biotechnology and Food Science IPCBEE 7, **2011**, 184–188.
31. N. Barka, S. Qourzal, A. Assabbane, A. Nounah, Y. Ait-Ichou, *J. Saudi Chem. Soc.* **2011**, *15*, 263–267. DOI:10.1016/j.jscs.2010.10.002
32. D. C. Manatunga, R. M. de Silva, K. M. Nalin de Silva, N. de Silva, E. V. A. Premalal, *R. Soc. Open Sci.* **2018**, *5*, 171557–171571. DOI:10.1098/rsos.171557
33. S. Wongsakulphasatch, *Eng. J.* **2010**, *17*, 30–37. DOI:10.4186/ej.2013.17.2.29
34. W. Aili, L. Dong, Y. Hengbo, W. Huixiong, W. Yuji, R. Min, J. Tingshun, C. Xiaonong, X. Yiqing, *J. Mat. Sc. Eng.* **2007**, *C27*, 865–869. DOI:10.1016/j.jmse.2006.10.001
35. G. M. El Shafei, C. A. Philip, N. A. Moussa, *J. Coll. Interf. Sci.* **2004**, *277*, 410–416. DOI:10.1016/j.jcis.2004.05.002
36. K. S. W. Sing, D. H. Everett, R. A. W. Haul, L. Moscou, R. A. Pierotti, J. Rouquérol, T. Siemieniowska, *Pure Appl. Chem.* **1985**, *57*, 603–619. DOI:10.1351/pac198557040603
37. J. R. Nimmo, *Soil Sci. Soc. Am. J.* **1992**, *56*, 1723–1730. DOI:10.2136/sssaj1992.03615995005600060011x
38. R. Garcidueñas Piña, C. Cervantes, *Biol. Met.* **1996**, *9*, 311–316. DOI:10.1007/BF00817932
39. Z. Aly, A. Graulet, N. Scales, T. Hanley, *Environ. Sci. Pollut. Res.* **2014**, *21*, 3972–3986. DOI:10.1007/s11356-013-2305-6
40. S. A. Al-Muhtaseb, M. H. El-Naas, S. Abdallah, *J. Hazard. Mater.*, **2008**, *158*, 300–307. DOI:10.1016/j.jhazmat.2008.01.080
41. A. Ramdani, Z. Taleb, A. Guendouzi, A. Kadeche, H. Herbache, A. Mostefai, S. Taleb, A. Deratani, *Can. J. Chem.*, **2020**, *98*, 79–89. DOI:10.1139/cjc-2019-0315
42. I. Langmuir, *J. Am. Chem. Soc.* **1916**, *38*, 2221–2295. DOI:10.1021/ja02268a002
43. H. Freundlich, *Zeitschrift für Physikalische Chemie* **1906**, *57*, 385–470. DOI:10.1515/zpch-1907-5723
44. C. H. Giles, D. Smith, A. Huitson, *J. Coll. Interf. Sci.* **1974**, *47*, 755–765. DOI:10.1016/0021-9797(74)90252-5
45. M. M. Dubinin, L. V. Radushkevich, *Physical Chemistry Section USSR*, **1947**, *55*, 331–333.
46. M. Temkin, *Zhurnal Fizicheskoi Khimii* **1941**, *15*, 296–332.
47. S. Lagergren, B. K. Svenska, *R. Swed. Acad. Sci. Doc. Band.* **1898**, *24*, 1–13.

48. G. McKay, Y. S. Ho, *Proc. Biochem.* **1999**, *34*, 451–465. DOI:10.1016/S0032-9592(98)00112-5
49. W. J. Jr. Weber, J. C. Morris, *J. Sanit. Eng. Div. Am. Soc. Civ. Eng.* **1963**, *89*, 31–59. DOI:10.1061/JSEDAI.0000430
50. J. E. B. Cayllahua, M. L. Torem, (2010) *Chem. Eng. J.* **2010**, *161*, 1–8. DOI:10.1016/j.cej.2010.03.025
51. M. Á. Lobo-Recio, F. R. Lapolli, T. J. Belli, C. T. Folzke, R. R. Zepon Tarpani, *Des. Water Treat.* **2013**, *51*, 1735–1743. DOI:10.1080/19443994.2012.715133

Povzetek

V tem delu predstavljamo rezultate sposobnosti adsorpcije aluminija iz onesnažene vode s hidroksiapatitom pripravljenim na različne načine. Eksperimenti so bili izvedeni v šaržnem načinu pri različnih pH vrednostih, temperaturi, količini adsorbenta, kontaktnem času in začetni koncentraciji aluminija. Termodinamska analiza je pokazala, da je proces adsorpcije aluminija na hidroksiapatit spontan in endotermen. Eksperimentalnim podatkom smo prilagajali Langmuirjev, Freundlichov, Flory-Hugginsov, Dubinin-Radushkevichov in Temkinov ravnotežni model, pri čemer smo najboljše ujemanje dosegli z Langmuirjevim modelom. Kinetične podatke smo ovrednotili s kinetičnim modelom psevdo-prvega in psevdo-drugega reda ter modelom znotrajdelčne difuzije. Hitrost adsorpcije aluminija lahko najboljše opišemo s psevdo-drugega reda. Rezultati so pokazali, da ima najvišjo adsorpcijsko kapaciteto aluminija hidroksiapatit pri katerem smo uporabili surfaktant Pluronic P123 (117.65 mg g^{-1}), sledi mu hidroksiapatit s surfaktantom Pluronic F127, najnižjo pa hidroksiapatit pripravljen brez uporabe surfaktanta (104.17 mg g^{-1}).



Except when otherwise noted, articles in this journal are published under the terms and conditions of the Creative Commons Attribution 4.0 International License

Scientific paper

The Removal of Binary Mixture of Dyes by Heterogeneous Fenton Oxidation: Kinetics, Product Identification and Toxicity Assessment

John Elisa Kumar,¹ Tsungom Mulai,¹ Wanshanlang Kharmawphlang,¹
Rajeshwar Nath Sharan² and Mihir Kumar Sahoo^{1*}

¹ Centre for Advanced Studies in Chemistry, Department of Chemistry, North-Eastern Hill University, Shillong– 793 022, India

² Radiation & Molecular Biology Unit, Department of Biochemistry, North-Eastern Hill University, Shillong– 793 022, India

* Corresponding author: E-mail: mksahoo@nehu.ac.in; mihirs2107@gmail.com
Tel.: +91-364-2722632; Cell: +91-9436706767; Fax: +91-364-2551634

Received: 03-19-2021

Abstract

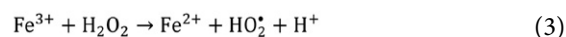
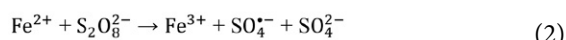
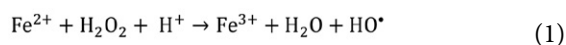
The removal of mixture of two azo dyes, Acid blue 29 and Ponceau xylidine, was studied by heterogeneous Fenton and Fenton-type processes using hydrogen peroxide and sodium persulphate as oxidants in the presence of and nano and micro-Fe₂O₃ particles as catalysts. The synthesised nano-Fe₂O₃ particles were characterised using analytical techniques viz. FT-IR, TEM, EDX, powder XRD and VSM. We have examined the effects of particle size on the COD removal efficiency and the reusability of the catalyst after optimising pH, and concentrations of catalyst and oxidant. Combination of nano-Fe₂O₃ and hydrogen peroxide possessed higher COD removal efficiency, which was accelerated in acidic pH and inhibited at pH > 6. Total consumption of hydrogen peroxide confirmed the efficiency of the optimised parameters. The mechanism of the formation of intermediate ions and products are proposed. COD removal and consumption of hydrogen peroxide follow pseudo-first-order kinetics. The toxicity of the solutions was assessed using *Aliivibrio fischeri* light loss and *Escherichia coli* growth inhibition assays. Both the assays showed different toxicity levels for the same solution.

Keywords: Binary mixture of dyes; Heterogeneous Fenton processes; COD removal kinetics; Identification of ions and products; Toxicity assessment using *Escherichia coli* and *Aliivibrio fischeri*

1. Introduction

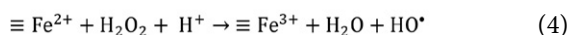
The wastewater generated by the textile industries usually contains a higher concentration of Chemical Oxygen Demand (COD), Biochemical Oxygen Demand (BOD), alkalinity and colour,¹ which should be normalised before releasing into the water bodies to contain pollution. Advanced Oxidation Processes (AOPs), which involve *in situ* generation of hydroxyl radicals, have achieved the above goals to a great extent.^{2–4} The oldest AOPs, involving activation of hydrogen peroxide (HP) and sodium persulphate (SPS) to generate hydroxyl and sulphate radicals^{5–7} using Fe²⁺ as a catalyst, are popularly known as Fenton (Fe²⁺/HP) and Fenton-type process (Fe²⁺/SPS) (Eqs. (1) and (2)). Apart from being a simple and efficient reaction requiring no electrical energy input, the Fe²⁺/HP pro-

cess requires only a catalytic amount of Fe²⁺ since it is regenerated from the Fe³⁺ ion in a process called Fenton-like reaction (Eq. (3)).⁸



These advantages are masked by its narrow operational pH range, and sludge generation at the end of the process.^{5,9} So, a search for a low cost and stable catalyst, which can be easily separated from the reaction medium and reused in successive cycles, thereby reducing the cost of operation, is needed. A heterogeneous catalyst has been

shown to meet the requirements mentioned above and, therefore, can be used in the Fenton process, the heterogeneous Fenton process. Among the various heterogeneous catalysts, zero-valent iron nano-particles,^{10,11} and iron oxide minerals^{12–15} have been widely used for environmental remediation. Iron is fixed in the structure of a heterogeneous catalyst that activates the oxidant (Eq. (4)) over a broad range of pH values depending on the point of zero charge (PZC) of the catalyst.¹⁶ Hence, the biggest advantage of the heterogeneous over homogeneous Fenton process is that the catalyst can be separated by an external magnet.



(Where \equiv represents the surface of the catalyst)

Most publications in this domain have utilized low concentrations of dyes varying from 10 to 30 ppm. Although the literature is rich in reports on degradation of individual dyes by different AOPs, that for mixture of dyes is scanty even though textile industries invariably use mixture of dyes. Keeping this lacuna in mind, we decided to study the removal of mixture of two dyes, viz. Acid Blue 29 (AB) and Ponceau Xylidine (PX) at higher concentrations (92 ppm and 72 ppm, respectively, equivalent to 0.15 mM for both) by heterogeneous Fenton and Fenton-type processes. COD removal efficiency (COD_{eff}) was used as an indicator for the removal of dyes. In this study, two types of iron oxide particles as catalysts: nano- Fe_2O_3 (synthesised, average particle size 26–35 nm) and micro- Fe_2O_3 particles (commercially available, < 5 μm) and two different oxidants, i.e. HP and SPS, were used. AB and PX were selected as the model dye pollutants because of their extensive use in textile industries for dyeing wool, cotton, silk, polyester and rayon etc. They are also used in paint, ink, plastic and leather industries. Moreover, the dyes, being azo dyes, are recalcitrant and carcinogenic due to the presence of $-\text{N}=\text{N}-$ bond.^{17,18} Since the activation of HP and SPS depends on the specific surface area of the catalyst; we proposed to investigate the ability of iron (III) oxide nano-particles (n- Fe_2O_3) and micro- Fe_2O_3 (m- Fe_2O_3) particles to decompose HP and SPS and produce hydroxyl and sulphate radicals. This study also examined the influence of catalyst loading, HP dosage, and pH on the efficiency of the process. Apart from these in this study, we attempted to optimize the operational parameters to maximize HP efficiency by ensuring its total consumption in the process, COD removal and HP consumption kinetics. Assessment of the effect of residual hydrogen peroxide on the COD removal efficiency was another important objective of the study. Different ions and end products formed in the process were analysed by Ion chromatography. The degradation mechanism of the mixture of dyes based on end-product analysis and supported by literature data has been proposed.

Despite the enhanced efficiency of the AOPs, complete mineralisation of the organic compounds may not always be possible. Under such a situation, the intermedi-

ate oxidation by-products may contribute to increased toxicity.¹⁹ On the contrary, there are instances of increased toxicity of the solutions even when Fenton and Fenton-type processes achieve mineralisation to the extent of >90%.^{7,20} Therefore, it is essential to test the toxicity of industrial wastewater after treatment, after a complete mineralisation is achieved. Some authors have used *Aliivibrio fischeri* and some *Escherichia coli* for the toxicity assessment. But no attempt has been made to compare the toxicity of a given sample using these two assessment methods. In this study, we have compared the toxicity of the pure dye solution and the solutions obtained at different stages of the treatment process.

2. Materials and Methods

2.1. Chemicals and Materials

The diazo dye, Acid Blue 29 (Synonym: Amacid Navy Blue B; Cetil Black M; Fabracid Navy S-BL; Mor-dant Blue 82; CI number: 20460; molecular formula: $\text{C}_{22}\text{H}_{14}\text{N}_2\text{Na}_2\text{O}_9\text{S}_2$; molecular weight: 616.49 (g mol^{-1}); $\lambda_{\text{max}} = 602 \text{ nm}$; pH of the dye solution in water: 6.7) and the anionic diazo dye, Ponceau Xylidine (Synonym: 1-(2,4-xylylazo)-2-naphthol-3,6-disulphonic acid disodium salt; C.I. number: 16150; molecular formula: $\text{C}_{18}\text{H}_{14}\text{N}_2\text{Na}_2\text{O}_7\text{S}_2$; molecular weight: 480.42 (g mol^{-1}); $\lambda_{\text{max}} = 504 \text{ nm}$; pH of the dye solution in water: 6.2) were procured from Sigma Aldrich (Germany). The molecular structures of AB 29 and PX are shown in Fig. 1.

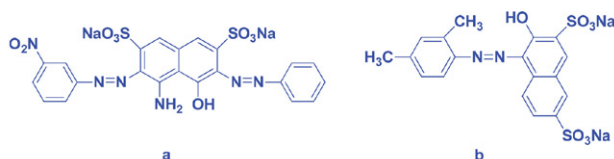


Figure 1. Structures of Acid blue 29 (a) and Ponceau xylidine (b).

The other chemicals viz. sulphuric acid (H_2SO_4 , GR), sodium hydroxide (NaOH, GR), hydrogen peroxide (H_2O_2 , 30% w/w, purified), sodium peroxodisulphate ($\text{Na}_2\text{S}_2\text{O}_8$, for analysis), iron (II) sulphate ($\text{FeSO}_4 \cdot 7\text{H}_2\text{O}$, GR), iron (II) chloride anhydrous (FeCl_2 , purified), iron (III) chloride tetrahydrate ($\text{FeCl}_3 \cdot 4\text{H}_2\text{O}$), hydrochloric acid (HCl, min 35% GR), nitric acid (HNO_3 , min 65% GR), and methanol (CH_3OH , GR) were obtained from Merck. Ethanol (absolute, 99.9%) was obtained from Changshu Yangyuan Chemical, China. Solution 1' (mercuric sulphate and sulphuric acid) and 'Solution 2' for low range COD (silver sulphate, chromic acid, sulphuric acid and demineralised water) required for the determination of COD were supplied by HACH, USA. The chemicals used for ion chromatographic analysis were sodium hydroxide (NaOH, 50–52% in water, Sigma), methane sulphonic acid ($\text{CH}_3\text{SO}_3\text{H}$,

HIMEDIA), acetonitrile (CH_3CN , HPLC grade, HIME-DIA), ammonium acetate ($\text{CH}_3\text{COONH}_4$, Merck, Emparta ACS). All the chemicals were used as received.

2. 2. Catalysts

2. 2. 1. Fe_2O_3 Micro-particles

Iron (III) oxide powder ($< 5\mu\text{m}$), i.e. $\text{m-Fe}_2\text{O}_3$ used as one of the catalysts in the heterogeneous process, was supplied by Sigma-Aldrich.

2. 2. 2. Fe_2O_3 Nano-particles

Iron (III) oxide nano-particles ($\text{n-Fe}_2\text{O}_3$) were synthesised by chemical co-precipitation of Fe(II) and Fe(III) ions as described earlier.²¹ Briefly, 3.1 g of $\text{FeCl}_2 \cdot 4\text{H}_2\text{O}$ and 5.2 g of FeCl_3 (molar ratio of 1:2) were successively added to 25 mL of deionised water acidified with 0.85 mL of 12.1 N HCl with constant stirring. The resulting solution was added dropwise to 250 mL of 1.5 M NaOH solution under vigorous stirring when an instant black precipitate was observed. The paramagnetic character of the particles was checked *in situ* by placing a magnet near the deposit. The precipitate was filtered using a vacuum pump after continuously stirring for 6 h and washed with deionised water until neutral pH was achieved. Finally, the precipitate was washed with ethanol, dried, ground and stored. The black precipitate turned light brown after drying due to calcination.

The surface functional groups of the prepared $\text{n-Fe}_2\text{O}_3$ particles were qualitatively identified using the FTIR spectrum (Bruker, Model: Alpha II). The morphology of the synthesised $\text{n-Fe}_2\text{O}_3$ was determined by transmission electron microscopy (TEM) with an instrument (JEOL, JEM-2100) operating at 200 kV. The purity of $\text{n-Fe}_2\text{O}_3$ was confirmed by energy dispersive X-rays (EDX) analysis. To check the crystallinity, powder X-ray diffraction (XRD) patterns of the dried $\text{n-Fe}_2\text{O}_3$ were recorded in reflection mode using a high resolution diffractometer (GNR Analytical Instrument, Explorer, Italy) with $\text{CuK}\alpha$ radiation ($\lambda = 1.54 \text{ \AA}$) within the 2θ values ranging from 20 to 80° with a step size of 0.05° and step time of 2 min. The operating voltage and current were 40 kV and 35 mA, respectively. The vibrating sample magnetometry (VSM) analysis was performed using Vibrating Sample Magnetometer (Lakeshore, 7410 series) to confirm the paramagnetic nature of the prepared nano-particles.

2. 3. Experimental

This section highlights details of the experiments performed and their procedures. The procedure for the heterogeneous Fenton-process has been described in Sec. 2.3.1. We have worked with various concentration of the catalysts (nano-particles) ranging from 0.1 to 1.0 g/L and HP ranging from 5.0 to 9.0 mM (Sec. 3.2) for their opti-

misation. The procedure of the heterogeneous Fenton-process is valid for each concentration of catalyst and oxidant. The determination of the size of the catalysts has been discussed in Sec. 3.1. The optimisation of the catalyst was done by running the reaction for 90 min and varying its concentration, and keeping other parameters (Conc. of oxidant and dye, pH) constant (Sec. 3.2). Sec. 2.3.2 describes the methods of determination of decolorisation, COD removal efficiency, identification of various ions and intermediate products formed during the treatment and iron content of the catalyst before and after the treatment.

2. 3. 1. Heterogeneous Fenton Procedure

Stock solutions of AB and PX of desired concentration were prepared separately by dissolving in the required amount of Millipore water (Elix3 Century, Millipore India, Bangalore). A mixture of 15 mL of each of the dyes was adjusted to 100 ml in a volumetric flask.

The concentrations of both the dyes in the mixture were calculated to be 0.15 mM each. The content in the volumetric flask was transferred to a 250 mL round bottom flask (RB). After adjusting the pH to the desired value, 4.0 g/L $\text{n-Fe}_2\text{O}_3$ were added to the mixture. The mixture was stirred for 90 min when complete equilibrium was established. The equilibrium point was established by measuring the concentration of the dyes from time to time until no change in concentration was observed. The concentration was measured spectrophotometrically using a UV-vis spectrophotometer (HACH, USA; DR 6000) and by following Beer-Lambert law. The reaction was started by adding 0.5 mL of HP of desired concentration after equilibration. After centrifuging for 6 min at 4800 rpm after the selected reaction period, the mixture was used for decolorisation and COD removal studies.

All reactions were carried out in the presence of air and at room temperature (varying between 19 and 25°C). The body and the mouth of the RB were wrapped with aluminium foil to prevent the passage of light. Two holes were pierced through aluminium foil covering the mouth to allow free passage of air. It may be mentioned that the temperature was not controlled during the experiments. Each RB was designated to be sacrificed for analysis after a predetermined time interval. The initial pH of the solution was adjusted to the desired value with H_2SO_4 (the strength ranging between 0.05–0.35 N depending on the pH necessary) or NaOH (the strength ranging between 0.025–0.125 N depending on the pH necessary) using a digital pH meter (Eutech instrument pH-Tutor). All solutions used in this study were freshly prepared except the dye solution, which was stored at 4°C and used within three days.

2. 3. 2. Analytical Methods

The decolorisation studies were carried out by measuring the absorbance at 539 nm (for PX) and 604 nm (AB

29) with the help of a UV-vis spectrophotometer (HACH, USA; DR 6000). COD was measured using a COD digester (HACH, USA; DRB 200) and UV-vis spectrophotometer (HACH, USA; DR 6000). HACH, USA, provided the procedure for the determination of COD.²

Decolorisation and COD_{eff} are calculated according to the following equations:

$$\text{Decolorisation (\%)} = \frac{A_0 - A_t}{A_0} \times 100 \%$$

$$\text{COD}_{\text{eff}} = \frac{\text{COD}_0 - \text{COD}_t}{\text{COD}_0} \times 100\%$$

Where the initial absorbance and COD of the solution are A_0 , and COD_0 respectively; the corresponding values at time 't' are A_t , and COD_t .

The COD value for the samples containing H_2O_2 was corrected quantitatively using Eq. (5), as proposed by Kang et al.²² The degradation rate constants in terms of COD removal was determined according to the pseudo-first-order rate laws (Eq. (6)).

$$\text{COD (mg/L)} = \text{COD}_m - (0.4706 \cdot [\text{H}_2\text{O}_2] - 4.06 \times 10^{-5} \cdot [\text{H}_2\text{O}_2]^2) \quad (5)$$

Where COD_m is the measured COD (mg/L)

$$-\ln(\text{COD}/\text{COD}_0) = k_{\text{COD}} \cdot t \quad (6)$$

Where, COD_0 is the initial COD at time $t = 0$, and COD is its value at any time t (min). The first-order rate constant (k_{COD}) for COD removal is the slope of the straight line obtained by plotting $-\ln(\text{COD}/\text{COD}_0)$ vs. time. The kinetics of HP consumption was determined by replacing COD with HP and COD_0 with HP_0 in Eq. (6), where HP_0 the initial [HP] at time $t = 0$, and HP is its value at any time t (min).

Anions, cations, organic acids, phenols and concentration of residual HP were analysed using Ion Chromatography System (ICS) supplied by Thermo Scientific, USA (Dionex, ICS-1100). For anions and organic acids, IonPac AS11 analytical column (4×250 mm) with a suitable guard column and an automatic electrolytic suppressor (AERS 500, 4 mm) was used. The current of the suppressor was maintained at 30 mA for anions and 38 mA for organic acids. The mobile phase was NaOH (12 mM for anion and 15 mM for organic acids) with a flow rate of 1 mL min^{-1} . Cations were analysed using IonPac CS17 analytical column (4×250 mm) with a suitable guard column and an automatic electrolytic suppressor (CERS 300, 4 mm) with a current of 15 mA. The mobile phase was 5 mM MSA with a flow rate of 1 mL min^{-1} . The concentration of residual HP was analysed using CarboPac PA20 analytical column (3×150 mm) with a suitable guard column and an electrochemical detector (ED 50A).

The mobile phase was 50 mM NaOH with a flow rate of 0.5 mL min^{-1} . Phenols were analysed using a VWD variable wavelength absorbance UV-vis detector (cell path length: 10mm; cell volume: 11 μL). The wavelengths selected for the purpose were 270 nm and 320 nm. The mobile phase was 0.1 M ammonium acetate solution with a flow rate of 1 mL min^{-1} . It was prepared by mixing an appropriate amount of ammonium acetate with a mixture of water and acetonitrile (1:1). All the experiments were repeated at least three times, and the error was always found to be within $\pm 5\%$. The data presented in the text and figures were analysed by standard deviation using 'Origin 7' (Microcal Inc.) and rounded up to significant values.

The iron content of the catalysts was determined by ICP-OES (ICP-OES: Model No. iCap 7600 Duo, Thermo Fisher). The sample preparation involves solubilising 0.02 g of the catalyst in 5 mL conc. HNO_3 by heating and evaporating to less than 1 mL. After solubilisation, the samples were diluted to 100 mL with distilled water and submitted for analysis by ICP-OES.²³

2. 4. Toxicity Assay

We have adapted two methods for the toxicity assessment of the treated solutions. The first method is based on the *E. coli* growth inhibition (metabolic inhibition) bioassay.^{7,24} Luria Bertani (LB) agar, LB broth and ampicillin used in the toxicity assessment study were acquired from Himedia, India. The lyophilised luminescent bacteria, *A. fischeri* used for the toxicity assessment by light loss assay was supplied by Modern Water Inc, USA.

2. 4. 1. Escherichia Coli Growth Inhibition Assay

The procedure involves dissolving 40 g of LB agar in 1000 mL of water followed by autoclaving for 30 min. Upon cooling down to about 40°C , ampicillin (1 μL for each mL of LB agar solution) was added, mixed, and aliquots of approximately 10 mL of the medium were poured into sterilised Petri plates. LB broth (25 g) was separately dissolved in 1000 mL of water, aliquoted (9 mL) in 100 mL conical flasks and sterilised by autoclaving for 30 min. Ampicillin (10 μL), *E. coli* culture inoculum (100 μL) and 1 mL of the dye or other test solution were added to the sterilised LB broth. The cultures were grown at 37°C overnight in a rotary shaker. The following day, the mid-log phase culture was diluted 10,000 times, and 10 μL of the diluted culture was spread over the LB agar plates prepared earlier. The plates were incubated for 16 h in a 37°C incubator as described earlier.²⁵ Colony forming units (CFUs) formed in each plate was counted. All steps of the experiment were performed under sterilized conditions. The relative toxicities of the treated solutions, measured as reduction in CFU, were with respect to the control.

2. 4. 2. *Aliivibrio fischeri* Luminescent Assay

In this method, the toxicity was measured using a Microtox FX test system (Modern Water Inc, USA). This method is based on the principles suggested by ISO (2007).²⁶ The relative toxicity of each sample was measured using an 81.9% screening test, the procedure of which was supplied by Modern Water Inc, USA. The assay was conducted at 15–22 °C by adding an osmotic adjusting solution (OAS) containing 22% NaCl. The test is called the 81.9% screening test, as all the samples are diluted at 81.9% of the initial sample concentration by adding a 22% NaCl solution.²⁷ The purpose of using 22% NaCl in OAS is to bring the salinity of the samples to approximately 2‰ to allow the regular cellular activity of *A. fischeri* and emission of luminescence (Sourced from “Microtox FX analyser user manual supplied by Modern Water Inc, USA”). The inhibition of luminescence or light loss (%) by the bacterium was analysed by the Microtox FX photometer. The light loss (%) was used as a measure of the relative toxicity of the samples.

3. Results and Discussion

As already discussed, not adequate information has been documented in the literature on the removal of mixture of dyes by AOPs. In this section, the removal of mixture of two dyes (AB and PX) by heterogeneous Fenton process has been discussed. Reduction in COD has been taken as an indication of removal of dyes. The critical step in the removal process lies in the ability of both nano and micro iron (III) oxide particles to decompose HP and SPS producing hydroxyl and sulphate radicals. To maximize the COD removal, we have first optimized various parameters such as catalyst load, concentration of oxidant, pH in n-Fe₂O₃/HP system. These optimized parameters were used for other systems as well. Further studies such as (i) COD removal and its dependency on particle size, (ii) reusability of catalysts, (iii) kinetics of COD removal and HP

consumption, (iv) product identification, and (v) toxicity assessment were also carried out under the same optimized conditions.

3. 1. Characterisation of n-Fe₂O₃ Catalyst

The nano-particles were characterised by FTIR, TEM, EDS, powder XRD and VSM. The FTIR spectrum of the n-Fe₂O₃ particles are shown in Fig. 2. The peak at 604

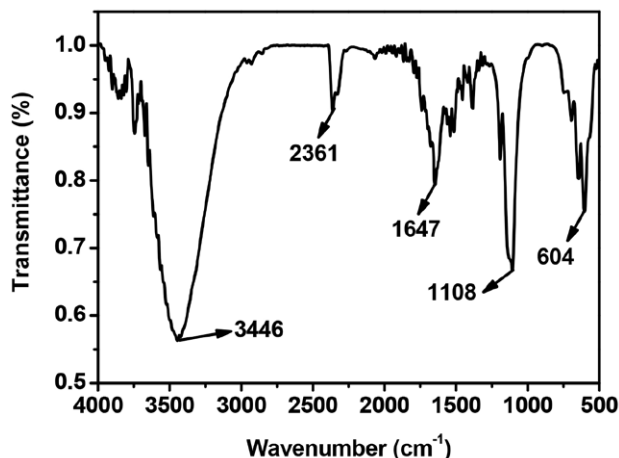


Figure 2. FTIR spectrum of n-Fe₂O₃ particles.

cm⁻¹ is assigned to Fe-O stretching band indicating the presence of Fe₂O₃, that at 3446 cm⁻¹ to the characteristic stretching vibrations of –OH moieties probably belonging to the adsorbed water molecules on the surface during the preparation process of the catalyst and that at 1647 cm⁻¹ to H–OH bending vibrations at γ -Fe₂O₃ surface.^{28–30} The weight (%) of iron and oxygen on the surface of n-Fe₂O₃ as analysed by EDX, was found to be 83.71 and 16.29%, respectively (Fig. 3).

The morphology of the nano-particles particle size distribution, powder XRD and VSM are shown in Fig. 4. It is observed that the shape of the particles is spherical (Fig.

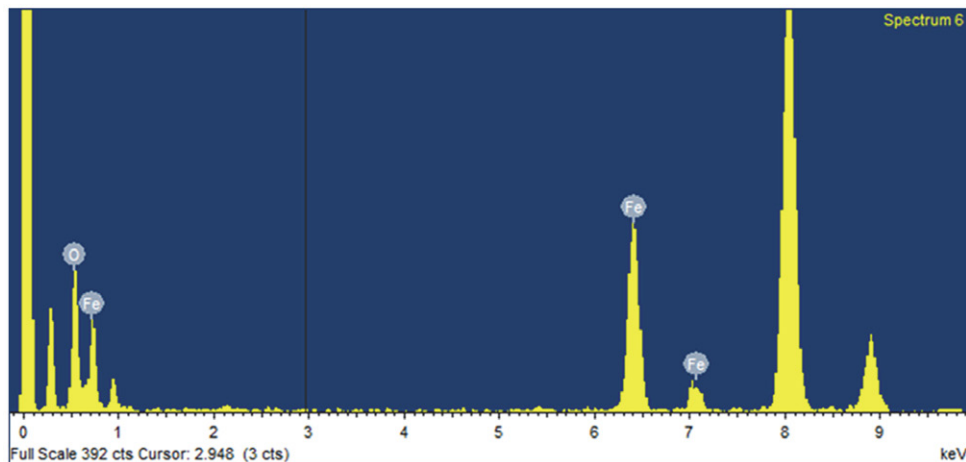


Figure 3. EDX analysis of n-Fe₂O₃ particles.

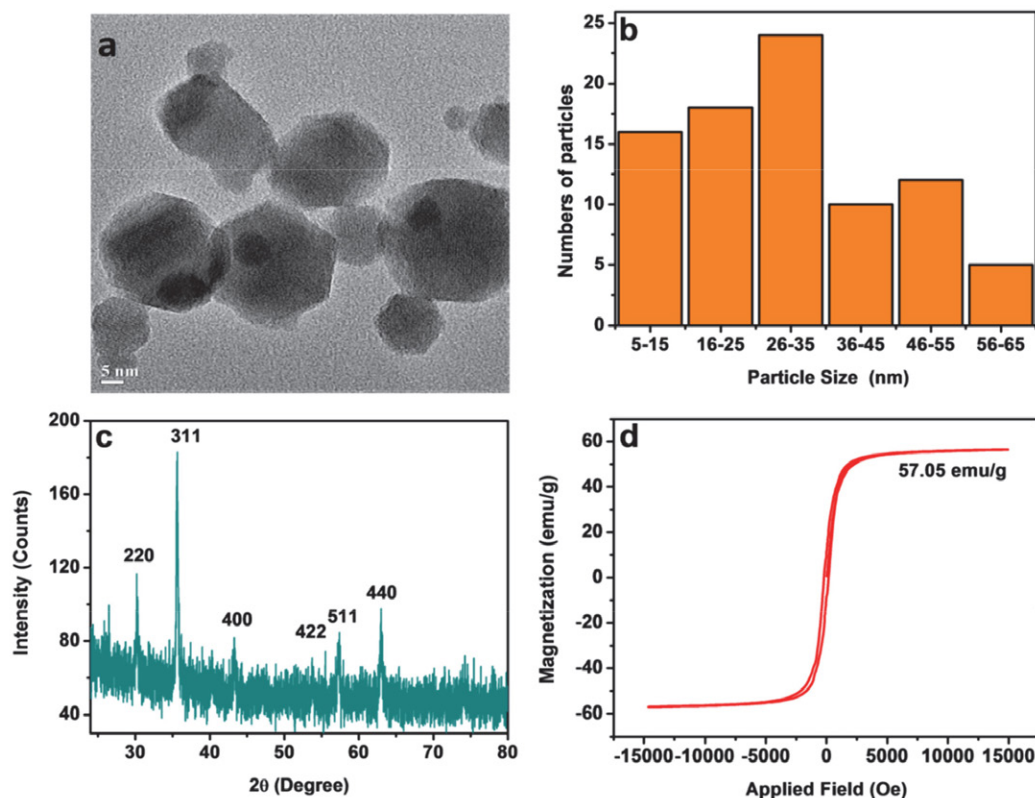


Figure 4. Characterisation of n-Fe₂O₃ particles: a. TEM image; b. Particle size distribution; c. XRD diffractogram; d. Magnetisation curve.

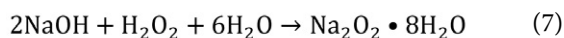
4a). The size range of the particles calculated using image j software was found to vary from 5–65 nm, and the average particle size lies within 26–35 nm (Fig. 4b). The XRD diffractogram shows diffraction peaks at angles $2\theta = 30.22^\circ$, 35.64° , 43.25° , 53.75° , 57.45° , and 62.98° which correspond to the 220, 311, 400, 422, 511, 440 planes of Fe₂O₃ NPs (Fig. 4c).^{24,31,32} The XRD data suggests that the Fe₂O₃ particles are γ -Fe₂O₃.³⁰ The VSM analysis shows that the nano-catalysts possessed super paramagnetic property with a saturation magnetisation of 57.05 emu/g (Fig. 4d).

3. 2. Optimisation of Operational Parameters for n-Fe₂O₃/oxidant Systems

The optimization of catalyst load in n-Fe₂O₃/oxidant systems was initially done on the basis of decolorisation efficiency. The concentration of the nano-particles was increased from 0.1 to 1.0 g/L keeping other parameters constant: [HP] = [SPS] = 7.0 mM; [AB] = [PX] = 0.15 mM; pH = 3; treatment period = 90 min. While decolorisation remained practically constant (95.0 and 91.4% for AB and PX, respectively) from 0.4 g/L onwards for the systems n-Fe₂O₃/HP, maximum decolorisation (97.0 and 91.4% for AB and PX, respectively) was observed at 0.6 g/L in n-Fe₂O₃/SPS system (Table 1).

The effect of pH on decolorisation at the optimum load of the nano-particles (0.4 g/L) was also considered. It was found that decolorisation was highest at pH 3 (95.0

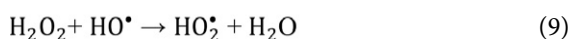
and 91.4% for AB and PX, respectively) and nil at pH ≥ 5.9 (the natural pH of the mixture of dyes). The higher efficiency at pH 3 may be due to the higher oxidation potential of HO[•] radicals, leaching of more iron species into the solution and forming catalyst-pollutant inner-sphere complexes.^{33–35} The higher decolorisation efficiency at lower pH and lower at higher pH may also be attributed to the surface properties of the catalyst. It is known that degradation in heterogeneous catalysis takes place at the catalyst's surface, the adsorption of the target molecule on its surface plays a vital role in the degradation process. The adsorption depends on the charge on the target molecule and surface of the catalyst. The point of zero charge (PZC) of a catalyst is the pH at which the surface is neutral. Therefore, the surface is acidic at pH < PZC and basic at pH > PZC. Since, AB and PX are anionic dyes, they are attracted towards the surface at pH < PZC. In the case of n-Fe₂O₃, the PZC lies between 6.0 and 6.8, and therefore, AB and PX are attracted towards the surface at pH < 6, i.e. in acidic pH.^{36,16} Since there is no adsorption of the dyes on the catalyst at pH > 6, no decolorisation was observed at pH ≥ 5.9 . The reduced decolorisation at higher pH may also be attributed to the oxidation of NaOH by HP (Eq. (7)).³⁷



The effect of pH on decolorisation in n-Fe₂O₃/SPS system was established by carrying out the reaction at pH

3.0, 5.9, 9.0 and 11.0. Table 1 shows that significant decolorisation was achieved within a wide range of pH values, although maximum decolorisation was achieved only at pH 3.

The optimization of HP was done by varying its concentration from 5.0 to 9.0 mM while keeping other parameters constant ($[AB] = [PX] = 0.15$ mM; pH = 3; $[n\text{-Fe}_2\text{O}_3] = 0.4$ g/L). The decolorisation concerning both the components of the dye solution was found to increase up to 7.0 mM, beyond which a slight decrease was observed (Table 1). A similar result was also obtained in $n\text{-Fe}_2\text{O}_3$ /SPS system. The initial increase in decolorisation with HP was due to the higher generation of hydroxyl radicals and decrease at higher conc. is due to the self-scavenging of hydroxyl radicals as well as by HP (Eqs. (8) and (9)).³⁷ Apart from being less reactive than HO^\bullet , the resulting hydroperoxyl radicals (HO_2^\bullet) further reduce the availability of HO^\bullet (Eq. (10)), a factor which is responsible for a lower degree of decolorisation.³⁸



Going by the discussion above, the optimum parameters for decolorisation in $n\text{-Fe}_2\text{O}_3$ /oxidant systems may be summarized as: $[AB] = [PX] = 0.15$ mM; pH = 3; $[n\text{-Fe}_2\text{O}_3] = 0.4$ g/L (for HP system) and 0.6 g/L (for SPS system), $[HP] = [SPS] = 7.0$ mM. A comparison of decolorisation in both the systems shows that they possess equal efficiency at their optimum parameters even though a higher concentration of catalyst is required for SPS system than for HP.

3. 3. COD removal Studies at Optimum Parameters for $n\text{-Fe}_2\text{O}_3$ /HP and $n\text{-Fe}_2\text{O}_3$ /SPS Systems

As it is known that HP interference results in the over estimation of COD values,²² we have calculated the actual

COD values at optimum parameters by eliminating the interference due to HP. The COD values presented in the text are inclusive of the HP factor (represented as m-COD) unless otherwise stated. Nevertheless, the result gives a qualitative idea about the COD value, which would obviously be higher than the value obtained after eliminating the HP factor.

In order to find COD_{eff} of both the systems at their respective optimal parameters, we have varied the treatment period up to 300 min. To our surprise, the COD_{eff} was found to be very low (1.4 and 6.8% respectively for HP and SPS systems) at 300 min of reaction even though complete decolorisation was achieved under the present conditions. So, it was decided to increase the catalyst load further to see if there is an increase in COD_{eff} . The reaction with catalyst load varying from 1.0 to 6.0 g/L was carried out under optimum parameters, i.e. $[HP] = 7.0$ mM; treatment period = 300 min; $[AB] = [PX] = 0.15$ mM; pH = 3; equilibrium period = 90 min. Although complete decolorisation was obtained from 0.4 g/L onwards, an increase in $\text{m-COD}_{\text{eff}}$ from 45.6% to 72.1% at 300 min was observed when the load was increased from 1.0 to 4.0 g/L. A slight decrease in the value was observed when the load was increased to 6.0 g/L (Fig. 5). Thus, 4.0 g/L was taken as the optimum concentration of $n\text{-Fe}_2\text{O}_3$ throughout the study. This initial increase in $\text{m-COD}_{\text{eff}}$ may be attributed to the acceleration of iron leaching and HP activation generating more HO^\bullet radicals due to an increase in the number of active sites on the catalyst surface area available for degradation. The decrease at higher catalyst concentration may be due to the agglomeration of nano-particles. Another reason may be due to the scavenging of HO^\bullet and HO_2^\bullet (Eq. (9) radicals on the oxide surface (Eqs. (11) – (13)).^{39–42} As already discussed earlier, the presence of HP in the solution results in the over estimation of COD. Hence, there is a need to eliminate the interference due to HP.

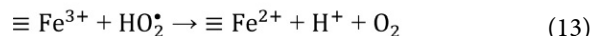
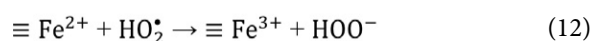
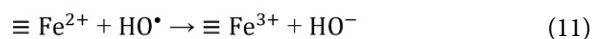


Table 1. Optimization of operational parameters of mixture of dyes for $n\text{-Fe}_2\text{O}_3$ /HP and $n\text{-Fe}_2\text{O}_3$ /SPS systems: $[AB] = [PX] = 0.15$ mM; $[n\text{-Fe}_2\text{O}_3] = 0.4$ g/L; $[n\text{-Fe}_2\text{O}_3] = 0.6$ g/L; $[HP] = [SPS] = 7.0$ mM; pH = 3; treatment period = 90 min.

Catalyst		Oxidant				pH								
$[n\text{-Fe}_2\text{O}_3]$ (g/L)	Decolorization (%)		$[\text{Oxidant}]$ (mM)	Decolorization (%)		pH	Decolorization (%)							
	$n\text{-Fe}_2\text{O}_3$ / HP system	$n\text{-Fe}_2\text{O}_3$ / SPS system		$n\text{-Fe}_2\text{O}_3$ / HP system	$n\text{-Fe}_2\text{O}_3$ / SPS system		$n\text{-Fe}_2\text{O}_3$ / HP system	$n\text{-Fe}_2\text{O}_3$ / SPS system	AB	PX	AB	PX		
	AB	PX	AB	PX	AB	PX	AB	PX	AB	PX	AB	PX		
0.1	62.0	51.7	39.9	15.8	5.0	66.1	54.3	94.3	79.7	3.0	95.0	91.4	97.0	91.4
0.2	82.4	72.0	47.1	23.1	6.0	86.1	84.4	96.5	89.2	5.9	No		95.4	84.5
0.4	95.0	91.4	88.2	64.3	7.0	95.0	91.4	97.0	91.4	–	decolorisation	–	–	–
0.6	95.2	91.0	97.0	91.4	8.0	93.4	90.0	93.8	85.5	9.0	was		94.2	82.8
0.8	94.2	91.0	92.2	72.9	9.0	91.2	85.9	93.0	76.9	11.0	observed		25.6	03.0
1.0	95.2	91.4	89.5	66.4	–	–	–	–	–	–	–	–	–	–

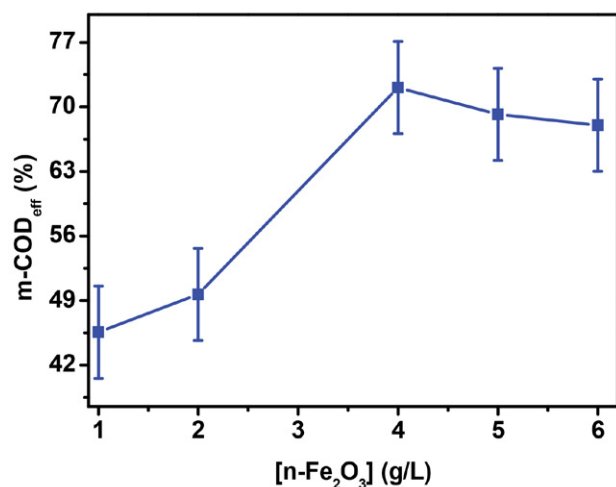


Figure 5. Effect of catalyst load on the m-COD_{eff} of mixture of dyes (AB+PX): [HP] = 7.0 mM; [AB] = [PX] = 0.15 mM; pH = 3; equilibrium period = 90 min; treatment period = 300 min.

To see the increase in m-COD_{eff} pattern with time, we have carried out the reaction from 10 to 360 min. Table 2 summaries the effect of HP on the m-COD_{eff} of the process. It is thus apparent that the presence of HP leads to a reduction of m-COD_{eff} values. Therefore, our result is in good agreement with the findings of Kang et al.²². It is apparent from Table 2 that the COD removal process takes place in two stages – a slow induction period (1st stage) followed by a fast degradation process (2nd stage). During the induction period, which lasted up to 60 min, the COD_{eff} practically remained constant (31.3% in 10 min to 35.7% in 60 min), beyond which an increase was observed, and the value reached 83.8% in 360 min. This is also evident from the consumption of HP, which follows the same trend as COD_{eff} (Table 2). On the other hand, complete decolorisation was achieved at 120 min of the reaction. From Table 2, it is evident that 67.2% of HP is consumed in 60 min with a corresponding COD_{eff} of 35.7%. On the other hand, rest

of the HP was consumed in the next 300 min for an additional 48.1% COD_{eff}. Therefore, the HP, which is consumed rapidly up to 60 min, mainly was used towards the decolorisation.

Previous studies have suggested that iron leaching from the surface of n-Fe₂O₃ into the solution forms the rate determining step of this reaction^{43,44} and therefore, the slow leaching of iron takes place in the first stage, i.e. induction period. It appears that during the induction period sufficient amount of HO· radicals are not formed through the activation of HP by n-Fe₂O₃. Further, part of the HO· radicals might be recombined or scavenged quickly in the presence of high conc. of HP (Eqs. (8) and (9)) and sizeable active surface (Eq. (11)) and partly might be engaged to a great extent in breaking the N=N bond leading to decolorisation and a lesser extent in removing the dyes and intermediate products and hence COD. The second and fast process primarily involves the interaction of HO· radicals, generated through the activation of HP with dissolved iron (Fe²⁺) (Eq. (4)), with the dyes leading to their degradation. The HO· radicals generated during the process are involved in the colour and COD removal process by acting in two different ways: by attacking the –N=N– chromophore or the carbon attached to the azo bond.^{45,46} In both cases, the dye molecules are fragmented, causing colour and COD removal.

Heterogeneous Fenton-type reactions (n-Fe₂O₃/SPS) were carried out with 4.0 g/L of Fe₂O₃ in the presence of SPS as an oxidant. To study the effect of the equimolar concentration of oxidants, we have considered the concentration of SPS as 7.0 mM. The other parameters taken were same as with heterogeneous Fenton process, e.g. [AB] = [PX] = 0.15 mM; pH = 3, equilibrium period = 90 min. Under these operational parameters, COD_{eff} was found to be only 28.5% in 360 min. The effect of pH was also studied on this system, and it was observed that COD_{eff} was highest at pH 3 and negligible at other pHs.

Table 2. COD removal efficiency of mixture of dyes (AB+PX): [AB] = [PX] = 0.15 mM; [n-Fe₂O₃] = 4.0 g/L; [HP] = 7.0 mM; pH = 3; equilibrium period = 90 min.

Treatment period (Min)	Decolorisation (%)		Consumption of [HP] (%)	m-COD _{eff} (%)	COD _{eff} (%)
	AB	PX			
10	71.6	65.3	64.0	4.1	31.3
30	83.6	77.6	64.0	6.1	33.2
60	97.9	96.9	67.2	10.9	35.7
120	100.0	100.0	76.3	29.3	45.1
180	100.0	100.0	87.3	47.4	58.8
240	100.0	100.0	95.4	55.7	74.9
300	100.0	100.0	98.9	72.1	83.1
360	100.0	100.0	99.8	78.2	83.8

m-COD_{eff} – COD removal efficiency in the presence of residual HP

COD_{eff} – COD removal efficiency in the absence of residual HP

3. 4. Effect of Particle Size on COD_{eff} of the Mixture of Dyes

To establish the effect of particle size of Fe₂O₃ particles on the COD_{eff}, we have used particles of two different sizes. The effect of n-Fe₂O₃ has already been described in the earlier section. The other iron oxide used in this work is m-Fe₂O₃ particles with particle size <5 μm. The oxidants used in this reaction were HP and SPS. The operational parameters used in n-Fe₂O₃/HP system as described in Sec. 3.3 was also employed in this reaction ([m-Fe₂O₃] = 4.0 g/L; [Oxidant] = 7.0 mM; [AB] = [PX] = 0.15 mM; pH = 3; equilibrium period = 90 min). m-COD_{eff} with a value of 51% in 360 min in the presence of HP, was completely inhibited in the presence of SPS. It may be noted that under similar conditions, m-COD_{eff} was 78.2% in n-Fe₂O₃/HP system. A comparison of the effectiveness of all the systems at their optimum parameters is shown in Fig. 6. It is apparent from the figure that SPS inhibits m-COD_{eff} in both the systems (n-Fe₂O₃ and m-Fe₂O₃), more so in m-Fe₂O₃ than n-Fe₂O₃. Hence, study with the only n-Fe₂O₃ system was considered further.

3. 5. Reusability of n-Fe₂O₃ in Heterogeneous Fenton Reaction

The economy of the heterogeneous Fenton process lies in the stability and reusability of the catalyst in multiple cycles. After each cycle of reaction under optimum parameters, the catalysts were separated from the solution with the help of a vacuum pump. The particles were then washed with 500 mL water followed by 250 mL methanol repeatedly until the solution's pH after washing was maintained at 7. In the end, the particles were washed with 1000 mL water to make them free of methanol. The particles were dried in an oven for 8 hours, cooled at room temperature, grinded and stored for the following reaction cycle. Four cycles of reaction were performed, and the result is

presented in Fig. 6. It is observed that the m-COD_{eff} remains constant until the 2nd cycle, after which a rapid decrease in efficiency was observed, and the value reached 11.6% in the 4th cycle. The lower efficiency from the 3rd cycle onwards may be attributed to diverse factors such as lower leaching of iron, resulting in a lower contribution to homogeneous Fenton process, catalyst surface area reduction due to aggregation, and deactivation of active sites by adsorption of organic intermediates etc.^{35,39,47} The nano-particles lose their colloidal stability due to dipole-dipole interaction, causing them to agglomerate.⁴⁸ As seen in Fig. 7, the number of black spots increases in each cycle, indicating the occurrence of agglomeration. As the number of agglomeration increases with the treatment period, a decrease in the number of nano-particles and hence surface area is observed. This explains a reduction in m-COD_{eff} in successive cycles. Nevertheless, complete decolorisation was achieved in all the cycles. To verify the amount of iron leaching from n-Fe₂O₃, the samples at the end of each of the four cycles were analysed by ICP-OES and was found to be 8.3, 41.1, 42.3, and 50.1%, respectively.

3. 6. Kinetics of COD Removal and HP Consumption in n-Fe₂O₃/HP System

As discussed before, the COD removal process consists of a slow and a fast process. Both the processes have been shown to follow pseudo-first-order kinetics (Fig. 8). The slow process takes place within the first 60 min of the reaction with a rate constant of 1.49 and 1.32 (10⁻³ min⁻¹) from 0–60 min with and without HP interference respectively, and the corresponding values of the faster process from 120–300 min are 7.94 and 6.73 (10⁻³ min⁻¹) respectively (Table 3). Data beyond 300 min was not considered for kinetic study as no appreciable change in COD_{eff} value was observed, and the reaction appeared to have completed with ≈99% consumption of HP (Table 2). The higher rate constant with HP interference compared to that with-

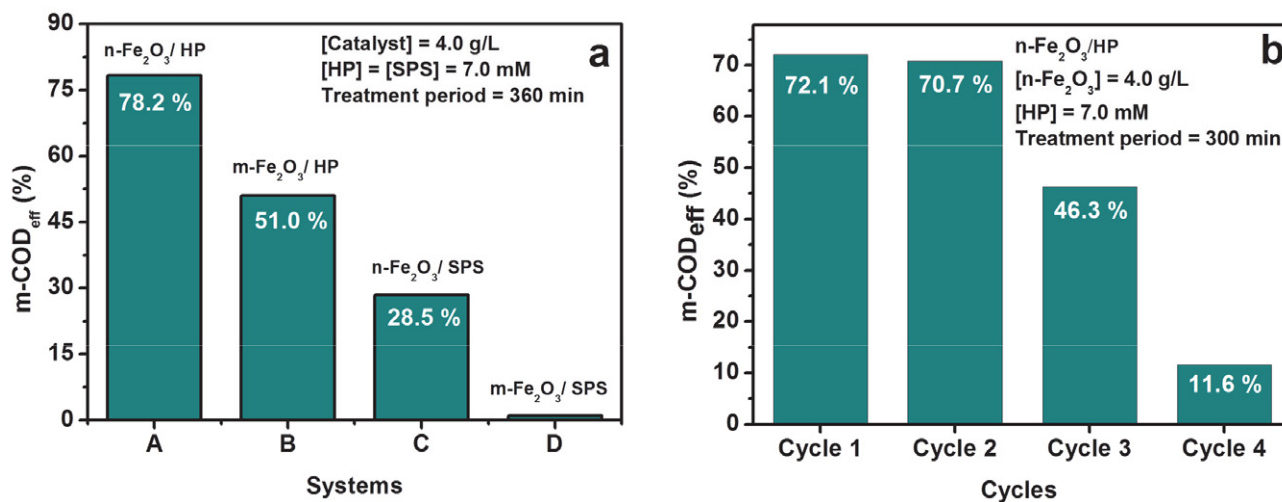


Figure 6. Effect of particle size of catalyst on m-COD_{eff} (a) and reusability of catalyst (b): [AB] = [PX] = 0.15 mM; equilibrium period = 90 min; pH= 3.

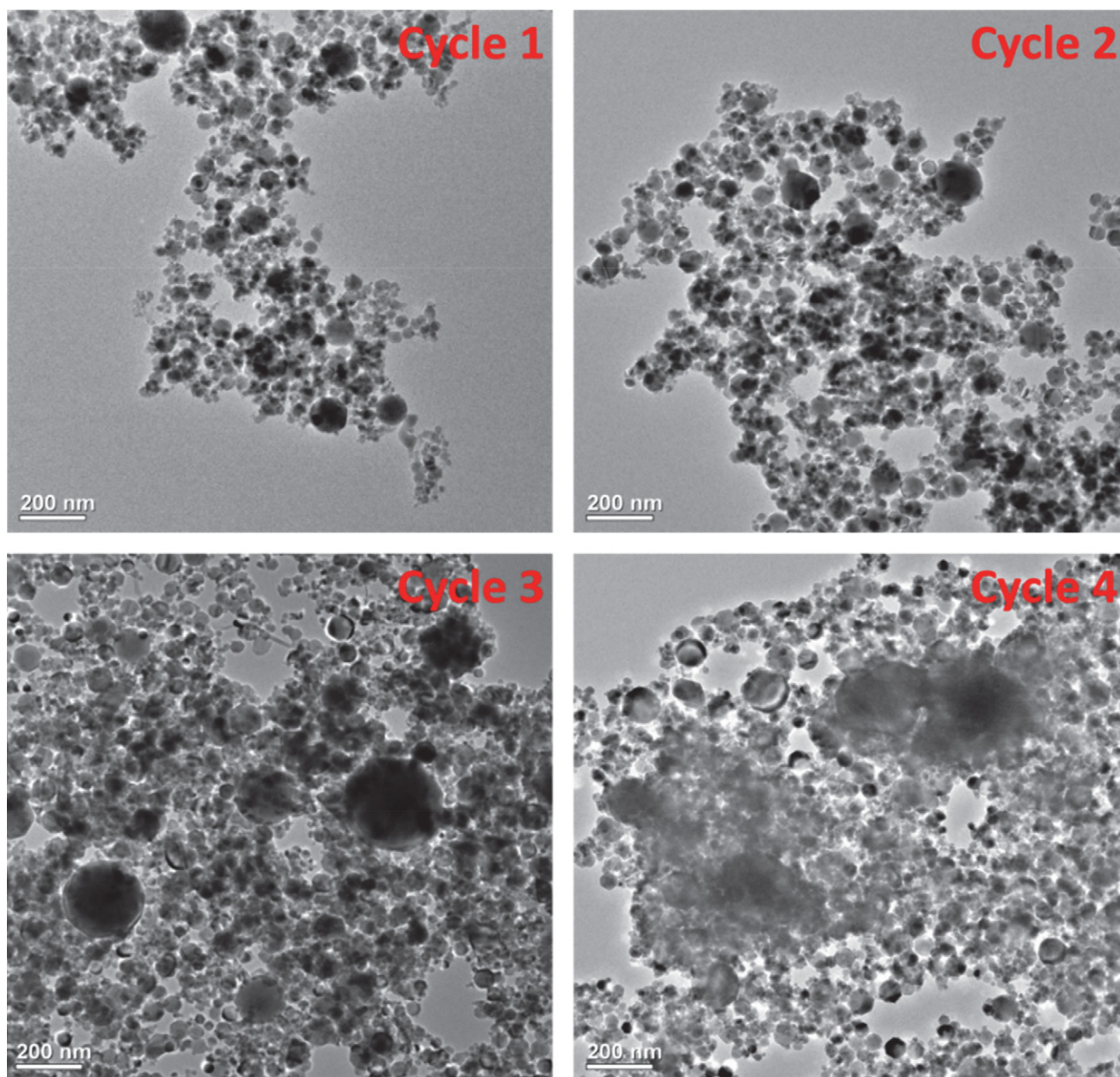


Figure 7. TEM images of $n\text{-Fe}_2\text{O}_3$ particles after different cycles of treatment: $[\text{AB}] = [\text{PX}] = 0.15 \text{ mM}$; $[\text{n-Fe}_2\text{O}_3] = 4.0 \text{ g/L}$; $[\text{HP}] = 7.0 \text{ mM}$; treatment period = 300 min; $\text{pH} = 3$.

Table 3. COD removal and HP consumption rate constants for the mixture of dyes (AB + PX) by $n\text{-Fe}_2\text{O}_3/\text{HP}$ system at different time intervals

Time scale	Rate constant (10^{-3} min^{-1})		R^2	
	COD removal rate constants			
	HP interference	No HP interference	HP interference	No HP interference
0–60 (min)	1.49	1.32	0.98555	0.99926
120–300 (min)	7.94	6.73	0.98394	0.99036
	HP consumption rate constants			
Time scale				
0–60 min	1.96		0.8813	
120–300 min	17.17		0.9684	

$m\text{-COD}_{\text{eff}}$ – COD removal efficiency in the presence of residual HP COD_{eff} – COD removal efficiency in the absence of residual HP

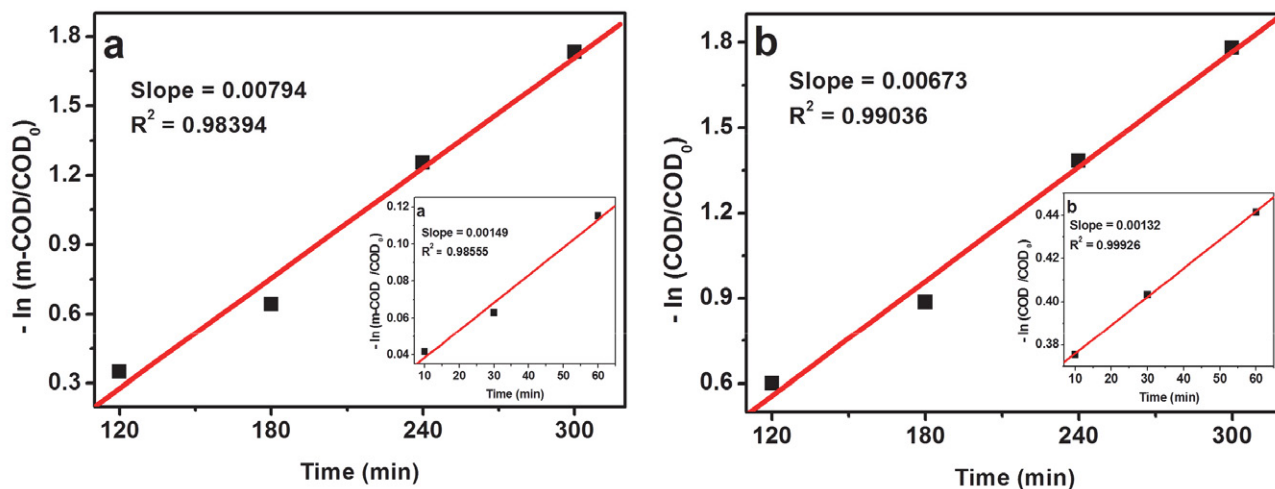


Figure 8. COD removal kinetics in n-Fe₂O₃/HP system: (a) with interference due to HP from 120 min to 300 min (inset: from 0–60 min); (b) Without interference due to HP from 120 to 300 min (inset: from 0–60 min).

out HP interference established the influence of HP on the COD removal process. As discussed before, the HP used in the process was almost entirely consumed in 300 min of the treatment. The kinetics of HP consumption and the rate constants during 0–60 and 120–300 min are given in Fig. 9 and Table 3, respectively.

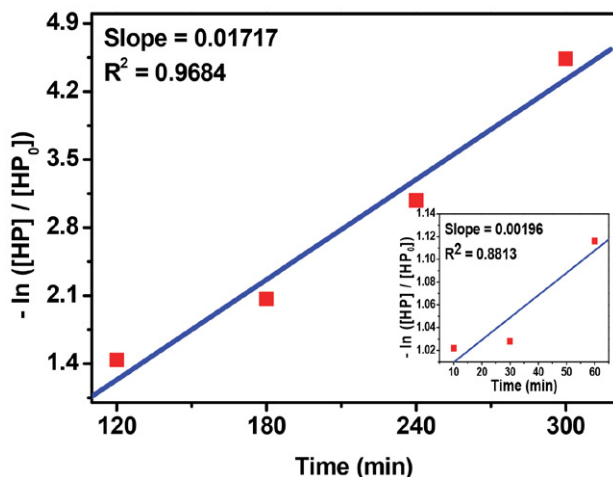


Figure 9. Kinetics of HP consumption in n-Fe₂O₃/HP system from 120 min to 300 min. (Inset: from 05 min to 60 min)

3. 7. Analysis of Ions and Intermediate Products Formed in n-Fe₂O₃/HP System

Different ions and intermediate products identified by ion chromatography during the degradation process are listed in Table 4. Both AB and PX have two sources of nitrogen: four azo nitrogen atoms on AB and two on PX, one on AB as –NO₂ substituent. The formation of –Na⁺ as the dissociation product of both AB and PX and SO₄^{2–}, formed as a result of the substitution of SO₃[–] group by HO[•] radicals has been identified.^{49–51} The aryl radical formed after

the elimination of SO₄^{2–} gets converted to hydroxyaromatic compounds on interacting with HO[•] radicals.⁵² Apart from these ions, NH₄⁺, –NO₂[–] and –NO₃[–] are identified in the process. The NH₄⁺ ions are reported to have been formed from the azo bonds. In the first step, azo bonds are attacked by HO[•] radicals and convert them into –NH₂ groups, which accounts for the formation of aromatic amino derivatives. It may be noted that in the present case, the azo group attached to the nitrophenyl group of AB is electron-deficient and hence the HO[•] radicals attack the other azo bond attached to the unsubstituted phenyl group preferentially.⁵² In the next step –NH₂ groups undergo protonation and the subsequent attack of HO[•] radicals at the nitrogen bearing carbon of the aromatic ring are converted into NH₄⁺ ions.^{50,53} This accounts for the formation of phenols. There is a report that N₂ is generated by the attack of HO[•] radicals on the azo bond bearing carbon of the aromatic ring⁵⁰ which accounts for an additional route to the formation of aromatic hydroxyl derivatives. The conversion of NH₄⁺ to NO₂[–], NO₃[–] as a result of the attack of HO[•] radicals was suggested by Reddy and Mahajani.⁵⁴ All these sequences of events are presented in Scheme 1. The formation of CO₃^{2–} ions indicate the partial, if not complete, mineralisation of the dyes to carbon dioxide.

The different intermediate products identified during the process are phenol, 2- and 3-aminophenol (Table 4). A peak appeared at retention time (RT) 2.95, but could not be identified using ion chromatography. Although we have been able to identify nitro aromatic compounds in other studies (data not published), the presence of these products couldn't be established in this study. Besides these products, smaller aliphatic acids like formic acid, malonic acid, maleic acid and fumaric acid were also identified. The presence of these acids indicates that the dyes are not completely mineralised. As per another report, the attack of HO[•] radicals to azo bond takes place with ~60% probability leading to decolorisation. Successive attack on

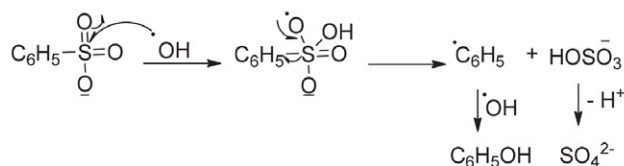
azo bond by HO[•] radicals leads to the formation of nitroso (Scheme 1) followed by nitro aromatic compounds.⁵⁵ The formation of aromatic amino compounds has been described earlier. Since complete decolorisation was achieved at 360 min with a COD_{eff} of 83.8% by consuming 100% HP (Table 2), it may be concluded that the azo bonds have broken completely, forming aromatic amines and other products (Scheme 1). Further attack of HO[•] radicals on nitro aromatic compounds leads to the formation of hydroxybenzenes, which ultimately generate the aliphatic acids through the formation of quinones.⁵⁶ The displaced O₂N[•] radical in its term undergoes oxidation to form HNO₃.⁵⁷ The attack of HO[•] radicals onto the nitro group may also result in the formation of HNO₃,^{52,58} in addition to an aromatic radical, which on further interaction with HO[•] radicals generate aromatic hydroxyl derivatives (Scheme 1).

The absence of nitro derivatives suggests that all the nitro groups are immediately substituted by HO[•] radicals and generate aromatic hydroxyl derivatives. It is observed that phenol is obtained at 120 min and 2- and 3-aminophenol at 60 min of the reaction. This indicates that phenol is not formed from aminophenols. Instead, they are formed in different routes. Based on the above analysis and with support from literature data,^{55,59,60} a mechanism of degradation of the mixture of dyes (AB+PX) has been proposed (Scheme 2).

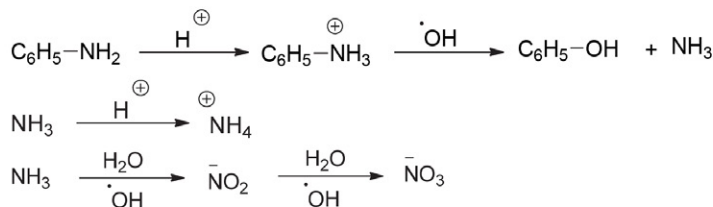
3. 8. Comparison of Toxicity Assessed by CFU and Light Loss Measurements

The relative toxicity of the pure dye solution and those obtained after different treatment periods in

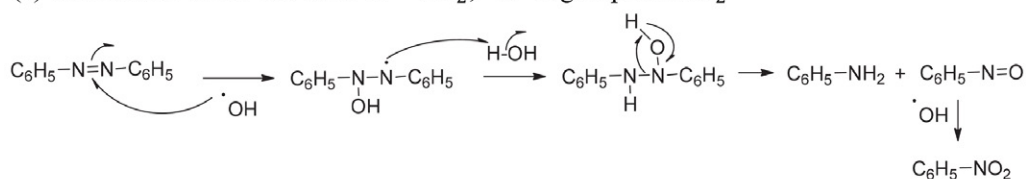
(a) Formation of SO₄²⁻ and C₆H₅OH



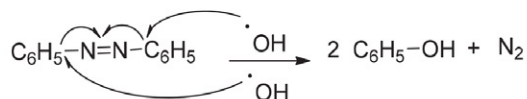
(b) Formation of Phenol, NH₄⁺, NO₂⁻, NO₃⁻



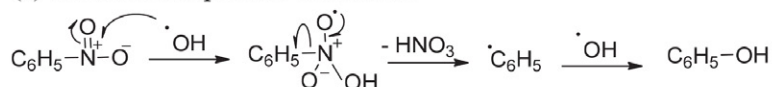
(c) Conversion of the azo bond to -NH₂, -N=O group and NO₂



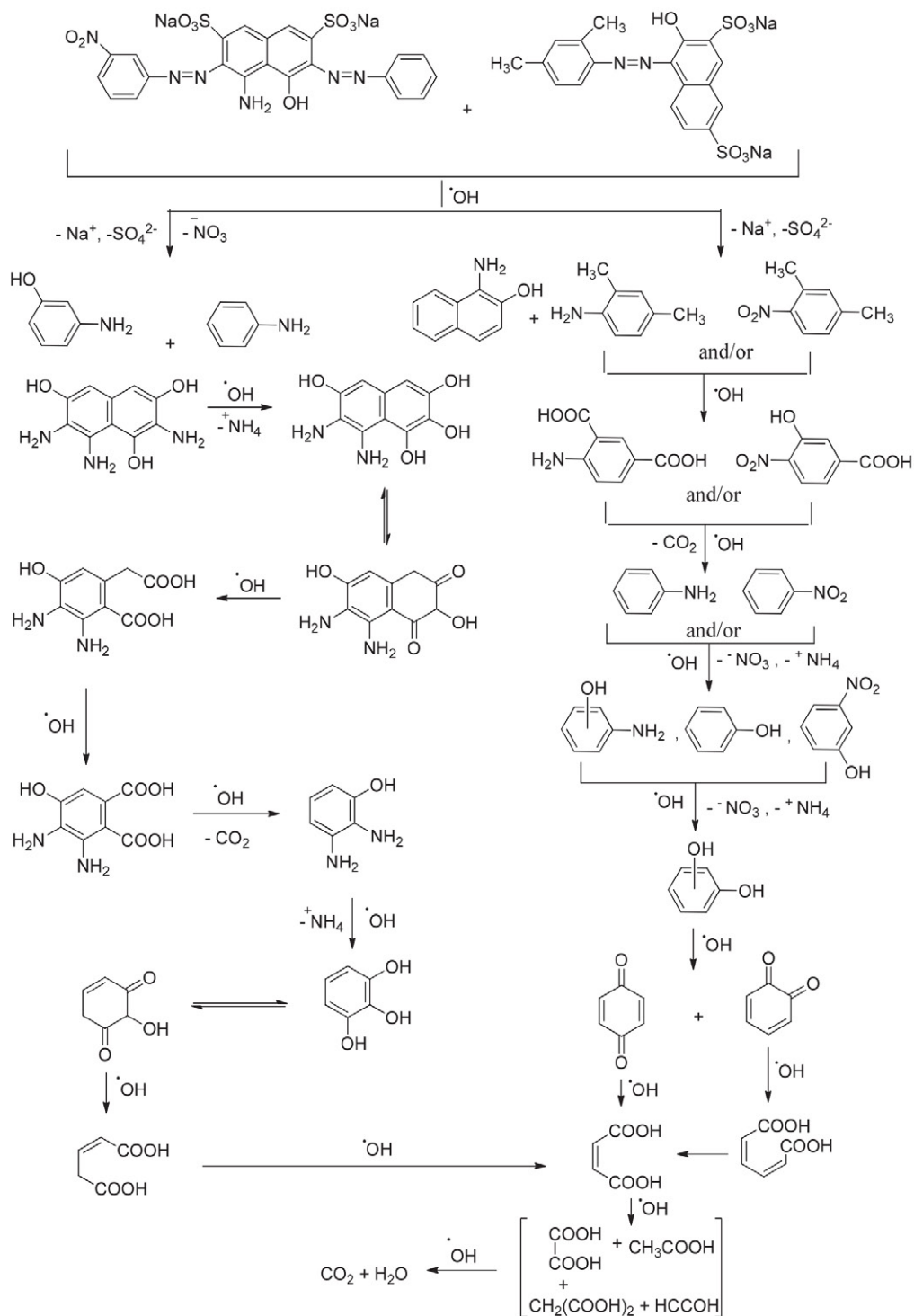
(d) Conversion of -N=N- to phenolic group



(e) Formation of phenols and amines



Scheme 1. Mechanism of formation of different ions and products from azo compounds



Scheme 2. Mechanism of degradation of the mixture of dyes (AB+PX)

$n\text{-Fe}_2\text{O}_3/\text{HP}$ system at optimal parameters was measured as a function of CFU and light loss percentage.

A comparison of the results by the two methods (Fig. 10) shows different relative toxicity levels for the same sample when measured with *A. fischeri* and *E. coli*. As seen from the figure, the untreated dye solution was most toxic

in both assay systems. A sharp decrease in relative toxicity with an increase in treatment period was observed with the former (*A. fischeri*-based assay) than the later (*E. coli*-based assay) method. A gradual decrease was observed, indicating that both assay systems possessed differential sensitivities towards the chemical toxicity. The *A. fischeri*-based as-

Table 4. Ions and intermediate products identified by ion chromatography

Sr. No.	Ions		Intermediate products	
	R.T (min)	Name	R. T (min)	Name
1	4.27	Na ⁺	1.54	Formic acid
2	4.54	NH ₄ ⁺	2.63	Malonic acid
3	2.12	NO ₂ ⁻	2.81	Maleic acid
4	3.65	NO ₃ ⁻	3.37	Fumaric acid
5	4.26	CO ₃ ²⁻	2.95	Not identified
6	5.56	SO ₄ ²⁻	3.86	3- Amino phenol
7	–	–	4.57	2- Amino phenol
8	–	–	7.91	Phenol

say measured by loss of emitted fluorescence, or light, was much more sensitive than the *E. coli*-based assay measuring the reproductive ability of the organism expressed as CFU. Thus, the results in Fig. 10 suggest that depending on the need and circumstances, either of the two parameters may be applied to measure the extent of dye detoxification. While complete detoxification was achieved in 360 min based on the loss of light assay utilising *A. fischeri* assay system, the later assay system based on *E. coli* CFU measurements showed that the detoxification was not complete in 360 min and the solution still possessed about 37% relative toxicity. The different sensitivity levels of the two test systems may be attributed to an assay of diverse end points of biological parameters. Looking at the slopes of the two toxicity curves for loss of light and loss of CFU, one may postulate that *E. coli*, a fresh water bacterium, may be more resistant to the aromatic intermediates formed during the beginning of the reaction (Scheme 1) than *A. fischeri*, a marine bacterium, which could be more resistant to organic acids formed at the end of the reaction.⁶¹

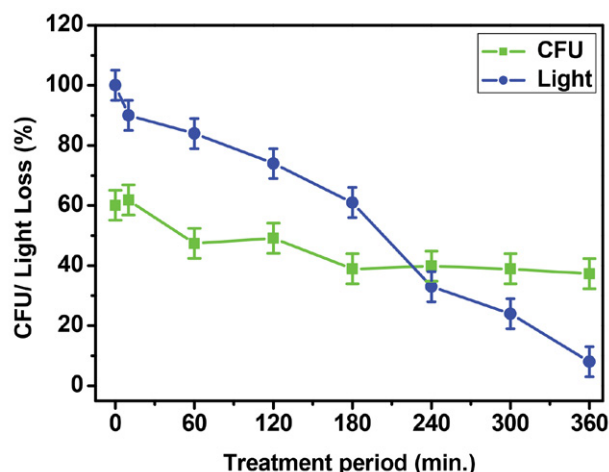


Fig. 10. *E. coli* and *A. fischeri* response in n-Fe₂O₃/HP system: [AB] = [PX] = 0.15 mM; pH of treatment = 3; pH of *E. coli* growth = 7; [n-Fe₂O₃] = 4.0 g/L; [HP] = 7.0 mM. Their response has been recorded as a function of CFU or light loss (%), respectively.

4. Conclusions

Colour and COD removal studies of a mixture of two dyes (AB+PX) were carried out by heterogeneous Fenton process using two different types of iron oxides: n-Fe₂O₃ and m-Fe₂O₃ particles, and two different oxidants, HP and SPS. Among them, n-Fe₂O₃ and HP were found to be the efficient catalyst and oxidant, respectively. Although, m-Fe₂O₃ caused very low COD reduction in the presence of HP, it was completely inhibited in the presence of SPS. Decolorisation and, therefore, COD removal was accelerated in an acidic pH and inhibited at pH > 6 due to surface characteristics of the nano-particles. The over estimation of COD values due to the interference of H₂O₂ has been verified, and our results are in good agreement with the results reported earlier. The COD removal is a two-stage process, a slow induction period and a fast degradation process, each following pseudo-first-order kinetics. The rate constants for COD_{eff} were found to be 1.32 (10⁻³ min⁻¹) and 6.73 (10⁻³ min⁻¹) during 0–60 and 120–300 min respectively after eliminating the interference due to HP and those for HP consumption during 0–60 and 120–300 min were found to be 1.96 and 17.17 (10⁻³ min⁻¹).

The catalyst's efficiency decreased from the 3rd cycle onwards due to various factors, such as lower leaching of iron resulting in a lower contribution to homogeneous Fenton process, catalyst surface area reduction due to agglomeration, deactivation of active sites by adsorption of organic intermediates etc. Hence, more work is required to identify the exact causes of deactivation, find some regeneration measures to restore the catalyst efficiency. The different ions formed during the process were identified as Na⁺, SO₄²⁻, NH₄⁺, NO₂⁻ and NO₃⁻ and the intermediate products as phenol, 2- and 3-aminophenol, formic acid, malonic acid, maleic acid and fumaric acid. Using two different toxicity assays, *A. fischeri* assay system measuring fluorescence and *E. coli* assay system giving CFU measurement, we found differential expression of relative toxicities for the same solution.

Acknowledgements

The authors gratefully acknowledge the use of facilities acquired through the DAE-BRNS grant (2013/36/50-BRNS/2485, dated 05.12.2013) to MKS; DST-FIST grant (SR/FST/CSI-194-2008) of the Department of Science and Technology, Govt. of India and UGC-SAP CAS-I grant (F.540/21/CAS/2013(SAP I)) of UGC to the Department of Chemistry, North-Eastern Hill University (NEHU), Shillong. The services provided by the Sophisticated Analytical Instrumentation Facility, NEHU for TEM, EDX and ICP-OES analysis and Department of Nanotechnology, NEHU for XRD measurements are duly acknowledged. It is further declared that this research did not receive any specific grant from funding agencies in the public, commercial, or not-for-profit sectors.

5. References

1. A. Yadav, S. Mukherji, A. Garg, *Ind. Eng. Chem. Res.* **2013**, *52*, 10063–10071. DOI:10.1021/ie400855b
2. A. Eslami, M. Moradi, F. Ghanbari, F. Mehdipour, *J. Environ. Health Sci. Eng.* **2013**, *11*, 1–8. DOI:10.1186/2052-336X-11-31
3. I. Oller, S. Malato, J. A. Sánchez-Pérez, *Sci. Total Environ.* **2011**, *409*, 4141–4166. DOI:10.1016/j.scitotenv.2010.08.061
4. P. Ghosh, A. N. Samanta, S. Ray, *Can. J. Chem. Eng.* **2010**, *88*, 1021–1026. DOI:10.1002/cjce.20353
5. A. Durán, J. M. Monteagudo, I. S. Martén, F. J. Amunategui, D. A. Patterson, *Chemosphere*, **2017**, *186*, 177–184. DOI:10.1016/j.chemosphere.2017.07.148
6. X. -R. Xu, X. -Z. Li, *Sep. Purif. Technol.* **2010**, *72*, 105–111. DOI:10.1016/j.seppur.2010.01.012
7. M. K. Sahoo, J. E. Kumar, B. Sinha, M. Marbaniang, R. N. Sharan, *Water Sci. Tech.* **2018**, *77*, 2917–2928. DOI:10.2166/wst.2018.290
8. F. Haber, J. Weiss, *Proc. Roy. Soc. A*, **1934**, *147*, 332–351. DOI:10.1098/rspa.1934.0221
9. G. P. Anipsitakis, D. D. Dionysiou, *Environ. Sci. Technol.* **2004**, *38*, 3705–3712. DOI:10.1021/es035121o
10. I. Grčić, S. Papić, K. Žižek, N. Koprivanac, *Chem. Eng. J.* **2012**, *195/196*, 77–90. DOI:10.1016/j.cej.2012.04.093
11. L. Xu, J. Wang, *J. Hazard. Mater.* **2011**, *186*, 256–264. DOI:10.1016/j.jhazmat.2010.10.116
12. Y. Wang, Y. Gao, L. Chen, *Catal. Today*, **2015**, *252*, 107–112. DOI:10.1016/j.cattod.2015.01.012
13. M. C. Pereira, L. C. A. Oliveira, E. Murad, *Clay Miner.* **2012**, *47*, 285–302. DOI:10.1180/claymin.2012.047.3.01
14. S. P. Sun, A. T. Lemley, *J. Mol. Catal. A: Chem.* **2011**, *349*, 71–79. DOI:10.1016/j.molcata.2011.08.022
15. X. Xue, K. Hanna, N. Deng, *J. Hazard. Mater.* **2009**, *166*, 407–414. DOI:10.1016/j.jhazmat.2008.11.089
16. D. B. Hasan, S. R. Pouran, A. R. A. Aziz, S. M. Nashwan, W. M. A. W. Daud, M. G. Shaaban, *J. Indust. Eng. Chem.* **2015**, *25*, 186–191. DOI:10.1016/j.jiec.2014.10.033
17. S. Sarkar, A. Banerjee, U. Halder, R. Biswas, R. Bandopadhyay, *Water Conserv. Sci. Eng.* **2017**, *2*, 121–131. DOI:10.1007/s41101-017-0031-5
18. R. G. Saratale, G. D. Saratale, J. S. Chang, *J. Taiwan Inst. Chem. Eng.* **2011**, *42*, 138–157. DOI:10.1016/j.jtice.2010.06.006
19. X. Yi, E. Kim, H. J. Jo, D. Schlenk, J. Jung, *Ecotoxicol. Environ. Saf.* **2009**, *72*, 1919–1924. DOI:10.1016/j.ecoenv.2009.04.012
20. M. K. Sahoo, B. Sinha, M. Marbaniang, D. B. Naik, R. N. Sharan, *Chem. Eng. J.* **2012**, *209*, 147–154. DOI:10.1016/j.cej.2012.07.121
21. R. Massart, *IEEE Trans. Magn.* **1981**, *17*, 1247–1248. DOI:10.1109/TMAG.1981.1061188
22. Y. W. Kang, M. -J. Cho, K. -Y. Hwang, *Water Res.* **1999**, *33*, 1247–1251. DOI:10.1016/S0043-1354(98)00315-7
23. APHA, Standard methods for the examination of water and wastewater. 19th Ed. Wahington DC, New York, **1995**.
24. Y. Zhang, N. Zhang, T. Wang, H. Huang, Y. Chen, Z. Li, Z. Zou, *Appl. Catal. B: Environ.* **2019**, *245*, 410–419. DOI:10.1016/j.apcatb.2019.01.003
25. R. N. Sharan, H. Ryo, T. Nomura, *Int. J. Radiat. Biol.* **2007**, *83*, 89–97. DOI:10.1080/095553000601121140
26. A. Karczmarczyk, A. Celebanska, W. Nogala, V. Sashuk, O. Chernyaeva, M. Opallo, *Electrochim. Acta*, **2014**, *117*, 211–216. DOI:10.1016/j.electacta.2013.11.049
27. T. X. H. Le, T.V. Nguyen, Z. A. Yacouba, L. Zoungrana, F. Avril, E. Petit, J. Mendret, V. Bonniol, M. Bechelany, S. Lacour, G. Lesage, M. Cretin, *Chemosphere*, **2016**, *161* 308–318. DOI:10.1016/j.chemosphere.2016.06.108
28. S. M. El-Khouly, N. A. Fathy, *Asia-Pac. J. Chem. Eng.* **2018**, *13*, 1–11. DOI:10.1002/apj.2184
29. P. Djomgoue, D. Njopwouo, *J. Surf. Eng. Mater. Adv. Technol.* **2013**, *3*, 275–282. DOI:10.4236/jsemat.2013.34037
30. C. Liang, H. Liu, J. Zhou, X. Peng, H. Zhang, *J. Chem.* **2015**, *2015*, 1–8. DOI:10.1155/2015/791829
31. A. Phuruangrat, A. Manechote, P. Dumrongrojthanath, N. Ekthammathat, S. Thongtem, T. Thongtem, *Superlattice. Microstruct.* **2015**, *78* 106–115. DOI:10.1016/j.spmi.2014.11.038
32. P. Dumrongrojthanath, T. Thongtem, A. Phuruangrat, S. Thongtem, *Superlattice. Microstruct.* **2013**, *64*, 196–203. DOI:10.1016/j.spmi.2013.09.028
33. N. K. Daud, B. H. Hameed, J. Hazard. Mater. **2010**, *176*, 938–944. DOI:10.1016/j.jhazmat.2009.11.130
34. N. Masomboon, C. Ratanatamskul, M. C. Lu, *Environ. Sci. Technol.* **2009**, *43*, 8629–8634. DOI:10.1021/es802274h
35. S. X. Zhang, X. L. Zhao, H. Y. Niu, Y. L. Shi, Y. Q. Cai, G. Jiang, *J. Hazard. Mater.* **2009**, *167*, 560–566. DOI:10.1016/j.jhazmat.2009.01.024
36. H. Watanabe, J. Seto, *Bull. Chem. Soc. Jpn.* **1986**, *59*, 2683–2687. DOI:10.1246/bcsj.59.2683
37. G. V. Buxton, C. L. Greenstock, W. P. Helman, A. B. Ross, *J. Phys. Chem. Ref. Data*, **1988**, *17*, 513–886. DOI:10.1063/1.555805
38. S. R. Pouran, A. Bayrami, M. S. Shafeeyan, A. A. B. Raman, W. M. A. W. Daud, *Acta Chim. Slov.* **2018**, *65*, 166–171. DOI:10.17344/acsi.2017.3732
39. F. Velichkova, C. Julcour-Lebigue, B. Koumanova, H. Delmas, *J. Environ. Chem. Eng.* **2013**, *1*, 1214–1222. DOI:10.1016/j.jece.2013.09.011
40. K. Rusevova, F. D. Kopinke, A. Georgi, *J. Hazard. Mater.* **2012**, *241/242*, 433–440. DOI:10.1016/j.jhazmat.2012.09.068
41. D. N. Thi, H. P. Ngoc, H. D. Manh, T. N. Kim, *J. Hazard. Mater.* **2011**, *185*, 653–661. DOI:10.1016/j.jhazmat.2010.09.068
42. J. H. Ramirez, F. J. Maldonado-Hódar, A. F. Pérez-Cadenas, C. Moreno-Castilla, C. A. Costa, L. M. Madeira, *Appl. Catal. B: Environ.* **2007**, *75*, 312–323. DOI:10.1016/j.apcatb.2007.05.003
43. L. Xua, J. Wang, *Appl. Catal. B: Environ.* **2012**, *123–124*, 117–126. DOI:10.1016/j.apcatb.2012.04.028
44. T. R. Gordon, A. L. Marsh, *Catal. Lett.* **2009**, *132*, 349–354. DOI:10.1007/s10562-009-0125-6
45. S. Das, P. V. Kamat, S. Padmaja, V. Au, S. A. Madison, Free radical induced oxidation of the azo dye Acid Yellow 9, *J. Chem. Soc. Perkin Trans.* **1999**, *2*, 1219–1224.

- DOI:10.1039/a809720h
46. J. T. Spadaro, L. Isabelle, V. Renganathan, *Environ. Sci. Technol.* **1994**, *28*, 1389–1393. DOI:10.1021/es00056a031
47. J. Guo, M. Al-Dahhan, *Appl. Catal. A*, **2006**, *299*, 175–184. DOI:10.1016/j.apcata.2005.10.039
48. S. P. Yeap, J. Lim, B. S. Ooi, A. Ahmad, *J. Nanopart Res.* **2017**, *368*, 1–15. DOI:10.1007/s11051-017-4065-6
49. M. Karkmaz, E. Puzenat, C. Guillard, J. M. Herrmann, *Appl. Catal. B: Environ.* **2004**, *51*, 183–194. DOI:10.1016/j.apcatb.2004.02.009
50. H. Lachheb, E. Puzenat, A. Houas, M. Ksibi, E. Elaloui, C. Guillard, J. Herrmann, *Appl. Catal. B: Environ.* **2002**, *39*, 75–90. DOI:10.1016/S0926-3373(02)00078-4
51. C. Galindo, P. Jacques, A. Kalt, J. *Photochem. Photobiol. A: Chem.* **2000**, *130*, 35–47. DOI:10.1016/S1010-6030(99)00199-9
52. M. A. Meetani, S. M. Hisaindee, F. Abdullah, S. S. Ashraf, M. A. Rauf, *Chemosphere*, **2010**, *80*, 422–427. DOI:10.1016/j.chemosphere.2010.04.065
53. K. Sahel, N. Perol, H. Chermette, C. Bordes, Z. Derriche, C. Guillard, *Appl. Catal. B-Environ.* **2007**, *77*, 100–109. DOI:10.1016/j.apcatb.2007.06.016
54. G. R. Reddy, V. V. Mahajani, *Ind. Eng. Chem. Res.* **2005**, *44*, 7320–7328. DOI:10.1021/ie050438d
55. J. M. Joseph, H. Destailats, H. –M. Hung, M. R. Hoffmann, *J. Phys. Chem. A*. **2000**, *104*, 301–307. DOI:10.1021/jp992354m
56. J. H. Fendler, G. L. Gasowski, *J. Org. Chem.* **1968**, *33*, 1865–1868. DOI:10.1021/jo01269a035
57. A. Kotronarou, G. Mills, M. R. Hoffmann, *J. Phys. Chem.* **1991**, *95*, 3630–3638. DOI:10.1021/j100162a037
58. M. Holčapek, K. Volná, D. Vaněrková, *Dyes Pigm.* **2007**, *75*, 156–165. DOI:10.1016/j.dyepig.2006.05.040
59. J. R. Steter, W. R. P. Barros, M. R. V. Lanza, A. J. Motheo, *Chemosphere*, **2014**, *117*, 200–207. DOI:10.1016/j.chemosphere.2014.06.085
60. E. Neyens, J. Baeyens, *J. Hazard. Mater. B*, **2003**, *98*, 33–50. DOI:10.1016/S0304-3894(02)00282-0
61. M. Munoz, Z. M. de Pedro, J. A. Casas, J. J. Rodriguez, *Chem. Eng. J.* **2012**, *198–199*, 275–281. DOI:10.1016/j.cej.2012.05.097

Povzetek

Preučevali smo odstranjevanje mešanice dveh azo barvil, »adic blue 29« in »ponceau xylydine« (imenovano tudi »acid red 26«), s pomočjo heterogenega Fentonovega in Fentonu podobnega procesa z uporabo vodikovega peroksida in natrijevega persulfata kot oksidanta, v prisotnosti katalizatorja v obliki nano in mikro Fe₂O₃ delcev. Sintetizirane Fe₂O₃ delce smo okarakterizirali z uporabo FT-IR, TEM, EDX, praškovne XRD in VSM. Preučili smo vpliv velikosti delcev na zmanjševanje COD (kemijske potrebe po kisiku), kot tudi večkratnosti uporabe katalizatorja po optimizaciji pH vrednosti ter koncentracije katalizatorja in oksidanta. Kombinacija nano-Fe₂O₃ in vodikovega peroksida se je izkazala kot najučinkovitejša za zmanjševanje COD, ki je bila hitrejša v kislem območju in inhibirana pri pH > 6. Celokupna poraba vodikovega peroksida je potrdila učinkovitost procesa pod optimiziranimi pogoji. Predpostavili smo reakcijski mehanizem nastajanja vmesnih ionov in produktov. Zmanjševanje COD in vodikovega peroksida je sledilo kinetiki pseudo-prvega reda. Toksičnost raztopine smo preverjali preko zmanjševanja svetilnosti *Aliivibrio fischeri* in inhibicije rasti *Escherichia coli*. Metodi sta pokazali različno stopnjo toksičnosti iste raztopine.



Except when otherwise noted, articles in this journal are published under the terms and conditions of the Creative Commons Attribution 4.0 International License

Scientific paper

Reactivity of Microcrystalline Cellulose with Methyltrimethoxysilane and 3-(2-Aminoethylamino)propyltrimethoxysilanes

Przemysław Pietras,^{1,*} Hieronim Maciejewski^{1,2} and Bartłomiej Mazela³¹ Adam Mickiewicz University Foundation, Poznań Science and Technology Park, Rubież 46, 61-612 Poznań, Poland² Faculty of Chemistry, Adam Mickiewicz University, Uniwersytetu Poznańskiego 8, 61-614 Poznań, Poland³ Poznań University of Life Sciences, Institute of Wood Chemical Technology, Faculty of Wood Technology, Wojska Polskiego 28, 60-637 Poznań, Poland

* Corresponding author: E-mail: przemyslaw.pietras@ppnt.poznan.pl

Received: 03-25-2021

Abstract

In the presented research, two trialkoxysilanes were used to investigate their reactivity with microcrystalline cellulose (MCC) applied as a model material. As a continuation of the previous study, the research aimed at evaluation of the durability and potential reversibility of the silane treatment. Two different solvents and a mixture thereof were used for cellulose modification. The influence of amino group/pH, an excess of silanes and re-soaking with water on binding with cellulose was examined. The results obtained confirm that both selected silanes can effectively modify MCC. However, the treatment with 3-(2-aminoethylamino)propyltrimethoxysilane occurred more effective than with Methyltrimethoxysilane due to the presence of amino groups. Among the three tested solvents, the most effective was pure water. In contrast, the use of ethanol and a mixture of ethanol and water gave significantly worse results. Summarising, the presented research clearly shows how important the type of the functional group in alkoxy silanes is for its chemical reactivity with natural polymers, which is crucial for their application in waterlogged wood conservation.

Keywords: Cellulose, alkoxy silane, silane modification, microcrystalline cellulose

1. Introduction

Polymer-based materials play a significant role in modern industry. However, due to the depletion of fossil fuels, increasing health concerns, as well as heightened environmental awareness triggered by anthropogenic climate change, more emphasis is currently placed on developing environmentally friendly bio-based products.^{1,2}

As renewable plant raw materials, natural polymers are an attractive alternative to synthetic petroleum-based supplies, that comply with principles of green chemistry, ecology, and sustainability.^{2,3} Potentially limitless susceptibility of natural fibres to various modifications enhancing their performance characteristics makes them perfect materials of the future.^{4,5}

Cellulose is one of the most commonly employed natural polymers for many industrial purposes.^{6,7} Among others, it is widely applied as a reinforcement for polymeric hydrogels, aerogels, and composites.^{8–10} One of the

forms of cellulose used i.a. as reinforcing agents are microcrystalline cellulose (MCC) or cellulose nanocrystals (CNCs).^{2,8,11–13} The main advantages of MCC and CNCs are their excellent mechanical properties (high strength and stiffness) along with their low weight, large surface area, biodegradability and renewability.^{14,15} However, some shortcomings, such as moisture absorption, susceptibility to high temperature or incompatibility with most polymeric matrices significantly limit the possibility of employing cellulose crystals for specific applications.^{15,16} Therefore, a variety of modifications has been recently tested to overcome these disadvantages.^{17,18}

One of the solutions to enhance the performance of different forms of cellulose and override the problems concerning i.a. divergences between the polar and hydrophilic nature of cellulose and non-polar and hydrophobic character of a synthetic polymer matrix is creating organic-inorganic hybrids.¹⁹ A sol-gel technique is one of the significant

methods to obtain this, and due to the specific chemical structure and the resulting reactivity, silicate systems (in particular trialkoxysilanes) became the most extensively studied among all compositions used in this technique.^{20,21}

Organotrialkoxysilanes are the most common silicon derivatives. They are bifunctional molecules that contain both readily hydrolysable alkoxy groups and an organic functional group which determines their specific features. In the presence of water, alkoxy groups can hydrolyse and react with hydroxyl groups present on the surface of natural fibres forming siloxy bonds (Si-O-C). Simultaneously, they can also react with other silane particles forming more stable Si-O-Si bonds.^{22,23} The series of hydrolysis and condensation reactions is called the sol-gel process, and it results in the formation of a spatial network consisting of polysiloxane and natural polymers.^{24,25}

Silanes have been widely used as coupling agents and surface modifiers i.e. for cellulose and other lignocellulosic materials.^{26–30} The silane modification proved to be effective in improving mechanical properties and fire performance of composites containing modified materials, reducing the hydrophilic character of the modified fibres, and limiting their susceptibility to biodegradation by fungi.²² It is also efficient in facilitating dispersivity of natural polymers with synthetic matrix and making them more compatible with human-made polymers.^{31–37} Silane modification can be widely applied not only to natural fibres but also i.e. metals, pigments, glass and others. Such modifications provide new or improved functionalities of silane treated material.^{38–41}

The unique structure and the resulting reactivity of organosilicons make them also useful in the conservation of wooden artefacts. The results of our previous study proved the effectiveness of some organosilicon compounds (including methyltrimethoxysilane and 3-(2-aminoethylamino)propyltrimethoxysilane) in the stabilisation of waterlogged archaeological wood.⁴² However, the mechanism behind the dimensional stabilisation remains unclear, as well as issues related to durability and potential reversibility of the treatment that are important from the conservation perspective. Hence the concept of research presented herewith.

The proposed hypothesis assumes that silanes can form chemical bonds with the cell wall polymers (including cellulose) via alkoxy groups that results in reinforcement of the degraded cell wall leading to wood dimensional stabilisation. Moreover, due to the low chemical stability of alkoxy bonds, the interactions between silanes and cellulose are presumably reversible. Thus silane treatment under particular conditions (i.e. presence of water) could turn out to be impermanent. It is also assumed that the reactivity of particular alkoxy silanes with cellulose differs depending on the type of organofunctional group present in their molecules.

Given the above, the presented research aimed to investigate the reactivity of two trialkoxysilanes differing in

the type of an organofunctional group (methyltrimethoxysilane and 3-(2-aminoethylamino)propyltrimethoxysilane) with microcrystalline cellulose used as a model material, which has not been studied before. Two different solvents and a mixture thereof were used for microcrystalline cellulose modification. The influence of the presence of pH, excess of silane and re-soaking with water on binding stability with cellulose was examined.

2. Materials and Methods

2.1. Materials

Microcrystalline cellulose (MCC) and ethylenediamine were purchased at Sigma-Aldrich, ethanol (99.8%) was purchased at P.O.CH. and used as received. methyltrimethoxysilane (MTMS) and 3-(2-aminoethylamino)propyltrimethoxysilane (AEAPTMS) were synthesised in Poznan Science and Technology Park.

2.2. Methods

2.2.3. Modification of Microcrystalline Cellulose

Influence of the solvent/water content

Three different solvents were tested in the experiment:

- water,
- 99.8% ethanol,
- a mixture of ethanol and water (3:1, v/v).

0.5 g of MCC and 10 g of a particular solvent was placed in a beaker and stirred vigorously. After obtaining an MCC suspension, 0.5 g (or 3 g in the experiment with the excess of silanes, the details are described below) of an appropriate silane was added and stirred briskly for 2 hours. Microcrystalline cellulose was treated with MTMS and AEAPTMS in an MCC:silane mass ratio of 1:1 and 1:6, respectively. Unmodified MCC was suspended only in the appropriate solvent for 2 hours. The unmodified and modified MCC was then filtered off without additional washing and air-dried for 72 hours.

Air-dried MCC samples still contain physically bound water which can influence the results of an infrared spectroscopy analysis that was performed to assess the effectiveness of the silane treatment (the measurement of the number of hydroxyl groups – the details are described below in the *Infrared spectroscopy* section). Moreover, the presence of particular functional groups in modified MCC, originating in the silanes applied, can also increase the amount of bound water, altering the results of the spectroscopy measurements. Therefore, to clarify the actual amount of hydroxyl groups in unmodified MCC, a batch of MCC sample was oven-dried at 120 °C for 24 h, cooled down to room temperature and analysed using an FT-IR technique. Then the oven-dried MCC was divided into two parts, and modification with silanes was performed

according to the above-described procedure. After modification, the samples were air-dried for 72 h, and then oven-dried at 120 °C for 24 h, cooled-down and analysed.

Influence of pH

The modification was carried out as described above, using water as a solvent. Before adding an MTMS silane, pH of cellulose suspension was adjusted to the desired value of 10.2 (it was a pH value of the AEAPTMS solution applied for MCC modification) by the addition of ethylenediamine (EDA). Modified and unmodified MCC sample were filtered off without additional washing and air-dried.

Influence of re-soaking in water

The modification process was conducted following the procedure mentioned above (in a paragraph *Influence of the solvent/water content*) using water as a solvent. Then, after 48 h of air-drying, part of the samples was placed in

distilled water and stirred for 10 minutes (re-soaking). In the next step, samples were filtered off and air-dried.

All the obtained cellulose-silane composites are presented in Table 1.

Infrared spectroscopy

All the modification reactions were controlled using Fourier Transform Infrared Spectroscopy (FT-IR). Infrared spectra for particular dried samples were recorded on a Bruker Tensor 27 FT-IR Spectrometer equipped with a SPECAC Golden Gate diamond ATR unit with 2 cm⁻¹ resolution in the 4000–600 cm⁻¹ absorbance range. Sixteen scans were collected for each spectrum. The spectra were baseline corrected.

Since modification with silanes involves the chemical reaction of hydroxyl groups present on the MCC surface with hydrolysed silane alkoxy groups, it is expected to observe a decrease in the number of free hydroxyls in

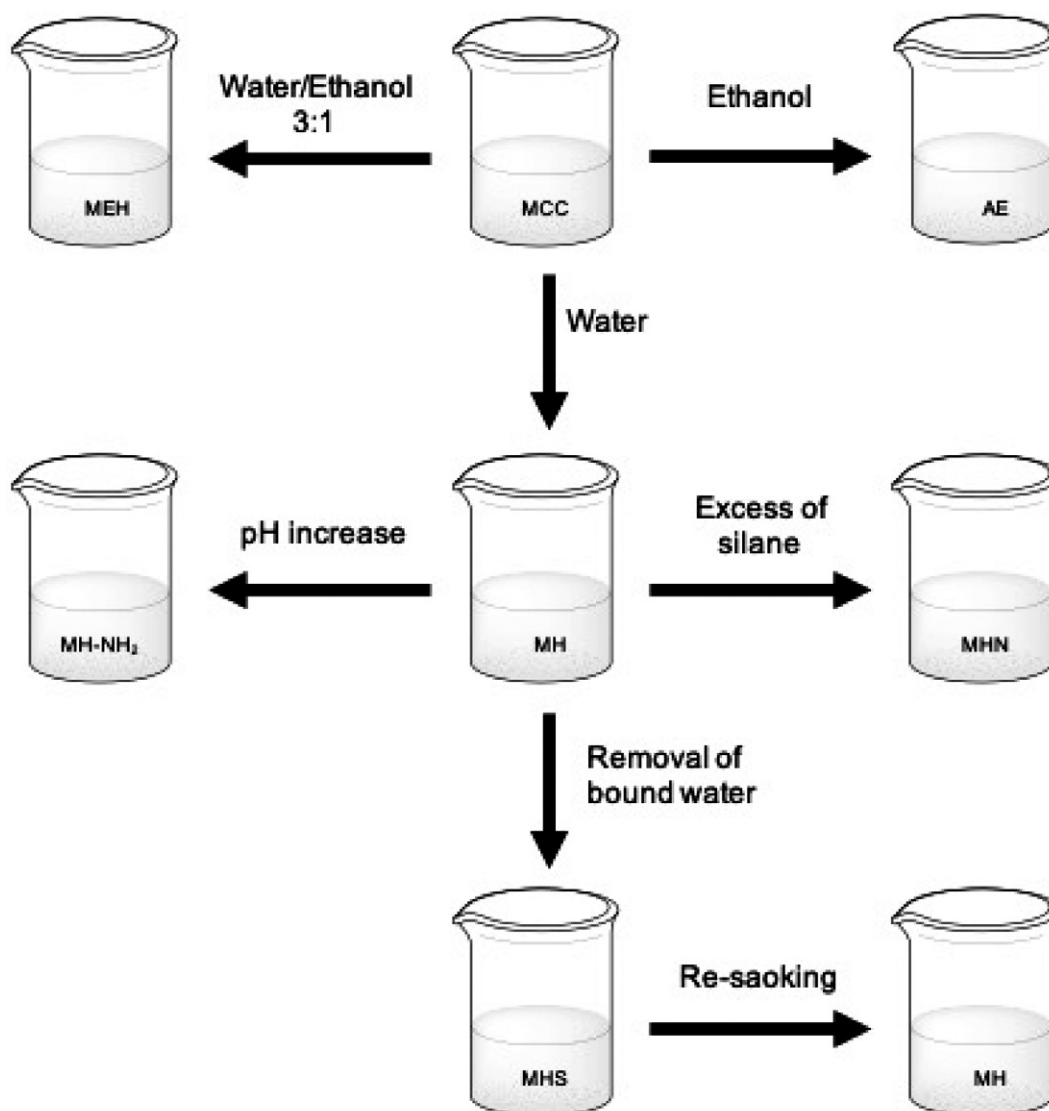


Fig. 1 Flowchart of chemical modification of MCC

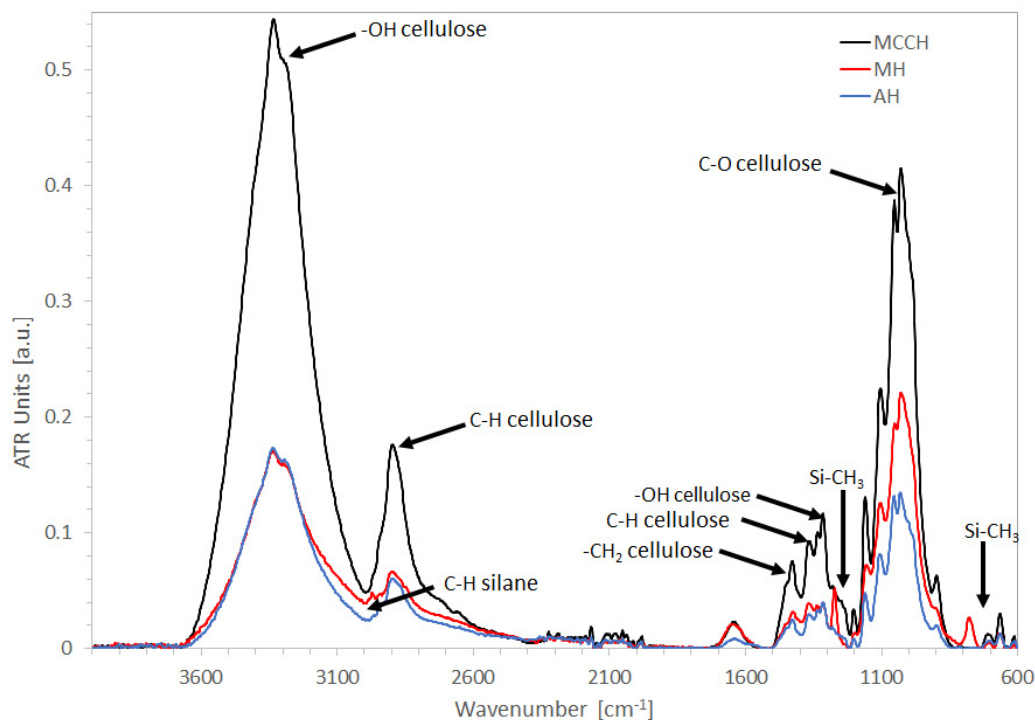
Table 1. Composition of obtained MCC samples

Sample code	silane Used	silane to cellulose Ratio (w/w)	Solvent	Additional information
MH	MTMS	1:1	Water	
AH	AEAPTMS	1:1	Water	
MCCH			Water	
ME	MTMS	1:1	Ethanol	
AE	AEAPTMS	1:1	Ethanol	
MCCE			Ethanol	
MEH	MTMS	1:1	Water:Ethanol 1:3	
AEH	AEAPTMS	1:1	Water:Ethanol 1:3	
MCCEH			Water	
MHN	MTMS	6:1	Water	
AHN	AEAPTMS	6:1	Water	
MCCS				Dried at 120 °C for 24h
MHS	MTMS	1:1	Water	Dried at 120 °C for 24h
AHS	AEAPTMS	1:1	Water	Dried at 120 °C for 24h
MH-NH ₂	MTMS	1:1	Water	pH adjusted to 10.2
MCCH-NH ₂			Water	pH adjusted to 10.2

modified MCC. Thus, to evaluate the effectiveness of the treatment, the hydroxyl content for unmodified and modified MCC was estimated by comparing the relative peak area of the absorption peak at 3300 cm⁻¹ assigned to hydroxyl groups. The hydroxyl peak area (HPA) within the range of 3650–3000 cm⁻¹ was calculated and expressed in arbitrary units (a.u.).

3. Results and Discussion

According to literature, the surface treatment of cellulose can be carried out with a silane solution in a commonly used concentration rate from 0.5 to 5% by weight. Such conditions offer several advantages: a) an increase in silane solubilisation in the medium, b) better control of the substrate film thickness on the surface, c) more uniform

**Fig. 2** FT-IR spectra of MCCH, MH and AH

coverage of the surface. The water-induced stepwise hydrolysis of the silane results in the formation of the corresponding silanols, which promotes the silane adsorption onto hydroxyl-rich substrates through hydrogen bonding. After solvent evaporation, the residual silanol groups may undergo a further condensation with the substrate hydroxyl groups. Moreover, they can also undergo self-condensation to form a polysiloxane network on the surface. Continued condensation leads to the formation of a gel-like network, which precipitates in the form of colloidal particles. Hydrolysis and condensation of the silanol groups are affected by the structure of the organic group of the silane and by the solvent characteristics (pH, temperature, amount of water, concentration).^{48–49} Therefore, a set of different experiments were performed to investigate the effect of type of the solvent, amount of a silane applied, pH and substrate re-soaking in the water on the reactivity of the selected silanes with MCC. The modification process was controlled using Fourier Transform Infrared Spectroscopy (FT-IR). Infrared spectra of untreated and silane-treated samples are presented in Figure 2.

Natural polymers and materials based on them form a complex network whose characteristics at the molecular level are often complicated. The intricacy of the chemicals contained in the material reflects in the variability of the functional groups present, which hinders interpretation of their infrared spectra.

In the FT-IR spectra of untreated and treated MCC (Figure 2), bands specific to cellulose can be observed, i.e. at 3380 (–OH), 2730 (C–H), 1427 (–CH₂), 1370 (C–H) and 1315 cm^{–1} (–OH), as well as at 1100, 1050 and 1030 cm^{–1}

(attributed to the stretching vibrations of C–O).⁴⁶ They are characterised by a high absorbance in untreated MCCH, while in treated MH and AH samples they are significantly reduced. Bands characteristic for silica are not visible in the spectra obtained, which can suggest that microcrystalline cellulose was not coated by silica but chemically modified by silanes. The band at 2960 cm^{–1} assigned for stretching vibrations of C–H and bands at 1260 and 802 cm^{–1} attributed to the vibrations of Si–CH₃, that are present in the MH, indicate the formation of a chemical bond between MTMS and MCC.⁴⁷ Unfortunately, bands that are specific to amino silane (particularly to –NH₂) are overlapped with bands characteristic for cellulose (especially –OH), thus hardly visible. However, when comparing spectra of MCCH and AH samples with pure AEAPTMS used for modification (Figure 3), a change in the shape of the band at 1640 cm^{–1} attributed to the presence of water can be observed. Comparison of normalised AH and MCCH spectra highlights differences between them in this region. Much broader band in the AH spectrum seems to consist of two overlapping bands: a band at 1640 cm^{–1} and a band specific to AEAPTMS, which indicates the presence of amino silane in the modified AH sample.

3. 1. Influence of the Solvent/water Content on Silane Reactivity

3. 1. 1. Impregnation in Different Solvents

The influence of the type and composition of the applied solvent on the MCC modification efficiency with

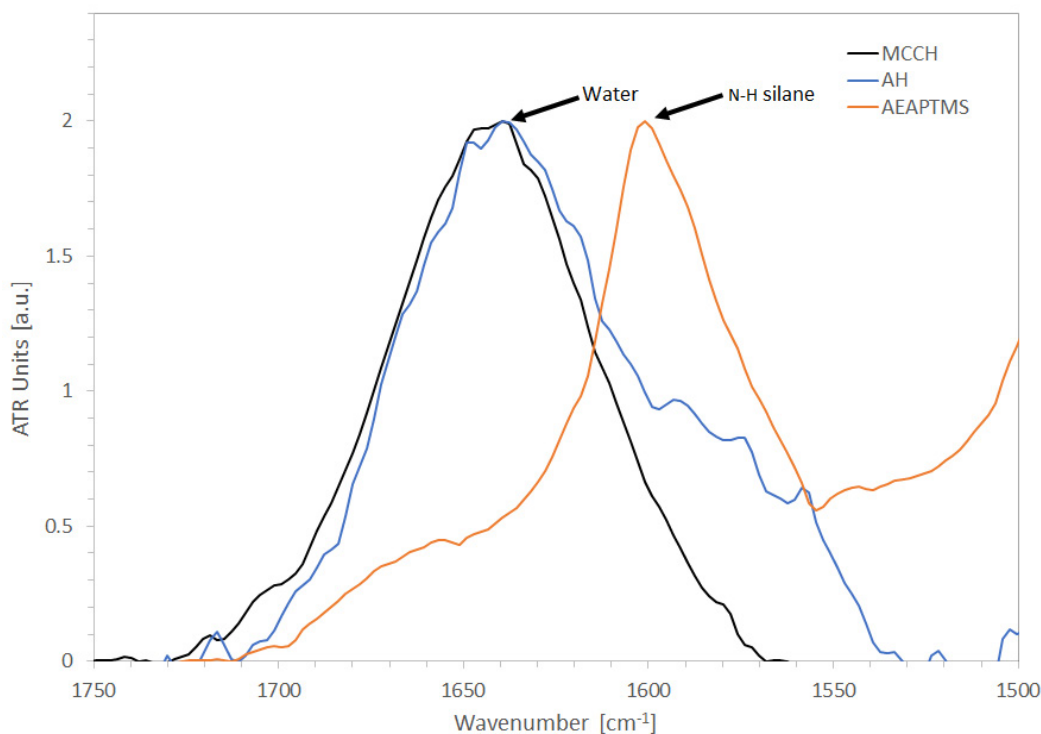


Fig. 3 FT-IR spectra of MCCH, AH and AEAPTMS

silanes (mass ratio 1:1) was investigated using water, ethanol and a mixture thereof (1:3). The changes in HPAs are presented on a graph in Figure 4. The graph starts only after 5 h of samples air-drying because directly after treatment the obtained infrared spectra were dominated by the bands specific to the particular solvents, and the measurement of the HPA was meaningless.

Starting with MCC treated with the use of water as a solvent. As it is clear from Figure 4, for all the samples, HPA decreases upon drying. The high initial HPA values result from the adsorption of water used as a solvent by the samples. They are similar for untreated MCCH and AEAPTMS-treated AH, and slightly lower from MTMS-treated MH. The observed difference between MCCH and MH can be explained by chemical modification of MH with silane, which limits the number of hydroxyl groups on its surface and increases its hydrophobicity thus reducing the number of water molecules interacting with MCC. AH, however, despite its chemical modification, has a stronger affinity to water due to the hydrophilic character of amino groups from the silane applied, which is visible as higher HPA, almost equal to highly hydrophilic unmodified MCCH. The different character of the functional groups of the used silanes also reflects in the rate of drying of particular samples. More hydrophilic AH dries slower than MH. The final HPA values after 72 h of air-drying for both treated samples are similar (about 40 a.u.). However, they are only almost half a size of HPA for unmodified cellulose (about 90 a.u.), which confirms their effective modification with silanes. However, since there is still bound water present in the air-dried cellulose samples (and it is included in the HPA value), the comparison of the effectiveness between particular silanes is unjustified.

An entirely different trend can be seen for samples suspended in ethanol (ME, AE and MCCE in Figure 4). First of all, the initial HPA values are significantly lower in comparison with samples suspended in water: about 3 times for unmodified MCC, about 2.5 times for MTMS-treated and more than 5 times for AEAPTMS-treated, respectively. It results from considerably lower water content in the solvent (only about 0.2% in comparison with the former 100%) thus the lower total number of hydroxyl groups present.

Interestingly, for samples suspended in ethanol, the HPAs after 5 h of air-drying are the lowest, and they increase and then decrease slightly upon drying. This phenomenon can suggest further silane hydrolysis due to the absorption of water molecules from the air and their condensation with a release of other water molecules. Although, in the end (after 72 h), HPAs remain higher than in the beginning. They are also significantly higher than those obtained for modification in water (MH and AH). This indicates lower effectiveness of the modification process due to the highly limited water content in the solvent, which occurred insufficient for full hydrolysis of the silanes applied. Lower HPA for AE indicates higher effectiveness of amino silane as against MTMS. It suggests that more hydrophilic amino groups can be more effective in attracting water molecules from a solvent and the air, providing better conditions for silane hydrolysis. On the other hand, their alkaline nature can create better conditions for silane condensation resulting in higher reactivity with hydroxyls present on MCC surface than MTMS.

Surprisingly, HPA for the sample treated with MTMS (ME) is higher in comparison with untreated MCCE, and even its slight increase upon air-drying can be observed. The presence of ethanol can explain this phenomenon. It

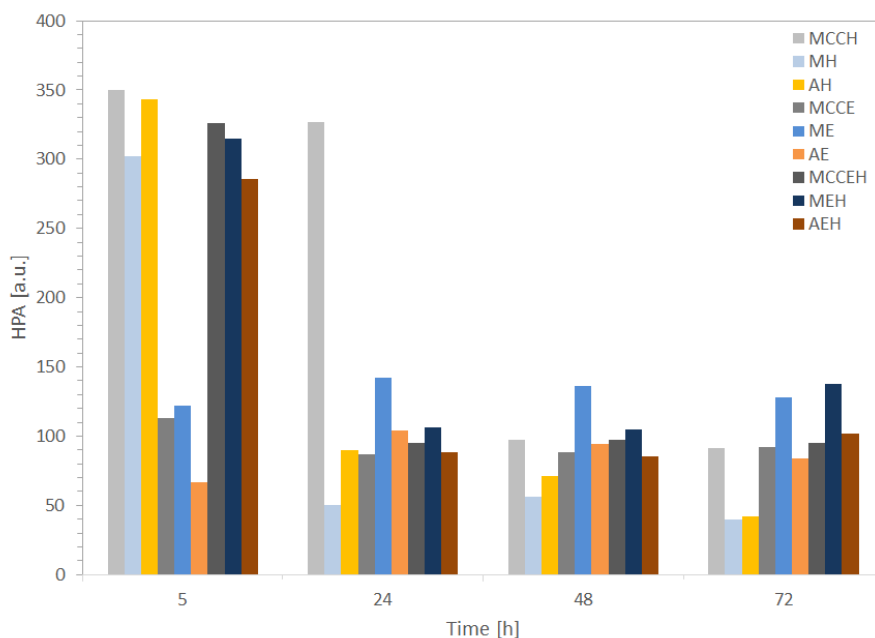


Fig. 4 Changes in hydroxyl peak area (HPA) during air-drying for MCC untreated and silane-treated (mass ratio 1:1) using tested solvents.

promotes silane hydrolysis leading to the formation of silanols, but simultaneously it inhibits their further condensation. It is possible then that under such conditions, MTMS can hydrolyse using all the available water molecules and bind to cellulose. However, it still contains free hydroxyls connected with silicon atoms (Si–OH) whose presence can be seen in an infrared spectrum as a band at 3300 cm^{-1} . Free Si–OH groups located close to each other can additionally trap water molecules by the formation of hydrogen bonds, and they can add to the intensity of the infrared band specific to hydroxyls. The observed phenomenon indicates lower effectiveness of modification in ethanol than in water. In the case of the samples treated with amino silane, the observed effect is lower, which confirms higher reactivity of this chemical with cellulose.

As can be seen from Figure 4 (MEH, AEH, MCEH), application of an ethanol/water mixture as a solvent resulted in high HPAs shortly after impregnation (5 h, similarly to the impregnation performed using water only), but also in the highest HPAs after air-drying (72 h, comparable with HPAs for samples treated in pure ethanol). The former results from the presence of water molecules in the solvent, the latter suggests that the presence of ethanol promotes silane hydrolysis leading to the formation of silanols, but simultaneously it inhibits further condensation which reflects in lower modification rate (i.e. higher amount of hydroxyls measured). Lower HPA for AEH in comparison with MEH indicates higher effectiveness of amino silane treatment, as described above.

Comparison of the results for all treated samples (Figure 4) can lead to the conclusion that water was definitely the solvent assuring the highest saturation of hydroxyls present on MCC with the applied silanes.

3. 1. 2. Impregnation in Water with a 6-fold Excess of Silanes

The changes of HPS's of MCC modification with an excess of silanes (mass ratio 1:6) is presented in Figure 5.

When comparing the results for MH and MHN, it is clear that although 5 h after silane treatment the HPA is similar for both samples, it differs significantly upon further drying, and after 72 h it is almost 2.5 times higher for the sample treated with an excess of MTMS. The significantly higher number of free hydroxyls in the MHN sample can result from a higher number of silanols attached only by one Si–O–C bond or by hydrogen bond and two free Si–OH groups which can increase HPA.

The different effect of an excess of silane applied can be observed in the case of AEAPTMS-treated samples, where HPA for AHN is continuously lower than for AH during drying. It can be explained by the specific properties of amino groups present in the silane, which promotes silane condensation. As a result, considerably higher effectiveness of MCC modification can be observed than for MHN sample, while in comparison with AH sample the reactivity with MCC only slightly improved.

3. 1. 3. The Effect of Bound Water on the Number of Hydroxyls Measured and Silanes Reactivity with MCC

Figure 6 presents the changes in HPAs obtained for MCC samples which were oven-dried, silane-modified, air-dried and then oven-dried again to exclude the effect of bound water on the hydroxyl peak area measured.

When comparing the results for MH and MHS, it is clear that after additional oven-drying HPA increases 2

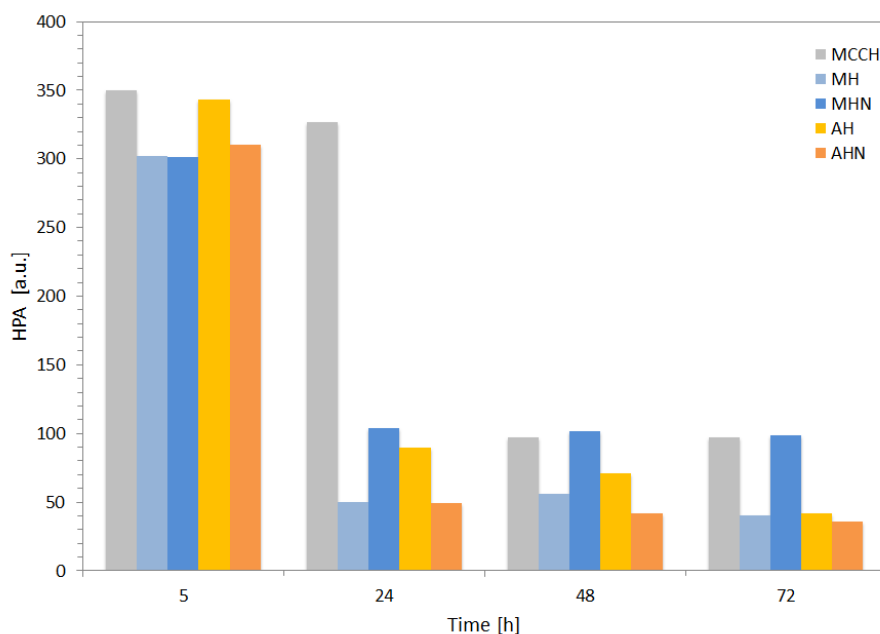


Fig. 5 Comparison of changes in hydroxyl peak area (HPA) during air-drying for MCC treated in water using MCC:silane mass ratio of 1:1 (MH, AH) and 1:6 (MHN, AHN), respectively.

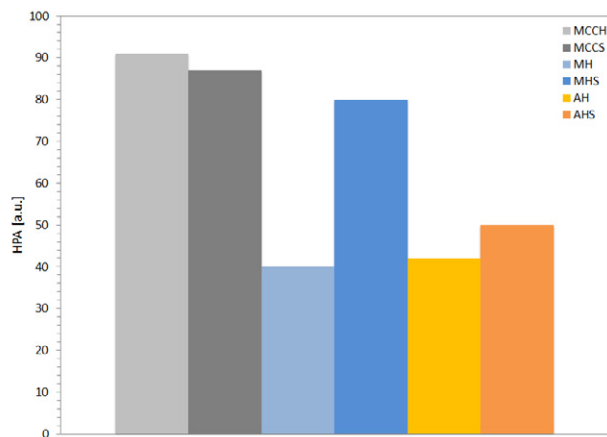


Fig. 6 Changes in hydroxyl peak area (HPA) for unmodified and modified MCC samples after air-drying (MCC, MH, AH) and oven-drying (MCCS, MHS, AHS)

times (from 40 a.u. for MH up to 80 a.u. for MHS) for MHS. The significantly higher number of free hydroxyl groups in the MHS sample can indicate that after hydrolysis of MTMS to a silanol, it only partially binds to MCCS hydroxyls, and the most of the formed silanol molecules are attached by hydrogen bonding. The formation of hydrogen bonds results in a decrease of HPAs on infrared spectra what corresponds with the previous results. During drying in 120 °C, hydrogen bonds break and silanols can easily evaporate from the surface (MTMS boiling point 102–104 °C). In the case of AEAPTMS the situation is similar, however, an increase in HPA is lower (from 42 a.u. for AH up to 50 a.u. for AHS). The higher pH of the reaction environment results in a higher condensation rate, which limits the formation of hydrogen bonds and can be the reason for a lower increase of HPA after oven-drying. Besides, because a boiling point for AEAPTMS is at 232 °C, much less of silanol molecules has a chance to evaporate during oven-drying.

3. 1. 4. The Effect of Re-soaking in the Water on Silanes Reactivity with Cellulose

The influence of re-soaking in the water on silane reactivity with MCC in the form of changes in the hydroxyl peak area (HPA) are presented in Figure 7.

In the first part of the graph (Figure 7), a typical decrease in HPA during air-drying can be seen. The initial high HPA values, resulting from the adsorption of water used as a solvent, are similar for both unmodified and modified MCC. After 48 h of air-drying, however, a significant difference can be observed between the MCC samples. HPA for treated MH and AH is 2× and 4× lower than for untreated MCCH, respectively, which confirms their effective modification with silanes.

Air-dried samples (after 48 h) were then re-soaked in water for 10 minutes and air-dried again. The effect of re-soaking is clearly visible in Figure 7, since after 24 hours from this point (72 h on the graph) HPA for MCCH in-

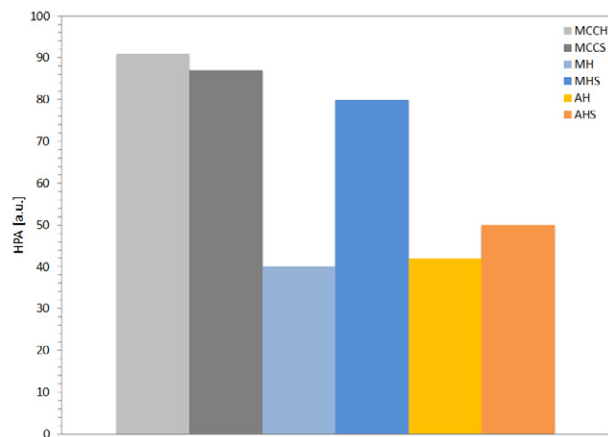


Fig. 7 Effect of re-soaking of unmodified and modified MCC

creased 3,5– (up to 353 a.u.), over 3– for MH (up to 189 a.u.) and 1,5– for AH (up to 43 a.u.) in comparison with dry samples after 48 h. Further 24-hour drying (96 h on the graph) resulted in a decrease in HPAs, reaching about the same level as before re-soaking for MCCH and AH (about 97 a.u. and 31 a.u., respectively) but significantly higher for MH (81 a.u. after re-soaking versus 58 a.u. before re-soaking, respectively). The observed phenomenon can indicate that a part of MTMS molecules was not chemically bonded with MCC and was washed out during re-soaking, leaving unoccupied hydroxyls on its surface. Another explanation could be that MH was not completely modified/covered with MTMS; therefore, during re-soaking, water molecules could penetrate the sample. The presence of additional water-induced further polymerisation of the silane which could cover water molecules connected to MCC, so that even after 48 h of air-drying an increased in HPA originated from water hydroxyls can be observed.

The results of the experiment with re-soaking of the previously treated samples confirmed that MCC modification with MTMS was less efficient than with AEAPTMS. Moreover, it also showed that part of MTMS molecules could be washed out from the modified MCC surface, which means that this type of modification is not permanent.

3. 1. 5. Influence of pH on Silanes Reactivity with Cellulose

The results of the experiments mentioned above point to the conclusion that the higher effectiveness of AEAPTMS in MCC modification can result from an alkaline reaction environment provided by amino groups present in the silane molecules. Therefore, to find out how alkaline pH affects silane reactivity with cellulose, the next modification process was carried out in the water with ethylenediamine at pH adjusted to 10.2 (pH level of AEAPTMS solution in water).

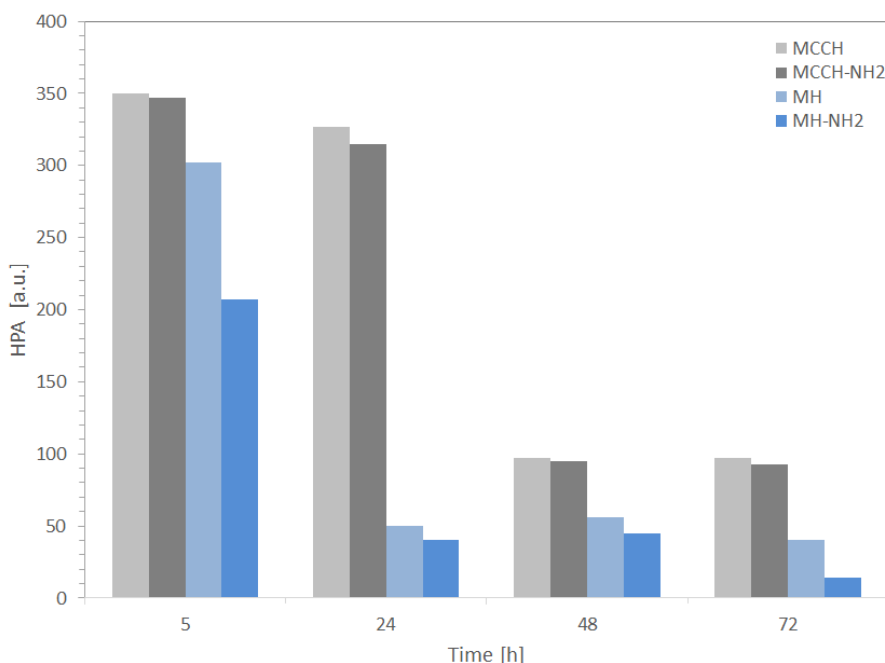


Fig. 8 Comparison of changes in hydroxyl peak area (HPA) during air-drying for MCC treated in water (MH) and water with ethylenediamine (MCCH-NH₂, MH-NH₂), respectively

As can be seen from Figure 8, alkalisation of the reaction environment increased the effectiveness of MCC modification with MTMS which can be seen as a significant decrease in HPA for dry samples from 40 a.u. for MH to 14 a.u. for MH-NH₂. However, the analysis of the FT-IR spectrum in the entire measured range clearly suggests that the addition of ethylenediamine changes the path of the reaction, which can be seen in Figure 8.

The FT-IR spectra of MCC untreated and treated with MTMS without ethylenediamine (Figure 9) reveal primarily the bands specific to cellulose, i.e. at 3380 cm⁻¹ (-OH), 2730 cm⁻¹ (C-H), 1427 cm⁻¹ (-CH₂), 1370 cm⁻¹ (C-H), 1315 cm⁻¹ (-OH) as well as 1100 cm⁻¹, 1050 cm⁻¹ and 1030 cm⁻¹ (attributed to the stretching of C-O). Additionally, the band at 2960 cm⁻¹ assigned for stretching vibrations of C-H and bands at 1260 and 802 cm⁻¹ (at-

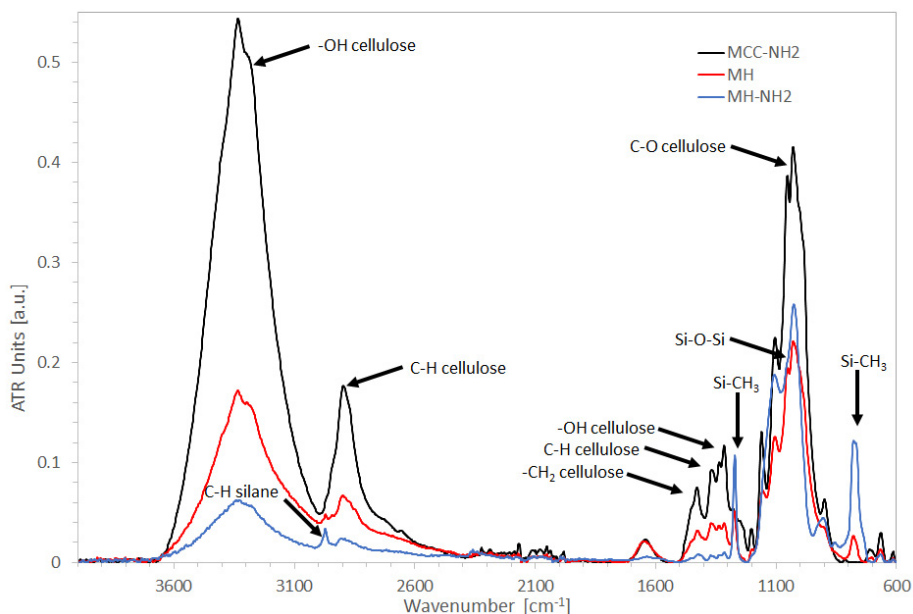


Fig. 9 The FT-IR spectra of MCCH, MH and MH-NH₂

tributed to the vibrations of Si–CH₃) are present in the MH spectrum, which indicates the formation of a chemical bond between MTMS and MCC. The spectrum of MCC treated with MTMS in the presence of ethylenediamine, however, looks different. In this spectrum, the bands specific to cellulose at 1427 cm⁻¹ (–CH₂), 1370 cm⁻¹ (C–H), 1315 cm⁻¹ (–OH) cannot be observed, and the band at 2730 cm⁻¹ (C–H) is significantly decreased. On the other hand, the bands characteristic to silane at 2960 cm⁻¹ (C–H) as well as at 1260 and 802 cm⁻¹ (attributed to the vibrations of Si–CH₃) can be clearly seen. Additionally, a band at 1140–1080 cm⁻¹ takes the shape of the band characteristic to Si–O–Si. It can indicate that MTMS-treated MCC in the presence of ethylenediamine is covered/encapsulated by obtained silica instead of being modified by silane.

4. Conclusions

The results of the presented research confirm hypothesis that silanes can react with cellulose, whereby the chemical structure of silane molecules affect effectiveness and stability of modification. As was shown, both selected silanes can efficiently modify microcrystalline cellulose. However, treatment with 3-(2-aminoethylamino)propyltrimethoxysilane generally occurred far more effective and durable than with methyltrimethoxysilane, including the reaction using an excess of silanes. It seems that the presence of amino groups in the amino silane molecules enhances its reactivity. On the one hand, it attracts water molecules (e.g. from the moist air) in a water-deficient environment (like ethanol) enabling hydrolysis of silanes; on the other hand, it provides an alkaline reaction environment supporting condensation of silanols, which results in the full polymerisation reaction.

For methyltrimethoxysilane, the results show that the polymerisation reaction may not be complete during MCC treatment and some of the silane molecules may remain in the form of silanols which can form only hydrogen bonds with MCC. This is in line with the results of our previous research when the DVS experiments revealed a similar phenomenon in waterlogged elm treated with MTMS. The full condensation, and thus stabilisation of the silane/wood system was achieved only after 12 cyclic sorption stages.⁴³ However, further experiments using waterlogged oak wood did not show such instability of the silane.⁴⁴ These observations are essential from the wood conservation perspective since they all point out that in the case of using a high concentration of MTMS, an additional stage of seasoning the conserved material is necessary to stabilise (fully polymerise) MTMS.

Another result of probable incomplete polymerisation of MTMS is the fact that the silane molecules can be washed out from the modified MCC surface, which means that this type of modification is not permanent. This par-

tially confirms the hypothesis that silane treatment can be reversible under particular conditions (presence of water promoting their hydrolysis). However, as was shown, the stability of silane-cellulose interactions depends on the organofunctional group of the silane.

Moreover, in the case of MTMS, an increase in pH to the level obtained in the reaction with amino silane leads to the encapsulation of microcrystalline cellulose by the silica formed in this reaction rather than to its modification. It suggests that alkaline reaction environment is not the only condition necessary for an effective modification process. The possibility of silica formation seems particularly essential from the conservation perspective. On the one hand, such an inner “skeleton” made of silica inside the wood structure could strengthen or reinforce its mechanical properties, but on the other side, it could also damage the already weakened and decomposed wooden tissue. Therefore, this issue requires further study before the application of silanes could be proposed as an accepted method for waterlogged wood conservation.

The use of dried MCC for modification with silanes decreases its effectiveness, which points out the essential role of bound water in the reaction process.

Among the three tested solvents, the most effective was pure water which assured the highest saturation of hydroxyls present on MCC with the silanes applied. The use of ethanol and a mixture of ethanol and water gave significantly worse results. Additionally, although the presence of ethanol promotes hydrolysis of a silane leading to the formation of silanols, it also simultaneously inhibits their further condensation. From the conservation perspective, these results demonstrate that using ethanol as a solvent will enable penetration of silane monomers into the wooden tissue; however, it should be remembered that the presence of water is necessary for its further polymerisation.

5. References

1. S. Kalia, B. Kaith, I. Kaur (Eds.), *Cellulose Fibers: Bio- and Nano-polymer Composites: Green Chemistry and Technology*. Springer Science & BusinessMedia, **2011**, pp. 97–119.
2. D. Trache, M. H. Hussin, C. T. H. Chuin, S. Sabar, M. N. Fazita, O. F. Taiwo, M. K. Hassan, M. M. Haafiz, *Int. J. Biol. Macromol.* **2016**, 93,789–804.
DOI:10.1016/j.ijbiomac.2016.09.056
3. A. Gholampour, T. Ozbakkaloglu, *J. Mater. Sci.* **2020**, 55, 829–892. DOI:10.1007/s10853-019-03990-y
4. H. A. Khalil, A. H. Bhat, A. I. Yusra, *Carbohydr. Polym.* **2012**, 87(2), 963–979. DOI:10.1016/j.carbpol.2011.08.078
5. Y. K. Kim, V. Chalivendra, Natural fibre composites (NFCs) for construction and automotive industries. In *Handbook of Natural Fibres*, Woodhead Publishing, **2020**, pp. 469–498.
6. L. Berglund, Cellulose-based nanocomposites. In: A. K. Mohanty, M. Misra, L. T. Drzal (Eds.), *Natural Fibers, Biopolymers, and Biocomposites*, CRC Press, **2005**, pp. 807–832.

7. A. Boldizar, C. Klason, J. Kubat, P. Näslund, P. Saha, , *Int. J. Polym. Mater.* **1987**, 11(4), 229–262. DOI:10.1080/00914038708078665
8. D. de Morais Zanata, L. C. Battirola, M. do Carmo Gonçalves, *Cellulose* **2018**, 25(12), 7225–7238. DOI:10.1007/s10570-018-2090-y
9. R. A. Ilyas, S. M. Sapuan, M. R. Ishak, E. S. Zainudin, *Carbohydr. Polym.* **2018**, 202, 186–202. DOI:10.1016/j.carbpol.2018.09.002
10. J. Yang, C. R. Han, F. Xu, R. C. Sun, *Nanoscale* **2014**, 6(11), 5934–5943. DOI:10.1039/c4nr01214c
11. H. P. S. Khalil, Y. Y. Tye, C. K. Saurabh, C. P. Leh, T. K. Lai, E. W. N. Chong, N. M. Fazita, J. Hafidz, A. Banerjee, M. I. Syakir, *Express Polym. Lett.* **2017**, 11, 244–265. DOI:10.3144/expresspolymlett.2017.26
12. S. Parveen, S. Rana, R. Fanguero, M. C. Paiva, *Cement Concrete Comp.* **2017**, 78, 146–161. DOI:10.1016/j.cemconcomp.2017.01.004
13. M. Rico, S. Rodriguez-Llamazares, L. Barral, R. Bouza, B. Montero, *Carbohydr. Polym.* **2016**, 149, 83–93. DOI:10.1016/j.carbpol.2016.04.087
14. A. Chartrand, J. M. Lavoie, M. A. Huneault, *J. Appl. Polym. Sci.* **2016**, 133, 44348. DOI:10.1002/app.44348
15. C. A. Murphy, M. N. Collins, *Polym. Composite.* **2018**, 39(4), 1311–1320. DOI:10.1002/pc.24069
16. S. T. Sundar, M. M. Sain, K. Oksman, *Carbohydr. Polym.* **2010**, 80(1), 35–43. DOI:10.1016/j.carbpol.2009.10.072
17. L. Xiao, Y. Mai, F. He, L. Yu, L. Zhang, H. Tang, G. Yang, *J. Mater. Chem.* **2012**, 22(31), 15732–15739. DOI:10.1039/c2jm32373g
18. X. Yu, X. Huang, C. Bai, X. Xiong, *Environ. Sci. Pollut. R.* **2019**, 26(32), 32859–32865. DOI:10.1007/s11356-019-06317-1
19. Y. Dong, J. Liang, Y. Cui, S. Xu, N. Zhao, *Carbohydr. Polym.* **2018**, 197, 183–193. DOI:10.1016/j.carbpol.2018.05.086
20. L. Meng, H. Zhu, B. Feng, Z. Gao, D. Wang, S. Wei, *Prog. Org. Coat.* **2020**, 141, 105540. DOI:10.1016/j.porgcoat.2020.105540
21. M. Yanilmaz, Y. Lu, J. Zhu, X. Zhang, *J. Power. Sources.* **2016**, 313, 205–212. DOI:10.1016/j.jpowsour.2016.02.089
22. S. Donath, H. Militz, C. Mai, *Wood Sci. Technol.* **2004**, 38(7), 555–566. DOI:10.1007/s00226-004-0257-1
23. D. Levy, M. Zayat (Eds.), *The Sol-Gel Handbook*, 3 Volume Set: Synthesis, Characterisation, and Applications (Vol. 2). John Wiley & Sons, **2015**, pp. 17–21.
24. D. Panov, N. Terziev, *Int. Biodeter. Biodeg.* **2009**, 63(4), 456–461. DOI:10.1016/j.ibiod.2008.12.003
25. Y. Xie, C.A. Hill, D. Sun, Z. Jalaludin, Q. Wang, C. Mai, *BioResources* **2011**, 6(3), 2323–2339.
26. H. Abdellaoui, R. Bouhfid, A. E. K. Qaiss, Lignocellulosic fibres reinforced thermoset composites: preparation, characterisation, mechanical and rheological properties. In *Lignocellulosic Composite Materials*. Springer, Cham. 2018, pp. 215–270. DOI:10.1007/978-3-319-68696-7_5
27. K. L. Mittal, Silanes and other coupling agents. VSP, Leiden, **2009**, pp. 51–64.
28. M. S. Sreekala, S. Thomas, *Compos. Sci. Technol.* **2003**, 63(6), 861–869. DOI:10.1016/S0266-3538(02)00270-1
29. Y. Xie, C. A. S. Hill, Z. Xiao, H. Militz, C. Mai, *Compos. Part A-Appl. S.* **2010**, 41(7), 806–819. DOI:10.1016/j.compositesa.2010.03.005
30. Z. Zhang, G. Sèbe, D. Rentsch, *Chem. Mater.* **2014**, 26, 2659–2668. DOI:10.1021/cm5004164
31. M. de Oliveira Taipina, M. M. F. Ferrarezi, I. V. P. Yoshida, M. D. C. Gonçalves, *Cellulose* **2013**, 20, 217–226. DOI:10.1007/s10570-012-9820-3
32. S. Donath, H. Militz, C. Mai, *Holzforschung* **2006**, 60(2), 210–216. DOI:10.1515/HF.2006.035
33. R. M. Neves, H. L. Ornaghi Jr, A. J. Zattera, S. C. Amico, *Carbohydr. Polym.* **2020**, 230, 115595. DOI:10.1016/j.carbpol.2019.115595
34. L. D. Rajapaksha, H. A. D. Saumyadi, A. M. P. B. Samarasekara, D. A. S. Amarasinghe, L. Karunanayake, Development of cellulose based light weight polymer composites. In: 2017 Moratuwa Engineering Research Conference (MERCon). IEEE, **2017**, pp. 182–186. DOI:10.1109/MERCon.2017.7980478
35. M. K. Thakur, R. K. Gupta, V. K. Thakur, *Carbohydr. Polym.* **2014**, 111, 849–855. DOI:10.1016/j.carbpol.2014.05.041
36. M. Wang, T. Yu, Z. Feng, J. Sun, X. Gu, H. Li, B. Fei, S. Zhang, *Polym. Advan. Technol.* **2020**, 1–9. DOI:10.1002/pat.4863
37. M. Fir, J. Vince, A. S. Vuk, A. Vilcnik, V. Jovanovski, G. Mali, B. Orel, B. Simoncic, *Acta Chim. Slov.* **2007**, 144–148.
38. I. Milosev, *Acta Chim. Slov.* **2019**, 511–533. DOI:10.17344/acsi.2019.5162
39. E. Soleimani, N. Zamano, *Acta Chim. Slov.* **2017**, 644–653. DOI:10.17344/acsi.2017.3459
40. N. Demirkiran, E. Ekinci, *Acta Chim. Slov.* **2012**, 302–306.
41. M. Steinbuecher, P. Venturini, J. Hafner, M. Zupancic, P. Gregoric, I. Golobic, *Acta Chim. Slov.* **2017**, 938–944. DOI:10.17344/acsi.2017.3637
42. M. Broda, I. Dąbek, A. Dutkiewicz, M. Dutkiewicz, C-M. Popescu, B. Mazela, H. Maciejewski, *Sci. Rep.* **2020**, 10(1), 1–13. DOI:10.1038/s41598-020-59240-8
43. M. C. Brochier Salon, M. Abdelmouleh, S. Boufi, M. N. Belgacem, A. Gandini, *J. Colloid. Interf. Sci.* **2005**, 289(1), 249–261. DOI:10.1016/j.jcis.2005.03.070
44. M. W. Daniels, L. F. Francis, *J. Colloid. Interf. Sci.* **1998**, 205(1) 191–200. DOI:10.1006/jcis.1998.5671
45. N. Nishiyama, K. Horie, T. Asakura, *J. Colloid. Interf. Sci.* **1989**, 129(1), 113–119. DOI:10.1016/0021-9797(89)90420-7
46. D. M. Panaitescu, D. Donescu, C. Bercu, D. M. Vuluga, M. Iorga, M. Ghiurea, *Polym. Eng. Sci.* **2007**, 47(8), 1228–1234. DOI:10.1002/pen.20803
47. Z. Olejniczak, M. Leczka, K. Cholewa-Kowalska, K. Wojtach, M. Rokita, W. Mozgawa, *J. Mol. Struc.* **2005**, 744, 465–471. DOI:10.1016/j.molstruc.2004.11.069
48. M. Broda, J. Majka, W. Olek, B. Mazela, *Int. Biodeter. Biodeg.* **2018**, 133, 34–41. DOI:10.1016/j.ibiod.2018.06.007
49. M. Broda, S. F. Curling, M. J. Spear, C. A. Hill, *Wood Sci. Tech.* **2019**, 53(3), 703–726. DOI:10.1007/s00226-019-01095-y

Povzetek

V tej raziskavi smo uporabili dva trialkoksisilana za študij reaktivnosti z mikrokristalinično celulozo (MCC), ki je bila uporabljena kot modelni material. Kot nadaljevanje prešnje študije je bila raziskava namenjena oceni trajnosti in potencialne reverzibilnosti obdelave s silanom. Za modifikacijo silana smo uporabili dve različni topili in njuno mešanico. Raziskali smo vpliv amino skupin, pH, presežka silana in ponovnega namakanja z vodo pri vezavi s celulozo. Dobljeni rezultati so potrdili, da lahko oba izbrana silana učinkovito spremenita MCC. Vendar pa je bila obdelava s 3-(2-aminoetilamino)-propiltrimetoksisilanom zaradi prisotnosti amino skupin učinkovitejša kot z metil-tri-metoksisilanom. Med tremi testiranimi topili je bila najbolj učinkovita čista voda. Uporaba etanola in mešanice etanola in vode pa je, nasprotno, dala bistveno slabše rezultate. Predstavljena raziskava presenetljivo jasno pokaže, kako pomemben za kemijsko reaktivnost z naravnimi polimeri je tip funkcionalnih skupin v alkoksisilanih, kar je ključnega pomena za njihovo uporabo pri ohranjanju lesa, zalitega z vodo.



Except when otherwise noted, articles in this journal are published under the terms and conditions of the Creative Commons Attribution 4.0 International License

Scientific paper

Development and Evaluation of Lyophilized Methotrexate Nanosuspension using Quality by Design Approach

Trupti Powar,^{1,*} Ashok Hajare,² Ravindra Jarag³ and Sopan Nangare⁴¹ Department of Pharmaceutics, Smt. Kashibai Navale College of Pharmacy, Kondhwa, Pune (Maharashtra) 411048, India.² Department of Pharmaceutics, Bharati Vidyapeeth College of Pharmacy, Kolhapur (Maharashtra) 416013, India.³ Department of Pharmacology, Bharati Vidyapeeth College of Pharmacy, Kolhapur (Maharashtra) 416013, India.⁴ Department of Pharmaceutics, H. R. Patel Institute of Pharmaceutical Education and Research, Shirpur (Maharashtra) 425405, India.* Corresponding author: E-mail: E-mail: truptipowar51@gmail.com
Mobile: +91 9766196512

Received: 06-29-2021

Abstract

With the application of the quality by design (QbD) approach, a high-pressure homogenizer (HPH) methodology was employed to develop methotrexate nanosuspension (MTX-NS) to boost bioavailability. The Ishikawa diagram was used to analyze potential risk factors in formulation development. To screen and study the impact of various formulation and process factors on the critical quality attributes (CQA), the Plackett–Burman design and central composite design were utilized. The number of HPH cycles, poloxamer 188 concentration, and tween 80 concentration were shown to be significant parameters ($P < 0.05$), that were further optimized using Central Composite Design. The zeta potential of optimized lyophilized MTX-NS was determined to be -11.6 ± 7.52 mV and the average particle size was 260 ± 0.25 nm. In vitro cytotoxicity experiments revealed a greater than 80% inhibition, with apoptotic cells shrinking, fragmentation, and cell death. Furthermore, the C_{max} and AUC_{0-t} were increased by 2.53 and 8.83 folds, respectively. The relative bioavailability of MTX-NS was found to be 8.83 times higher than that of MTX-aqueous dispersion. As a result, the QbD method resulted in the development of a lyophilized MTX-NS with process understanding and control based on quality risk management.

Keywords: Nanosuspension; Lyophilized, QbD approach; Central Composite Design; Plackett–Burman Design; *In-vivo* study.

1. Introduction

Pharmaceutical experts have long struggled with the formulation and development of poorly water-soluble drugs, and these challenges are projected to worsen since more than 40% of new chemical entities discovered by drug discovery are poorly aqueous soluble.¹ Whereas, it is more problematic in the case of poorly soluble drugs with poor absorption profile, and bioavailability because it is dissolution rate-limited and can be affected by patient fed or fasted state condition². Traditional approaches including solubilization by surfactant, surfactant dispersion, micronization, use of the oily solution, permeation enhancers, which evolved too earlier, that address the challenges of formulation and have limited use.^{2,3} The major mile-

stone has been achieved in the development of poorly water-soluble drugs using various newer technology, but to date, there is no universal thumb approach applicable to all active pharmaceutical ingredients.³ Consequently, a new approach has been progressively required to deal with formulation issues that are associated with the delivery of poorly soluble drugs, to enhance their therapeutic efficacy and maximize their pharmacodynamics therapy.²

A drug delivery aims to deliver a sufficient amount of drug to a proper side in the body such that, the optimal concentration of the drug is reached rapidly and then sustained. The development of a proper dosage form is an essential element to achieve this objective.⁴ From its inception, oral drug delivery is the most commonly used route of administering the drug in various dosage forms due to

its simple administration, flexibility in the design of dosage form, and its high patient compliance.⁵

The Methotrexate (MTX) (2, 4-diamino-N10-methyl propyl glutamic acid) is an anticancer agent belong to biopharmaceutical classification system class IV (BCS-IV) employed for different solid tumors viz. Breast cancer, lung cancer, etc. treatment.⁶ It has poor water solubility (0.01 mg/mL), low permeability hence consequently very low bioavailability (30–40%).^{7,8} Besides, MTX showed multidrug resistance (MDR) in cancer treatment and produced toxicity to a normal cell of the body. Also, MTX produces several adverse reactions like hepatotoxicity, ulcerative colitis, nephrotoxicity, which resulted in the restriction of its clinical applications.⁷

Nano-formulation is a comparatively new scientific field that applies Nano-engineering to health and medicines. Although nanotechnology has multiple applications in the drug delivery system, the development of nanoparticles (nanoscale: 10^{-9} m) based formulation has been a key application in pharmaceuticals.³ In recent decades, nanoparticle engineering for pharmaceutical applications has been developed and reported by researchers.⁹ Among the assorted strategy of conversion of nanoparticles, Nanosuspension (NS) is offering plentiful advantages over conventional oral drug delivery. NS can be defined as a sub-micron colloidal dispersion of nanosized (1–1000 nm) pure drug particles that are stabilized by surfactant/polymer or a mixture of both.¹⁰ NS is gaining a lot of attention in the scientific community because of its numerous benefits, including improved dissolution rate and, as a result, increased bioavailability of poorly soluble and permeable drugs, improved physical and chemical stability of drugs, higher drug loading, dose reduction, and so on.^{2,3} It also improves the AUC and C_{max} of the drug and consequently improves drug safety and efficacy.¹¹ Besides, in the last two decades, NS has been drawing much attention in the pharmaceutical industry and also has been executed commercially.¹⁰ For productive formulation development of the NS various strategy have been reported including top-down (viz. high-pressure homogenization, sonication, etc.) and bottom-up approach (viz. nano-precipitation), etc.^{3,11,12}

For the production of nanosuspensions of poorly soluble medicines, high pressure homogenization is a typical approach. This procedure entails forcing a drug-and-stabilizer suspension through a valve with a small opening under pressure. High-pressure homogenization is usually divided into two categories: (i) Dissocubes (aqueous media homogenization), (ii) Nanopure (homogenization in water-free media or water mixtures). The size of the particles is reduced in homogenization by forcing suspension under high pressure (100–1000 bars) through a small-aperture valve. Cavitation-induced implosion pressures and shock waves in the liquid medium break down microparticles (25 m) into the nano-size range as the static pressure drops due to a sudden drop in fluid velocity. Shear

forces caused by particle collisions and high velocity also aid in the fracture of particles with inherent crystal flaws. Viscosity enhancers can aid the nanosizing process by increasing particle density inside the dispersion area and inhibiting crystal formation. Homogenization can convert metastable amorphous particles generated by precipitation into stable crystal form. To create particles in the desired size ranges, numerous cycles are usually required. The method's main advantages are its ease of scaling up, adaptability to dilute or concentrate suspensions, low risk of contamination, and aseptic manufacturing viability. The approaches include difficulties such as the need for micronized particles, multiple cycles, high energy technique, and the danger of contamination from the container's metal wall.^{13–16}

Further, the physical stability problem of NS has been overcome by various solidification techniques including rotary evaporation, spray drying, lyophilization, etc. Generally, the technique selection has been done based on the physical properties of active pharmaceutical ingredients and the characteristics of the final formulation.¹⁰ Among these techniques, lyophilization is predominately employed for the solidification of NS, which provides several benefits such as suitability for drying of thermolabile drugs, enhanced long-term storage stability, easy reconstitution of the formulation before use, and manufacture of high-value formulation without excessive damage.^{10,11} Furthermore, the development of an oral drug delivery system for anticancer drugs provides the most suitable and easiest way.⁷ Therefore, the development of MTX in lyophilized NS form can be a useful tool to attempt the above-mentioned facts.

Owing to the fast onset of action, permeability, solubility, and bioavailability, a novel drug delivery system (NDDS) is well known for its toxicities. Whereas, the cost of such an advanced NDDS is increasing because of a lack of proper understanding and various manufacturing variability.¹¹ The International Conference on Harmonization (ICH Q8) proposed to use the concepts of quality by design (QbD) to formulate the pharmaceutical products as technical criteria.¹⁷ Owing to the high incomprehension about the effect of critical processing parameters (CPPs), critical material attributes (CMAs) on the attainment of admirable smaller particle size, and narrow polydispersity index (PDI), researchers stressed for the most challenging manufacturing variability during NS formulation development.¹¹

Hence, the present study is aimed to develop MTX-NS to improve its oral bioavailability that can increase its clinical efficacy by reducing the oral dose which is required to achieve the same effect and thus reduces its side effects. QbD approach was applied to obtain the effect of CMAs and CPPs on critical quality attributes (CQAs) viz., particle size, drug content, zeta potential, dissolution profile and bioavailability of MTX-NS, reduction in the manufacturing variability, upgrading of safety and quality in a for-

mulation, and controlling the manufacturing cost. QbD approach was applied to understand and optimize the lyophilized preparation of MTX-NS. In the first step, all the possible potential independent variables were screened by the Plackett-Burman design. A predictive model was then developed for critical response variables to evaluate optimal value by Central composite design (CCD) to produce extremely stable and soluble MTX-NS by the High-Pressure Homogenizer (HPH) technique. The MTX-NS developed was stabilized using the lyophilization process. The MTX-NS was evaluated for their saturation solubility, particle size, and zeta potential analysis, polydispersity index (PDI), crystallinity study, topographical analysis, dissolution efficiency, Apoptosis, and in-vitro cytotoxicity study. Moreover, the in vivo bioavailability and stability study of MTX-NS was also performed.

2. Material and Methods

2. 1. Materials

MTX sample was gifted by Cipla Ltd, Goa (India). Tween 80 and mannitol (MNT) was procured from Merck Specialties Pvt. Ltd. Mumbai, (India). Soya lecithin (SL) (Phospholipon R 90 H) was obtained from Lipoid GmbH (Germany). HPLC grade methanol was purchased from Thermo Fisher Scientific Pvt. Ltd. Mumbai, (India). All other reagents used in the experiments were of analytical grade.

2. 2. Methods

2. 2. 1. Screening of the Stabilizer and Polymers for MTX-NS

For the formulation development of MTX-NS, appropriate stabilizers were obtained from 20 stabilizers as enlisted beneath.

2. 2. 1. 1. Suspending Effect of Stabilizers

Initially, the suitable polymers and stabilizers were screened based on suspending concentration of stabilizers viz., Carbomer 940, cremophor EL-40, poloxamer 407, soya lecithin (SL), hydroxypropyl methylcellulose (HPMC), tween 80, sodium lauryl sulfate (SLS), poloxamer 188 (F68), polyethylene glycol (PEG) 6000, span 80, sodium deoxycholate (SDS), polyvinyl pyrrolidone (PVP) K 30, and/or their mixtures on MTX. About 0.5 mg of MTX was added in 0.2 % w/v surfactant solution, followed by shearing with a high-speed homogenizer for 1.5 h (3000 rpm), followed by centrifugation at 4000 rpm for 30 min duration. The supernatant was diluted using water as a solvent and drug content was measured by UV visible spectrophotometer at 303 nm. As composites for the development of NS, the stabilizer which has shown an effective suspending effect on MTX, smaller particle size, and lower sedimentation rate were optimized.^{18–20}

2. 2. 1. 2. Docking Tool and Algorithm

The virtual interaction among MTX and above-enlisted stabilizers were performed via molecular docking using VLife MDS version 4.6. The chemical structures of enlisted stabilizers and MTX were drawn in a 2D format which was followed by 3D conversion. Finally, these structures were optimized for the docking score. Generally, biopredicta (docking algorithm) is used to predict and study the modes of interaction between two compounds. Herein, the possible interaction between stabilizers and MTX was optimized based on ligand-receptor binding geometry within chemical structures of compounds. Finally, the molecular interaction among stabilizers and MTX were screened to establish the stabilizer's ability to enhance drug solubility and NS stability purpose.

2. 2. 2. Formulation and Lyophilization of MTX-NS

MTX-NS was fabricated by HPH (Panda PLUS 2000, GEA Niro Soavi, Germany). Pre-nanosuspension was first fabricated using a high-speed homogenizer to avoid blockage of the HPH valve. Here, the 0.5 mg/mL coarse powder of MTX was¹⁷ dispersed in an aqueous stabilizer solution of (0.15 % v/v tween 80 and 30 mg of SL) by digital homogenizer (3000 rpm, 1.5 h). Then, the pre-NS was subjected to HPH processing, with three HPH cycles at fixed 250, 700, and 1200 bars. Moreover, this obtained NS was shifted for 1500 bars for maximum cycles. Interestingly, the number of cycles of HPH at constant process temperature can affect the particle size of the formulation. Therefore the MTX-NS showed different particle sizes, concerning process temperature and several cycles. Finally, the obtained NS was shifted to the lyophilization process using a lyophilizer (Freezone12, Labconco, MO, USA) along with the optimized concentration of cryoprotectant (6% w/w mannitol). Initially, the pre-freezing of MTX-NS was performed at $-30\text{ }^{\circ}\text{C}$ for 12 h. Then, the primary drying process of NS was performed at $-53\text{ }^{\circ}\text{C}$ and 0.016 mBar for 24 h. Finally, the secondary drying was carried out at $10\text{ }^{\circ}\text{C}$ for 8 h followed by $25\text{ }^{\circ}\text{C}$ for 4 h. Further drying of obtained lyophilized NS was done by gradually increasing the drying process temperature by $1\text{ }^{\circ}\text{C}/\text{min}$. to finish the process. The temperature of the cold trap was maintained at $-53\text{ }^{\circ}\text{C}$ until the end of the drying process.

2. 2. 3. Quality by Design

2. 2. 3. 1. Quality Target Product Profile (QTPP)

The primary step in QbD is to define the potential target product profile (TPP) and critical quality attributes (CQA) of the formulation. To this study, the CQAs were enlisted based on a literature survey and preliminary research on the formulation. For the study, CMAs, CPPs have been chosen to satisfy the predefined objective.²² The QTPP, CMAs, and CPPs listed are presented in Table S1.

2. 2. 3. 2. Risk Assessment

In the context of risk assessment, the main critical material and process parameters that influence the formulation quality were established. An Ishikawa fishbone diagram is also referred to as a cause-effect diagram, developed to define the CPPs and CMAs. Only three-parameter were indicated as important factors influencing formulation i.e. drug content (DC), and average particle size, as CQAs following the risk analysis using the diagram and preliminary studies. In addition, failure mode effects analysis (FMEA) was utilized for risk assessment, followed by risk rating and filtering following the ICH Q9 recommendations. As shown in Table S2, the risk associated with each element [critical method parameters (CMPs) and critical process parameters (CPPs)] on responses was critically assessed, and the risks were then labeled using the FMEA approach, which measures risk severity. Severity (effect on end method output), regularity of occurrence, and detectability are three major categories which were all used further to define risk variables. The impact of these factors on responses was evaluated from 1 to 3 scale (Table S3). Table S3 lays up the rankings. The sum of the severity, regularity, and detectability was used to calculate the risk priority number (RPN). As stated in Table S4, the RPN values were utilized to rank failure modes, CMPs, and CPPs.^{21, 23, 22, 30}

2. 2. 3. 3. Experimental Design

Eight independent variables were selected based on risk analysis, (Table 1) namely speed of high-speed homogenizer (pre-NS) (X1), time of homogenizer (pre-NS) (X2), homogenization pressure (X3), number of cycles (X4), the concentration of poloxamer 188 (X5), the concentration of sodium lauryl sulfate (X6), the concentration

of tween 80 (X7), the concentration of MTX (X8). For the optimization study of NS, the response surface method was employed. Furthermore, each of these factors were evaluated at two levels, including six center points; Plackett-Burman Design (PB design) was used to study the effect of these variables on the preparation of NS. Design-Expert (Version 11.0.5.0, Stat-Ease Inc., MN) software was used for the analysis of three response variables viz., particle size (Y1), and DC (Y2). The experiment was conducted in random order according to the runs or trials organized by design expert software. Besides, the variable analysis (ANOVA) was used to estimate the significance of interaction and key effects. Factors that have a marginal effect on the reaction variables at a significance level of 95% have been analyzed and CCD further optimizes the remaining important factors influencing the response variables.

2. 2. 3. 4. Central Composite Design (CCD) for Optimization of MTX-NS

After the identification of critical formulation and process variables using PB screening design, CCD response surface methods were used to inspect the optimum levels of the variables. This consisted of two groups of design points, which include two-level factorial design points as -1 and $+1$, axial, or star points as $-\alpha$ and $+\alpha$ along with center points as 0. Thus, the effect of three independent variables viz., the concentration of tween 80 (A), the concentration of poloxamer 188 (B), and the number of cycles (C) was studied at five different levels, with the coding of $-\alpha$, -1 , 0, $+1$, and $+\alpha$. Alpha value, 1.6817 fulfills the rotatability in the CCD. Dependent variables selected for the formulation of MTXNPs by CCD were particle size (Y1), & DC (Y2). Table 2 suggests the coded and actual values of variables. The Design Expert® software was used to gener-

Table 1. Plackett–Burman Design with independent variables and their responses

Factors		Levels	
		High	Low
X1	Speed of Homogenizer (Preliminary Stage) (rpm)	8000	6000
X2	Time of Homogenizer (Preliminary Stage) (min.)	45	30
X3	Homogenization Pressure (Bars * 1000)	25	5
X4	Number of Cycles	25	5
X5	Concentration of Poloxamer 188 (mg)	75	50
X6	Concentration of Sodium Lauryl Sulphate (mg)	75	50
X7	Concentration of Tween 80 (mL)	0.75	0.50
X8	Concentration of Methotrexate (mg)	150	100

Table 2. Central Composite Design with factors and their responses

Factors		Levels				
		$-\alpha$	-1	0	$+1$	$+\alpha$
A	Concentration of Tween 80 (mL)	0.05	0.15	0.25	0.35	0.45
B	Concentration of Poloxamer 188 (mg)	25	50	75	100	125
C	Number of cycles	10	20	30	40	50

ate a CCD matrix with 20 runs, which includes six replicated center points, one axial point, and one replication of fractional point.

2. 2. 4. Process Analytical Technology (PAT) – Particle Size Analysis, EE, and DC

The particle size analysis of developed NS was measured by Zetasizer 300 HAS (Malvern Instruments, Malvern, UK). The DC were calculated by using a UV-visible spectrophotometer (Jasco V-530, Japan) at 303 nm wavelengths. It was used for PAT for NS particle size, and DC.^{23,24}

2. 2. 5. Characterization of MTX-NS

2. 2. 5. 1. Particle Size Analysis

MTX-NS particle size, polydispersity index (PDI), and zeta potential were measured at 25 °C by dynamic light scattering (DLS) method using Zetasizer 300 HAS (Malvern Instruments, Malvern, UK) in triplicates in a 1 ml disposable polystyrene cuvette. For sample preparation, the 1 mg of lyophilized MTX-NS was diluted in 10 ml water, and analysis was performed for independent samples (n = 6.18). The values shown on average are the hydrodynamic sample diameter and the PDI value measured is the size distribution width. Besides, the zeta potential of NS was measured at the above-mentioned zeta sizer. It is determined at an average of measurements based on the electrical mobility of particles in an electric field.^{11,24}

2. 2. 5. 2. Scanning Electron Microscopy (SEM)

The morphology of MTX-NS was determined by SEM (JEOL JSM-6360, Japan). Imaging was performed on SEM at a voltage of 20 kV and a high vacuum. Lyophilized MTX-NS was placed on two-sided carbon tape and sputtered using gold-palladium alloy (3–5 nm of thickness) and imaging was captured using SEM.²⁵

2. 2. 5. 3. X-ray Crystallography (XRD)

Powder XRD analysis of pure drug, physical mixture (PM), and optimized NS were performed using an X-ray diffractometer (Philips analytical XRD, PW 3710) with Cu-K α radiation (1.54 Å), at 40 kV, 40 mA by passing through a nickel filter. The samples were prepared by spreading the powder samples on the specimen holding ring and further it was subjected to sample angular scan. The samples were analyzed in the 2 θ angle range of 5 to 80°. The range and the chart speed were 5 \times 10³ CPS and 10 mm/ $^{\circ}$ 2 θ , respectively.²⁵

2. 2. 5. 4. Differential Scanning Calorimetry (DSC)

The samples of pure drug, physical mixture (PM), and optimized NS were accurately weighed and filled in aluminum pans followed by a sealing process and then shifted to DSC using Perkin-Elmer Pyris 6 DSC, coupled

with Pyris software and equipped with a thermal analyzer (Perkin-Elmer Instruments, Norwalk, USA). Thermograms were taken from 35 to 300 °C with a heating rate of 10 °C min⁻¹ using a bare aluminum pan as a reference by heating the sample in the nitrogen atmosphere.¹¹

2. 2. 5. 5. Fourier Transform Infrared Spectroscopy (FTIR)

The FTIR of the drug, physical mixture (PM), and optimized lyophilized NS were obtained using the FTIR spectrophotometer (Agilent CARY 630 FTIR). The above-mentioned samples were crushed to a fine powder, milled with potassium bromide, and pressed to form a thin pellet, and subjected to analysis.²⁵

2. 2. 5. 6. Saturation Solubility Studies

Excess pure drug (MTX) and lyophilized MTX-NS in 10 mL of distilled water were added to their saturation, followed by agitation using an orbital shaker for 48 h at 25 °C. The obtained samples were subjected to centrifugation. Then the supernatant layer was analyzed using a UV-visible spectrophotometer at 303 nm.^{11,26}

2. 2. 5. 7. Total Drug Content

About 10 mg of MTX-NS was dissolved in water followed by filtration using 0.45 μ m filter paper. Finally, the filtrate was collected and subjected to total DC analysis using a UV-visible spectrophotometer (Shimadzu-1700, Japan) at λ max of 303 nm. The total DC (TDC) and percentage TDC were calculated from equations 1 and 2.²⁰

$$\text{TDC} = (\text{Vol. total} / \text{Vol. aliquot}) \times \text{drug in aliquot} \times 100 \quad (1)$$

$$\% \text{TDC} = \text{TDC} / \text{TAD} \times 100 \quad (2)$$

where, TAD: vol. total/vol. an aliquot is the total volume of NS to the taken aliquot volume and the total amount of drug i.e. TAD is the drug used for the fabrication of NS.

2. 2. 5. 8. Entrapment Efficiency

About 10 mg of MTX-NS was dissolved in 10 ml of water and % EE was determined by ultracentrifugation for 30 min at 10,000 rpm using a cold centrifuge (at 4 °C, Remi CM 12 Plus, Mumbai). The supernatant obtained was quantified in triplicates at 303 nm using a UV-visible spectrophotometer. EE is the percentage of drug entrapped in nanoparticles and can be calculated using a given formula.^{11,29}

$$\% \text{EE} = \frac{\text{Total drug content (mg)} - \text{Free Drug (mg)}}{\text{Total drug content (mg)}} \times 100 \quad (3)$$

2. 2. 5. 9. In-vitro Drug Release

Dissolution studies on MTX powder and optimized MTX-NS were performed using USP type-I apparatus (Basket). About 50 mg of weighed quantities of samples

were transferred into the dissolution apparatus (Electro lab TDT-08 L, India) containing 900 mL of simulated intestinal fluid (SIF) with pH 6.8 as a medium at 50 rpm with 37 ± 0.5 °C temperature. For analysis, 5 mL samples were withdrawn at 10, 20, 30, 40, 50, and 60 min. of time points, and the fresh buffer was added for sink condition maintenance. The samples were collected and filtered using the Whatman filter paper (0.25 μ m, Whatman Inc., USA) and subjected to UV spectrophotometer analysis at 303 nm.¹⁹

2. 2. 5. 10. Cytotoxicity Activity on Human Breast Cancer Cell Line (MCF-7 Cells)

Cell Culture: Cytotoxicity of optimized MTX-NS and aqueous dispersion (AQD) was studied on human MCF-7 breast cancer cell lines, which were procured from NCCS (National Centre for Cell Sciences), Pune, India. They were stored and nurtured in DMEM (Dulbecco's modified eagles medium of Sigma Aldrich, USA). Cell lines were cultured and maintained in a 25 cm² flask of tissue culture with DMEM which was boosted with L-glutamine, 10% FBS, sodium bicarbonate (Merck, Germany), and with an antibiotic solution containing streptomycin (100 μ g/ml), amphotericin B (2.5 μ g/ml) and penicillin (100U/ml). These cultured cells were then kept in a CO₂ incubator at 37 °C with 5% humidity.

MTT assay: In each well of 96 well microtiter plates, about 50 μ L 1×10^5 cells/mL cell suspension was seeded and end volume was made to 150 μ L by adding DMEM media. Dilutions of NS were made in DMEM media and about 100 μ L of different concentrations of NS and their aqueous dispersion (AQD) (62.5, 125, 250, 500, 1000 μ g/mL) were added and incubated for 48 h in presence of CO₂ incubator at 37 °C with 5 % humidity. After 48 h, 20 μ L 3-(4,5-dimethylthiazol-2-yl)-2,5-diphenyl tetrazolium bromide (MTT) reagent (5 mg/mL) was added to the wells and the plates were kept for 4 h to incubate in a dark place at room temperature. The plates were covered with aluminum foil as the MTT reagent is photosensitive. Without disturbing the precipitated formazan crystals, the supernatant was removed carefully and 100 μ L dimethyl sulfoxide (DMSO) was added to dissolve the formed crystals. The OD (optical density) was measured using the ELISA microplate reader at 492 nm. The baseline was obtained using a culture medium and the wells with only cells were used as control. With an assessment of colorimetry and spectrophotometry, the *in-vitro* growth inhibition effect of NS and AQD was measured by the conversion of MTT into "Formazan blue" by living cells. The study was performed in triplicates. The generated dose-response curve was used to estimate the IC₅₀ of test samples required to inhibit the growth of 50% cells. The % growth inhibition was calculated using the following formula (equation 4),

$$\text{Growth inhibition (\%)} = 1 - \frac{\text{Mean OD of the test compound}}{\text{Mean OD at untreated cells}} \times 100 \quad (4)$$

2. 2. 5. 11. Direct Microscopy

The entire plate was observed under an inverted phase-contrast tissue culture microscope after 48 h of treatment with NS and AQD and observations were recorded as a microscopic image. A change in the morphology of cells, like rounding or shrinking, vacuolization, and granulation in the cell cytoplasm is an indication of cytotoxicity.

2. 2. 5. 12. Apoptosis Study by Fluorescent Microscopy using Eb (Ethidium Bromide) and AO (Acridine Orange) Double Staining Method.

The MCF-7 cells were washed using cold phosphate buffer saline solution (PBS) after treating them with different concentrations of NS and AQD as 13.2262 μ g/mL, 26.4524 μ g/mL (LD 50 Concentration), 52.9048 μ g/mL for forty-eight-hour, following AO (100 μ g/ml) and EtBr (100 μ g/ml) stains for 10 min at RT. Further, with 1X PBS solution the cells which are stained are washed twice and were observed under a fluorescent microscope using a blue filter (Zhang et al., 1998). Based on staining reactions, the cells were grouped as normal green nucleus (living cells), bright green colored nucleus with fragmented or condensed chromatin (early apoptotic), orange-colored nuclei with condensation or fragmentation of chromatin (late apoptotic), and uniformly orange-stained cell nuclei (necrotic cells).

2. 2. 5. 13. Pharmacokinetic and Biodistribution Study in Rats

Sprague- Dawley rats (mean weight 200–220 g) were purchased from Global Bioresearch Solutions Pvt. Ltd., Pune. The pharmacokinetic (PK) and biodistribution studies of MTX were performed using the Sprague- Dawley rats model (BVCPK / CPCSEA /IAEC / 01/14/2017-2020). Initially, rats were kept on fast overnight with free access to water *ad libitum*. For the study, rats were randomly divided into three groups (n = 3). Group I was selected as the test group (MTX-NS), the standard group (group II) was treated with MTX-AQD, and group III (control group) was given a normal saline solution. On the day of the study, the rats have been dosed (40 mg/kg) with optimized MTX-NS and MTX-AQD via oral feeding cannula. Blood samples (0.5 mL) were obtained from the retro-orbital vein at predetermined intervals of 0, 2, 3, 4, 6, 12, 24, 36, 48 hours under mild anesthesia and transferred into a tube containing EDTA. Finally, blood samples were centrifuged immediately at 3,000 rpm for 10 min at 4 °C, and separated plasma and samples were stored at -20 °C. The rats were sacrificed (n = 3) using the cervical dislocation method. The distribution of the drug in vital organs is measured after 72 h of dosing. Spleen, liver, heart, brain, lungs, stomach, and kidney tissue samples were homoge-

nized and centrifuged to get clear tissue samples, further stored at $-20\text{ }^{\circ}\text{C}$.

Plasma and tissue sample preparation: The tissue and plasma blood samples have been combined with $20\text{ }\mu\text{L}$ (MTX) solution ($5\text{ }\mu\text{g}/\text{mL}$) and deproteinization of the sample was achieved by applying $100\text{ }\mu\text{L}$ acetonitrile to a $50\text{ }\mu\text{L}$ plasma sample and $300\text{ }\mu\text{L}$ acetonitrile to $200\text{ }\mu\text{L}$ of clear homogenates of tissue followed by cold centrifugation ($6,000\text{ rpm}$, 15 min) at $4\text{ }^{\circ}\text{C}$. The collected transparent supernatant was filtered by a syringe filter ($0.20\text{ }\mu\text{m}$) and injected into the HPLC for the determination of MTX content in tissue and blood samples.^{23,27}

2. 2. 5. 14. Pharmacokinetic Analysis

A non-compartmental model was used to perform the PK study of the plasma concentration-time profile using Microsoft Excel (Microsoft office 2016). PK parameters obtained directly from plasma data, includes AUC_{0-t} (AU plasma concentration-time curves), T_{max} (the time to reach maximum plasma concentration), C_{max} (maximum plasma concentration), K_{el} (elimination rate constant), $t_{1/2}$ (elimination half-life), Cl (clearance), VD (volume of distribution), MRT (mean residence time), and F_{rel} (relative bioavailability). Lyophilized MTX-NS F_{rel} after oral administration was measured with the AQD as a reference using the following formula (Equation 5).

$$F_{\text{rel}} = \frac{\text{AUC}_{\text{test}}}{\text{AUC}_{\text{reference}}} \times 100 \quad (5)$$

All data were revealed as \pm SD (mean) and the level of significance was taken as $P < 0.05$ ²². While the Absolute bioavailability ($F\%$) is calculated by comparing exposure of drug by extra vascular route of MTX NS to its i.v. an administration which is assumed to be 100%. It is calculated by the given formula (equation 6):

$$F\% = \frac{\text{AUC}_{e.v.}}{\text{AUC}_{i.v.}} \times \frac{\text{Dose}_{i.v.}}{\text{Dose}_{e.v.}} \times 100 \quad (6)$$

2. 2. 5. 15. HPLC Analysis of MTX

The MTX content was analyzed through reverse-phase (RP)- HPLC (UV detector system, intelligent HPLC pump, Model Jasco PU-2080) using a reverse-phase C18 column ($5\text{ }\mu\text{m}$ pore size, $150 \times 4.6\text{ mm}$, Phenomenex). The optimized mobile phase was ($70:30\text{ v/v}$) water and acetonitrile mixture. For separation, HPLC analysis was performed using a constant flow rate ($1.0\text{ mL}/\text{min}$), with a $20\text{ }\mu\text{L}$ injection at $25\text{ }^{\circ}\text{C}$ column temperature, and 303 nm wavelengths under isocratic conditions. The curve of calibration for MTX in plasma was found within the linear concentration range of $15\text{--}100\text{ }\mu\text{g}/\text{mL}$ ($R^2 = 0.9865$) with pazopanib as an internal standard. The experimental outcomes indicate a mean \pm SD and < 0.05 level of significance.

2. 2. 5. 16. Stability Studies

The stability studies of optimized lyophilized MTX-NS and liquid MTX-NS were performed [ICH Q1A (R2)].

In brief, the developed formulations were wrapped into aluminum foils and stored in a refrigerator at $4\text{ }^{\circ}\text{C}$, room temperature, and $40^{\circ} \pm 2\text{ }^{\circ}\text{C}/75 \pm 5\%$ relative humidity (in the stability chamber) for 6 months. As per the defined time interval, the DC and particle size were calculated to check the chemical as well as physical stability of developed MTX-NS.¹¹

2. 2. 5. 17. Statistical Analysis

The outcomes of the study were analyzed using ANOVA, multilinear regression analysis, and lack-of-fit tests. Student's t-test where appropriate, was used and expressed as mean \pm SD ($n=3$), to test the statistical significance.¹¹

3. Results and Discussion

3. 1. Screening of the Stabilizer for MTX-NS

3. 1. 1. Suspending Effect of Stabilizers on MTX

In the development of NS, stabilizers and polymers play a crucial role. A lack of adequate stabilizers causes aggregation of nano-sized drug particles due to extremely free of surface energy. An admirable stabilizer efficiently decreases the nanoparticle's surface energy by dispersing them at a water and particle interface to avoid particulate accumulation in the NS. Moreover, the ionic/steric barrier is therefore stopped from Ostwald's ripening. A stable MTX-NS system with a suitable stabilizer was optimized by various factors such as sedimentation effect, suspending effects, and particle size analysis (Table S5).^{18,28}

The combination of poloxamer 188/ tween 80/SLS ($198.87 \pm 0.01\text{ }\mu\text{g}/\text{ml}$) presented superior suspending effect on MTX, followed by poloxamer 188 ($126 \pm 0.05\text{ }\mu\text{g}/\text{ml}$), tween 80 ($119.14 \pm 0.04\text{ }\mu\text{g}/\text{ml}$), and SLS ($112.83 \pm 0.05\text{ }\mu\text{g}/\text{ml}$). While the particle size of the formulation prepared by poloxamer 188/ tween 80/SLS, poloxamer 188, tween 80, and SLS was found to be 332.45 ± 1.03 , 293.46 ± 3.32 , 301.65 ± 1.45 , and $349.09 \pm 2.18\text{ nm}$ respectively. Poloxamer 188, tween 80, and SLS did not produce stratification and sedimentation. The high surface free energy of nanosized particles makes NS a highly unstable thermodynamic system. Thus, to optimize the surfactant and stabilizer system and to stabilize the nanosuspension, the CCD response surface was designed to finalize the surfactant and their concentration from the above results, with the highest electric repulsions.

3. 1. 2. Molecular Docking

The interactions between MTX and stabilizers show that stabilizers can solubilize drugs to improve their stability in the present study. Figure 1 shows the virtual interaction between MTX and stabilizers. In this study, the MTX and stabilizers lead to strong interaction by using less

binding energy with strong hydrogen, hydrophobic, and Vander Waal interactions. This means that stronger hydrogen bonding between the MTX and stabilizers like Poloxamer 188 and Tween 80 can virtually improve the stability and solubility of MTX.

3. 3. Quality by Design

3. 3. 1. Risk Assessment

For identification of possible risks of process and formulation variables on the CQAs, viz., DC, EE, and particle

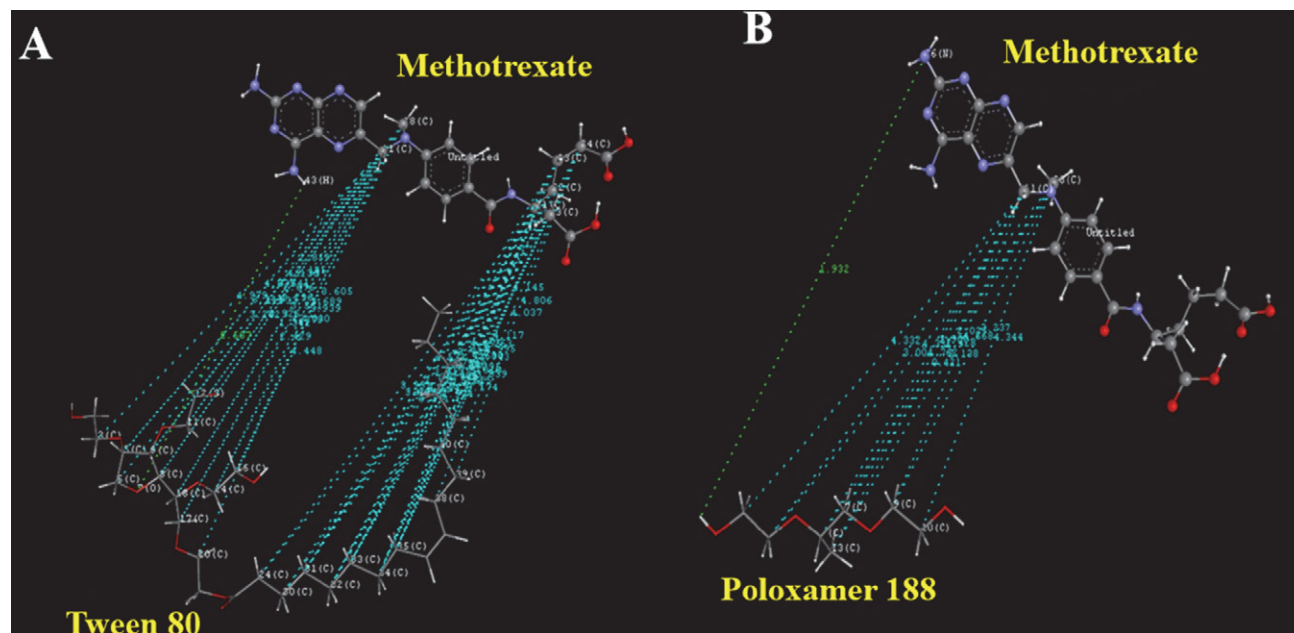


Figure 1. Docking study: a) interaction of MTX with Poloxamer 188, b) interaction of MTX with tween 80. *Colour code Light blue: Vander Waal interaction, Green: Hydrogen bonding

3. 2. Process Analytical Technology (PAT): – Particle Analysis, %EE, and DC

MTX-NS was developed using Tween 80 as a stabilizer and Poloxamer 188 as polymers with the applications of the QbD.¹⁷ As a result of the PAT study, the particle size, EE, and DC of the developed NS were found to be in the range of 239.30–309.60 nm, 99.42–99.96%, and 87.56–88.32% respectively.

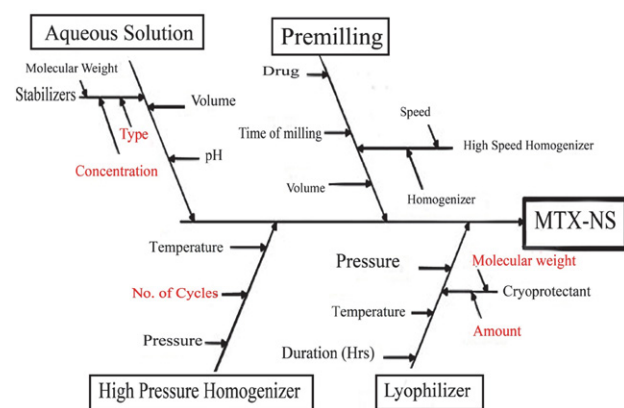


Figure 2. Ishikawa Diagram illustrating process and formulation variables that may have an influence on the properties of MTX-NS

size of MTX-NS an Ishikawa diagram was established (Figure 2). As a result of risk analysis, the 8 possible risk factors were identified based on preliminary experiments and prior knowledge and were further evaluated using experimental designs.¹¹

3. 3. 2. Plackett–Burman Design

PB design is carried out by introducing 8 factors, at 2 levels, with 12 runs to screen the significant formulation and process variables for the development of MTX-NS. The formulations were piloted and the resulting response values are listed in Table 3. The significant and most contributing factors for the first response i.e. particle size (Y1) were the speed of homogenizer (X1, pre-NS), the concentration of tween 80 (X7), and the concentration of poloxamer (X5) respectively (Table 4). The value of R^2 found was 0.8990, which indicates a significant model fitting of the tested model. From ANOVA the p-value for main effects obtained was 0.1750, which was not statistically significant. Hence, by using CCD most significant factors were further evaluated. The particle size plays a crucial role for MTX-NS as they affect the stability, drug release, bio-availability and biodistribution, and cellular uptake of drugs.

Following polynomial equation 7 can describe Y1,

Table 3. Plackett–Burman experimental design matrix with observed values of response variables.

Batch code	X1 (rpm)	X2 (min.)	X3 (Bars *1000)	X4	X5 (mg)	X6 (mg)	X7 (mg)	X8 (mg)	Y1* (nm)	Y2* (%)
1	1	-1	1	1	-1	1	1	1	141 ± 0.12	76.13 ± 0.16
2	-1	-1	-1	-1	-1	-1	-1	-1	208 ± 0.10	73.55 ± 0.19
3	-1	-1	-1	1	-1	1	1	-1	167 ± 0.22	64.36 ± 0.13
4	-1	-1	1	-1	1	1	-1	1	215 ± 0.15	74.63 ± 0.11
5	-1	1	-1	1	1	-1	1	1	152 ± 0.11	92.56 ± 0.17
6	-1	1	1	1	-1	-1	-1	1	228 ± 0.21	77.13 ± 0.19
7	1	1	-1	1	1	1	-1	-1	188 ± 0.19	97.5 ± 0.20
8	1	1	1	-1	-1	-1	1	-1	202 ± 0.10	69.28 ± 0.22
9	-1	1	1	-1	1	1	1	-1	199 ± 0.13	76.5 ± 0.13
10	1	1	-1	-1	-1	1	-1	1	151 ± 0.16	76.5 ± 0.15
11	1	-1	-1	-1	1	-1	1	1	175 ± 0.21	72.92 ± 0.17
12	1	-1	1	1	1	-1	-1	-1	220 ± 0.24	67.98 ± 0.12*

Mean ± SD (n = 3).

Table 4. ANOVA analysis for response variables in Plackett – Burman design matrix

Factors	Y1: Particle size (nm)		Y2: Drug content (%)	
	p value	% Contribution	p value	% Contribution
β ₀ : Constant	0.1750	–	0.2884	–
A : Speed of homogenizer* (rpm)	0.0715	25.23	0.1953	13.78
B : Time of homogenizer* (min.)	0.8133	0.22	0.1761	15.52
C : Homogenization pressure* (Bar*1000)	0.8591	0.13	0.3962	4.87
D : Number of cycles	0.5473	1.54	0.1283	21.72
E : Concentration of Poloxamer 188 (mg)	0.0550	31.52	0.1339	20.80
F : Concentration of SLS* (mg)	0.5473	1.54	0.5495	2.26
G : Concentration of Tween 80 (mg)	0.0594	29.56	0.4109	4.53
H : Concentration of Methotrexate* (mg)	0.8361	0.17	0.6175	1.54

$$\text{Particle size} = +187.17 - 14.17^*A + 1.33^*B - 1.00^*C + 3.50^*D - 15.83^*E + 3.50^*F + 15.33^*G - 1.17^*H \quad (7)$$

The equation represents, with an increase in the concentration of SLS and concentration of tween 80, there is an increase in average particle size, while increasing the concentration of poloxamer 188, decreases the average particle size (Y1). Particle size also decreases with an increasing speed of homogenizer and pressure of high-pressure homogenizer, with increasing MTX concentration. The decreased size of particles is also seen with the increasing time of homogenizer and the number of cycles of

ber of cycles (X4), and the concentration of poloxamer 188 (X5), respectively (Table 1). The R² value was 0.8502 indicating a significant fit for the model being tested. From ANOVA the *p*-value for main effects obtained was 0.2884, which was not statistically significant. Hence, CCD was used for further significant factors evaluation. DC has a chief part in a therapeutic activity at a given dose of MTX in NS.

Following polynomial equation 8 describes Y2,

$$\text{DC} = +86.58 + 2.18^*A + 2.31^*B - 1.30^*C + 2.74^*D - 2.67^*E - 0.88^*F - 1.25^*G + 0.73^*H \quad (8)$$

HPH. Thus, from all the process variables, the percentage contribution for average particle size is a concentration of tween 80 (29.56%), the concentration of poloxamer 188 (31.52%), and the speed of homogenizer (25.23%), respectively. The smallest particle of 141 nm could be achieved by experimenting using 0.5 mL of tween 80, 75 mg of poloxamer 188 at 8000 rpm speed.

For the DC (Y2), the most contributed and significant factors were the time of homogenizer (X2), the num-

Polynomial equation 8 represents that, DC (Y2) was increased with increasing concentration of MTX and speed of homogenizer, while it decreases with an increasing concentration of poloxamer 188, SLS, and tween 80, respectively. It also increases with an increasing number of HPH cycles and the time of homogenizer. DC also decreases with the increasing pressure of HPH. From all the process variables, the % contribution of a time of homogenizer (15.52%), number of cycles (21.72%), and concentra-

tion of poloxamer 188 (20.80%) influence DC, respectively. Thus, achieving 97.50% of DC in MTX-NS could be achieved by experimenting using 50 mg of poloxamer 188 for 45 min homogenization at 25 cycles of HPH.

3. 3. 3. Optimization of MTX-NS by Central Composite Design

3. 3. 3. 1. Model Fitting

By design of expert (DOE), 20 runs were proposed and the input of predicted and observed values for Y1, and Y2, responses range from 229.3 to 300.6 nm, and 85.56 to 89.43%, respectively (Table 5). Using DOE software, the obtained responses were fitted to cubic, 2FI, quadratic and linear models (Table S6). As the R^2 values were greater than 0.9, and both the predicted and observed values were less comparable with standard deviations (SD) (< 1.0%) and precision values, the best-fitted model for Y1, Y2, and Y3 were quadratic.²⁵ As the ratios of maximum to minimum responses values were less than 10, transformation is not necessary (Y1 = 5.61; Y2 = 2.46; Y3 = 8.22).

Effect on Size of Particle (Y1)

The proposed polynomial equation 9 for particle size is as follows,

$$Y1 = +268.92 + 2.83 (A) - 0.10 (B) - 4.14 (C) \quad (9)$$

Where, Y1 is particle size, (A) concentration of tween 80, (B) concentration of poloxamer 188, (C) number of cycles for MTX-NS formulation by HPH.

The F value was 2.89, which demonstrated that the used model was significant. While their model terms were not significant as the Prob>F p-value is <0.0567, hence these models are used to develop the design space. The impact of independent factors on particle size was studied using 3D response surface plots. The Y1 responses predicted values range from 244.34 to 299.02 nm. The positive value of the coefficient represents an increasing particle size. Figure 3A and Figure S1, predicts that as the concentration of tween 80 (A) increases from 0.05 to 0.45 ml, the particle starts to aggregate. It may be because of the saturation of surfactant in NS, as formed particles are adsorbed by an excess concentration of surfactant present in NS.

Table 5. CCD matrix with predicted and observed values of responses

Batch	Independent variables			Dependent variables		Predicted values	
	A (mg)	B (mg)	C	Observed values Y1* (nm)	Y2* (%)	Y1 (nm)	Y2 (%)
1	-1	1	1	280.60 ± 0.10	87.67 ± 0.07	280.09	86.85
2	0	0	0	272.80 ± 0.08	88.64 ± 0.11	268.92	88.43
3	0	0	0	270.30 ± 0.03	88.58 ± 0.09	268.92	88.43
4	0	0	0	269.40 ± 0.07	88.13 ± 0.06	268.92	88.43
5	0	0	1.68179	260.40 ± 0.05	86.80 ± 0.04	274.21	86.96
6	-1.68179	0	0	289.40 ± 0.11	85.89 ± 0.08	289.51	86.56
7	1	1	-1	278.20 ± 0.09	88.39 ± 0.11	281.22	86.85
8	0	0	0	268.50 ± 0.10	88.12 ± 0.1	268.92	88.43
9	0	-1.68179	0	250.00 ± 0.05	86.32 ± 0.06	244.69	86.95
10	1	-1	-1	300.60 ± 0.06	87.32 ± 0.09	294.22	86.95
11	1	-1	1	273.20 ± 0.08	89.43 ± 0.11	277.25	88.64
12	1	1	1	275.40 ± 0.12	86.74 ± 0.08	252.95	86.76
13	0	0	0	263.80 ± 0.07	88.96 ± 0.12	268.92	88.43
14	0	0	-1.68179	292.20 ± 0.08	85.26 ± 0.09	288.12	86.78
15	0	0	0	270.40 ± 0.06	88.44 ± 0.05	268.92	88.43
16	-1	-1	1	277.40 ± 0.07	85.62 ± 0.06	267.50	85.96
17	-1	-1	-1	240.20 ± 0.10	86.84 ± 0.10	255.77	85.63
18	-1	1	-1	290.60 ± 0.09	88.73 ± 0.09	279.66	88.32
19	1.68179	0	0	289.40 ± 0.05	86.57 ± 0.11	299.02	87.59
20	0	1.68179	0	229.30 ± 0.11	86.56 ± 0.09	244.34	87.62

* Y1= Particle size; *Y2=Drug content; *Y3=Entrapment efficiency. *Mean ± SD (n = 3).

3. 3. 3. 2. Analysis of Response Surface Plots

Response surface plots were extensively employed for the study of the interaction effects of selected factors on their responses and relationships. Thus, we have constructed a surface response plot for three responses (Y1, and Y2), which are depicted in Figure 3.

When the concentration of poloxamer (B) increases from 25 to 105 mg respectively, it prohibits the re-aggregation of dispersed particles leading to the existence of smaller bodies in NS. Further, it resulted in the decreased particle size of NS. The number of cycles (C) for HPH shows a direct relationship with particle size, with increased C the size of

particle decreases. Effectively, the coefficient with a negative value is represented by decreasing particle size. An increase in the number of cycles leads to a reduction in the size of the particle of NS by increasing the viscosity of the system, which inhibits the Ostwald ripening. This is the reason for particle size reduction. Thus, it is a CQA and the factors i.e. concentration of poloxamer 188 and number of the cycle that affects particle size was optimized by CCD.

Effect on DC (Y2)

The proposed polynomial equation 10 for DC is as follows,

$$Y2 = +88.42 + 0.3055(A) + 0.1995(B) + 0.0560(C) \quad (10)$$

The predicted Y2 response values range from 85.63 to 88.78 %. The design was not significant as the F value was 1.63, while model terms were not significant as the

$\text{Prob} > F$, a p -value is < 0.2292 , hence these models were not used to develop the design space. Here as 'A' increases, there is an increase in DC. While the concentration of 'B' shows an increasing effect on DC (Figure 3B and Figure S1). DC also increases with increasing 'C'. The amount of drug i.e. dose present in nanoparticles is significant to study for the dissolution and pharmacokinetic parameters. However, DC had the most important effect on drug dissolution, which directly affects drug absorption and thus bioavailability.

3. 3. 4. Optimization Model Validation

To achieve the predicted (software suggestions) composition, targeted criteria were fed into the software. The software-suggested values were selected as a region of interest based on desirability values and were practically used for their verification. The design expert software was

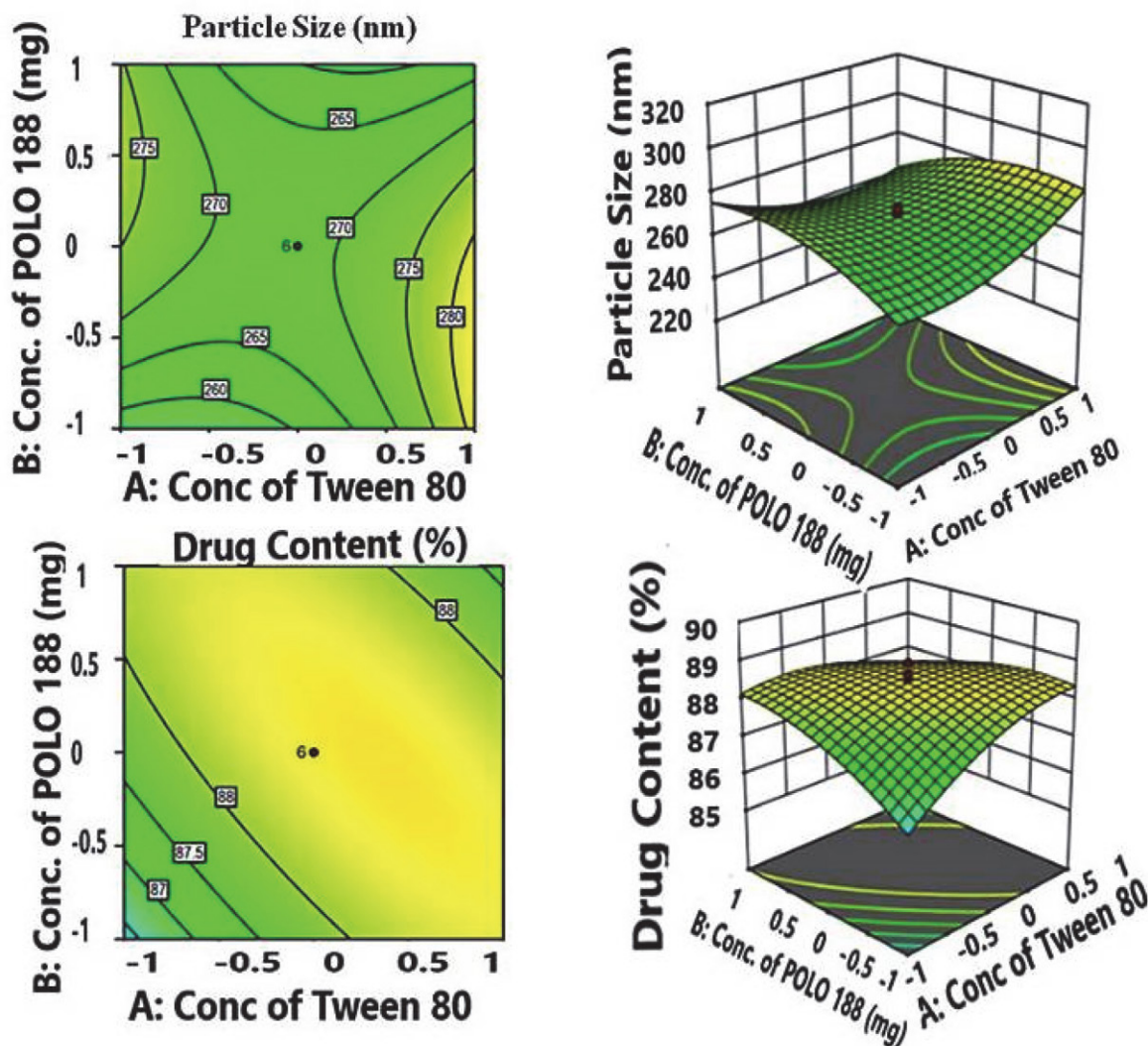


Figure 3. A) 3D surface response plot showing: a) The effect of factor A (Concentration of tween 80) and factor B (concentration of poloxamer 188) on response Y1 (particle size). B) The effect of factor A (Concentration of tween 80) and factor B (concentration of poloxamer 188) on response Y2 (drug content). C) The effect of factor A (Concentration of tween 80) and factor B (concentration of poloxamer 188) on response Y2 (drug content).

used to statistically validate the obtained polynomials by ANOVA. The design space was constructed using a graphical method for this study. The desirability values based on selected software suggestions were observed as 1, providing 100 % assurances to achieve the targeted product with efficient CPPs and CMAs (Table S7). Thus greater desirability value more possibility to gain the target product (Figure S2). The final formulation was prepared with optimized CPPs and CMAs, and its CQAs were analyzed. The predicted and actual results of CQAs were used to calculate the values of residuals to ensure the attainment of the design space. The calculation of residual values is also a verification/validation of the model and CQAs. The values of residuals were calculated as percent residual using the following formula:

$$\text{Percent residual} = \frac{\text{Software suggested results} - \text{Actual obtained results}}{\text{Software suggested results}} \times 100 \quad (11)$$

The residuals were observed with very low values (–1.27 to –0.07) which indicates that the obtained results with software predicted one has a very strong correlation. Residuals with lower values have more reproducibility and lesser variation of CQAs with the optimized CPPs and CMAs. The impact of concentration of tween 80 and concentration of poloxamer 188 (independent variables) was observed as more predominant from DOE results. The number of cycles favors the size of particles and the DC of MTX-NS. Thus to enhance the adaptability of the method, the number of cycles was fixed to 25 cycles and by using the remaining two factors the design space was developed. The overlay plot obtained from DOE software shows the design space to select the optimum tween 80 and poloxamer 188 concentrations to prepare highly stable NS with a lower size of particles (Figure S3). The three points that are located in the design space predict good responses. By changing the composition of factors 'A' and 'B' as per design space and keeping the number of cycles fix, three formulations, MTX-NS1, MTX-NS2, MTX-NS3 were developed and then characterized for three dependent variables. The plots constructed between observed and predicted responses showed a better relationship between the observed (actual) and theoretical (predicted) values for particle size (Y1), and DC (Y2) responses (Table 6). Negligible changes were seen in DC and particle size of MTX-NS1, MTX-NS2, and MTX-NS3 as compared to the above for-

mulations. The MTX-NS3 was selected as an optimized MTX-NS formulation based on the data obtained from the two responses. Further, they were dried using Lyophilizer with 6% of mannitol as an optimized cryoprotectant to stabilize the system.

3. 3. 5. Particle Size and Zeta-potential Analysis

MTX is a coarse micronized powder with fine texture, poor flow property, and aqueous solubility. The average particle diameter of pure MTX was 16.64 ± 8.55 μm , indicating broad particle size distribution (PI: 0.945). The freshly prepared NS was lyophilized to enhance product stability. The lyophilized MTX-NS powder was smooth in appearance with a particle size of 260 ± 0.25 nm, respec-

tively (Figure 4A) which was easily re-dispersed upon gentle shaking. The PDI represents size distribution and the potency of the measured average diameter of the drug components determined by the DLS system. Optimized lyophilized MTX-NS, showed, PDI values 0.212 ± 0.33 , respectively indicating a narrow distribution of particle size. The lower PDI value indicates better stability of NS. Narrow and uniform particle size distribution favors dissolution enhancement, boosts intestinal absorption, and improves oral bioavailability.

Another important significant index is zeta potential, which directly affects the dispersion system stability, as it reflects steric or electrostatic barriers preventing agglomeration and aggregation of

nanoparticles. When drug particles possess very low values of zeta it provides appropriate steric or electric repulsion between each other, aggregation of particles is likely to occur. The zeta of reconstituted MTX-NS was found to be -11.6 ± 7.52 mV, which indicates the admirable physical stability of the developed nanosystem (Figure 4 B).

3. 3. 6. Saturation Solubility Studies

The saturation solubility (SS) studies of pure drug MTX with their optimized lyophilized formulations viz., MTX-NS was done using double distilled water. The SS of MTX-NS was 1487.23 ± 0.064 $\mu\text{g/ml}$, respectively. While

Table 6. Results of optimized batches obtained from an overlay plot of Design expert software

Optimized batch	Independent variables			Dependent variables		Predicted value Y1 (nm)	Predicted value Y2 (%)	Zeta Potential (mV)
	A	B	C	Observed value Y1 (nm)	Observed value Y2 (%)			
MTX-NS1	0.12	75.8	25	271 ± 0.32	88.45 ± 0.33	272.43	88.23	-5.97 ± 7.01
MTX-NS2	0.13	74.2	25	267 ± 0.24	87.20 ± 0.54	266.16	87.80	-9.06 ± 6.19
MTX-NS3	0.10	76	25	260 ± 0.25	88.65 ± 0.24	259.71	87.35	-11.6 ± 7.52

[†]Mean \pm SD (n = 3).

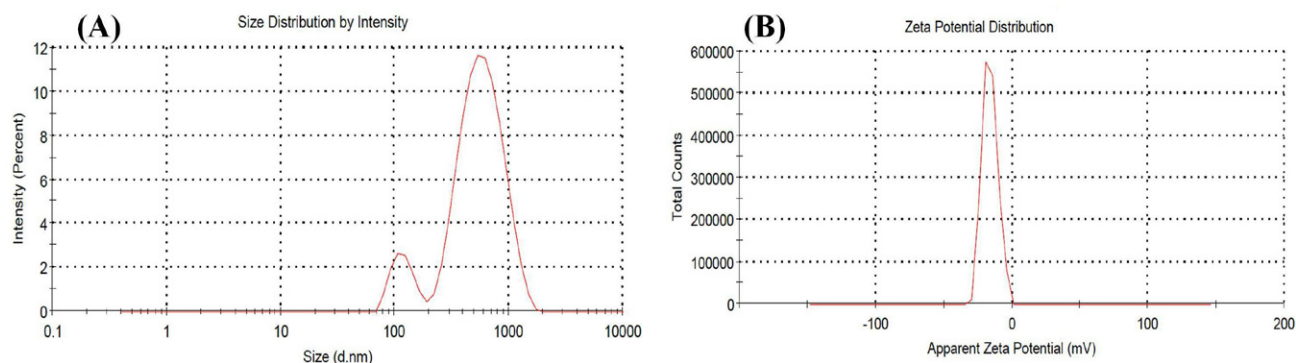


Figure 4. A) Average particle size for optimized batch MTX-NS. B) Zeta potential for MTX-NS optimized batch

for coarse MTX, the SS was $178.96 \pm 0.02 \mu\text{g/ml}$. Here the SS of MTX, in NS form is increased by 8.31 folds. This is because of the decreased size of particles and the enhanced surface area of NS as compared to pure drugs. Ostwald Freundlich equation states that decreasing particle size increases saturation solubility (C_s)

$$\frac{\log C_s}{C} = \frac{2sV}{2.303RT r_1 r} \quad (12)$$

Where, s = substance interfacial tension, R = gas constant, C = solids solubility with large particles, r_1 = density of the solid, C_s = solubility, r = radius, V = particle molar volume, and T = absolute temperature. Another reason that increases saturation solubility is explained by the Kelvin equation, which suggests that with increased curvature the dissolution pressure increases with decreasing particle size. The particle size when reduced to the nanometer range, the curvatures then formed are enormous.

3. 3. 7. Surface Topographical Studies

3. 3. 7. 1. Scanning Electron Microscopy (SEM)

SEM of MTX shown that the coarse MTX particles bear an average size of particle $16.64\text{--}17.5 \mu\text{m}$ with broad

size distribution and mostly composed of drug crystals that are fragmented (Figure 5 a). The SEM (Figure 5 b) of optimized lyophilized MTX-NS showed that particles were discrete and aligned in intimate contact as fiber-like structures with an absence of agglomeration that may be assigned by the presence of a stabilizer. Thus, indicated that lyophilization avoids aggregation of particles. The NS had a porous surface and were found slightly elongated but not completely spherical. These pores may be developed because of solvent evaporation from the surface of MTX-NS during lyophilization. Thus SEM confirms that the larger scaly particles of MTX were successfully converted to nearly elongated, smaller-sized nanoparticles with a smoother surface on size reduction. This concludes that the crystalline nature of MTX was lost during the fabrication of the MTX-NS. The obtained NS particles were readily redispersible. SEM analysis also revealed that stabilizer-drug interaction leads to a matrix structure that is different from pure drug SEM images. This means that drug molecules are completely dispersed in the surfactant structures leading to the formation of nanoparticles. After lyophilization, the size of the MTX-NS particle was increased to a lesser extent but smaller than MTX. SEM images of MTX-NS showed quasispherical spheres and the

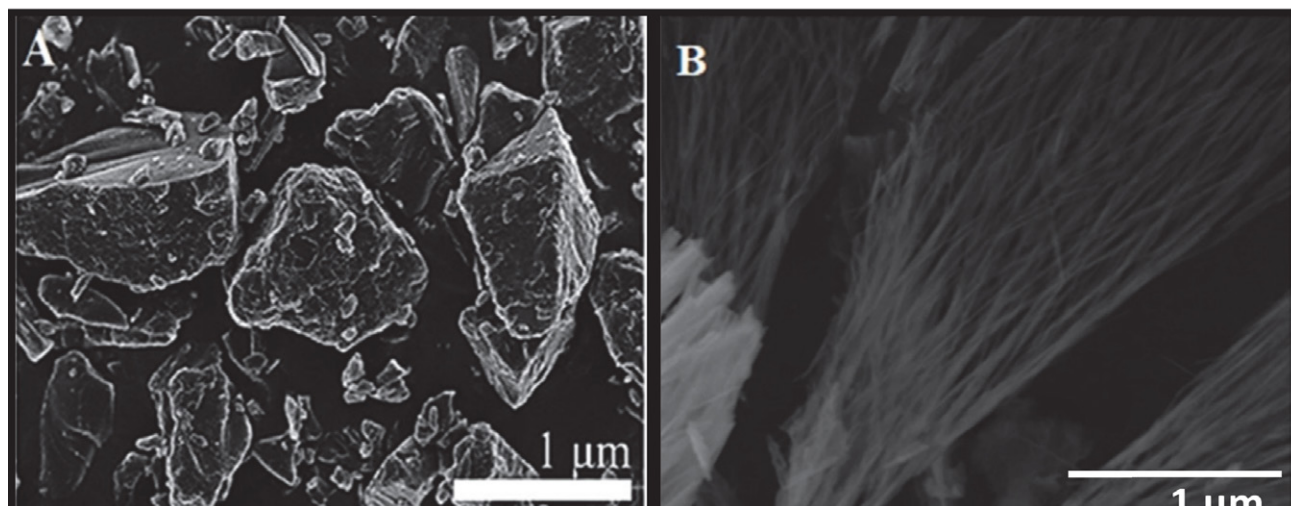


Figure 5 A) SEM images of pure MTX (B) Optimized MTX-NS

size of the particle obtained was in correlation with the results of DLS.

3. 3. 8. Crystallographic Investigation

3. 3. 8. 1. Differential Scanning Calorimetry (DSC)

The stability and dissolution behavior of compounds are influenced by their crystalline state. During the HPH process, a high-energy input was generated because of the high powered density in the piston gap of the homogenizer. This increases the amorphous portion or complete amorphization of drug particles by changing their crystalline state. These extents of changes depend on applied pressure along with the physical hardness and chemical nature of the drug compound. Thermal analysis of MTX, physical mixtures of MTX, and optimized formulations were performed to study the differences in the solid state of MTX. The results of the DSC analysis are displayed in Figure 6. Coarse MTX powder showed a sharp distinct endothermic peak at 117.45 °C, which was the marked intrinsic melting point peak of MTX, while DSC of the physical mixture was showed two distinct melting endotherm at 48.62 °C and 167.02 °C, respectively. Whereas, the freeze-dried MTX-NS powder were recorded a sharp melting endotherm at 167.54 °C respectively.

The mannitol showed a sharp endothermic peak at 168.74 °C, which confirms the high crystalline nature of mannitol. The characteristic peak of MTX extinct in the thermogram of lyophilized optimized MTX-NS, and physical mixture. These changes are predicted because of the dilution effect of excipients on MTX, especially at a higher concentration of mannitol that had covered the MTX melting peak. Thus, the crystallinity of MTX disappeared or decreased because of its encapsulation by stabi-

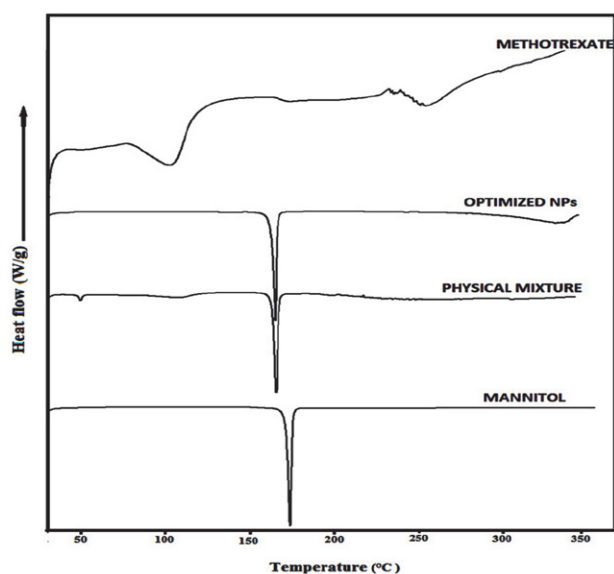


Figure 6. DSC Thermogram of A) Pure MTX B) Optimized MTX-NS C) Physical mixture D) Mannitol

lizers. The state of MTX in NS was not simply physically mixed but may exist as either amorphous or as molecular dispersion form in NS; these changes are because of the interactions between MTX, poloxamer 188, and tween 80. Data obtained from DSC fails to explain factual changes that occurred in drug crystals during formulation processing. The results of the XRD analysis further confirmed the existing state of MTX loaded in MTX-NS.

3. 3. 8. 2. X-ray Powder Diffraction (XRPD)

The crystalline state of lyophilized MTX-NS was confirmed by performing XRPD of coarse MTX powder, physical mixture, and optimized lyophilized MTX-NS. XRPD was used to analyze the probable changes in the physical nature of MTX-NS that occurred because of the development of a high-energy disintegration process. The chemical nature and physical hardness of the drug along with applied pressure are responsible for such changes. The XRPD patterns of powder MTX, physical mixtures, and optimized lyophilized MTX-NS are displayed in Figure 7. Sharp characteristic diffraction peaks were exhibited by MTX at 2θ of 7.58°, 9.2°, 11.42°, 11.92°, 12.82°, 14.32°, 15.38°, 15.94°, 17.68°, 19.36°, 19.46°, 21.38°, 22.34°, 24.18°, 25.34°, 24.16°, 26.06°, 26.01°, 26.96° and 27.82° and several short peaks between 2θ of 30.66° and 80°, indicating its highly crystalline nature. The physical mixtures demonstrated reflections at 2θ of 9.44°, 13.4°, 17°, 18.5°, 20.12°, and 21.04° with similar intensities as compared to MTX and higher intensities than MTX-NS. The physical mixture showed additional peaks similar to that of the parent crystalline compound.

Lyophilized MTX-NS showed four diffraction lines but at lesser intensities, as compared to MTX at 2θ of 9.62°, 13.6°, 17.16°, 19.8°, 20.32°, 21.26°, 22.02°, 24.62° and 36.16° with the additional peaks because of the presence of mannitol. In the PXRD spectra of lyophilized MTX-NS, the characteristic peaks of MTX were absent because of the dilution effect influenced by mannitol, without any qualitative variations in the diffractogram of MTX. This pattern revealed that the MTX-NS, were not completely amorphous in the state, hence the crystalline state of MTX and optimized lyophilized MTX-NS, were different, indicating the HPH technique, and lyophilization process did induce polymorphic transition or crystalline changes in the drug. Thus, amorphous form conversion enhances the solubility, thus enhances the rate of dissolution and the bioavailability of MTX. The state of MTX in NS was not simply physically mixed but may exist as either amorphous or as molecular dispersion form in NS, these changes are because of the interactions between MTX, poloxamer 188, and tween 80. Moreover, the same induced properties and results were confirmed by previously mentioned studies.

3. 3. 9. FTIR

FTIR provides information about the feasible molecular interactions between MTX and excipients used for the

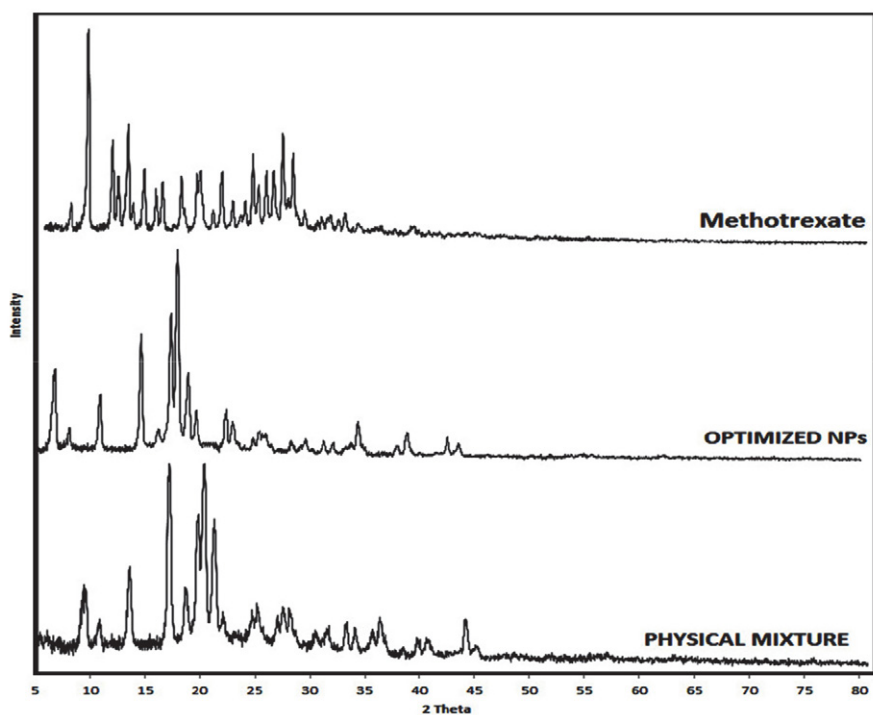


Figure 7. PXRD Spectra of A) Pure MTX B) Optimized MTX-NS C) Physical mixture

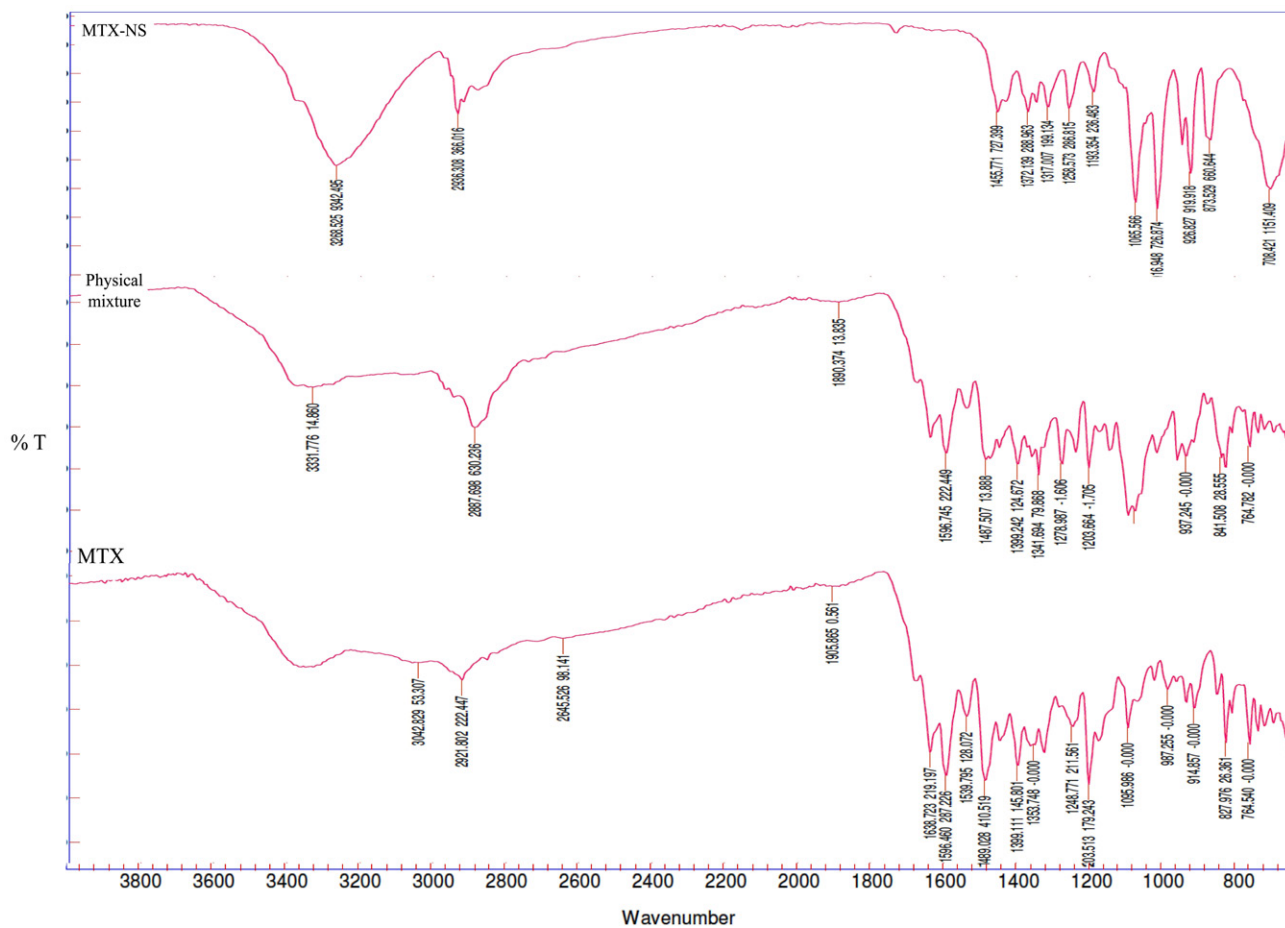


Figure 8. FTIR spectrum of A) pure MTX B) optimized NS(MTX-NS) and C) physical mixture

development of formulation. The FTIR spectra of MTX coarse powder, physical mixture, and optimized lyophilized MTX-NS are disclosed in Figure 8. The FTIR spectra of MTX coarse powder revealed that the characteristic peaks at 1638.723 cm^{-1} , 1596.460 cm^{-1} , 1539.795 cm^{-1} , 1203.513 cm^{-1} , 1489.028 cm^{-1} , and 1305 cm^{-1} had attributed to C=C stretching and O–H stretching and deformation. The FTIR spectra of MTX-NS show a broadening of peaks at 3268.52 cm^{-1} of OH bonding and C–H stretching at 2936.308 cm^{-1} because of the diluting effect of mannitol or by H-bond formation between the poloxamer 188 and tween 80. An extra peak was observed in MTX-NS at 1456.77 cm^{-1} that imputable because of the interaction between mannitol and excipients used for the development of MTX-NS. This showed that MTX was adsorbed onto the nanoparticle surface either by weak H-bonding between the COO-groups of MTX and the OH-groups of poloxamer 188 or by ionic bonds formed between the NH_2 groups of MTX and the COO-groups present in mannitol and tween 80. MTX has dispersed in the tween 80 and poloxamer 188 matrices in the microcrystalline form without polymorphic changes or transition into an amorphous form. Broadening at 708.421 cm^{-1} is because of the H-bond formation between the MTX and tween 80. The absence of characteristic peaks of MTX at 1638.723 cm^{-1} , 1596.460 cm^{-1} , and 1489.028 cm^{-1} in MTX-NS is because of overlapping peaks of mannitol and tween 80. Furthermore, the shifting of peaks to its lower wave number and broadening of characteristic peaks of MTX is seen in FTIR of MTX-NS, which is because of intermolecular H-bonding. While in the physical mixture all characteristic peaks of MTX were retained with the slight shifting of wavenumber. Because of physical interactions between different functional groups of the excipients and drugs, a weak hydrogen bond was formed. The physical interactions found here could be beneficial for the size and shape of the NS and their drug release pattern.

3. 3. 10. *In-vitro* Drug Release

The dissolution behaviors of pure drug MTX, along with their optimized lyophilized formulations viz., MTX-NS in SIF pH 6.8 is represented in Figure 9. The rate of MTX and MTX-NS dissolution was $28.575 \pm 0.021\%$ and $99.27 \pm 0.04\%$ within 60 min in SIF pH 6.8 respectively. The MTX-NS showed a dramatically enhanced rate of dissolution as compared to MTX coarse powder by 3.45 folds. Moreover, the MTX-NS displayed a marked increase in dissolution velocities, more than 70% as compared to MTX coarse powder (2.5%) within 10 min. These suggested that the profile of the dissolution of lyophilized MTX-NS was distinctly superior as compared to MTX. As the size of MTX-NS particles was much smaller than that of MTX, it has a much larger surface area, hence a higher dissolution rate. Besides the particle size, the shape also plays a crucial role that may affect the dissolution of the drug. A

particle that is irregular, flaky, and long may increase its average hydrodynamic thickness (h) at the boundary layer. Thus, the value of ' h ' would be increased with decreased dissolution rate. The SEM image of MTX showed rod-shaped particles in different sizes. Thus, concluded that enhancement in dissolution was because of the reduction in the size of the particle rather than shape alteration.

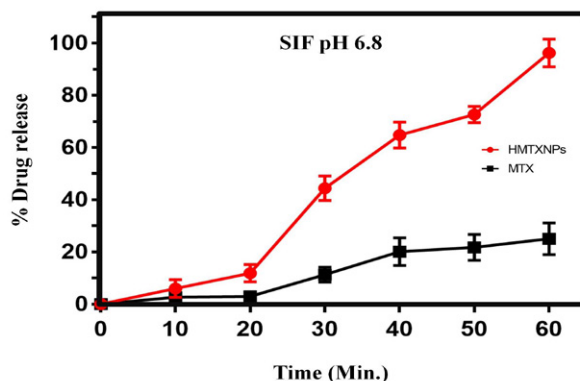


Figure 9. Dissolution profiles of optimized NS (MTX-NS) with a pure drug in simulated intestinal fluid (SIF) with pH 6.8

3. 3. 11. Cytotoxicity Activity

The MCF-7 breast cancer cells were cultured with MTX-NS, along with their aqueous dispersions (MTX-AQD) to study the impact of drugs on cell proliferation of MCF-7. By MTT assay, the cell inhibition ratio was evaluated. The IC_{50} values were obtained by calculating non-linear regression values of the cytotoxicity data by using the sigmoidal dose-response equation with the help of Graph Pad Prism software 7. The obtained results show that the inhibition of MCF-7 cell growth by optimized MTX-NS was dose and time-dependent. However, significant inhibition of MCF-7 cell proliferation was observed when treated with the previously mentioned MTX-NS with a concentration above or at $6.25\text{ }\mu\text{g/mL}$. MTX-NS treated cells had a notable enhancement in growth inhibition rates as compared to MTX-AQD treated cells. These findings might be because of three possible aspects. First, the ability of MTX-NS to incarnate into cells by endocytosis or phagocytosis mechanism. Second, by increasing contact time and the area between drug and cells, as the smaller size NS initiates its adhesion to MCF-7 cells. As NS enhanced solubility and dissolution rates, it helps to induce sufficient molecular concentration of drugs around the cells. Thus, the MTX-NS was highly toxic to MCF-7 cells compared to free drugs. The values of IC_{50} of the MTX-NS solution were $27.73\text{ }\mu\text{g/mL}$. Whereas, the MTX-AQD was showed an IC_{50} value of about $59.56\text{ }\mu\text{g/mL}$ (Figure S4). The outcomes of this study indicated that the values of IC_{50} of NS are lower than MTX-AQD at the same incubation time (48 h).

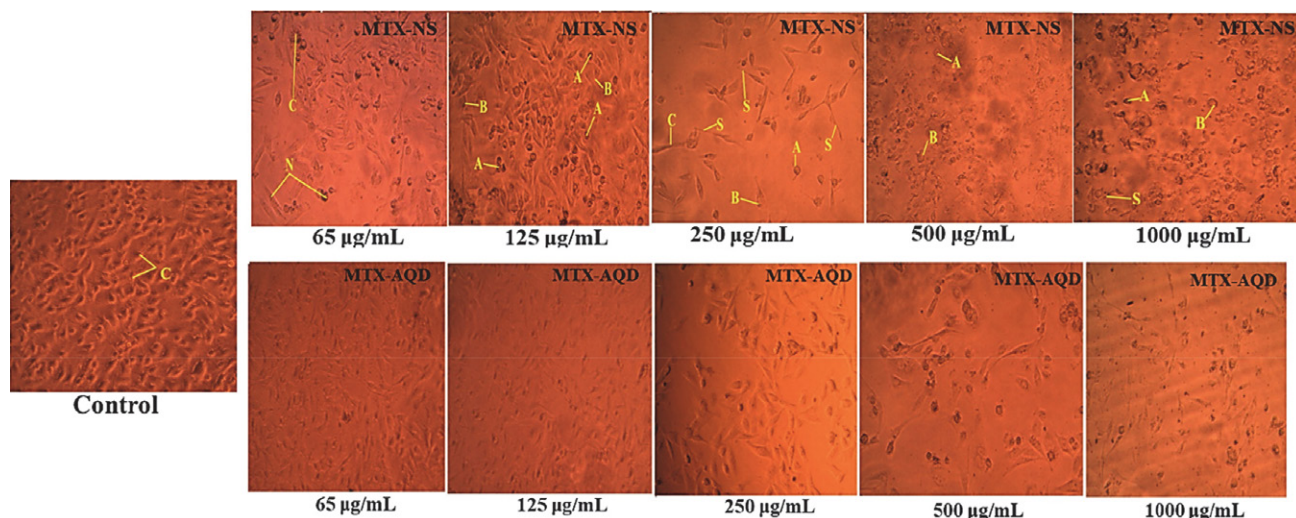


Figure 10. Photomicrographs (light microscopy; magnification, $\times 200$) showing morphological and growth inhibitory changes of MCF-7 cells following exposure to, MTX-NS for 48 h

Noticeable morphological changes were seen in cells, which include membrane blebbing, nuclear fragmentation, and shrinkage of cells after exposure to MTX-NS and MTX-AQD for 48 h. Further, more changes that are obvious were observed in NS treated cells as compared to untreated cells (control), Figure 10. [Control cells (C), Membrane blebbing (B), Condensed nuclei (N), Cell shrinkage (C), Apoptotic bodies (A), Echinoid spikes (S & E)]

3. 3. 12. Apoptosis Study on MCF-7 Cells

Apoptosis study of MTX-NS by double staining method reveals the ability of drugs and especially the MTX to induce apoptosis. As displayed in Figure 11 A, the green-colored nucleus indicates living cells in the control group, which are untreated. While Figure 11 B and 11 C showed a decreasing ratio of living cells with increased concentration of AQD and NS. Herein, of AQD and NS (12.5 $\mu\text{g}/\text{mL}$) treated cells showed uniformly orange-stained fluorescent nuclei but at a lesser amount as com-

pared to NS treated cells, indicating necrosis of cells followed by the death of cells. The changed morphological of apoptosis cells, when treated with NS, include shrinkage of cells, followed by fragmentation and irregular shape. Such changes in morphology were observed in larger amounts with cells treated by NS as compared to AQD. Thus, the reduction in living cells of MCF-7 indicates an increase in the ratio of apoptotic cells.

3. 3. 13. Pharmacokinetic and Biodistribution Study in Wistar and Sprague-Dawley Rats

To confirm the positive impact of NS on oral bio-availability enhancement of MTX *in-vivo* PK studies of NS and their AQD in rats were carried out and obtained results were correlated with each other. The mean concentration-time profile in the rat plasma for MTX is displayed in Figure 12, obtained when the single dose of 40 mg/kg of MTX was administered orally from NS and AQD and their PK parameters obtained are reported in Table 7 respective-

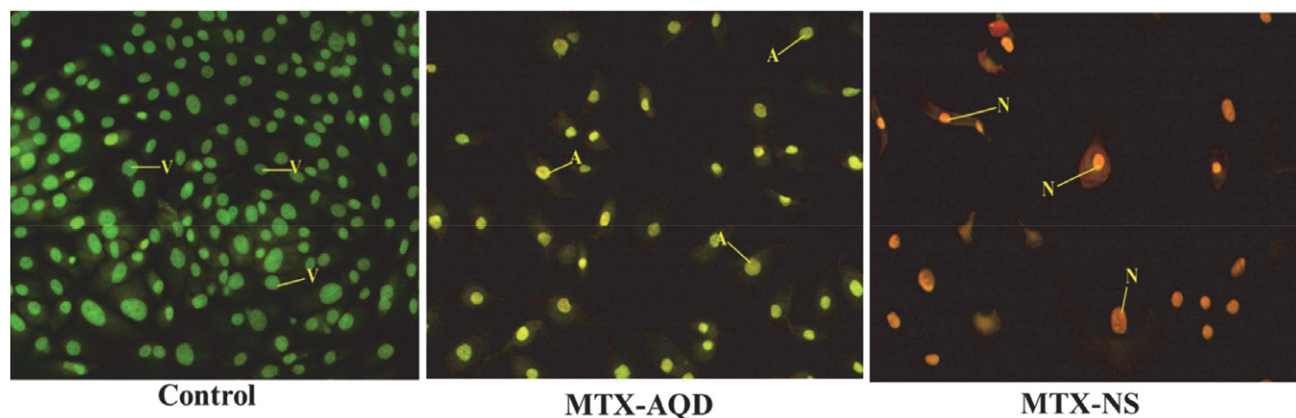


Figure 11. Apoptosis study of MST-NS on MCF-7 cells. A) Untreated cell lines that are intact and with green nucleus B) Cells treated with 25 $\mu\text{g}/\text{mL}$ of AQD C) Cells treated with 25 $\mu\text{g}/\text{mL}$ of NS; N- necrotic Cells, A- Apoptotic cells, and V- Viable cells.

ly. Following the oral administration of MTX-NS and MTX-AQD, the plasma concentration of MTX from MTX-NS in rats was significantly reached to a higher level than that of MTX-AQD at every time interval. The MTX-NS exhibited higher C_{max} and T_{max} , which indicates greater drug absorption but at a slower rate. The C_{max} of MTX-NS increased by 2.53 folds. The reduced C_{max} of MTX-AQD is because of the rapid distribution and metabolism of MTX. The coating of tween 80 and poloxamer 188 helps the circulation of formulation in the body for a prolonged period, thus T_{max} of MTX-NS is higher than free MTX. The mean residence time (MRT) of MTX-NS and MTX-AQD was 27.61 ± 2.10 and 38.62 ± 2.03 hours, respectively. Thus, the $t_{1/2}$ of MTX from MTX-NS was reduced to ~ 8 h, then free MTX, with $t_{1/2}$ of 18.78 h. This drug is available in the body for a longer period in NS form for absorption. The relative and absolute bioavailability of MTX-NS was 8.83 fold high as compared to MTX-AQD. The area under the curve (AUC) is a vital PK parameter that explains the circulation and exposure time of the drug in bloodstreams. The AUC_{0-t} of MTX-NS and MTX-AQD were $3932.79 \mu\text{g/ml} \cdot \text{h}$ and $445.39 \mu\text{g/ml} \cdot \text{h}$, respectively. This increase in AUC indicated that the MTX oral absorption in rats was enhanced notably in lyophilized NS form.

Thus, the oral bioavailability of MTX was improved by decreased particle size, increased dissolution rate, and thus enhances membrane permeation of the drug. Here the size of MTX particle was reduced to nanometers from microscale. This significant reduction in the size of particles leads to tremendous enhancement in surface area which fastens the drug dissolution velocity as per Noyes–Whitney equation. Moreover, reduction in the size of the particle improved the uptake of drugs not only by dissolution enhancement but also by other mechanisms like increased mucosal adhesion to GI surfaces that helps to prolong GI transit time and leads to efficient oral bioavailability. Thus, reduction in the size of the particle

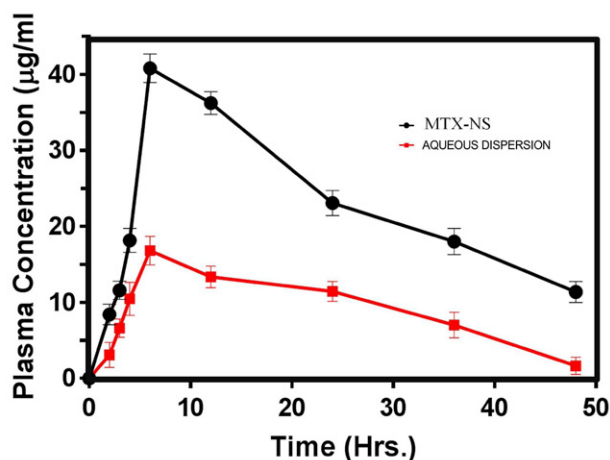


Figure 12. Plasma concentration-time profiles of MTX after oral intake of MTX-NS and the MTX-AQD formulation in rats. Each value represents the mean \pm S.D. ($n = 3$)

and increased rates of drug dissolutions were the reason for higher C_{max} and AUC_{0-t} of MTX after oral administration. As a stabilizer moreover, poloxamer 188 has a thick coat on the surface of MTX-NS, which plays a chief role in bioavailability enhancement. It is an amphiphilic surfactant, that may enhance the MTX penetration ability and thus promote rapid permeation of the MTX nanoparticles through the intestinal epithelium, and finally into blood i.e. systemic circulation.

Table 7. Plasma pharmacokinetic parameters of MTX-AQD and Lyophilized MTX-NS in Sprague Dawley rats after oral administration

Pharmacokinetic parameter	MTX-AQD	Lyophilized MTX-NS
C_{max} ($\mu\text{g/ml}$)	15.7 ± 1.12	$39.70 \pm 1.32^{**}$
T_{max} (h)	5.00 ± 1.59	$6.00 \pm 1.41^{**}$
$t_{1/2}$ (h)	26.76 ± 1.68	$18.78 \pm 1.36^{**}$
MRT (h)	38.62 ± 2.03	$27.61 \pm 2.10^{**}$
AUC_{0-t} ($\mu\text{g/ml} \cdot \text{h}$)	445.39 ± 3.99	$3932.79 \pm 3.09^{**}$
$AUC_{0-\infty}$ ($\mu\text{g/ml} \cdot \text{h}$)	485.16 ± 3.25	$6788.86 \pm 3.33^{**}$
VD (mL)	109.24 ± 2.22	$16.10 \pm 2.45^{**}$
Cl ($\text{mL} \cdot \text{h}^{-1}$)	2.83 ± 2.24	$0.059 \pm 2.55^{**}$
KE (h^{-1})	0.026 ± 2.15	$0.0037 \pm 2.35^{**}$
F_{rel}	–	8.83 ± 1.19
F%	4.45	67.88

After oral administration, the biodistribution study of MTX-NS and MTX-AQD showed a higher collection of MTX in the spleen, liver, stomach, and kidney (Figure S5). The liver is the major organ of the reticuloendothelial system (RES) that accumulates and metabolizes nanoparticles. The biodistribution data revealed the maximum concentration of MTX by liver, spleen, stomach, and kidney were 8.15 ± 4.22 , 16.15 ± 5.12 , 9.40 ± 4.72 and $4.73 \pm 5.12 \mu\text{g/g}$, for MTX-NS, respectively, after 72 h of oral administration. However, the MTX-AQD concentration in the liver, spleen, stomach, and kidney were 8.24 ± 2.28 , 4.02 ± 3.36 , 3.26 ± 5.43 , and $2.45 \pm 3.22 \mu\text{g/g}$, respectively. This may be because of the faster elimination of MTX because of higher particle size as compared to MTX-NS. The higher uptake of MTX in the spleen, liver, and stomach is because of enhanced lymphatic uptake. After oral intake of MTX-NS, no weight loss, no systemic toxicity, or fatalities, or any other toxic effects were seen during the entire study in rats. The increased biodistribution of MTX-NS in the stomach as compared to MTX-AQD was maybe because of increased intimate contact of MTX with GIT absorptive cells because of increased surface area and adhesion properties of nanoparticles. Before the maceration, the stomach was cleaned for all waste or any food material to measure the levels of the stomach to the actual tissues. The concentration of MTX-NS in the brain was $5.03 \pm 4.21 \mu\text{g/g}$ and MTX-AQD was $1.56 \pm 4.18 \mu\text{g/g}$, which indicates

that the MTX-NS can deliver MTX to the brain. Early studies suggest that the size of NS in a nanometer plays a key role to deliver the drug to the brain and it crosses the blood-brain barrier (BBB). Thus MTX-NS in lesser doses can be used to treat primary central nervous system lymphoma (PCNSL). The concentration of MTX in lungs and heart were 6.57 ± 3.45 and 4.05 ± 3.25 $\mu\text{g/g}$ for MTX-NS, while for MTX-AQD it was 2.00 ± 4.62 and 2.12 ± 3.45 $\mu\text{g/g}$ respectively. A comparison of MTX-AQD with MTX-NS was not statistically significant ($p > 0.05$). Thus, biodistribution studies conclude the accumulation of MTX-NS in the spleen, liver, stomach, and lungs in larger amounts as compared to the brain, lungs, and heart.¹¹

3.3.14. Stability Studies

The six-month stability data for lyophilized MTX-NS with liquid MTX-NS are reported in Table 8. MTX-NS stored at room temperature showed an increased particle size from 260 to 365 nm, within six months. While, storage under refrigerated conditions, showed there was a nominal increase from 260 to 300 nm indicating better stability under these conditions. The NS store at $40^\circ \pm 2$ °C/75 \pm 5% RH showed an increase in the size of particles from 260 to 388 nm. Results conclude, temperature influences the aggregation of nanoparticles, thus the stability and aggregation were higher at RT and stability chamber as compared to refrigerator storage conditions for liquid NS. For liquid, MTX-NS particle size ranges from 260 to 300 nm for samples stored at the refrigerator that shows better stability of NS than other storage conditions (Table 8). The refrigerated condition does not have a significant effect on average particle size, whereas room temperature and stability chamber condition has a more deleterious effect. This concluded that higher temperature leads to greater particle aggregation which results in increased size of particles. Thus aggregation of particles at room temperature and stability chamber increases its particle size and thus they are less stable. Probably Ostwald ripening may be the second reason resulting in fluctuations at RT. The chemical stability results of formulation during various conditions of storage are featured in Table 8. Results suggest no signifi-

cant change in the DC of MTX-NS and their lyophilized MTX-NS when stored at three storage conditions. Thus, it concluded that both the liquid and lyophilized MTX-NS are chemically stable at three storage conditions. Noteworthy, for physical stability of liquid NS, lyophilization, and storage at refrigerated conditions are recommended²⁸.

4. Conclusion

Lyophilized MTX-NS was fabricated and characterized using the QbD approach to enhance solubility, bioavailability, and stability of MTX. To understand the impact of CMAs and CPPs on CQAs the QbD approach was applied. The main reason to use the QbD approach is to improve the quality and safety of NS formulation. By using the statistical experimental designs like Plackett-Burman and Central Composite design within a QbD concept, the effect of process and formulation parameters which affects the CQAs of NS, and that influences the stability and solubility of MTX in NS were optimized. The particle size distribution of optimized MTX products from the CCD overlay plot showed an average particle size of 260 ± 0.2 nm, with a zeta potential of -11.6 ± 7.52 mV. The SEM and TEM studies conclude particles were spherical. The XRPD, FTIR, and DSC studies conclude the crystalline nature of MTX was intact in NS form, but there was a significant increase in dissolution velocity and release rate of MTX-NS, due to the reduced size of particles and larger surface area of MTX. The lyophilized NS was found to be stable in refrigerator storage conditions. The plasma pharmacokinetic parameters viz., C_{max} , T_{max} , $t_{1/2}$, AUC_{total} , and MRT of NS on rats were significantly higher than MTX-AQD. The relative and absolute bioavailability of MTX-NS was enhanced by more than 8.83 folds. Higher MTX concentration was found in the liver within 72 hrs, concluded from the biodistribution study. *In vitro* cytotoxicity study proves the significant inhibitory effect of the MTX-NS against human breast cancer cells MCF-7 at a very low dose. Apoptosis studies conclude MTX-NS treated cells at a 12.5 $\mu\text{g/mL}$ concentration showed uniformly orange-stained flu-

Table 8. Physical stability data of lyophilized and liquid MTX-NS

Formulation	Storage Temperature	Initial Particle Size	Particle Size After			Initial Drug Content	Drug Content After		
			2M	4M	6 M		2 M	4 M	6 M
Lyophilized MTX-NS	4 °C	260 \pm 4.6	274.9 \pm 4.6	289.3 \pm 8.2	300.8 \pm 4.5	88.65 \pm 0.33	88.46 \pm 4.2	88.32 \pm 5.8	88.11 \pm 3.5
	Room temperature		295.2 \pm 5.9	325.9 \pm 7.1	365.7 \pm 6.8		87.23 \pm 6.8	87.10 \pm 6.6	87.09 \pm 2.6
	40 °C		280.4 \pm 5.4	336.9 \pm 5.6	388.5 \pm 7.2		87.99 \pm 7.2	87.57 \pm 8.2	87.65 \pm 4.5
Liquid MTX-NS	4 °C	246.8 \pm 8.23	254.9 \pm 4.2	269.3 \pm 3.6	280.8 \pm 6.3	99.86 \pm 7.4	99.70 \pm 7.8	99.55 \pm 6.1	99.29 \pm 6.6
	Room temperature		268.2 \pm 4.6	290.9 \pm 4.2	321.7 \pm 2.8		99.64 \pm 5.9	99.44 \pm 8.1	99.05 \pm 7.2
	40 °C		250.4 \pm 5.5	283.9 \pm 5.3	338.5 \pm 3.3		99.74 \pm 9.1	99.45 \pm 5.6	99.37 \pm 7.8

*Mean \pm SD (n = 3).

orescent nuclei at a higher amount as compared to AQD treated cells at the same concentration, indicating necrosis of cells followed by the death of cells i.e. they induce apoptosis. The stability studies conclude physical as well as chemical stability of NS, by inhibiting the reaggregation of particles by adsorption of stabilizers on drug particles. Thus, the pieces of evidence obtained from QbD results prove that it is a helpful tool in the fabrication of NS to improve quality and safety, reduce the manufacturing variability, and reduce the manufacturing cost, a requirement of USFDA.

Conflict of interest

The authors declare no conflict of interest. The authors alone are responsible for the content and writing of the article.

Acknowledgments

The authors are grateful to Dr. Babasaheb Ambedkar Research and Training Institute (BARTI), Pune for providing funds to carry out the research work smoothly.

5. References

1. C. Lipinski, *Am Pharm Rev* **2002**, 5, 82–85. DOI:10.1016/S0338-9898(02)80223-2
2. V. Patravale, A. A. Date and R. Kulkarni, *J Pharm Pharmaco* **2004**, 56, 827–840. DOI:10.1211/0022357023691
3. V. R. Patel, Y. K. Agrawal, *J. Adv. Pharm. Technol. & Res.*, **2011**, 2 (2), 81–87. DOI:10.4103/2231-4040.82950
4. B. Vora, A. Khopade, V. Jain, S. Jain, and N. Jain, *Indian Drugs* **1996**, 33, 365–373.
5. Gennaro AR. Remington: The Science and Practice of Pharmacy. 19th edition. *Mace Publishing Co.*, **1995**, 976, 1267.
6. S. S. Abolmaali, A. M. Tamaddon, and R. Dinarvand, *Cancer Chemother Pharmacol* **2013**, 71, 1115–1130. DOI:10.1007/s00280-012-2062-0
7. P. Jadhav, C. Bothiraja and A. Pawar, *J Pharm Innov* **2018**, 13, 213–225. DOI:10.1007/s12247-018-9314-4
8. E. Van Roon and M. Van de Laar, *Clinical and Experimental Rheumatology-Incl Supplements* **2010**, 28, S27. DOI:10.1007/s12247-018-9314-4
9. I. S. Desai, D. Bhagwat, S. Shinde And J. Desouza, *Int J App Pharm* **2019**, 11, 43–48. DOI:10.22159/ijap.2019v11i3.30578
10. A. H. Ibrahim, E. Rosqvist, J.-H. Smätt, H. M. Ibrahim, H. R. Ismael, M. I. Afouna, A. M. Samy and J. M. Rosenholm, *Int J Pharm* **2019**, 563, 217–227. DOI:10.1016/j.ijpharm.2019.03.064
11. T. A. Powar and A. A. Hajare, *Acta Chim Slov* **2020**, 67, 283–303. DOI:10.17344/acsi.2019.5441
12. R. Yadollahi, K. Vasilev and S. Simovic, *J Nanomater* **2015**, 1–13. DOI:10.1155/2015/216375
13. S. Jacob, A. Nair, and J. Shah, *Bio Res* **2020**, 24 (3), 1–16. DOI:10.1186/s40824-020-0184-8
14. R. Jayaprakash, K. Krishnakumar, B. Dineshkumar, R. Jose and S. Nair, *Sch Acad J Pharm* **2016**, 5(5), 138–141. DOI:10.36347/SAJP
15. H. Purkayastha and S. Imanur Hossian, *Int J Curr Pharm Res* **2019**, 11(3), 1–3. DOI:10.22159/ijcpr.2019v11i3.34098
16. S. Hussain, A. Baquee Ahmed, and J. Debnath, *Int J Pharm Sci Res* **2020**, 11(10), 4822–4832. DOI:10.13040/IJPSR.0975-8232
17. J. Cook, M. T. Cruaños, M. Gupta, S. Riley and J. Crison, *AAPS PharmSciTech* **2014**, 15, 140–148. DOI:10.1208/s12249-013-0043-1
18. Q. Huang, H. Yu, and Q. Ru, *J Food Sci* **2010**, 75, R50–R57. DOI:10.1111/j.1750-3841.2009.01457.x
19. S. Kalvakuntla, M. Deshpande, Z. Attari and K. Kunnatur, *Adv Pharma Bull* **2016**, 6, 83. DOI:10.15171/apb.2016.013
20. C. P. Dora, S. K. Singh, S. Kumar, A. K. Datusalia and A. Deep, *Acta Pol Pharm* **2010**, 67, 283–90. DOI:acta_pol_2010/3_2010/283-290
21. N. S. K. Srinivas, R. Verma, G. P. Kulyadi and L. Kumar, *Int J Nanomed* **2017**, 12, 15. DOI:10.2147/IJN.S122729
22. F. Yerlikaya, A. Ozgen, I. Vural, O. Guven, E. Karaagaoglu, M. A. Khan and Y. Capan, *J Pharm Sci* **2013**, 102, 3748–3761. DOI:10.1002/jps.23686
23. L. Rabelo, N. Monteiro, R. Serquiz, P. Santos, R. Oliveira, A. Oliveira, H. Rocha, A. H. Morais, A. Uchoa and E. Santos, *Marine drugs* **2012**, 10, 727–743. DOI:10.3390/md10040727
24. A. A. Abdelbary, A. M. Al-Mahallawi, M. E. Abdelrahim, and A. M. Ali, *Int J Nanomed* **2015**, 10, 6339–6353. DOI:10.2147/IJN.S91631
25. H. C. Vadlamudi, P. R. Yalavarthi, B. R. M. Venkata, J. Thaniruru, K. Vandana and C. Sundaresan, *J Acute Dis* **2016**, 5, 315–325. DOI:10.1016/j.joad.2016.05.004
26. P. F. Yue, Q. Zheng, B. Wu, P.-Y. Hu, Z.-F. Wu and M. Yang, *J Dispers Sci Technol* **2012**, 33, 213–222. DOI:10.1080/01932691.2011.561162
27. J. He, Y. Han, G. Xu, L. Yin, M. N. Neubi, J. Zhou and Y. Ding, *RSC Advances* **2017**, 7, 13053–13064. DOI:10.1039/C6RA28676C
28. A. Sattar, D. Chen, L. Jiang, Y. Pan, Y. Tao, L. Huang, Z. Liu, S. Xie and Z. Yuan, *Sci Rep* **2017**, 7, 1–9. DOI:10.1038/s41598-017-02523-4
29. A. Fernandes, C. Pydi, R. Verma, J. Jose, and L. Kumar, *Braz J Pharm Sci* **2020**, 1–14. DOI:10.1590/s2175-97902019000318069
30. N. Bhaskaran, L. Kumar, M. Reddy, and G. Pai, *Acta Pharm* **2021**, 71(1), 57–79. DOI:10.2478/acph-2021-0008

Povzetek

Z uporabo pristopa »Quality by design« (QbD) je bila za razvoj nanosuspenzije metotreksata (MTX-NS) uporabljena metodologija visokotlačnega homogenizatorja (HPH) za povečanje biološke uporabnosti. Diagram Ishikawa je bil uporabljen za analizo možnih dejavnikov tveganja pri razvoju formulacij. Za pregled in proučevanje vpliva različnih formulacijskih in procesnih dejavnikov na kritične attribute kakovosti (CQA) sta bila uporabljena zasnova Plackett-Burman in osrednja kompozitna zasnova. Število ciklov HPH, koncentracija poloksamera 188 in koncentracija tween 80 so se izkazali za pomembne parametre ($P < 0.05$), ki so bili dodatno optimizirani z uporabo osrednje kompozitne zasnove. Zeta potencial optimiziranega liofiliziranega MTX-NS je bil -11.6 ± 7.52 mV, povprečna velikost delcev pa je bila 260 ± 0.25 nm. Poskusi citotoksičnosti *in vitro* so pokazali več kot 80 % inhibicijo, pri čemer je prišlo do skrčenja apoptotičnih celic, fragmentacije in celične smrti. Poleg tega sta se C_{\max} in AUC_{0-t} povečala za 2.53, oziroma 8.83 krat. Ugotovljeno je bilo, da je relativna biološka uporabnost MTX-NS 8.83-krat večja kot pri vodni disperziji MTX. Posledično je metoda QbD omogočila razvoj liofiliziranega MTX-NS z razumevanjem procesov in nadzorom, ki temelji na obvladovanju tveganja kakovosti.



Except when otherwise noted, articles in this journal are published under the terms and conditions of the Creative Commons Attribution 4.0 International License

Scientific paper

QSAR Studies and Structure Property/Activity Relationships Applied in Pyrazine Derivatives as Antiproliferative Agents Against the BGC823

Fatima Soualmia,^{1,2} Salah Belaidi,^{2,*} Nouredine Tchouar,¹ Touhami Lanez³
and Samia Boudergua^{1,4}

¹ Laboratoire Génie des Procédés et Environnement (GPE), Faculté de chimie, Université des sciences et technologies d'Oran (USTO) BP 1503 Oran 31000, Algérie

² University of Biskra, Group of Computational and Medicinal Chemistry, LMCE Laboratory, BP 145 Biskra 07000, Algeria

³ University of El-Oued, Faculty of Sciences and Technology, VTRS Laboratory, B.P.789, 39000, El-Oued, Algeria

⁴ University of KhemisMiliana, Faculty of Sciences and Technology, 44225, Ain Defla, Algeria

* Corresponding author: E-mail: s.belaidi@univ-biskra.dz.

Received: 04-08-2021

Abstract

Electronic structures, the effect of the substitution, structure physicochemical property/activity relationships and drug-likeness applied in pyrazine derivatives, have been studied at *ab initio* (HF, MP2) and B3LYP/DFT (density functional theory) levels. In the paper, the calculated values, i.e., NBO (natural bond orbitals) charges, bond lengths, dipole moments, electron affinities, heats of formation and quantitative structure-activity relationships (QSAR) properties are presented. For the QSAR studies, we used multiple linear regression (MLR) and artificial neural network (ANN) statistical modeling. The results show a high correlation between experimental and predicted activity values, indicating the validation and the good quality of the derived QSAR models. In addition, statistical analysis reveals that the ANN technique with (9-4-1) architecture is more significant than the MLR model. The virtual screening based on the molecular similarity method and applicability domain of QSAR allowed the discovery of novel anti-proliferative activity candidates with improved activity.

Keywords: Pyrazine; DFT; QSAR; MLR; ANN.

1. Introduction

Pyrazine is a heterocyclic compound containing two nitrogen atoms in its aromatic ring with molecular formula $C_4H_4N_2$.¹ It is a symmetrical molecule with point group D_{2h} .

Pyrazine is less basic than pyridine, pyridazine and pyrimidine. Tetramethyl pyrazine (also known as ligustrazine) is reported to scavenge superoxide anion and decrease nitric oxide production in human polymorph nuclear leukocytes and is a component of some herbs in traditional Chinese medicine. Some pyrazine derivatives contain various pharmacological effects: anti-cancer, anti-depressant and anxiolytic, tuberculosis, an anti-diabetic drug and pulmonary hypertension and cardiac valve.²⁻⁷

Quantum chemistry methods play an important role in obtaining molecular structures and predicting various

properties. To obtain highly accurate geometries and physical properties for molecules that are built from electronegative elements, expensive *Ab initio*/MP2 electron correlation methods are required.⁸ Density functional theory methods⁹⁻¹⁴ offer an alternative use of inexpensive computational methods which could handle relatively large molecules.¹⁵⁻²⁰

Quantitative structure-activity relationships (QSAR)²¹⁻²⁵ are attempts to correlate molecular structure, or properties derived from molecular structure, with a particular kind of chemical or biochemical activity. The kind of activity is a function of the interest of the user. QSAR is widely used in pharmaceutical, environmental and agricultural chemistry in the search for particular properties. The molecular properties used in the correla-

tions relate as directly as possible to the key physical or chemical processes taking place in the target activity.²⁶

This work is planned to illuminate the theoretical determination of the optimized molecular geometries, MESP, NBO charges of pyrazine compounds. In addition, we calculated important quantities such as the HOMO–LUMO energy gap.²⁷

Lipinski's 'Rule of Five'²⁸ as well as other parameters is useful a tools to aid in choosing oral drug candidates. Drug-likeness is described to encode the balance among the molecular properties of a compound that influences its pharmacodynamics, pharmacokinetics and ADME (absorption, distribution, metabolism and excretion) in a human body like a drug.²⁹

These parameters allow estimating oral absorption or membrane permeability, which occurs when evaluated molecules obey Lipinski's rule-of-five. Other parameters that are included the number of rotatable bonds, molecular volume, molecular polar surface area and the in vitro plasma protein binding.

The present paper deals with a specific organizational form of molecular matter. Other forms are given for example in the References.^{30–34}

Many different chemometric methods, such as multiple linear regression (MLR),³⁵ partial least squares regression (PLS),³⁶ different types of artificial neural networks (ANN),^{37–40} genetic algorithms (GA)⁴¹ and support vector machine (SVM) can be employed to deduce correlation models between the molecular structure and properties. At present, we derive a quantitative structure-activity relationship (QSAR) model using multiple linear regression (MLR) as well as artificial neural network (ANN) methods for the series of pyrazine derivatives.

The goal of the present study is to validate a suitable methodology for the accurate prediction of molecular geometries and energetic properties of potentially active compounds, and to determine the best molecular descriptors to be used in conjunction with linear (MLR) and non-linear (ANN) QSAR models to identify the best candidates for antiproliferative agents against the BGC823. The obtained QSAR models were finally employed to identify biological activities of potentially novel active compounds using in silico screening procedures.

2. Materials and Methods

All calculations were performed using HyperChem 8.0.6 software⁴² and Gaussian 09 program package⁴³, Marvin Sketch 6.2.1 software⁴⁴, Molinspiration online database⁴⁵ and JMP 8.0.2 software.⁴⁶

The geometries of pyrazine and their methyl, ethyl, bromo, fluoro derivatives were fully optimized with *ab initio*/HF, MP2 and DFT/B3LYP methods, using both basis set 6-311G ++(d,p) and cc-pVDZ integrated with Gaussian 09 program package. The calculation of QSAR proper-

ties is performed through the module QSAR properties (HyperChem version 8.0.6), which allows several properties commonly used in QSAR studies to be calculated.

Molinspiration, web-based software was used to obtain parameters such as TPSA (topological polar surface area), nrotb (number of rotatable bonds) and drug-likeness.

Multiple Linear Regression MLR analysis and artificial neural networks ANN were carried out using the software JMP 8.0.2.

The calculated results have been reported in the present work.

3. Results and Discussion

3.1. Geometric and Electronic Structure of Pyrazine

The optimized geometrical parameters of pyrazine with *ab initio*/HF, *ab initio*/MP2 and DFT method using 6-311G ++ (d, p) and cc-pVDZ basis set. Results concerning bond length values for pyrazine are listed in (Table 1), bond angles are listed in (Table 2) with the experimental results⁴⁷ and charge densities are listed in (Table 3) are following the numbering scheme given in (Fig. 1).

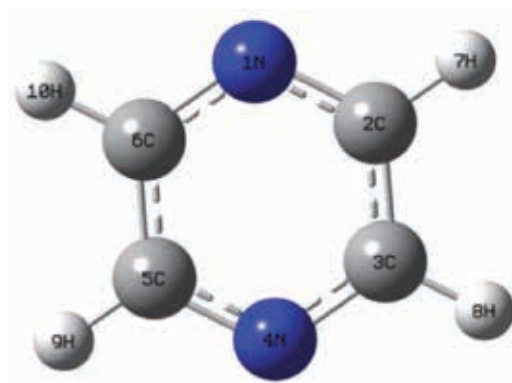


Fig. 1. 3D conformation of pyrazine (GaussView 5.0.8).

The efficiency of the DFT/B3LYP method with cc-pVDZ basis set may be scrutinized by comparison with the results obtained by more elaborate calculations such as *ab initio*/HF and MP2 methods. A very good agreement between predicted geometries (bond lengths and bond angles) and corresponding experimental data was obtained especially through the DFT/B3LYP results.

From that, we can say that the DFT method is more appropriate for further study on the pyrazine rings. Charge densities calculated by DFT/B3LYP are almost similar to *ab initio*/HF and MP2 methods. The geometry of the pyrazine is symmetric and planar; as all the dihedral angles are either nearly 0° or 180°, which makes this conforma-

tion more stable. The total atomic charges of pyrazine obtained from NBO charges with DFT/B3LYP and *ab initio*/HF and MP2 methods with cc-pVDZ basis set are listed in Table 3. The atoms N have negative charges which lead to an electrophilic attack, the atoms C and H have a positive charges which leads to the preferential site to nucleophilic attack.

The molecular electrostatic potential surface (MESP) is a plot of electrostatic potential mapped on to the constant electron density surface. In the majority of the MESP the maximum negative region which preferred the site for an electrophilic attack is indicated in red color, while the maximum positive region which preferred the site for a nucleophilic attack is symptoms indicated in blue color.⁴⁸ MESP has been found to be a very useful tool in the investigation of the correlation between the molecular structure and the physicochemical property relationship of molecules including biomolecules and drugs.^{49–53}

The MESP surface and contour map of pyrazine (Fig. 2) show the three regions characterized by red color (negative electrostatic potential) around the two cyclic nitrogen atoms which explain the ability of an electrophilic at-

tack on these positions, also the blue color (positive electrostatic potential) around the four hydrogen atoms which explain that these regions are susceptible for a nucleophilic attack. The green color situated in the middle between the red and blue regions explains the neutral electrostatic potential surface.

Table 3. NBO charges of pyrazine molecule.

Pyrazine Atoms	DFT/B3LYP cc-pVDZ	Ab initio/HF cc-pVDZ	Ab initio/MP2 cc-pVDZ
C	0.013	0.044	0.033
N	-0.456	-0.492	-0.487
H	0.215	0.202	0.210

3. 2. Substitution Effect on Pyrazine Structure

Calculated values of the two studied series indicated that in the first series methyl and ethyl groups with effects of electron donors, however, in the second series bromo and fluoro groups with effects of electron acceptors in po-

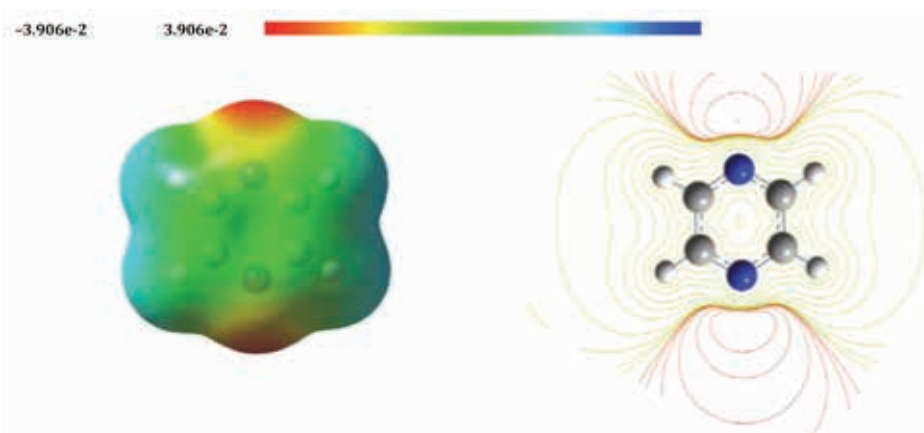


Fig. 2. 3D MESP surface map and 2D MESP contour map for pyrazine (Gauss view 5).

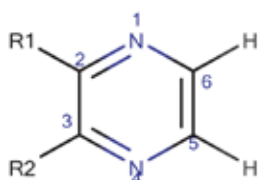
Table 1. Calculated bond lengths (angstrom) of pyrazine molecule.

Distance	EXP ⁴⁷	DFT/B3LYP		Ab initio/HF		Ab initio/MP2	
		6-311G ++ (d, p)	cc-pVDZ	6-311G ++ (d, p)	cc-pVDZ	6-311G ++ (d, p)	cc-pVDZ
C-N	1.338	1.335	1.339	1.317	1.320	1.343	1.349
C-C	1.397	1.394	1.398	1.386	1.388	1.399	1.405
C-H	1.083	1.086	1.095	1.075	1.082	1.087	1.096

Table 2. Angles in degree of pyrazine molecule.

Angle	EXP ⁴⁷	DFT/B3LYP		Ab initio/HF		Ab initio/MP2	
		6-311G++(d, p)	cc-PVDZ	6-311G++ (d, p)	cc-pVDZ	6-311G++(d, p)	cc-pVDZ
CCH	120.0	120.0	120.8	120.8	120.8	120.7	120.6
CNC	115.7	116.1	115.6	116.6	116.3	115.2	114.6

sitions C2 and C3 in the same series are given in (Table 4) and (Table 5), the heat of formation, dipole moment (μ) and HOMO (Highest Occupied Molecular Orbital) and LUMO (Lowest Unoccupied Molecular Orbital) energies of pyrazine systems are presented in (Fig. 3), NBO charges of pyrazine derivatives are reported in (Table 6) for the first series and in (Table 7) for the second series. This calculation is performed with DFT/B3LYP method using the cc-pVDZ basis set.

**Series 1**

- (A1) R1 = H, R2 = H
 (A2) R1 = CH₃, R2 = H
 (A3) R1 = CH₃, R2 = CH₃
 (A4) R1 = C₂H₅, R2 = H
 (A5) R1 = C₂H₅, R2 = C₂H₅

Series 2

- (B1) R1 = H, R2 = H
 (B2) R1 = Br, R2 = H
 (B3) R1 = Br, R2 = Br
 (B4) R1 = F, R2 = H
 (B5) R1 = F, R2 = F

Fig. 3. Structure of pyrazine derivatives (Marvin sketch15.8.31).

For each addition of methyl, ethyl and fluoro, the heat of formation decreases approximately 6, 12 or 39 (kcal · mol⁻¹) respectively but the addition of the bromo group leads to the increase of the heat of formation with 6 (kcal · mol⁻¹) approximately.

The Frontier orbitals, the highest occupied molecular orbital (HOMO) and lowest unoccupied molecular orbital (LUMO) are important factors in quantum chemistry⁵⁴ as these determine the way the molecule interacts with other species. The frontier reactivity and kinetic stability of the molecule. A molecule with a small frontier orbital gap

is more polarizable and is generally associated with a high chemical reactivity, low kinetic stability and is also termed a soft molecule.⁵⁵

For the first series, it was found that electron donors of compound A4 (2-ethyl pyrazine) has the lowest energy gap HOMO-LUMO (0.1958) and compound B3 (2,3-dibromopyrazine) has the lowest energy gap (0.1927) for the second series (Fig. 4).

From HSAB (Hard Soft Acid and Base) principle the lowest energetic gap allows an easy flow of electrons which makes the molecule soft and more reactive,⁵⁶ which means that A4 and B3 compounds are the most reactive in the two series of pyrazine derivatives. For each addition of alkyl-substituted, the energy of the HOMO and LUMO increase respectively but the addition of the fluoro, bromo substituted leads to the decrease of the LUMO energy an exception increase of the bromo substituted and decrease of the fluoro substituted of the HOMO. The carbon C2 has the most important positive charge (0.206) in the compound A4 (2-ethyl pyrazine) for the first series, also for compound B3 (2,3-dibromopyrazine) of the second series, the most important positive charges are on carbon C2 (0.102) and C3 (0.102) as shown in (Table 5), these positions C2 and C3 with the important positive charges lead to preferential sites of nucleophilic attack. The compound B3 is predicted to be the most reactive with a smaller HOMO-LUMO energy gap and with sites of nucleophilic attack, more stable with the maximum value in the heat of formation.

The contour plots of the π like frontier orbital for the ground state of the compound B3 are shown in (Fig. 4).

From the plots, we can observe that the HOMO is a π bonding molecular orbital developed on C5 and C6 atoms, and the LUMO is a π^* anti-bonding molecular orbit-

Table 4. Energies of pyrazine and methyl, ethyl-substituted pyrazine.

		ΔH_f [kcal/mol]	HOMO [au]	LUMO [au]	ΔE [au]	μ [Debye]
A1	Pyrazine	44.09	-0.252	-0.055	0.197	0.00
A2	2-methyl pyrazine	37.05	-0.247	-0.051	0.196	0.59
A3	2,3-di-methyl pyrazine	31.78	-0.243	-0.044	0.199	0.80
A4	2-ethyl pyrazine	30.97	-0.247	-0.051	0.195	0.59
A5	2,3-di-ethyl pyrazine	20.48	-0.242	-0.045	0.196	0.69

Table 5. Energies of pyrazine and fluoro, bromo-substituted pyrazine.

		ΔH_f [kcal/mol]	HOMO [au]	LUMO [au]	ΔE [au]	μ [Debye]
B1	Pyrazine	44.09	-0.253	-0.055	0.197	0.00
B2	2-bromopyrazine	49.73	-0.269	-0.068	0.201	1.50
B3	2,3-dibromopyrazine	55.88	-0.268	-0.075	0.192	2.05
B4	2-fluoro pyrazine	04.15	-0.272	-0.065	0.207	1.33
B5	2,3-di-fluoropyrazine	-33.52	-0.280	-0.069	0.211	2.24

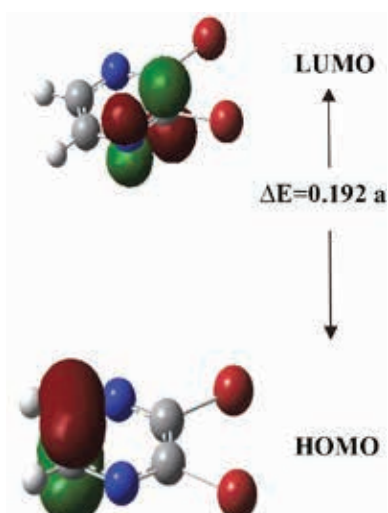
Table 6. NBO charges of pyrazine series 1.

	A1	A2	A3	A4	A5
N1	-0.456	-0.472	-0.471	-0.476	-0.476
N4	-0.456	-0.452	-0.473	-0.452	-0.472
C2	0.013	0.204	0.215	0.206	0.216
C3	0.013	0.016	0.208	0.020	0.213
C5	0.013	0.003	0.010	0.004	0.013
C6	0.013	0.022	0.012	0.023	0.015
C-methyl- 2	-	-0.665	-0.669	-	-
C-methyl- 3	-	-	-0.673	-	-
C ¹ -ethyl- 2	-	-	-	-0.458	-0.459
C ² -ethyl- 2	-	-	-	-0.628	-0.627
C ¹ -ethyl- 3	-	-	-	-	-0.461
C ² -ethyl-3	-	-	-	-	-0.627

Table 7. NBO charges of pyrazine series 2.

	B1	B2	B3	B4	B5
N1	-0.456	-0.458	-0.446	-0.497	-0.485
N4	-0.456	-0.441	-0.446	-0.441	-0.485
C2	0.013	0.112	0.102	0.634	0.586
C3	0.013	0.018	0.102	-0.040	0.586
C5	0.013	0.006	0.018	-0.008	0.002
C6	0.013	0.024	0.018	0.024	0.002
Brome-2	-	0.064	0.100	-	-
Brome-3	-	-	0.100	-	-
Fluor-2	-	-	-	-0.338	-0.327
Fluor-3	-	-	-	-	-0.327

al developed on the N1 and C2 atoms. This further demonstrates the existence of the delocalization of the conjugated π -electron system in 2, 3-dibromopyrazine molecule. Dipole moment equal to zero which confirms the symmetry group D_{2h} of pyrazine. The compound B5 (2, 3-di-fluoropyrazine) also shows a high dipole moment value (2.2435 Debye).

Fig. 4. π like frontier orbitals of the compound B3.

3. 3. Structure Activity/Property Relationship for Pyrazine Derivatives

For the series of pyrazine derivatives (Fig. 8) we have studied seven physicochemical properties with respect to their anti-proliferative activity against the BGC823 (human gastric cell).⁵⁷ The properties involved are: Surface area grid (SAG), molar volume (V), hydration energy (HE), partition coefficient octanol/water (log P), molar refractivity (MR), polarizability (Pol) and molecular weight (MW).

The results obtained using HyperChem 8.0.8 software are shown in Table 8. For example, Fig. 5 shows the favored conformation in 3D of compound 1.

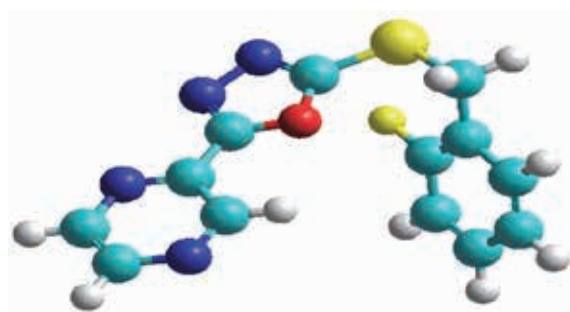


Fig. 5. 3D Conformation of compound 1 (HyperChem 8.03).

Table 8. QSAR properties of pyrazine derivatives.

Compounds	MW [amu]	SAG [Å ²]	V [Å ³]	Pol [Å ³]	MR [Å ³]	LogP	HE [kcal/mol]
1	288.30	466.47	770.17	28.82	79.14	1.94	-12.54
2	304.75	474.61	791.62	30.84	83.73	2.32	-12.63
3	349.20	485.20	810.26	31.54	86.54	2.60	-12.58
4	304.75	498.29	809.75	30.84	83.73	2.32	-13.29
5	349.20	505.96	828.55	31.54	86.54	2.6	-13.24
6	320.81	512.80	828.87	33.20	90.17	2.67	-11.30
7	304.36	486.18	800.84	31.18	85.58	2.29	-11.39
8	320.81	498.70	822.05	33.20	90.17	2.67	-12.25
9	424.32	628.79	1054.66	41.91	118.37	3.13	-11.55
10	363.41	543.20	948.38	39.20	110.97	2.48	-11.54
11	379.87	550.54	984.28	41.21	115.56	2.86	-10.69
12	424.32	554.53	997.06	41.91	118.37	3.13	-10.63
13	379.87	562.49	980.74	41.21	115.56	2.86	-11.45
14	363.41	543.20	948.38	39.20	110.97	2.48	-11.54
15	270.31	475.71	769.23	28.91	79.01	2.55	-13.67
16	286.37	490.32	789.01	31.27	85.45	2.89	-12.89
17	349.20	517.21	832.69	31.54	86.54	2.60	-14.62
18	306.29	476.68	771.74	28.73	79.26	1.34	-13.64

Molar refractivity and polarizability relatively increase with the size and the molecular weight of the studied pyrazine derivatives (Table 8 and fig.6). This result is in agreement with the formula of Lorentz-Lorenz, which gives a relationship between polarizability, molar refractivity and molecular size.

From the obtained results presented in Table 8 and figure 6, we observed that polarizability data and molecular refractivity are generally proportional to the size and the molecular weight of pyrazine derivatives. This explains the congruity of our results with Lorentz-Lorenz expression. For instance, compound 9 and compound 12 show the same maximum values of polarizability (41.91 (Å³)) and refractivity (118.37(Å³)). These compounds have also

high values of molecular weight (424.32 uma), and a slight difference in surfaces and volumes.

Hydration energy in absolute value, the most important is that of the compound 17 (14.62 kcal · mol⁻¹) and the smallest value is that of the compound 12 (10.63 kcal · mol⁻¹). Indeed, in biological environments, the polar molecules are surrounded by water molecules. They have established hydrogen bonds between them.

Hydrophobic groups in pyrazine derivatives induce a decrease of hydration energy.

However, the lipophilie increases proportionally with the hydrophobic features of the substituent. As seen in Table 8, compound 17 is expected to have the highest hydrophilicity, whereas compound number 12 should be

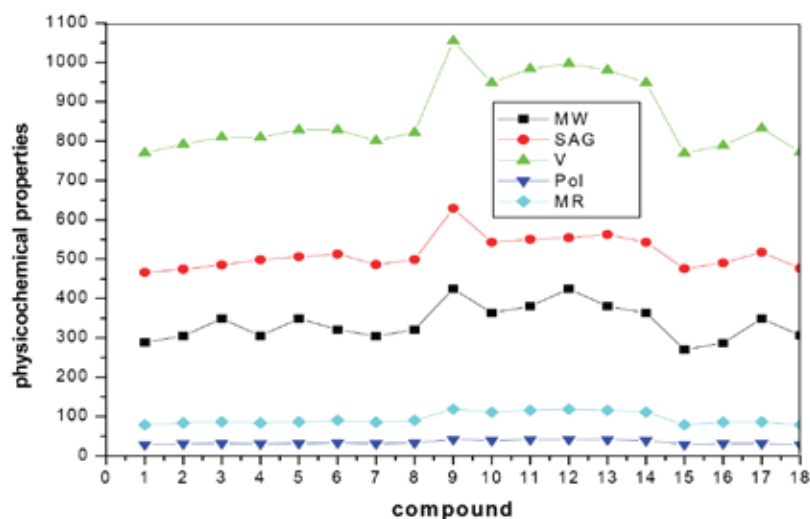


Fig. 6. Graphical representation of physicochemical properties.

most lipophilic. This implies that these compounds should have poor permeability across the cell membrane.

We noticed that compound 17 possess seven hydrogen bond acceptors (HBA) and no hydrogen bond donors (HBD), the presence of hydrophilic groups in this compound result in an increase of the hydration energy. This property explains the ability of these compounds, not only to fix the receptor but also to activate it. Hydration energy measures the degree of agonist character of a potential drug molecule.

Almost ($\log P$) of studied molecules have optimal values. For good oral bioavailability, the $\log P$ must be greater than zero and less than 3 ($0 < \log P < 3$). For very high values of $\log P$, the drug has low solubility and for very low values of $\log P$, the drug has difficulty penetrating the lipid membranes. Thus, compound 17 has the most important hydration energy and the optimal value of $\log P$, the small value of molecular weight leading to better distribution and solubility in fabrics, good oral bioavailability and permeability in cellular membranes respectively (Fig. 7).

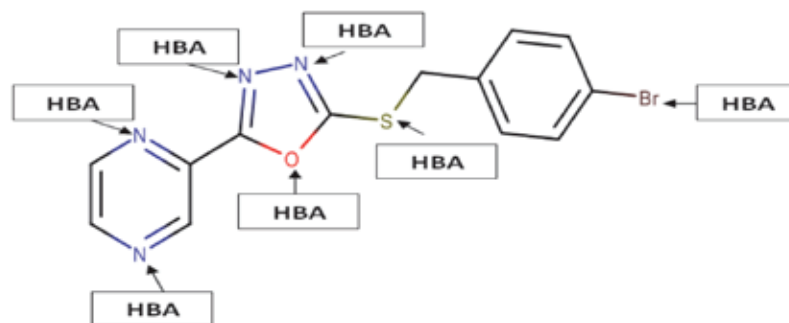


Fig. 7. Acceptor sites of proton for compound 17.

Table 9. Pharmacological activities and properties involved in MPO methods for drug-likeness of pyrazine derivatives.

N°	pIC ₅₀ _{BGC823} ⁵⁷	logP <5	Lipinski's rule			Veber rules	
			MW [amu]	HBA <10	HBD <5	NRB <10	TPSA[A ^{o2}] <140
1	4.74	1.94	288.30	5	0	4	64.71
2	4.56	2.32	304.75	5	0	4	64.71
3	4.76	2.60	349.20	5	0	4	64.71
4	4.8	2.32	304.75	5	0	4	64.71
5	4.94	2.6	349.20	5	0	4	64.71
6	4.87	2.67	320.81	4	0	4	51.57
7	4.73	2.29	304.36	4	0	4	51.57
8	4.69	2.67	320.81	4	0	4	51.57
9	4.70	3.13	424.32	5	0	5	56.50
10	4.53	2.48	363.41	4	0	4	51.57
11	4.46	2.86	379.87	5	0	5	56.50
12	4.44	3.13	424.32	5	0	5	56.50
13	4.69	2.86	379.87	5	0	5	56.50
14	4.57	2.48	363.41	5	0	5	56.50
15	4.60	2.55	270.31	5	0	4	64.71
16	4.67	2.89	286.37	4	0	4	51.57
17	4.59	2.60	349.20	5	0	4	64.71
18	4.48	1.34	306.29	5	0	4	64.71

3. 4. Drug-Likeness Screening Applied in Pyrazine Derivatives

We have applied rules of thumb and calculated metrics of eighteen derivatives of pyrazine (Fig. 8) taken from literature with their anti-proliferative activity against the BGC823.⁵⁷

The properties involved are: octanol/water partition coefficient ($\log P$), molecular weight (MW), hydrogen bond donors (HBD), hydrogen bond acceptors (HBA), number of rotatable bonds (NRB) and polar surface area (TPSA). All the results have been calculated using HyperChem 8.0.8 and Marvin Sketch 6.2.1 software, which are listed respectively in Table 9, we have studied Lipinski and Veber rules to identify “drug-like” compounds:^{58,59}

- (1) There are less than 5 H-bond donors (expressed as the sum of OHs and NHs).
- (2) The molecular weight is under 500 DA.
- (3) The $\log P$ is under 5.
- (4) There are less than 10 H-bond acceptors (expressed as the sum of Ns and Os).

(5) Rotatable bonds are under 10.

(6) TPSA is under 140 \AA^2

All the compounds of the series have the MW under 500 DA, thus they can easily pass through the cell membrane and the better the absorption will be.

There are less than 10 H-bond acceptors and 0 H-bond donors, the fat solubility will be high and therefore the drug will be able to penetrate the cell membrane to reach the inside of the cell. If two of these rules are unsatisfied, the compound will have a problem in absorption and permeability.⁶⁰

TPSA of pyrazine derivatives was found in the range of $52.325\text{--}65.217 \text{ \AA}^2$ and is well below 140 \AA^2 , indicating that these compounds should have good cellular plasmatic membrane permeability. All the screened compounds were flexible, especially; compounds 9 and 11–14 which have 5 rotatable bonds (table 9).

3. 5. Quantitative Structure-Activity Relationships Studies (QSAR) of Pyrazine Derivatives

When chemical or physical properties and molecular structures are derived from numbers, it is often possi-

ble to propose mathematical relations connecting them, which allow making quantitative predictions. The obtained mathematical expressions can then be used as a predictive means of the biological response for similar structures. They are widely used in the pharmaceutical industry to identify promising compounds, especially at the early stages of drug discovery.⁶¹

Relationships between the physicochemical properties of chemical substances and their biological activities can be derived using QSAR (Quantitative Structure-Activity Relationships) concept. These models can also be used to predict the activities of new chemical entities and for their design.⁶² therefore, the biological activity is quantitatively expressed as the concentration of substance necessary to obtain a certain biological response. For that purpose, multiple linear regression, MLR, and artificial neural networks (ANNs) are used. The accuracy of such models is mainly evaluated by the correlation coefficient R^2 .⁶³ The MLR and ANN models were generated using JMP 8.0.2 software.

The equilibrium geometries and the highest occupied molecular orbital energy (E_{HOMO}) and lowest unoccupied molecular orbital energy (E_{LUMO}) and dipole moment (μ) of pyrazine derivatives were determined at the B3LYP/cc-pVDZ level of theory. We list in table 10 of the

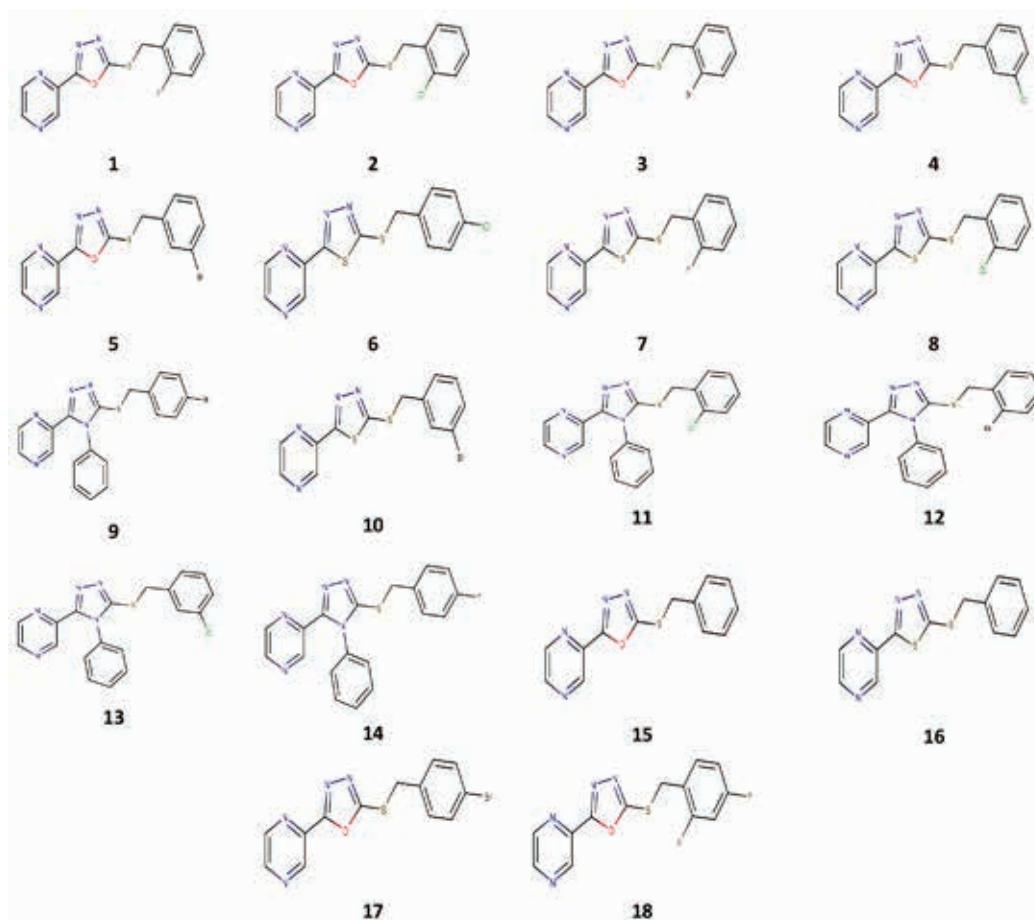


Fig. 8. Structural comparison of pyrazine derivatives.

Table 10. Values of molecular descriptors.

N°	pIC50 _{BGC823} ⁵⁷	V [Å ³]	HE [kcal/mol]	Log P	MR [Å ³]	SAG [Å ²]	MW [amu]	Pol [Å ³]	E _{HOMO} [au]	E _{LUMO} [au]	μ [Debye]
1	4.740	770.170	-12.540	1.940	79.140	466.470	288.300	28.820	-0.239	-0.079	0.886
2	4.560	791.620	-12.630	2.320	83.730	474.610	304.750	30.840	-0.249	-0.081	5.144
3	4.760	810.260	-12.580	2.600	86.540	485.200	349.200	31.540	-0.240	-0.080	0.887
4	4.800	809.750	-13.290	2.320	83.730	498.290	304.750	30.840	-0.243	-0.081	1.269
5	4.940	828.550	-13.240	2.600	86.540	505.960	349.200	31.540	-0.247	-0.082	1.498
6*	4.870	828.870	-11.300	2.670	90.170	512.800	320.810	33.200	-0.236	-0.086	2.564
7	4.730	800.840	-11.390	2.290	85.580	486.180	304.360	31.180	-0.234	-0.084	5.024
8	4.690	822.050	-12.250	2.670	90.170	498.700	320.810	33.200	-0.235	-0.086	5.023
9*	4.700	1054.660	-11.550	3.130	118.370	628.790	424.320	41.910	-0.223	-0.065	4.262
10	4.530	948.380	-11.540	2.480	110.970	543.200	363.410	39.200	-0.223	-0.064	4.275
11*	4.460	984.280	-10.690	2.860	115.560	550.540	379.870	41.210	-0.220	-0.063	4.963
12	4.440	997.060	-10.630	3.130	118.370	554.530	424.320	41.910	-0.220	-0.063	4.949
13	4.690	980.740	-11.450	2.860	115.560	562.490	379.870	41.210	-0.224	-0.067	4.190
14	4.570	948.380	-11.540	2.480	110.970	543.200	363.410	39.200	-0.223	-0.064	4.275
15	4.600	769.230	-13.670	2.550	79.010	475.710	270.310	28.910	-0.240	-0.081	4.278
16	4.670	789.010	-12.890	2.890	85.450	490.320	286.370	31.270	-0.233	-0.083	1.449
17	4.590	832.690	-14.620	2.600	86.540	517.210	349.200	31.540	-0.241	-0.081	4.127
18	4.480	771.740	13.640	1.340	79.260	476.680	306.290	28.730	-0.243	-0.084	4.472

* denotes the selected compounds for external validation (test set).

supplementary material the Cartesian coordinates of the optimized pyrazine derivatives equilibrium structures. Then, the QSAR properties module from Hyper Chem 8.08 was used to calculate: molar weight (MW), surface area (SAG), volume (V), molar refractivity (MR), polarizability (Pol), octanol-water partition coefficient (log P) and hydration energy (HE).

3. 5. 1. Multiple Linear Regression (MLR)

Despite being the oldest, MLR^{64,65} still remains one of the most popular approaches to build QSAR models. This is due to its simple practical use, ease of interpretation and transparency. Indeed, the key algorithm is available and accurate predictions can be provided.⁶⁶ The values of the calculated descriptors are those listed in Table 10. Data were randomly divided into two groups: a training set (internal validation) and a testing set (external validation) at a ratio of 80:20. A correlation matrix between parameters was performed on all nine descriptors. Nevertheless, the analysis revealed six independent descriptors for the development of the model. The significant correlation analysis between biological activity and descriptors is represented by the following equation:

$$\begin{aligned} \text{pIC50}_{\text{BGC823}} = & -6.878 + 0.0115 \\ & \text{V} - 0.0134\text{HE} + 0.1763\text{MR} - 0.0087 \\ & \text{SAG} - 0.004355\text{MAG} - 0.5185\text{Pol} - 15.46 \\ & \text{E}_{\text{HOMO}} - 66.309\text{E}_{\text{LUMO}} - 0.067 \mu \end{aligned} \quad (1)$$

Where, pIC50 is the response or dependent variable (V, HE, MR, SAG, MAG, Pol, E_{HOMO}, E_{LUMO} and μ) are

descriptors (features or independent variables). Within the regression, the coefficients in front of these descriptors are optimized.

The F value (F = 11.84) was found to be statistically significant at 95% level, since all the calculated F value is higher as compared to tabulated values.

For validation of the model, we plot in Fig. 9 the experimental activities against the predicted values as determined by equation (1). We can observe that the predicted pIC50 values are in an acceptable agreement and regular distribution with experimental ones with correlation coefficient (R²) for the training set (R²_{inter} = 0.955) and test set (R²_{ext} = 0.930) indicate the significant correlation between different independent variables with anti-proliferative activity against the BGC823.

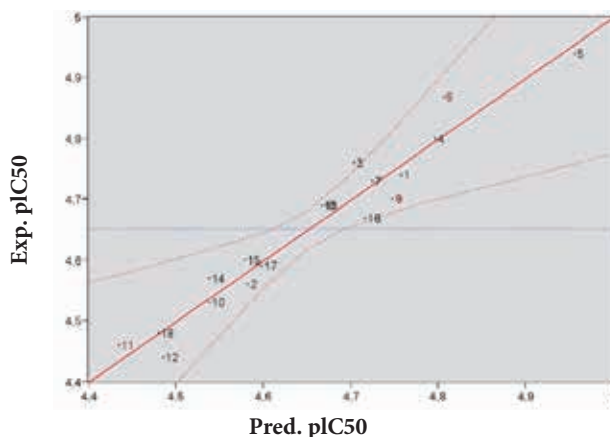


Fig. 9. Correlation of experimental and predicted pIC50 values as derived using MLR.

3. 5. 2. Artificial Neural Networks

ANN^{67–70} is a popular nonlinear model, used to predict the biological activity (i.e. IC₅₀) of the datasets of therapeutic molecules. It presents several benefits like better prediction, adaptation and generalization capacity beyond the studied sample, and better stability of the coefficients. It is employed in complex drug design, drug engineering and medicinal chemistry domains.⁷¹ In this work, the neural network is a system of fully interconnected neurons arranged in three layers. The input layer is made of nine neurons, where each of them receives one of the nine descriptors selected from the correlation matrix of the model. The intermediate (hidden) layer is composed of four neurons that form the deep internal pattern that discovers the most significant correlations between

predicted and experimental data. One neuron constitutes the output layer, which returns the value of pIC₅₀ (Fig. 10).⁷²

As it can be seen in Fig. 10, a good agreement between experimental data and predicted pIC₅₀ issued from the ANN model is observed. Indeed, the statistical parameters for this model, reveal a correlation coefficient close to 1 (= 0.995), indicating that the ANN one is more reliable. Furthermore, the robustness of the model was further confirmed by the significant value of the test data set (= 0.920).

3. 5. 3. Virtual Screening Application

The aim of this study is to identify new structures of pyrazines⁷³ with improved anti-proliferative activity against BGC823 that has to be within the applicability do-

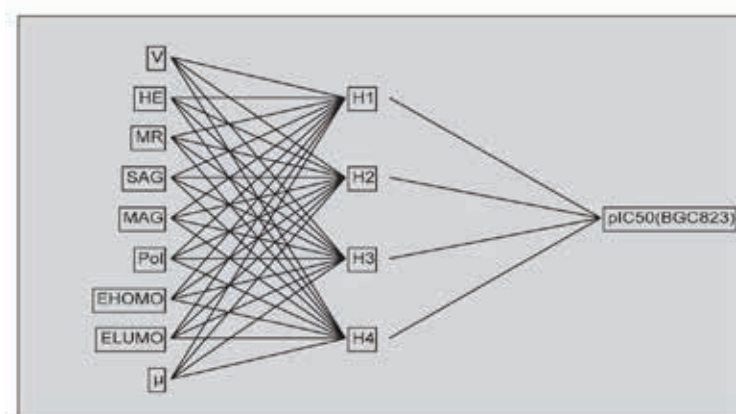


Fig. 10. Structure of ANN.

Table 11. Experimental and predicted pIC₅₀ values using MLR and ANN methods.

N°	Exp. pIC ₅₀ (BGC823)	Pred. pIC ₅₀ (BGC823)	
		MLR	ANN
1	4.740	4.757	4.736
2	4.560	4.582	4.562
3	4.760	4.704	4.764
4	4.800	4.796	4.804
5	4.940	4.956	4.931
6*	4.870	4.806	4.869
7	4.730	4.724	4.717
8	4.690	4.671	4.696
9*	4.700	4.748	4.642
10	4.530	4.537	4.550
11*	4.460	4.434	4.521
12	4.440	4.485	4.443
13	4.690	4.666	4.686
14	4.570	4.537	4.550
15	4.600	4.579	4.603
16	4.670	4.716	4.672
17	4.590	4.598	4.595
18	4.480	4.480	4.481

* denotes the compounds selected for external validation (test set).

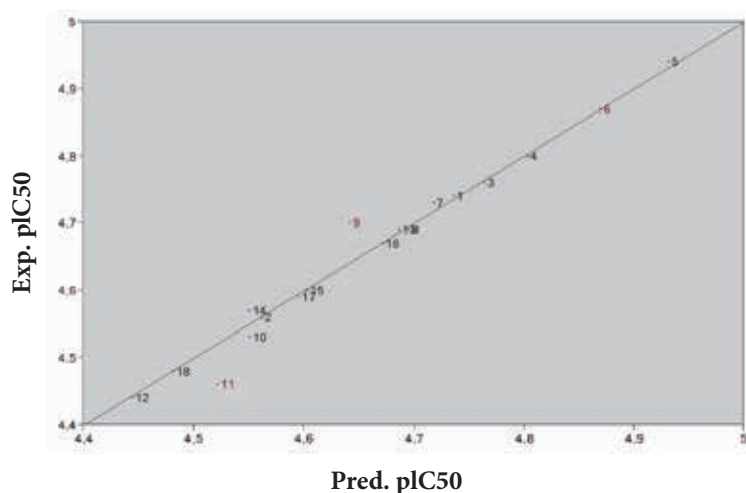
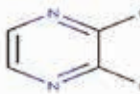
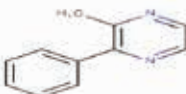
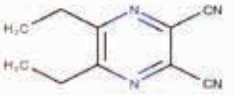
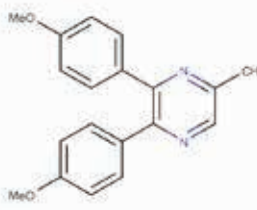
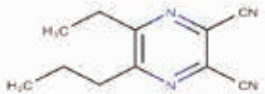
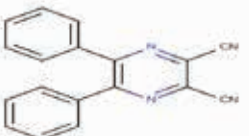
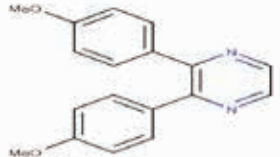
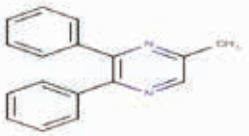
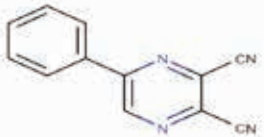
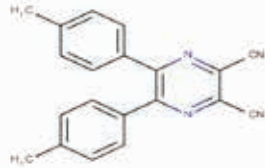
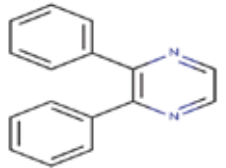
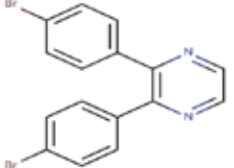


Fig. 11. Correlation of experimental and predicted pIC50 values obtained using ANN.

Table 12. Proposed structural compounds and predicted activities.

No.	Compound structure	pIC50	No.	Compound structure	pIC50
1		6.251	7		2.884
2		5.789	8		3.205
3		4.495	9		7.570
4		2.941	10		3.770
5		6.907	11		7.632
6		3.878	12		4.931

main of the developed model. The structures and activities of these compounds are reported in table 12.

4. Conclusion

The present work deals with the molecular properties of pyrazine. The HF, MP2 and DFT methods, the DFT method is more appropriate for further study on pyrazine rings. The geometry of the pyrazine is symmetric and planar, as all the dihedral angles are either nearly 0° or 180°, which makes this conformation more stable. The compound B3(2,3-dibromo pyrazine) is predicted to be the most reactive with a smaller HOMO–LUMO energy gap of all pyrazine systems, C2 and C3 positions are the most preferential site of nucleophilic attack.

Afterward, we showed that both ANN and MLR methods provide similar QSAR model accuracy. As can be seen in Table 11, the ANN network has substantially better predictive capabilities compared to MLR, leading to pIC50 values closer to the experimental determinations. Nevertheless, both models remain satisfactory and exhibit a high predictive power, thus validating their use to explore and propose new molecules as anti-proliferative activity against the BGC823.

Based on the obtained QSAR equation we have identified a series of potential novel compounds of pyrazine. This series has been used as a primary step for predicting the anti-proliferative activity against the BGC823. It is worth testing the reliability of these predictions in vitro, our work should help in identifying new compounds targeting anti-proliferative activity against the BGC823.

5. References

1. V. M. Baldwin, S. D. Arikatt, T. J. Sindhu, M. Chanran, A. R. Bhat, K. Krishnakumar, *World J. Pharm. Sci.* **2014**, *3*, 1124–1132.
2. D. L. Trump, H. Payne, K. Miller, J. S. de Bono, J. Stephenson, H. Burris, F. Nathan, M. Taboada, T. Morris, A. Hubner, *J. of Prostate*, **2011**, *71*, 1264–1275. DOI:10.1002/pros.21342
3. C. P. Meher, A. M. Rao, Md. Omar, *Asian J. Pharm. Sci. & Res.* **2013**, *3*, 52–56.
4. L. E. Schechter, Q. Lin, D. L. Smith, G. Zhang, Q. Shan, B. Platt, M. R. Brandt, L. A. Dawson, D. Cole, R. Bernotas, A. Robichaud, S. Rosenzweig-Lipson, C.E. Beyer, *Int. J. Neuropsychopharmacol.* **2008**, *33*, 1323–1335. DOI:10.1038/sj.npp.1301503
5. S. Spaia, I. Magoula, G. Tsapas, G. Vayonas, *Perit. Dial. Int.* **2002**, *20*, 47–52. DOI:10.1177/089686080002000109
6. K. Whalen, “*Pharmacology*”, 6th edition, University of Florida, College of Pharmacy Gainesville, Gainesville, Florida, USA, **2014**.
7. S. Rosenzweig-Lipson, J. Zhang, H. Mazandarani, L. H. Boyd, A. sabb, J. Sabalski, G. Stack, G. Welmaker, J. E. Barrett, *J. Dunlop, Brain Res.* **2006**, *1073–1074*, 240–251. DOI:10.1016/j.brainres.2005.12.052
8. W. J. Hehre: Practical Strategies for Electronic Structure Calculations, Wave functions, Irvine, California, USA, **1995**.
9. I. H. Nazli, D. B. Celepci, G. Yakali, D. Topkaya, M. Aygün, S. Alp, *Acta Chim. Slov.* **2018**, *65*, 86–96. DOI:10.17344/acsi.2017.3613
10. F. Odame, *Acta Chim. Slov.* **2018**, *65*, 328–332. DOI:10.17344/acsi.2017.4001
11. S. Belaidi, R. Mazri, H. Belaidi, T. Lanez, D. Bouzidi, *Asian J. Chem.* **2015**, *25*, 9241–9245. DOI:10.14233/ajchem.2013.15199
12. Z. Haddadi, H. Meghezzi, A. Amar, A. Boueckkine, *J. Theor. Comput. Chem.* **2019**, *31*, 595–601. DOI:10.1142/S0219633619500019
13. A. K. Sachan, S. K. Pathak, S. Chand, R. Srivastava, O. Prasad, S. Belaidi, L. Sinha, *Spectrochim. Acta A Mol. Biomol. Spectrosc.* **2014**, *132*, 568–581. DOI:10.1016/j.saa.2014.05.011
14. S. Belaidi, Z. Almi, D. Bouzidi, *J. Comput. Theor. Nanosci.* **2014**, *11*, 2481–2488. DOI:10.1166/jctn.2014.3665
15. C. M. Chang, H. L. Tseng, A. F. Jalbout, A. de Leon, *J. Comput. Theor. Nanosci.* **2013**, *10*, 527–533. DOI:10.1166/jctn.2013.2730
16. T. L. Jensen, J. Moxnes, E. Unneberg, *J. Comput. Theor. Nanosci.* **2013**, *10*, 464–469. DOI:10.1166/jctn.2013.2720
17. M. Ibrahim, H. Elhaes, *Rev. Theor. Sci.* **2013**, *1*, 368–376. DOI:10.1166/rits.2013.1012
18. E. C. Anota, H. H. Cocolletzi, M. Castro, *J. Comput. Theor. Nanosci.* **2013**, *10*, 2542–2546. DOI:10.1166/jctn.2013.3244
19. F. Bazooyar, M. Taherzadeh, C. Niklasson, K. Bolton, *J. Comput. Theor. Nanosci.* **2013**, *10*, 2639–2646. DOI:10.1166/jctn.2013.3263
20. E. R. Davidson : Quantum Theory of Matter, *Chem. Rev.*, guest editor, department of chemistry, Indiana university, India, **1991**, *91*, 649. DOI:10.1021/cr00005a600
21. S. Belaidi, H. Belaidi, D. Bouzidi, *J. Comput. Theor. Nanosci.* **2015**, *12*, 1737–1745. DOI:10.1166/jctn.2015.3952
22. B. Souyei, A. Hadj Seyd, F. Zaiz, A. Rebiai, *Acta Chim. Slov.* **2019**, *66*, 315–325. DOI:10.17344/acsi.2018.4793
23. R. A. Gupta, A. K. Gupta, S. G. Kaskhedikar, *Acta Chim. Slov.* **2009**, *56*, 977–984.
24. E. Zerroug, S. Belaidi, I. Benbrahim, S. Leena, *J. King Saud Univ. Sci.* **2019**, *31*, 595–601. DOI:10.1016/j.jksus.2018.03.024
25. F. Soualmia, S. Belaidi, N. Tchouar, T. Lanez, *J. Fundam. Appl. Sci.* **2020**, *12*, 392–415. DOI: 10.4314/jfas.v12i1S.28.
26. Y. C. Martin: Quantitative Drug Design, Marcel Dekker, New York, USA, **1978**.
27. I. Almi, S. Belaidi, E. Zerroug, M. Alloui, R. G. Ben Said, R. Linguerrri, M. Hochlaf, *J. Mol. Struct.* **2020**, *1211*, 128015. DOI:10.1016/j.molstruc.2020.128015
28. C. A. Lipinski, V. Lombardo, B. W. Dominy, P. J. Feeney, *Adv. Drug Deliv. Rev.* **2001**, *46*, 3–26. DOI:10.1016/S0169-409X(00)00129-0
29. E. L. Pankratov, E. A. Bulaeva, *Rev. Theor. Sci.* **2013**, *1*, 58–82. DOI:10.1166/rits.2013.1004

30. Q. Zhao, *Rev. Theor. Sci.* **2013**, *1*, 83–101.
DOI:10.1166/rits.2013.1005
31. A. Khrennikov, *Rev. Theor. Sci.* **2013**, *1*, 34–57.
DOI:10.1166/rits.2013.1003
32. V. Paitya, K. P. Ghatak, *Rev. Theor. Sci.* **2013**, *1*, 165–305.
DOI:10.1166/rits.2013.1008
33. D. Fisaletti, *Rev. Theor. Sci.* **2013**, *1*, 103–144.
DOI:10.1166/rits.2013.1006
34. D. M. Segall, *J. Curr. Pharm. Des.* **2012**, *18*, 1292–1310.
DOI:10.2174/138161212799436430
35. R. Darnag, B. Minaoui, M. Fakir, *Arab. J. Chem.* **2017**, *10*, 600–608. DOI:10.1016/j.arabjc.2012.10.021
36. P. Xuan, Y. Zhang, T. J. Tzeng, X. F. Wan, F. Luo, *Glycobiology*, **2012**, *22*, 554–560. DOI:10.1093/glycob/cwr163
37. S. Kothiwale, C. Borza, A. Pozzi, J. Meiler, *Molecules*. **2017**, *22*, 1576–1586. DOI:10.3390/molecules22091576
38. Z. Hajimahdi, A. Ranjbar, A. A. Suratgar, A. Zarghi, *Iran. J. Pharm. Res.* **2014**, *14*, 69–74.
39. M. Ghamri, D. Harkati, S. Belaidi, S. Boudergua, R. Ben Said, R. Linguierri, G. Chambaud, M. Hochlaf, *Spectrochim. Acta A Mol. Biomol. Spectrosc.* **2020**, *242*, 118724.
DOI:10.1016/j.saa.2020.118724
40. S. Boudergua, M. Alloui, S. Belaidi, M. Mogren Al Mogren, U. A. Abd Ellatif Ibrahim, M. Hochlaf, *J. Mol. Struct.* **2019**, *1189*, 307–314. DOI:10.1016/j.molstruc.2019.04.004
41. E. Pourbasheer, S. Vahdani, D. Malekzadeh, R. Aalizadeh, A. Ebadi, *Iran. J. Pharm. Res.* **2017**, *16*, 966–980.
42. HyperChem (Molecular Modeling System) Hypercube, Inc., 1115 NW, 4th Street, Gainesville, FL 32601, USA (2008).
43. Gaussian 09, M. J. Frisch, G. W. Trucks, H. B. Schlegel, G. E. Scuseria, M. A. Robb, J. R. Cheeseman, G. Scalmani, V. Barone, B. Mennucci, G. A. Petersson, H. Nakatsuji, M. Caricato, X. Li, H. P. Hratchian, A. F. Izmaylov, J. Bloino, G. Zheng, J. L. Sonnenberg, M. Hada, M. Ehara, K. Toyota, R. Fukuda, J. Hasegawa, M. Ishida, T. Nakajima, Y. Honda, Y. Kitao, H. Nakai, T. Vreven, J. A. Montgomery, J. E. Peralta, F. Ogliaro, M. Bearpark, J. J. Heyd, E. Brothers, K. N. Kudin, V. N. Staroverov, T. Keith, R. Kobayashi, J. Normand, K. Raghavachari, A. Rendell, J. C. Burant, S. S. Iyengar, J. Tomasi, M. Cossi, N. Rega, J. M. Millam, M. Klene, J. E. Knox, J. B. Cross, V. Bakken, C. Adamo, J. Jaramillo, R. Gomperts, R. E. Stratmann, O. Yazyev, A. J. Austin, G. A. Cammi, R. Pomelli, C. Ochterski, J. W. Martin, R. L. Morokuma, K. Zakrzewski, V. G. Voth, P. Salvador, J. J. Dannenberg, S. Dapprich, A. D. Daniels, O. Farkas, J. B. Foresman, J. V. Ortiz, J. Cioslowski, D. J. Fox, Gaussian Inc., Wallingford, CT (2010).
44. MarvinSketch15.8.31, Chemaxon (<http://www.chemaxon.com>) (2015).
45. Database, (<http://www.molinspiration.com>).
46. JMP 8.0.2, SAS Institute Inc., (2009).
47. M. Kanno, Y. Ito, N. Shimakura, S. Koseki, H. Kono, Y. Fujimura, *J. Phys. Chem. - Chem. Phys.* **2015**, *17*, 2012–2024.
DOI:10.1039/C4CP04807E
48. P. Govindasamy, S. Gunasekaran, *J. Mol. Struct.* **2015**, *1081*, 96–109. DOI:10.1016/j.molstruc.2014.10.011
49. J. S. Murray, K. Sen, Molecular Electrostatic Potentials, 1st Edition, Concepts and Applications, Elsevier, Amsterdam, Holland, 1996.
50. I. Alkorta, J. J. Perez, *Int. J. Quantum Chem.* **1996**, *57*, 123–135.
DOI:10.1002/(SICI)1097-461X(1996)57:1<123::AID-QUA14>3.0.CO;2-9
51. E. Scrocco, J. Tomasi, *Adv. Quantum Chem.* **1978**, *11*, 115–193. DOI:10.1016/S0065-3276(08)60236-1
52. F. J. Luque, M. Orozco, P. K. Bhadane, S. R. J. Gadre, *J. Phys. Chem.* **1993**, *97*, 9380–9384. DOI:10.1021/j100139a021
53. J. Sponer, P. Hobza, *J. Quantum Chem.* **1996**, *57*, 959–970.
DOI:10.1002/(SICI)1097-461X(1996)57:5<959::AID-QUA16>3.0.CO;2-S
54. J. M. Seminario, Recent Developments and Applications of Modern Density Functional Theory, Elsevier, Amsterdam, Holland, **1996**. DOI:10.1016/S1380-7323(96)80082-3
55. I. Fleming: Frontier orbitals and organic chemical reactions, Wiley, New York, USA, **1976**.
56. G. L. Miessler, D. A. Tarr: *Inorganic Chemistry*, 2nd edition, Prentice-Hall Upper Saddle River, New Jersey, USA, **1999**.
57. Y. B. Zhang, X. L. Wang, W. Liu, Y. S. Yang, J. F. Tang, H. L. Zhu, *Bioorg. Med. Chem.* **2012**, *20*, 6356–6365. DOI:10.1016/j.bmc.2012.08.059
58. C. A. Lipinski, F. Lombardo, B. W. Dominy, P. J. Feeney, *J. Adv. Drug Deliv. Rev.* **2012**, *64*, 4–17.
DOI:10.1016/j.addr.2012.09.019
59. D. F. Veber, S. R. Johnson, H. Y. Cheng, B. R. Smith, K. W. Ward, K. D. Kopple, *J. Med. Chem.* **2002**, *45*, 2615–2623.
DOI:10.1021/jm020017n
60. M. Aurélien, Ph.D. Dissertation, Orleans University, France, **2006**.
61. F. Soualmia, S. Belaidi, H. Belaidi, N. Tchouar, Z. Almi, *J. Biomed. Sci.* **2017**, *11*, 584–591.
DOI:10.1166/jbns.2017.1476
62. B. Jhanwarb, V. Sharma, R. K. Singla, B. Shrivastava, *Pharmacologyonline*. **2011**, *1*, 306–344.
63. R. Darnag, B. Minaoui, M. Fakir, *Arab. J. Chem.* **2017**, *10*, 600–608. DOI:10.1016/j.arabjc.2012.10.021
64. I. Hammoudan, S. Matchi, M. Bakhouch, S. Belaidi, *Chemistry*, **2021**, *3*(1):391–401. DOI:10.3390/chemistry3010029
65. R. Dahmani, M. Manachou, S. Belaidi, S. Chtita, S. Boughdiri, *New J. Chem.* **2021**, *45*(3), 1253–1262.
DOI:10.1039/D0NJ05298A
66. K. Roy, S. Kar, R. N. Das, A Primer on QSAR/QSPR Modeling: Fundamental Concepts, Springer, New York, USA, **2015**.
67. S. Erić, M. Kalinić, A. Popović, M. Zloh, I. Kuzmanovski, *Int. J. Pharm.* **2012**, *437*, 232–241.
DOI:10.1016/j.ijpharm.2012.08.022
68. R. Lowe, H. Y. Mussa, J. B. Mitchell, R. C. Glen, *J. Chem. Inf. Model.* **2011**, *51*, 1539–1544. DOI:10.1021/ci200128w
69. E. Zerroug, S. Belaidi, S. Chtita, *J. Chin. Chem. Soc.* **2021**, *68*(2), 197–384. DOI:10.1002/jccs.202000457
70. F. Z. Fadel, N. Tchouar, S. Belaidi, F. Soualmia, O. Oukil, and K. Ouadah, *J. Fundam. Appl. Sci.*, **2021**, *13*(2), 942–964.
DOI:10.4314/jfas.v13i2.17.
71. C. Feng, S. Vijaykumar, *Clin. Exp. Pharmacol.* **2012**, *2*, 2–3.
DOI:10.4172/2161-1459.1000e113

72. B. D. Ripley, Pattern Recognition and Neural Networks, Cambridge University Press, NY United States, USA, 1996.

73. P. Ghosh, A. Mandal, Green Chem. Lett. Rev., 2012, 5(2), 127–134. DOI:10.1080/17518253.2011.585182

Povzetek

Preučevali smo elektronske strukture, vpliv substitucije, povezavo med strukturno fizikalno-kemijskimi lastnostmi ter aktivnostjo in učinkovinske podobnosti (ang. drug-likeness) pirazinskih derivatov s pomočjo *ab initio* (HF, MP2) in B3LYP/DFT (teorijo gostotnega funkcionala). V članku smo izračunali vrednosti naboja NBO (naravnih veznih orbital), dolžino vezi, dipolne momente, elektronsko afiniteto, tvorbeno entalpijo in QSAR lastnosti. Študij QSAR smo izvedli s pomočjo statističnih modelov multiple linearne regresije in nevronske mreže (ANN). Rezultati so pokazali visoko korelacijo med eksperimentalnimi in napovedanimi vrednostmi, s čimer smo preverili in pokazali ustreznost QSAR modelov. Statistična analiza je pokazala, da je ANN z arhitekturo 9-4-1 bolj ustrezna kot MLR. Pregled različnih molekul na osnovi molekularne podobnosti in uporabe QSAR domen je pokazal več kandidatov z izboljšanim antiproliferativnim delovanjem.



Except when otherwise noted, articles in this journal are published under the terms and conditions of the Creative Commons Attribution 4.0 International License

Scientific paper

Medicinal Plants Extracts Impact on Oxidative Stress in Mice Brain under the Physiological Conditions: the Effects of Corn Silk, Parsley, and Bearberry

Marijana Vranješ,¹ Dubravka Štajner,² Dejan Vranješ,¹ Bojana Blagojević,^{2,*} Ksenija Pavlović,³ Dubravka Milanov⁴ and Boris M. Popović²

¹ Emergency Centre, Clinical Centre of Vojvodina, Hajduk Veljkova 1, 21000 Novi Sad, Serbia

² Chemistry and Biochemistry Laboratory, Department of Field and Vegetable Crops, Faculty of Agriculture, University of Novi Sad, Trg Dositeja Obradovića 8, 21000 Novi Sad, Serbia

³ Department of Chemistry, Biochemistry and Environmental Protection, Faculty of Sciences, University of Novi Sad, Trg Dositeja Obradovića 3, 21000 Novi Sad, Serbia

⁴ Scientific Veterinary Institute "Novi Sad", Rumenački put 20, 21113 Novi Sad, Serbia

* Corresponding author: E-mail: bojana.blagojevic@polj.uns.ac.rs

Received: 04-13-2021

Abstract

This study was performed to examine the effects of medicinal plant extracts of corn silk (*Stigma maydis*), parsley leaf (*Petroselinum folium*), and bearberry leaf (*Uvae ursi folium*) on antioxidant status of the brain of experimental animals (mice) under the physiological conditions. Biological properties of these plants are insufficiently investigated and the aim was to explore their possible antioxidant effects that can alleviate oxidative damage of the brain tissue. Corn silk extract showed positive effect on activities of antioxidant enzymes in mice brain tissue. Parsley extract induced the increase in glutathione content and decrease of lipid peroxidation. Bearberry leaf extract induced catalase activity and decrease of hydroxyl radical content, while malonyldialdehyde accumulation was maintained at the control level. Results obtained in this study support the use of corn silk, parsley and bearberry leaves as natural antioxidant sources in the prevention and treatment of brain tissue damages and different diseases caused by oxidative stress.

Keywords: corn silk; parsley; bearberry; brain; oxidative stress; antioxidants

1. Introduction

Oxidative stress is one of the biggest threats to brain cells because of their large oxygen consumption.¹ Brain oxidative stress can be monitored primarily by superoxide and hydroxyl radical, hydrogen peroxide, other reactive oxygen species (ROS) and lipid peroxidation (LP) products.² Moreover, brain damages caused by free radicals can lead to serious neurological disorders such as stroke, dementia, and Alzheimer's disease.³ Traumatic brain injuries (TBI) are followed by increased reactive species production and LP process that can further cause severe damages and fatal consequences.⁴ Human clinical trials still did not result in efficient neuroprotective therapies for TBI and this disorder is among the most severe health problems and causes of death worldwide.⁵

When nerve injury occurs, the first minutes and hours are critical because of the activation of numerous sources of superoxide anion radical ($O_2^{\cdot-}$). The brain, like the other organs in aerobic organisms, has potent defenses against superoxide, including enzymatic antioxidants such as superoxide dismutase (SOD), catalase (CAT), guaiacol peroxidase (GPx), glutathione peroxidase (GSH-Px) and reduced glutathione as nonenzymatic antioxidant (GSH).⁶ By reduction of oxidative stress, they play important roles in neurotoxicity and neurological disorders.⁷

Over the last time period, the accent is given to the substances with antioxidant properties, designed to scavenge reactive species responsible for LP induction and its neurotoxic effects.⁴ Natural products can enhance antioxidant defense activities and minimize different tissue oxi-

dativ damages.^{8,9} It was shown that high dietary intake of some vitamins, carotenoids and flavonoids from food and medicinal plants can reduce the risk of Alzheimer's disease and exhibit a protective effect on neural tissue.¹⁰

Although the bioactive potential of corn silk (*Stigma maydis*), parsley leaf (*Petroselinum folium*) and bearberry leaf (*Uvae ursi folium*) is insufficiently tested, these medicinal plants showed the antioxidative and protective roles in treatment and prevention of many diseases, especially renal diseases, nephritis, kidney stones, chronic cystitis, for weakened kidneys, liver or pancreas.¹¹⁻¹³ The aim of this study was to explore their protective antioxidative and free radical scavenging effects that could prevent oxidative damage of the mice brain tissue.

2. Experimental

2.1. Chemicals and Reagents

Folin-Ciocalteu's reagent, guaiacol (2-methoxyphenol), NBT (Nitro Blue Tetrazolium), DPPH (2,2-diphenyl-1-picrylhydrazyl), TPTZ (2,4,6-tripyridyl-triazine), TBA (2-thiobarbituric acid), iron(III) chloride and potassium dihydrogen phosphate, methanol (HPLC gradient grade) and standard substances were obtained from Sigma-Aldrich (Belgrade, Serbia). All other reagents and chemicals were of analytical grade.

2.2. Plant Extracts Preparation

Corn silk (*Stigma maydis*; *Zea mays* L.), parsley leaf (*Petroselinum folium*; *Petroselinum crispum* L.) and bearberry leaf (*Uvae ursi folium*; *Arctostaphylos uva-ursi* L.) originated from Serbia and were bought commercially (Dr. Josif Pančić Institute, Belgrade, Serbia). Dried plant material was ground into a fine powder and macerated in 96% ethanol (1:20, w/v) for 72 h in the dark. Ethanol was evaporated under reduced pressure at 40 °C. The yields (Y) of obtained extracts were 6.12%, 8.28% and 34.93% for corn silk, parsley leaves and bearberry leaves, respectively. Dry residues were redissolved in water to obtain 5% (w/v) extracts.

2.3. Experimental Animals

Three months old male mice (*Mus musculus*, NMRI strain), weighing 31–46 g, were housed at the Department of Pharmacology, Toxicology and Clinical Pharmacology, Medical Faculty, University of Novi Sad, Serbia. Animals were handled in accordance with the European Union principles established for research on animal models (EU Directive 2010/63/EU) and Serbian national guideline (No. 41/09). Animals were bred at controlled temperature (21 ± 1 °C) and humidity (55% ± 1.5%), with 12 h day/12 h night cycle. They were fed standard laboratory mice feed, produced by the Veterinary Institute in Zemun,

Serbia. During the treatment, every animal was kept in a separate metabolic plexiglas cage. Ten animals were regarded as one group. The first group served as control and had *ad libitum* access to water and feed. Instead of water, animals in the other three groups were given appropriate plant extract: corn silk, parsley and bearberry leaf extract, respectively. After 28 days of the treatment, animals were sacrificed under urethane anesthesia. Brain tissue was removed and homogenized.

2.4. Preparation of Brain Homogenate

According to the method of Vranješ et al.¹³, after washing the brain tissue in saline solution, it was homogenized in 1.15% potassium chloride solution and 0.05 M potassium phosphate buffer solution (pH 7.4) to yield 10% homogenate (w/v). The mixture was ultrasonicated for 15 minutes and then centrifuged 5 minutes at 4000 × g and 4 °C. Supernatants were kept at –20 °C until analyses. Samples prepared as described were used for all assays except for those where it was differently stated (LP and GSH determinations).

2.5. Assessment of Prooxidant / Antioxidant Activity

The activity of the enzyme superoxide dismutase (SOD) was estimated by the ability of extract to inhibit photosensitive reduction of nitro blue tetrazolium chloride (NBT) reagent.¹⁴ Reaction medium was prepared by mixing 2.6 mL of 50 mM phosphate buffer (pH 7.8), 100 µL of 13 mM methionine, 100 µL of 75 µM NBT, 100 µL of 0.1 mM EDTA, and 50 µL of 2 µM riboflavin. Supernatant (10–50 µL) was added in test samples, while the same volume of buffer was added for blanks (maximum formazan production). The absorbance was read at 560 nm. The quantity of the enzyme needed for 50% inhibition of the NBT-formazan formation was expressed as one unit (U). Final results were calculated as U per milligram of proteins.

Catalase (CAT) activity was determined by measuring the reduction of absorbance at 240 nm, as a consequence of the degradation of H₂O₂.¹⁵ Blank was prepared by mixing 50 µL of supernatant and 3 mL of phosphate buffer (0.05 M, pH 7). In test tubes there were mixed 50 µL of supernatant, 2 mL of buffer and 1 mL of freshly prepared H₂O₂ (0.1%) was added to start the reaction. The quantity of the enzyme that degrades 1 µmol H₂O₂ in 1 min at 25 °C was expressed as one unit (U).

Guaiacol peroxidase (GPx) activity was determined by transformation of guaiacol to tetraguaiacol.¹⁶ The change of absorbance was measured at 436 nm. Supernatant (100 µL) was added to reaction medium containing 3 mL of phosphate buffer (0.1 M, pH 7), 50 µL of guaiacol solution (prepared by diluting 220 µL of guaiacol in 100 mL of water) and 30 µL of 12.3 mM H₂O₂. The one unit

(U) is the GPx activity that transforms 1 μmol of guaiacol to tetraguaiacol during 1 min at 25 °C.

The activity of glutathione peroxidase (GSH-Px) was assessed using cumene hydroperoxide and reduced glutathione (GSH) as the substrate.¹⁷ Supernatant (100 μL) was mixed with 700 μL TRIS buffer (pH 7.6). After 5 min of incubation, 100 μL of GSH (6 mg GSH dissolved in 10 mL TRIS buffer) and 100 μL of cumene hydroperoxide (5 μL diluted in 10 mL TRIS buffer) were added. After 10 min of incubation, 20% trichloroacetic acid (TCA) was added. The mixture was centrifuged for 5 minutes at $4000 \times g$ and 4 °C. The volume of 1 mL of supernatant was mixed with 2 mL TRIS buffer and 100 μL of 0.01 M DTNB (5,5'-dithio-bis(2-nitrobenzoic acid) reagent) was added. The GSH-Px activity was determined by the absorbance change at 412 nm and expressed as U/mg protein. The quantity of the enzyme that catalyses the oxidation of 1 μmol of GSH in 1 min at 25 °C was expressed as one unit (U).

Soluble protein content was set by the method of Bradford.¹⁸ The Bradford reagent was prepared by dissolving 100 mg of Coomassie Brilliant Blue G-250 in 3% perchloric acid. The absorbance of the complex was read at 595 nm. The calibration curve was prepared with bovine serum albumin.

For lipid peroxidation (LP), brain tissue (0.5 g) was homogenized with 4.5 mL of LP reagent. The LP reagent was composed of 0.5% thiobarbituric acid (TBA; prepared in 10% HClO_4) and 20% TCA, mixed in ratio 1:3. The homogenate was boiled at 100 °C for 30 min, centrifuged for 10 min at $4000 \times g$. The intensity of lipid peroxidation (LP) was expressed as the amount of malonyldialdehyde (MDA), which is one of the final products of lipid membrane degradation.¹⁹ The absorbances were read at 532 nm and 600 nm, and the final absorbance was calculated as $A_{532} - A_{600}$. The results were expressed as nmol MDA/mg protein.

Power of the tissue antioxidant systems capable to scavenge hydroxyl radical was measured by the deoxyribose degradation test.²⁰ In the reaction medium composed of 250 μL mL of 0.003% H_2O_2 (diluted in 12 mM phosphate buffer, pH 7.4), 250 μL of 0.1 mM FeSO_4 , and 250 μL of 10 mM 2-deoxyribose, 500 μL of supernatant was added. In control tubes, supernatant was replaced with buffer solution. The tubes were incubated for 30 min at 37 °C. Produced MDA was measured with LP reagent, as described above. Final results were calculated by the difference between sample and control, and were expressed as the hydroxyl radical quantity.

The quantity of GSH was determined with Ellman reagent (DTNB).²¹ The tissue (0.5 g) was homogenized with 4 mL of 5% TCA and centrifuged for 10 min at $4000 \times g$. Supernatant (100 μL) was added to reaction medium containing 2 mL TRIS buffer (0.4 M, pH 8.9) and 100 μL DTNB (6 mM, dissolved in methanol). Absorbance was read at 412 nm after 5 min and the results were expressed as μmol GSH/mg protein.

Antioxidant capacity was determined by free radical scavenging capacity and FRAP (Ferric Reducing Antioxidant Power) test.

Free radical scavenging capacity was determined using 90 μM DPPH (1,1-diphenyl-2-picrylhydrazyl) radical.²² At first, the proteins were precipitated with 20% TCA. Afterwards, there were mixed 200 μL of sample and 2 mL of DPPH and the absorbance was read at 515 nm after 30 min. Scavenging capacity was calculated by Eq 1:

$$\text{Inhibition (\%)} = (A_{\text{control}} - A_{\text{sample}}) / A_{\text{control}} \times 100\% \quad (1)$$

where control was without sample and presented 100% of radical content. The concentration of the homogenate that inhibits 50% of the DPPH radical was defined as IC_{50} value.

FRAP test was performed according to the method of Benzie and Strain (1999),²³ measuring the total antioxidant potential of the sample through the reduction of ferric ions (Fe^{3+}) to ferrous ions (Fe^{2+}). FRAP reagent was consisted of 300 mM acetate buffer pH 3.6, 10 mM TPTZ dissolved in 40 mM HCl, and 20 mM FeCl_3 mixed in ratio 10:1:1. The volume of 100 μL of sample was added to 2 mL of FRAP reagent and the absorbance was read at 593 nm after 5 min. Results were expressed as FRAP units. FRAP unit is equal to the concentration of 100 $\mu\text{mol/L}$ Fe^{2+} .

2. 6. Plant Extracts Polyphenol Characterization by HPLC-PDA Method

Separation and identification of polyphenol compounds were performed using the reversed phase high pressure liquid chromatography (RP-HPLC) with a photodiode array (PDA) detector. The spectra were acquired in the range 190–600 nm and chromatograms were plotted at 280 nm (hydroxybenzoic acids), 320 nm (hydroxycinnamic acids), 350 nm (flavonoids). The results were expressed as μg of the polyphenol compound per mL of the extract. For the flavonoid derivatives calibration curve of corresponding flavonoid glucoside was used for calculation and derivatives of hydroxycinnamic acids were calculated as corresponding aglycones.²⁴ The compounds were identified by comparing the retention time, and UV-Vis spectra with appropriate standards and literature data. Quercetin derivatives had absorption maximum at 356 nm, apigenin derivatives at 338 nm, and luteolin derivatives at 347 nm.²⁵

2. 7. Statistical Analysis

All determinations were performed in triplicate. Data were expressed as mean \pm standard error (SE). Values are given as means for ten mice. For statistical evaluation of data *Statistica 12* software (StatSoft Inc., USA) was used. Statistical significance of differences between means was tested by Duncan's multiple range test ($p < 0.05$).

3. Results and Discussion

The results of the antioxidant enzymes SOD and CAT activities in mice brain tissue are presented in Figure 1a and 1b, respectively. The only favorable and the highest SOD activity was observed after corn silk treatment (2.78 U/mg protein). SOD isoenzymes play an important role in cerebral ischemia, particularly in reperfusion injury when brain cells are resupplied with oxygen that leads to overproduction of ROS and LP process. Therefore, altering SOD activity can reduce neurotoxicity.²⁶ Bearberry extract treatment elevated CAT activity (1.17 U/mg protein), but more effective was the influence of corn silk extract (1.92 U/mg protein).

During oxidative stress, it is important that all scavenging mechanisms are active²⁷, which was achieved by corn silk extract in our experiment.

The effect of investigated medicinal plant extracts on soluble protein and GSH content in mice brain is shown in the Figure 2a and 2b. In comparison with the control (104.0 mg/g), protein content was significantly decreased after corn silk treatment (55.21 mg/g), while after bearberry extract treatment it was elevated (114.41 mg/g).

In mice brains treated with corn silk and parsley (162.53 and 89.59 nmol GSH/mg protein) quantities of GSH were above the control value (77.65 nmol GSH/mg protein, Figure 2b). The increase of GSH quantity is favorable for oxidative stress protection because of its role in peroxide

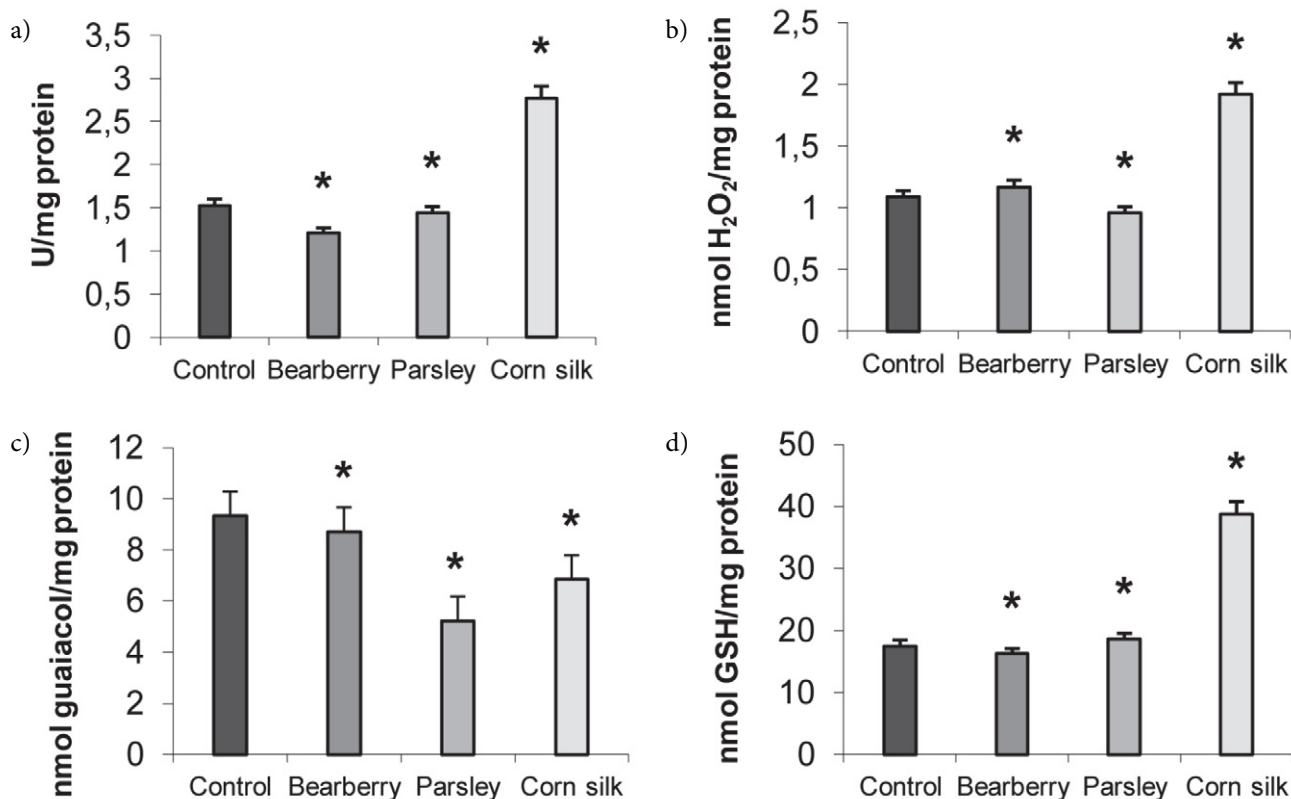


Figure 1. The activity of antioxidant enzymes SOD (a), CAT (b), GPx (c) and GSH-Px (d) in mice brain after the plant extract treatment. *Marked values significantly differ from control according to the Duncan's multiple range test results ($p < 0.05$).

The results presented in Figure 1c show that GPx activity in mice brain tissue decreased under the influence of all studied plant extracts. The lowest enzyme activity was obtained after the parsley extract intake (5.22 nmol guaiacol/mg protein). In comparison to the control and to the other examined extracts, corn silk extract significantly enhanced the activity of GSH-Px (38.78 nmol GSH/mg protein, Figure 1d). Mice GSH-Px activity is very important for the detoxification of H₂O₂ in brain cells in physiological conditions. It was proved that if GSH-Px is inhibited, CAT compensates its activity and *vice versa*, but in meta-

detoxification, as it is the substrate of the GSH-Px enzyme. Also, as an endogenous molecular antioxidant, it is important for neutralizing other reactive species. Thus, GSH is very important for intracellular redox status maintenance.²⁸

Table 1 shows DPPH free radical scavenging activity and the ability of ferric ion reduction (FRAP test) of the brain tissue of treated animals. Radical scavenging capacity was improved under the bearberry and parsley leaf treatment, while the effect of corn silk extract was at the control level. FRAP values were improved after treatments with all examined medicinal plant extracts.

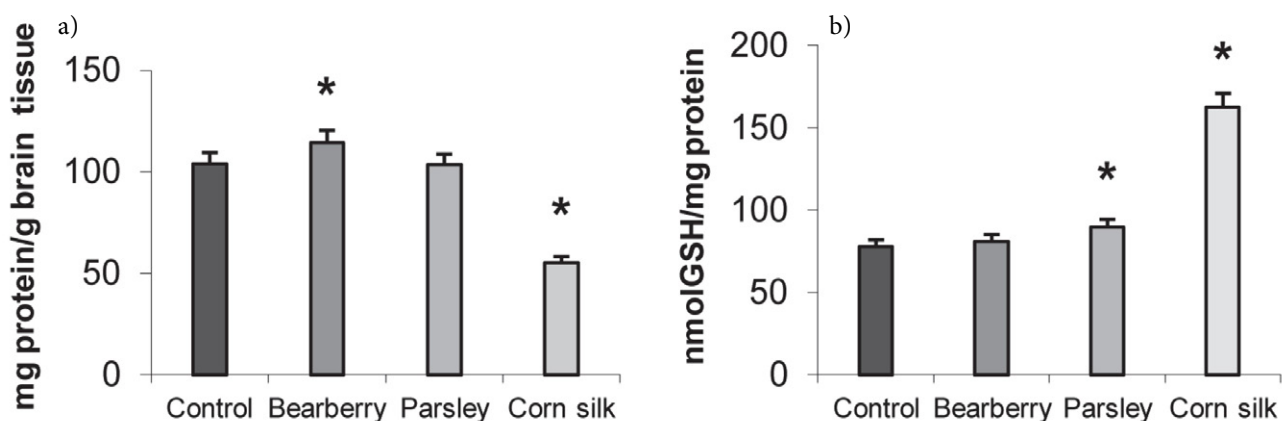


Figure 2. The soluble protein content (a) and reduced glutathione content (GSH; b) in mice brain after the plant extract treatment. *Marked values significantly differ from control according to the Duncan's multiple range test results ($p < 0.05$).

Table 1. DPPH radical scavenging capacity and ferric reducing antioxidant power (FRAP) of brain cells after the plant extract treatment

Sample	DPPH (IC ₅₀ , mg/mL)	FRAP units
Control	31.40 a	33.30 a
Bearberry	27.13 b	36.23 b
Parsley	29.52 ab	36.41 b
Corn silk	30.86 a	36.52 b

Values with the different letters are significantly different according to Duncan's multiple range test results ($p < 0.05$).

DPPH and FRAP tests are used for overall antioxidant potential assessment. Concerning the damages induced by free radicals and other highly reactive species, the increase of the antioxidant power of the cells is crucial to prevent different diseases.²⁹ Our results show that there are no significant differences among the effects of examined plant extracts and that all of them induced slightly better antioxidant status of brain cells in comparison to the control. It could be possibly achieved by the promoted activity of endogenous antioxidants or by the action of polyphenol

compounds present in the extracts. Plants rich in flavonoid compounds, like plants examined in our study (Table 1), promote DPPH free radical scavenging activity.³⁰

The effects of medicinal plant extracts on $\cdot\text{OH}$ scavenging activity and level of LP in mice brains are shown in Figure 3.

A significant decrease in $\cdot\text{OH}$ accumulation was observed in the brain tissue of mice drinking all three herb extracts (Figure 3a). Hydroxyl radical is one of the most harmful reactive species because of its high reactivity, small size and easy transport through cell compartments. It attacks proteins, DNA, lipids and carbohydrates leading to their dysfunctions and severe tissue damages. Since it initiates LP, potential of scavenging $\cdot\text{OH}$ is very important for brain cells, because lipids are responsible for normal structure and function of neural membranes.³¹

The LP in brain cells of mice drinking medicinal plant extracts was at the lower level than in the control group of animals. Accumulation of MDA, the product of LP, was significantly reduced under the influence of corn silk and parsley extract (1.09 and 1.43 nmol MDA/mg protein, Figure 3b). Brain cells are rich in polyunsaturated fat-

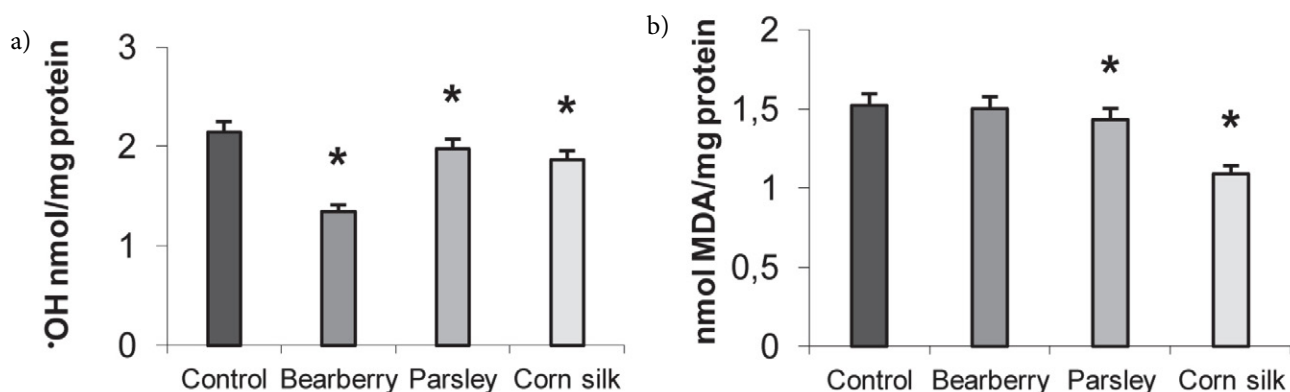


Figure 3. Hydroxyl radical scavenging activity (a) and level of lipid peroxidation (b) in mice brain after the plant extract treatment. *Marked values significantly differ from control according to the Duncan's multiple range test results ($p < 0.05$).

ty acids, which are very susceptible to LP, so the decrease of LP is very important, also because many neurological disorders, like Alzheimer's, Parkinson's, Huntington disease, schizophrenia, and many CNS traumas, involve dysfunction of lipid metabolism.³¹

All examined extracts were rich in phenolic content (Table 2) and phenolic compounds are generally known for their strong antioxidant activities, therefore they could be responsible for the decrease of LP in mice brain.³²

Polyphenol profile of medicinal plant extracts investigated in this study is presented in Table 2.

Table 2. Polyphenol compounds content in plant extracts.

Polyphenol compound	Bearberry leaves µg/mL extract	Parsley leaves µg/mL extract	Corn silk µg/mL extract
Gallic acid	162.99	4.14	3.16
Protocatechuic acid	-	2.69	1.20
Catechin	-	51.60	-
<i>p</i> -Hydroxybenzoic	-	0.42	0.69
Vanilic acid	-	-	1.63
Syringic acid	20.02	-	-
<i>p</i> -Coumaric acid derivative	-	-	0.75
<i>p</i> -Coumaric acid	-	7.53	1.47
Ferulic acid derivative	-	-	2.40
Ferulic acid	-	-	5.94
Quercetin derivatives	208.74	-	-
Quercetin	4.16	-	-
Kaempferol derivatives	-	211.80	-
Apigenin 7-glucoside	-	491.97	-
Apigenin derivative	-	192.44	-
Apigenin	-	0.22	-
Luteolin 7-glucoside	-	-	31.93
Luteolin derivatives	-	-	584.07
Luteolin	-	-	35.34
TOTAL	395.91	962.80	668.58

The polyphenol profile and content varies among the plant extracts, but all of them were pointed out with high flavonoid content, although flavonoid subgroups differ. Parsley and corn silk were rich in flavones. Apigenin derivatives predominated in parsley, while in corn silk extract the most dominant were luteolin derivatives. Flavonols, in particular, quercetin derivatives, were present in bearberry leaf extract, and kaempferol derivatives were present in parsley leaf extract.

Quercetin and galloyl derivatives, as well as other phenolic constituents, were found in bearberry leaves.³³ Within the same species phenolic content could vary due to many factors, including intrinsic biological or environmental factors. Aside from the most abundant bearberry phenolic glycoside arbutin, the contents of quercetin glucoside, myricetin, catechin, and caffeic acid showed geographic and climatic dependence.³⁴ Although our results

showed no significant effect of bearberry leaves on lipid peroxidation in mice brain, bearberry leaves extract *in vitro* delayed lipid oxidation showed due to its antioxidant activity and scavenging ability.³⁵ Very high contribution of phenolic content to antioxidant capacity of bearberry leaves was established.³⁶

De Menezes Epifanio et al. (2020) identified 30 different flavonoid glycosides in parsley leaves and showed that the antioxidant potential was directly related to the synergistic effect of all constituents present in the extract. Further, they proved that, unlike apigenin, its glycosylated derivative, apiin, could protect cells from oxidative stress caused by hydrogen peroxide.³⁷

Similarly to our results, cinnamic acids derivatives and luteolin derivatives were shown to be the most dominant phenolic constituents of corn silk.^{38,39} Wang et al. (2019) identified 76 phenolic compounds in corn silk aqueous extract, and shown that, after oral administration, phenolic compounds were metabolized and reached the blood predominantly in the forms of glucuronide conjugates.⁴⁰ Conjugation/deconjugation process in organism presents the key process that allows phenolic compounds to circulate through the organism and express their activities.⁴¹

Our results suggest that luteolin derivatives from corn silk extract may be responsible for the very potent reducing capacity of corn silk extract and protection against LP. Many studies showed strong antioxidant activities of corn silk extracts.⁴² Flavon compounds from corn silk showed better LP inhibition activity, and radical scavenging capacity than commercially used antioxidants.⁴³ Besides, maysin, luteolin derived flavone from corn silk, was shown to possess neuroprotective effects.⁴⁴ Polyphenol compounds from examined plant extracts could also induce higher antioxidant response which led to a better $\cdot\text{OH}$ scavenging activity in the brains of animals that were subjected to the treatments.

4. Conclusion

The intake of corn silk, parsley leaf and bearberry leaf extracts affected the metabolism of mice brain tissue. Corn silk showed a significant positive effect on activities of antioxidant enzymes SOD, CAT, and GSH-Px. The quantity of GSH was the highest under the influence of corn silk extract, while the accumulation of $\cdot\text{OH}$ and MDA was the lowest, suggesting its protective effect against LP. Parsley leaf extract induced the increase in GSH content and the decrease in $\cdot\text{OH}$ and MDA accumulation. Bearberry leaf extract induced CAT activity and the decrease in the accumulation of $\cdot\text{OH}$, while MDA accumulation was maintained at the control level. All three plant extracts were rich in polyphenol compounds, especially in flavonoids, which may be responsible for beneficial effects. Our results support the use of these medicinal plants as natural antioxidants in the prevention of oxidative stress provoked

damages of brain tissue, but further investigations are required to clarify their mechanisms of action.

Acknowledgment

This research was funded by the Ministry of Education, Science and Technological Development, Republic of Serbia, Contract No. 451-03-9/2021-14/200117

Conflicts of Interest

The authors declare that they have no conflict of interest.

5. References

- L. M. Haces, T. L. Montiel, L. Massieu, *Neurosci. J.* **2010**, *165*, 28–38. DOI: 10.1016/j.neuroscience.2009.10.003
- G. P. Marrazzo, P. Bosco, F. La Delia, *Neurosci. Lett.* **2011**, *504*, 252–256. DOI: 10.1016/j.pmp.2008.04.002
- M. Bains, E. D. Hall, *Biochim. Biophys. Acta, Mol. Basis Dis.* **2012**, *1822*, 675–684. DOI: 10.1016/j.bbdis.2011.10.017
- T. S. Anthonymuthu, E. M. Kenny, H. Bayır, *Brain. Res.* **2016**, *1640*(Pt A), 57–7. DOI: 10.1016/j.brainres.2016.02.006
- A. Kumar, D. J. Loane, *Brain. Behav. Immun.* **2012**, *26*, 1191–1201. DOI: 10.1016/j.bbi.2012.06.008
- L. B. Ceretta, G. Z. Réus, H. M. Abelaira, K. F. Ribeiro, G. Zappellini, F. F. Felisbino, A. V. Steckert, F. Dal-Pizzol, J. Quevedo, *J. Diabetes. Res.* **2012**, Article ID 302682, DOI: 10.1155/2012/302682
- J. C. Hanish Singh, V. Alagarsamy, S. Sathesh Kumar, Y. Narasimha Reddy, *Willd. Phytother. Res.* **2011**, *25*, 1061–1067. DOI: 10.1016/j.jep.2011.08.048
- D. Štajner, B. M. Popović, J. Čanadanović-Brunet, S. Đilas, G. Četković, *LWT-Food Sci. Technol.* **2014**, *55*, 408–413. DOI: 10.1016/j.lwt.2013.08.025
- D. Štajner, B. M. Popović, D. Čalić, M. Štajner, *Sci. World. J.* **2014**, *7* pages, DOI: 10.1155/2014/767392 –b.
- M. J. Engelhart, M. I. Geerlings, A. Ruitenber, J. C. van Swieten, A. Hofman, J. C. Witteman, M. M. Breteler, *JAMA*, **2002**, *287*(24): 3223–3229. DOI: 10.1001/jama.287.24.3223
- B. Hua, H. Chunx, X. Miaomiao, L. Xin, L. Rui, *Plant Food Hum. Nutr.* **2010**, *65*(3), 271–276. DOI: 10.1007/s11130-010-0172-6
- H. Jia, W. Aw, M. Hanate, S. Takahashi, K. Saito, H. Tanaka, M. Tomita, H. Kato, *J. Funct. Foods.* **2014**, *11*, 438–448. DOI: 10.1016/j.jff.2014.09.018
- M. Vranješ, B. M. Popović, D. Štajner, V. Ivetić, A. Mandić, D. Vranješ, *J. Funct. Foods.* **2016**, *21*, 272–282. DOI: 10.1016/j.jff.2015.12.016
- S. Mandal, A. Mitra, N. Mallick, *Physiol. Mol. Plant Path.* **2008**, *72*, 56–61. DOI: 10.1016/j.pmp.2008.04.002
- T. Iwase, A. Tajima, S. Sugimoto, K. Okuda, I. Hironaka, Y. Kamata, K. Takada, Y. Mizunoe, *Sci. Rep.* **2013**, *3*, 3081. DOI: 10.1038/srep03081
- I. Morkunas, J. Gmerek, *J. Plant. Physiol.* **2007**, *164*, 185–194. DOI: 10.1016/j.jplph.2005.11.005
- R. Ždero Pavlović, B. Blagojević, D. Latković, D. Agić, N. Mičić, D. Štajner, B. M. Popović, *Baltic Forestry*, **2020**, *26*(2), 420. DOI: 10.46490/BF420
- D. Štajner, B. M. Popović, D. Čalić-Dragsavac, Đ. Malenčić, S. Zdravković-Korać, *Phytother. Res.* **2011**, *25*(11), 1618–1622. DOI: 10.1002/ptr.3394
- J. K. Moon, T. Shibamoto, *J. Agric. Food Chem.* **2009**, *57*, 1655–1666. DOI: 10.1021/jf803537k
- J. M. Gardner, S. D. Aust, *J. Cataract Refractive Surg.* **2009**, *35*(12), 2149–2153. DOI: 10.1016/j.jcrs.2009.06.030
- D. Štajner, B. M. Popović, P. Boža, *Phytother. Res.* **2007**, *21*(12), 1242–1245. DOI: 10.1002/ptr.2244
- J. Čanadanović-Brunet, G. Četković, V. Tumbas Šaponjac, S. Stajčić, S., J. Vulić, J., S. Djilas, D. Štajner, B. Popović, *Ind. Crops Prod.* **2014**, *62*, 1–7. DOI: 10.1016/j.indcrop.2014.08.009
- I. F. F. Benzie, J. J. Strain, *Methods. Enzymol.* **1999**, *299*, 15–27. DOI: 10.1016/S0076-6879(99)99005-5
- B. Popović, B. Blagojević, R. Ždero Pavlović, N. Mičić, S. Bijelić, S. Bogdanović, A. T. Serra, *Food Chem.* **2020**, *302*:125373. DOI: 10.1016/j.foodchem.2019.125373
- T. Mabry, K. R. Markham, M. B. Thomas: The systematic identification of flavonoids. Springer Science & Business Media, **2012**, pp. 35–57.
- S. Fukui, T. Ookawara, H. Nawashiro, K. Suzuki, K. Shima, *Free Rad. Biol. Med.* **2002**, *32*, 289–298. DOI: 10.1016/S0891-5849(01)00804-8
- P. Klivenyi, O. A. Andreassen, R. J. Ferrante, N. Dedeoglu, G. Mueller, E. Lancelot, M. K. Bogdanov, J. K. Andersen, D. Jiang, M. F. Beal, *J. Neurosci.* **2000**, *20*, 1–7. DOI: 10.1523/JNEUROSCI.20-01-00001.2000
- F. Favilli, T. Iantomasi, M. Marraccini, M. Stio, B. Lunghi, C. Treves, M. T. Vincenzini, *Neurobiol. Aging* **1994**, *15*(4), 429–433. DOI: 10.1016/0197-4580(94)90074-4
- I. Álvarez-González, F. Fernando Garcia-Melo, V. R. Vásquez-Garzón, A. E. Saúl Villa-Treviño, O. Madrigal-Santillán, J. A. Morales-González, J. A. Mendoza-Peres, E. Madrigal-Bujaidar, *Evid. Based Complement. Alternat. Med.* **2014**, Article ID 379890, 8 pages. DOI: 10.1155/2014/379890
- I. Baranowska, S. Bajkacz, *Food Chem.* **2018**, *256*, 333–341. DOI: 10.1016/j.foodchem.2018.02.138
- R. M. Adibhatla, J. F. Hatcher, *Future Lipidol.* **2007**, *2*(4), 403–422. DOI: 10.2217/17460875.2.4.403
- A. Scalbert, I. T. Johnson, M. Saltmarsh, *Am. J. Clin. Nutr.* **2005**, *81*, 215S–217S. DOI: 10.1093/ajcn/81.1.215S
- M. Wrona, S. Blasco, R. Becerril, C. Nerin, E. Sales, E. Asensio, *Talanta*, **2019**, *196*, 498–509. DOI: 10.1016/j.talanta.2018.12.057
- E. Asensio, D. Vitales, I. Pérez, L. Peralba, J. Viruel, C. Montaner, J. Vallès, T. Garnatje, E. Sales, *Plants* **2020**, *9*(9), 1250. DOI: 10.3390/plants9091250
- N. A. Mohd Azman, M. G. Gallego, F. Segovia, S. Sureena Abdullah, S. M. Shaarani, M. P. Almajano Pablos, *Antioxidants* **2016**, *5*(11), 11. DOI: 10.3390/antiox5020011

36. X. C. Song, E. Canellas, E. Asensio, C. Nerin, *Talanta*, **2020**, 213, 120831. DOI: 10.1016/j.talanta.2020.120831
37. N. M. de Menezes Epifanio, L. R. I. Cavalcanti, K. F. Dos Santos, P. S. C. Duarte, P. Kachlicki, M. Ożarowski, C. J. Riger, D. S. de Almeida Chaves, *Food Funct.* **2020**, 11(6), 5346–5356. DOI: 10.1039/d0fo00484g
38. S. Žilić, M. Janković, Z. Basić, J. Vančetović, V. Maksimović, *J. Cereal Sci.* **2016**, 69, 363–370. DOI: 10.1016/j.jcs.2016.05.003
39. J. Tian, H. Chen, S. Chen, L. Xing, Y. Wang, J. Wang, *Food Funct.* **2013**, 10, 1526–1534. DOI: 10.1039/C3FO60171D
40. Y. Wang, Q. Liu, S. Fan, X. Yang, L. Ming, H. Wang, J. Liu, *J. Sep. Sci.* **2019**, 42(19), 3054–3066. DOI: 10.1002/jssc.201900407
41. F. Perez-Vizcaino, J. Duarte, C. Santos-Buelga, *J. Sci. Food Agric.* **2012**, 92(9), 1822–1825. DOI: 10.1002/jsfa.5697
42. K. Hasanudin, P. Hashim, S. Mustafa, *Molecules* **2012**, 17(8), 9697–9715. DOI: 10.3390/molecules17089697
43. S. C. Ren, Q. Q. Qiao, X. L. Ding, *Czech J. Food Sci.* **2013**, 31(2), 148–155.
44. D. J. Choi, S. L. Kim, J. W. Choi, Y. I. Park, *Life Sci.* **2014**, 109(1), 57–64. DOI: 10.1016/j.lfs.2014.05.020

Povzetek

Ta raziskava je bila izvedena z namenom proučitve učinkov zdravilnih rastlinskih izvlečkov koruznih laskov (*Stigma maydis*), peteršiljevih listov (*Petroselinum folium*) in listov vednozelenega gornika (*Uvae ursi folium*) na antioksidativni status možganov poskusnih živali (miši) pod fiziološkimi pogoji. Biološke lastnosti teh rastlin niso dovolj raziskane, zato je bil cilj raziskati njihove možne antioksidativne učinke, ki bi lahko ublažili oksidativne poškodbe možganskega tkiva. Izvleček koruznih laskov je pozitivno vplival na delovanje antioksidativnih encimov v možganskem tkivu miši. Ekstrakt peteršilja je spodbudil povečanje vsebnosti glutaciona in zmanjšal lipidno peroksidacijo. Izvleček listov vednozelenega gornika je spodbudil povečanje aktivnosti katalaze in zmanjšanje vsebnosti hidroksilnih radikalov, medtem ko se je kopičenje malonildialdehida ohranjalo na ravni kontrole. Rezultati, pridobljeni v tej raziskavi, podpirajo uporabo koruznih laskov, listov peteršilja in vednozelenega gornika kot naravnih virov antioksidantov pri preprečevanju in zdravljenju poškodb možganskega tkiva in različnih bolezni, ki jih povzročata oksidativni stres.



Except when otherwise noted, articles in this journal are published under the terms and conditions of the Creative Commons Attribution 4.0 International License

Scientific paper

Synthesis and Spectral Studies of Some Homo Dinuclear Lanthanide(III) Complexes of a Mesogenic Schiff Base

Prem Kumar Shrestha and Pawan Raj Shakya*

Department of Chemistry, Padma Kanya Multiple Campus, Tribhuvan University, Kathmandu, Nepal

* Corresponding author: E-mail: pawansh2003@yahoo.com

Tel.: +977-1-4218218

Received: 04-14-2021

Abstract

A mesogenic Schiff base, *N,N'*-di(4-decyloxysalicylidene)-1',8'-diamino-3',6'-dioxaoctane (H_2L) and a series of homo dinuclear lanthanide(III) complexes of the type $[Ln_2(LH_2)_3(NO_3)_4](NO_3)_2$, ($Ln = La, Pr, Nd, Sm, Eu, Gd, Tb, Dy, \text{ and } Ho$) were synthesized and characterized by elemental analysis, mass spectrometry, FTIR, and NMR spectral techniques. The IR and NMR spectral evidences imply bonding of a neutral bidentate H_2L species through two phenolate oxygen atoms in its zwitterionic form to Ln^{III} , rendering the overall geometry of the complexes as a seven-coordinate polyhedron – possibly distorted mono-capped octahedron. Differential scanning calorimetry (DSC) and polarizing optical microscopic (POM) studies reveal mesogenic properties (smectic-X, smectic-A and nematic mesophases) in the ligand over a wide range of temperature but none mesomorphism in the Ln^{III} complexes synthesized under this study. Luminescence studies exhibit emissions of H_2L and Tb^{III} complex.

Keywords: Mesogenic Schiff base; Ln^{III} Complexes; Zwitterionic-coordination; Mono-capped octahedron; Luminescence

1. Introduction

Lanthanide(III) complexes have received much attention due to their potential scientific applications in design of various luminescent metallomesogens,^{1,2} chemosensors,^{1,3} and photoluminescence materials and devices.⁴ Schiff base ligands having N and/or O donor atoms may assemble coordination architectures in which the Ln^{III} ions can promote Schiff base condensation.⁵ Mesomorphisms (an anisotropic liquid) in Schiff base ligands, may be obtained by their careful design in which the molecular order is in between the crystalline and isotropic liquid state.⁶ By incorporating Ln^{III} ions into the mesogenic Schiff base, one can obtain useful metallomesogens for the design of emissive LCDs.

The mesogenic properties of the ligands may often be influenced by the nature of coordinated metal ions.^{7,8} A metallomesogen has the greater tendency to exhibit intermolecular dative coordination in solid state.^{7,9} The design of metallomesogens is rather difficult because of their high coordination numbers incompatible with the structural anisotropy, the basics for showing liquid crys-

talline behavior.⁹ However, the columnar type of Ln^{III} ion containing metallomesogens was first synthesized by Piechocki *et al.*,¹⁰ in 1985 followed by the first calamitic Ln^{III} ion containing metallomesogens by Galyametdinov *et al.*,¹¹ in 1991. Lanthanide(III) complexes with high coordination number may be obtained by choice of nitrate as the counter-ion because it can coordinate in a bidentate fashion. In continuation of our earlier work on metallomesogens,¹²⁻¹⁷ we now report here synthesis and spectral studies of a mesogenic Schiff base (having terminal alkoxy chain next to benzene ring) and of some homo dinuclear Ln^{III} complexes.

2. Experimental

2.1. Starting Materials

All the required reagents of analytical grade (AR) were obtained from commercial sources and used without further purification; 1-bromodecane, 2,4-dihydroxybenzaldehyde and 1,8-diamino-3,6-dioxaoctane are from Sigma–Aldrich, USA; all the $Ln(NO_3)_3 \cdot xH_2O$ salts are

from Indian Rare Earths Ltd. and KI and KHCO_3 are from Merck. The organic solvents obtained from commercial vendors were dried using standard methods.¹⁸

2. 2. Synthesis

Experimental details given in Scheme 1 show synthesis of N,N' -di-(4-decyloxysalicylidene)-1',8'-diamino-3',6'-dioxaoctane (H_2L), **2**, by a two-step process, alkylation of 2,4-dihydroxybenzaldehyde with 1-bromodecane followed by condensation with 1,8-diamino-3,6-dioxaoctane. The Ln^{III} complexes, $[\text{Ln}_2(\text{LH}_2)_3(\text{NO}_3)_4](\text{NO}_3)_2$ ($\text{Ln} = \text{La, Pr, Nd, Sm, Eu, Gd, Tb, Dy, and Ho}$), **3**, were synthesized by reacting the H_2L and appropriate metal nitrate in solution state at room temperature.

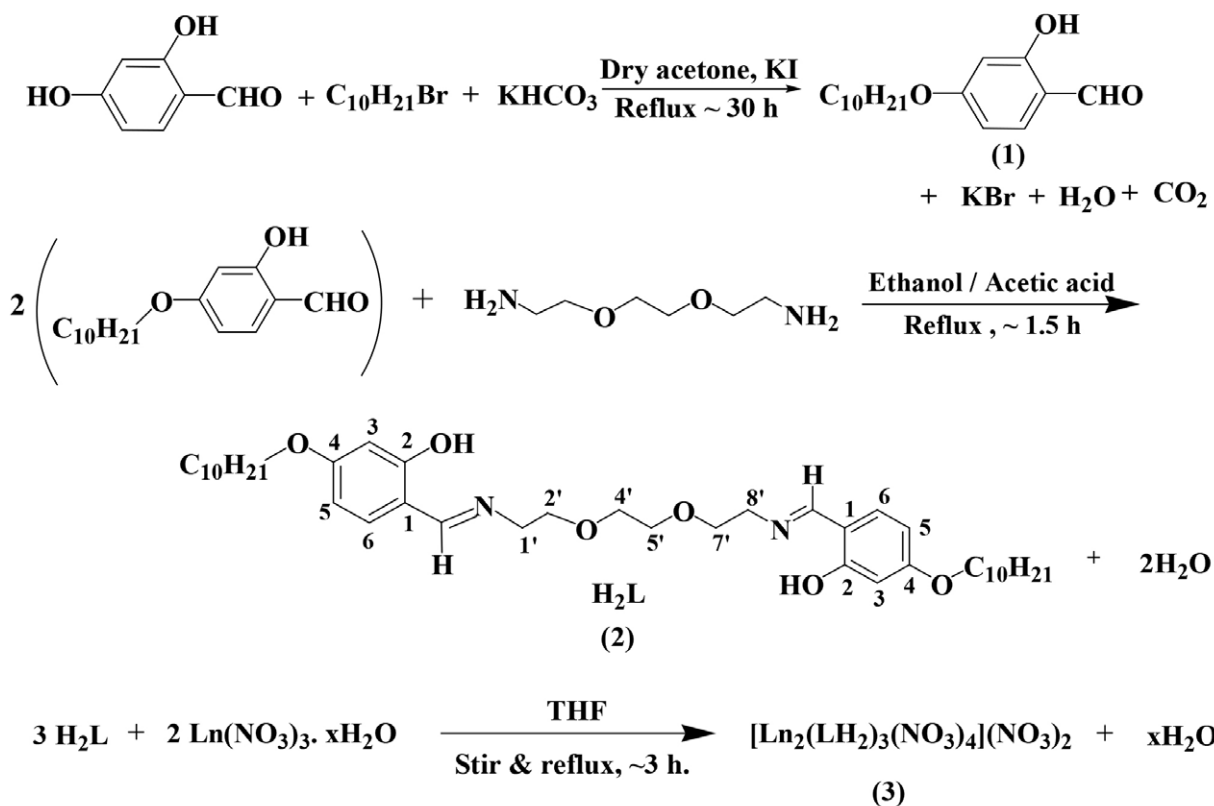
2. 2. 1. Preparation of 4-decyloxysalicylaldehyde, **1**

Equimolar amounts of 2,4-dihydroxybenzaldehyde (50 mmol, 6.91 g) and 1-bromodecane (50 mmol, 10.4 mL) were mixed with 100 mL of dry acetone and added potassium bicarbonate (55 mmol, 5.51 g). The reaction mixture was refluxed for 30 h in the presence of KI (0.1–0.2 g) as a catalyst. Insoluble solids were removed through hot fil-

tration and subsequently, the filtrate was made neutral by adding 6N hydrochloric acid little at a time and extracted the product twice with 100 mL portions of CHCl_3 . A straw-yellow solid was obtained upon concentration of the chloroform extracts which was purified by column chromatography over SiO_2 by eluting first with n-hexane and then with a mixture of n-hexane and chloroform (v/v, 1/1). The product, 4-decyloxysalicylaldehyde (**1**) was obtained in the form of a white solid upon evaporation of this purified extract; yield: 68% (9.47 g).

2. 2. 2. Synthesis of N,N' -di-(4-decyloxysalicylidene)-1',8'-diamino-3',6'-dioxaoctane (H_2L), **2**

A mixture of absolute ethanolic solutions of 4-decyloxysalicylaldehyde, **1**, (8.34 g, 30 mmol in 50 mL) and 1,8-diamino-3,6-dioxaoctane (2.22 g, 15 mmol in 15 mL) was refluxing together for 1.5 h in the presence of a few drops of glacial acetic acid. Yellow colored solid, **2**, was obtained after the resulting mixture left overnight which was filtered off under suction, thoroughly washed with cold ethanol and dried at room temperature. Yield: 74% (7.43 g), m.p.165 °C. Anal. Calcd for $\text{C}_{40}\text{H}_{64}\text{N}_2\text{O}_6$ (%): C, 71.82; H, 8.64; N, 4.19.



Where,

$\text{Ln} = \text{La, Pr, Nd, Sm, Eu, Gd, Tb, Dy and Ho}$

Scheme 1. Reaction steps involved in the synthesis of 4-decyloxysalicylaldehyde, **1**; N,N' -di-(4-decyloxysalicylidene)-1',8'-diamino-3',6'-dioxaoctane (H_2L), **2**, and Ln^{III} complexes, **3**.

Found (%): C, 71.85; H, 9.65; N, 4.21. ^1H NMR (300 MHz; DMSO- d_6 ; J (Hz), ppm) (Figure S1) δ = 0.85 (t, J = 5.7, 3H, $-\text{CH}_3$), 1.73–1.26 (m, 16H, $-(\text{CH}_2)_8-$), 3.51 (t, J = 6.6, 2H, $-\text{NCH}_2$), 3.96 (t, J = 6.3, 2H, $-\text{OCH}_2$), 6.28 (d, J = 11.4, 1H, Ar-H), 6.33 (s, 1H, Ar-H), 7.19 (d, J = 8.7, 1H, Ar-H), 8.32 (s, 1H, $-\text{N}=\text{CH}$), 13.80 (s, br, 1H, Ph-OH); $^{13}\text{C}\{^1\text{H}\}$ NMR: (75.45 MHz; DMSO- d_6 ; ppm) (Figure S2) δ = 165.39, 163.82, 162.36, 132.45, 111.70, 105.56, 101.40, 67.27; FAB Mass (m/e , fragment, % intensity): the molecular ion as base peak (668, M^+ , 100) generates simultaneously four fragments, M_1 – M_4 ; M_1 : 349, $\text{C}_{10}\text{H}_{21}\text{OC}_6\text{H}_3(\text{OH})\text{CH}=\text{NC}_2\text{H}_4\text{OCH}_2\text{CH}_2^+$, 28%; M_2 : 321, $\text{C}_{10}\text{H}_{21}\text{OC}_6\text{H}_3(\text{OH})\text{CH}=\text{NCH}_2\text{CH}_2\text{O}^+$, 25%; M_3 : 305, $\text{C}_{10}\text{H}_{21}\text{OC}_6\text{H}_3(\text{OH})\text{CH}=\text{NCH}_2\text{CH}_2^+$, 35%; M_4 (generated from M_3): 164, $(\text{OH})\text{C}_6\text{H}_3(\text{OH})\text{CH}=\text{NCH}_2\text{CH}_2^+$, 25%; IR (cm^{-1} , KBr disk): 3458 (ν -OH), 1628 (ν -C=N), 1150 (ν - C_{ph} -O).

2. 2. 3. Synthesis of La^{III} Complex, $[\text{Ln}_2(\text{LH}_2)_3(\text{NO}_3)_4](\text{NO}_3)_2$, **3**

Mixing of THF solutions of H_2L (2.01 g, 3.0 mmol in 30 mL) and of $\text{La}(\text{NO}_3)_3 \cdot 6\text{H}_2\text{O}$ (0.87 g, 2.0 mmol in 20 mL) under magnetic stirring turned the resultant solution cloudy after 15 min. A light yellow colored solid separated upon continuous stirring for 3 h at room temperature was filtered off under suction, washed repeatedly with cold methanol, and dried over fused CaCl_2 in a desiccator. Yield: 65% (1.73 g) as yellow solid; m.p. 245 °C (decompose); Anal. Calcd for $\text{La}_2\text{C}_{120}\text{H}_{192}\text{N}_{12}\text{O}_{36}$ (%): C, 54.25; H, 7.28; N, 6.33; La, 10.46; Found (%): C, 54.30; H, 7.30; N, 6.37 and La, 10.51; ^1H NMR (300 MHz; DMSO- d_6 ; J (Hz), ppm) (Figure S3) δ = 0.88 (t, J = 5.4, 3H, $-\text{CH}_3$), 1.71–1.29 (m, 16H, $-(\text{CH}_2)_8-$), 3.54 (t, J = 6.3, 2H, $-\text{NCH}_2$), 3.98 (t, J = 6.3, 2H, $-\text{OCH}_2$), 6.34 (d, J = 6.6, 1H, Ar-H), 6.36 (s, 1H, Ar-H), 7.22 (d, J = 8.7, 1H, Ar-H), 8.36 (s, 1H, $-\text{N}=\text{CH}$), 9.27 (s, br, 1H, $-\text{N}^+\text{H}$); $^{13}\text{C}\{^1\text{H}\}$ NMR: (75.45 MHz; DMSO- d_6 ; ppm) (Figure S4) δ = 166.07, 162.61, 164.02, 132.75, 111.67, 105.64, 101.56, 67.35; IR (cm^{-1} , KBr disk): 3046 (ν - N^+H), 1658 (ν -C=N), 1124 (ν - C_{ph} -O).

All the other Ln^{III} complexes ($\text{Ln} = \text{Pr}$, Nd , Sm , Eu , Gd , Tb , Dy , and Ho) were synthesized in an analogous way by using the appropriate hydrated salt of Ln^{III} nitrate; the physical properties and the analytical data of all the complexes are given in Table 1 while the NMR data of the ligand (H_2L) and the La^{III} complex are presented as supplementary data. Infrared spectral data of the ligand and complexes are given in Table 2; the data of two representative complexes are given below: $[\text{Gd}_2(\text{LH}_2)_3(\text{NO}_3)_4](\text{NO}_3)_2$: IR (cm^{-1} , KBr disk): 3026 (ν - N^+H), 1654 (ν -C=N), 1124 (ν - C_{ph} -O); $[\text{Ho}_2(\text{LH}_2)_3(\text{NO}_3)_4](\text{NO}_3)_2$: IR (cm^{-1} , KBr disk): 3038 (ν - N^+H), 1654 (ν -C=N), 1124 (ν - C_{ph} -O).

2. 3. Physical Measurements

The Ln^{III} ions in the complexes were determined complexometrically by titrating against the standard EDTA

solution using xylenol orange as a metal ion indicator. The elemental contents (C, H and N) were analyzed on an Exeter Analyzer, Model CE-440 CHN. Bruker Av III HD (DRX) 300 MHz FT-NMR multinuclear spectrometer was used to record the ^1H and ^{13}C NMR spectra while Bruker IFS66 FTIR spectrometer recorded IR spectra within the 4000–400 cm^{-1} region using KBr pellets. Mass spectra were recorded on JEOL SX-102 FAB mass spectrometer. UV-vis spectra were recorded on Shimadzu spectrophotometer, model Pharmaspec-UV 1700. The molar conductance of the complexes was determined in 10^{-3} M solutions on a digital conductivity meter (Model alpha-06, ESICO International) using a commercial conductivity ‘dip cell’ of cell constant, 1.03. Magnetic susceptibility measurements were made at room temperature on a Cahn–Faraday balance using $\text{Hg}[\text{Co}(\text{NCS})_4]$ as the calibrant. Mesophases were identified by the optical textures using an Olympus BX60 Polarizing Optical Microscope (POM) equipped with a Linkam THMS600 hot stage and a Linkam TMS93 programmable temperature controller (heating and cooling rates of 2 °C/min). Differential Scanning Calorimetry (DSC) studies were made on a Mettler-Toledo DSC822e module (scan rate 10 °C/min under a helium flow, aluminum cups). Fluorescence measurements were recorded at room temperature in a mixed solvent of $\text{CHCl}_3/\text{DMSO}$ solutions (3:1 v/v; 10^{-4} mol L^{-1} ; λ_{ex} , 380 nm) on a Perkin Elmer LS-45 luminescence spectrometer (10 nm slit width on both excitation and emission).

3. Results and Discussion

3. 1. Properties of the Complexes

The analytical data on elemental analyses, general behavior and some important physical properties of the Ln^{III} complexes are given in Table 1. The Ln^{III} complexes synthesized under the study are of the type $[\text{Ln}_2(\text{LH}_2)_3(\text{NO}_3)_4](\text{NO}_3)_2$ indicating 2:3 metal to ligand stoichiometry with nitrate groups present both outside and within the coordination sphere. The molar conductivity measurements in 10^{-3} M DMF solutions (110 – 125 $\Omega^{-1} \text{cm}^2 \text{mol}^{-1}$) of the Ln^{III} complexes imply 2:1 electrolytic behavior.¹⁹

3. 2. FAB-mass Spectral Study of H_2L

The formation of the Schiff base ligand (H_2L), in addition to the IR and NMR spectral techniques to be discussed later, was further confirmed by the FAB mass spectrum. The molecular ion peak as well as base peak that corresponds to the m/e value of 668, matches with the molecular weight of the ligand (668.95) having the molecular formula, $\text{C}_{40}\text{H}_{64}\text{N}_2\text{O}_6$. The 100% intensity of the molecular ion peak as the base peak is as expected for the molecule on the basis of its predominant aromatic character; the major fragment peaks ($m/e = 349$, 321, 305, 164) are due to $\text{C}_{10}\text{H}_{21}\text{OC}_6\text{H}_3(\text{OH})\text{CH}=\text{N}$ -

Table 1. General and analytical data of H₂L and of Ln^{III} metal complexes.

H ₂ L/complex formula weight (empirical formula)	Colour, yield	m.p. (°C)	Found (Calcd.)%				μ_{eff} (van Vleck) value, B.M.
			C	H	N	M	
H ₂ L, 668.95 (C ₄₀ H ₆₄ N ₂ O ₆)	Yellow, 74%	165	71.85 (71.82)	9.65 (9.64)	4.21 (4.19)	–	–
[La ₂ (LH ₂) ₃ (NO ₃) ₄](NO ₃) ₂ 2656.68 (La ₂ C ₁₂₀ H ₁₉₂ N ₁₂ O ₃₆)	Light yellow, 65%	245 ^d	54.30 (54.25)	7.30 (7.28)	6.37 (6.33)	10.51 (10.46)	Diamag.
[Pr ₂ (LH ₂) ₃ (NO ₃) ₄](NO ₃) ₂ 2660.69 (Pr ₂ C ₁₂₀ H ₁₉₂ N ₁₂ O ₃₆)	Light yellow, 66%	242 ^d	54.15 (54.12)	7.28 (7.27)	6.38 (6.32)	10.66 (10.59)	3.90 (3.40-3.60)
[Nd ₂ (LH ₂) ₃ (NO ₃) ₄](NO ₃) ₂ 2667.35 (Nd ₂ C ₁₂₀ H ₁₉₂ N ₁₂ O ₃₆)	Light yellow, 72%	238 ^d	54.10 (54.03)	7.28 (7.26)	6.28 (6.30)	10.90 (10.82)	3.94 (3.50-3.60)
[Sm ₂ (LH ₂) ₃ (NO ₃) ₄](NO ₃) ₂ 2679.59 (Sm ₂ C ₁₂₀ H ₁₉₂ N ₁₂ O ₃₆)	Light yellow, 69%	240 ^d	53.82 (53.79)	7.26 (7.22)	6.30 (6.27)	11.30 (11.22)	1.87 (1.50-1.60)
[Eu ₂ (LH ₂) ₃ (NO ₃) ₄](NO ₃) ₂ 2682.80 (Eu ₂ C ₁₂₀ H ₁₉₂ N ₁₂ O ₃₆)	Light yellow, 74%	255 ^d	53.75 (53.72)	7.23 (7.21)	6.32 (6.27)	11.37 (11.33)	4.56 (3.40-3.60)
[Gd ₂ (LH ₂) ₃ (NO ₃) ₄](NO ₃) ₂ 2693.37 (Gd ₂ C ₁₂₀ H ₁₉₂ N ₁₂ O ₃₆)	Light yellow, 70%	258 ^d	53.49 (53.51)	7.23 (7.19)	6.29 (6.24)	11.71 (11.68)	10.84 (7.80-8.00)
[Tb ₂ (LH ₂) ₃ (NO ₃) ₄](NO ₃) ₂ 2696.72 (Tb ₂ C ₁₂₀ H ₁₉₂ N ₁₂ O ₃₆)	Light yellow, 67%	260 ^d	53.47 (53.45)	7.21 (7.18)	6.28 (6.23)	11.86 (11.79)	11.84 (9.40-9.60)
[Dy ₂ (LH ₂) ₃ (NO ₃) ₄](NO ₃) ₂ 2703.87 (Dy ₂ C ₁₂₀ H ₁₉₂ N ₁₂ O ₃₆)	Light yellow, 70%	257 ^d	53.35 (53.30)	7.20 (7.16)	6.27 (6.22)	12.09 (12.02)	12.47 (10.40-10.50)
[Ho ₂ (LH ₂) ₃ (NO ₃) ₄](NO ₃) ₂ 2608.73 (Ho ₂ C ₁₂₀ H ₁₉₂ N ₁₂ O ₃₆)	Light Yellow, 68%	258 ^d	53.22 (53.21)	7.19 (7.14)	6.26 (6.21)	12.25 (12.18)	14.36 (10.30-10.50)

d = decomposition

C₂H₄OCH₂CH₂⁺, C₁₀H₂₁OC₆H₃(OH)CH=NCH₂CH₂O⁺, C₁₀H₂₁OC₆H₃(OH)CH=NCH₂CH₂⁺, and (OH)C₆H₃(OH)CH=NCH₂CH₂⁺ species respectively.

3. 3. IR Spectral Studies

The important infrared spectral data of H₂L and its Ln^{III} complexes are presented in Table 2.

The broad absorption, centered at 3458 cm⁻¹ and characteristic of $\nu(\text{O-H})_{\text{phenolic}}$ ²⁰ involving considerable H-bonding, disappears in spectra of the complexes due to shifting of the phenolic proton to the azomethine nitrogen, resulting in formation of the zwitterion. The weak/medium intensity bands of the H₂L centered at 1150 cm⁻¹ are assigned to $\nu(\text{C-O})_{\text{phenolic}}$. The strong intensity band

appearing at 1628 cm⁻¹, which is assignable²¹ to $\nu(\text{C=N})$ of azomethine, undergoes a hypsochromic shift in all the complexes on account of zwitterion formation. Thus, the complexation of the H₂L to Ln^{III} results in migration of phenolic protons onto the two uncoordinated imino nitrogen atoms, which then are intramolecularly hydrogen bonded to metal-bound phenolate oxygen atoms to give the zwitterionic structure, N⁺-H...O⁻. Such zwitterionic behavior is in consistent with the study of Binnemans *et al.*,²² who also reported similar observation for acyclic Schiff base lanthanide complexes. The band frequencies of $\nu(\text{C=N})$ shifting to higher wave numbers upon complexation, also provide further evidence implying the presence of the C-N⁺ and the non-involvement of nitrogen in complex formation.²³ Further, the present complexes are

Table 2. IR Spectral data* (cm⁻¹) of H₂L and of Ln^{III} metal complexes

H ₂ L/Complexes	$\nu(\text{O-H})_{\text{phenol}}$	$\nu(\text{N}^+\text{H})$	$\nu(\text{C=N})$	$\nu(\text{C-O})_{\text{phenolic}}$	$\nu(\text{NO}_3)$				
					ν_5	Ionic	ν_1	ν_2	$\nu_5 - \nu_1$
H ₂ L	3458 b	–	1628 s	1150 m	–	–	–	–	–
[La ₂ (LH ₂) ₃ (NO ₃) ₄](NO ₃) ₂	–	3046w	1656	1124	1470	1386	1290	794	180
[Pr ₂ (LH ₂) ₃ (NO ₃) ₄](NO ₃) ₂	–	3042	1654	1118	1469	1386	1294	794	175
[Nd ₂ (LH ₂) ₃ (NO ₃) ₄](NO ₃) ₂	–	3040	1654	1126	1470	1380	1292	791	178
[Sm ₂ (LH ₂) ₃ (NO ₃) ₄](NO ₃) ₂	–	3042	1654	1124	1470	1382	1292	792	180
[Eu ₂ (LH ₂) ₃ (NO ₃) ₄](NO ₃) ₂	–	3030	1654	1124	1468	1381	1288	793	181
[Gd ₂ (LH ₂) ₃ (NO ₃) ₄](NO ₃) ₂	–	3026	1654	1124	1467	1372	1290	791	177
[Tb ₂ (LH ₂) ₃ (NO ₃) ₄](NO ₃) ₂	–	3036	1654	1122	1471	1378	1294	792	177
[Dy ₂ (LH ₂) ₃ (NO ₃) ₄](NO ₃) ₂	–	3028	1654	1126	1472	1378	1292	793	180
[Ho ₂ (LH ₂) ₃ (NO ₃) ₄](NO ₃) ₂	–	3038	1654	1124	1470	1382	1290	794	180

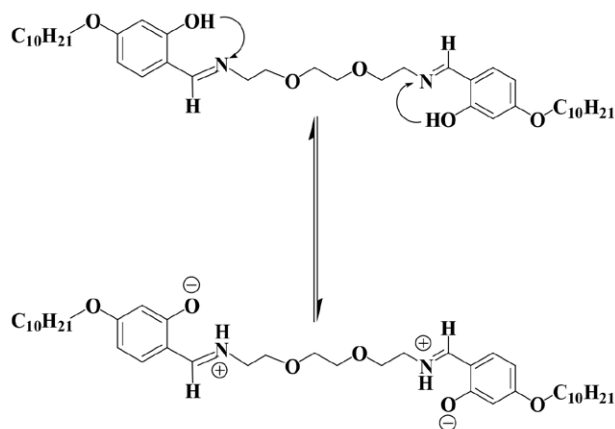
* Spectra recorded as KBr pellets; b: broad; w: weak; s: sharp; m: medium

characterized by a strong band at 1656–1654 cm^{-1} due to $\nu(\text{C}=\text{N})$ and a weak broad band at 3046–3026 cm^{-1} due to H-bonded $\text{N}^+\text{H}\cdots\text{O}^-$ vibration of the protonated imine.²³ Thus, the above evidence supports for none involvement of bonding between lanthanide and the imine nitrogen; instead the ligand coordinates to the Ln^{III} ions *via* the negatively charged phenolic oxygen.

The Ln^{III} complexes also exhibit three additional characteristic bands of the vibrational modes of the coordinated nitrate groups (C_{2v} symmetry) at 1472–1467, 1294–1288, and 794–791 cm^{-1} .²⁴ Besides, the mono- and bidentate chelating nitrates in the complexes may be distinguished on the basis of the profile and separation of the modes associated with asymmetric nitrate vibrations. Accordingly, a bidentate coordinated nitrate is indicated by the magnitude of splitting (181–175 cm^{-1}) at higher energies.^{24,25} The non-coordinated nitrate present in the ionization sphere is supported by additional bands at 1386–1372 cm^{-1} .

3. 4. ^1H and ^{13}C NMR Spectral Studies

A comparison of ^1H NMR spectral data of the ligand with that of the La^{III} complex shows the phenolic $-\text{OH}$ signal (δ , 13.80) that appear in the ligand, disappears later upon complexation. Further, the ^1H NMR spectral data imply the shifting of phenolic protons to the two uncoordinated imino nitrogen atoms, which give zwitterionic structure ($=\text{N}^+\text{H}\cdots\text{O}^-$) by intramolecularly hydrogen-bonding to the metal-bound phenolate oxygen atoms; as such is designated as LH_2 .²⁶ Besides, the La^{III} complex (δ , 8.36) shows a signal corresponding to the imine hydrogen, $-\text{CH}=\text{N}$, that got broadened when compared with that of the ligand (δ , 8.32). Further, the La^{III} complex shows a new signal, characteristic of $-\text{N}^+\text{H}$ resonance, at 9.27 δ while such a signal is absent in the ligand. The results are in accordance with similar observations made by Binnemans *et al.*,²⁷ on metallomesogens, $[\text{Ln}(\text{LH})_3(\text{NO}_3)_3]$, where LH



Scheme 2. Depiction of migration of phenolic protons to imine nitrogens of the ligand, H_2L , during the formation of zwitter ion.

= 4-alkoxy-N-alkyl-2-hydroxy benzaldimine. Thus, the metal complex has its Schiff base ligand existing in a zwitterionic form, with the phenolic oxygen deprotonated and the imine nitrogen protonated (Scheme 2), as supported evidently by IR and NMR spectral data.

The $^{13}\text{C}\{^1\text{H}\}$ NMR spectral data show a significant shift of the $-\text{NCH}$ signal (δ , 165.39 in case of H_2L and δ , 166.07 in the La^{III} complex) implying the two phenolate oxygen atoms of H_2L bonded to La^{III} in the zwitterionic form. The carbons directly attached to the phenolate group showed similar shifts while those for the other carbon signals were of lower magnitude.

3. 5. Magnetic and Electronic Spectral Studies

The μ_{eff} values (at room temperature) of all the Ln^{III} complexes (Table 1) under the present study have been found to be higher than the reported van Vleck values. These abnormal μ_{eff} values, attributed to metal–metal interactions, are in good agreement with similar complexes reported in literatures.^{28–30}

The electronic spectra of only the Pr^{III} , Nd^{III} , Sm^{III} , and Dy^{III} complexes (Table 3) were recorded in qualitative solution state from 200 to 1100nm, in view of their ability to show hypersensitive bands. The considerable red shifts in the λ_{max} values of the above complexes compared to those of the corresponding aqua ions,³¹ are attributed to

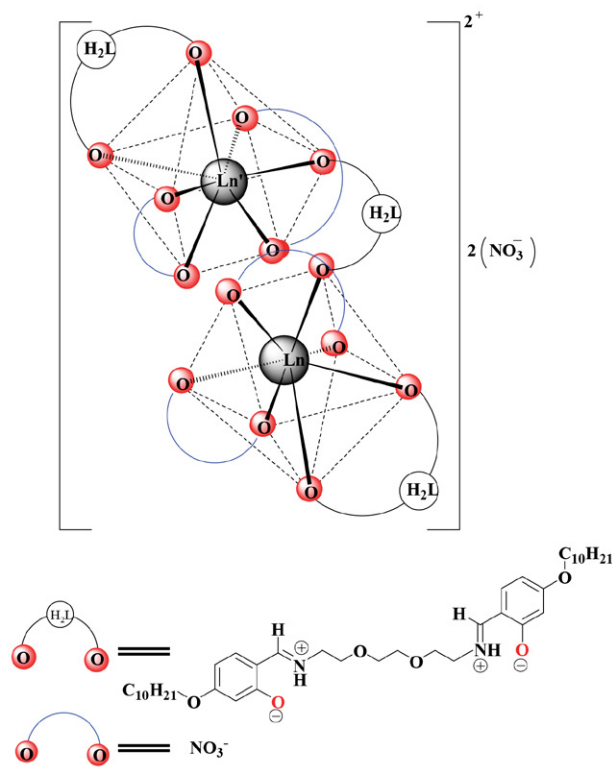


Figure 1. Proposed Polyhedron (Mono-capped Octahedron) for $[\text{Ln}_2(\text{LH}_2)_3(\text{NO}_3)_4](\text{NO}_3)_2$: Ln = La, Pr, Nd, Sm, Eu, Gd, Tb, Dy and Ho

Table 3. Electronic spectral data of the selected metal complexes of H₂L.

Pr(III)			Nd(III)		
Transitions/ Bonding parameters	λ_{\max} (cm ⁻¹) aq. ion	λ_{\max} (cm ⁻¹) complex	Transitions/ Bonding parameters	λ_{\max} (cm ⁻¹) aq. ion	λ_{\max} (cm ⁻¹) complex
¹ G ₄ ← ³ H ₄	9900	9800	⁴ F _{3/2} ← ⁴ I _{9/2}	11,450	11,435
¹ D ₂ * ←	16850*	16,840	⁴ F _{5/2} ←	12,500	12,484
³ P ₀ ←	20800	20,760	⁴ S _{3/2} , ⁴ F _{7/2} ←	13,500	13,430
			⁴ F _{9/2} ←	14,800	14,694
			² H _{11/2} ←	15,900	15,850
			² G _{7/2} * ←	17,400*	17,196
			⁴ G _{7/2} ←	19,100	19,015
β		0.993			0.995
$b^{1/2}$		0.059			0.050
% δ		0.705			0.503
η		0.003			0.002
Sm(III)			Dy(III)		
⁶ F _{9/2} ← ⁶ H _{5/2}	9200	9174	⁶ H _{7/2} ← ⁶ H _{15/2}	9100	–
⁶ F _{11/2} ←	10,500	10,352	⁶ F _{9/2} ←		
⁴ G _{5/2} ←	17,900	–	⁶ H _{5/2} ←	10,200	10,156
⁶ P _{7/2} * ←	26,750*	26,197	⁶ F _{7/2} ←	11,000	10,952
⁴ D _{7/2}	29,100	29,185	⁶ F _{5/2} ←	12,400	12,392
			⁴ F _{7/2} ←	25,800	25,828
β		0.991			0.998
$b^{1/2}$		0.067			0.032
% δ		0.908			0.200
η		0.004			0.001

* Hypersensitive band.

the Nephelauxetic effect,³² which is regarded as a measure of covalency of the bonding between the metal ions and the ligands. Various bonding parameters (Table 3), viz., Nephelauxetic ratio (β), bonding parameter ($b^{1/2}$), Sinha's parameter (% δ), and covalency angular overlap parameter (η), calculated by the procedures as reported,³³ suggest a weak covalent nature of the metal–ligand bonds.

Based on the above spectral evidences, the seven-coordinate geometry, possibly in a distorted mono-capped octahedron (Figure 1) may be proposed to all the present complexes in which the mesogenic Schiff base, *N,N'*-di-(4-decyloxysalicylidene)-1',8'-diamino-3',6'-dioxaoctane (H₂L), **2**, coordinates to the Ln^{III} ions in a neutral bidentate fashion.

3. 6 Optical and Thermal Studies

The DSC (recorded in the second heating and cooling cycle with heating rate of 10°C/min) and POM (heating and cooling rates of 2 °C/min) were employed to study liquid crystalline (mesogenic) properties of the ligand and those of the Ln^{III} complexes. The corresponding transition temperatures, enthalpy, and entropy changes are given in Table 4.

Table 4. Thermodynamic data (transition temp., enthalpy and entropy changes).

Ligand	Transition ^a	<i>T</i> ^b (°C)	ΔH^b (kJ mol ⁻¹)	ΔS (J mol ⁻¹ K ⁻¹)
H ₂ L	Cr – SmX	91.84	10.62	29.11
	SmX – SmA	116.96	10.52	26.98
	SmA – N	131.93	16.52	40.80
	N – I	162.85	6.09	13.97
	I – N	148.53	2.39	5.67
	N – SmX	141.73	1.12	2.70
	SmX – Cr	89.96	20.20	55.65

^a Cr: Crystalline; SmX: Smectic-X; SmA: Smectic-A; N: Nematic; I-Iso-tropic liquid ^b Data as obtained from the DSC cycle

The POM study revealed optical textures of the H₂L (Figure 2) implying smectic-X (*SmX*), smectic-A (*SmA*) and nematic (*N*) mesophases while none of the Ln^{III} complexes reported here exhibited mesomorphism. The non-mesomorphism in the Ln^{III} complexes may be attributed to very high thermal energy required to melt completely the alkoxy chains of the complexes. Under the

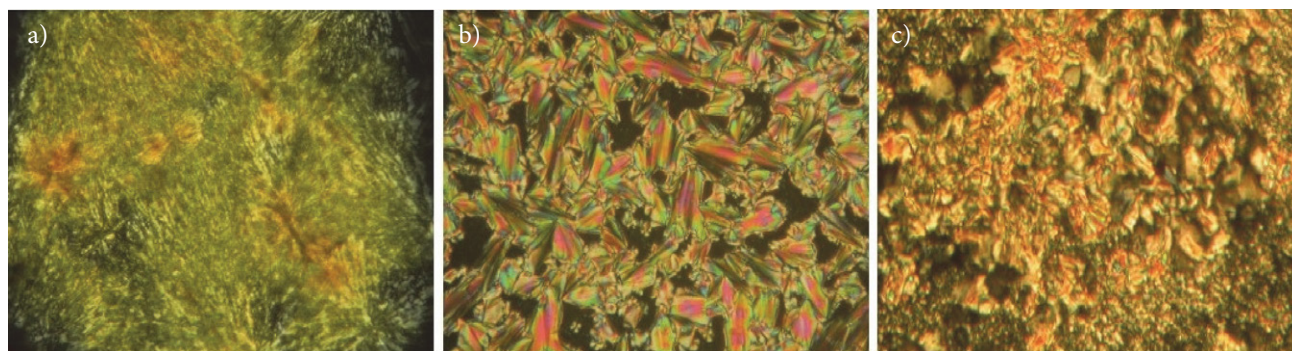


Figure 2. Optical textures of Schiff base (H_2L): (a) Smectic-X (SmX), (b) Smectic-A (SmA) and (c) Nematic (N)

given situation of high energy level, the layered structure in the complexes breaks down prior to the alkoxy chains, losing thereby the mesogenic properties of the materials.²⁷

3. 7. Luminescence Studies

The H_2L shows fluorescence (Figure 3a) with an emission band at 410 nm due to intra-ligand transition

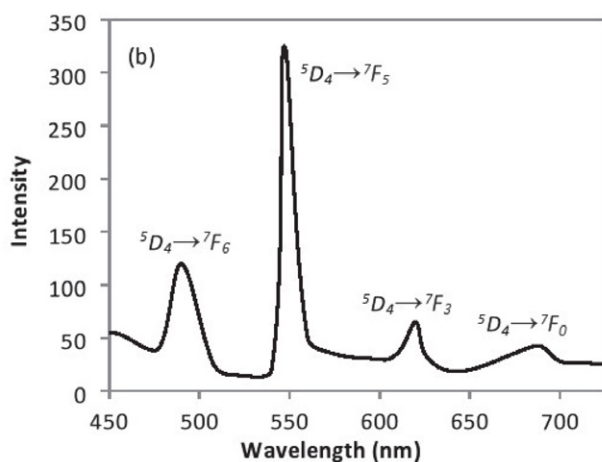
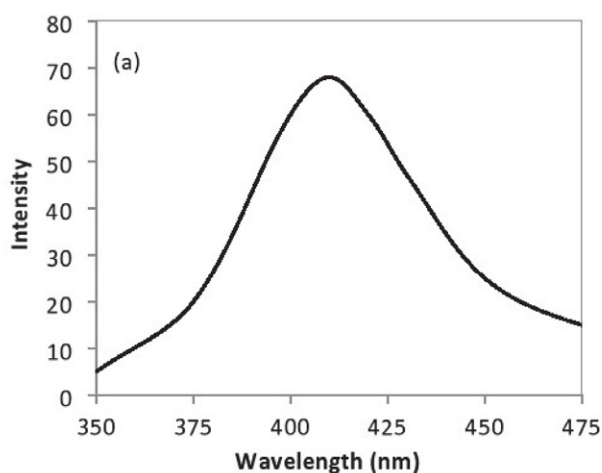


Figure 3. The fluorescence spectra of (a) H_2L and (b) Tb^{III} complex.

and the Tb^{III} complex (Figure 3b) with four typical metal-centered emission bands at 490 nm ($^5D_4 \rightarrow ^7F_6$), 547 nm ($^5D_4 \rightarrow ^7F_5$), 620 nm ($^5D_4 \rightarrow ^7F_3$), and 685 nm ($^5D_4 \rightarrow ^7F_0$) respectively.³⁴

Under the same experimental conditions, the observed fluorescence intensities of the Sm^{III} , Eu^{III} and Dy^{III} complexes were observed to be weak (spectra not shown) and their emission spectra also did not show any bands characteristic of metal-centered emission. Thus, it may be inferred that the H_2L is likely to be a suitable organic chelator to absorb energy and transfer the same to Tb^{III} ion, implying the well-known intramolecular energy transfer mechanism exhibited by lanthanide Schiff base complexes.³⁵

4. Conclusion

The mesogenic (SmX , SmA and N) Schiff base, N,N' -di-(4-decyloxysalicylidene)-1',8'-diamino-3',6'-dioxaoctane (H_2L), coordinates to Ln^{III} ions ($Ln = La, Pr, Nd, Sm, Eu, Gd, Tb, Dy, Ho$) as a neutral bidentate species to yield seven-coordinate non-mesogenic complexes of the formula, $[Ln_2(LH_2)_3(NO_3)_4](NO_3)_2$, the polyhedron being possibly distorted mono-capped octahedron. The neutral bidentate H_2L coordinates to Ln^{III} in a zwitterionic form through two phenolate oxygen atoms along with bonding of nitrate groups in similar bidentate fashion. Luminescence of the H_2L and Tb^{III} complex arises due to intra-ligand and metal-centered emissions respectively.

Acknowledgements

One of the authors, P.R. Shakya gratefully acknowledges the University Grants Commission (UGC), Kathmandu, Nepal, for research fellowship.

5. References

1. D. Parker, R. S. Dickins, H. Puschmann, C. Crossland, J. A. K. Howard, *Chem. Rev.* **2002**, *102*, 1977–2010; DOI: 10.1021/cr010452+

2. C. Piguet, J. C. G. Bunzli, B. Donnio, D. Guillon, *Chem. Commun.* **2006**, 3755–3768; DOI: 10.1039/B605737C
3. L. J. Charbonniere, R. Ziessel, M. Montalti, L. Prodi, N. Zaccaroni, C. Boehme, G. Wipff, *J. Am. Chem. Soc.* **2002**, *124*, 7779–7788; DOI: 10.1021/ja0200847
4. H. J. Zhang, R. H. Gou, L. Yan, R. D. Yang, *Spectrochim. Acta Part A* **2007**, *66*, 289–294; DOI: 10.1016/j.saa.2006.02.054
5. M. Tsiouri, N. Hadjiliadis, T. Arslan, B. M. Kariuki, J. C. Plakatouras, *Inorg. Chem. Commun.* **2006**, *9*, 429–432; DOI:10.1016/j.inoche.2005.12.018
6. K. Lodewyckx, R. V. Deun, K. Binnemans, *Mater. Sci. Eng. C* **2001**, *18*, 217–221; DOI:10.1016/S0928-4931(01)00361-7
7. A. M. Giroud-Godquin, P. M. Maitlis, *Angew. Chem.* **1991**, *30*, 375–402; DOI:10.1002/anie.199103751
8. D. W. Bruce, In *Inorganic Materials*, 2nd ed.; Bruce, D. W., O'Hare, D., Eds.; Wiley: Chichester, Chapter 8, **1996**, pp 405–490.
9. K. Binnemans, K. Lodewyckx, *Angew. Chem.* **2001**, *13*, 248–244; DOI:10.1002/1521-3773(20010105)40:1<242::AID-ANIE242>3.0.CO;2-O
10. C. Piechocki, J. Simon, J. J. Andre, D. Guillon, P. Petit, A. Skoulios, P. Weber, *Chem. Phys. Lett.* **1985**, *122*, 124–128; DOI:10.1016/0009-2614(85)85490-7
11. Y. G. Galyametdinov, G. I. Ivanova, I. V. Ovchinnikov, *Bull. Acad. Sci. USSR, Div. Chem. Sci.*, **1991**, *40*, 1109–1115. <https://doi.org/10.1007/BF00961392>
12. P. R. Shakya, A. K. Singh, T. R. Rao, *Spectrochim. Acta A* **2011**, *79*, 1654–1659; DOI:10.1016/j.saa.2011.05.030
13. P. R. Shakya, A. K. Singh, T. R. Rao, *Mater. Sci. Eng. C* **2012**, *32*, 1906–1911; DOI:10.1016/j.msec.2012.05.039
14. P. R. Shakya, A. K. Singh, T. R. Rao, *J. Coord. Chem.* **2012**, *65*, 3519–3529; DOI:10.1080/00958972.2012.719225
15. P. R. Shakya, A. K. Singh, T. R. Rao, *Synth. Rect. Inorg. Met. Org. Chem.* **2014**, *44*, 739–747; DOI:10.1080/15533174.2013.790056
16. A. K. Singh, S. Kumari, P. R. Shakya, T. R. Rao, *Mater. Sci. Eng. C* **2011**, *31*, 1111–1114; DOI:10.1016/j.msec.2011.04.006
17. P. K. Shrestha, P. R. Shakya, *J. Nepal Chem. Soc.* **2020**, *41*, 16–25; DOI:10.3126/jncs.v41i1.30509
18. A. Weisberger, F. S. Praskver, *Organic Solvents*, International Publishers Inc., New York, **1956**, p. 1263.
19. W. J. Geary, *Coord. Chem. Rev.* **1971**, *7*, 81–122; DOI:10.1016/S0010-8545(00)80009-0
20. R. M. Silverstein, F. X. Webster, *Spectrometric Identification of Organic Compounds*, 6th Ed., John Wiley & Sons Inc., New York, **2002**.
21. N. B. Colthup, L. H. Daly, S. E. Wiberley, *Introduction to Infrared and Raman Spectroscopy*, 3rd Ed., Academic Press, New York, **1990**.
22. K. Binnemans, D. W. Bruce, S. R. Collinson, R. Van Deun, Y. G. Galyametdinov, F. Martin, *Philos. Trans. R. Soc. Lond., Ser. A* **1999**, *357*, 3063–3077; DOI:10.1098/rsta.1999.0481
23. K. Binnemans, R. van Deun, Christiane G. Walrand, W. Haase, D. W. Bruce, L. Malykhina, Y. G. Galyametdinov, *Mater. Sci. Eng. C* **2001**, *18*, 247–254; DOI:10.1016/S0928-4931(01)00369-1
24. B. Keshavan, P. G. Chandrashekhara, N. M. Made Gowda, *J. Mol. Struct.* **2000**, *553*, 193–197; DOI:10.1016/S0022-2860(00)00551-2
25. J. Nawrocka, V. Patroniak, *J. Alloys Compd.* **2004**, *380*, 159–162; DOI:10.1016/j.jallcom.2004.03.079
26. P. Bag, U. Flörke, K. Nag, *Dalton Trans.* **2006**, *26*, 3236–3248; DOI:10.1039/B516306D
27. K. Binnemans, Y. G. Galyametdinov, R. van Deun, D. W. Bruce, S. R. Collison, A. P. Polishchuk, I. Bikechantaev, W. Hasse, A. V. Prosvirin, L. Tinchurina, I. Litvinov, A. Gubajdullin, A. Rakhmatullin, K. Uytterhoeven, L. VanMeervelt, *J. Am. Chem. Soc.* **2000**, *122*, 4335–4344; DOI:10.1021/ja993351q
28. W. Plass, G. Fries, *Z. Anorg. Allg. Chem.* **1997**, *623*, 1205–1207; DOI:10.1002/zaac.19976230804
29. J. P. Costes, F. Dahan, A. Dupuis, S. Lagrave, J. P. Laurent, *Inorg. Chem.* **1998**, *37*, 153–155; DOI:10.1021/ic9712481
30. J. P. Costes, A. Dupuis, J. P. Laurent, *Inorg. Chim. Acta* **1998**, *268*, 125–130; DOI:10.1016/S0020-1693(97)05628-4
31. R. Reisfeld, C.K. Jorgensen, *Lasers and Excited States of Rare Earths*, SpringerVerlag, Berlin, **1977**. <https://doi.org/10.1007/978-3-642-66696-4>
32. W. T. Carnall, P. R. Fields, K. Rajnak, *J. Chem. Phys.* **1968**, *49*, 4424–4442; DOI:10.1063/1.1669893
33. T. R. Rao, P. A. Kumar, *Synth. Rect. Inrg. Met. Org. Chem.* **1995**, *25*, 1011–1026; DOI:10.1080/15533179508218277
34. T. Gao, P. F. Yan, G. M. Li, G. F. Hou, J. S. Gao, *Inorg. Chim. Acta* **2008**, *361*, 2051–2058; DOI:10.1016/j.ica.2007.10.021
35. R. D. Archer, H. Chen, L. C. Thompson, *Inorg. Chem.* **1998**, *37*, 2089–2095; DOI:10.1021/ic960244d

Povzetek

Sintetizirali smo mezogeno Schiffovo bazo, *N,N'*-di(4-deciloksaliciliden)-1',8'-diamino-3',6'-dioksaoktan (H_2L) in serijo homo dvojedrnih lantanoidnih(III) kompleksov tipa $[Ln_2(LH_2)_3(NO_3)_4](NO_3)_2$, ($Ln = La, Pr, Nd, Sm, Eu, Gd, Tb, Dy, Ho$) ter jih okarakterizirali z elementno analizo, masno spektrometrijo, FTIR in NMR spektroskopijo. IR in NMR analizi nakazujeta vezavo nevtralne dvovezne H_2L zvrsti preko dveh fenolatnih kisikovih atomov v zwitterionski obliki na Ln^{III} , kar vodi do kompleksa s koordinacijskim številom sedem – verjetno popačen oktaeder s sedmim donorskim ligandom nad stransko ploskvijo. DSC in polarizacijski optični mikroskop (POM) razkrijeta mezogene lastnosti (smektična X, smektična A in nematična mezofaze) liganda v širokem temperaturnem območju, vendar nobenega mezomorfizma pri Ln^{III} kompleksih, sintetiziranih pri tej študiji. Študij luminescence pokaže emisije pri H_2L in Tb^{III} kompleksih.



Except when otherwise noted, articles in this journal are published under the terms and conditions of the Creative Commons Attribution 4.0 International License

Scientific paper

Determination of Some Elements in Legumes Using ICP-MS and EDXRF Methodology Applications

Lovro Sinkovič,^{1,*} Marijan Nečemer,² Barbara Pipan¹
and Vladimir Meglič¹

¹ Crop Science Department, Agricultural Institute of Slovenia, Hacquetova ulica 17, SI-1000 Ljubljana, Slovenia

² Department of Low and Medium Energy Physics, "Jožef Stefan" Institute, Jamova 39, SI-1000 Ljubljana, Slovenia

* Corresponding author: E-mail: lovro.sinkovic@kis.si
phone: +386 (0)1280 52 78

Received: 08-16-2021

Abstract

The current study involves two analytical research techniques, inductively coupled plasma-mass spectrometry (ICP-MS) and energy dispersive X-ray fluorescence (EDXRF) spectroscopy, used to determine the elemental composition of different legumes usually produced and consumed in Slovenia. Results indicate that data obtained using these methods are in agreement with certified reference materials. In total, nineteen elements were determined from twenty legume samples. An intercomparison between four macro- (P, S, K, Ca) and three microelements (Fe, Zn, Mo) measured using ICP-MS and EDXRF methods showed a strong correlation. The EDXRF was found to be a cheaper, simpler and more environmentally friendly method for determination of elements P, S, Cl, K, Ca, Fe, Zn, Mo, Sr, Rb, Ti and Br in legumes, while for the identification and determination of Na, Mg, V, Cr, Mn, Co and Cu content ICP-MS was the method of choice due to its excellent sensitivity and accuracy. Using principal component analysis (PCA), the samples of the studied legumes were classified into four groups according to their elemental composition.

Keywords: EDXRF; elemental composition; ICP-MS; legumes.

1. Introduction

Legumes are of prime importance in human or animal nutrition with a great variety of plants.¹ These include crops grown for grains (e.g. common bean, runner bean, lupins, lentil, chickpea), fresh vegetables (e.g. snap bean, green pea) and livestock forage (e.g. soybean, field pea). Legumes play a distinct role in agricultural ecosystems with their ability to fix nitrogen symbiotically.² Grains of food legumes are an important source of elements such as P, Ca, K, N, Fe, Mg and Zn, essential for a human well-being. Legume grains not only play a vital role in many traditional diets worldwide but are valuable for the food and animal feed industries.³ The common bean is the most important grain legume for direct human consumption which provides 10 – 20% of the adult requirements for nutrients, namely Fe, P, Mg, Mn, and to a lesser degree for Zn, Cu and Ca.⁴ Chickpea applies the third most important grain legume for human consumption after beans and peas.⁵ According to the FAO, in 2019 the total world production was the highest for soybeans, followed by beans

(*Phaseolus* spp.), peas, chickpeas, lentils, faba beans and lupins.⁶

The main objective in multi-elemental analysis of foods is to ensure food quality and safety. Therefore, with the increased crop production to meet the growing demands, product quality becomes an important issue.⁷ Elemental fingerprinting has been proven effective way for quality and authentication of foods.⁸ Besides, it serves as an important tool for plant breeding programmes and nutritional biofortification purposes.^{9,10,11} Around twenty of the known elements are defined as essential since they act as important phytochemicals and have a significant role in the maintenance of human health. Essential elements are classified into macroelements or major minerals, namely Na, K, Mg, Ca, Cl, P and S, and microelements or trace minerals such as Fe, Cu, Mn, Zn, Co and Mo.¹² The levels of these elements are measured to provide valuable nutritional information about foods. Over the past decade, with the development of advanced analytical techniques, the element composition of various food samples can be

successfully measured using inductively coupled plasma-mass spectrometry (ICP-MS), energy dispersive X-ray fluorescence (EDXRF) spectroscopy, among others.¹³ Although ICP-MS is frequently the most accurate technique for elemental analysis due to the simplicity, easily interpreted spectra and the exceptionally low limits of detection, on the other hand, requires expensive reagents, gases and laborious sample preparation.⁸ EDXRF spectroscopy is a good alternative to ICP-based methods, in which sample digestions are needed since hardly any sample treatment is required to carry out multi-elemental analysis in solid samples. Despite huge progress made in EDXRF instruments few works were published in the field of elemental characterization of organic matrices such as plant foods using this technique. Nevertheless, EDXRF is characterized by detection limits at the low mg/kg level, which are about three orders of magnitude higher than those obtained by the ICP-MS method.¹⁴

Within the framework of the current studies at the Agricultural Institute of Slovenia, the capabilities of two analytical techniques, ICP-MS and EDXRF spectroscopy, were compared through the determination of elements in several legume samples. The present research aims to provide data on elemental composition of legumes usually produced and consumed in Slovenia which can be used in the ongoing plant breeding programs (e.g. common bean). The purpose of the study was: (i) to determine the multi-elemental composition of different legumes; (ii) to assess the appropriateness of two analytical methods ICP-MS and EDXRF for element determination of different legumes, thus (iii) evaluating the correlation between used analytical methods.

Table 1. List of studied legume samples and their origin

Sample name	Legume species	Latin name	Variety/ accession	Seed provider	Sample type
KIS_GL1	common bean	<i>Phaseolus vulgaris</i> L.	Ribničan	Semenarna Ljubljana	grains
KIS_GL2	common bean	<i>Phaseolus vulgaris</i> L.	SRGB204	Slovenian Plant Gene Bank	grains
KIS_GL3	common bean	<i>Phaseolus vulgaris</i> L.	Zorin	Semenarna Ljubljana	grains
KIS_GL4	common bean	<i>Phaseolus vulgaris</i> L.	Ribničan	Semenarna Ljubljana	Pods
KIS_GL5	common bean	<i>Phaseolus vulgaris</i> L.	SRGB204	Slovenian Plant Gene Bank	Pods
KIS_GL6	common bean	<i>Phaseolus vulgaris</i> L.	Zorin	Semenarna Ljubljana	Pods
KIS_GL7	common bean	<i>Phaseolus vulgaris</i> L.	Etna	Semenarna Ljubljana	grains
KIS_GL8	common bean	<i>Phaseolus vulgaris</i> L.	Golden gate	Semenarna Ljubljana	grains
KIS_GL9	common bean	<i>Phaseolus vulgaris</i> L.	SRGB196	Slovenian Plant Gene Bank	grains
KIS_GL10	white lupin	<i>Lupinus albus</i> L.	Energy	Feldsaaten Freudenberger	grains
KIS_GL11	faba bean	<i>Vicia faba</i> L. var. minor	Zoran	Agricultural Institute of Slovenia	grains
KIS_GL12	faba bean	<i>Vicia faba</i> L. var. minor	Merkur	Semenarna Ljubljana	grains
KIS_GL13	blue lupin	<i>Lupinus angustifolius</i> L.	Sonet	Feldsaaten Freudenberger	grains
KIS_GL14	yellow lupin	<i>Lupinus luteus</i> L.	Mister	Feldsaaten Freudenberger	grains
KIS_GL15	red lentil	<i>Lens culinaris</i> Medik.	rdeča leča	food retail market	grains
KIS_GL16	brown lentil	<i>Lens culinaris</i> Medik.	rjava leča	food retail market	grains
KIS_GL17	chickpea	<i>Cicer arietinum</i> L.	čičerika	food retail market	grains
KIS_GL18	soybean	<i>Glycine max</i> L. Merr.	ES Mentor	Saatbau Slovenia	grains
KIS_GL19	field pea	<i>Pisum sativum</i> L.	Eso	Semenarna Ljubljana	grains
KIS_GL20	runner bean	<i>Phaseolus coccineus</i> L.	SRGB222	Slovenian Plant Gene Bank	grains

2. Experimental

2.1. Materials

A set of twenty homogenised plant samples consists of several legume species as presented in Table 1. Analysed samples were as follows: common bean grains (6 samples), common bean pods (3 samples), lupin (3 samples), faba bean (2 samples), lentil (2 samples), chickpea (1 sample), soybean (1 sample), field pea (1 sample) and runner bean (1 sample). Most of the analysed legumes were produced at the experimental fields of Infrastructure Centre Jablje at the Agricultural Institute of Slovenia (304 m a.s.l.; 46.151°N 14.562°E). Chickpea, brown and red lentil samples were purchased from the Slovenian food retail market. The legume grain samples were air-dried after harvest to reduce the moisture content, to levels below 11%. The common bean pods were immediately after harvesting frozen using liquid nitrogen and lyophilized. Before determination of elements, all legume samples were homogenised and powdered using a laboratory ball mill (Retsch MM 400, GmbH) at a high frequency of 30 Hz for 2–5 min.

2.2. Determination of Elements Using ICP-MS

Digestion of plant samples (decomposition of organic matter). The powdered legume samples were digested using a high-pressure microwave oven (Milestone ETHOS 1600). Separate samples were weighed (250 mg) into PTFE vessels and 6 mL of 65% nitric acid (HNO₃, SUPRAPUR, Merck) and 2 mL 30% hydrogen peroxide (H₂O₂, SUPRAPUR, Merck) was added. The digestion was conduct-

ed according to the following programme: step 1, 300 W, 5 min at 100 °C; step 2, 400 W, 5 min at 150 °C; step 3, 500 W, 5 min at 180 °C; step 4, 600 W, 7 min at 210 °C; step 5, 550 W, 15 min at 210 °C; step 6, 0 W, 20 min cooling.

Preparation of test solution. Digested samples were cooled to room temperature and the solution was quantitatively transferred into 50 mL plastic tubes (Sarstedt, USA) and filled up to full volume with Milli-Q water. Before analysis, the digested samples were diluted by a factor of 20 and consisted of 1% HNO₃ (v/v).

Determination of elements by ICP-MS. For the determination of elements in samples, the Agilent 7900 ICP-MS was used. This instrument includes a 4th generation collision/reaction cell, the Octopole reaction System (ORS⁴) which provides optimized operational conditions for the removal of polyatomic interferences using helium (He) collision mode. In this manner, smaller and faster analyte ions are separated from larger, slower interference ions using kinetic energy discrimination. The following isotopes were monitored: ²³Na, ²⁴Mg, ³¹P, ³⁴S, ³⁹K, ⁴³Ca, ⁵¹V, ⁵²Cr, ⁵⁵Mn, ⁵⁶Fe, ⁵⁹Co, ⁶³Cu, ⁶⁶Zn and ⁹⁵Mo. Due to the high sensitivity of the 7900 ICP-MS most elements of interest could be measured in He mode, only phosphorus (P) and sulphur (S) were measured in the high helium (HEHe) mode. The ICP-MS operating conditions were optimized using autotuning functions within the ICP-MS MassHunter software. Other instruments operating conditions were as follows: general-purpose plasma mode; peri-pump sample introduction; micro-mist nebuliser; nickel cones interface; He gas flow was 5 mL/min in He mode and 10 mL/min in HEHe mode; spectrum acquisition mode; one point peak pattern; three replicates and 100 sweeps per replicate.

Calibration of the instrument. Quantitative analysis was performed with the external calibration method. Calibration standards for most of the elements were prepared using IV-STOCK-50 standard solution containing: 1000 mg/L of Na, Mg, K, Ca and Fe and 10 mg/L of V, Cr, Mn, Co, Cu, Zn and Mo (matrix 5% v/v HNO₃, Inorganic Ventures). Phosphorus (1000 mg/L P, matrix H₂O, CGP1, Inorganic Ventures) and sulphur (1000 mg/L S, matrix H₂O, CGS1, Inorganic Ventures) single standard solutions were added separately to the mixture. A five-point calibration from 0.05 µg/L to 50 µg/L was carried out for the elements V, Cr, Mn, Co, Cu, Zn and Mo, and from 5 µg/L to 5000 µg/L for the elements Na, Mg, S, P, K and Fe. Only for Ca a six-point calibration was used between 5 µg/L and 10000 µg/L due to the higher concentrations expected in plant samples. Final multi-element calibration solutions were prepared daily and contained 1% HNO₃ (v/v). The internal standards used to compensate for sensitivity drift and matrix effects during the analytical run were Sc, Rh, In and Lu (Agilent PN 5188-6525). They were added online in a concentration of 200 µg/L (in 1% v/v HNO₃).

Quality control. For quality control analytical blanks, independent QC standards and standard reference mate-

rial (SRM) were used. In each test series, a blank sample containing only acids was included. The QC standards were prepared in the concentrations of 2 µg/L, 20 µg/L and 2000 µg/L over the analytical range from ICP-MS multi-standard solution VIII (MERCK, Certipur, PN 1.09492) and ICP-MS multi-standard solution XVI (MERCK, Certipur, PN 1.09487) and were analysed in the beginning, in the middle and at the end of each analysis run. Finally, a National Institute of Standards and Technology (NIST) Standard Reference Material (SRM) Tomato Leaves (1573a) was used to check the accuracy of the analytical procedures and recovery. Analytical data was processed using the ICP-MS MassHunter Workstation Software (Rev. C.01.02, G7201C, Agilent technologies, 2015). The software calculates the correlation coefficient of the calibration curve (R), the limit of detection (LOD) and the background equivalent concentration (BEC) for each element. Data along with the accuracy (as % recovery) is shown in Table 2 and accuracy data using NIST SRM Tomato Leaves (1573a) in Table 3. The data are expressed as macro- (g/kg) or microelements (mg/kg).

Table 2. ICP-MS calibration coefficients, method detection limits and background equivalent concentration data

Element	R ²	LOD (mg/kg)	BEC (mg/kg)	Recovery (%)
²³ Na	1.0000	1.07	6.63	82.5
²⁴ Mg	1.0000	0.53	0.74	84.9
³¹ P	1.0000	10.8	8.2	92.7
³⁴ S	1.0000	223	3360	95.7
³⁹ K	1.0000	6.8	318.0	91.4
⁴³ Ca	1.0000	48	125	89.9
⁵¹ V	1.0000	0.0001	0.0041	71.8
⁵² Cr	1.0000	0.085	0.342	86.6
⁵⁵ Mn	1.0000	0.038	0.093	90.9
⁵⁶ Fe	1.0000	0.021	3.522	86.3
⁵⁹ Co	1.0000	0.003	0.035	85.8
⁶³ Cu	1.0000	0.041	0.160	98.5
⁶⁶ Zn	1.0000	0.254	0.759	89.7
⁹⁵ Mo	1.0000	0.010	0.217	73.3

R, calibration coefficient; LOD, method detection limit; BEC, background equivalent concentration.

2. 3. Determination of Elements Using EDXRF

Identification of twelve elements (P, S, Cl, K, Ca, Ti, Fe, Zn, Br, Rb, Sr, Mo) in a single measurement was carried out using non-destructive EDXRF spectrometry. Pellets prepared from 0.5 g to 1.0 g of powdered legume samples were set using a pellet die and a hydraulic press. The disc radioisotope excitation sources Fe-55 (25 mCi) and Cd-109 (20 mCi) from Eckert & Ziegler (Germany) was used for fluorescence excitation. The emitted fluorescence

radiation was measured using the EDXRF spectrometer with an XR-100 SDD detector (Amptek), a PX5 digital pulse processor (Amptek), and a PC-based, multichannel analyser software package DPPMCA. In Fe-55 mode, the spectrometer was equipped with a vacuum chamber to measure the three light elements (P, S, Cl), and in Cd-109 mode, the multi-element measurement was performed in the air for the nine elements K, Ca, Ti, Fe, Zn, Br, Rb, Sr and Mo. The energy resolution setting of the spectrometer was 125eV at 5.9keV. The analysis of complex X-ray spectra was performed using the AXIL spectral analysis program.¹⁵ The evaluated uncertainty of this procedure included the statistical uncertainty of measured intensities and the uncertainty of the mathematical fitting procedure. The overall uncertainty of spectral measurement and analysis was in most cases better than 1%.

Quantification was performed using the QAES (Quantitative Analysis of Environmental Samples) software.¹⁶ The estimated uncertainty of the analysis was around 5% to 10%, LOD for Zn was from 5 µg/g to 10 µg/g. A high total estimated uncertainty is mainly due to contributions of matrix correction and geometry calibration procedures, which include errors of tabulated fundamental parameters, and also contributions of spectrum acquisition and analysis. The uncertainty due to the inhomogeneity of the sample was not included. Accuracy of the data

Table 3. Accuracy of the data using the National Institute of Standards and Technology (NIST) Standard Reference Material (SRM) Tomato Leaves (1573a)

Element	NIST SRM Tomato Leaves (1573a)		
	EDXRF results	ICP-MS results	Certified values
	g/kg		
K	27.80 ± 0.28	24.47 ± 0.04	26.76 ± 0.48
P	1.930 ± 0.023	2.004 ± 0.001	2.161 ± 0.028
S	8.82 ± 0.90	9.19 ± 0.18	9.60*
Ca	50.10 ± 0.49	45.37 ± 0.07	50.45 ± 0.55
Mg	/	10.18 ± 0.01	12.00*
Cl	6.50 ± 0.65	/	6.60*
	mg/kg		
Fe	353.0 ± 3.6	317.3 ± 1.5	367.5 ± 4.3
Mn	246.1 ± 2.8	223.8 ± 0.6	246.3 ± 7.1
Zn	29.10 ± 3.01	27.75 ± 0.27	30.94 ± 0.55
Na	/	112.3 ± 0.2	136.1 ± 3.7
Cu	/	4.63 ± 0.02	4.70 ± 0.14
Rb	15.90 ± 0.21	/	14.83 ± 0.31
Br	12.70 ± 1.30	/	13.00*
Sr	83 ± 9	/	85*
Mo	/	0.34 ± 0.1	0.46*
Cr	/	1.721 ± 0.011	1.988 ± 0.034
Co	/	0.4952 ± 0.0001	0.5773 ± 0.0071
V	/	0.599 ± 0.005	0.835 ± 0.034

*noncertified values

using the 1573a (Tomato Leaves) is presented in Table 3. The quantified twelve elements were expressed as macro-(g/kg) or microelements (mg/kg).

2. 4. Statistical Evaluation

Statistical calculations and multivariate analysis were carried out using the XLSTAT software package (Addinsoft, New York, USA). The multivariate analysis involved principal component analysis (PCA).

3. Results and Discussion

A common characteristic of both analytical techniques applied ICP-MS and EDXRF is their multi-element capability. Preparation of legume samples was simple and non-destructive in the case of EDXRF, while, ICP-MS required skilled personnel and decomposition of samples. ICP-MS was a more sensitive method in this study with LODs in the range of ng/g. Results of the LOD, BEC and accuracy of multi-elemental determination performed by ICP-MS with certified reference material (NIST SRM Tomato Leaves 1573a) are presented in Tables 2 & 3. The sensitivity of EDXRF according to estimated uncertainty was from 5% to 10% and LODs for the analysed elements in the range from a hundred to a few µg/g. This means that LODs of ICP-MS were approximately two orders of magnitude lower compared to EDXRF. The determination of element Cl by ICP-MS was impossible since it forms negative ions, while EDXRF enables its determination as an essential element (dietary mineral) being one of the main electrolytes in the body. On the other hand, ICP-MS enables the determination of elements Na, Mg, Mn and Cu which are according to the European Food Safety Authority (EFSA) essential required substances as nutrients necessary by the body to perform a variety of functions. Considering the cost per sample, EDXRF was cheaper, simpler and more environmentally friendly when compared to ICP-MS and much more suitable for determination of P, S, Cl, K, Ca, Fe, Zn, Mo, Sr, Rb, Ti and Br in legume samples. However, for determination of Na, Mg, V, Cr, Mn, Co and Cu content ICP-MS was a method of choice due to its excellent sensitivity and accuracy.

The macroelement composition of twenty legume samples determined by ICP-MS and/or EDXRF is presented in Table 4 and the microelement composition in Table 5. A total of nineteen elements were determined and divided into six macro- (Mg, P, S, K, Cl, Ca) and thirteen microelements (Mn, Fe, Cu, Na, Cr, Co, Zn, V, Rb, Ti, Br, Sr, Mo). The results of macroelements are expressed as g/kg (Table 4) and those of microelements as mg/kg (Table 5). Based on the average values the order is $K > P > S > Ca > Mg > Cl$ of for the macro- and $Fe > Mn > Zn > Na > Cu > Rb > Br > Ti > Sr > Mo > Cr > Co > V$ for the microelements in analysed legume samples. The ranges of individual macroelements in the analysed legumes were as follows: K (7.5–22.6 g/kg),

P (2.7–7.5 g/kg), S (0.9–4.7 g/kg), Ca (0.2–5.0 g/kg), Mg (0.8–2.9 g/kg), and Cl (0.1–51.0 g/kg). The highest coefficient of variation was calculated for the Ca (66.49%), followed by Cl (58.30%) and S (38.40%). Among different legume species, the highest concentrations of K was found in common bean pods (snap beans) and soybean grains and the lowest for lentil. The P concentration was the highest for faba bean and the lowest for chickpea. The lupins and soybean contained the most S, and common bean pods the most Ca. When compared with other legumes, lentil had the lowest concentration of Ca and Mg. The ranges of essential microelements in the analysed legumes were the following: Fe (37.2–126.0 mg/kg), Mn (8.3–487.7 mg/kg), Zn (17.5–64.6 mg/kg), Na (1.7–91.8 mg/kg), Cu (4.9–16.3 mg/kg), and Mo (0.2–8.5 mg/kg). Among determined microelements the highest coefficients of variation were calculated for the Mn, Cr and Na (> 102.12%) while the lowest for Cu, Zn and Fe (< 38.72%). The highest concentration of Fe was found for soybean and the lowest for field peas. All three lupin samples (white, blue and yellow) were the richest source of microelement Mn compared to other legumes. The Na concentration was the highest for common bean pods and lupins. These elemental compositions are consistent with literature data for common bean grains^{17,18} and pods,^{19,20} lupin,^{21,22} faba bean,^{22,23} lentil,^{3,24,25} chickpea,^{3,5} soybean,²¹ field pea²⁵ and runner bean.^{26,27}

The EFSA set dietary reference values for the following fourteen essential elements Ca, Cl, Cu, F, I, Fe, Mg, Mn, Mo, P, K, Se, Na and Zn. Using laboratorial developed

ICP-MS multi-element method for plant samples ten (Ca, Cu, Fe, Mg, Mn, Mo, P, K, Na, Zn) of these fourteen elements were determined. The three elements, namely Cl, F and I, belong to halogen elements and for these due to the presence of interferences formed in the Ar plasma operating under conventional conditions or due to the matrix effects, their determination by ICP-MS is still considered a challenging task. Despite quadrupole ICP-MS is by far the most used instrumentation for multi-element determination, there are some drawbacks particularly associated with its application for halogen determination.²⁸ Furthermore, the Se is another element which determination by ICP-MS remains particularly difficult. For Se analyses, conventional quadrupole ICP-MS operation suffers from inadequate sensitivity due to the high ionization potential of Se in the plasma as well as isobaric and polyatomic interferences. Selenium has six stable isotopes (⁷⁴Se 0.87%, ⁷⁶Se 9.02%, ⁷⁷Se 0.58%, ⁷⁸Se 23.52%, ⁸⁰Se 49.82%, ⁸²Se 9.19%), which adds complexity to the analysis.²⁹ When using the EDXRF multi-element method seven (Ca, Cl, Fe, Mo, P, K, Zn) of fourteen above mentioned elements was determined. However, EDXRF is a non-destructive and simultaneous method with simple sample preparation steps.³⁰ After the sample preparation procedure, the EDXRF analysis presented high analytical frequency and most equipment counts on an automatic sample holder.³¹

Out of a total of nineteen elements determined using ICP-MS and EDXRF, the following seven P, S, K, Ca, Fe, Zn and Mo were determined by both methods. The

Table 4. Macroelement composition of 20 legume samples determined by ICP-MS and EDXRF

Sample name	Legume species	Macroelements (g/kg)											
		K		P		S		Ca		Mg		Cl	
		ICP-MS	ED XRF	ICP-MS	ED XRF	ICP-MS	ED XRF	ICP-MS	ED XRF	ICP-MS	ED XRF	ICP-MS	ED XRF
KIS_GL1	CB (grains)	13.9	12.8	4.8	5.0	2.1	1.9	1.0	0.8	1.4	0.2		
KIS_GL2	CB (grains)	19.1	17.3	5.9	5.9	2.3	1.9	1.2	1.0	1.6	0.3		
KIS_GL3	CB (grains)	14.4	13.1	5.0	4.6	2.2	1.4	0.9	0.9	1.5	0.1		
KIS_GL4	CB (pods)	17.1	18.3	3.1	3.5	1.4	1.2	2.5	2.2	1.7	0.7		
KIS_GL5	CB (pods)	18.5	18.7	3.1	3.9	1.7	1.5	4.1	3.3	2.0	0.6		
KIS_GL6	CB (pods)	20.9	22.6	3.7	4.7	1.5	1.8	5.0	3.7	2.1	1.0		
KIS_GL7	CB (grains)	13.5	13.4	4.2	4.5	2.0	1.5	1.3	1.1	1.5	0.1		
KIS_GL8	CB (grains)	16.3	15.4	5.9	5.8	2.4	2.1	1.2	1.1	1.7	0.3		
KIS_GL9	CB (grains)	17.8	15.9	5.9	5.6	2.2	1.7	0.8	0.9	1.7	0.1		
KIS_GL10	white lupin	15.3	11.9	5.3	6.2	2.4	2.5	3.0	1.8	1.7	0.1		
KIS_GL11	faba bean	12.5	11.4	6.5	6.5	1.5	0.9	1.1	0.9	1.4	0.6		
KIS_GL12	faba bean	12.7	12.9	6.2	6.5	1.6	1.1	1.0	1.0	1.4	0.5		
KIS_GL13	blue lupin	11.1	10.4	4.9	4.9	2.2	2.0	2.2	2.1	1.8	0.2		
KIS_GL14	yellow lupin	12.1	11.6	7.5	7.0	4.7	4.6	1.9	1.6	2.9	0.6		
KIS_GL15	red lentil	9.2	9.1	3.7	3.5	1.8	1.5	0.2	0.2	0.8	0.5		
KIS_GL16	brown lentil	7.8	7.5	3.1	3.1	1.6	1.2	0.8	0.8	0.8	0.7		
KIS_GL17	chickpea	10.1	9.4	2.9	2.7	2.1	1.4	1.3	1.1	1.3	0.6		
KIS_GL18	soybean	18.2	17.1	5.5	4.9	3.0	2.5	1.8	1.6	2.4	0.1		
KIS_GL19	field pea	9.1	8.8	3.7	3.6	1.6	1.3	0.9	0.8	1.3	0.5		
KIS_GL20	runner bean	17.8	16.3	4.6	5.1	2.0	2.3	1.1	1.2	1.8	0.5		
Correlation		0.96		0.94		0.94		0.98		n.a.		n.a.	
Coefficient of variation (%)		26.85		25.54		38.40		66.49		29.27		58.30	

CB, common bean; n.a., not applicable.

Table 5. Microelement composition of 20 legume samples determined by ICP-MS and EDXRF

Sample name	Legume species	Microelements (mg/kg)																									
		Fe		Mn		Zn		Na		Cu		Rb		Br		Ti		Sr		Mo		Cr		Co		V	
		ICP-MS	ED XRF	ICP-MS	ED XRF	ICP-MS	ED XRF	ICP-MS	ED XRF	ICP-MS	ED XRF	ICP-MS	ED XRF	ICP-MS	ED XRF	ICP-MS	ED XRF	ICP-MS	ED XRF	ICP-MS	ED XRF	ICP-MS	ED XRF	ICP-MS	ED XRF	ICP-MS	ED XRF
KIS_GL1	CB (grains)	64.6	69.2	12.0	28.1	26.6	6.1	8.7	5.9	1.3	1.6	0.9	0.6	0.9	0.2	0.03	0.003										
KIS_GL2	CB (grains)	69.9	79.0	12.4	27.9	26.7	3.3	9.5	3.7	1.2	2.2	0.9	3.2	1.9	0.1	0.04	0.000										
KIS_GL3	CB (grains)	57.7	91.6	11.0	28.9	22.3	2.4	5.9	9.0	1.7	3.5	1.1	0.9	0.9	0.3	0.03	0.004										
KIS_GL4	CB (pods)	54.0	65.8	13.6	21.5	17.5	67.2	7.1	6.2	6.9	3.5	3.0	0.4	1.1	0.1	0.03	0.026										
KIS_GL5	CB (pods)	44.2	76.6	14.7	22.0	23.9	53.5	5.8	3.9	2.9	4.4	4.1	0.2	1.3	0.1	0.02	0.002										
KIS_GL6	CB (pods)	50.6	68.0	16.7	24.2	25.4	91.8	4.9	8.2	13.9	3.3	4.8	0.4	1.8	0.2	0.02	0.014										
KIS_GL7	CB (grains)	77.3	84.0	13.6	26.8	25.1	3.0	8.3	2.4	1.5	3.0	4.6	5.8	4.5	0.2	0.04	0.045										
KIS_GL8	CB (grains)	58.7	76.0	11.9	27.6	27.1	38.3	5.8	7.8	1.8	2.4	3.1	8.5	6.6	0.2	0.15	0.019										
KIS_GL9	CB (grains)	56.9	84.7	9.4	20.3	19.4	1.7	5.2	6.7	1.6	3.8	0.8	4.7	3.5	0.2	0.05	0.008										
KIS_GL10	white lupin	37.2	57.5	487.7	42.4	48.6	58.8	8.0	23.3	2.0	2.0	2.0	2.2	1.6	0.1	0.09	0.008										
KIS_GL11	faba bean	43.3	74.7	16.4	49.1	43.1	9.0	16.3	5.6	1.3	2.0	0.9	0.9	1.1	0.2	0.20	0.005										
KIS_GL12	faba bean	46.9	84.9	16.8	44.6	43.0	10.0	16.3	3.4	1.5	2.1	1.8	1.0	0.9	0.2	0.16	0.007										
KIS_GL13	blue lupin	43.9	58.3	79.5	34.9	33.1	58.6	6.1	8.9	3.5	2.4	5.7	1.7	1.4	1.7	0.04	0.031										
KIS_GL14	yellow lupin	64.9	95.6	82.9	63.3	64.6	78.3	10.7	3.3	2.1	4.1	2.2	1.4	1.1	2.9	0.07	0.022										
KIS_GL15	red lentil	65.9	87.6	13.6	33.0	33.0	10.7	9.1	4.1	3.8	2.7	1.8	5.3	4.4	0.1	0.03	0.008										
KIS_GL16	brown lentil	47.3	70.8	9.6	19.6	22.1	6.9	8.1	3.1	1.3	2.8	1.8	0.5	0.9	0.2	0.04	0.006										
KIS_GL17	chickpea	55.5	71.1	25.8	28.6	26.0	33.8	8.0	6.7	10.8	0.6	5.5	2.7	1.7	1.0	0.12	0.027										
KIS_GL18	soybean	86.0	126.0	22.7	36.8	35.9	10.3	13.4	7.6	6.6	3.7	2.0	0.7	2.0	2.7	0.13	0.034										
KIS_GL19	field pea	46.8	79.3	8.3	26.3	24.3	16.2	7.3	4.9	1.6	1.1	1.8	0.6	1.0	0.2	0.03	0.027										
KIS_GL20	runner bean	52.7	77.6	12.6	23.0	20.8	1.8	5.4	3.4	2.6	1.0	2.6	2.4	1.9	0.3	0.04	0.013										
Correlation		0.72		n.a.		0.97		n.a.		n.a.		n.a.		n.a.		0.95		n.a.		n.a.		n.a.					
Coefficient of variation (%)		25.96		232.72		35.83		102.12		38.72		68.38		97.13		39.79		59.72		89.18		146.10		77.30		79.13	

CB, common bean; n.a., not applicable.

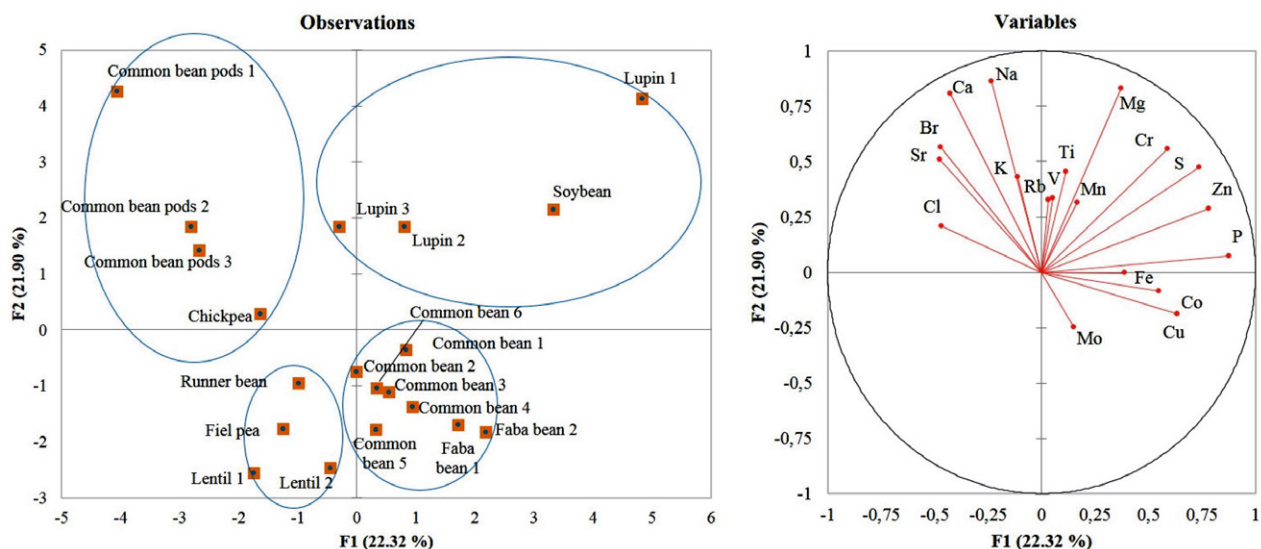


Fig. 1. PCA score plot (left) and discriminant loadings plot (right)

correlations between these two methods for the macroelements P, S, K and Ca are presented in Table 4 and for the microelements Fe, Zn and Mo in Table 5. A very strong correlations were detected for the elements Ca (0.98), Zn (0.97), K (0.96), Mo (0.95), P and S (0.94), while strong correlation was observed for Fe (0.72). For the elements K,

S, Ca and Zn brought to evidence a tendency that EDXRF values were lower, when compared with ICP-MS values. Phosphorus values were comparable between methods while Fe EDXRF values were higher compared to ICP-MS values. These discrepancies can be due to the inhomogeneity of the samples.

Statistical evaluation of results was performed on the dataset using PCA to identify the elements responsible for differentiating legume samples. The discrimination score plot and loadings across the original dataset are shown in Fig. 1. When the PCA was applied to the data (20 samples, 19 variables), discriminant functions were obtained where Function 1 explained 22.31% and Function 2 21.90% of the total variance. According to the multi-elemental composition, the analysed legumes can be divided into four groups as seen in Fig. 1. The first group included samples of common bean pods and chickpea with the most influential elements Ca, Na, Sr and Cl. Second group involved soybean and lupin samples, where the most influential elements were Na, Mg, S, Zn and P. The third group consisted of runner bean, field pea and lentil samples with most influential elements Mg, S, Zn and P. Finally, the faba bean and common bean grain samples formed the fourth group with most influential elements Mo, Cu and Co.

4. Conclusion

There is a need for reliable legumes element concentration data to provide information about nutritional uptake, especially for essential macro- and microelements. Besides, the multi-elemental composition, it provides important information for the plant breeding programmes and can potentially serve as a base for nutrient biofortification purposes (e.g. Fe, Zn). This paper provides some interesting comparisons between two different techniques (ICP-MS, EDXRF) in the determination of the multi-elemental composition of different legumes. An intercomparison of seven elements (P, S, K, Ca, Fe, Zn and Mo) showed satisfactory agreement between both methods. The simple, fast and cheaper EDXRF method when combined with ICP-MS, was found the most appropriate technique for determination of Na, Mg, V, Cr, Mn, Co and Cu, and used to provide the first evaluation of multi-elemental composition to differentiate between several legume samples usually produced and consumed in Slovenia. Despite these encouraging data, there remain some limitations and further research base on a larger dataset of legume species will be important in establishing more reliable databases in elemental composition.

Acknowledgements

This research was a part of the research programme Agrobiodiversity (P4-0072) and the research project L4-7520 financially supported by the Slovenian research agency (ARRS), Ljubljana, Slovenia, and the Public Service in vegetables and herbs financed by the Ministry of Agriculture, Forestry and Food, Republic of Slovenia. The authors would like to thank Peter Kump, PhD, for kindly providing the QAES (Quantitative Analysis of Environmental Samples) software (XRF), and to the national curator of SPGB

(Slovene Plant Gene Bank) Jelka Šuštar Vozlič, PhD, for providing the legumes genetic resources.

5. Reference

1. E. Rööös, G. Carlsson, F. Ferawati, M. Hefni, A. Stephan, P. Tidåker, C. Witthöft, *Renew. Agr. Food Syst.* **2020**, *35*(2), 192–205. DOI:10.1017/S1742170518000443
2. D. Rubiales, A. Mikić, *Crit. Rev. Plant Sci.*, **2015**, *34*, 2–3. DOI:10.1080/07352689.2014.897896
3. M. Farooq, M. Hussain, M. Usman, S. Farooq, S. S. Alghamdi, K. H. Siddique, *J. Agric. Food Chem.* **2018**, *66*(34), 8887–8897. DOI:10.1021/acs.jafc.8b02924
4. C. Pinheiro, J. P. Baeta, A. M. Pereira, H. Domingues, C. P. Ricardo, *J. Food Comp. Anal.* **2010**, *23*(4), 319–325. DOI:10.1016/j.jfca.2010.01.005
5. K. I. Ereifej, G. N. Al-Karaki, M. K., Hammouri, *Int. J. Food Prop.* **2001**, *4*(2), 239–246. DOI:10.1081/JFP-100105190
6. FAOSTAT, 2020. Food and Agriculture Organisation (FAO) of the United Nations. Crops. Available form: <http://www.fao.org/faostat/en/#data/QC> (Accessed on 8/4/2021).
7. G. Alandia, C. Pulvento, M. H. Sellami, N. Hoidal, T. Anemone, E. Nigussie, J. J. Agüero, A. Lavini, S. E. Jacobsen, in: A. Hirich, R. Choukr-Allah, R. Ragab (Eds.): *Emerging Research in Alternative Crops, Environment & Policy*, vol 58. Springer, Cham, **2020**, 25–53. DOI:10.1007/978-3-319-90472-6_2
8. M. Markiewicz-Keszycka, R. Cama-Moncunill, M. P. Casado-Gavalda, C. Sullivan, P. J. Cullen, *Curr. Opin. Food Sci.* **2019**, *28*, 96–103. DOI:10.1016/j.cofs.2019.10.002
9. S. Kumar, G. Pandey, *Helvion* **2020**, *6*(3), p.e03682. DOI:10.1016/j.helivon.2020.e03682
10. B. M. Freire, R. M. Pereira, C. N. Lange, B. L. Batista, in: *Sustainable Solutions for Elemental Deficiency and Excess in Crop Plants*. Springer, Singapore, **2020**, pp. 135–182. DOI:10.1007/978-981-15-8636-1_7
11. N. Petry, E. Boy, J. P. Wirth, R. F. Hurrell, *Nutrients*, **2015**, *7*(2), 1144–1173. DOI:10.3390/nu7021144
12. M. A. Zoroddu, J. Aaseth, G. Crisponi, S. Medici, M. Peana, V. M. Nurchi, *J. Inorg. Biochem.* **2019**, *195*, 120–129. DOI:10.1016/j.jinorgbio.2019.03.013
13. H. Zhao, J. Tang, Q. Yang, *J. Food Comp. Anal.* **2021**, p.103900. DOI:10.1016/j.jfca.2021.103900
14. M. Ghidotti, S. Papoci, C. Dumitrascu, T. Zdiniakova, Y. Fiamegos, M. B. de la Calle Gutiñas, *Talanta Open*, **2021**, p.100040. DOI:10.1016/j.talo.2021.100040
15. M. Nečemer, P. Kump, J. Ščančar, R. Jačimovič, J. Simčič, P. Pelicon, M. Budnar, Z. Jeran, P. Pongrac, *Spectrochim. Acta B* **2008**, *63*, 1240–1247. DOI:10.1016/j.sab.2008.07.006
16. M. Nečemer, P. Kump, K. Vogel-Mikuš, in: *Use of X-ray fluorescence-based analytical techniques in phytoremediation*, Nova Science Publishers, Inc., New York, USA, **2011**, 331–358
17. A. P. de Oliveira, B. D. S. O. Mateó, A. M. Fioroto, P. V. de Oliveira, J. Naozuka, *J. Food Comp. Anal.* **2018**, *67*, 135–140. DOI:10.1016/j.jfca.2018.01.012

18. G. E. Guild, N. G. Paltridge, M. S. Andersson, J.C. Stangoulis, *Plant Soil* **2017**, *419*(1), 457–466. DOI:10.1007/s11104-017-3352-4
19. G. R. Gomes, G. H. Freiria, L. Vinicius Constantino, S. M. Alves, D. M. Zeffa, L. S. A. Takahashi, *Semina: Ciênc. Agrár.* **2020**, *41*(5), 1469–1482. DOI:10.5433/1679-0359.2020v41n5p1469
20. T. Celmeli, H. Sari, H. Canci, D. Sari, A. Adak, T. Eker, C. Toker, *Agronomy* **2018**, *8*(9), p.166. DOI:10.3390/agronomy8090166
21. S. Lukin, *Vestnik Russian Agric. Sci.* **2018**, *6*, 76–79. DOI:10.30850/vrsn/2018/6/76-79
22. C. I. Lizarazo, M. Yli-Halla, F. L. Stoddard, *Nutr. Cycl. Agroecosystems* **2015**, *103*(3), 311–327. DOI:10.1007/s10705-015-9743-0
23. H. Khazaei, A. Vandenberg, *Agronomy* **2020**, *10*(4), p.511. DOI:10.3390/agronomy10040511
24. Z. Türk, *J. Plant Nutr.* **2020**, *43*(4), 563–577. DOI:10.1080/01904167.2019.1685099
25. G. Ciurescu, I. Toncea, M. Ropotă, M. Hăbeanu, *Rom. Agric. Res.* **2018**, *35*, 101–108. <https://www.incda-fundulea.ro/rar/nr35/rar35.14.pdf>
26. L. X. Lopez-Martinez, in: H. N. Murthy, K. Y. Paek (Eds.) *Bioactive Compounds in Underutilized Vegetables and Legumes. Reference Series in Phytochemistry.* Springer, Cham, **2020**, 1–17. DOI:10.1007/978-3-030-44578-2_31-1
27. M. T. Mosisa, *Afr. J. Food Sci.* **2017**, *11*(3), 74–81. DOI:10.5897/AJFS2016.1475
28. E. M. Flores, P. A. Mello, S. R. Krzyzaniak, V. H. Cauduro, R. S. Picoloto, *Rapid Commun. Mass Spectrom.* **2020**, *34*, p.e8727. DOI:10.1002/rcm.8727
29. M. W. Donner, T. Siddique, *Can. J. Chem.* **2018**, *96*(8), 795–802. DOI:10.1139/cjc-2017-0637
30. G. G. A. de Carvalho, M. B. B. Guerra, A. Adame, C. S. Nomura, P. V. Oliveira, H. W. P. de Carvalho, D. Santos, L. C. Nunes, F. J. Krug, *J. Anal. Atom. Spectrom.* **2018**, *33*(6), 919–944. DOI:10.1039/C7JA00293A
31. E. de Almeida, N. M. Duran, M. H. Gomes, S. M. Savassa, T. N. da Cruz, R. A. Migliavacca, H. W. Pereira de Carvalho, *X-Ray Spectrometry* **2019**, *48*(2), 151–161. DOI:10.1002/xrs.3001

Povzetek

V raziskavi smo z dvema analiznima tehnikama, induktivno sklopljeno plazemsko-masno spektrometrijo (ICP-MS) in energijsko disperzijsko rentgensko fluorescenčno spektroskopijo (EDXRF), določili elementarno sestavo različnih stročnic, ki se pogosto pridelujejo in uživajo v Sloveniji. Rezultati kažejo, da se podatki, pridobljeni z uporabo teh metod, dobro ujemajo s certificiranimi referenčnimi materiali. Skupno smo v dvajsetih vzorcih stročnic določili devetnajst elementov. Medsebojna primerjava štirih makro- (P, S, K, Ca) in treh mikroelementov (Fe, Zn, Mo) izmerjenih z ICP-MS in EDXRF, je pokazala visoko korelacijo med uporabljenima metodama. EDXRF se je izkazala za cenejšo, enostavnejšo in okolju prijaznejšo metodo za določanje elementov P, S, Cl, K, Ca, Fe, Zn, Mo, Sr, Rb, Ti in Br v stročnicah, medtem ko je za določanje vsebnosti Na, Mg, V, Cr, Mn, Co in Cu ustrežnejša ICP-MS metoda, predvsem zaradi visoke občutljivosti in natančnosti. Z analizo glavnih komponent (PCA) smo uspeli razvrstiti vzorce preučevanih stročnic glede na elementarno sestavo v štiri skupine.



Except when otherwise noted, articles in this journal are published under the terms and conditions of the Creative Commons Attribution 4.0 International License

Scientific paper

Zinc Complexes Derived from 5-Bromo-2-(((2-isopropylamino)ethyl)imino)methyl)phenol: Microwave-Assisted Synthesis, Characterization, Crystal Structures and Antibacterial Activities

Wei-Guang Zhang^{1,*} and Ji-Hong Liang²¹ College of Chemistry and Chemical Engineering, Qiqihar University, Qiqihar 161006, P. R. China² Library, Qiqihar University, Qiqihar 161006, P. R. China

* Corresponding author: E-mail: zhangweiguang1230@163.com

Received: 04-22-2021

Abstract

Three new zinc complexes $[\text{Zn}_3\text{L}_2(\mu_2\text{-}\eta^1\text{-CH}_3\text{COO})_2(\mu_2\text{-}\eta^2\text{-}\eta^0\text{-CH}_3\text{COO})_2]$ (**1**), $[\text{ZnCl}_2(\text{HL})]$ (**2**) and $[\text{ZnBr}_2(\text{HL})]$ (**3**), where L = 5-bromo-2-(((2-isopropylamino)ethyl)imino)methyl)phenolate, HL = 5-bromo-2-(((2-isopropylammonio)ethyl)imino)methyl)phenolate, have been synthesized under microwave irradiation. The complexes were characterized by elemental analyses, IR, UV-Vis spectra, molar conductivity, and single crystal X-ray diffraction. X-ray analysis revealed that the Zn atoms in complex **1** are in square pyramidal and octahedral coordination, and those in complexes **2** and **3** are in tetrahedral coordination. The molecules of the complexes are linked through hydrogen bonds and $\pi\cdots\pi$ interactions. In order to evaluate the biological activity of the complexes, *in vitro* antibacterial against *Staphylococcus aureus*, *Bacillus subtilis*, *Escherichia coli* and *Pseudomonas aeruginosa* was assayed.

Keywords: Schiff base; zinc complex; X-ray diffraction; antibacterial activity

1. Introduction

In the past few years, microwave-assisted preparation has attracted enormous interest in the fields of coordination chemistry and inorganic synthesis.¹ Microwave irradiation can accelerate many chemical reactions. This method of synthesis has also advantages in providing a clean, cheap and easy handling heating way, which achieves higher yields with less reaction time.² Penicillins and cephalosporins disrupt the formation of the bacterial cell wall, but many bacteria strains have developed resistance to them.³ Thus, to explore new antibacterial drugs is a hot topic in chemical and biological areas.⁴ Schiff bases have been known for a long time for their interesting biological activities and coordination capability for metal ions.⁵ When bioorganic molecules or drugs are bound to metal ions, there is drastic change in their biomimetic properties, therapeutic effects and pharmacological properties. Zinc complexes are found to be antitumor active, catalytic active, antimicrobial and cytotoxic.⁶ In this study, the synthesis, characterization and antibacterial properties of three new zinc complexes $[\text{Zn}_3\text{L}_2(\mu_2\text{-}\eta^1\text{-}\eta^1\text{-CH}_3\text{COO})_2(\mu_2\text{-}$

$\eta^2\text{-}\eta^0\text{-CH}_3\text{COO})_2]$ (**1**), $[\text{ZnCl}_2(\text{HL})]$ (**2**) and $[\text{ZnBr}_2(\text{HL})]$ (**3**), where L = 5-bromo-2-(((2-isopropylamino)ethyl)imino)methyl)phenolate, HL = 5-bromo-2-(((2-isopropylammonio)ethyl)imino)methyl)phenolate, are presented.

2. Experimental

2.1. Materials and Physical Methods

All the starting materials and solvents used in the present investigation were of analytical grade and used without further purification. 4-Bromosalicylaldehyde and *N*-isopropylethane-1,2-diamine were purchased from TCI. WX-4000 microwave digestion system was used in microwave synthesis. Elemental analyses were performed on a Perkin-Elmer 2400 Elemental Analyzer. IR spectra were recorded as KBr pellets on a Bio-Rad FTS 135 spectrophotometer in the range of 4000–400 cm^{-1} . Electronic spectra were recorded on a Lambda 35 spectrometer. Conductivities of 10^{-3} M solutions in acetonitrile were measured on a DDS-11A conductivity meter. Single crystal

X-ray diffraction was carried out with a Bruker Smart 1000 CCD diffractometer.

2. 2. Synthesis of Complex 1

4-Bromosalicylaldehyde (0.20 g, 1.0 mmol), *N*-isopropylethane-1,2-diamine (0.10 g, 1.0 mmol), zinc acetate dihydrate (0.22 g, 1.0 mmol) and methanol (20 mL) were placed in a 30-mL Teflon-lined autoclave, which was then inserted into the cavity of a microwave reactor. The reaction mixture was maintained at 350 K and 200 W for 10 min. Then natural cooling was followed for about 1 h. The resulting solution was then filtered and allowed to evaporate slowly at room temperature for 5 days. The diffraction quality colorless single crystals were collected by filtration and washed with methanol. The yield was 0.22 g (66%). Anal. Calcd. for $C_{32}H_{44}Br_2N_4O_{10}Zn_3$ (%): C, 38.41; H, 4.43; N, 5.60. Found (%): C, 38.27; H, 4.52; N, 5.71. IR data (KBr, cm^{-1}): 3093, 1648, 1581, 1523, 1459, 1431, 1401, 1370, 1318, 1292, 1252, 1230, 1188, 1161, 1133, 1075, 1061, 956, 926, 911, 868, 788, 775, 670, 615, 545, 470. UV-Vis data in methanol [λ_{max} (nm), ϵ ($L \cdot mol^{-1} \cdot cm^{-1}$)]: 239, 15370; 273, 9260; 340, 4535.

2. 3. Synthesis of Complex 2

4-Bromosalicylaldehyde (0.20 g, 1.0 mmol), *N*-isopropylethane-1,2-diamine (0.10 g, 1.0 mmol), zinc chloride (0.14 g, 1.0 mmol) and methanol (20 mL) were placed in a

30-mL Teflon-lined autoclave, which was then inserted into the cavity of a microwave reactor. The reaction mixture was maintained at 350 K and 200 W for 10 min. Then natural cooling was followed for about 1 h. The resulting solution was then filtered and allowed to evaporate slowly at room temperature for 8 days. The diffraction quality colorless single crystals were collected by filtration and washed with methanol. The yield was 0.26 g (62%). Anal. Calcd. for $C_{12}H_{17}BrCl_2N_2OZn$ (%): C, 34.20; H, 4.07; N, 6.65. Found (%): C, 34.33; H, 4.15; N, 6.56. IR data (KBr, cm^{-1}): 3105, 1634, 1585, 1576, 1525, 1468, 1447, 1401, 1344, 1282, 1237, 1182, 1158, 1131, 1071, 1039, 960, 913, 847, 785, 608, 583, 532, 465. UV-Vis data in methanol [λ_{max} (nm), ϵ ($L \cdot mol^{-1} \cdot cm^{-1}$)]: 227, 16250; 246, 17100; 273, 9250; 365, 4520.

2. 4. Synthesis of Complex 3

4-Bromosalicylaldehyde (0.20 g, 1.0 mmol), *N*-isopropylethane-1,2-diamine (0.10 g, 1.0 mmol), zinc bromide (0.23 g, 1.0 mmol) and methanol (20 mL) were placed in a 30-mL Teflon-lined autoclave, which was then inserted into the cavity of a microwave reactor. The reaction mixture was maintained at 350 K and 200 W for 10 min. Then natural cooling was followed for about 1 h. The resulting solution was then filtered and allowed to evaporate slowly at room temperature for 6 days. The diffraction quality colorless single crystals were collected by filtration and washed with methanol. The yield was 0.26 g (62%).

Table 1. Crystallographic data for the complexes

Complex	1	2	3
Formula	$C_{32}H_{44}Br_2N_4O_{10}Zn_3$	$C_{12}H_{17}BrCl_2N_2OZn$	$C_{12}H_{17}Br_3N_2OZn$
Formula weight	1000.64	421.46	510.38
Crystal system	Triclinic	Monoclinic	Monoclinic
Space group	$P-1$	$P2_1/n$	$P2_1/n$
a (Å)	8.6285(12)	6.2574(16)	6.3937(8)
b (Å)	11.3804(13)	11.6604(17)	11.9598(12)
c (Å)	19.8737(15)	22.1717(19)	21.9993(13)
α (°)	86.433(1)	90	90
β (°)	89.601(1)	94.109(1)	95.186(1)
γ (°)	84.145(1)	90	90
V (Å ³)	1937.6(4)	1613.6(5)	1675.3(3)
λ (Å)	0.71073	0.71073	0.71073
ρ_{calcd} ($g \cdot cm^{-3}$)	1.715	1.735	2.023
Z	2	4	4
μ (mm^{-1})	3.962	4.322	8.614
θ ranges (°)	1.80–25.50	1.84–25.50	1.86–25.50
Reflections collected	10470	8194	8790
Independent reflections	7180	2999	3120
Observed reflections ($I \geq 2\sigma(I)$)	4961	2398	2409
Restraints	26	0	0
Parameters	515	173	174
Goodness-of-fit on F^2	1.022	1.167	1.040
Final R indices [$I \geq 2\sigma(I)$]	0.0405, 0.0824	0.0684, 0.1780	0.0332, 0.0724
R indices (all data)	0.0731, 0.0929	0.0813, 0.1828	0.0513, 0.0781

Anal. Calcd. for $C_{12}H_{17}Br_3N_2OZn$ (%): C, 28.24; H, 3.36; N, 5.49. Found (%): C, 28.33; H, 3.29; N, 5.61. IR data (KBr, cm^{-1}): 3096, 1633, 1585, 1575, 1521, 1466, 1446, 1401, 1344, 1280, 1238, 1182, 1152, 1131, 1070, 1037, 958, 913, 847, 785, 608, 581, 532, 465. UV-Vis data in methanol [λ_{max} (nm), ϵ ($L \cdot mol^{-1} \cdot cm^{-1}$)]: 227, 16250; 246, 17100; 273, 9250; 365, 4520.

2. 5. X-Ray Structure Determination

Single-crystals X-ray diffraction analyses of the complexes were carried out on a Bruker Smart 1000 CCD

diffractometer equipped with a graphite monochromated Mo K α radiation ($\lambda = 0.71073 \text{ \AA}$) at 298(2) K. Raw frame data were integrated with the SAINT program.⁷ The structures were solved by direct methods and refined by full-matrix least-squares on F^2 using SHELXL.⁸ An empirical absorption correction was applied with the program SADABS.⁹ All non-hydrogen atoms were refined anisotropically. The N2-C26-C27-C28 moiety of complex **1** is disordered over two sites, with occupancies of 0.44(2) and 0.56(2). The N3-C8-C9-N4 moiety of complex **1** is disordered over two sites, with occupancies of 0.61(2) and 0.39(2). Molecular graphics software used was ORTEP

Table 2. Selected bond distances (\AA) and bond angles ($^\circ$) for the complexes

1			
Zn1–O1	2.117(3)	Zn1–O3	1.984(3)
Zn1–O4	2.020(3)	Zn1–N3	2.014(4)
Zn1–N4	2.175(4)	Zn2–O2	2.047(3)
Zn2–O1	2.113(3)	Zn2–O4	2.155(3)
Zn3–O7	1.990(3)	Zn3–N1	2.031(4)
Zn3–O6	2.095(3)	Zn3–O9	2.123(3)
Zn3–N2	2.176(4)	Zn4–O8	2.050(3)
Zn4–O6	2.107(3)	Zn4–O9	2.144(3)
O3–Zn1–N3	115.48(17)	O3–Zn1–O4	103.27(12)
N3–Zn1–O4	140.15(16)	O3–Zn1–O1	94.56(12)
N3–Zn1–O1	86.40(13)	O4–Zn1–O1	81.44(10)
O3–Zn1–N4	97.54(14)	N3–Zn1–N4	82.07(15)
O4–Zn1–N4	102.48(14)	O1–Zn1–N4	166.00(13)
O2–Zn2–O2A	180	O2–Zn2–O1A	89.96(11)
O2–Zn2–O1	90.04(11)	O1–Zn2–O1A	180
O2–Zn2–O4A	90.27(11)	O1–Zn2–O4A	101.49(10)
O2–Zn2–O4	89.73(11)	O1–Zn2–O4	78.51(10)
O4–Zn2–O4A	180	O7–Zn3–N1	110.33(16)
O7–Zn3–O6	96.20(12)	N1–Zn3–O6	86.91(14)
O7–Zn3–O9	96.93(12)	N1–Zn3–O9	150.95(15)
O6–Zn3–O9	80.15(11)	O7–Zn3–N2	93.5(2)
N1–Zn3–N2	81.08(18)	O6–Zn3–N2	166.63(15)
O9–Zn3–N2	107.9(2)	O8–Zn4–O8B	180
O8–Zn4–O6B	89.91(12)	O8–Zn4–O6	89.98(11)
O6–Zn4–O6B	180	O6–Zn4–O9B	100.61(11)
O8–Zn4–O9B	90.72(11)	O8–Zn4–O9	90.72(11)
O6–Zn4–O9	79.39(12)	O9–Zn4–O9B	180
Symmetry codes: A) 2 – x, 1 – y, 1 – z; B) 1 – x, 1 – y, – z.			
2			
Zn1–Cl1	2.246(3)	Zn1–Cl2	2.228(3)
Zn1–O1	1.936(6)	Zn1–N1	2.004(7)
O1–Zn1–N1	97.1(3)	O1–Zn1–Cl2	108.1(2)
N1–Zn1–Cl2	112.6(2)	O1–Zn1–Cl1	111.4(2)
N1–Zn1–Cl1	109.9(2)	Cl2–Zn1–Cl1	116.12(11)
3			
Zn1–Br1	2.3658(6)	Zn1–Br2	2.3784(7)
Zn1–O1	1.939(3)	Zn1–N1	2.000(3)
O1–Zn1–N1	97.55(12)	O1–Zn1–Br1	109.65(8)
N1–Zn1–Br1	110.19(9)	O1–Zn1–Br2	111.09(9)
N1–Zn1–Br2	111.26(9)	Br1–Zn1–Br2	115.62(3)

III.¹⁰ The crystal data for the complexes are listed in Table 1. Selected bond lengths and angles for the complexes are listed in Table 2.

2. 6. Antibacterial Activity

The free Schiff base and the zinc complexes were screened *in vitro* for their antibacterial property against two Gram-positive (*Staphylococcus aureus* MTCC 96, *Bacillus subtilis* MTCC 121) and two Gram-negative (*Escherichia coli* MTCC 1652, *Pseudomonas aeruginosa* MTCC 741) bacterial strains by agar well diffusion method.¹¹ DMSO was used as a negative control, and Ciprofloxacin was used as positive control.

2. 7. Determination of Minimum Inhibitory Concentration (MIC)

MIC of the compounds against bacterial strains was tested through a modified agar well diffusion method.¹² A twofold serial dilution of each compound was prepared by first reconstituting the compound in DMSO followed by dilution in sterile distilled water to achieve a decreasing concentration range 256 μM . A 100 μL volume of each dilution was introduced into wells in the agar plates already seeded with 100 μL of standardized inoculums (10^6 cfu mL^{-1}) of the test microbial strain. All test plates were incubated aerobically at 37 $^{\circ}\text{C}$ for 24 h and observed for the inhibition zones.

3. Results and Discussion

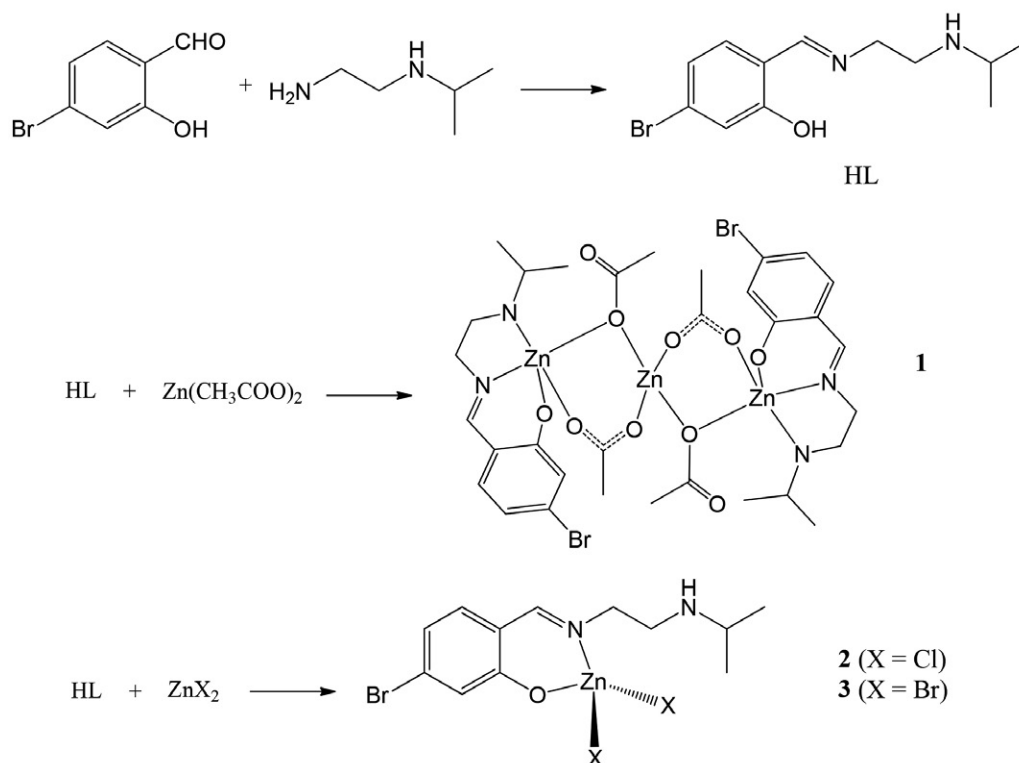
3. 1. Chemistry

Reaction of the newly formed Schiff base HL with zinc acetate, zinc chloride and zinc bromide, respectively, afforded the trinuclear zinc complex **1** and mononuclear zinc complexes **2** and **3** (Scheme 1). The poor conductivity of complexes **1–3** ($20\text{--}40 \Omega^{-1} \text{cm}^2 \text{mol}^{-1}$) indicates they are non-electrolytes in solution.¹³

3. 2. Infrared and Electronic Spectra

In the infrared spectra of the complexes, the weak absorptions in the range $3093\text{--}3177 \text{ cm}^{-1}$ are assigned to the N-H vibrations of the Schiff base ligands. The characteristic imine stretching is observed at $1633\text{--}1648 \text{ cm}^{-1}$ as strong signal.¹⁴ The asymmetric and symmetric stretching vibrations of the acetate groups in **1** appear at 1581 and 1431 cm^{-1} , respectively. The difference between $\nu_{\text{asym}}(\text{COO})$ and $\nu_{\text{sym}}(\text{COO})$ ($\Delta\nu = 150 \text{ cm}^{-1}$), which is smaller than 164 cm^{-1} observed in ionic acetate, reflects the bidentate bridging coordination mode.¹⁵ The Schiff base ligands coordination is substantiated by the phenolic C–O stretching bands at $1175\text{--}1188 \text{ cm}^{-1}$ in the complexes.¹⁶ Coordination of the Schiff bases is further confirmed by the appearance of weak bands in the low wave numbers $400\text{--}600 \text{ cm}^{-1}$, corresponding to $\nu(\text{M–N})$ and $\nu(\text{M–O})$.¹⁷

In the UV-Vis spectra of the complexes, the bands at $225\text{--}246 \text{ nm}$ and $257\text{--}273 \text{ nm}$ are attributed to the $\pi\text{--}\pi^*$



Scheme 1. The synthetic procedure for the Schiff base and the complexes.

and $n-\pi^*$ transitions.¹⁸ The bands at 340–380 nm can be attributed to the ligand to metal charge transfer transition (LMCT).¹⁹

3. 3. Structure Description of Complex 1

The molecular structure of the acetate and phenolate bridged trinuclear zinc complex is shown in Fig. 1. There are two halves of coordination molecules in the asymmetric unit of the complex. Each molecule possesses crystallographic inversion center symmetry, with the center located at Zn2 atom. The outer and inner Zn atoms are linked through three kinds of bridging groups, including phenolate oxygen, $\mu_2-\eta^1:\eta^1$ -acetate, and $\mu_2-\eta^2:\eta^0$ -acetate. The distance between the Zn atoms is 3.064(1) Å. The outer Zn atom is coordinated in square pyramidal geometry, as evidenced by the τ value.²⁰ The

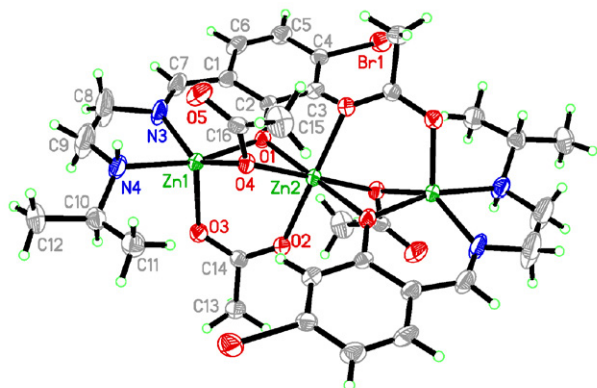


Fig. 1. Molecular structure of complex 1. Unlabeled atoms are related to the symmetry operation $2-x, 1-y, 1-z$. Displacement ellipsoids are drawn at the 30% probability level.

basal plane is defined by the phenolate oxygen, imino and amino nitrogen of the Schiff base ligand, and one O atom of the $\mu_2-\eta^2:\eta^0$ -acetate ligand. The apical position is occupied by one O atom of the $\mu_2-\eta^1:\eta^1$ -acetate ligand. The Zn atoms deviate from the corresponding basal planes by 0.440(3) Å for Zn1 and 0.320(3) Å for Zn3. The square pyramidal coordination is distorted from ideal model, as evidenced by the bond angles. The *cis* and *trans* angles in the basal planes are in the ranges of 81.48(11)–102.49(15)° and 140.15(18)–166.06(14)° for Zn1, and 80.15(12)–107.9(2)° and 151.02(16)–166.59(16)° for Zn3, respectively. The bond angles among the apical and basal donor atoms are in the ranges of 94.58(13)–115.49(18)° for Zn1 and 93.4(2)–110.28(17)° for Zn3. The inner Zn atom is coordinated in octahedral geometry. The equatorial plane is defined by two phenolate oxygen from two Schiff base ligands, and two O atoms from two $\mu_2-\eta^2:\eta^0$ -acetate ligands. The axial positions are occupied by two O atoms from two $\mu_2-\eta^1:\eta^1$ -acetate ligands. The octahedral coordination is distorted from ideal model, as evidenced by the bond angles. The *cis* and *trans* angles in the equatorial planes are in the ranges of 78.48(11)–101.52(11)° and 101.52(11)° for Zn2, and 79.37(12)–100.63(12)° and 180.00(16)° for Zn4, respectively. The bond angles among the apical and basal donor atoms are in the ranges of 89.78(12)–90.22(12)° for Zn2 and 89.22(12)–90.78(12)° for Zn4. The Zn–O and Zn–N bond lengths are comparable to those observed in Schiff base zinc complexes with acetate ligands.²¹

In the crystal structure of the complex, the molecules are linked through C–H...O hydrogen bonds (Table 3), to form one-dimensional chains along the *c* axis (Fig. 2).

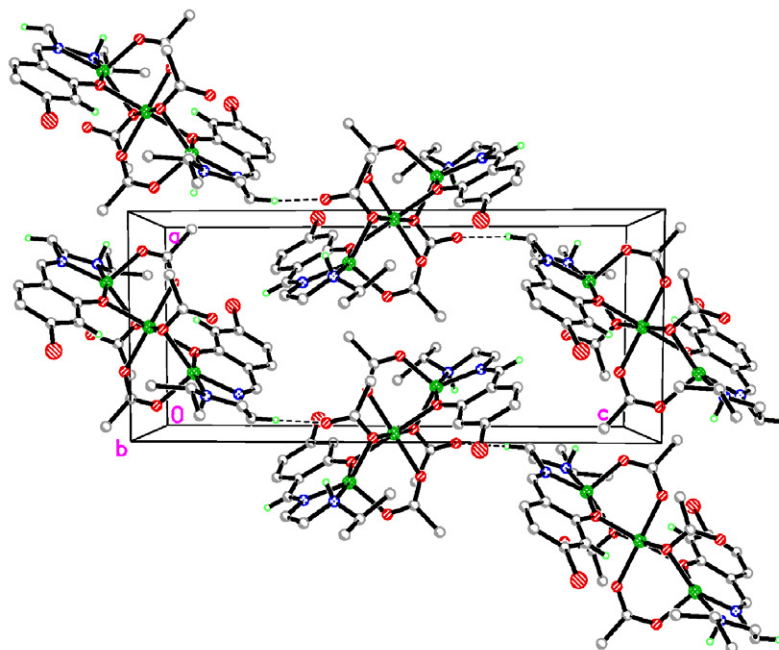


Fig. 2. Molecular packing structure of complex 1. Hydrogen bonds are drawn as dashed lines.

3. 4. Structure Description of Complexes 2 and 3

Molecular structures of complexes 2 and 3 are shown in Figs. 3 and 4, respectively. The complexes are isostruc-

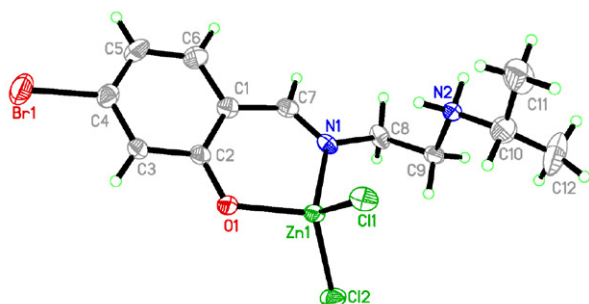


Fig. 3. Molecular structure of complex 2. Displacement ellipsoids are drawn at the 30% probability level.

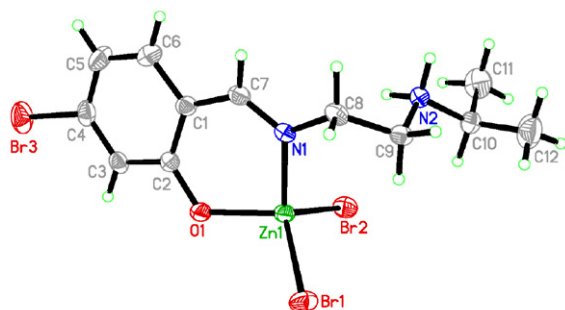


Fig. 4. Molecular structure of complex 3. Displacement ellipsoids are drawn at the 30% probability level.

tural mononuclear zinc compounds. The Zn atom in each complex is coordinated by the phenolate oxygen and imino nitrogen of the Schiff base ligand and two halide atoms, *viz.* Cl for 2 and Br for 3, forming tetrahedral geometry. The tetrahedral coordination is distorted from ideal model, as evidenced by the bond angles. The coordinate bond angles in complexes 2 and 3 are in the ranges of 97.1(3)-

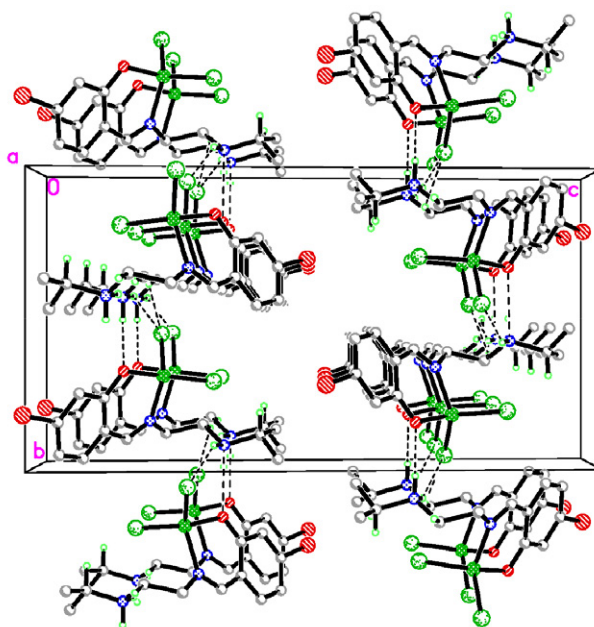


Fig. 5. Molecular packing structure of complex 2. Hydrogen bonds are drawn as dashed lines.

Table 3. Hydrogen bond distances (Å) and bond angles (°) for the complexes

<i>D</i> -H... <i>A</i>	<i>d</i> (<i>D</i> -H)	<i>d</i> (H... <i>A</i>)	<i>d</i> (<i>D</i> ... <i>A</i>)	Angle (<i>D</i> -H... <i>A</i>)
1				
N4-H4A...O5	0.91	2.45	3.055(6)	124(5)
N4-H4A...Br1 ^{#1}	0.91	3.00	3.863(5)	160(5)
C7-H7...O10 ^{#2}	0.93	2.60	3.445(5)	151(5)
C19-H19...O9 ^{#3}	0.93	2.51	3.285(5)	141(5)
C24-H24B...O5 ^{#4}	0.97	2.52	3.292(5)	136(5)
2				
N2-H2B...Cl1	0.90	2.91	3.440(8)	119(6)
N2-H2B...Cl2 ^{#5}	0.90	2.57	3.316(8)	141(6)
N2-H2A...O1 ^{#5}	0.90	1.99	2.850(9)	160(6)
C9-H9B...Cl2 ^{#6}	0.97	2.72	3.463(8)	133(6)
C10-H10...Cl1	0.98	2.78	3.522(8)	133(6)
3				
N2-H2B...Br2	0.90	3.14	3.638(3)	117(5)
N2-H2B...Br1 ^{#7}	0.90	2.67	3.441(3)	145(5)
N2-H2A...O1 ^{#7}	0.90	2.04	2.886(4)	157(5)
C9-H9A...Br1 ^{#8}	0.97	2.84	3.561(4)	132(5)
C10-H10...Br2	0.98	2.92	3.660(4)	133(5)

Symmetry codes: #1: $x, 1 + y, z$; #2: $1 - x, 1 - y, 1 - z$; #3: $1 - x, 1 - y, -z$; #4: $-x, 1 - y, 1 - z$; #5: $-x, -1 - y, 1 - z$; #6: $5/2 - x, 1/2 + y, 1/2 - z$; #7: $3/2 - x, 1/2 + y, 1/2 - z$; #8: $5/2 - x, 1/2 + y, 1/2 - z$.

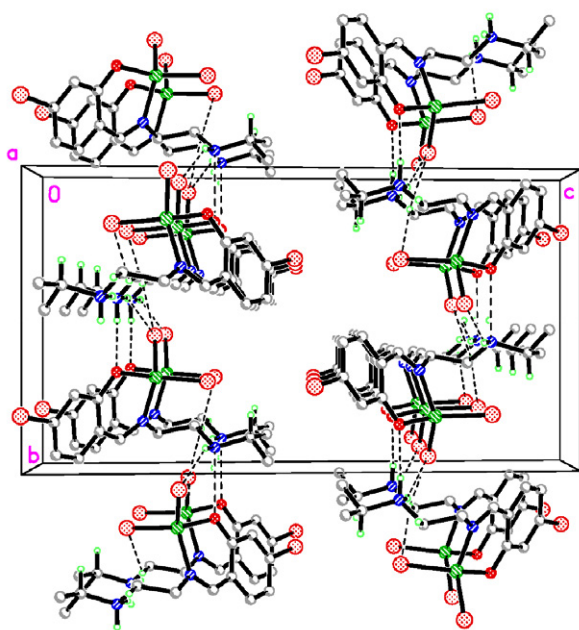


Fig. 6. Molecular packing structure of complex 3. Hydrogen bonds are drawn as dashed lines.

116.12(11)° and 97.55(12)–115.62(3)°, respectively. The Zn–O, Zn–N, Zn–Cl and Zn–Br bond lengths are comparable to those observed in Schiff base zinc complexes.²²

As shown in Fig. 5, the molecules of complex 2 are linked through N–H...O and N–H...Cl hydrogen bonds (Table 3), to form one-dimensional chains along the *b* axis. The chains are further linked through C–H...Cl hydrogen bonds (Table 3) along the *a* axis to form two-dimensional sheets parallel to the *ab* plane. As shown in Fig. 6, the molecules of complex 3 are linked through N–H...Br hydrogen bonds (Table 3), to form one-dimensional chains along the

b axis. The chains are further linked through C–H...Br hydrogen bonds (Table 3) along the *a* axis to form two-dimensional sheets parallel to the *ab* plane.

3. 5. Antibacterial Activities

The antibacterial results are listed in Tables 4 and 5. The studies suggested that the complexes showed somewhat enhanced antibacterial activities in comparison to the free Schiff base. Ciprofloxacin produced significantly sized inhibition zones against the tested bacteria, while DMSO, the negative control, produced no inhibitory effect against any of the tested organisms. The free Schiff base HL showed zones of inhibition in the range of 3.4–13.2 mm against the four bacteria. All the complexes have been observed to show increased zones of inhibition against the four bacterial strains as compared to the free Schiff base. The MIC results indicated that complexes 2 and 3 have similar activities against the bacterial strains, which are better than complex 1. Complex 1 have weak activities against the four bacteria. However, complexes 2 and 3 have strong activities against *Bacillus subtilis* and *Escherichia coli*, and weak activities against the remaining two bacteria. MIC results also revealed that the complexes are more effective against the antibacterial strains as compared to the free Schiff base. The results of this study are in accordance with those reported previously.²³ The overtone's concept²⁴ and Tweedy's chelation theory²⁵ might be used to explain the enhanced in antibacterial activity of the metal complexes.

4. Conclusion

Using microwave assisted heating, three new zinc(II) complexes derived from the Schiff base ligand 5-bro-

Table 4. Diameter of growth of inhibition zone (mm)

Compounds	<i>Staphylococcus aureus</i>	<i>Bacillus subtilis</i>	<i>Escherichia coli</i>	<i>Pseudomonas aeruginosa</i>
HL	6.1	13.2	7.5	3.4
1	8.6	15.5	9.2	5.1
2	9.8	17.6	15.1	11.3
3	9.5	16.8	16.4	12.7
Ciprofloxacin	25.1	20.8	24.9	22.6

Table 5. MIC values (μM)

Compounds	<i>Staphylococcus aureus</i>	<i>Bacillus subtilis</i>	<i>Escherichia coli</i>	<i>Pseudomonas aeruginosa</i>
HL	128	32	64	256
1	64	16	64	128
2	32	8	8	32
3	32	8	8	32
Ciprofloxacin	16	8	16	16

mo-2-(((2-isopropylamino)ethyl)imino)methyl)phenol have been synthesized and characterized by infrared and electronic spectra, and conductance measurement. Structures of the complexes have been confirmed by single crystal X-ray determination. The complexes show interesting antibacterial activities on the bacteria *Staphylococcus aureus* and *Escherichia coli*, which deserves further study.

Supplementary Materials

The X-ray crystallographic data in the CIF format for the structures of the complexes reported in this paper have been deposited with the Cambridge Crystallographic Data Center, and the supplementary crystallographic data can be obtained free of charge on request at www.ccdc.cam.ac.uk/conts/retrieving.html [or from The Director, Cambridge Crystallographic Data Center, CCDC, 12 Union Road, Cambridge CB2 1EZ, UK; fax: +44(0)1223-336033; email: deposit@ccdc.cam.ac.uk], quoting the CCDC numbers 2061673, 2061674 and 2061675.

Acknowledgments

This project was supported by the Qiqihar University.

5. References

- (a) R. T. Liu, C. L. Yuan, Y. Feng, J. Y. Qian, X. T. Huang, Q. T. Chen, S. Y. Zhou, Y. Ding, B. B. Zhai, W. J. Mei, L. Z. Yao, *RSC Advances* **2021**, *11*, 4444–4453; DOI:10.1039/D0RA09418H
- (b) D. L. Zhou, W.-P. To, E. N. S. M. Tong, G. Cheng, L. L. Du, D. L. E. Phillips, C. M. Che, *Angew. Chem. Int. Ed.* **2020**, *59*, 6375–6382; DOI:10.1002/anie.201914661
- (c) L. R. Piquer, S. Dey, L. Castilla-Amoros, S. J. Teat, J. Cirera, G. Rajaraman, E. C. Sanudo, *Dalton Trans.* **2019**, *48*, 12440–12450; DOI:10.1039/C9DT02567G
- (d) L. R. Piquer, E. C. Sanudo, *Polyhedron* **2019**, *169*, 195–201; DOI:10.1016/j.poly.2019.05.011
- (e) L. L. S. Melo, G. P. Castro, S. M. C. Goncalves, *Inorg. Chem.* **2019**, *58*, 3265–3270. DOI:10.1021/acs.inorgchem.8b03340
- (a) S.-H. Zhang, Y.-L. Zhou, X.-J. Sun, L.-Q. Wei, M.-H. Zeng, H. Liang, *J. Solid State Chem.* **2009**, *182*, 2991–2996; DOI:10.1016/j.jssc.2009.08.009
- (b) S.-H. Zhang, C. Feng, *J. Mol. Struct.* **2010**, *977*, 62–66. DOI:10.1016/j.molstruc.2010.05.010
- J. R. Anaconda, M. Lorono, D. Marpa, C. Ramos, F. Celis, *Appl. Organomet. Chem.* **2020**, *34*, e5755. DOI:10.1002/aoc.5755
- (a) X.-D. Wang, W. Wei, P.-F. Wang, L.-C. Yi, W.-K. Shi, Y.-X. Xie, L.-Z. Wu, N. Tang, L.-S. Zhu, J. Peng, C. Liu, X.-H. Li, S. Tang, Z.-P. Xiao, H.-L. Zhu, *Bioorg. Med. Chem.* **2015**, *23*, 4860–4865; DOI:10.1016/j.bmc.2015.05.026
- (b) Z.-P. Xiao, W. Wei, P.-F. Wang, W.-K. Shi, N. Zhu, M.-Q. Xie, Y.-W. Sun, L.-X. Li, Y.-X. Xie, L.-S. Zhu, N. Tang, H. Ouyang, X.-H. Li, G.-C. Wang, H.-L. Zhu, *Eur. J. Med. Chem.* **2015**, *102*, 631–638; DOI:10.1016/j.ejmech.2015.08.025
- (c) W. Wei, W.-K. Shi, P.-F. Wang, X.-T. Zeng, P. Li, J.-R. Zhang, Q. Li, Z.-P. Tang, J. Peng, L.-Z. Wu, M.-Q. Xie, C. Liu, X.-H. Li, Y.-C. Wang, Z.-P. Xiao, H.-L. Zhu, *Bioorg. Med. Chem.* **2015**, *23*, 6602–6611; DOI:10.1016/j.bmc.2015.09.018
- (d) Z.-P. Xiao, X.-D. Wang, P.-F. Wang, Y. Zhou, J.-W. Zhang, L. Zhang, J. Zhou, S.-S. Zhou, H. Ouyang, X.-Y. Lin, M. Mustapa, A. Reyinbaike, H.-L. Zhu, *Eur. J. Med. Chem.* **2014**, *80*, 92–100; DOI:10.1016/j.ejmech.2014.04.037
- (e) X.-D. Wang, W. Wei, P.-F. Wang, Y.-T. Tang, R.-C. Deng, B. Li, S.-S. Zhou, J.-W. Zhang, L. Zhang, Z.-P. Xiao, H. Ouyang, H.-L. Zhu, *Bioorg. Med. Chem.* **2014**, *22*, 3620–3628; DOI:10.1016/j.bmc.2014.05.018
- (f) X.-D. Wang, W. Wei, R.-C. Deng, S.-S. Zhou, L. Zhang, X.-Y. Lin, Z.-P. Xiao, *Chin. J. Org. Chem.* **2014**, *34*, 1773–1779; DOI:10.6023/cjoc201404042
- (g) X.-D. Wang, R.-C. Deng, J.-J. Dong, Z.-Y. Peng, X.-M. Gao, S.-T. Li, W.-Q. Lin, C.-L. Lu, Z.-P. Xiao, H.-L. Zhu, *Bioorg. Med. Chem.* **2013**, *21*, 4914–4922. DOI:10.1016/j.bmc.2013.06.066
- (a) H. Kargar, *Trans. Met. Chem.* **2014**, *39*, 811–817; DOI:10.1007/s11243-014-9863-4
- (b) A. Sahraei, H. Kargar, M. Hakimi, M. N. Tahir, *J. Mol. Struct.* **2017**, *1149*, 576–584; DOI:10.1016/j.molstruc.2017.08.022
- (c) A. Sahraei, H. Kargar, M. Hakimi, M. N. Tahir, *Trans. Met. Chem.* **2017**, *42*, 483–489; DOI:10.1007/s11243-017-0152-x
- (d) A. Jamshidvand, M. Sahihi, V. Mirkhani, M. Moghadam, I. Mohammadpoor-Baltork, S. Tangestaninejad, H. A. Rudbari, H. Kargar, R. Keshavarzi, S. Gharaghani, *J. Mol. Liquids* **2018**, *253*, 61–71; DOI:10.1016/j.molliq.2018.01.029
- (e) H. Kargar, R. Behjatmanesh-Ardakani, V. Torabi, M. Kashani, Z. Chavoshpour-Natanzi, Z. Kazemi, V. Mirkhani, A. Sahraei, M. N. Tahir, M. Ashfaq, K. S. Munawar, *Polyhedron* **2021**, *195*, 114988; DOI:10.1016/j.poly.2020.114988
- (f) H. Kargar, F. Aghaei-Meybodi, R. Behjatmanesh-Ardakani, M. R. Elahifard, V. Torabi, M. Fallah-Mehrjardi, M. N. Tahir, M. Ashfaq, K. S. Munawar, *J. Mol. Struct.* **2021**, *1230*, 129908; DOI:10.1016/j.molstruc.2021.129908
- (g) H. Kargar, A. A. Ardakani, M. N. Tahir, M. Ashfaq, K. S. Munawar, *J. Mol. Struct.* **2021**, *1233*, 130112. DOI:10.1016/j.molstruc.2021.130112
- (a) N. Farahani, M. Khalaj, *J. Mol. Struct.* **2021**, *1228*, 129747; DOI:10.1016/j.molstruc.2020.129747
- (b) Y.-L. Sang, X.-S. Lin, W.-D. Sun, *Acta Chim. Slov.* **2020**, *67*, 581–585; DOI:10.17344/acsi.2019.5595
- (c) F.-M. Wang, L.-J. Li, G.-W. Zang, T.-T. Deng, Z.-L. You, *Acta Chim. Slov.* **2020**, *67*, 1155–1162; DOI:10.17344/acsi.2020.6056
- (d) H. Kargar, R. Behjatmanesh-Ardakani, V. Torabi, M. Kashani, Z. Chavoshpour-Natanzi, Z. Kazemi, V. Mirkhani, A. Sahraei, M. N. Tahir, M. Ashfaq, K. S. Munawar, *Polyhedron* **2021**, *195*, 114988; DOI:10.1016/j.poly.2020.114988
- (e) N. S. Rukk, L. G. Kuzmina, R. S. Shamsiev, G. A. Davydova, E. A. Mironova, A. M. Ermakov, G. A. Buzanov, A. Y. Skryabina, A. N. Streletskii, G. A. Vorobeve, V. M. Retivov, P.

- A. Volkov, S. K. Belus, E. I. Kozhukhova, V. N. Krasnoperova, *Inorg. Chim. Acta* **2019**, 487, 184–200. DOI:10.1016/j.ica.2018.11.036
7. Siemens, SAINT: Area Detector Control and Integration Software, Siemens Analytical X-ray Instruments Inc., Madison, WI, USA, **1996**.
8. G. M. Sheldrick, SHELXL97 and SHELXTL Software Reference Manual, Version 5.1, Bruker AXS Inc., Madison, WI, USA, **1997**.
9. G. M. Sheldrick, SADABS, University of Göttingen, Germany, **1996**.
10. M. N. Burnett, C. K. Jonsson, ORTEP III, Report ORNL-6895, Oak Ridge National Laboratory, Tennessee, USA, **1996**.
11. K. Singh, Y. Kumar, P. Puri, C. Sharma, K. R. Aneja, *Med. Chem. Res.* **2012**, 21, 1708–1716. DOI:10.1007/s00044-011-9683-4
12. M. I. Okeke, C. U. Iroegbu, E. N. Eze, A. S. Okoli, C. O. Esimone, *J. Ethnopharmacol.* **2001**, 78, 119–127. DOI:10.1016/S0378-8741(01)00307-5
13. W. J. Geary, *Coord. Chem. Rev.* **1971**, 7, 81–122. DOI:10.1016/S0010-8545(00)80009-0
14. G. Kastas, C. A. Kastas, A. Tabak, *Spectrochim. Acta A* **2019**, 222, 117198. DOI:10.1016/j.saa.2019.117198
15. U. Kumar, J. Thomas, N. Thirupathi, *Inorg. Chem.* **2010**, 49, 62–72. DOI:10.1021/ic901100z
16. S. Daravath, A. Rambabu, N. Vamsikrishna, N. Ganji, S. Raj, *J. Coord. Chem.* **2019**, 72, 1973–1993. DOI:10.1080/00958972.2019.1634263
17. A. A. El-Sherif, A. Fetoh, Y. K. Abdulhamed, G. M. Abu El-Reash, *Inorg. Chim. Acta* **2018**, 480, 1–15. DOI:10.1016/j.ica.2018.04.038
18. A. Jayamani, M. Sethupathi, S. O. Ojwach, N. Sengottuvelan, *Inorg. Chem. Commun.* **2017**, 84, 144–149. DOI:10.1016/j.inoche.2017.08.013
19. S. Shit, P. Talukder, J. Chakraborty, G. Pilet, M. S. El Fallah, J. Ribas, S. Mitra, *Polyhedron* **2007**, 26, 1357–1363. DOI:10.1016/j.poly.2006.11.013
20. A. W. Addison, T. N. Rao, J. Reedijk, J. van Rijn, G. C. Verschoor, *J. Chem. Soc. Dalton Trans.* **1984**, 7, 1349–1356. DOI:10.1039/DT9840001349
21. Y. Luo, J. Wang, X. Ding, R. Ni, M. Li, T. Yang, J. Wang, C. Jing, Z. You, *Inorg. Chim. Acta* **2021**, 516, 120146. DOI:10.1016/j.ica.2020.120146
22. A. Guha, T. Chattopadhyay, N. D. Paul, M. Mukherjee, S. Goswami, T. K. Mondal, E. Zangrando, D. Das, *Inorg. Chem.* **2012**, 51, 8750–8759. DOI:10.1021/ic300400v
23. K. Singh, Y. Kumar, P. Puri, M. Kumar, C. Sharma, *Eur. J. Med. Chem.* **2012**, 52, 313–321. DOI:10.1016/j.ejmech.2012.02.053
24. N. Raman, A. Kulandaisamy, K. Jayasubramanian, *Polish J. Chem.* **2002**, 76, 1085–1094.
25. B. G. Tweedy, *Phytopathology* **1964**, 55, 910–915.

Povzetek

Z mikrovalovnim obsevanjem smo sintetizirali tri nove cinkove komplekse: $[\text{Zn}_3\text{L}_2(\mu_2\text{-}\eta^1\text{-}\eta^1\text{-CH}_3\text{COO})_2(\mu_2\text{-}\eta^2\text{-}\eta^0\text{-CH}_3\text{COO})_2]$ (**1**), $[\text{ZnCl}_2(\text{HL})]$ (**2**) in $[\text{ZnBr}_2(\text{HL})]$ (**3**), pri čemer je L = 5-bromo-2-(((2-izopropilamino)etil)imino)metil)fenolat, HL = 5-bromo-2-(((2-izopropilamonijev)etil)imino)metil)fenolat. Produkte smo karakterizirali z elementno analizo, IR, UV-Vis spektri, meritvami molske prevodnosti in monokristalno rentgensko difrakcijo. Strukturna analiza je pokazala, da so cinkovi atomi v spojini **1** kvadratno – piramidalno in oktaedrično koordinirani, medtem ko so v spojinah **2** in **3** tetraedrično koordinirani. Molekule v kompleksih so povezane z vodikovimi vezmi in $\pi\cdots\pi$ interakcijami. Biološko aktivnost produktov smo preverili z *in vitro* antibakterijskim delovanjem na bakterije *Staphylococcus aureus*, *Bacillus subtilis*, *Escherichia coli* in *Pseudomonas aeruginosa*.



Except when otherwise noted, articles in this journal are published under the terms and conditions of the Creative Commons Attribution 4.0 International License

Scientific paper

Some Nitrogen Rich Energetic Material Synthesis by Nucleophilic Substitution Reaction from Polynitro Aromatic Compounds

Kübra Gürpınar,¹ Yaprak Gürsoy Tuncer,¹ Ş. Betül Sopacı,²
M. Abdulkadir Akay,¹ Hasan Nazır,¹ Ingrid Svoboda,³ Orhan Atakol¹
and Emine Kübra İnal^{1,*}

¹ Ankara University, Faculty of Science, Department of Chemistry, 06100, Ankara, Turkey

² Kırşehir Ahi Evran University, Faculty of Art and Science, Department of Chemistry, 40100, Kırşehir, Turkey

³ TU-Darmstadt, Materialwissenschaft, Strukturforchung, Alarich-Weiss Strasse 2, 64287, Darmstadt, Germany

* Corresponding author: E-mail: inal@science.ankara.edu.tr

Received: 04-22-2021

Abstract

Three new nitrogen-rich energetic compounds, *N*-(5-chloro-2,4-dinitrophenyl)hydrazine (1), *N*-(5-chloro-2,4-dinitrophenyl)guanidine (2) and *N*-(5-chloro-2,4-dinitrophenyl)-4-aminopyrazole (3) prepared by the nucleophilic substitution reaction of 1,3-dichloro-4,6-dinitrobenzene with hydrazine, guanidinium carbonate and 4-aminopyrazole. The compounds were characterized by ¹H NMR, ¹³C NMR, IR and mass spectroscopy. Only compound 2 could be prepared in a suitable crystal and molecular model was determined by X-ray analysis. Compounds were investigated by TG and DSC. Thermal degradation and thermokinetic behavior were investigated by Ozawa–Flynn–Wall and Kissinger–Akihira–Sunose techniques. Compounds were observed to be prone to exothermic thermal decomposition. HOMO and LUMO levels, theoretical formation enthalpy and electrostatic maps were calculated by Gaussian09. The detonation velocity and pressure were calculated by Kamlet–Jacobs equation. The compounds were assayed for antimicrobial properties.

Keywords: Energetic material; nitrogen-rich material; formation enthalpy; thermokinetic analysis; Kamlet–Jacobs equation; antimicrobial activity

1. Introduction

As known, in today's energetic research, the aim is to produce nitrogen-rich energetic materials.^{1–3} In explosion reactions, nitrogen atoms are assumed to turn into N₂ gas. The N₂ molecule is very stable, and therefore, the higher the number of nitrogen atoms in the energetic molecule, the higher the enthalpy of the explosion reaction.³ In this study, according to this suggestion, three new nitrogen-rich energetic materials were prepared using nucleophilic substitution reactions and examined by thermal analysis methods. Starting from this fact, 1,3-dichloro-4,6-dinitrobenzene is reacted with three nitrogen-rich nucleophiles, namely hydrazine, guanidine and 4-aminopyrazole in non-aqueous solvents and thus are prepared three new nitrogen-rich energetic materials, *N*-(5-chloro-2,4-dinitrophenyl)hy-

drazine, *N*-(5-chloro-2,4-dinitrophenyl)guanidine and *N*-(5-chloro-2,4-dinitrophenyl)-4-aminopyrazole (Figure 1).

In the aromatic ring, usually, nucleophilic substitution reactions do not occur, on the contrary, electrophilic substitution reactions occur. But nitro groups can change the behavior of the aromatic ring and nitro group is a strong electron-withdrawing group and it strongly affects the electron distribution of the molecule to which it is attached.^{4–6} Although many aromatic substances predominantly undergo electrophilic substitution reactions, when more than one nitro group is bonded to the aromatic ring the electron density of the aromatic ring decreases due to the high electron withdrawing effect of the nitro groups, and this ring can then undergo nucleophilic substitution reactions and the electron distribution of the ring is unbal-

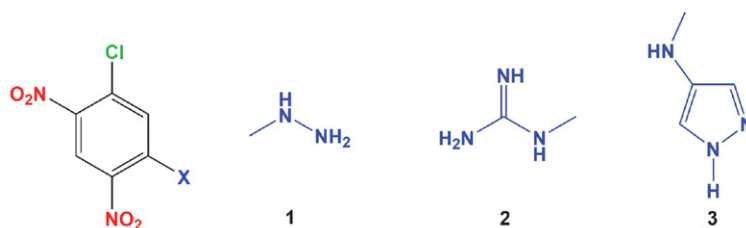


Figure 1. The structural formulas of the nitrogen-rich energetic materials.

anced.^{7–9} A large number of energetic substances prepared by this method were reported in the literature.^{10–14}

Our choice of hydrazine and guanidine is since they are rich in nitrogen and the choice of 4-aminopyrazole is because of its heterocyclic structure. If hydrazine and guanidine are employed in nucleophilic substitution reactions, it is highly probable that two amino groups may be substituted which may result in symmetric molecules and the final product is a mixture. To obviate such a situation, guanidinium carbonate and hydrazine were added above their stoichiometric quantities. Since the second nucleophilic substitution is much more cumbersome after the first one, we only carried out one substitution. Before anything else, these energetic compounds were characterized by the use of C, H, N element analysis, IR spectroscopy and then their structures were elucidated by ¹H NMR and ¹³C NMR spectroscopy after determining the molecular signals from direct inlet (DI) unit of mass spectroscopy. Among these energetic materials, only *N*-(5-chloro-2,4-dinitrophenyl) guanidine was obtained as suitable crystals for the determination of its molecular structure and unit cell parameters by the use of X-ray diffraction methods. Then, the thermal decomposition of the compounds was examined by TG at different heating rates. The TG data obtained were used in the determination of activation energy (E_a) and pre-exponential factor A of the thermal decomposition reactions utilizing the nonisothermal-isoconversional Ozawa–Flynn–Wall (OFW)^{15–23} and Kissinger–Akahira–Sunose (KAS)^{19–26} and isothermal Coats–Redfern (CR)^{27–29} methods.

Also, theoretical calculations were made using the basic set programs included in the Gaussian program in molecules.³⁰ First, the theoretical formation enthalpies of the energetic materials were calculated by the use of the CBS-4M algorithm present in Gaussian09 software. Then the electron distribution and dipole moments of the energetic molecules were determined using DFT method and the differences between HOMO and LUMO of the energetic material were computed and evaluated. Finally, the detonation pressure and detonation velocity of the energetic materials prepared were calculated theoretically according to the literature.³

The energetic materials were also subjected to anti-microbial activity tests due to the lack of these types of tests in the literature using seven different bacteria, namely *Escherichia coli*, *Pseudomonas aeruginosa*, *Salmonella en-*

teritidis, *Enterococcus faecalis*, *Bacillus subtilis*, *Staphylococcus aureus*, and *Bacillus licheniformis*. Anti-microbial activity results were evaluated according to the groups attached to the energetic compounds investigated. There are two important reasons for antimicrobial activity studies. The first one is to have a better insight into the effect of the groups attached to them. The energetic compounds are strained molecules due to nitro groups and these strained molecules can have highly anti-bacterial activity. Secondly, the energetic materials that contain nitrogen are of good nutritional value for the microscopic organisms and promote their growth. Therefore the microscopic investigation of these compounds is of great importance as regards the protection of the environment and human health.

2. Experimental

In the syntheses, 1,3-dichloro-4,6-dinitrobenzene, guanidinium carbonate, hydrazine hydrate and 4-aminopyrazole were used without previous purification. IR spectra were taken with a Shimadzu IRAffinity-1 FTIR spectrometer equipped with a three-reflection ATR unit, all IR spectra were recorded at a resolution of 4 cm⁻¹. Thermal analyses were conducted with a Shimadzu DTG 60H and Shimadzu DSC 60 under N₂ atmosphere with a heating rate of 10 °C min⁻¹ in Pt pans. The temperature and heat calibrations of TG were carried out using In and Zn samples and DSC was calibrated using In. The NMR spectra of the ligands were recorded on a Varian Mercury 400 MHz NMR spectrometer in DMSO-*d*₆. C, H, N elemental analyses were carried out using Eurovector 3018 CHNS analyzer. Electron impact mass spectra (EI-MS) were recorded on a Shimadzu QP2010 Plus GCMS apparatus equipped with a direct inlet unit.

2. 1. X-Ray Analysis

A single crystal of compound **2** was analyzed with an Oxford Diffraction Xcalibur (TM) Single Crystal X-ray Diffractometer with a sapphire CCD detector using MoK_α radiation ($\lambda = 0.71073 \text{ \AA}$) operating in the $\omega/2\theta$ scan mode. The unit-cell dimensions were determined and refined by using the angular settings of 25 automatically centered reflections in $2.98 \leq \theta \leq 27.788$ range. The empirical absorption corrections were applied by the semi-empirical method via the CrysAlis CCD software.³¹ Models were obtained from the

results of the cell refinement and the data reductions were carried out using the solution software SHELXL 2014-6.³² The structures of the energetic materials were resolved by direct methods implemented in the WinGX package.³³

2. 2. Kinetic Analysis

Kinetic analyses for the decomposition reactions of compounds **1**, **2** and **3** were carried out by applying KAS, FOW and Coats–Redfern methods to thermograms at heating rates of 1.0, 5.0, 10.0, 15.0, 20.0 and 25.0 °C min⁻¹ for **2** and **3**; 0.5, 0.6, 0.75 and 1.0 °C min⁻¹ for **1**. Since 1.0 °C min⁻¹ heating rate leads to $\ln\beta = 0$, the other heating rates were employed for FOW and KAS calculations; nonetheless, 1.0 °C min⁻¹ was used in CR calculations. FOW calculation was not applicable to **1** because there was not sufficient data for the three heating rates used. The fact that the compound decomposes very rapidly at higher heating rates does not make any calculations possible.

The activation energies and pre-exponential factors were calculated with the help of graphical methods using the temperatures corresponding to $g(\alpha)$ values of 0.2, 0.4, 0.5, 0.6 and 0.8 at different heating rates according to both KAS and FOW methods. On the other hand, CR calculations were separately carried out at a chosen heating rate for different $g(\alpha)$ values.

The calculations were carried out by the use of KAS (1), FOW (2) and CR (3,4) equations given below:

$$\ln \frac{\beta}{T^2} = \ln \frac{AE_a}{Rg(\alpha)} - \frac{E_a}{RT} \quad (1)$$

$$\ln \beta = \ln \frac{0.0048 A E_a}{R g(\alpha)} - 1.0516 \frac{E_a}{RT} \quad (2)$$

$$\ln \frac{g(\alpha)}{T^2} = \ln \left[\frac{AR}{\beta E_a} \left(1 - \frac{2RT}{E_a} \right) \right] - \frac{E_a}{RT} \quad (3)$$

Because of the term $\frac{2RT}{E_a} \leq 0.1$ in most cases the equation 3 is rearranged as.

$$\ln \frac{g(\alpha)}{T^2} = \ln \left[\frac{AR}{\beta E_a} \right] - \frac{E_a}{RT} \quad (4)$$

In the equations β is the heating rate in °C min⁻¹, R is the universal gas constant, E_a is the activation energy for thermal decomposition, A is the Arrhenius pre-exponential factor, T is the temperature in K and $g(\alpha)$ is the fraction of completion of the decomposition reaction. Note that these methods assume that the reaction order is 1. There-

fore one can sketch the plots of $\ln\beta$, $\ln \frac{\beta}{T^2}$, and $\ln \frac{g(\alpha)}{T^2}$ against $\frac{1}{T}$. E_a and A values can simply be calculated using the slope and the intercept of these plots. Besides, employing E_a and A values, other thermodynamic parameters such as entropy (S), enthalpy (H) and Gibbs free energy (G) changes for the thermal decompositions were calculated. The entropy change in a thermal reaction can be approximated by using the pre-exponential factor²⁸ (Equations 5 and 6):

$$\Delta S = 2.303 \left(\log \frac{Ah}{kT} \right) R \quad (5)$$

The change in enthalpy is calculated from the activation energy according to the first law of thermodynamics (Equation 6):

$$\Delta H = E_a - R\Delta T \quad (6)$$

Using these values the Gibbs free energy can be calculated from equation 7:

$$\Delta G = \Delta H - T\Delta S \quad (7)$$

2. 3. Theoretical Calculation

The enthalpies (H) and free energies (G) were calculated using the CBS-4M method embedded in the Gaussian G09 W (revision D.01) software package.³⁰ The CBS-4M begins with a HF/3-21G(d) to structure optimization and zero-point energy calculations. Then using MP2/6-31+G and MP4(SDQ)/6-31+G(d,p) basis sets it is possible to calculate the corrected energy and to estimate the correlation contributions of a higher-order respectively. The stabilization of the optimized structures was controlled by the number of imaginary (NImag = 0) at the same theory level.

Table 1. CBS-4M results.

Compound	p.g. ^a	NImag ^b	-H ₂₉₈ /a.u. ^c	ΔH°/kJ mol ⁻¹
1,3-dichloro-4,6-dinitrobenzene	C1	0	1558.715040	-3.30
1	C1	0	1210.104523	119.57
2	C1	0	1303.467180	74.90
3	C1	0	1379.535864	205.04
C			37.786156	716.682 ^d
H			0.500991	217.100 ^d
N			54.522462	472.679 ^d
O			74.991202	249.178 ^d

^a Point group, ^b Number of imaginary frequencies, ^c CBS-4M calculated enthalpy, ^d Ref. 35

The formation enthalpies were calculated according to the atomization energy method, with respect to the equation given below^{34–36} (Table 1).

$$\Delta_f H^0(g, M) = H(M) - \sum_{atoms} H^0 + \sum_{atoms} \Delta_f H^0 \quad (8)$$

In this equation, $\Delta_f H^0(g, M)$ stands for the gas-phase enthalpy of formation of the molecule M , under investigation, $H(M)$ represents the CBS-4M calculated enthalpy of the molecule M (H_{298} in Table 1), $\sum_{atoms} H^0$ denotes the CBS-4 M calculated enthalpies for the individual atoms (1 a.u. = 2625.50 kJ mol⁻¹), and $\sum_{atoms} \Delta_f H^0$ values were quoted from NIST database.³⁷

Also, the detonation heat (Q), detonation velocity (D) and detonation pressure (P_{C-J}) of the compounds were calculated using the Kamlet–Jacobs equation, using the theoretical density (ρ) and oxygen balance (Ω) values according to the equation given below³:

$$P_{C-J} = 15.88\rho^2 NM^{1/2} Q^{1/2}, \text{ as kbar} \quad (9)$$

$$D = 1.01(NM^{1/2} Q^{1/2})^{1/2} (1 + 1.30\rho), \quad (10)$$

as mm μs^{-1} or m s^{-1}

Here, Q is the heat of explosion in kcal g⁻¹, N is the number of moles gas per gram explosive and M is the mass of gas in gram per mole of gas. The explosion reaction is written according to the oxygen balance equation. The detonation heat (Q) is calculated according to Hess's law by using the moles of product in the explosion reaction, standard enthalpy of formation and theoretical enthalpy of formation of energetic compounds.

2. 4. Determination of Biological Activity

Antibacterial activity was tested against Gram negative (*E. coli*, *P. aeruginosa*, *S. enteritidis*) and Gram positive (*E. faecalis*, *B. subtilis*, *S. aureus*, *B. licheniformis*) bacterial species.^{24,38–40} Bacterial species were grown in Hinton Müeller Agar (HMA) and suspensions (10⁶ cfu/mL) were prepared from 24 h cultures. *N*-(5-chloro-2,4-dinitrophenyl)hydrazine (**1**), *N*-(5-chloro-2,4-dinitrophenyl)guanidine (**2**) and *N*-(5-chloro-2,4-dinitrophenyl)-4-aminopyrazole (**3**) suspensions were prepared in DMSO. Agar dilution tests were performed for Minimum Inhibitory Concentration (MIC) determination. 10 μL bacterial suspensions were placed into plates and results were recorded after 24 h cultivation.

2. 5. Preparation of Energetic Materials

Aromatic polynitrohalides can easily undergo nucleophilic substitution reactions.^{7,8} The energetic materials used in the study were prepared in hydrothermal conditions, accordingly chlorine atoms in 1,3-dichloro-4,6-dinitrobenzene can be replaced by strong nucleophiles. Since the nitrogen nucleophiles used are strong nucleophiles,

the chlorine atom in 1,3-dichloro-4,6-dinitrobenzene and the amino groups of the nucleophile molecules were displaced in amphiprotic solvents under hydrothermal conditions in 2 or 3 hours of reaction time and energetic substances were obtained.

3. Results and Discussion

3. 1. Synthesis

Three energetic compounds were prepared from amino compounds, hydrazine, guanidinium carbonate and 4-aminopyrazole with 1,3-dichloro-4,6-dinitrobenzene as a result of nucleophilic substitution reactions in MeOH or EtOH under reflux for 3 h. 4-Aminopyrazole was used in an equivalent amount of 1,3-dichloro-4,6-dinitrobenzene in the medium, while more than the equivalent amount of guanidinium carbonate and hydrazine was added to the medium. A second possibility expected here was the replacement of two chlorine atoms in 1,3-dichloro-4,6-dinitrobenzene and there was a possibility of a mixed product, but it was observed that a single chlorine was eventually replaced.

***N*-(5-Chloro-2,4-dinitrophenyl)hydrazine (1).** Yield 77–80%. Anal. Calcd for C₆H₅N₄O₄Cl: C, 30.98; H, 2.17; N, 24.08. Found: C, 31.34; H, 2.29; N, 24.02. ¹H NMR (DMSO-*d*₆) δ 9.30 (s, 1H, broad), 8.88 (s, 1H), 7.19 (s, 1H), 4.75 (d, J = 0.004 Hz, 2H). ¹³C NMR (DMSO-*d*₆) δ 149.44, 128.39, 122.35. IR, ν , cm⁻¹: 3462.22, 3361.93, 3265.49 (NH), 3101.54 (CH), 1636.64 (C=N), 1595.13 (C=C), 1280.73 (N=O), 837.11, 738.14 (CH). MS m/z : 232 [M]⁺, 214, 149, 113, 85, 76, 57, 43.

***N*-(5-Chloro-2,4-dinitrophenyl)guanidine (2).** Yield 85–90%. Anal. Calcd for C₇H₆N₅O₄Cl: C, 32.29; H, 2.33; N, 26.96. Found: C, 31.81; H, 2.53; N, 25.03. ¹H NMR (DMSO-*d*₆) δ 8.56 (s, 1H), 8.48, (s, 1H), 7.72 (s, 1H), 7.07 (s, 1H), 6.81 (s, 2H, broad). ¹³C NMR (DMSO-*d*₆) δ 158.95, 153.34, 151.01, 138.22, 132.69, 124.87. IR, ν , cm⁻¹: 3462.22, 3421.72, 3381.90 (NH), 3101.54 (CH), 1636.64 (C=N), 1595.13, 1550.77 (C=C), 1280.73 (N=O), 827.44, 738.79 (CH). MS m/z : 259 [M]⁺, 229, 187, 132, 97, 57, 43.

***N*-(5-Chloro-2,4-dinitrophenyl)-4-aminopyrazole (3).** Yield 67–70%. Anal. Calcd for C₉H₆N₅O₄Cl: C, 37.33; H, 2.13; N, 24.68. Found: C, 36.59; H, 2.45; N, 24.23. ¹H NMR (DMSO-*d*₆) δ 12.81 (s, 1H), 10.20 (s, 1H), 8.86 (s, 1H), 8.43 (s, 1H), 7.79 (s, 1H), 6.33 (s, 1H). ¹³C NMR (DMSO-*d*₆) δ 146.93, 142.53, 134.89, 133.40, 129.99, 126.07, 119.31, 98.26. IR, ν , cm⁻¹: 3310.42, 3298.26 (NH), 3147.83 (CH), 1610.56 (C=N), 1591.27, 1552.70 (C=C), 1317.38 (N=O), 827.46, 738.74 (CH). MS m/z : 283 [M]⁺, 237, 191, 156, 129.

Warning: The synthesized compounds are in the energetic material class, working temperatures should be in

hydrothermal conditions. High temperature may result in explosion and sample amount should not be higher than 10 mg in thermal analysis experiments.

Elemental analysis results are in close agreement with expected values. Specific N–H stretching vibrations in the IR spectra were observed at the expected value between 3462–3265 cm^{-1} . It is thought that the middle signal observed at 1610–1636 cm^{-1} in three energetic materials is due to the C=N imine bond formed as a result of resonance. N=O stretching vibration signals of nitro groups were observed at 1280–1317 cm^{-1} . In the EI-MS spectra, the molecular peaks $[M]^+$ were observed at the expected values and also as the base peak of the spectrum. The m/z values of the $[M]^+$ signals are in agreement with the nitrogen rule.

In the ^1H NMR spectrum of *N*-(5-chloro-2,4-dinitrophenyl)hydrazine, 4 signals with δ values of 9.30, 8.88, 7.19 and 4.75 were observed, respectively. This result is expected, because there are 4 different hydrogens in the molecule. It is probable that the signal observed at δ 9.30 is the signal of the NH group proton and the signal observed at δ 4.75 belongs to the NH_2 group protons. In the ^{13}C NMR spectrum of this substance, 4 different signals are observed, actually the number of different carbon nuclei is 6. It is possible that the signals of aromatic carbons with nitro groups and H bonded carbons signals overlap, because two signals in the spectrum were observed to be more intense than the others.

In the ^1H NMR spectrum of *N*-(2,4-dinitro-5-chlorophenyl)guanidine, 5 signals are observed with δ values of 8.56, 8.48, 7.72, 7.07 and 6.81. There are 5 different types of hydrogen in the molecule, similarly, there are 7 different carbon nuclei in this molecule and as a result, 7 different signals were found in the ^{13}C NMR spectrum. Similarly, there are 6 different hydrogen atom nuclei in the *N*-(5-chloro-2,4-dinitrophenyl)-4-aminopyrazole molecule and 6 different signals are observed in the ^1H NMR spectrum. The signal of δ 12.81 is most likely the signal of the hydrogen in the NH group of the pyrazole ring. There are 9 different carbon atoms in the *N*-(5-chloro-2,4-dini-

trophenyl)-4-aminopyrazole molecule, but 8 signals are observed in the spectrum. It is possible that the two carbon signals in the pyrazole ring overlap.

3. 2. Thermal Analysis

The TG plots of three new energetic materials at a heating rate of 15 $^\circ\text{C min}^{-1}$ are shown in Figure 2a. The plots reveal the fact that *N*-(5-chloro-2,4-dinitrophenyl)hydrazine (**1**) acts as a typical explosive. The compound shows a rapid mass loss at 235 $^\circ\text{C}$ which culminates at 268 $^\circ\text{C}$ in a complete degradation with a mass loss of 97%. On the other hand, the compounds *N*-(5-chloro-2,4-dinitrophenyl)guanidine (**2**) and *N*-(5-chloro-2,4-dinitrophenyl)-4-aminopyrazole (**3**) display two decomposition processes in their respective TG plots. Figure 2b shows the differential thermal analysis (DTA) curves of the energetic compounds investigated in this study. It is obvious that the decomposition is exothermic. The first mass losses of the thermal reactions of the compounds at a heating rate of 15 $^\circ\text{C min}^{-1}$ were 48% and 41% and these were followed by the second mass losses of 21% and 18%.

Compound **1** gives a strong exothermic signal around 260 $^\circ\text{C}$ without a melting process. On the other hand, **2** starts to melt down at 215 $^\circ\text{C}$ and gives three weak exothermic signals at 241, 330 and 379 $^\circ\text{C}$ after 226 $^\circ\text{C}$. Finally, **3** melts down at 189–190 $^\circ\text{C}$ and gives two weak exothermic signals at 351 $^\circ\text{C}$ and 407 $^\circ\text{C}$.

As seen from Figure 2a, **1** gives a single step decomposition above a heating rate of 10 $^\circ\text{C min}^{-1}$, this is exactly the behavior expected from a typical explosive compound.⁴¹ However, it gives a two-step decomposition below this critical value. Figures 3a and 3b show TG and DTA curves at scan rates of 0.6, 0.75, 1.0 and 5.0 $^\circ\text{C min}^{-1}$. Figure 3a shows that the mass loss takes place slowly at the first step and in an explosive manner in the second step. As the heating rate is increased, the second step appears more distinctively. The DTA curves given in Figures 2b and 3b are not in the expected format. The curves display first an

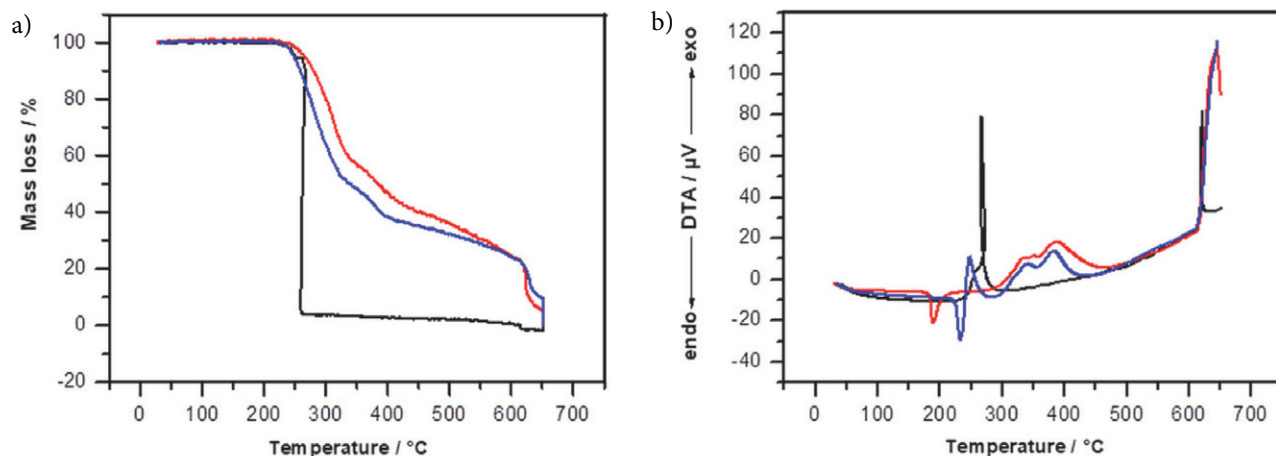


Figure 2. a. Thermogravimetric curves at 15 $^\circ\text{C min}^{-1}$ heating rate, b. DTA curves [black: *N*-(5-chloro-2,4-dinitrophenyl)hydrazine (**1**), blue: *N*-(5-chloro-2,4-dinitrophenyl)guanidine (**2**), red: *N*-(5-chloro-2,4-dinitrophenyl)-4-aminopyrazole (**3**)].

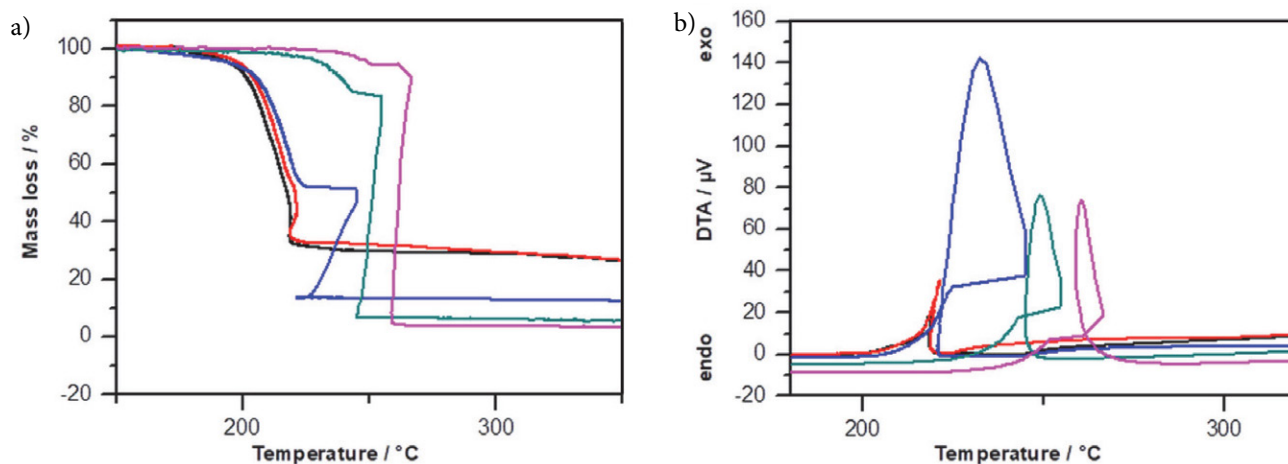


Figure 3. a. Thermogravimetric curves, b. DTA curves of *N*-(5-chloro-2,4-dinitrophenyl)hydrazine (**1**) recorded at different low heating rates [black: 0.6 °C min^{-1} , red: 0.75 °C min^{-1} , blue: 1 °C min^{-1} , darkcyan: 5 °C min^{-1} , purple: 15 °C min^{-1}].

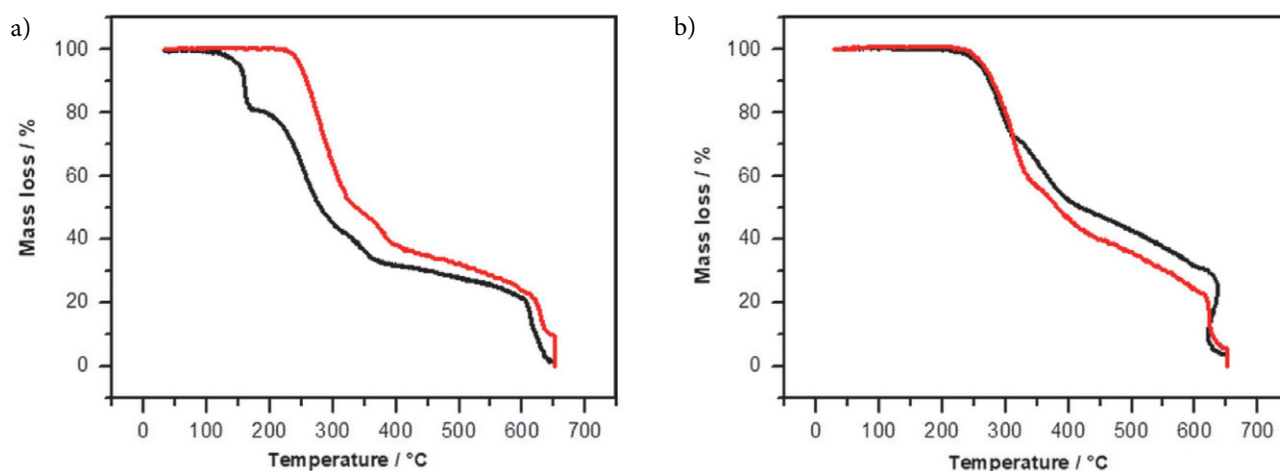


Figure 4. TG curves at different heating rate a. *N*-(5-chloro-2,4-dinitrophenyl)guanidine (**2**), b. *N*-(5-chloro-2,4-dinitrophenyl)-4-aminopyrazole (**3**) [black: 5 °C min^{-1} , red: 15 °C min^{-1}].

increase then a decrease in temperature. The reason for that is thermal decomposition taking place with an explosion. In a rapid explosion reaction, the gas products leave the pan rapidly taking away the heat they absorbed with them. This decreases the temperature of the pan resulting in the abnormal curves given in Figures 2b and 3b.

A similar case exists for the energetic materials of **2** and **3** as the heating rate has decreased the shape and mass loss of TG curves change. Figure 4a shows the TG curves of energetic material of **2** recorded at two different heating rates. Figure 4b illustrates analogous curves for **3**. The shapes of the curves change at lower heating rates. The thermoanalytical data belonging to TG-DTA curves of the energetic compounds prepared in this study are listed in Table 2.

When TG curves are examined in Figure 2a, at a heating rate of 15 °C min^{-1} , the compound **1** undergoes a complete single-step decomposition with almost a complete mass loss between $250\text{--}260\text{ °C}$ just like an explosive material. The other two materials, on the other hand, give

two distinctive reactions at the same heating state. However, these TG curves change at lower heating rates. The compound **1** is observed to give a distinct two-step reaction at a heating rate of 5 °C min^{-1} or lower (Figures 3a and 3b). TG curves of compounds **2** and **3** vary with decreasing heating rates.

The fact that compounds **2** and **3** show distinct changes at 5 °C min^{-1} is apparent in Figure 4. The decompositions of compounds **2** and **3** in two steps are more clearly observed at low heating rates. The mass losses of compounds **2** and **3** are 65% and 56%, respectively as a result of thermal decomposition.

A fact that is known about energetic materials since 1958 is that if there is a nitrogen-containing group neighboring a nitro group, the thermal decomposition takes place though a furoxan ring.^{8,42–45} This situation is particularly apparent in picrylazide molecule where the 1st nitrogen of the azide group forms a furoxan ring with the oxygen of the neighboring nitro group releasing two nitrogens of the azide group as an N_2 molecule.^{11,42} If the heating

process continues, the resulting furoxan will also decompose. A similar case exists for the compounds investigated here. Figure 5 shows the furoxan conversion reactions of the compounds prepared. As a result of the decomposition process, it is thought that 5-chloro-6-nitrofuroxane is formed by the release of a small group in gaseous form. Table 2 lists the thermoanalytical results drawn from the TG data. The mass losses for the first stage of decomposition at a thermal heating rate of $5\text{ }^{\circ}\text{C min}^{-1}$ for compounds

2 and 3 are 16.89 ± 0.46 and 25.76 ± 1.08 . In Figure 5 the theoretical mass loss values of energetic compounds 2 and 3 for the second step were 16.95% and 24%. These results prove that the first stage thermal decomposition reaction of compounds 2 and 3 takes place as written below. However since the thermal decomposition rate of compound 1 is much higher than those of compounds 2 and 3, it was not possible to accurately define its mass losses at the first and second stage decomposition reactions even at very low

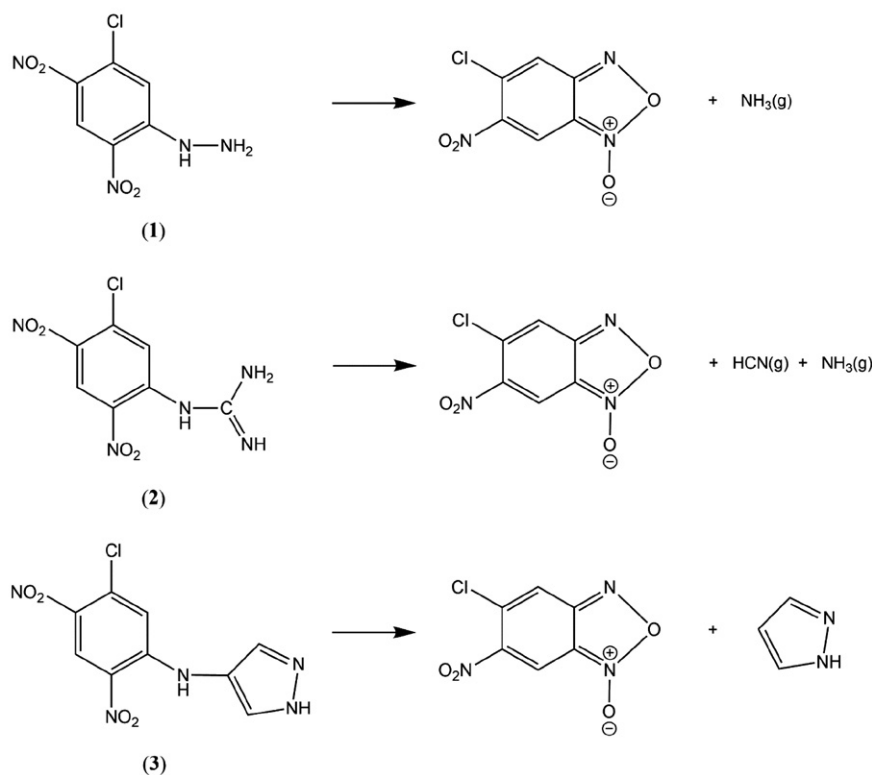


Figure 5. Probable first decomposition reaction of the energetic materials prepared.

Table 2. Thermoanalytical data of energetic materials prepared.

Energetic Compound	M.P. $^{\circ}\text{C}$	Heating rate $^{\circ}\text{C min}^{-1}$	First Thermal Reaction		Second Thermal Reaction	
			Temperature range / $^{\circ}\text{C}$	Mass loss / %	Temperature range / $^{\circ}\text{C}$	Mass loss / %
N-(5-chloro-2,4-dinitrophenyl)hydrazine (1)	NO	5	211–240 DTA peak: 216	94.73 ± 0.87	–	–
			236–268 DTA peak: 261	96.76 ± 0.48	–	–
N-(5-chloro-2,4-dinitrophenyl)guanidine (2)	NO	5	144–173 DTA peak: 162	16.89 ± 0.46	201–384 DTA peak: 353	49.20 ± 3.45
			228–347 DTA peak: 241	48.2 ± 2.64	347–426 DTA peak: 379	17.23 ± 2.92
N-(5-chloro-2,4-dinitrophenyl)-4-aminopyrazole (3)	188	5	221–307 DTA peak: 293	25.76 ± 1.08	311–407 DTA peak: 351	26.15 ± 1.23
			235–338 DTA peak: 322	41.13 ± 3.19	338–420 DTA peak: 379	15.23 ± 2.07

NO: Not observed

heating rates. Although the decomposition reaction is observed to take place in two staged manners at low heating rates in Figure 3a the mass loss is erratic. Especially since the second thermal decomposition reaction is very fast, there were observed anomalies both in TG and DTA curves. Nevertheless, if one looks at TG curve of compound 1 at 5 °C min⁻¹ one sees that it is a two-stage process. It is seen that there is a small mass loss at the beginning in both the TG curves taken at heating rates of 5 °C

min⁻¹ and 15 °C min⁻¹. However, the mass loss observed at the start constantly increases with the heating rate which makes it impossible to do any calculations for compound 1.

3. 3. X-Ray Studies

Only compound 2 amongst the energetic materials prepared in this study was obtained in suitable crystal size therefore only the structure of this compound was deter-

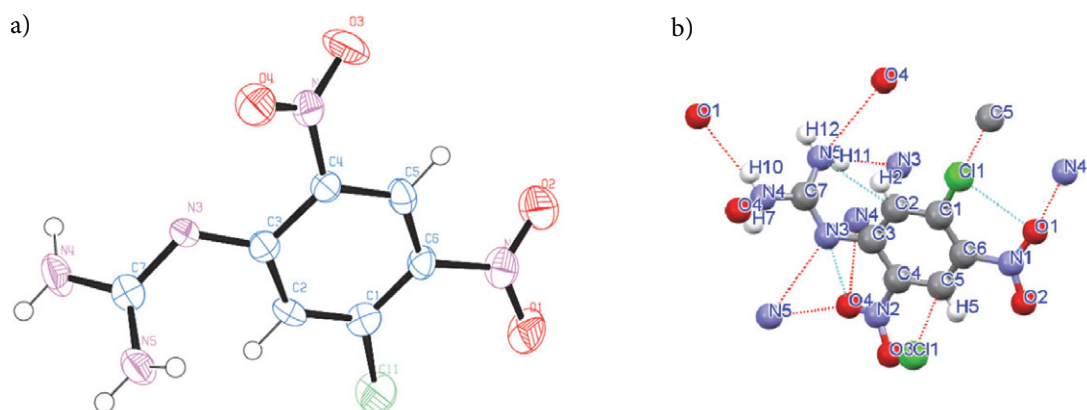


Figure 6. a. The Ortep drawing of *N*-(5-chloro-2,4-dinitrophenyl)guanidine (2), b. inter- and intramolecular hydrogen bonds and other interactions of *N*-(5-chloro-2,4-dinitrophenyl)guanidine (2), obtained using Mercury software.

Table 3. *N*-(5-chloro-2,4-dinitrophenyl)guanidine (2) crystal data and data collection conditions.

Molecular Formula	C ₇ H ₆ ClN ₅ O ₄	Molar Mass/g mol⁻¹	259.62
T/ K	293(2)	F (000)	528
Crystal Colour	yellow	Crystal System	orthorhombic
Space Group	<i>Pna</i> 2	Index Ranges	-5 ≤ <i>h</i> ≤ 9, -2 ≤ <i>k</i> ≤ 9, -23 ≤ <i>l</i> ≤ 22
<i>a</i> / Å	7.3082(4) Å	Reflections Collected	3687
<i>b</i> / Å	7.5105(4) Å	Reflections Unique	2067
<i>c</i> / Å	17.8511(9) Å	R1, wR2 (2θ)	0.0473, 0.0882
α	90°	R1, wR2 (all)	0.0711, 0.0991
β	90°	Data / Parameters	2062/ 154
γ	90°	GOOF of F²	1.114
V/ Å³	979.82(9)	Largest Difference Peak Hole / e Å⁻³	0.367 and -0.269
Z	4	Crystal Size / mm	0.44 × 0.22 × 0.06
Calc. density / g cm⁻³	1.760	CCDC No	1943903
μ / mm⁻¹	0.404		

Table 4. The list of inter- and intramolecular hydrogen bonds.

<i>D-H</i> ... <i>A</i>	<i>D</i> ... <i>H</i> (Å)	<i>H</i> ... <i>A</i> (Å)	<i>D</i> ... <i>A</i> (Å)	<i>D-H</i> ... <i>A</i> (°)
<i>N4-H7</i> ... <i>N3'</i>	0.92	2.58	2.934 (6)	109
<i>N4-H7</i> ... <i>O4</i>	0.92	2.49	3.371 (6)	161
<i>N4-H10</i> ... <i>O1</i>	0.81	2.27	3.063 (6)	167
<i>N5-H11</i> ... <i>N3'</i>	0.82	2.10	2.911 (6)	169
<i>N5-H12</i> ... <i>O1</i>	0.78	2.54	3.229 (6)	148

Symmetry codes: -1/2 + *x*, -5/2 - *y*, *z*; -1/2 + *x*, -5/2 - *y*, *z*; -*x*, -3 - *y*, 1/2 + *z*; 1/2 + *x*, -5/2 - *y*, *z*; -1/2 - *x*, -1/2 + *y*, 1/2 + *z* (respectively)

mined. Single crystal data collection conditions and crystal data are listed in Table 3, important bond lengths and angles are shown in Supporting Information (Table S1), the intra- and intermolecular hydrogen bonds are listed in Table 4, and the molecular structure is drawn with Ortep program and hydrogen bonds and molecular interactions model is presented in Figures 6a and 6b.⁴⁶

As seen from Figure 6a, not all groups in the structure of the molecule **2** are in the same plane. There is an angle of 61.22° between the plane of the N3C7N4N5 atoms that make up the guanidine unit and the plane of the aromatic ring. Similarly, the plane formed by the nitro groups is not parallel to the plane of the aromatic ring. The model is found to contain two NH₂ on C7 atom. Under these circumstances, the hydrogen atoms on N3, N4, and N5 are very labile and dislocate constantly due to resonance phenomena. A similar situation has been observed recently in X-ray investigation of picrylguanidine.^{13,47}

The resonance in the guanidine unit is clearly visible in the IR spectra. The double bond is constantly shifting around C7, but distancing from the plane of the molecule decreases the resonance, consequently, asymmetry can be observed around C7. The angles around the C7 atom are 119.9(4), 122.8(4) and 117.5(5)°. These values are close to 120°, despite to the bonds around C7 were found to be 1.329(6), 1.337(6) and 1.317(6) Å and these values indicate the probability of a C=N double bond around C7. However, there are two NH₂ groups bounded to C7 atom in the molecular structure. As can be seen from Table 4 and Figure 6b, important intra- and intermolecular five hydrogen bonds were found, one of which can be considered strong intermolecular hydrogen bond. The angle of the hydrogen bond formed between the hydrogen in N5 atom and N3 atom of the neighboring molecule is 169° and the length is 2.911 Å, this cannot be classified as a strong hydrogen bond since strong hydrogen bonds are shorter than this.^{48–51} In this study, it was not possible to obtain *N*-(5-chloro-2,4-dinitrophenyl)hydrazine (**1**) in suitable crystal sizes. Although X-ray study of picrylhydrazine has been recently reported, the compound possesses a higher number of inter- and intramolecular bonds with much shorter bond lengths with predominating intermolecular interactions.⁹

Again, the hydrogen bond between the hydrogen in N4 atom and N3 atom of the neighboring molecule is in the class of strong hydrogen bonds. These strong hydrogen bonds increase intermolecular interaction, which is observed in thermal analysis, due to the strong intermolecular hydrogen bond, the molecule does not have a melting point up to 200 °C, and the molecule gives a rapid thermal decomposition reaction around 240 °C and this thermal decomposition reaction is an explosion-like reaction.

3. 4. Thermokinetic Analysis

The graphically calculated activation energy and Arrhenius pre-exponential factor values obtained by the use

of OFW and KAS methods are tabulated in Table 5 and ΔH^0 , ΔS^0 and ΔG^0 calculated using these data in Table 6. The thermokinetic analysis of **1** could only be possible at low heating rates. Since this compound gives a rapid explosion at higher heating rates, there is a temperature decrease shortly after that and this makes the slopes of the curves positive which does not give any result. To overcome this problem, the kinetic studies were limited with the heating rates of 0.4, 0.5, 0.6, 0.75 and 1.0 °C min⁻¹. However, this causes the emergence of a new problem for the OFW. The logarithms of the values smaller than 1.0 are negative. Under such a situation, the OFW method is of no use. Therefore, only KAS method was employed for the thermokinetic investigation of this compound. There is no such problem for the other energetic materials **2** and **3**. E_a and A values for the two-step thermal decomposition of these compounds were separately determined.

As seen from Table 5, the results obtained from thermokinetic studies for compound **1** are not satisfactory. At the heating rates below 1 °C min⁻¹ OFW technique is not useable since the logarithm of a number smaller than 1 is negative and it is not possible to compute the activation energy under these conditions. Although they can be calculated by the use of KAS and CR methods, the results are not reliable. Since TG curves change with the increasing heating rate the regression coefficients at high $g(\alpha)$ values are far from the acceptable limits. The values calculated for compound **1** in Table 6 are not statistically reliable. On the other hand, the values given for compounds **2** and **3** are comparable. Especially the results obtained for compound **2** by the use of OFW and KAS methods are very close to each other. This situation verifies the fact the nonisothermal-isoconversional calculations in the thermokinetic computations indicated by ICTAC in 2011 are much more reliable.^{52–54} The OFW and KAS results of compound **3** are comparable. However, its CR calculation is different than those of OFW and KAS results. Since both OFW and KAS are non-isothermal graphic techniques the similarity between the results is an expected outcome. Table 6 lists the enthalpy (ΔH^0) values of the decomposition reactions of the energetic compounds investigated in this study. It was not possible to use OFW method for compound **1** for the use of lower heating rates. Since it is not possible to define the boundaries of the first and the second decomposition reactions of compound **1** all the calculations were carried out on the assumption that the compound gives a single step decomposition reaction at heating rates of 0.6, 0.75 and 1.0 °C min⁻¹. However, the ΔH^0 value of compound **1** calculated by the assumption of single-step decomposition reaction is of comparable dimension with those of compounds **2** and **3** calculated based upon two-step decomposition. This shows the fact that the approach is not bad at all. However, the difficulty of the thermokinetic studies of energetic compounds is obvious. For very rapid reactions one has to use very low heating rates but if the thermal

Table 5. The thermokinetic analysis results of energetic materials.

Energetic Material	g(α)	Methods						
		OFW		KAS			CR	
		$E_a / \text{kJ mol}^{-1}$	A / min^{-1}	$E_a / \text{kJ mol}^{-1}$	A / min^{-1}	$\theta / ^\circ\text{C min}^{-1}$	$E_a / \text{kJ mol}^{-1}$	A / min^{-1}
compound 1 $\text{C}_6\text{H}_5\text{N}_4\text{O}_4\text{Cl}$	0.2			160.50 ± 1.26	$5.53 \pm 0.90 \times 10^9$	0.50	142.29 ± 1.86	$2.09 \pm 0.06 \times 10^{10}$
	0.4			179.33 ± 8.74	$5.99 \pm 0.59 \times 10^{11}$	0.75	231.97 ± 3.79	$1.44 \pm 0.08 \times 10^{20}$
	0.5			183.14 ± 21.63	$1.55 \pm 0.37 \times 10^{12}$	1.00	200.69 ± 1.86	$5.11 \pm 0.09 \times 10^{16}$
	0.6			204.27 ± 41.17	$2.06 \pm 0.84 \times 10^{14}$			
	0.8			162.44 ± 43.88	$1.04 \pm 0.56 \times 10^{10}$			
				177.94 ± 17.79			191.65 ± 45.52	
compound 2 $\text{C}_7\text{H}_6\text{N}_5\text{O}_4\text{Cl}$	0.2	76.01 ± 0.37	$5.11 \pm 0.05 \times 10^9$	76.98 ± 0.14	46.35 ± 0.02	5.0	79.51 ± 0.95	$7.63 \pm 0.17 \times 10^3$
	0.4	72.75 ± 0.07	$2.78 \pm 0.01 \times 10^9$	66.69 ± 0.02	5.59 ± 0.01	10.0	76.39 ± 0.47	$3.63 \pm 0.04 \times 10^3$
	0.5	71.66 ± 0.36	$2.22 \pm 0.02 \times 10^9$	68.17 ± 0.62	7.81 ± 0.13	15.0	59.88 ± 0.49	68.75 ± 0.10
	0.6	70.65 ± 0.27	$1.76 \pm 0.01 \times 10^9$	65.65 ± 0.48	4.56 ± 0.06	20.0	66.17 ± 0.60	299.93 ± 0.05
	0.8	65.01 ± 0.56	$4.84 \pm 0.07 \times 10^8$	48.78 ± 5.76	0.14 ± 0.00			
1. Thermal Step	71.22 ± 4.01			65.25 ± 10.24			70.49 ± 9.08	
2. Thermal Step	0.2	64.12 ± 0.81	$4.28 \pm 0.09 \times 10^7$	57.39 ± 0.74	0.085 ± 0.0	5.0	66.93 ± 0.10	32.69 ± 0.01
	0.4	83.82 ± 0.70	$2.64 \pm 0.04 \times 10^9$	77.84 ± 0.66	4.81 ± 0.07	10.0	68.57 ± 0.50	130.04 ± 0.02
	0.5	97.50 ± 2.45	$3.01 \pm 0.12 \times 10^{10}$	92.60 ± 2.03	58.09 ± 0.20	15.0	132.12 ± 1.31	$1.03 \pm 0.02 \times 10^7$
	0.6	108.21 ± 1.71	$2.26 \pm 0.06 \times 10^{11}$	103.17 ± 1.62	377.51 ± 0.09	20.0	140.74 ± 3.22	$8.09 \pm 0.28 \times 10^7$
	0.8	115.08 ± 0.92	$7.91 \pm 0.10 \times 10^{11}$	110.17 ± 0.87	$1.26 \pm 0.01 \times 10^3$			
2. Thermal Step	93.75 ± 20.34			88.23 ± 21.11			102.09 ± 39.81	
compound 3 $\text{C}_9\text{H}_6\text{N}_5\text{O}_4\text{Cl}$	0.2	41.63 ± 0.55	$1.72 \pm 0.04 \times 10^6$	34.60 ± 0.46	0.52 ± 0.01	5.0	107.99 ± 0.50	$1.47 \pm 0.01 \times 10^6$
	0.4	46.13 ± 0.25	$6.44 \pm 0.06 \times 10^6$	39.08 ± 0.22	0.47 ± 0.01	10.0	102.62 ± 0.23	$9.80 \pm 0.04 \times 10^5$
	0.5	47.00 ± 0.09	$8.57 \pm 0.03 \times 10^6$	39.83 ± 0.08	0.55 ± 0.01	15.0	78.06 ± 0.19	$2.70 \pm 0.01 \times 10^3$
	0.6	47.92 ± 0.09	$1.13 \pm 0.01 \times 10^7$	40.70 ± 0.08	0.59 ± 0.01	20.0	122.28 ± 0.41	$2.64 \pm 0.02 \times 10^7$
	0.8	48.00 ± 0.07	$1.26 \pm 0.01 \times 10^7$	40.63 ± 0.05	0.97 ± 0.01			
1. Thermal Step	46.14 ± 2.63			38.97 ± 2.53			102.74 ± 18.42	
2. Thermal Step	0.2	110.88 ± 0.89	$1.60 \pm 0.02 \times 10^{11}$	97.15 ± 1.92	55.20 ± 0.17	5.0	85.05 ± 0.94	595.95 ± 0.10
	0.4	135.06 ± 2.70	$1.97 \pm 0.06 \times 10^{13}$	101.25 ± 1.76	160.48 ± 0.04	10.0	97.85 ± 2.53	$1.05 \pm 0.04 \times 10^4$
	0.5	142.48 ± 3.70	$6.98 \pm 0.28 \times 10^{13}$	104.44 ± 2.94	268.45 ± 0.11	15.0	93.43 ± 1.49	$4.35 \pm 0.11 \times 10^3$
	0.6	139.67 ± 3.63	$3.70 \pm 0.14 \times 10^{13}$	103.80 ± 4.13	228.05 ± 0.14	20.0	112.23 ± 3.37	$1.74 \pm 0.08 \times 10^5$
	0.8	150.98 ± 3.18	$2.00 \pm 0.06 \times 10^{14}$	120.11 ± 4.13	$2.87 \pm 0.14 \times 10^3$			
2. Thermal Step	135.81 ± 15.09			105.35 ± 8.73			97.14 ± 11.37	

Table 6. The calculated thermodynamic values of the energetic materials prepared for the thermal decomposition reactions.

Energetic Material	Methods									
	OFW			KAS			CR			
	$\Delta H / \text{kJ mol}^{-1}$	$\Delta S / \text{J K}^{-1}$	$\Delta G / \text{kJ mol}^{-1}$	$\Delta H / \text{kJ mol}^{-1}$	$\Delta S / \text{J K}^{-1}$	$\Delta G / \text{kJ mol}^{-1}$	$\Delta H / \text{kJ mol}^{-1}$	$\Delta S / \text{J K}^{-1}$	$\Delta G / \text{kJ mol}^{-1}$	
$\text{C}_6\text{H}_5\text{N}_4\text{O}_4\text{Cl}$ (1)				176.27	-15.82	184.17	189.98	136.74	121.74	
$\text{C}_7\text{H}_6\text{N}_5\text{O}_4\text{Cl}$ (2)	1. Thermal Step	69.21	-70.93	107.49	63.24	-232.79	192.65	68.48	-181.72	166.55
	2. Thermal Step	91.04	-50.46	122.52	85.52	-217.31	221.10	99.38	-210.61	230.78
$\text{C}_9\text{H}_6\text{N}_5\text{O}_4\text{Cl}$ (3)	1. Thermal Step	44.05	-117.29	108.54	36.88	-255.01	177.10	100.65	-135.32	175.06
	2. Thermal Step	133.09	13.96	124.36	102.63	-204.60	230.54	94.42	-174.11	203.27

decomposition reaction gives the curve expected from TG analysis as is the case for the energetic compounds 2 and 3, the results are highly useable. What is the logic for

the thermokinetic studies of energetic compounds? This point is under discussion as is the validity of Kissinger equation.⁵⁵

3. 5. Computational Results

The electron density maps and HOMO-LUMO overlap images are illustrated in Figure 7. The calculated formation enthalpies (kJ mol^{-1}) and the smallest HOMO-LUMO energy differences (eV) are listed in Table 7. In

electron density maps the blue areas correspond to the electron-rich and the red areas correspond to the electron-poor regions. According to the Kamlet–Jacobs equation the calculated oxygen balance (Ω), theoretical detonation velocity (D) and detonation pressure (P) values are given in Table 8.

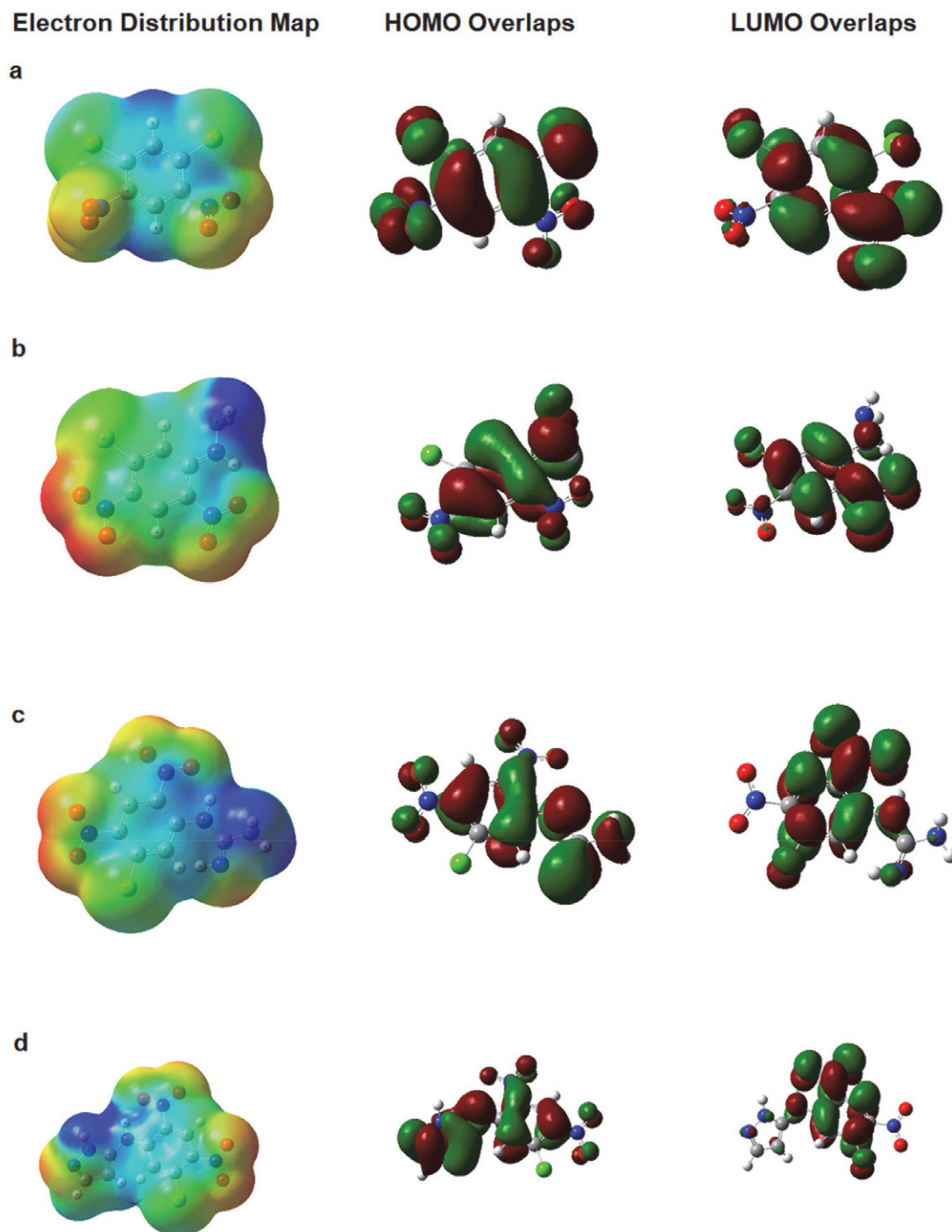


Figure 7. Electron density distribution and HOMO and LUMO images of the energetic molecules prepared, a: 1,3-dichloro-4,6-dinitrobenzene, b: *N*-(5-chloro-2,4-dinitrophenyl)hydrazine (1), c: *N*-(5-chloro-2,4-dinitrophenyl)guanidine (2), d: *N*-(5-chloro-2,4-dinitrophenyl)-4-aminopyrazole (3)

Table 7. The energy levels of the highest energy HOMO and lowest energy LUMO, calculated theoretical dipole moment and formation enthalpy values of the energetic materials prepared.

Energetic Compound	$E_{\text{HOMO}} / \text{eV}$	$E_{\text{LUMO}} / \text{eV}$	$\Delta E / \text{eV}$	μ / D	$\Delta H_f^0 / \text{kJ/mol}$
1,3-dichloro-4,6-dinitro-benzene	-7.948	-3.193	4.755	3.55	458.832
1	-6.905	-2.902	4.003	7.66	386.290
2	-7.073	-3.215	3.858	5.01	372.217
3	-6.711	-3.203	3.508	4.10	338.506

Table 8. Calculated detonation properties of the energetic materials prepared.

Component	$V_{\text{calc}} / \text{cm}^3 \text{mol}^{-1}$	$\rho_{\text{calc}} / \text{g cm}^{-3}$	$\Omega / \%$	$Q / \text{kcal g}^{-1}$	$D / \text{km s}^{-1}$	P / kbar
1,3-dichloro-4,6-dinitrobenzene	129.140	1.15	-0.54	835.8	3.92	4.99
1	127.646	1.82	-0.69	1047.4	6.54	19.07
2	173.358	1.76 ^a	-0.77	918	6.17	16.66
3	172.192	1.25	-0.93	949.9	4.75	7.81

^a X-ray data

The theoretical results are tabulated in Table 7. The formation enthalpies or ΔH_f^0 values of the compounds **1**, **2** and **3** are listed as 386.290, 372.217, and 338.506 kJ mol⁻¹, respectively which also indicate the order of the stability of these compounds. The most stable one among them is compound **3** with the smallest ΔH_f^0 value. This is highly commendable since there are two aromatic rings connected to each other in this compound. The theoretically calculated dipole moments also show parallelism with this result. Since dipole moments are the measure of electron distribution the homogeneity of the electron distribution changes in parallel with the dipole moment and ΔH_f^0 values. The only unexpected result of the theoretical calculations is the difference in energy between HOMO and LUMO levels which is the measure of the thermal sensitivity of energetic materials.⁵⁶ Theoretically calculated detonation heat, detonation pressure and detonation velocity values are given in Table 8 using the formation enthalpy values, densities and oxygen balance values of the energetic substances prepared. Only the density value of energetic compound **2** was determined with X-ray study, others were theoretically calculated. The detonation velocity and detonation pressure values were calculated in parallel with the formation enthalpy values of energetic substances and this is an expected result. This case shows the success of the Gaussian09 program because the experimental density of the energetic substance **2** lies within a suitable range between theoretical densities.

The smaller is this difference, the smaller is the thermal sensitivity. Therefore, the compound with the highest thermal sensitivity is compound **3**. However, this is also the compound with the highest thermal decomposition temperature. This contradiction is attributed to probable intermolecular interactions. When we consider the dipole moments the compound with the highest intermolecular

forces is compound **1**. By the effect of these forces, the molecule may preserve its solid-state properties up to a certain temperature and have a sudden decomposition. There are numerous examples of this situation in the literature.⁵⁷ Therefore, the compound **1** behaves differently than compounds **2** and **3**.

3. 6. Antibacterial Activity

For bioactivity determination, Gram negative (*Escherichia coli*-ATCC 25922, *Pseudomonas aeruginosa*-ATCC 27853, *Salmonella enteritidis*-ATCC35311) and Gram positive (*Enterococcus faecalis*, *Bacillus subtilis*-DSM 1971, *Staphylococcus aureus*-ATCC 25953, *Bacillus licheniformis*-DSM 13) bacterial strains were tested against **1**, **2**, and **3** in 8–512 mg/L concentration range. It was shown that compounds **1**, **2**, and **3** were especially effective against Gram negative species and compound **2** is the most effective compound concerning antibacterial activity having 8–16 mg/L MIC values for Gram negative strains and being the only effective agent against Gram positive strains. *B. licheniformis* was found to be the most susceptible bacterial strain against the energetic compounds tested in this study. The complete results are given in Table 9. Generally speaking, *E. coli* is not affected by these energetic substances, however *P. aeruginosa* is affected even at low concentrations and the bacterial population is decreased. There are two major reasons to investigate the antimicrobial properties of energetic compounds. The first one is to determine whether they have any lethal effect upon the microbial organisms. The second reason was just the opposite of whether they might have nutritious effect on the bacteria. The results listed in Table 9 show the fact that the energetic materials do not have any lethal effect upon the bacteria. On the contrary, they may provide a nutrition

Table 9. The antimicrobial tests results of the energetic materials toward seven different bacteria.

Energetic Material (mg L ⁻¹)	<i>E. coli</i>			<i>E. faecalis</i>			<i>B. subtilis</i>			<i>S. aureus</i>			<i>P. aeruginosa</i>			<i>S. enteritidis</i>			<i>B. licheniformis</i>		
	1	2	3	1	2	3	1	2	3	1	2	3	1	2	3	1	2	3	1	2	3
512	+	-	+	+	-	+	+	-	-	-	-	-	+	+	+	+	+	-	-	-	-
256	+	+	+	+	-	+	+	-	-	-	-	-	+	+	+	+	+	-	-	-	-
128	+	+	+	+	-	+	+	-	-	+	-	-	+	+	+	+	+	+	-	-	-
64	+	+	+	+	-	+	+	-	-	+	-	-	+	+	+	+	+	+	+	-	-
32	+	+	+	+	+	+	+	+	+	+	-	-	+	+	+	+	+	+	+	+	+
16	+	+	+	+	+	+	+	+	+	+	-	+	+	+	+	+	+	+	+	+	+
8	+	+	+	+	+	+	+	+	+	+	+	+	+	+	+	+	+	+	+	+	+

Note: + sign indicates that the bacterial population has increased, and the - sign indicates that the bacterial population does not increase.

source to microbial organisms. The compound **1** acted as a nutrition source for all the microorganisms investigated. The energetic compounds are rich in nitrogen. Nitrogen is in positive oxidation state in nitro group and in negative oxidation state in amino groups attached to the molecule. That is why all the bacteria among the compounds used especially compound **1** as a nutrition source in cultured medium. The energetic compounds **2** and **3** showed an antimicrobial effect on a microbial concentration of 64 mg/L. The compound with the highest antimicrobial effect is compound **2**. This is due to guanidine group attached to the molecule. Guanidines have been used as an antiseptic agents in gastro systems.⁵⁸

Also, the antimicrobial studies must be extended to environmental dimensions. The elimination of the ammunition which completed their practical lives constitutes a very big problem. The only solution today is burning the outdated material. This is a dangerous and risky process. Microbial degradation can be a much less risky alternative to it.

4. Conclusion

Three new energetic materials were prepared using 1,3-dinitro-4,6-dichlorobenzene with nucleophilic substitution reactions and these energetic materials were investigated by thermogravimetry. It was observed that thermal decomposition of these energetic materials occurs in two steps and these two-step reaction can be observed at low heating rates. Thermogravimetric results showed that the intermediate product is furoxane ring in thermal decomposition. Besides, although these energetic materials contained nitro groups, it was seen that they do not have a strong toxic effect on seven different bacteria and on the contrary they are nutrient materials for some bacteria.

Acknowledgments

This research did not receive any specific grant from funding agencies. The authors declare that there is no conflict of interest.

5. References

- J. P. Agrawal: High Energy Materials, Wiley-VCH, Weinheim, Germany, **2010**, pp. 141–144.
- D. M. Badgajar, M. B. Talawar, S. N. Asthana, P. P. Mahulikar, *J. Hazard. Mat.* **2008**, *151*(2-3), 289–305. DOI:10.1016/j.jhazmat.2007.10.039
- T. M. Klapötke: Chemistry of the High Energy Materials, Walter de Gruyter, Berlin, Germany, **2017**, pp. 299–305. DOI:10.1515/9783110536515
- F. A. Carey, R. J. Sundberg: Advanced Organic Chemistry, Springer, New York, USA, **2007**, pp. 817–821.
- N. Ono: The Nitro Group in Organic Synthesis, Wiley-VCH, Weinheim, Germany, **2001**, pp. 309–316. DOI:10.1002/0471224480
- J. P. Agrawal, R. D. Hodgson: Organic Chemistry of Explosives, John Wiley & Sons, West Sussex, England, **2007**, pp. 157–159.
- J. P. Agrawal: High Energy Materials, Wiley-VCH, Weinheim, Germany, **2010**, pp. 82–102.
- A. B. Sheremetev, N. S. Aleksandrova, N. V. Ignat'ev, M. Schulte, *Mendeleev Comm.* **2012**, *22*(2), 95–97. DOI:10.1016/j.mencom.2012.03.015
- A. Ö. Yiğiter, M. K. Atakol, M. L. Aksu, O. Atakol, *J. Therm. Anal. Calorim.* **2017**, *127*, 2199–2123. DOI:10.1007/s10973-016-5766-2
- M. K. Atakol, A. Atakol, A. Ö. Yiğiter, I. Svoboda, O. Atakol, *J. Therm. Anal. Calorim.* **2017**, *127*, 1931–1940. DOI:10.1007/s10973-016-5800-4
- E. Özkaramete, N. Şenocak, E. K. İnal, S. Öz, I. Svoboda, O. Atakol, *Propellants, Explosives, Pyrotechnics* **2013**, *38*(1), 113–119. DOI:10.1002/prop.201200075
- M. B. Talawar, R. Sivabalan, T. Mukundan, H. Muthurajan, A. K. Sikder, B. R. Gandhe, A. S. Rao, *J. Hazard. Mat.* **2009**, *161*(2-3), 589–607. DOI:10.1016/j.jhazmat.2008.04.011
- T. M. Klapötke, F. Mieskes, J. Stierstorfer, M. Weyrauther, *Propellants, Explosives, Pyrotechnics* **2016**, *41*(2), 217–222. DOI:10.1002/prop.201500338
- P. Leonard, P. Bowden, M. Shorty, M. Schmitt, *Propellants, Explosives, Pyrotechnics* **2019**, *44*(2), 203–206. DOI:10.1002/prop.201800144

15. N. Koga, *J. Therm. Anal. Calorim.* **2013**, *113*, 1527–1541. DOI:10.1007/s10973-012-2882-5
16. S. Kullyakool, K. Siriwong, P. Noisong, C. Danvirutai, *J. Therm. Anal. Calorim.* **2017**, *127*, 1963–1974. DOI:10.1007/s10973-016-5837-4
17. L. Abdelouahed, S. Leveneur, L. V. Hassimi, L. Balland, B. Taouk, *J. Therm. Anal. Calorim.* **2017**, *129*, 1201–1213. DOI:10.1007/s10973-017-6212-9
18. K. Jayaraman, M. V. Kok, I. Gokalp, *J. Therm. Anal. Calorim.* **2017**, *127*, 1361–1370. DOI:10.1007/s10973-016-6042-1
19. J. Zhao, B. Jin, R. Peng, Q. Liu, B. Tan, S. Chu, *J. Therm. Anal. Calorim.* **2016**, *124*, 1431–1439. DOI:10.1007/s10973-016-5315-z
20. Y. F. Li, L. J. Zhai, K. Z. Xu, B. Z. Wang, J. R. Song, F. Q. Zhao, *J. Therm. Anal. Calorim.* **2016**, *126*, 1167–1173. DOI:10.1007/s10973-016-5662-9
21. F. Bao, G. Zhang, S. Jin, C. Zhang, H. Niu, *J. Therm. Anal. Calorim.* **2018**, *132*, 805–811. DOI:10.1007/s10973-018-6973-9
22. L. Luo, B. Jin, R. Peng, Y. Shang, L. Xiao, S. Chu, *J. Therm. Anal. Calorim.* **2019**, *135*, 3005–3013. DOI:10.1007/s10973-018-7481-7
23. X. Yin, J. Li, G. Zhang, H. Gu, Q. Ma, S. Wang, J. Wang, *J. Therm. Anal. Calorim.* **2019**, *135*, 2317–2328. DOI:10.1007/s10973-018-7390-9
24. A. Krajníková, A. Rotaru, K. Györyová, K. Homzová, H. O. Manolea, J. Kovářová, D. Hudecová, *J. Therm. Anal. Calorim.* **2015**, *120*, 73–83. DOI:10.1007/s10973-014-4212-6
25. A. Suekkhayad, P. Noisong, C. Danvirutai, *J. Therm. Anal. Calorim.* **2017**, *129*, 123–134. DOI:10.1007/s10973-017-6156-0
26. E. C. Moine, R. Bouamoud, A. El Hamidi, M. Khachani, M. Halim, S. Arsalane, *J. Therm. Anal. Calorim.* **2018**, *131*, 993–1004. DOI:10.1007/s10973-017-6632-6
27. N. S. Abdel-Kader, R. M. Amin, A. L. El-Ansary, *J. Therm. Anal. Calorim.* **2016**, *123*, 1695–1706. DOI:10.1007/s10973-015-5015-0
28. J. Naktiyok, H. Bayrakçeken, A. K. Özer, M. Ş. Gülaboğlu, *J. Therm. Anal. Calorim.* **2017**, *129*, 531–539. DOI:10.1007/s10973-017-6149-z
29. G. Ganeshan, K. P. Shadangi, K. Mohanty, *J. Therm. Anal. Calorim.* **2018**, *131*, 1803–1816. DOI:10.1007/s10973-017-6597-5
30. M. J. Frisch, G. W. Trucks, H. B. Schlegel, G. E. Scuseria, M. A. Robb, J. R. Cheeseman, G. Scalmani, V. Barone, B. Mennucci, G. Petersson, H. Nakatsuji: Gaussian 09, Revision D. 01, Gaussian, Inc., Wallingford CT, **2009**.
31. CrysAlis C. CrysAlis RED, Version 1.171. Oxford Diffraction Ltd., Abdingdon, UK, **2002**.
32. G. M. Sheldrick, *Acta Cryst. C.* **2015**, *71*, 3–8. DOI:10.1107/S2053229614024218
33. L. J. Farrugia, *J. Appl. Crystallogr.* **1999**, *32*, 837–838. DOI:10.1107/S0021889899006020
34. L. A. Curtiss, K. Raghavachari, P. C. Redfern, J. A. Pople, *J. Chem. Phys.* **1997**, *106*, 1063–1079. DOI:10.1063/1.473182
35. E. F. C. Byrd, B. M. Rice, *J. Phys. Chem. A* **2009**, *110*(3), 1005–1013. DOI:10.1021/jp0536192
36. B. M. Rice, S. V. Pai, J. Hare, *Combust. Flame* **1999**, *118*(3), 445–458. DOI:10.1016/S0010-2180(99)00008-5
37. P. J. Linstrom, W. G. Mallard, NIST standard reference database number 69, National Institute of Standards and Technology, <http://webbook.nist.gov> (accessed: July, 2018).
38. D. S. Y. Gaele, D. M. Yufanyi, R. Jagan, M. O. Agwara, *Cogent Chem.* **2016**, *2*(1), 1253201. DOI:10.1080/23312009.2016.1253201
39. H. F. Abd El-Halim, M. M. Omar, M. N. Anwar, *J. Therm. Anal. Calorim.* **2017**, *130*, 1069–1083. DOI:10.1007/s10973-017-6491-1
40. O. A. M. Ali, *J. Therm. Anal. Calorim.* **2017**, *128*, 1579–1590. DOI:10.1007/s10973-016-6055-9
41. J. Akhavan: The Chemistry of Explosives, Royal Society of Chemistry Publishing, Cambridge, UK, **1998**.
42. A. S. Bailey, J. R. Case, *Tetrahedron* **1958**, *3*, 113–131. DOI:10.1016/0040-4020(58)80003-4
43. G. O. Reddy, B. K. M. Murall, A. K. Chotterjee, *Propellants, Explosives, Pyrotechnics* **1983**, *8*(1), 29–33. DOI:10.1002/prop.19830080107
44. J. Kehler, A. Püschl, O. Dahl, *Acta Chem. Scand.* **1996**, *50*, 1171–1173. DOI:10.3891/acta.chem.scand.50-1171
45. P. Cardillo, L. Gigante, A. Lunghi, P. Zanirato, *J. Therm. Anal. Calorim.* **2010**, *100*(1), 191–198. DOI:10.1007/s10973-009-0572-8
46. A. L. Spek: PLATON Program for Crystal Molecular Drawing, University of Utrecht, Netherlands, **2000**.
47. G. Smith, U. D. Vermuth, J. M. White, *Acta Cryst. E* **2007**, *63*, o3759. DOI:10.1107/S1600536807038068
48. T. Steiner, *Angew. Chem. Int. Ed.* **2002**, *41*(1), 48–76. DOI:10.1002/1521-3773(20020104)41:1<48::AID-ANIE48>3.0.CO;2-U
49. G. R. Desiraju, *Acc. Chem. Res.* **1996**, *29*(9), 441–449. DOI:10.1021/ar950135n
50. P. K. Thallapally, A. K. Katz, H. L. Carrel, G. R. Desiraju, *Cryst. Eng. Comm.* **2003**, *5*, 87–92. DOI:10.1039/b301677c
51. S. MirDYa, M. G. B. Drew, A. K. Chandra, A. Banerjee, A. Frontera, S. Chattopadhyay, *Polyhedron*, **2020**, *179*, 114374. DOI:10.1016/j.poly.2020.114374
52. S. Vyazovkin, A. K. Burnham, J. M. Criado, L. A. Perez-Magueda, C. Popescu, N. Sbirazzuoli, *Thermochim. Acta* **2011**, *520*(1-2), 1–19. DOI:10.1016/j.tca.2011.03.034
53. S. Vyazovkin, K. Chrissafis, M.L. Di Lorenzo, N. Koga, M. Pijolat, B. Roduit, N. Sbirazzuoli, J. J. Suñol, *Thermochim. Acta* **2014**, *590*, 1–23. DOI:10.1016/j.tca.2014.05.036
54. M. E. Brown, M. Maciejewski, S. Vyazovkin, R. Nomen, J. Sempere, A. Burnham, J. Opfermann, R. Strey, H. L. Anderson, A. Kemmler, R. Keuleers, J. Janssens, H. O. Desseyn, C. R. Li, T. B. Tang, B. Roduit, J. Malek, T. Mitsushashi, *Thermochim. Acta* **2000**, *355*(1-2), 125–143. DOI:10.1016/S0040-6031(00)00443-3
55. J. Sestak, *J. Therm. Anal. Calorim.* **2014**, *117*, 3–7. DOI:10.1007/s10973-014-3810-7
56. X. Liu, Z. Su, W. Ji, S. Chen, Q. Wei, G. Xie, X. Yang, S. Gao, *J. Phys. Chem. C* **2014**, *118*(41), 23487–23498. DOI:10.1021/jp5062418

57. T. M. Klapötke: Chemistry of the High Energy Materials, Walter de Gruyter, Berlin, Germany, 2017, pp. 7.
DOI:10.1515/9783110536515

58. L. F. Fieser, M. Fieser: Lehrbuch der Organischen Chemie, Verlag Chemie GMBH, Weinheim, Germany, 1954, pp. 1176–1178.

Povzetek

Z reakcijo nukleofilne substitucije smo iz 1,3-dikloro-4,6-dinitrobenzena s hidrazinom, gvanidinijevim karbonatom oz. 4-aminopirazolom pripravili tri nove dušikove energetske spojine: *N*-(5-kloro-2,4-dinitrofenil)hidrazin (**1**), *N*-(5-kloro-2,4-dinitrofenil)gvanidin (**2**) in *N*-(5-kloro-2,4-dinitrofenil)-4-aminopirazol (**3**). Spojine smo karakterizirali z ¹H NMR, ¹³C NMR, IR in masno spektroskopijo. Samo spojino **2** smo lahko pripravili v obliki kristalov, primernih za rentgensko difrakcijsko analizo. Spojine smo raziskali tudi s TG in DSC. Termični razpad in termokinetično obnašanje smo raziskali s pomočjo metod, ki so jih razvili Ozawa–Flynn–Wall ter Kissinger–Akahira–Sunose. Opazili smo, da z raziskovanimi spojinami lahko poteka eksotermen termični razpad. S pomočjo Gaussian09 smo izračunali HOMO in LUMO nivoje, teoretične tvorbenne entalpije in porazdelitev elektrostatskega naboja. Eksplozijske hitrosti in tlake smo izračunali s pomočjo Kamlet–Jacobsovih enačb. Spojinam smo določili tudi antimikrobne lastnosti.



Except when otherwise noted, articles in this journal are published under the terms and conditions of the Creative Commons Attribution 4.0 International License

Scientific paper

Synthesis of CuO by Electrospinning Method for Sensing of Hydrogen and Carbon Monoxide Gases

Abdollah Fallah Shojaei^{1*} and Parisa Fallah Komsari^{1*}¹ Department of Chemistry, Faculty of Science, University of Guilan, P. O. Box, 41335-1914, Rasht, Iran

* Corresponding author: E-mail: shoja47@yahoo.com, a.f.shojaie@guilan.ac.ir

Received: 05-01-2021

Abstract

The pure CuO nanofibers were synthesized via the electrospinning method successfully. The calcinated CuO nanofibers were investigated for sensing hydrogen and carbon monoxide gases. Structural properties of the synthesized calcinated nanofibers were studied using Fourier –transform infrared spectroscopy (FTIR), X-ray diffraction (XRD), Energy-dispersive X-ray spectroscopy (EDX), and particle morphology by scanning electron microscopy (SEM). SEM images confirmed string-like structures, nanofibers. The sensor based on the calcinated CuO nanofibers exhibited excellent gas sensing performance at the low operating temperature of 175 °C and the fast response and recovery characteristics at a low concentration. Moreover, good stability, prominent reproducibility, and excellent selectivity are also observed based on the calcinated nanofibers. These results demonstrate the potential application of calcinated CuO nanofibers for sensing hydrogen (10–200 ppm) and carbon monoxide (400–700 ppm) gases.

Keywords: CuO, Carbon Monoxide, Electrospinning, Hydrogen, Calcinated nanofibers

1. Introduction

Metal oxide semiconductor (MOS) gas sensors have gained special focus driven by their diverse applications in air quality detection, inflammable gas inspection, environmental monitoring, healthcare, defense, security, and so on.¹ Semiconducting metal oxides have been extensively used as sensing materials; resistance changes in oxide based semiconductor gas sensors are used to monitor reducing, toxic and inflammable gases, such as NH₃, NO₂, H₂ and CO.²

In recent years, huge efforts have been made to develop nanostructured metal oxides with p-type semiconductivity.³ Copper oxide (CuO) has a narrow band gap (1.2 eV)⁴ as a p-type semiconducting oxide is known for being an excellent catalyst of Hydrogen gas.⁵ Copper oxide has increasingly attracted interest for both fundamental and practical reasons. It was shown to be an industrially important material that can be widely used in applications such as gas sensors, magnetic storage media, solar energy transformation, semiconductors, and catalysis⁶. A variety of methods such as thermal oxidation,⁷ hydrothermal,⁸ and electrochemical deposition⁹ have been proposed and investigated for the fabrication of low dimensional CuO. Among these methods, electrospinning is one of the most attractive strategies for producing nanofibers of CuO. The

electrospinning method involves the following steps: (1) Preparation of sol with suitable inorganic precursor and polymer content and achieving the right rheology for electrospinning, (2) Spinning of the solution to obtain fibers of polymer/inorganic composite, (3) Calcination of the composite fibers to obtain final oxide fibers. It is important; however, to control all of the above three stages to obtain high quality fibers with the desired final properties.¹⁰ It has the merits of simplicity, high efficiency, low cost, and high reproducibility.¹¹ In the other hand, many studies have reported on H₂ and CO gases sensing. For example, in 1950, Wagner et al. reported the variation of electrical properties when ZnO is exposed to reducing gases.¹² After that, a series of research works about the sensing behavior of MOS to reducing gases were reported by Seiyama, et al. since the 1960s.¹³ Up to the present, many kinds of MOS were investigated as hydrogen and carbon monoxide sensing materials, Some of the MOS were studied for measuring hydrogen gas include the following: ZnO which measures a mixture of H₂, CO, CH₄ gases at 300–500 °C,¹⁴ group-III-element-doped ZnO,¹⁵ SnO_x/Pt (Response to 3000 ppm at 250 °C.),¹⁶ Cu/SnO₂ (Response to 435 ppm at 270 °C.),¹⁷ In₂O₃ (Sensitivity values (S) for CO and H₂ (1000 ppm) in air were obtained at 350 °C.),¹⁸ SrCe_{0.95}Yb_{0.05}O₃ (The response of hydrogen to 30,000–90000 at 1000 °C.),¹⁹ Cd-doped SnO₂ (Sensitivity to 1000 ppm H₂ and 1000 ppm

CO at 300 °C.),²⁰ CuO- and ZnO-doped SnO₂ (The response to 200 ppm H₂ and CO at 310 °C.)²¹ F-doped SnO₂ (Response to 100 ppm H₂ gas is 2.2 approximately.)²² Co-doped SnO₂ (Response to 100 ppm of H₂ gas at 330 °C),²³ Pd-doped SnO₂ (gas sensing to 100 ppm H₂ and 100 ppm CO at 385 °C.),²⁴ SnO₂ (Response to 10000 ppm H₂ gas at 150 °C.)²⁵ CuO (The sensitivity of the sensor in response to 100 ppm H₂ at 300 °C is ~2.5.)²⁶ SnO₂ (Response to 1000 ppm H₂ at 400 °C.),²⁷ TiO₂ (The sensitivity of the sensor in response to 1000 ppm H₂ at 300 °C is ~3.75.)²⁸

And some of MOS were studied to measure CO gas are: Cu-doped ZnO (Its Sensitivity to carbon monoxide at 350 °C is ~ 3.)²⁹, SnO₂ (The sensitivity of the sensor in response to 1000 ppm carbon monoxide at 200 °C is 3.5.)³⁰ SnO₂ doped with Pd and Pt (CO sensing at 450 °C),³¹ Nb–TiO₂ (Response to CO (1000 ppm) at 550–950 °C.),³² In₂O₃/ SnO₂ (The selectivity to CO gas at 200 °C.),³³ CuO (Sensitivity to CO gas at 300 °C.),³⁴ ZnO-doped SnO₂ (The response to carbon monoxide at 300 °C.)³⁵ ZnO₂ (measured CO concentrations ranging from 100 ppm to 1000 ppm.).³⁶

In this paper, we reported a simple and facile approach to fabricate high quality calcinated CuO nanofibers by electrospinning and their H₂ and CO sensing characteristics are investigated. The study focuses on the design of CO and H₂ sensors with minimum interference with other Volatile organic compounds. The high response, quick response, and recovery, and good selectivity are observed in our investigation, which indicates the potential application of calcinated CuO nanofibers for the fabrication of high performance H₂ and CO sensors.

1. 1. Gas Sensing Performances

The gas sensing properties of unloaded and loaded-MOS nanoparticles sensing films are characterized in terms of response, response time, and recovery time as a function of operating temperature, gas concentration, and metal loading. The resistance of the p-type metal oxide surface increases because generated electrons recombine with holes, decreasing the hole concentration. The response for p-type semiconducting oxide to reducing gas (S^p) becomes:

$$S^p = \frac{R_g}{R_a} \quad (1)$$

where R_g and R_a are the electrical resistances of the sensors measured in the presence of reducing gas and pure dry air, respectively. The response time, T_{res} is defined as the time required reaching 90% of the steady response signal. The recovery times, T_{rec} denotes the time needed to recover 90% of the original baseline resistance. Moreover, the selectivity defined as the response ratio of target gas to that of another gas is used to assess the relative performance of Semiconducting metal oxides (MOXs) sensors towards different gases.³⁷ In this paper the sensitivity (S) was defined as $S = R_g/R_a$.

A possible sensing mechanism is described as follows to discover the gas sensing reaction process of the CuO sensor against H₂ and CO gases and illustrate the enhanced H₂ and CO sensing properties of the calcinated CuO nanofibers.

As described in Figure 1, under an air atmosphere the oxygen molecules can get adsorbed on the surface of

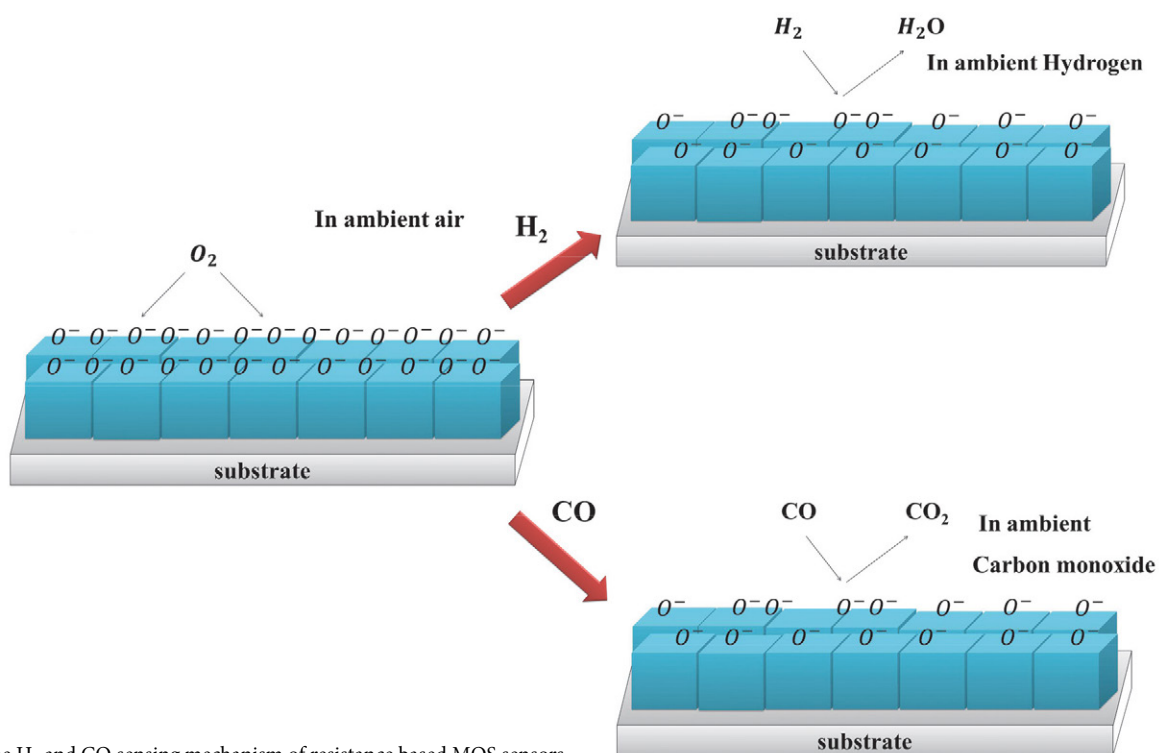
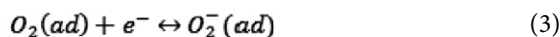
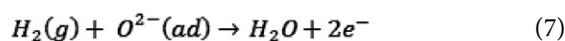
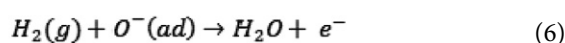


Figure 1. The H₂ and CO sensing mechanism of resistance based MOS sensors

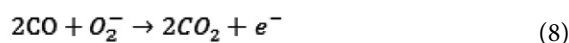
the semiconductor and extracts electrons from the conduction band to form oxygen ions.³⁸ The adsorption of oxygen forms ionic species such as O_2^- , O^- and O^{2-} , which acquire electrons from the conduction band. The reaction kinetics may be explained by the following reactions:^{39,40}



H_2 and CO sensing mechanisms of the MOS can be explained from the following reaction paths:⁴¹



And:⁴²



2. Experimental

2.1. Materials and Methods

Ethanol (>99%), N, N-dimethyl formamide (>99%, DMF), $CuCl_2 \cdot 6H_2O$ were used and purchased from Merck Company. Poly vinyl pyrrolidone (PVP, Mw = 1,300,000) and poly vinyl alcohol (PVA, Mw = 31,000–50,000) were obtained from Sigma Aldrich and also distilled water was used. All chemicals were analytical grade and used as received without any further purification.

The Fourier transforms infrared spectroscopy (FT-IR) of the calcinated CuO nanofibers were recorded on Thermo Nicolet Avatar spectrophotometer in the range of 500–4000 cm^{-1} using KBr pellets. The X-ray diffraction (XRD) technique (PHILIPS XRD diffractometer using $Cu K\alpha$ ($K\alpha = 1.540 \text{ \AA}$ and $2\theta = 10\text{--}90$ radiation as X-ray source) was used to verify the structure of the calcinated CuO nanofibers. Scanning electron microscopy (SEM) calcinated nanofibers images were performed on an LEO 1450 VP (Germany) instrument, Energy Dispersive X-ray spectroscopy (EDX) was attained on a TESCAN S8000 microscope, Atomic Absorption Spectrometer (AAS) of calcinated nanofibers were performed on an Agilent 240 AA instrument and Spin coating Device (Institute for Research and Technology Development of Modern Industry, Made in Iran) was a used to deposit uniform thin films onto flat glass.

2.2. Synthesis of CuO nanofibers

The electrospinning process was employed for CuO nanofibers synthesis. A mixed solution of polyvinyl alcohol (PVA, Mw: 31,000–50,000) and Copper (II) chloride ($CuCl_2 \cdot 6H_2O$) was used for electrospinning. In the typical experimental procedure, a PVA solution (10 wt %) was first prepared by dissolving PVA powder in distilled water and stirred for 5 h at 60 °C. A 20 wt% $CuCl_2$ solution and PVP powder was added to this solution. After stirring for 12 h, this mixed solution was introduced in a 20 mL syringe equipped with a metal needle tip in a controlled electrospinning setup. The parameters for electrospinning were selected as; applied voltage: 20 kV, feeding rate of the solution: 0.2 mL/h, distance between glass substrate attached to the copper sheet, and the tip of the needle: 10 cm. Finally, the fibers were peeled off from the collector with tweezers and placed in a crucible. The conversion of copper dichloride to CuO and the removal of organic constituents PVP and PVA in the as-spun nanofibers were achieved by calcining at 400 °C for 2 h in air.

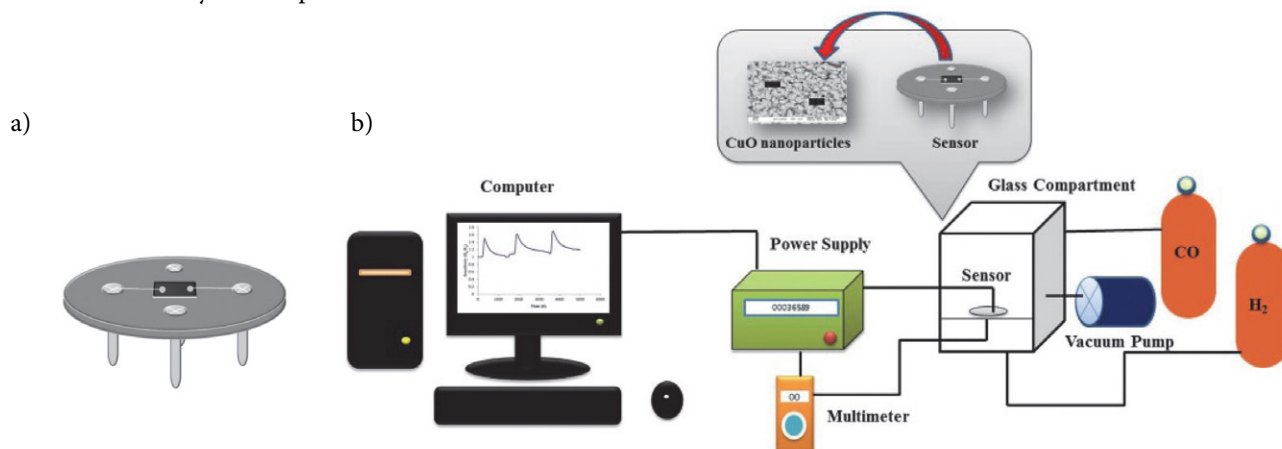


Figure 2. Schematic image of (a) sensor kit, and (b) the gas-sensing analysis system.

2. 3. Gas Identification System

Gas sensors were manufactured by Spin coating technique with planar glass substrates. Fig.2 (a) shows the schematic of the sensor. The as-prepared calcinated CuO nanofibers were blended with deionized water in a weight ratio of 100: 25 to form a paste. Then the paste was subsequently screen-printed onto the planar glass substrate to form a sensing film with a thickness of about 60 μm , the manufactured sensor was dried in air at room temperature to volatilize the water solvent and last aged in an aging test chamber for 24 h and after a Ni–Cr heating wire was inserted in the underneath to form a side-heated gas sensor. The efficiency of the gas sensors was determined in a gas testing chamber. Detail of the measurement setup can be observed in the schematic diagram is presented in Fig.2 (b). Electrical linkages to the gas sensors were achieved by physically connecting needle probes to the Pt electrodes of the sensors. A PC 510a (japan) multimeter was applied for measuring the changes of sensor resistance over time and a computer was used for logging data from the multimeter. At first, the responses of the sensors were measured in the presence of 200 ppm H_2 gas and 700 ppm CO gas in the ambient air where the temperatures were modified in the range 25–175 $^\circ\text{C}$ in order to ascertain their optimum operating temperature. The sensors were pre-heated at different operating temperatures for about 45 min. When the resistances of all the sensors were stable, saturated target gas was injected into the test chamber (20 L in volume) by a micro injector through a rubber plug. After its resistance value reached a new constant value, the test chamber was opened to recover. The sensor resistance and sensitivity were collected and analyzed by the system. And the environmental temperature, relative humidity, and working temperature were recorded.

3. Results and Discussion

3. 1. Identification of Sensor Structure

The X-ray diffraction pattern of the CuO nanofibers at 400 $^\circ\text{C}$ for 2h (calcinated CuO nanofibers) is shown

in Fig. 3. The CuO peaks appear at diffraction angles of 32/53 $^\circ$, 35/55 $^\circ$, 38/75 $^\circ$, 48/75 $^\circ$, 51/40 $^\circ$, 58/35 $^\circ$, 61/57 $^\circ$, 66/28 $^\circ$, 68/14 $^\circ$, 73/01 $^\circ$, 75/28 $^\circ$ corresponding to reflection from (1 1 0), (0 0 2), (1 1 1), (-2 0 2), (0 2 0), (2 0 2), (-1 1 3), (-3 1 1), (2 2 0), (3 1 1), and (-2 2 2) planes, respectively. The strongest diffraction pattern viewed at $2\theta = 35/55$ suggests that the CuO grows with a preferential orientation of (0 0 2) on the glass plate and illustrates the formation of the single-phase of monoclinic CuO. It was also viewed that the obtained XRD spectra are in very good agreement with reported 2θ values in JCPDS card no 48–1548.⁴³ Also, the average CuO particle size (D) was calculated using the Scherrer equation (11) is resulted 60 nm in one dimension, where D is the nanocrystal size; K is the shape factor, usually taken as 0.89 for ceramic materials (K has a typical value of about 0.9); λ is the wavelength of radiation in nanometer ($\lambda_{\text{CuK}\alpha} = 0.15405$ nm); θ is the diffracted angle of the peak; β is the full width at half maximum of the peak in radians.⁴⁴

$$D = \frac{K\lambda}{\beta \cos \theta} \quad (11)$$

Fig. 4(a) shows the SEM image of the nanofibers, this precursor at room temperature it has an average diameter of about 80 nanometers and several tens of micrometers in length. After calcination for 2h at 400 $^\circ\text{C}$, the length of the product, as shown in Fig. 4(b), is shorter than that of the precursor. The average diameter of calcinated CuO nanofibers at 400 $^\circ\text{C}$ is approximately 70 nm.

The FT-IR absorption peaks were performed to confirm the presence of characteristic vibrational peaks of calcinated CuO nanofibers. The FT-IR spectrum of the calcinated CuO nanofibers is presented in Fig. 5. The observed strong peaks at around 529, 585, and 672 cm^{-1} are attributed to the stretching from Cu-O along (-2 0 2) direction.⁴⁵ The absorption peak around 1100 cm^{-1} may be attributed to -OH bending vibrations of Cu-OH.⁴⁶ The transmittance peak that appeared at around 1377 cm^{-1} may be ascribed due to the presence of CO_2 , which is usually adsorbed from the air on the surface of sample materials during KBr pelletization.⁴⁷ The corresponding CH_2 bend placed at around 1460 cm^{-1} .⁴⁸ The weak band

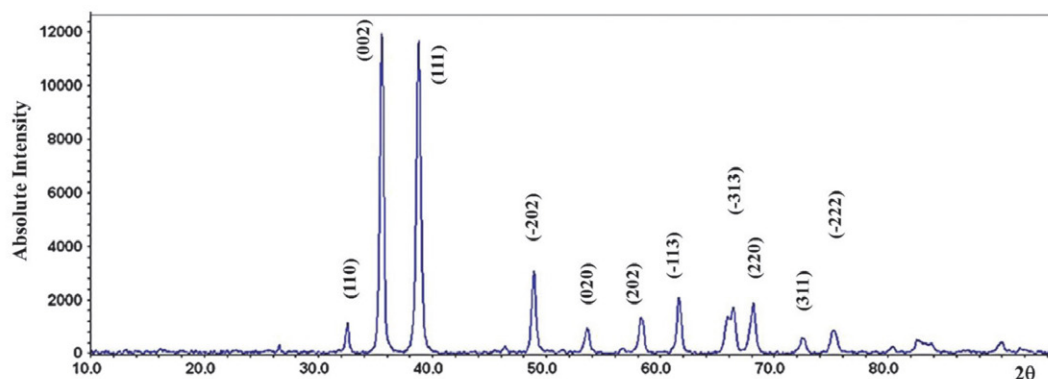


Figure 3. X-ray diffraction pattern of CuO nanofibers calcined at 400 $^\circ\text{C}$ for 2 h (calcinated CuO nanofibers).

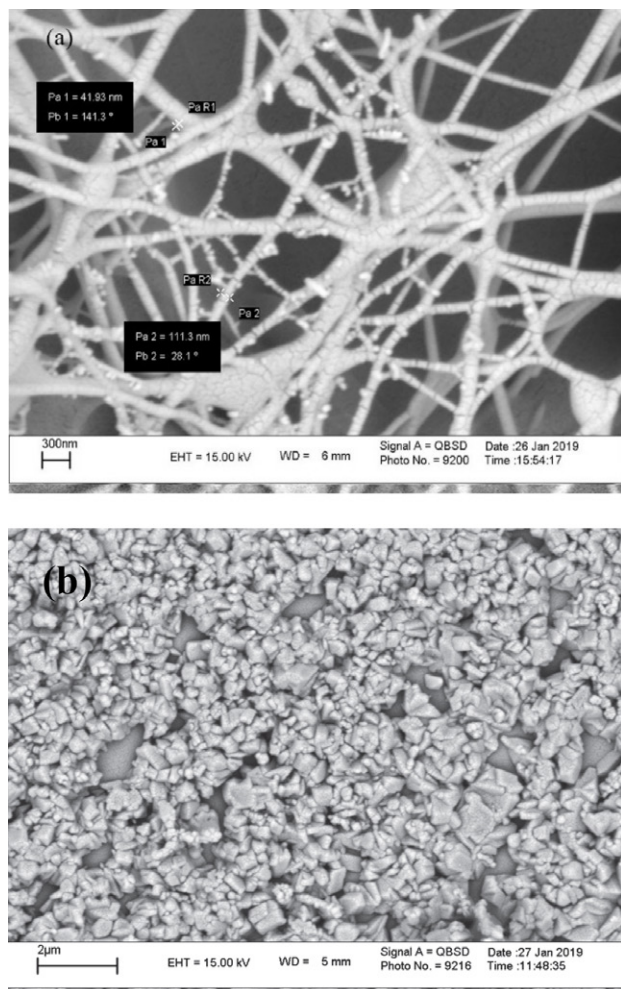


Figure 4. SEM image of (a) CuO nanofibers (b) CuO nanofibers calcinated at 400 °C for 2 h.

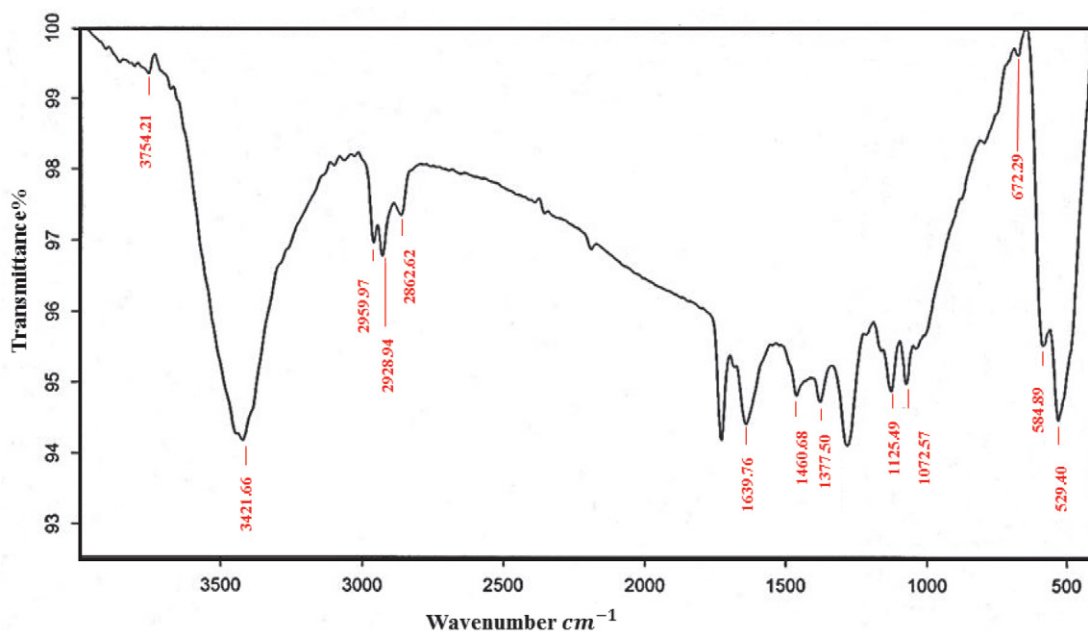


Figure 5. FTIR spectra of calcinated CuO nanofibers.

at 1639.76 cm^{-1} may be attributed to the bending vibration modes of O–H groups of these adsorbed H_2O molecules.⁴⁹ Further, three small bands at 2862.62, 2928.94, and 2959.97 cm^{-1} may be ascribed to the asymmetric and symmetric vibrational modes of the O–H bond of the H_2O molecules physisorbed on the surface of the CuO.⁵⁰ An intense broadband appeared in the 3400–3800 cm^{-1} region that was attributed to the O–H stretching vibration of surface hydroxyl groups of adsorbed water molecules,⁵¹ which arises because nanocrystalline materials having a high surface-to-volume ratio absorbs high moisture.

The EDX spectrum of the calcinated CuO nanofibers is reported in Fig. 6. Only Cu and O signals have been detected, indicating that the calcinated nanofibers were only built up of Cu and O. Weight percent of Cu was found to be 68.42 and that of O was 31.58. Thus the atomic ratio of Cu and O was 1:1. And 2.8 Peak is for the gold metal due to the preparation of the sample for EDX analysis.

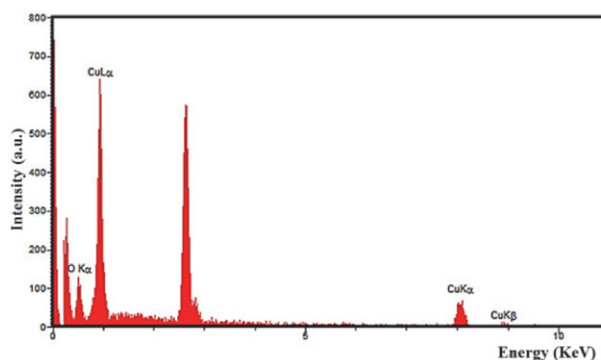


Figure 6. EDX spectra of calcinated CuO nanofibers.

3. 2. Gas Sensing Characteristics

To determine the optimum operating temperature, the responses of the calcinated CuO nanofibers gas sensor to 200 ppm H₂ and 700 ppm CO were measured continually at different operating temperatures. Fig. 7 shows the responses as a function of operating temperature from 25 to 300 °C. For each gas, the response is measured to increase rapidly with increasing operating temperature and arrive at the maximum and then decreases with a further rise of the operating temperature. The optimum operating temperatures of the calcinated CuO nanofibers are suggested at 175 °C for both H₂ and CO gases with response values of 5.43 and 9.14, respectively.

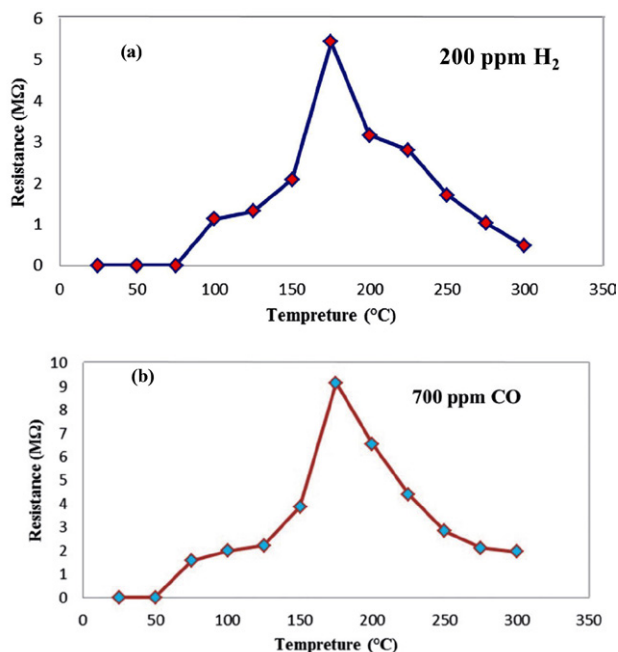


Figure 7. Responses of the calcinated CuO nanofibers sensors to (a) 200 ppm of H₂ and (b) 700 ppm of CO at different operating temperatures.

It is well known that response and recovery characteristics are important for evaluating the performances of semiconductor oxide sensors. The gas sensing transients of the calcinated CuO nanofibers sensor upon exposure to H₂ (200 ppm) and CO (700 ppm) are shown in Fig. 8. The gas responses and response speeds differed significantly according to the sensor temperature and type of gas. The times to reach 90% variation in resistance upon exposure to gas and air were defined as the 90% response time (τ_{res}) and the 90% recovery time (τ_{recov}), respectively. Most of the τ_{res} values were very short, indicating that both in the diffusion of analyte gas and the oxidation reaction between analyte gas and negatively charged chemisorbed oxygen occur very rapidly. Fast gas diffusion in the present study was attributed to the large surface area of calcinated nanofibers. Fig. 8 (a) shows the response time of the designed sensors for hydrogen and carbon monoxide gas was 39 s and 53 s at 175 °C, respective-

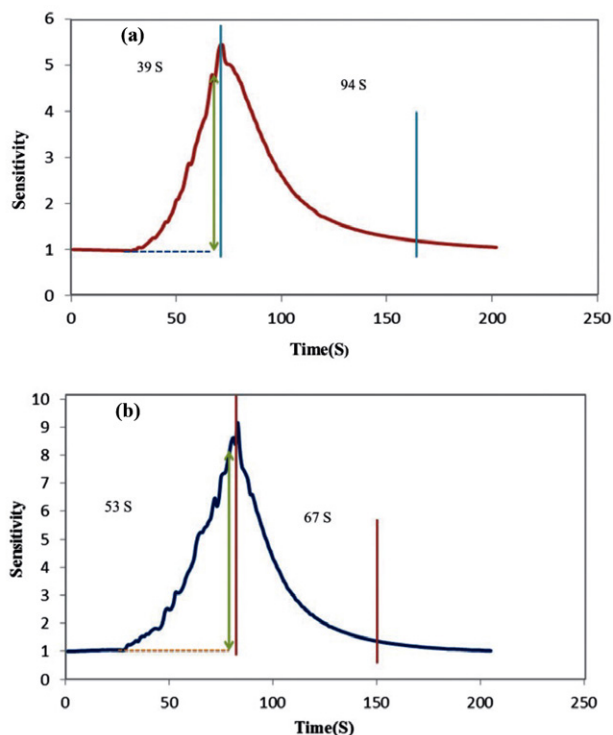


Figure 8. A single-cycle response–recovery characteristic curves of calcinated CuO nanofibers to (a) 200 ppm H₂ and (b) 700 ppm CO at 175 °C.

ly. The recovery time for hydrogen and carbon monoxide gas was 94 s and 67 s at 175 °C, respectively (Fig. 8 (b)).

Selectivity of H₂ and CO sensors couldn't be measured at the same time to justify the detection of one gas; there for Sensitivity of gases was measured separately during the experiment. To investigate the stability and repeatability of the calcinated CuO nanofibers sensor, it was sequentially exposed to different concentrations of H₂ gas Separately (10, 25, 50, 100, and 200 ppm) as shown in Figure 9 and shows the best response with more drastic resistance in concentration 200 ppm of H₂. also Fig. 10 (a-d) presents three reversible cycles response curve in the concentration range of 400–700 ppm of the that confirmed the calcinated CuO nanofibers had excellent stability and reversibility when alternately exposed to air and CO gas and it was found that calcinated CuO nanofibers showed extremely excellent CO sensing performances at concentration 700 ppm with the highest sensor response and the highest selectivity compared to the other CO concentrations. As shown in Figures 9 and 10, the sensor response increases rapidly when exposed to a certain concentration of H₂ and CO and decreases dramatically when exposed to air for recovery. Meanwhile, the gas response of the sensor always returns to its initial value during the continuous test period, implying a very satisfying reproducibility of the prepared sensor.

The concentration dependence of calcinated CuO nanofibers was investigated in the concentration range of 10–200 ppm of H₂ and the concentration range of 400–700 ppm CO the plots of the gas response against gas concentration

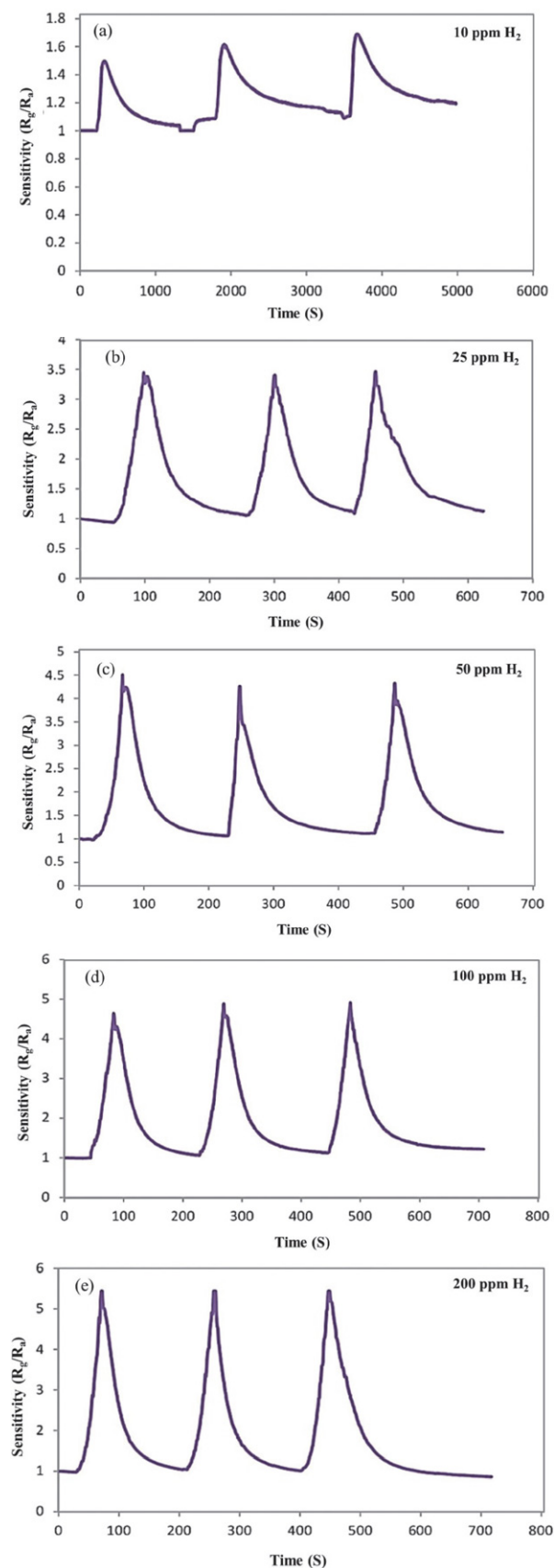


Figure 9. Reproducibility of the calcinated CuO nanofibers sensor on successive exposure (3 cycles) to (a) 10 ppm (b) 25 ppm (c) 50 ppm (d) 100 ppm (e) 200 ppm of H_2 at $175^\circ C$.

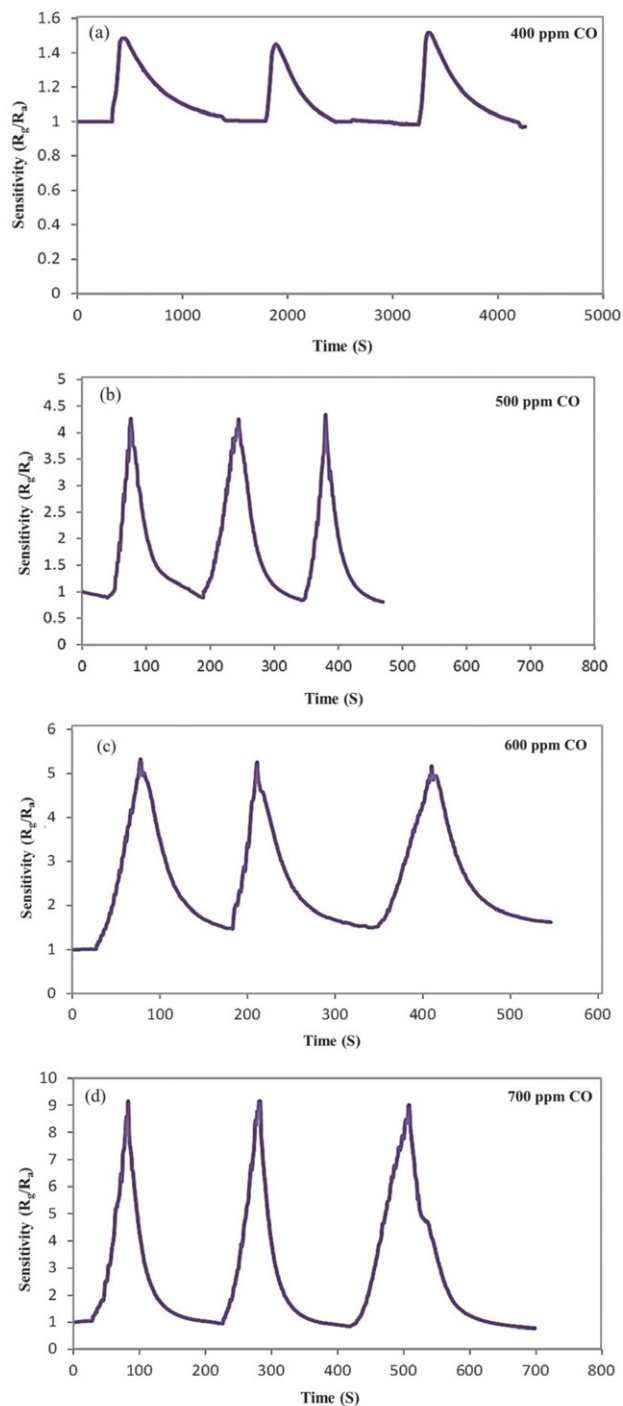


Figure 10. Reproducibility of the calcinated CuO nanofibers sensor on successive exposure (3 cycles) to (a) 400 ppm (b) 500 ppm (c) 600 ppm (d) 700 ppm of CO at $175^\circ C$.

are shown in Figure 11(a–b). As shown in Figure 11 (a), as the H_2 concentration increases to 50 ppm, the gas response increases linearly, and at 100 and 200 ppm the graph's slope decreases but the response is still rapid. This indicates that the sensor is not saturated. Thus, the calcinated CuO nanofibers sensor has a relatively linear relation to detecting H_2 at concentrations 10, 25 and 50 ppm at the log scale, and

also the calcinated CuO nanofibers sensor has a linear relationship to detect CO at the log scale. Thus calcinated CuO nanofibers sensor is favorable to detect H₂ and CO.

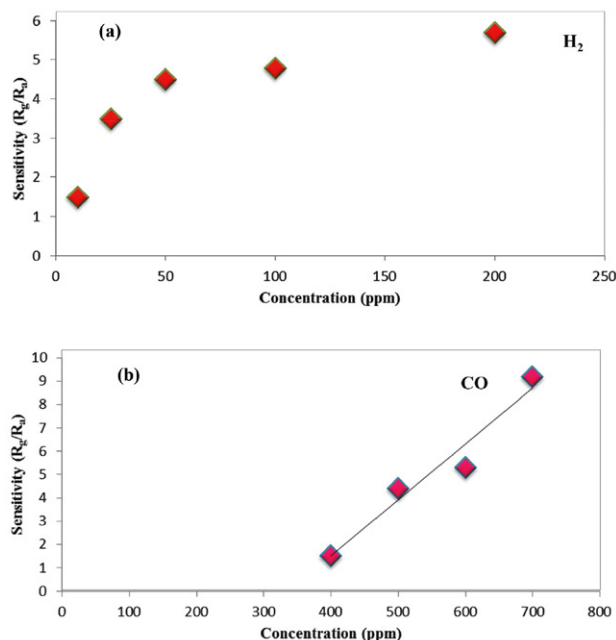


Figure 11: Responses of the calcinated CuO nanofibers sensor to different concentrations of (a) H₂ and (b) CO at 175 °C.

The gas sensing selectivity is another very important parameter to appraise the sensing ability of metal oxide semiconductor materials. Fig. 12 describes the histogram of the gas response of the calcinated CuO nanofibers sensor to 10 ppm of various gases, including n-hexane, methanol, ethanol, acetaldehyde, formaldehyde, and hydrogen at 175 °C. To demonstrate the sensor's high sensitivity to hydrogen gas than various gases, 10 ppm of various gases including: n-hexane, methanol, ethanol, acetaldehyde, and formaldehyde) are injected separately to test sensor sensitivity. And the sensitivity(S) results are presented in the form of a bar graph in Figure 12.

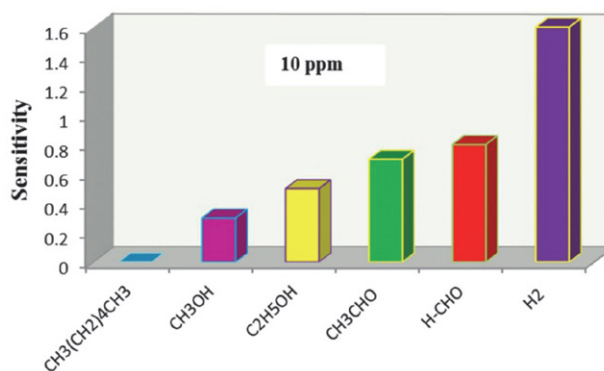


Figure 12. The selectivity of the calcinated CuO nanofibers sensor on successive exposure to 10 ppm of various gases at 175 °C.

This sensor shows an obvious hydrogen sensing response than other potential interface gases. Therefore, we believe that the calcinated CuO nanofibers gas sensor has an excellent selectivity to 10 ppm of H₂.

The comparison of calcinated CuO nanofibers sensor performance and recently reported data in the literature for hydrogen and carbon monoxide sensing applications are shown in Table 1. The sensitivity of calcinated CuO nanofibers at low temperature (175 °C) to 200 ppm of hydrogen gases with a response time of 39 s and 700 ppm of carbon monoxide with a response time of 53 s is 5.5 and 9.3, respectively. Low detection limit and low temperature, high sensitivity have shown promising results compared to other literature Table 1.

4. Conclusion

In summary, pure calcinated CuO nanofibers are synthesized via a simple electrospinning method and characterized by FT-IR, XRD, SEM, and EDX. The sensor exhibited the highest sensitivity (response: $R_g/R_a = 5.43$) to 200 ppm hydrogen and (response: $R_g/R_a = 9.14$) to 700 ppm Carbon monoxide at 175 °C. Short response and re-

Table 1. Comparison of calcinated CuO nanofibers sensors parameters and previous researches.

Sensing material	gas	Detection limit (ppm)	Operating temperature (°C)	Sensitivity (R_g/R_a)	Synthesis method	Response time	Ref.
CuO	H ₂	60000	300–800	3.72	Thermal oxidation	5 (min)	52
CuO	H ₂	1000	300	3	Sputtering	10 (S)	53
30Pd/CuO	H ₂	1000	200	4.5	Hydrothermal	10(min)	54
CuO	H ₂	1000	200	0.4	Anodization	~9(min)	55
Pd Doped TiO ₂ – CuO	H ₂	3000	150	–	Sol-gel	–	56
CuO	H ₂	200	175	5.5	Electrospinning	39 (S)	This work
CuO	CO	1000	300	1.6	Sputtering	–	53
CuO–ZnO	CO	800	500	–	Thermal evaporation	3.2 (min)	57
CuO–Cu _x Fe _{3–x} O ₄	CO	500	400	1.9	Sputtering	21(min)	58
0.4% Pt/ZnO–CuO	CO	1000	RT	2.64	Thermal	81(S)	59
CuO	CO	700	175	9.2	Electrospinning	53 (S)	This work

covery times and excellent selectivity are indicated based on calcinated CuO nanofibers that can be fabricated more quickly and at a lower cost. The simple method reported here can be used for further improving gas sensor performance such as enhancing the selectivity of the gas sensors to different test gases.

Acknowledgments

This study was supported by the Science and Research Branch, University of Guilan.

Conflict of Interest

The authors declare that there are no conflicts of interest regarding the publication of this manuscript.

5. References

1. L. Li, C. Guo, S. Li, L. Wang, Q. Dong, W. Li, *Sens. Actuators, B.* **2010**, *150*, 806–810. DOI:10.1016/j.snb.2010.07.022
2. C. C. Hsiao, L. S. Luo, *Sensors*, **2014**, *14*, 12219–12232. DOI:10.3390/s140712219
3. J. Jayaprakash, N. Srinivasan, P. Chandrasekaran, & E. K. Girija, *Spectrochim. Acta, Part A.* **2015**, *136*, 1803–1806. DOI:10.1016/j.saa.2014.10.087
4. H. Xiang, Y. Long, X. Yu, X. Zhang, N. Zhao, & J. Xu, *Cryst-EngComm.* **2011**, *13*, 4856–4860. DOI:10.1039/c0ce00980f
5. N. D. Hoa, S. Y. An, N. D. Dung, N. V. Quy, D. Kim, *Sens. Actuators, B.* **2010**, *146*, 239–244. DOI:10.1016/j.snb.2010.02.045
6. H. Guan, C. Shao, B. Chen, J. Gong, & X. Yang, *Inorg. Chem. Commun.* **2003**, *6*, 1409–1411. DOI:10.1016/j.inoche.2003.08.021
7. D. T. T. Le, N. Van Duy, N. D. Hoa, N. Van Hieu, *Phys. E (Amsterdam, Neth.)*. **2014**, *58*, 16–23. DOI:10.1016/j.physe.2013.11.013
8. M. A. Dar, Y. S. Kim, W. B. Kim, J. M. Sohn, H. S. Shin, *Appl. Surf. Sci.* **2008**, *254*, 7477–7481. DOI:10.1016/j.apsusc.2008.06.004
9. L. Chen, S. Shet, H. Tang, H. Wang, T. Deutsch, Y. Yan, J. Turner, M. Al-Jassim, *J. Mater. Chem.* **2010**, *20*, 6962–6967. DOI:10.1039/c0jm01228a
10. N. V. Dung, D. T. T. Le, N. D. Trung, H. N. Dung, N. M. Hung, N. V. Duy, & N. V. Hieu, *J. Nanosci. Nanotechnol.* **2016**, *16*, 7910–7918. DOI:10.1166/jnn.2016.12747
11. X. Shi, W. Zhou, D. Ma, Q. Ma, D. Bridges, Y. Ma, A. Hu, *J. Nanomater.* **2015**, *16*, 122. DOI:10.1155/2015/140716
12. C. Wagner, *J. Chem. Phys.* **1950**, *18*, 69–71. DOI:10.1063/1.1747459
13. T. Seiyama, A. Kato, K. Fujiishi, M. Nagatani, *Anal. Chem.* **1962**, *34*, 1502–1503. DOI:10.1021/ac60191a001
14. B. Bott, T. A. Jones, B. Mann, *Sens. Actuators.* **1984**, *5*, 65–73. DOI:10.1016/0250-6874(84)87007-9
15. H. Nanto, T. Minami, S. Takata, *J. Appl. Phys.* **1986**, *60*, 482–484. DOI:10.1063/1.337435
16. W. K. Choi, S. K. Song, J. S. Cho, Y. S. Yoon, D. Choi, H. J. Jung, S. K. Koh, *Sens. Actuators, B.* **1997**, *40*, 21–27. DOI:10.1016/S0925-4005(97)80194-3
17. A. Galdikas, V. Jasutis, S. Kačiulis, G. Matogno, A. Mironas, V. Olevano, D. Senulienė A. Šetkus, *Sens. Actuators, B.* **1997**, *43*, 140–146. DOI:10.1016/S0925-4005(97)00206-2
18. W. Y. Chung, G. Sakai, K. Shimano, N. Miura, D. D. Lee, N. Yamazoe, *Sens. Actuators, B.* **1998**, *46*, 139–145. DOI:10.1016/S0925-4005(98)00100-2
19. I. Kosacki, H. U. Anderson, *Sens. Actuators, B.* **1998**, *48*, 263–269. DOI:10.1016/S0925-4005(98)00055-0
20. Z. Tianshu, P. Hing, Y. Li, Z. Jiancheng, *Sens. Actuators, B.* **1999**, *60*, 208–215. DOI:10.1016/S0925-4005(99)00272-5
21. J. H. Yu, G. M. Choi, *Sens. Actuators, B.* **2001**, *75*, 56–61. DOI:10.1016/S0925-4005(00)00742-5
22. C. H. Han, S. D. Han, I. Singh, T. Toupance, *Sens. Actuators, B.* **2005**, *109*, 264–269. DOI:10.1016/j.snb.2004.12.115
23. L. Liu, C. Guo, S. Li, L. Wang, Q. Dong, W. Li, *Sens. Actuators, B.* **2010**, *150*, 806–810. DOI:10.1016/j.snb.2010.07.022
24. J. K. Choi, I. S. Hwang, S. J. Kim, J. S. Park, S. S. Park, U. Jeong, Y. C. Kang, J. H. Lee, *Sens. Actuators, B.* **2010**, *150*, 191–199. DOI:10.1016/j.snb.2010.07.013
25. R. Ab Kadir, Z. Li, A. Z. Sadek, R. Abdul Rani, A. S. Zoolfakar, M. R. Field, J. Z. Ou, A. F. Chrimes, K. Kalantar-Zadeh, *J. Phys. Chem. C.* **2014**, *118*, 3129–3139. DOI:10.1021/jp411552z
26. O. Lupan, V. Postica, N. Ababii, M. Hoppe, V. Cretu, I. Tiginyanu, V. Sontea, Th. Pauporté, B. Viana, R. Adelung, *Microelectron. Engin.* **2016**, *164*, 63–70. DOI:10.1016/j.mee.2016.07.008
27. N. Xue, Q. Zhang, S. Zhang, P. Zong, F. Yang, *Sensors*, **2017**, *17*, 2351. DOI:10.3390/s17102351
28. S. A. Mohd Chachuli, M. N. Hamidon, M. S. Mamat, M. Ertugrul, N. H. Abdullah, *Sensors*, **2018**, *18*, 2483. DOI:10.3390/s18082483
29. H. Gong, J. Q. Hu, J. H. Wang, C. H. Ong, F. R. Zhu, *Sens. Actuators, B.* **2006**, *115*, 247–251. DOI:10.1016/j.snb.2005.09.008
30. A. Salehi, *Sens. Actuators, B.* **2003**, *96*, 88–93. DOI:10.1016/S0925-4005(03)00490-8
31. P. Menini, F. Parret, M. Guerrero, K. Soulantica, L. Erades, A. Maisonnat, B. Chaudret, *Sens. Actuators, B.* **2004**, *103*, 111–114. DOI:10.1016/j.snb.2004.04.103
32. T. Anukunprasert, C. Saiwan, E. Traversa, *Sci. Technol. Adv. Mater.* **2005**, *6*, 359–363. DOI:10.1016/j.stam.2005.02.020
33. I. J. Kim, S. D. Han, C. H. Han, J. Gwak, H. D. Lee, J. S. Wang, *Sensors*, **2006**, *6*, 526–535. DOI:10.3390/s6050526
34. S. Steinhauer, E. Brunet, T. Maier, G. C. Mutinati, A. Köck, O. Freudenberg, C. Gspan, W. Grogger, A. Neuhold, R. Resel, *Sens. Actuators, B.* **2013**, *187*, 50–57. DOI:10.1016/j.snb.2012.09.034
35. E. Nikan, A. A. Khodadadi, Y. Mortazavi, *Sens. Actuators, B.* **2013**, *184*, 196–204. DOI:10.1016/j.snb.2013.04.089
36. C. C. Hsiao, L. S. Luo, *Sensors*, **2014**, *14*, 12219–12232. DOI:10.3390/s140712219
37. T. Samerjai, N. Tamaekong, K. Wetchakun, V. Kruefu, C. Liewhiran, C. Siri Wong, A. Wisitsoraat, S. Phanichphat, *Sens.*

- Actuators, B.* **2012**, *171*, 43–61.
DOI:10.1016/j.snb.2012.05.052
38. H. Gu, Z. Wang, Y. Hu, *Sensors*, **2012**, *12*, 5517–5550.
DOI:10.3390/s120505517
39. S. Phanichphant, C. Liewhiran, K. Wetchakun, A. Wisitsoraat, A. Tuantranont, *Sensors*, **2011**, *11*, 472–84.
DOI:10.3390/s110100472
40. L. F. Dong, Z. L. Cui, Z. K. Zhang, *Nanostruct. Mater.* **1997**, *8*, 815–823. DOI:10.1016/S0965-9773(98)00005-1
41. C. Wongchoosuk, A. Wisitsoraat, D. Phokharatkul, A. Tuantranont, T. Kercharoen, *Sensors*, **2010**, *10*, 7705–15.
DOI:10.3390/s100807705
42. C. C. Hsiao, L. S. Luo, *Sensors*, **2014**, *14*, 12219–12232.
DOI:10.3390/s140712219
43. Y. Zou, Y. Li, X. Lian, D. An, *Research of Materials Science*, **2014**, *3*, 44–51.
44. U. Holzwarth, & N. Gibson, *Nat. Nanotechnol.* **2011**, *6*, 534–534. DOI:10.1038/nnano.2011.145
45. M. A. Das, S. H. Nam, Y. S. Kim, W. B. Kim, *J. Solid State Electrochem.* **2010**, *14*, 1719–1726.
DOI:10.1007/s10008-010-1022-z
46. D. P. Dubal, G. S. Gund, C.D. Lokhande, R. Holze, *Mater. Res. Bull.* **2013**, *48*, 923–928.
DOI:10.1016/j.materresbull.2012.11.081
47. S. Sundar, G. Venkatachalam, S. J. Kwon, *Nanomaterials*, **2018**, *8*, 823. DOI:10.3390/nano8100823
48. N. Can, *Mater. Chem. Phys.* **2018**, *213*, 6–13.
DOI:10.1016/j.matchemphys.2018.03.069
49. A. Nezamzadeh-Ejehieh, H. Zabihi-Mobarakeh, *J. Ind. Eng. Chem.* **2014**, *20*, 1421–1431. DOI:10.1016/j.jiec.2013.07.027
50. P. K. Raul, S. Senapati, A. K. Sahoo, I. M. Umlong, R. R. Devi, A. J. Thakur, V. Veer, *RSC Adv.* **2014**, *4*, 40580–40587.
DOI:10.1039/C4RA04619F
51. M. Halder, M. M. Islam, Z. Ansari, S. Ahammed, K. Sen, S. K. M. Islam, *ACS Sustain. Chem. Eng.* **2017**, *5*, 648–657.
DOI:10.1021/acssuschemeng.6b02013
52. N. D. Hoa, S.Y. An, N. Q. Dung, N. Van Quy, & D. Kim, *Sens. Actuators, B.* **2010**, *146*, 239–244.
DOI:10.1016/j.snb.2010.02.045
53. P. Yadav, A. Kumar, A. Sanger, Y.K. Gautam, & B. P. Singh, *J. Electron. Mater.* **2021**, *50*, 192–200.
DOI:10.1007/s11664-020-08588-8
54. N. Sarica, O. Alev, L. Ç. Arslan, & Z. Z. Öztürk, *Thin Solid Films.* **2019**, *685*, 321–328. DOI:10.1016/j.tsf.2019.06.046
55. O. Şişman, N. Kılınc, & Z.Z. Öztürk, *Sens. Actuators, B.* **2016**, *236*, 1118–1125. DOI:10.1016/j.snb.2016.06.148
56. B. Biswas, A. Dey, S. Roy, S. Ray, & S. K. Sarkar, *IEEE.* **2019**, 202–205. DOI:10.1109/DEVIC.2019.8783477
57. N. Wu, M. Zhao, J. G. Zheng, C. Jiang, B. Myers, S. Li, & S. X. Mao, *Nanotechnology.* **2005**, *16*, 2878.
DOI:10.1088/0957-4484/16/12/024
58. L. Presmanes, A. Chapelle, F. Oudrhiri-Hassani, A. Barnabé, & P.H. Tailhades, *Sens. Lett.* **2011**, *9*, 587–590.
DOI:10.1166/sl.2011.1568
59. M. R. Yu, R. J. Wu, & M. Chavali, *Sens. Actuators, B.* **2011**, *153*, 321–328. DOI:10.1016/j.snb.2010.09.071

Povzetek

Z metodo elektrospredjenja (electrospinning) smo uspešno sintetizirali nanovlakna CuO. Nanodelce CuO smo preiskovali z namenom detekcije vodika in ogljikovega monoksida. Strukturne lastnosti sintetiziranih nanodelcev smo preučevali s Fourierjevo infrardečo spektroskopijo (FTIR), rentgensko difrakcijo (XRD), energijsko disperzivno rentgensko spektroskopijo (EDX) in morfologijo delcev z vrstično elektronsko mikroskopijo (SEM). Posnetki SEM so pokazali nanovlaknasto strukturo. Senzorji, zasnovani na nanodelcih CuO, so izkazali odlično sposobnost zaznavanja plinov pri temperaturi 175 °C in hiter odziv pri nizkih koncentracijah. Poleg tega smo opazili tudi dobro stabilnost, primerno ponovljivost in odlično selektivnost. Rezultati kažejo na možnost uporabe nanodelcev CuO pri detekciji H₂ (10–200 ppm) in CO (400–700ppm).



Except when otherwise noted, articles in this journal are published under the terms and conditions of the Creative Commons Attribution 4.0 International License

Scientific paper

Dehydrogenation of 1-Phenylethanol Catalyzed by Nickel(II)diphosphine Complexes

Reshma Geetha,¹ Meenu Kumar,¹ Naveen V. Kulkarni^{1,2*}
and William D. Jones^{2*}

¹ Department of Chemistry, Amrita Vishwa Vidyapeetham, Amritapuri, Kerala 690525, INDIA

² Department of Chemistry, University of Rochester, Rochester, New York 14450, USA

* Corresponding author: E-mail: dr.naveenvk@gmail.com; naveenvkulkarni@am.amrita.edu (NVK)
jones@chem.rochester.edu (WDJ)

Received: 05-12-2021

Abstract

Catalytic efficacy of the nickel(II)-diphosphine systems in the dehydrogenation of 1-phenylethanol to acetophenone under acceptorless conditions was investigated. Steric and electronic factors of the phosphine ligands were found to play an important role in the catalysis, while the nature of the base used and the reaction conditions, *viz.* time, temperature, and stoichiometry, have also shown major influence. Based on the preliminary analysis, a homogeneous pathway, perhaps involving nickel hydride species, was proposed. Due to the gradual disintegration of the catalytic species, deterioration of catalytic activity was observed resulting into low to moderate conversions. Among the series of catalysts examined, the highest conversion of 52% was exhibited by the catalyst C4, dichloro(1,2-bis(diphenylphosphino)ethane)nickel(II) (5 mol%), when loaded with 50 mol% of sodium ethoxide in toluene at 120 °C.

Keywords: Acceptorless dehydrogenation; dehydrogenation of alcohol; nickel(II)catalyst; 1,2 bis(alkyl/arylphosphino)alkane. homogeneous catalysis; Catalyst disintegration.

1. Introduction

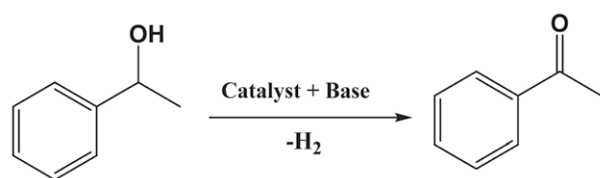
In recent years the acceptorless dehydrogenation process has gained much attention in academic and industrial research. It provides an efficient and atom-economical route for converting alcohols into synthetically useful carbonyl compounds, without the use of a sacrificial hydrogen acceptor. Moreover, the only byproduct formed in the reaction is highly valuable molecular hydrogen.^{1–3} Due to the vast significance of this catalytic reaction, a variety of homogeneous catalysts has been developed and employed in this process. It is often seen that the catalysts containing precious metal centres, *viz.*, Ru, Rh, Ir, and Os have exhibited better performance,^{4–7} nevertheless, with the meticulous tuning of structural features of the catalyst and reaction conditions, systems containing sustainable metals such as Fe, Co and Mn were also shown to exhibit comparable activities in this catalytic reaction.^{8–15} However, in comparison, nickel-based catalysts are underexplored in dehydrogenation chemistry; examples of single-molecule nickel catalysts capable of mediating acceptorless dehydrogenation of alcohols are extremely scarce. Key examples

are the Ni(II) complexes supported by tris(3,5-dimethylpyrazolyl)borate and 2-hydroxyquinoline mixed ligands developed by Jones *et al.*¹⁶ and Ni(II) complexes derived from 2,6-bis(diethylaminomethyl)pyridine pincer ligand reported by Zhang *et al.*¹⁷ It is important to notice that these catalysts involve either exotic ligand systems or special reaction conditions to achieve the desired reactivity. This prompted us to look for simple nickel-based systems, which can efficiently catalyse dehydrogenation of alcohols under mild to moderate reaction conditions. Incidentally, diphosphine nickel(II)chloride complexes attracted us due to their simple synthetic protocols, stability and well-established catalytic profile.^{18–25} Here in this article, we describe the use of diphosphine nickel(II)chloride complexes in the acceptorless dehydrogenation of alcohols.

2. Experimental

All of the synthesis and catalysis procedures were performed under N₂ atmosphere using Schlenk line techniques. All the solvents and reagents used in this work were

purified & dried using standard protocols²⁶ and stored over molecular sieves (4 Å). Ligands, bis(dimethylphosphanyl)ethane (**L1**), bis(diethylphosphanyl)ethane (**L2**), bis(diphenylphosphanyl)ethane (**L4**), triphenylphosphine (**L5**), bis(diphenylphosphanyl)methane (**L6**), 1,3-bis(diphenylphosphanyl)propane (**L7**) were purchased from Sigma Aldrich (Merck). Ligand, bis(diisopropylphosphanyl)ethane (**L3**)²⁷ and the nickel(II) catalysts, [1,2-bis(dimethylphosphino)ethane]dichloronickel(II) (**C1**),²⁸ [1,2-bis(diethylphosphino)ethane]dichloronickel(II) (**C2**),^{28,29} [1,2-bis(diisopropylphosphino)ethane]dichloronickel(II) (**C3**),³⁰ [1,2-bis(diphenylphosphino)ethane]dichloronickel(II) (**C4**),^{28,31} dichlorobis(triphenylphosphine)nickel(II) (**C5**),³² bis(diphenylphosphino)methane]dichloronickel(II) (**C6**)³¹ and bis(diphenylphosphino)propane]dichloronickel(II) (**C7**)³¹, were prepared by following the reported protocols.



Scheme 1: Catalytic acceptorless dehydrogenation of 1-phenylethanol

In a typical catalytic acceptorless dehydrogenation reaction (Scheme 1), 0.05 mmol of nickel(II)phosphine catalyst (**C1**–**C7**) and 0.5 mmol of base were loaded in a two necked Schlenk flask equipped with a water condenser under N₂ atmosphere. 2 mL of toluene (dried over benzophenone-sodium) was added and the mixture was stirred

for a couple of minutes. 0.122 mL (1 mmol) of 1-phenylethanol was added to the catalytic mixture using a syringe and the Schlenk flask was kept in a 120 °C preheated oil-bath and stirred vigorously for 16 h. A continuous bubbling of N₂ gas was maintained throughout the reaction. After the scheduled period of time, the reaction was stopped, allowed to cool to room temperature and opened to air. The product yield was analysed by gas chromatography analysis (*vide infra*) and in some cases, also by ¹H NMR spectroscopic analysis (*vide infra*). Product isolation was done by running the catalytic mixture through a silica gel column using ethyl acetate:hexane (1:3) eluant. The results are summarized in Table 1.

GC analysis details: After the reaction, the reaction mixture was diluted with 9 mL of dichloromethane and filtered through a short plug of Celite. 360 µL of filtrate and 25 µL of tridecane (internal standard) were taken in 3 mL of dichloromethane and analyzed on Shimadzu GC-17A – FID instrument, using Agilent DB-WAXETR column (30 m × 0.25 mm, thickness 0.50 µm) using helium as a carrier gas. Method used: starting oven temperature, 50 °C (hold for 5 min); maximum temperature, 240 °C; heating rate, 15 °C/min (hold for 5 min); column pressure: 24.5 psi; total flow: 273 mL/min, column flow: 2.64 mL/min, split ratio: 100, linear velocity: 49 cm/sec.

¹H NMR spectroscopic analysis details: Reaction mixture was evacuated under a weak vacuum to partially remove the solvent (toluene), followed by the addition of ~ 0.3 mL of CDCl₃ and thorough mixing. An aliquot from this solution was taken in an NMR tube, diluted with CDCl₃ and analyzed on a Bruker Ascend 500 NMR spectrometer operating at 500 MHz at RT). Relative area of integration of the methyl protons of 1-phenylethanol

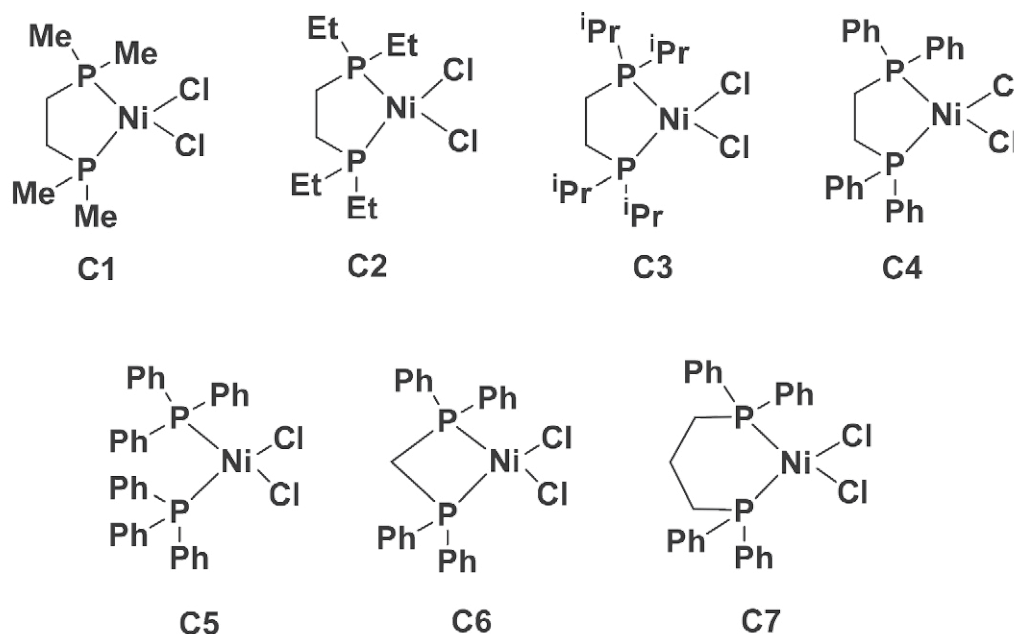


Figure 1: Nickel(II)diphosphine complexes used in the current study.

(doublet or broad, $\sim \delta$ 1.48) and acetophenone (singlet, $\sim \delta$ 2.57) were considered to calculate the percent of conversion.

$^{31}\text{P}\{^1\text{H}\}$ NMR analysis was done in CDCl_3 on a Bruker AMX 400 spectrometer operating at 162 MHz at RT; Chemical shift values are reported with reference to the external standard, H_3PO_4 . In the analysis of catalytic mixture, an aliquot of reaction mixture was taken in NMR tube, added with CDCl_3 and used for analyses.

3. Results and Discussion

Among the nickel(II) complexes supported by the substituted diphosphinoethane ligands (Figure 1), we found that the system bearing phenyl substitutions (i.e., **C4**) exhibited better activity, converting 52% of 1-phenylethanol to acetophenone, under the current reaction conditions (Entry 4, Table 1). The systems having methyl (**C1**) and isopropyl (**C3**) substitutions on the phosphorus donors yielded only 12 and 14% of acetophenone, respectively (Entries 1 and 3 in Table 1). With the nickel(II) diphosphine system substituted with ethyl groups on phosphorus, 30% conversion was observed (Entry 2, Table 1). This indicates the significant influence of electronic effects of the ligands on the stability and reactivity of the catalyst system.^{33,34} Incidentally, anhydrous nickel(II)chloride in the absence of any phosphine ligand showed no detectable conversions under our reaction conditions (Entry 8, Table 1). Sole use of the ligand, bis(diphenylphosphaneyl)ethane

(**L4**) did not provide any catalytic conversion (Entry 9, Table 1). Sodium ethoxide (50 mol%) in absence of nickel catalyst also did not show any detectable conversion (Entry 10, Table 1).

Table 1: Catalysis data for acceptorless dehydrogenation of 1-phenylethanol to yield acetophenone; catalyzed by nickel(II)diphosphine complexes **C1**–**C7**.*

Entry	Catalyst	Conversion (%) [#]	Yield (%) [§]
1	C1	12	–
2	C2	30	24
3	C3	14	–
4	C4	52	45
5	C5	30	25
6	C6	21	16
7	C7	34	26
8	NiCl_2	NIL	–
9	L4	NIL	–
10	–	NIL	–

*Catalytic reactions are conducted in dry toluene with 1 mmol of 1-phenyl ethanol, 0.05 mmol of catalyst (5 mol%) and 0.5 mmol (0.027 g, 50 mol%) of NaOEt, at 120 °C (oil bath temperature) for 16h, under the slow, continuous bubbling of nitrogen gas. [#] Data from GC analysis (Average value of two duplicate experiments). [§] Isolated yield.

Further, we examined the efficacy of different phosphinonickel(II)chloride complexes, bearing phenyl substituents on the phosphorus but with varying spacer groups in the acceptorless dehydrogenation of 1-phenyl-

Table 2: Catalysis data for acceptorless dehydrogenation of 1-phenylethanol to yield acetophenone; catalyzed by the nickel(II)diphosphine complex **C4** under various reaction conditions.

Entry	Catalyst (mol%)	Base (mol%)	Reaction conditions	Conversion (%) [*]	Yield (%) [#]
1	C4 (5)	NaOEt (50)	120 °C in Toluene, 16h, No N_2 bubbling.	8	–
2	C4 (5)	NaOMe (50)	120 °C in Toluene, 16h, With N_2 bubbling.	23	15
3	C4 (5)	KOH (50)	120 °C in Toluene, 16h, With N_2 bubbling.	4	–
4	C4 (5)	KO^tBu (50)	120 °C in Toluene, 16h, With N_2 bubbling.	50	45
5	C4 (5)	NaOEt (25)	120 °C in Toluene, 16h, With N_2 bubbling.	22	16
6	C4 (5)	NaOEt (10)	120 °C in Toluene, 16h, With N_2 bubbling.	11	–
7	C4 (10)	NaOEt (50)	120 °C in Toluene, 16h, With N_2 bubbling.	56	48
8	C4 (2)	NaOEt (50)	120 °C in Toluene, 16h, With N_2 bubbling.	12	–
9	C4 (5)	NaOEt (50)	120 °C in Toluene, 24h, With N_2 bubbling.	54	45
10	C4 (5)	NaOEt (50)	120 °C in Toluene, 48h, With N_2 bubbling.	55	45
11	C4 (5)	NaOEt (50)	120 °C in Toluene, 8h, With N_2 bubbling.	32	24
12	C4 (5)	NaOEt (50)	25 °C in Toluene, 16h, With N_2 bubbling.	Traces	–
13	C4 (5)	NaOEt (50)	60 °C in Toluene, 16h, With N_2 bubbling.	8	–
14	C4 (5)	NaOEt (50)	140 °C in Xylenes, 16h, With N_2 bubbling.	54	45
15 [¶]	C4 (5)	NaOEt (50)	120 °C in Toluene, 16h, With N_2 bubbling.	46	38
16 [¥]	C4 (5)	NaOEt (50)	120 °C in Toluene, 16h, With N_2 bubbling.	54	44
17 ^{##}	C4 (5)	NaOEt (50)	120 °C in Toluene, 16h, With N_2 bubbling.	52	43
18 [§]	C4 (5)	NaOEt (50)	120 °C in Toluene, 16h, With N_2 bubbling.	51	43

*Data from GC analysis (Average value of two duplicate experiments; Percent of conversion obtained from ^1H NMR spectroscopic analysis were comparable with the GC data, within the difference of $\pm 5\%$). [#] Isolated yield. [¶] 1-(p-tolyl)ethanol was used as substrate. [¥] 1-(4-fluorophenyl)ethanol was used as substrate. ^{##} A drop of metallic mercury (~ 50 mg) was added to the reaction mixture prior heating (Mercury poisoning test). [§] A drop of carbon disulphide (~ 0.1 mL) was added to the reaction mixture prior heating (CS_2 poisoning test).

lethanol, under the same reaction conditions. It was found that the phenylphosphine(II)nickel system with a propyl (three-carbons) spacer (C7) exhibited better activity yielding 34% of acetophenone (Entry 7, Table 1), over the system bearing a methylene (one-carbon) spacer (C6), which could dehydrogenate only 21% of the substrate (Entry 6, Table 1). On the other hand, the catalytic activity of the nickel catalyst containing two triphenylphosphine ligands (C5) was found to fall between the complexes C6 and C7 (30% conversion, Entry 5, Table 1). Nevertheless, the complex, C4, which bears an ethyl (two carbon) spacer was found to be the best catalyst among the systems employed in this study (Entry 4, Table 1), hence was chosen for the further exploration. The higher activity of the complex C4 can be correlated with its higher stability. Due to the presence of a stable five membered coordination ring (ring size effect) and near ideal bite angle β , this system is expected to be stabilized electronically.^{34–38}

Continuous bubbling of dry nitrogen/argon gas throughout the reaction period is found to be key to expel the molecular hydrogen produced and to access the better conversions.¹⁶ A drastic decrease in the yield (~8%) was observed, otherwise, due to the superseding backward, hydrogenation reaction³¹ (Entry 1, Table 2). Since alcohol dehydrogenation is a thermodynamically uphill process,³⁹ continuous removal of hydrogen gas will have a positive thermodynamic contribution and can favour the forward reaction.⁴⁰

The nature and stoichiometric ratio of the base used play an important role in the dehydrogenation-hydrogenation catalytic reactions.⁴¹ In the current studies, sodium ethoxide was found to be the most compatible base; replacing it with sodium methoxide, under similar reaction conditions, yielded lower conversion *viz.*, 23% (Entry 2, Table 2). Potassium hydroxide was found to be unsuitable for our system, which produced only about 4% of acetophenone (Entry 3, Table 2), while potassium tert-butoxide provided a comparable yield (50 % conversion, Entry 4, Table 2). Lowering the loading of the base sodium ethoxide to 25 mol% (Entry 5, Table 2) or 10 mol% (Entry 6, Table 2) resulted in a decrease in reactivity, yielding 22% and 11% of the product, respectively, indicating that the higher loading of 50 mol% of base is essential to maintain the catalytically active species during the course of the reaction.^{41,42}

In an attempt to improve the catalytic conversion, we tried varying the catalyst loading, keeping the stoichiometry of the sodium ethoxide unchanged (50 mol%) under the same reaction conditions. When the catalyst loading was increased to 10 mol% (Entry 7, Table 2) a slight improvement in the conversion (56%) was observed, indicating that higher catalyst loading is necessary to get better conversions. Conversely, when catalyst loading was reduced to 2 mol% (Entry 8, Table 2), a drastic decrease in the activity was observed, yielding only 12% conversion.

All the catalytic reactions in the above studies were run overnight (16h). In anticipation of increasing the con-

version, we extended the reaction period to 24h (Entry 9, Table 2). This resulted in a slight enhancement in the conversion providing 54% of the product. However, further extension of the reaction period to 48h did not show any significant improvement in the yield (Entry 10, Table 2), indicating gradual degeneration of the catalytic species over time.⁴² On the other hand, when the reaction time was limited to 8h, only 32% conversion was observed (Entry 11, Table 2).

To overcome the thermodynamic constraints, the process of dehydrogenation of alcohols often requires higher reaction temperatures¹⁶ or a suitable acceptor.⁴³ In our current acceptorless reaction conditions, we found that a higher reaction temperature, *viz.* 120 °C, is required to attain higher conversions. When the catalytic reaction was carried at room temperature (Entry 12, Table 2), no detectable catalytic activity was observed and the reaction conducted at 60 °C (Entry 13, Table 2) yielded only 8% conversion. On the other hand, when the reaction was conducted at higher temperature (140 °C, in xylenes), a slight improvement in the activity was observed, providing 54% conversion (Entry 14, Table 2).

Further, we examined the efficacy of our catalytic system in the dehydrogenation of a couple of *para* substituted 1-phenylethanol motifs. The substrate containing an electron donating group, 1-(*p*-tolyl)ethanol (Entry 15, Table 2), yielded slightly lower conversion (slower reaction) compared to the substrate bearing an electron withdrawing substituent, 1-(4-fluorophenyl)ethanol (Entry 16, Table 2) under the same reaction conditions. This reactivity pattern is in line with the earlier observations involving nickel-based catalysts.¹⁶ Due to the moderate reactivity of the catalyst system, we did not try to expand the substrate scope to other alcohols.

It has recently been shown that nickel(II)diphosphine complexes are very good catalysts in transfer hydrogenation, where various substituted ketones were converted nearly quantitatively to the corresponding alcohols using isopropanol as a sacrificial hydrogen donor as well as a solvent.³¹ However, in the current acceptorless conditions, in spite of our attempts with varying reaction stoichiometry and conditions, we were not able to improve the conversion. Gradual disintegration of the catalyst under the reaction conditions is envisaged to be the main cause for the deterioration of catalytic activity. However, the dominant backward hydrogenation reaction could also have some key role to play.^{16,31} During the course of the catalytic dehydrogenation reaction, a change in the colour of the reaction mixture from yellow to dark brown was observed, which is a typical indication for the formation of Ni(0) related nanoclusters.^{31,44} In order to investigate if the Ni(0) nanoclusters have any role to play in the catalysis, a mercury poisoning test (Entry 15, Table 2),^{16,47} as well as a carbon disulphide poisoning test (Entry 16, Table 2)⁴⁶ were performed. However, both tests turned out to be negative, as no significant difference in the catalytic reactivity/

conversion was observed, thus, ruling out any contribution from a metal nano-particle mediated heterogeneous pathway.⁴¹ Further, in the $^{31}\text{P}\{^1\text{H}\}$ NMR spectroscopic analysis, we found that, a single signal at δ 57.1 observed for the complex C4, experiences a significant shift upon addition of 2 equivalent amount of 1-phenyl ethanol and heating to 60 °C for five minutes with thorough shaking, forming a peak at δ 33.0 indicating the formation of a new compound, possibly an alkoxide species. Same signal ($\sim \delta$ 33.0) was observed in the $^{31}\text{P}\{^1\text{H}\}$ NMR spectrum of the catalytic mixture, when recorded at the initial stages (within 5 min), suggesting the formation of the same species as in the catalytic conditions. However, at the end of the catalytic reaction (24h), the appearance of a new signal at δ 198.5 along with the signal at $\sim \delta$ 33.0 indicates partial dissociation of the intermediate compound. All of these observations strongly suggest a catalytic mechanism involving a homogeneous route, perhaps mediated by nickel alkoxide and nickel hydride intermediates, as envisaged in the previous studies.^{16,31,47}

4. Conclusion

Overall, we have explored the catalytic efficacy of the nickel(II)diphosphine systems in the dehydrogenation of 1-phenylethanol under acceptorless conditions. Steric and electronic factors of the phosphine ligands were found to play an important role in the catalysis along with the nature of the base used, as well as the reaction conditions. The catalytic reaction was found to follow a homogeneous pathway, presumably involving nickel hydride species. The catalytic reaction suffers mostly due to the disintegration of the catalytic species, providing only low to moderate conversions. We are currently working on isolation of the nickel hydride species, as structural characterization of these reactive intermediates could help us in understanding the mechanistic aspects of the catalytic reaction which would, indeed, help in improving the efficacy and expanding the substrate scope of the catalytic systems.^{48,49} Perhaps, these systems can be tuned to efficiently promote Guerbet upgrading of ethanol to n-butanol, which is a reaction of great commercial importance and of our primary focus.^{41,50}

Acknowledgments

This work was partly supported by the NSF under the CCI Center for Enabling New Technologies through Catalysis (CENTC), CHE-1205189. NVK thanks Science and Engineering Research Board (SERB) for the TARE grant (TAR/2018/000881) and Prof. A. G. Samuelson, Indian Institute of Science, Bengaluru for his support. WDJ acknowledges partial summer support from the U.S. Department of Energy, Basic Energy Sciences (BES) Chemical Sciences, Geosciences, & Biosciences (CSGB) Division (DE-SC0020230).

5. References

1. R. H. Crabtree, *Chem. Rev.* **2017**, *117*, 9228–9246. DOI:10.1021/acs.chemrev.6b00556
2. P. Pandey, I. Dutta, J. K. Bera, *Proc. Natl. Acad. Sci., India, Sect. A Phys. Sci.* **2016**, *86*, 561–579. DOI:10.1007/s40010-016-0296-7
3. G. Guillena, D. J. Ramon, M. Yus, *Chem. Rev.* **2010**, *110*, 1611–1641. DOI:10.1021/cr9002159
4. G. Zeng, S. Sakaki, K.-I. Fujita, H. Sano, R. Yamaguchi, *ACS Catal.* **2014**, *4*, 1010–1020. DOI:10.1021/cs401101m
5. T. Zweifel, J. V. Naubron, H. Grützmacher, *Angew. Chem., Int. Ed.* **2009**, *48*, 559–563. DOI:10.1002/anie.200804757
6. I. Mena, M. A. Casado, V. Polo, P. Garcia-Orduña, F. J. Lahoz, L. A. Oro, *Angew. Chem., Int. Ed.* **2012**, *51*, 8259–8263. DOI:10.1002/anie.201202936
7. M. Bertoli, A. Choualeb, A. J. Lough, B. Moore, D. Spasyuk, D. G. Gusev, *Organometallics* **2011**, *30*, 3479–3482. DOI:10.1021/om200437n
8. S. Chakraborty, W. W. Brennessel, W. D. Jones, *J. Am. Chem. Soc.* **2014**, *136*, 8564–8567. DOI:10.1021/ja504523b
9. S. Chakraborty, P. O. Lagaditis, M. Förster, E. A. Bielinski, N. Hazari, M. C. Holthausen, W. D. Jones, S. Schneider, *ACS Catal.* **2014**, *4*, 3994–4003. DOI:10.1021/cs5009656
10. P. J. Bonitatibus, Jr., S. Chakraborty, M. D. Doherty, O. Siclovan, W. D. Jones, G. L. Soloveichik, *Proc. Natl. Acad. Sci. U. S. A.* **2015**, *112*, 1687–1692. DOI:10.1073/pnas.1420199112
11. G. Zhang, S. K. Hanson, *Org. Lett.* **2013**, *15*, 650–653. DOI:10.1021/ol303479f
12. G. Zhang, K. V. Vasudevan, B. L. Scott, S. K. Hanson, *J. Am. Chem. Soc.* **2013**, *135*, 8668–8681. DOI:10.1021/ja402679a
13. S. Elangovan, M. Garbe, H. Jiao, A. Spannenberg, K. Junge, M. Beller, *Angew. Chem., Int. Ed.* **2016**, *55*, 15364–5368. DOI:10.1002/anie.201607233
14. M. Andérez-Fernández, L. K. Vogt, S. Fischer, W. Zhou, H. Jiao, M. Garbe, S. Elangovan, K. Junge, H. Junge, R. Ludwig, M. Beller, *Angew. Chem., Int. Ed.* **2017**, *56*, 559–562. DOI:10.1002/anie.201610182
15. N. V. Kulkarni, W. D. Jones, *Chemistry of Mn and Co pincer compounds*, in: D. M. Morales (Ed), *Pincer Compounds: Chemistry and Applications*, **2018**, pp 491–518. DOI:10.1016/B978-0-12-812931-9.00024-4
16. S. Chakraborty, P. E. Pizsel, W. W. Brennessel, W. D. Jones, *Organometallics* **2015**, *34*, 5203–5206. DOI:10.1021/acs.organomet.5b00824
17. Z. Dai, Q. Luo, H. Jiang, Q. Luo, H. Li, J. Zhang, T. Peng, *Catal. Sci. Technol.* **2017**, *7*, 2506–2511. DOI:10.1039/C7CY00432J
18. V. Percec, G. M. Golding, J. Smidrkal, O. Weichold, J. Org. Chem. **2014**, *69*, 3447–3452. DOI:10.1021/jo049940i
19. H. Ke, X. Chen, G. Zou, *J. Org. Chem.* **2014**, *79*, 7132–7140. DOI:10.1021/jo501291y
20. X. Chen, H. Ke, G. Zou, *ACS Catalysis* **2014**, *4*, 379–385. DOI:10.1021/cs4009946
21. S. D. Ramgren, L. Hie, Y. Ye, N. K. Garg, *Org. Lett.* **2013**, *15*, 3950–3953. DOI:10.1021/ol401727y

22. P. Leowanawat, N. Zhang, M. Safi, D. J. Hoffman, M. C. Fryberger, A. George, V. Percec, *J. Org. Chem.* **2012**, *77*, 2885–2892. DOI:10.1021/jo3001194
23. L. Gan, T. L. Groy, P. Tarakeshwar, S. K. S. Mazinani, J. Shearer, V. Mujica, A. K. Jones, *J. Am. Chem. Soc.* **2015**, *137*, 1109–1115. DOI:10.1021/ja509779q
24. K. E. Dalle, J. Warnan, J. J. Leung, B. Reuillard, I. S. Karmel, E. Reisner, *Chem. Rev.* **2019**, *119*, 2752–2875. DOI:10.1021/acs.chemrev.8b00392
25. T. Li, B. Xie, J.-X. Cao, D. -L. Zhang, C. Lai, H.-J. Fan, B. Zhao, W.-Y. Mou, X.-X. Bai, *Appl. Organomet. Chem.* **2021**, *35*, 26123–26124.
26. A. I. Vogel. A Text book of Quantitative Inorganic Analysis, 3rd Edn, Longmans Green and Co. Ltd., London, **1961**.
27. M. Jimenez-Tenorio, M. C. Puerta, S. Valerga, D. L. Hughes, *J. Chem. Soc. Dalton Trans.* **1994**, 2431–2436.
28. G. Booth, J. Chatt, *J. Chem. Soc.* **1965**, 3238–3241. DOI:10.1039/jr9650003238
29. S. C. Davies, S. E. Duff, D. J. Evans, *Acta Cryst.* **2005**, *E61*, m1674–m1676. DOI:10.1107/S160053680502386X
30. F. Scott, C. Krüger, P. Betz, *J. Organomet. Chem.* **1990**, *387*, 113–121.
31. S. Venkatesh, R. R. Panicker, V. Lenin Kumar, B. B. Pavankumar, N. Viswanath, S. Singh, R. Desikan, A. Sivaramakrishna, *J. Coord. Chem.* **2020**, *73*, 2963–2977. DOI:10.1080/00958972.2020.1837784
32. J. Montgomery, *Science of Synthesis*, Georg Thieme Verlag KG, **2001**, vol. 1, pp. 11.
33. B. Stewart, A. Harriman, L. J. Higham, *Organometallics* **2011**, *30*, 5338–5343. DOI:10.1021/om200070a
34. C. A. Tolman, *Chem. Rev.* **1977**, *77*, 313–348. DOI:10.1021/cr60307a002
35. A. Chacko, U. R. Idem, C. H. Bains, L. M. Mihichuk, A. L. L. East, *Organometallics*, **2013**, *32*, 5374–5383. DOI:10.1021/om400667t
36. M. Kumar, R. V. Chaudhari, B. Subramaniam, T. A. Jackson, *Organometallics*, **2015**, *34*, 1062–1073. DOI:10.1021/om5012775
37. C. P. Casey, G. T. Whiteker, M. G. Melville, L. M. Petrovich, J. A. Gavney, D. R. Powell, *J. Am. Chem. Soc.* **1992**, *114*, 5535–5543. DOI:10.1021/ja00040a008
38. W. N. M. van Leeuwen, P. C. J. Kamer, J. N. H. Reek, P. Dierkes, *Chem. Rev.* **2000**, *100*, 2741–2770. DOI:10.1021/cr9902704
39. K. B. Wiberg, L. S. Crocker, K. M. Morgan, *J. Am. Chem. Soc.* **1991**, *113*, 3447–3450. DOI:10.1021/ja00009a033
40. L. A. Watson, O. Eisenstein, *J. Chem. Educ.* **2002**, *79*, 1269–1277. DOI:10.1021/ed079p1269
41. N. V. Kulkarni, W. W. Brennessel, W. D. Jones, *ACS Catal.* **2018**, *8*, 997–1002. DOI:10.1021/acscatal.7b03653
42. S. L. Scott, *ACS Catal.* **2018**, *8*, 8597–8599. DOI:10.1021/acscatal.8b03199
43. M. Zhao, Z. Yu, S. Yan, Y. Li, *Tetrahedron Let.* **2009**, *50*, 4624–462. DOI:10.1016/j.tetlet.2009.05.100
44. S. Chandra, A. Kumar, P. K. Tomar, *J. Saudi Chem. Soc.*, **2014**, *18*, 437–442. DOI:10.1016/j.jscs.2011.09.008
45. V. M. Chernyshev, A. V. Astakhov, I. E. Chikunov, R. V. Tyurin, D. B. Eremin, G. S. Ranny, V. N. Khrustalev, V. P. Ananikov, *ACS Catal.* **2019**, *9*, 2984–2995. DOI:10.1021/acscatal.8b03683
46. B. J. Hornstein, J. D. Aiken, R. G. Finke, *Inorg. Chem.* **2002**, *41*, 1625–1638. DOI:10.1021/ic010920y
47. N. A. Eberhardt, H. Guan, *Chem. Rev.* **2016**, *116*, 8373–8426. DOI:10.1021/acs.chemrev.6b00259
48. N. V. Kulkarni, C. Dash, N. B. Jayaratna, S. G. Ridlen, S. K. Khani, A. Das, X. Kou, M. Yousufuddin, T. R. Cundari, H. V. R. Dias, *Inorg. Chem.* **2015**, *54*, 11043–11045. DOI:10.1021/acs.inorgchem.5b02134
49. P. G. Gassman, D. W. Macomber, S. M. Willging, *J. Am. Chem. Soc.* **1985**, *107*, 2380–2388. DOI:10.1021/ja00294a031
50. G. Reshma, V. Padmanabhan, A. R. Varma, M. S. Gouri, U. R. Nair, P. B. Parvathy, N. V. Kulkarni, D. Senthurpandi, *J. Mol. Struct.* **2021**, *1226*, 129344. DOI:10.1016/j.molstruc.2020.129344

Povzetek

Proučili smo katalitično učinkovitost sistema nikel(II)-difosfin pri dehidrogenaciji 1-feniletanola do acetofenona brez prisotnosti akceptorja. Ugotovili smo, da imajo sterični in elektronski faktorji fosfinskega liganda pomemben vpliv na katalitične lastnosti sistema, pomembna pa je tudi izbira baze ter reakcijskih pogojev (čas reakcije, temperatura, stehiometrija). Glede na preliminarne analize predvidevamo homogen mehanizem, morda z udeležbo zvrsti, ki vsebuje nikljev hidrid. Nizke konverzije so posledica zmanjšanja katalitične aktivnosti sistema zaradi počasnega razkroja katalitične zvrsti. Med proučevanimi katalizatorji ima največjo konverzijo (52 %) katalizator **C4**, dikloro(1,2-bis(difenilfosfino)etan)nikel(II) (5 mol%), ob dodatku 50 mol% natrijevega etoksida v toluenu pri 120 °C.



Except when otherwise noted, articles in this journal are published under the terms and conditions of the Creative Commons Attribution 4.0 International License

Scientific paper

Synthesis, Characterization and Crystal Structures of Schiff Base Copper Complexes with Urease Inhibitory Activity

Shuang Han¹ and Yuan Wang^{2,*}¹ College of Chemistry and Chemical Engineering, Qiqihar University, Qiqihar 161006, P.R. China² Heilongjiang Province Qiqihar Ecological Environment Monitoring Center, Qiqihar 161005, P.R. China

* Corresponding author: E-mail: qqhrwangyuan@163.com

Received: 05-24-2021

Abstract

Urease inhibitors can inhibit the decomposition rate of urea, and decrease the air pollution caused by ammonia. In this paper, four new copper(II) complexes $[\text{CuL}(\text{ONO}_2)]_n$ (**1**), $[\text{Cu}_2\text{L}_2(\mu_{1,3}\text{-N}_3)_2]$ (**2**), $[\text{CuBrL}]$ (**3**), and $[\text{CuClL}]$ (**4**), where L = 5-bromo-2-(((2-methylamino)ethyl)imino)methylphenolate, have been synthesized and characterized. The complexes were characterized by elemental analyses, IR and UV-Vis spectroscopy, molar conductivity, and single crystal X-ray diffraction. X-ray analysis reveals that Cu atoms in complexes **1** and **2** are in square pyramidal coordination, and those in complexes **3** and **4** are in square planar coordination. The molecules of the complexes are linked through hydrogen bonds and $\pi\cdots\pi$ interactions. The inhibitory effects of the complexes on *Jack bean* urease were studied, which showed that the complexes have effective activity on urease.

Keywords: Schiff base; Copper complex; X-ray diffraction; Urease inhibitory activity

1. Introduction

Urea is a major nitrogen-containing soil fertilizer, with an annual production projected to reach 226 million tons in 2021.¹ Once deposited in soil, urea quickly hydrolyzes by urease to yield NH_3 .² This reaction causes a number of agronomic, environmental and economic problems and affects the global nitrogen cycle.³ In particular, too rapid increase of soil pH upon urea hydrolysis catalyzed by urease activity causes the loss of urea nitrogen as gaseous ammonia, which is toxic to plants and contributes to the production of fine inorganic particulate matter.⁴ This process causes tropospheric pollution by NO, NO_2 and N_2O , which is a greenhouse gas with 300 times the heat trapping capacity of CO_2 .⁵ Urease occurs widely in most bacteria, plants, algae, fungi and invertebrates.⁶ Urease enzyme catalyzes the decomposition of urea into ammonia in high efficiency, with the rate 10^{14} times faster than the non-catalyzed reaction.⁷ This process is harmful for the health of human beings and environment. The use of inhibitors proves to be a good way to solve this problem.⁸ Recent research indicated that metal complexes have interesting activities on urease.⁹ However, the study on this

topic is limited, and no definite relationship between structures and properties is given. Schiff bases are a kind of interesting ligands in the formation of metal complexes, which have received particular attention due to their facile synthesis, versatile structures, and good biological activities.¹⁰ Schiff base complexes of copper, cobalt, nickel and zinc are reported to have urease inhibitory activities.¹¹ In pursuit of exploring novel urease inhibitors, four new copper complexes $[\text{CuL}(\text{ONO}_2)]_n$ (**1**), $[\text{Cu}_2\text{L}_2(\mu_{1,3}\text{-N}_3)_2]$ (**2**), $[\text{CuBrL}]$ (**3**), and $[\text{CuClL}]$ (**4**), where L = 5-bromo-2-(((2-methylamino)ethyl)imino)methylphenolate, are presented.

2. Experimental

2.1. General Methods and Materials

4-Bromosalicylaldehyde and *N*-methylethane-1,2-diamine were purchased Lancaster and used as received. All other reagents were of analytical reagent grade. Elemental analyses of C, H and N were carried out in a 2400 Series-II CHN analyzer. FT-IR spectra were obtained on a Jasco FT/IR-4000 spectrometer with samples pre-

pared as KBr pellets. Electronic spectra were obtained with Lambda 35 spectrophotometer. Single crystal X-ray diffraction was carried out with a Bruker Apex II CCD diffractometer. Molar conductance was measured with a Shanghai DDS-11A conductometer.

Caution! Although our samples never exploded during handling, azide compounds are potentially explosive. Only a small amount of azide compound should be prepared and it should be handled with care.

2. 2. Synthesis of Complex 1

4-Bromosalicylaldehyde (0.20 g, 1.0 mmol) and *N*-methylethane-1,2-diamine (0.074 g, 1.0 mmol) were dissolved and mixed in methanol (30 mL). The mixture was stirred at room temperature for 10 min to give a yellow solution. To the solution was added dropwise a methanol solution (20 mL) containing copper nitrate (0.24 g, 1.0 mmol). The color changed to blue immediately. The mixture was further stirred at room temperature for 30 min and filtered. The filtrate was kept at ambient temperature. Single crystals of the complex, suitable for X-ray diffraction, were grown from the filtrate upon slow evaporation within a few days. The crystals were isolated by filtration, washed with methanol and dried in air. Yield: 0.23 g (61%). Anal. Calcd. for $C_{10}H_{12}BrCuN_3O_4$ (%): C, 31.47; H, 3.17; N, 11.01. Found (%): C, 31.28; H, 3.26; N, 11.23. IR data (KBr, cm^{-1}): 3151 (NH), 1647 (C=N), 1421, 1272, 1086 (NO_3). UV-Vis data in methanol [λ_{max} (nm)]: 230, 245, 271, 363.

2. 3. Synthesis of Complex 2

4-Bromosalicylaldehyde (0.20 g, 1.0 mmol) and *N*-methylethane-1,2-diamine (0.074 g, 1.0 mmol) were dissolved and mixed in methanol (30 mL). The mixture was stirred at room temperature for 10 min to give a yellow solution. To the solution was added dropwise a methanol solution (20 mL) containing copper bromide (0.22 g, 1.0 mmol) and sodium azide (0.065 g, 1.0 mmol). The color changed to blue immediately. The mixture was further stirred at room temperature for 30 min and filtered. The filtrate was kept at ambient temperature. Single crystals of the complex, suitable for X-ray diffraction, were grown from the filtrate upon slow evaporation within a few days. The crystals were isolated by filtration, washed with methanol and dried in air. Yield: 0.13 g (36%). Anal. Calcd. for $C_{20}H_{24}Br_2Cu_2N_{10}O_2$ (%): C, 33.21; H, 3.34; N, 19.36. Found (%): C, 33.37; H, 3.45; N, 19.20. IR data (KBr, cm^{-1}): 3172 (NH), 1645 (C=N), 2078 (N_3). UV-Vis data in methanol [λ_{max} (nm)]: 230, 248, 272, 361.

2. 4. Synthesis of Complex 3

4-Bromosalicylaldehyde (0.20 g, 1.0 mmol) and *N*-methylethane-1,2-diamine (0.074 g, 1.0 mmol) were

dissolved and mixed in methanol (30 mL). The mixture was stirred at room temperature for 10 min to give a yellow solution. To the solution was added dropwise a methanol solution (20 mL) containing copper bromide (0.22 g, 1.0 mmol). The color changed to deep blue immediately. The mixture was further stirred at room temperature for 30 min and filtered. The filtrate was kept at ambient temperature. Single crystals of the complex, suitable for X-ray diffraction, were grown from the filtrate upon slow evaporation within a few days. The crystals were isolated by filtration, washed with methanol and dried in air. Yield: 0.26 g (65%). Anal. Calcd. for $C_{10}H_{12}Br_2CuN_2O$ (%): C, 30.06; H, 3.03; N, 7.01. Found (%): C, 29.87; H, 3.12; N, 6.93. IR data (KBr, cm^{-1}): 3201 (NH), 1640 (C=N). UV-Vis data in methanol [λ_{max} (nm)]: 230, 245, 280, 365.

2.5. Synthesis of Complex 4

4-Bromosalicylaldehyde (0.20 g, 1.0 mmol) and *N*-methylethane-1,2-diamine (0.074 g, 1.0 mmol) were dissolved and mixed in methanol (30 mL). The mixture was stirred at room temperature for 10 min to give a yellow solution. To the solution was added dropwise a methanol solution (20 mL) containing copper chloride (0.13 g, 1.0 mmol). The color changed to deep blue immediately. The mixture was further stirred at room temperature for 30 min and filtered. The filtrate was kept at ambient temperature. Single crystals of the complex, suitable for X-ray diffraction, were grown from the filtrate upon slow evaporation within a few days. The crystals were isolated by filtration, washed with methanol and dried in air. Yield: 0.21 g (58%). Anal. Calcd. for $C_{10}H_{12}BrClCuN_2O$ (%): C, 33.82; H, 3.41; N, 7.89. Found (%): C, 33.95; H, 3.30; N, 7.81. IR data (KBr, cm^{-1}): 3198 (NH), 1640 (C=N). UV-Vis data in methanol [λ_{max} (nm)]: 230, 247, 278, 367.

2. 6. X-Ray Structure Determination

Single-crystal X-ray diffraction data for the complexes were collected on a Bruker Apex II CCD diffractometer at 298(2) K with Mo K_α radiation ($\lambda = 0.71073$ Å) by ω scan mode. The program SAINT was used for integration of the diffraction profiles.¹² The structures were solved by direct methods using the SHELXS program of the SHELXTL package and refined by full-matrix least-squares methods with SHELXL (semi-empirical absorption corrections were applied using the SADABS program).¹³ The positions of the non-hydrogen atoms were located in difference Fourier syntheses and least-squares refinement cycles, and finally refined anisotropically. All hydrogen atoms of the complexes were placed theoretically onto the specific atoms and refined isotropically as riding atoms. Crystallographic data and experimental details for structural analyses are summarized in Table 1. Selected bond lengths and angles for the complex are listed in Table 2.

Table 1. Crystallographic data and refinement details for the complexes.

	1	2	3	4
Formula	C ₁₀ H ₁₂ BrCuN ₃ O ₄	C ₂₀ H ₂₄ Br ₂ Cu ₂ N ₁₀ O ₂	C ₁₀ H ₁₂ Br ₂ CuN ₂ O	C ₁₀ H ₁₂ BrClCuN ₂ O
Formula weight	381.68	723.39	399.58	355.12
Crystal color, shape	Blue, block	Blue, block	Blue, block	Blue, block
Crystal system	Monoclinic	Orthorhombic	Orthorhombic	Orthorhombic
Space group	<i>P</i> 2 ₁	<i>Pbcn</i>	<i>Pbca</i>	<i>Pbca</i>
<i>a</i> (Å)	7.6706(10)	16.8624(12)	17.1761(11)	17.012(9)
<i>b</i> (Å)	8.1444(12)	7.1989(11)	6.8686(12)	6.930(4)
<i>c</i> (Å)	10.712(2)	21.0019(13)	21.3893(12)	21.828(11)
β (°)	94.035(2)	90	90	90
<i>V</i> (Å ³)	667.58(19)	2549.4(5)	2523.4(5)	2574(2)
<i>Z</i>	2	4	8	8
<i>D</i> _{calcd} (g cm ⁻³)	1.899	1.885	2.104	1.833
μ (Mo K α , mm ⁻¹)	4.641	4.843	8.044	4.990
Reflections collected	3909	12296	12465	12598
Unique	2304	2374	2348	2407
Observed reflections (<i>I</i> \geq 2 <i>s</i> (<i>I</i>))	2116	1714	1818	1931
Data/restraints/parameters	2304/1/173	2374/0/164	2348/0/146	2407/0/146
Goodness of fit on <i>F</i> ²	1.032	1.078	1.073	1.103
<i>R</i> ₁ , <i>wR</i> ₂ (<i>I</i> \geq 2 <i>s</i> (<i>I</i>)) ^a	0.0276, 0.0713	0.0435, 0.0888	0.0388, 0.0921	0.0431, 0.1029
<i>R</i> ₁ , <i>wR</i> ₂ (all data) ^a	0.0310, 0.0728	0.0710, 0.0985	0.0560, 0.0995	0.0563, 0.1091

$$^a R_1 = F_o - F_c/F_o, wR_2 = [\sum w(F_o^2 - F_c^2)/\sum w(F_o^2)]^{1/2}$$

Table 2. Selected bond distances (Å) and angles (°) for the complexes.

1			
Cu1–O1	1.913(4)	Cu1–O2	2.045(4)
Cu1–N1	1.929(5)	Cu1–N2	2.029(5)
O1–Cu1–N1	94.69(19)	O1–Cu1–N2	175.3(2)
N1–Cu1–N2	84.9(2)	O1–Cu1–O2	90.01(18)
N1–Cu1–O2	165.81(19)	N2–Cu1–O2	91.5(2)
2			
Cu1–O1	1.895(3)	Cu1–N1	1.938(4)
Cu1–N2	2.021(4)	Cu1–N3	1.969(4)
Cu1–N3A	3.184(5)	Cu1–N5A	2.565(5)
O1–Cu1–N1	92.84(15)	O1–Cu1–N3	88.92(16)
N1–Cu1–N3	176.27(19)	O1–Cu1–N2	170.86(17)
N1–Cu1–N2	84.39(17)	N3–Cu1–N2	93.37(18)
O1–Cu1–N3A	88.01(18)	N1–Cu1–N3A	72.81(18)
N2–Cu1–N3A	82.85(18)	N3–Cu1–N3A	103.99(18)
N5B–Cu1–N3A	162.34(18)	O1–Cu1–N5B	96.89(18)
N1–Cu1–N5B	89.96(18)	N2–Cu1–N5B	91.82(18)
N3–Cu1–N5B	93.09(18)		
Symmetry codes: A: 1 - <i>x</i> , 2 - <i>y</i> , 1 - <i>z</i> ; B: 1 - <i>x</i> , 1 - <i>y</i> , 1 - <i>z</i> .			
3			
Cu1–O1	1.892(4)	Cu1–N1	1.935(4)
Cu1–N2	2.017(4)	Cu1–Br2	2.3996(8)
O1–Cu1–N1	93.02(16)	O1–Cu1–N2	176.36(18)
N1–Cu1–N2	84.57(18)	O1–Cu1–Br2	89.01(11)
N1–Cu1–Br2	161.31(13)	N2–Cu1–Br2	94.15(13)
4			
Cu1–O1	1.918(3)	Cu1–N1	1.970(4)
Cu1–N2	2.044(4)	Cu1–Cl1	2.3001(17)
O1–Cu1–N1	93.14(14)	O1–Cu1–N2	174.39(16)
N1–Cu1–N2	84.56(16)	O1–Cu1–Cl1	89.63(10)
N1–Cu1–Cl1	161.44(12)	N2–Cu1–Cl1	94.18(12)

2. 7. Measurement of Urease Inhibitory Activity

The assay mixture, containing 25 μL (10U) of *jack bean* urease which was replaced by 25 μL of cell suspension (4.0×10^7 CFU/mL) for the urease assay of intact cells and 25 μL of the test compound, was pre-incubated for 1.5 h at room temperature in a 96-well assay plate. Urease activity was determined by measuring ammonia production using the indophenol method as described by Weatherburn.¹⁴

3. Results and Discussion

3. 1. General Chemistry

The Schiff base ligand was prepared by reaction of 4-bromosalicylaldehyde and *N*-methylethane-1,2-diamine in methanol. The ligand was not isolated and purified, and was used to prepare the complexes with copper salts (Scheme 1). Elemental analyses of the complexes are in accordance with the molecular structures proposed by the X-ray analysis. The complexes are stable in air at room temperature. The molar conductivity of complexes measured in methanol at concentration of 10^{-3} mol L⁻¹ is 20–45 Ω^{-1} cm² mol⁻¹, indicating the non-electrolytic nature of them in solution.¹⁵

3. 2. IR and UV-Vis Spectra

In the IR spectra the weak and sharp absorptions in the range 3150–3200 cm⁻¹ are assigned to the N–H vibrations of the Schiff base ligands. The characteristic C=N stretching is observed at 1630 cm⁻¹ as intense signals.¹⁶ The Schiff base ligand coordination to the copper atoms

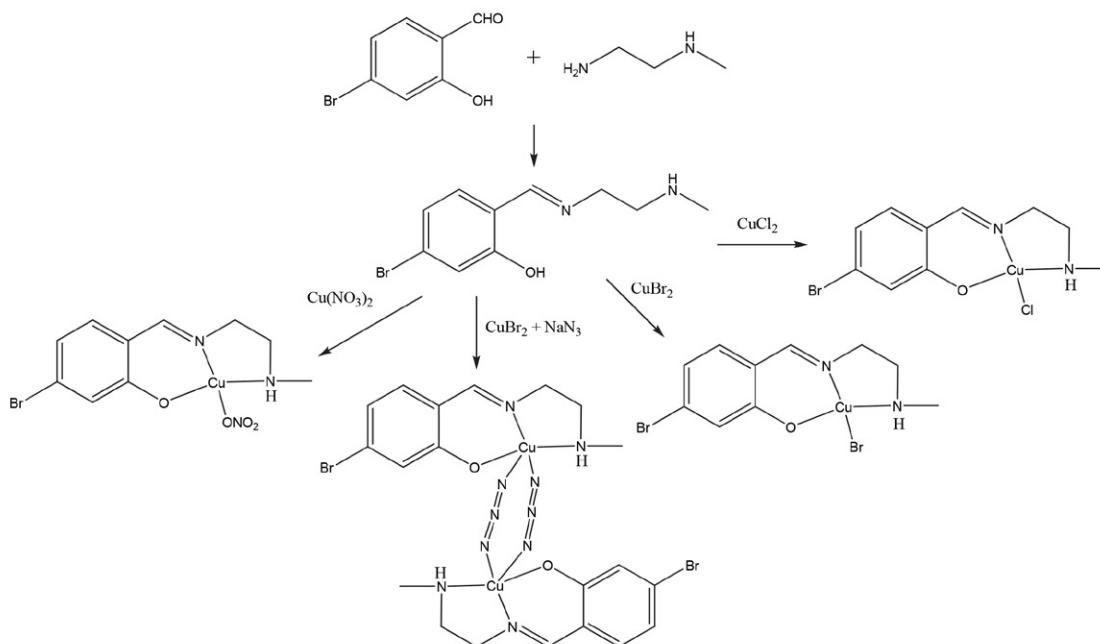
is substantiated by weak bands in the low wavenumbers 400–600 cm⁻¹ corresponding to $\nu(\text{Cu-N})$ and $\nu(\text{Cu-O})$. The IR spectrum of complex **2** shows the most intense absorption band at 2078 cm⁻¹ corresponding to the azide ligand.¹⁷ The Ar–O stretching bands are located at 1150–1200 cm⁻¹.¹⁸ The spectrum of complex **1** displays three absorption bands at 1421, 1272 and 1086 cm⁻¹ corresponding to the nitrate ligand.¹⁹

In the UV-vis spectra the bands at 230, 245–250 nm and 270–280 nm are attributed to the π - π^* and n - π^* transitions.²⁰ The bands at 360–370 nm can be assigned to the ligand to metal charge transfer transition (LMCT).²¹

3. 3. Structure Description of Complex 1

The molecular structure of complex **1** is shown in Fig. 1. The [CuL] units are linked by acetate ligand, to form one dimensional chain structure. The Cu atom is in a square pyramidal geometry, with the basal plane defined by the phenolate O, imino N and amino N atoms of the Schiff base ligand, and one acetate O atom, and with the apical position occupied by one acetate O atom. The Cu atom deviates from the plane defined by the four basal donor atoms by 0.078(2) Å. The square pyramidal coordination is distorted from ideal model, as evidenced by the bond angles in the basal plane, with *cis* and *trans* angles in the ranges of 84.9(2)–94.7(2)° and 165.8(2)–175.3(2)°, respectively. The Cu–O and Cu–N bond lengths are comparable to those observed in Schiff base copper complexes with acetate ligands.²²

In the crystal structure of the complex, the molecules are linked through N–H...O and C–H...O hydrogen bonds (Table 3), to form one dimensional chain along the *b* axis (Fig. 2).



Scheme 1. The synthetic procedure for the Schiff base and the complexes.

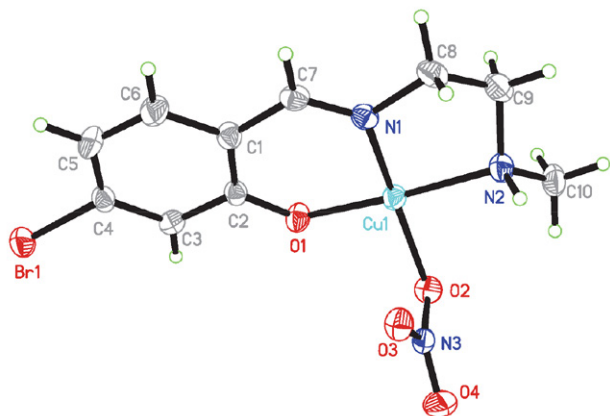


Fig. 1. A perspective view of the molecular structure of complex 1. Thermal ellipsoids are drawn at the 30% probability level.

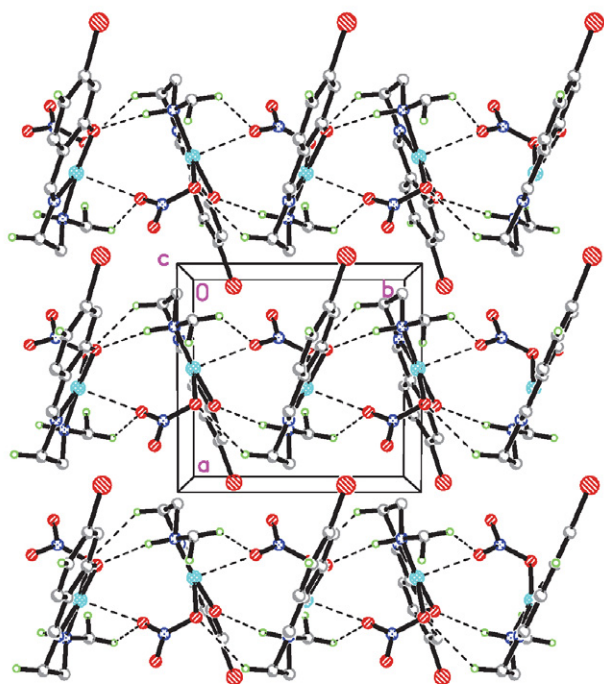


Fig. 2. Molecular packing structure of complex 1. Hydrogen bonds are drawn as dashed lines.

3. 4. Structure Description of Complex 2

The molecular structure of the $\mu_{1,1,3}$ -azido bridged polynuclear complex 2 is shown in Fig. 3. The adjacent two Cu atoms are bridged by two azide ligands, with distances of 3.314(1) and 5.000(1) Å, respectively. The Cu atom is coordinated in octahedral geometry, with the equatorial plane defined by the phenolate O, imino N and amino N atoms of the Schiff base ligand, and one azide N atom, and with the axial positions occupied by two azide N atoms. The Cu atom deviates from the equatorial plane by 0.102(2) Å. The octahedral coordination is distorted from ideal model, as evidenced by the bond angles. The *cis* and *trans* angles in the equatorial plane are in the ranges of

84.4(2)–93.4(2)° and 170.9(2)–176.3(2)°, respectively. The bond angles among the axial and equatorial donor atoms are in the range of 81.8(2)–96.9(2)°. The Cu–O and Cu–N bond lengths are comparable to those observed in Schiff base copper complexes with azide ligands.²³

In the crystal structure of the complex, the molecules are linked by azide ligands, to form one dimensional chain along the *b* axis. There are N–H...O and C–H...N hydrogen bonds (Table 3) within the chains (Fig. 4).

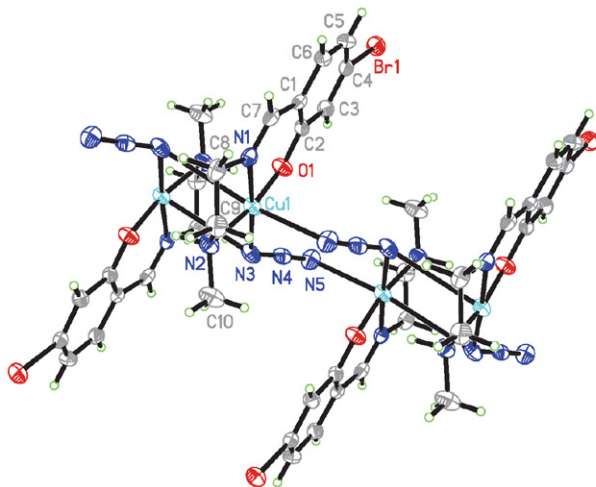


Fig. 3. A perspective view of the molecular structure of complex 2. Thermal ellipsoids are drawn at the 30% probability level. Unlabeled atoms are related to the symmetry operations $1 - x$, $2 - y$, $1 - z$ and B: $1 - x$, $1 - y$, $1 - z$.

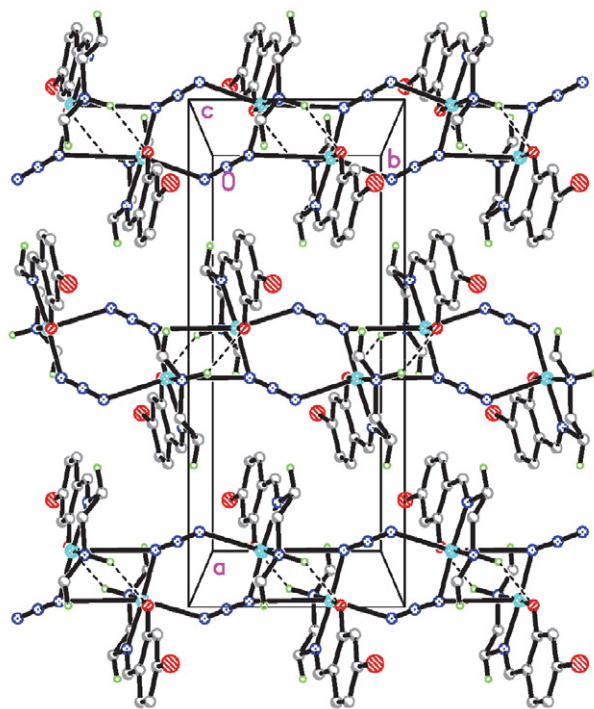


Fig. 4. Molecular packing structure of complex 2. Hydrogen bonds are drawn as dashed lines.

3. 5. Structure Description of Complexes 3 and 4

Molecular structures of complexes **3** and **4** are shown in Figs. 5 and 6, respectively. The two complexes are isostructural mononuclear copper compounds. The Cu atom in each complex is coordinated by the phenolate O, imino N and amino N atoms of the Schiff base ligand, and one halide atom, *viz.* Br for **3** and Cl for **4**. The Cu atoms deviate from the planes defined by the four donor atoms by 0.153(2) Å for **3** and 0.129(2) Å for **4**. The square planar coordination is distorted from ideal model, as evidenced by the bond angles, with *cis* and *trans* angles in the ranges of 84.6(2)–94.2(1)° and 161.3(1)–176.4(2)° for **3**, and 84.6(2)–94.2(1)° and 161.4(1)–174.4(2)° for **4**, respectively. The Cu–O and Cu–N bond lengths are comparable to those observed in Schiff base copper complexes with halide ligands.²⁴

In the crystal structure of complex **3**, the molecules are linked through N–H...O and C–H...Br hydrogen bonds (Table 3), to form zigzag chains along the *b* axis (Fig. 7). In the crystal structure of complex **4**, the molecules are linked through N–H...O hydrogen bonds (Table 3), to form zigzag chains along the *b* axis (Fig. 8).

Table 3. Hydrogen bond distances (Å) and bond angles (°) for the complexes.

D–H...A (D–H...A)	<i>d</i> (D–H)	<i>d</i> (H...A)	<i>d</i> (D...A)	Angle
		1		
N2–H2...O1 ^{#1}	0.98	2.08	3.037(6)	166(5)
C5–H5...O4 ^{#2}	0.93	2.59	3.448(6)	153(5)
C8–H8A...O2 ^{#1}	0.97	2.55	3.340(6)	139(5)
C10–H10C...O3 ^{#3}	0.96	2.51	3.145(6)	124(5)
		2		
N2–H2...O1 ^{#4}	0.98	2.24	3.067(5)	142(5)
C8–H8B...N5 ^{#5}	0.97	2.62	3.510(5)	152(5)
		3		
N2–H2B...O1 ^{#6}	0.98	2.48	3.311(6)	143(6)
N2–H2...Br2 ^{#6}	0.98	3.04	3.797(5)	135(6)
C7–H7...Br2 ^{#7}	0.93	2.88	3.779(5)	163(6)
		4		
N2–H2...O1 ^{#8}	0.98	2.39	3.240(6)	145(6)

Symmetry codes: #1: 1 – *x*, –1 – *y*, 1 – *z*; #2: *x*, *y*, 1 + *z*; #3: 1 – *x*, –½ + *y*, 1 – *z*; #4: –*x*, 1 – *y*, –*z*; #5: ½ – *x*, ½ + *y*, *z*; #6: –*x*, ½ + *y*, ½ – *z*; #7: ½ + *x*, *y*, ½ – *z*; #8: –*x*, –½ + *y*, ½ – *z*.

3. 6. Urease Inhibitory Activity

We investigated the urease inhibition of the complexes in an effort to find more potent compounds in comparison with previously reported compounds. The IC₅₀ values of complexes **1**, **3** and **4** are 1.72 ± 0.33, 1.05 ± 0.26 and 0.77 ± 0.15 μmol L⁻¹, respectively. However,

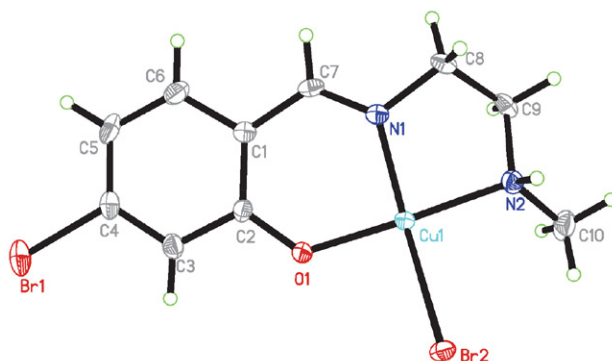


Fig. 5. A perspective view of the molecular structure of complex **3**. Thermal ellipsoids are drawn at the 30% probability level.

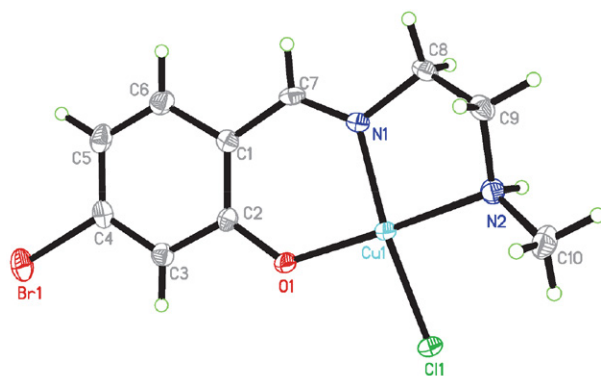


Fig. 6. A perspective view of the molecular structure of complex **4**. Thermal ellipsoids are drawn at the 30% probability level.

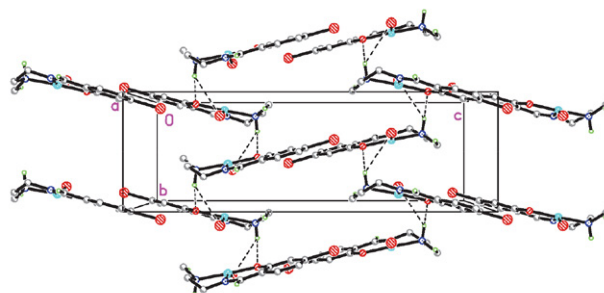


Fig. 7. Molecular packing structure of complex **3**. Hydrogen bonds are drawn as dashed lines.

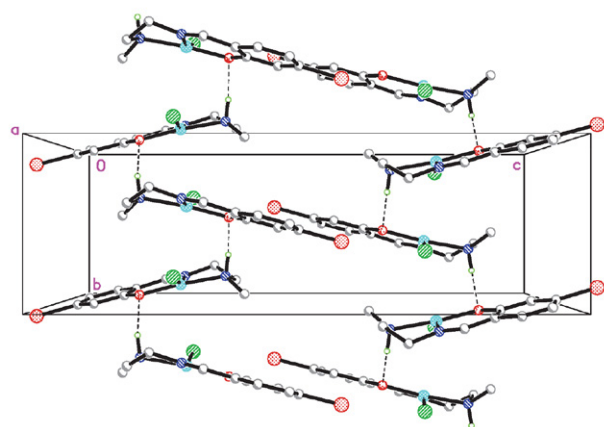


Fig. 8. Molecular packing structure of complex **4**. Hydrogen bonds are drawn as dashed lines.

complex **2** has medium activity, with IC_{50} value of $8.31 \pm 1.29 \mu\text{mol L}^{-1}$. The copper complexes have from medium to strong urease inhibitory activity, which is in accordance with those reported in literature.²⁵ Complex **2** has weaker activity than the other complexes, which might due to the larger size arise from polymerization. The hydrophobic area of the enzyme cannot comfortably accommodate the molecules with large sizes. Acetohydroxamic acid (AHA) was used as a reference, and with IC_{50} value of $27.8 \pm 2.12 \mu\text{mol L}^{-1}$. Thus, the copper complexes would be potential urease inhibitors that deserve further study.

4. Conclusion

In summary, four new copper complexes with the Schiff base ligand 5-bromo-2-(((2-methylamino)ethyl)imino)methyl)phenolate have been synthesized and characterized. X-ray single crystal structure analysis indicates that the Cu atoms in complexes **1**, **3** and **4** are in square planar geometry, and those in complex **2** are in octahedral geometry. The copper complexes have strong urease inhibitory activity, which deserves further study to explore new and efficient urease inhibitors.

Supplementary Materials

X-ray crystallographic data for the complexes have been deposited with the Cambridge Crystallographic Data Centre (The Director, CCDC, 12 Union Road, Cambridge, CB2 1 EZ, UK; e-mail: deposit@ccdc.cam.ac.uk; http://www.ccdc.cam.ac.uk; fax: +44-(0)1223-336033) and are available free of charge on request, quoting the deposition numbers CCDC 2083691–2083694.

Acknowledgments

This project was supported by the Heilongjiang Province Qiqihar Ecological Environment Monitoring Center.

5. References

1. L. Casali, L. Mazzei, O. Shemchuk, L. Sharma, K. Honer, F. Grepioni, S. Ciurli, D. Braga, J. Baltrusaitis, *ACS Sustainable Chem. Eng.* **2019**, *7*, 2852–2859. DOI:10.1021/acssuschemeng.8b06293
2. P. A. Karplus, M. A. Pearson, R. P. Hausinger, *Acc. Chem. Res.* **1997**, *30*, 330–337. DOI:10.1021/ar960022j
3. (a) B. Bano, Kanwal, K. M. Khan, A. Lodhi, U. Salar, F. Begum, M. Ali, M. Taha, S. Perveen, *Bioorg. Chem.* **2018**, *80*, 129–144; DOI:10.1016/j.bioorg.2018.06.007
(b) P. Y. Oikawa, C. Ge, J. Wang, J.R. Eberwein, L. L. Liang, L. A. Allsman, D. A. Grantz, G. D. Jenerette, *Nat. Commun.* **2015**, *6*, 8753; DOI:10.1038/ncomms9753
- (c) D. Coskun, D. T. Britto, W. Shi, H. J. Kronzucker, *Nat. Plants* **2017**, *3*, 17074. DOI:10.1038/nplants.2017.74
4. (a) S. V. Krupa, *Environ. Pollut.* **2003**, *124*, 179–221; DOI:10.1016/S0269-7491(02)00434-7 (b) J. L. Hand, B. A. Schichtel, M. Pitchford, W. C. Malm, N. H. Frank, *J. Geophys. Res. Atmos.* **2012**, *117*, D05209.
5. J. N. Galloway, F. J. Dentener, D. G. Capone, E. W. Boyer, R. W. Howarth, S. P. Seitzinger, G. P. Asner, C. C. Cleveland, P. A. Green, E. A. Holland, D. M. Karl, A. F. Michaels, J. H. Porter, A. R. Townsend, C. J. Vorosmarty, *Biogeochemistry* **2004**, *70*, 153–226. DOI:10.1007/s10533-004-0370-0
6. (a) A. Saeed, M. S. Khan, H. Rafique, M. Shahid, J. Iqbal. *Bioorg. Chem.* **2014**, *52*, 1–7; DOI:10.1016/j.bioorg.2013.10.001 (b) A. Hameed, K. M. Khan, S. T. Zehra, R. Ahmed, Z. Shafiq, S. M. Bakht, M. Yaqub, M. Hussain, A. de la Vega de Leon, N. Furtmann, J. Bajorath, H. A. Shad, M. N. Tahir, J. Iqbal, *Bioorg. Chem.* **2015**, *61*, 51–57. DOI:10.1016/j.bioorg.2015.06.004
7. F. Iftikhar, Y. Ali, F. A. Kiani, S. F. Hassan, T. Fatima, A. Khan, B. Niaz, A. Hassan, F. L. Ansari, U. Rashid, *Bioorg. Chem.* **2017**, *74*, 53–65. DOI:10.1016/j.bioorg.2017.07.003
8. (a) M. J. Todd, R. P. Hausinger, *Biochemistry* **2000**, *39*, 5389–5396; DOI:10.1021/bi992287m
(b) K. M. Khan, F. Rahim, A. Khan, M. Shabeer, S. Hussain, W. Rehman, M. Taha, M. Khan, S. Perveen, M. I. Choudhary, *Bioorg. Med. Chem.* **2014**, *22*, 4119–4123; DOI:10.1016/j.bmc.2014.05.057
(c) W.-W. Ni, H.-L. Fang, Y.-X. Ye, W.-Y. Li, C.-P. Yuan, D.-D. Li, S.-J. Mao, S.-E. Li, Q.-H. Zhu, H. Ouyang, Z.-P. Xiao, H.-L. Zhu, *Future Med. Chem.* **2020**, *12*, 1633–1645; DOI:10.4155/fmc-2020-0048
(d) Q. Liu, W.-K. Shi, S.-Z. Ren, W.-W. Ni, W.-Y. Li, H.-M. Chen, P. Liu, J. Yuan, X.-S. He, J.-J. Liu, P. Cao, P.-Z. Yang, Z.-P. Xiao, H.-L. Zhu, *Eur. J. Med. Chem.* **2018**, *156*, 126–136; DOI:10.1016/j.ejmech.2018.06.065
(e) W.-W. Ni, Q. Liu, S.-Z. Ren, W.-Y. Li, L.-L. Yi, H. Jing, L.-X. Sheng, Q. Wan, P.-F. Zhong, H.-L. Fang, H. Ouyang, Z.-P. Xiao, H.-L. Zhu, *Bioorg. Med. Chem.* **2018**, *26*, 4145–4152; DOI:10.1016/j.bmc.2018.07.003
(f) W.-K. Shi, R.-C. Deng, P.-F. Wang, Q.-Q. Yue, Q. Liu, K.-L. Ding, M.-H. Yang, H.-Y. Zhang, S.-H. Gong, M. Deng, W.-R. Liu, Q.-J. Feng, S. Tang, Z.-P. Xiao, H.-L. Zhu, *Bioorg. Med. Chem.* **2016**, *24*, 4519–4527; DOI:10.1016/j.bmc.2016.07.052
(g) Z.-P. Xiao, W.-K. Shi, P.-F. Wang, W. Wei, X.-T. Zeng, J.-R. Zhang, N. Zhu, M. Peng, B. Peng, X.-Y. Lin, H. Ouyang, X.-C. Peng, G.-C. Wang, H.-L. Zhu, *Bioorg. Med. Chem.* **2015**, *23*, 4508–4513; DOI:10.1016/j.bmc.2015.06.014
(h) Z.-P. Xiao, Z.-Y. Peng, J.-J. Dong, R.-C. Deng, X.-D. Wang, H. Ouyang, P. Yang, J. He, Y.-F. Wang, M. Zhu, X.-C. Peng, W.-X. Peng, H.-L. Zhu, *Eur. J. Med. Chem.* **2013**, *68*, 212–221; DOI:10.1016/j.ejmech.2013.07.047
(i) Z.-P. Xiao, Z.-Y. Peng, J.-J. Dong, J. He, H. Ouyang, Y.-T. Peng, C.-L. Lu, W.-Q. Lin, J.-X. Wang, Y.-P. Xiang, H.-L. Zhu, *Eur. J. Med. Chem.* **2013**, *63*, 685–695. DOI:10.1016/j.ejmech.2013.03.016

9. (a) M. K. Rauf, S. Yaseen, A. Badshah, S. Zaib, R. Arshad, Imtiaz-ud-Din, M. N. Tahir, J. Iqbal, *J. Biol. Inorg. Chem.* **2015**, *20*, 541–554; DOI:10.1007/s00775-015-1239-5
(b) X. Dong, Y. Li, Z. Li, Y. Cui, H. Zhu, *J. Inorg. Biochem.* **2012**, *108*, 22–29; DOI:10.1016/j.jinorgbio.2011.12.006
(c) Y. Gou, M. Yu, Y. Li, Y. Peng, W. Chen, *Inorg. Chim. Acta* **2013**, *404*, 224–229. DOI:10.1016/j.ica.2013.03.045
10. (a) H. Kargar, *Transit. Met. Chem.* **2014**, *39*, 811–817; DOI:10.1007/s11243-014-9863-4
(b) A. Sahraei, H. Kargar, M. Hakimi, M. N. Tahir, *J. Mol. Struct.* **2017**, *1149*, 576–584; DOI:10.1016/j.molstruc.2017.08.022
(c) A. Sahraei, H. Kargar, M. Hakimi, M. N. Tahir, *Transit. Met. Chem.* **2017**, *42*, 483–489; DOI:10.1007/s11243-017-0152-x
(d) A. Jamshidvand, M. Sahihi, V. Mirkhani, M. Moghadam, I. Mohammadpoor-Baltork, S. Tangestaninejad, H.A. Rudbari, H. Kargar, R. Keshavarzi, S. Gharaghani, *J. Mol. Liquids* **2018**, *253*, 61–71; DOI:10.1016/j.molliq.2018.01.029
(e) H. Kargar, R. Behjatmanesh-Ardakani, V. Torabi, M. Kashani, Z. Chavoshpour-Natanzi, Z. Kazemi, V. Mirkhani, A. Sahraei, M. N. Tahir, M. Ashfaq, K. S. Munawar, *Polyhedron* **2021**, *195*, 114988; DOI:10.1016/j.poly.2020.114988
(f) H. Kargar, F. Aghaei-Meybodi, R. Behjatmanesh-Ardakani, M. R. Elahifard, V. Torabi, M. Fallah-Mehrjardi, M. N. Tahir, M. Ashfaq, K. S. Munawar, *J. Mol. Struct.* **2021**, *1230*, 129908; DOI:10.1016/j.molstruc.2021.129908
(g) H. Kargar, A. A. Ardakani, M. N. Tahir, M. Ashfaq, K. S. Munawar, *J. Mol. Struct.* **2021**, *1233*, 130112. DOI:10.1016/j.molstruc.2021.130112
11. (a) H. Zhu, Z.-Z. Wang, B. Qi, T. Huang, H.-L. Zhu, *J. Coord. Chem.* **2013**, *66*, 2980–2991; DOI:10.1080/00958972.2013.821198
(b) L. Habala, A. Roller, M. Matuska, J. Valentova, A. Rompel, F. Devinsky, *Inorg. Chim. Acta* **2014**, *421*, 423–426; DOI:10.1016/j.ica.2014.06.035
(c) F.-M. Wang, L.-J. Li, G.-W. Zang, T.-T. Deng, Z.-L. You, *Acta Chim. Slov.* **2020**, *67*, 1155–1162; DOI:10.17344/acsi.2020.6056
(d) H. Zhao, X.-P. Tan, Q.-A. Peng, C.-Z. Shi, Y.-F. Zhao, Y. Cui, *Acta Chim. Slov.* **2020**, *67*, 638–643. DOI:10.17344/acsi.2019.5644
12. G. M. Sheldrick. SAINT (version 6.02), SADABS (version 2.03), Madison (WI, USA): Bruker AXS Inc, **2002**.
13. (a) G. M. Sheldrick, *Acta Crystallogr.* **2015**, *C71*, 3–8; (b) G. M. Sheldrick. SADABS Program for Empirical Absorption Correction of Area Detector, University of Gottingen, Germany **1996**.
14. M. W. Weatherburn, *Anal. Chem.* **1967**, *39*, 971–974. DOI:10.1021/ac60252a045
15. W. J. Geary, *Coord. Chem. Rev.* **1971**, *7*, 81–122. DOI:10.1016/S0010-8545(00)80009-0
16. K. R. Surati, B. T. Thaker, *Spectrochim. Acta A* **2010**, *75*, 235–242. DOI:10.1016/j.saa.2009.10.018
17. (a) S. S. Massoud, F. A. Mautner. *Inorg. Chim. Acta*, **2005**, *358*, 3334–3340; DOI:10.1016/j.ica.2005.05.007
(b) A. Ray, S. Banerjee, R. J. Butcher, C. Desplanches, S. Mitra, *Polyhedron* **2008**, *27*, 2409–2415. DOI:10.1016/j.poly.2008.04.018
18. Y.-M. Zhou, X.-R. Ye, F.-B. Xin, X.-Q. Xin, *Transit. Met. Chem.* **1999**, *24*, 118–120. DOI:10.1023/A:1006989707001
19. M. F. Iskander, T. E. Khalil, R. Werner, W. Haase, I. Svoboda, H. Fuess, *Polyhedron* **2000**, *19*, 949–958. DOI:10.1016/S0277-5387(00)00340-5
20. L. Pogany, J. Moncol, M. Gal, I. Salitros, R. Boca, *Inorg. Chim. Acta* **2017**, *462*, 23–29. DOI:10.1016/j.ica.2017.03.001
21. A. Jayamani, M. Sethupathi, S. O. Ojwach, N. Sengottuvelan, *Inorg. Chem. Commun.* **2017**, *84*, 144–149. DOI:10.1016/j.inoche.2017.08.013
22. (a) P. Bhowmik, S. Chattopadhyay, A. Ghosh, *Inorg. Chim. Acta* **2013**, *396*, 66–71; DOI:10.1016/j.ica.2012.10.003
(b) K. Abe, K. Matsufuji, M. Ohba, H. Okawa, *Inorg. Chem.* **2002**, *41*, 4461–4467. DOI:10.1021/ic020002f
23. (a) P. K. Bhaumik, K. Harms, S. Chattopadhyay, *Polyhedron* **2014**, *68*, 346–356; DOI:10.1016/j.poly.2013.10.031
(b) J. Wang, Y. Luo, Y. Zhang, Y. Chen, F. Gao, Y. Ma, D. Xian, Z. You, *J. Coord. Chem.* **2021**, *74*, 1028–1038. DOI:10.1080/00958972.2020.1861603
24. (a) H. Adams, D. E. Fenton, S. R. Haque, S. L. Heath, M. Ohba, H. Okawa, S. E. Spey, *J. Chem. Soc. Dalton Trans.*, **2000**, 1849–1856; DOI:10.1039/b001395l
(b) M. Das, S. Chattopadhyay, *J. Mol. Struct.* **2013**, *1051*, 250–258. DOI:10.1016/j.molstruc.2013.07.045
25. (a) L. Pan, C. Wang, K. Yan, K. Zhao, G. Sheng, H. Zhu, X. Zhao, D. Qu, F. Niu, Z. You, *J. Inorg. Biochem.* **2016**, *159*, 22–28; DOI:10.1016/j.jinorgbio.2016.02.017
(b) Y. Luo, J. Wang, B. Zhang, Y. Guan, T. Yang, X. Li, L. Xu, J. Wang, Z. You, *J. Coord. Chem.* **2020**, *73*, 1765–1777. DOI:10.1080/00958972.2020.1795645

Povzetek

Inhibitorji urease lahko inhibirajo proces razgradnje sečnine in zmanjšajo onesnaženje zraka zaradi sproščanja amoniaka. Sintetizirali smo štiri nove bakrove(II) komplekse $[\text{CuL}(\text{ONO}_2)]_n$ (**1**), $[\text{Cu}_2\text{L}_2(\mu_{1,3}\text{-N}_3)_2]$ (**2**), $[\text{CuBrL}]$ (**3**) in $[\text{Cu-CLL}]$ (**4**), kjer je L = 5-bromo-2-(((2-metilamino)etil)imino)metil)fenolat. Komplekse smo okarakterizirali z elementno analizo, IR in UV-Vis spektroskopijo, molsko prevodnostjo in monokristalno rentgensko difrakcijo. Rentgenska analiza razkiva, da imajo Cu atomi v kompleksih **1** in **2** kvadratno piramidalno koordinacijo in v kompleksih **3** in **4** kvadratno planarno koordinacijo. Molekule so povezane z vodikovimi vezmi in $\pi\cdots\pi$ interakcijami. S testiranjem smo ugotovili, da imajo kompleksi inhibitory vpliv na ureazo stročnice *Canavalia ensiformis*.



Except when otherwise noted, articles in this journal are published under the terms and conditions of the Creative Commons Attribution 4.0 International License

Scientific paper

Lomustine Incorporated Lipid Nanostructures Demonstrated Preferential Anticancer Properties in C6 Glioma Cell Lines with Enhanced Pharmacokinetic Profile in Mice

Bhabani Sankar Satapathy,^{1,*} Ladi Alik Kumar,² Gurudutta Pattnaik² and Binapani Barik²

¹ School of Pharmaceutical Sciences, Siksha 'O' Anusandhan (Deemed to be University), Bhubaneswar, Odisha, India

² Centurion University of Technology & Management, Odisha, India

* Corresponding author: E-mail: bhabanisatapathy@soa.ac.in

Received: 05-30-2021

Abstract

Effective treatment of glioma still stands as a challenge in medical science. The work aims for the fabrication and evaluation of lipid based nanostructures for improved delivery of lomustine to brain tumor cells. Experimental formulations (LNLs) were developed by modified lipid layer hydration technique and evaluated for different *in vitro* characteristics like particle size analysis, surface charge, surface morphology, internal structure, *in vitro* drug loading, drug release profile etc. Anticancer potential of selected LNLs was tested *in vitro* on C6 glioma cell line. Electron microscopic study depicted a size of less than 50 nm for the selected LNLs along with 8.8% drug loading with a sustained drug release tendency over 48 h study period. Confocal microscopy revealed reasonable internalization of the selected LNL in C6 cells. LNLs were found more cytotoxic than free drug and blank nanocarriers as depicted from MTT assay. The selected LNL showed improved pharmacokinetic profile both in blood and brain in the experimental mice models along with negligible hemolysis in mice blood cells. Further studies are warranted for the future translation of LNLs at clinics.

Keywords: Lomustine; lipid nanostructure; C6 glioma cells; cellular uptake; pharmacokinetic; hemolysis

1. Introduction

Effective treatment of brain tumor remains a challenge in medical science. Gliomas are the most common type of tumors of brain and central nervous system.¹ Based on the type of primary cells along with molecular characteristics, gliomas can be of astrocytomas, ependymomas, oligodendrogliomas etc. Glioma is characterized by its uncontrolled cellular proliferation, diffused infiltration along with significant angiogenesis.² Glioma at its fourth stage is referred to as glioblastoma multiforme, which is the most dangerous stage with poor prognosis and an average survival rate of 1–2 years.³ In spite of all the advanced medical strategies, death rate of glioma patients is increasing at an alarming rate all over the world. The treatment failures may be attributed to the delicate and sensitive characteristics of brain tissue, which limits effective application of surgery or radiation

therapy; whereas presence of blood-brain barrier (BBB) further worsens the case.⁴ BBB is the most complex, tight endothelial barrier, which strictly checks the entry of therapeutic molecules into the brain and thus stands as a serious challenge for chemotherapy.^{5,6} Although, many conventional anticancer drugs are available in clinical practice, but majority of them fails to maintain the desired therapeutic concentration in the brain tissue for a sufficient period of time due to their inability to pass effectively through BBB.⁷ Some lipophilic drugs like carmustine, temozolomide, bevacizumab etc. are being claimed to cross BBB, but shorter half-life along with severe dose related toxic effects associated with them throw additional challenges to get desired treatment outcomes.^{8,9} In this context, novel drug delivery strategies like nanoliposomes, nanoparticles, polymeric micelles, niosomes, dendrimers etc. have been investigated

widely in past years to improve the efficacy of conventional chemotherapeutic agents for the treatment of glioma.^{10,11,12} However, till today, very few of them have been approved to be used in clinical practice. Among various types of nanocarrier platforms, nanosize lipid based vesicular carriers have been largely preferred for successful delivery of toxic chemotherapeutic drugs to brain.^{13,14} Due to high lipophilic nature as well as ultra small size, they fulfill the prime requisite criteria to overcome BBB to get into the brain. Phospholipid based nanostructures (NLs) are the ultra-micron size phospholipid vesicles consisting of self assembled lipid bilayers enclosing small aqueous phase in their core.¹⁵ Due to this architectural uniqueness, they act as dual platform for both hydrophobic and hydrophilic molecules.¹⁶ The hydrophobic/lipophilic agents get entrapped in the outer lipid bilayer, where as the hydrophilic agents remain encapsulated in the aqueous core.¹⁵ NLs owing to their lipophilicity, biodegradability, non-immunogenicity, biocompatibility, sustained drug release property, ease of surface manipulation etc. have drawn the attention of formulation scientists as preferred drug delivery vehicles in nanomedicine based research.^{17,18} Due to sustained delivery of the loaded cargo as well as site-specific delivery, the dose of the cytotoxic anti-cancer drugs is expected to be reduced, which leads to better treatment outcome and fewer side effects.

Lomustine (LS) is a nitrosourea class of antineoplastic agent, which is used in the treatment of various types of malignancies, including glioma.¹⁹ It inhibits protein synthesis by causing alkylation and cross-linking in the nucleic acids (DNA/RNA). Being lipophilic in nature, it possesses the capacity to cross BBB, however, its short half life and deadly side effects like severe bone marrow depression, leucopenia, etc. limits its effective use in the treatment of glioma.^{20,21} Thus, there is a need to develop novel strategies for the safer and effective delivery of LS to brain and thereby reducing the dose-related side effects associated with the conventional forms.

Kevin A. Harvey et al. studied anticancer properties of LS in conjunction with docosahexaenoic acid (DHA) in glioblastoma cell lines. They studied effects of LS, alone and in combination with DHA in C6 human glioblastoma cell line.¹⁹ In another study, LS nanoparticles prepared by molecular envelope technology was tested on C6 glioblastoma bearing animal model.²¹ Another work reported an optimized method of development of poly (D,L-lactide-co-glycolide) based LS nanoparticles and investigated their anticancer potential in lung cancer cell line L132.²² However, to our knowledge, no reports are available on the anticancer potential of lomustine loaded lipid nanostructures (LNLs) on C6 glioma cells and also on their *in vivo* plasma/brain pharmacokinetic (PK) profile. Haemolysis assay for LNLs in mice RBC further adds novelty to the work, which is an important piece of information for safe biomedical application.

In the lieu of which, the present study aims to investigate the anticancer potential of optimized LNLs on rat glioma cells along with evaluation of both blood and brain PK profiles in experimental animal model. The LNLs were prepared by conventional method with optimization of critical manufacturing conditions to achieve the desired nanosize. Preferably, we wanted to keep the size of LNLs within a range of 50–100 nm to achieve effective permeation into brain as well as to escape from reticuloendothelial system. The experimental LNLs were evaluated by different *in vitro* techniques and the optimized formulation was tested for its *in vitro* anticancer effectiveness in C6 glioma cells. Further *in vivo* blood and brain PK study was also carried out in experimental mice to estimate the potentiality of the optimized formulation both qualitatively and quantitatively for the treatment of glioma.

2. Materials & Methods

2.1. Materials

LS was obtained as a gift sample from Cipla laboratories (Goa, India). Cholesterol (CHL), soya-L- α -lecithin (SL), 1,2-distearoyl-sn-glycero-3-phosphatidylethanolamine (DSPE) were procured from Merck (Mumbai, India). Chloroform, butylated hydroxytoluene (BHT), fluorescein isothiocyanate (FITC), were purchased from Hi-media Laboratories Pvt. Ltd (Mumbai, India). 4',6-Diamidino-2-phenylindole (DAPI) and tetrazolium dye 3-(4,5-dimethylthiazol-2-yl)-2,5-diphenyltetrazolium bromide (MTT) were purchased from Sigma-Aldrich (Bangalore, India). C6 glioma cells were procured from National Center for Cell Science (Pune, India). All other chemicals used in the experiment were of analytical grade.

2.1.1. Animals

For PK studies, healthy Swiss albino mice of either sex (male: female ratio 1:1) were used. All animal related experiments were in accordance with CPCSEA guidelines. Animals were kept in polypropylene cages and maintained in the Jadavpur university animal house at normal room temperature (20–25 °C), 55% relative humidity environment with normal day and night cycle. Before experiments, animals were properly fed standard diet and drinking water *ad libitum*. The guidelines of Animal Ethical Committee, Jadavpur University were followed strictly during the entire study period. The animals were kept for three weeks in the animal house environment before study. A total number of 72 mice were used for plasma PK study, where as 56 animals were used for brain PK study. For hemolysis assay, total 30 animals were used.

2. 2. Methods

2. 2. 1. Method of Development of Experimental LNLs

The experimental LNLs were prepared by conventional thin film hydration method with necessary modification of process parameters.²⁴ For the formulation development, soya-L- α -lecithin (SL) was used as the main phospholipid. Along with that, we used DSPE and CHL. Briefly, weighed amount of LS, SL, CHL along with DSPE were dissolved in a required volume of chloroform taken in a 250 ml round bottom flask. To this mixture, BHA (2% w/v) was added as an antioxidant, since all phospholipids are generally sensitive to oxidation. The prepared mixture was then subjected to gentle rotation along with evaporation of the solvent in a rotary vacuum evaporator (Rotavap, PBU-6, Superfit, Mumbai, India), connected with a water bath. The temperature of the water bath was kept at 40 °C. After, evaporation of chloroform, a thin film was formed along the inner wall of the round bottom flask. The flask was then kept in a dessicator overnight, which caused further removal of any residues of organic solvent still left in the thin film. On day 2, the formed thin film was hydrated with phosphate buffer saline (PBS), pH 7.4 for about an hour at a rotation of 130 rpm. During this period, the formed film was completely dispersed in the PBS. Following hydration, the mixture was subjected to sonication in a bath-type sonicator (Trans-o-sonic, Mumbai, India). Sonication helps the reduction of large size vesicles into desired ultra small size range. After sonication, the formulation was allowed to stand for 1 h at room temperature followed by storage in a refrigerator overnight at 4 °C. On next day (day 3), the sample was subjected to cold centrifugation at 15,000 rpm for 45 minutes (Sigma Lab Centrifuge, UK). After centrifugation, the supernatant was discarded and the sediments were collected, which was stored at –20 °C overnight. The pre-cooled samples were then lyophilized for 10 h (laboratory lyophilizer, Kolkata, India) to obtain dry powdered formulation and stored in a refrigerator (4 °C).

2. 2. 2. Development of Fluorescent LNLs

For cellular uptake study, fluorescent LNLs were prepared with FITC. For this, FITC at a concentration 0.4% w/v was dissolved in a required volume of chloroform and ethanol mixture. From this stock preparation, about 50 μ l was used added during the first step of preparation of LNLs. All other steps mentioned above remained unchanged.²⁵

2. 3. In vitro Studies of Experimental LNLs

2. 3. 1. Determination of Average Vesicle Diameter (Z-average) and Surface Potential

For the determination of mean vesicle diameter (Z-average), polydispersity index (PDI) and surface charge (zeta potential) of the experimental formulations, a weighed amount of the formulation was dispersed in milli-

Q water, sonicated for 5 minutes and observed under a dynamic light scattering (DLS) instrument (DLS-nano ZS, Zetasizer, Malvern Instrument Ltd, UK).²³ The data was interpreted by instrument software.

2. 3. 2. Percentage of Drug Loading and Loading Efficiency

For the calculation of amount of LS loaded in the experimental NLs, about 2 mg of the lyophilized LNLs was dissolved in required volume of acetonitrile. The sample was then sonicated in a bath sonicator for 10 min. After that, it was vortexed for another 3 min followed by centrifugation at 15,000 rpm. After centrifugation, the sediments were discarded and the absorbance of the collected supernatant was measured at 230 nm in UV-visible spectrophotometer (Advanced Microprocessor UV-Visible single beam, Intech 295, India).^{24,27}

The amount of LS loaded in the experimental LNLs was calculated by applying following formula

$$\% \text{ LS loading} = \frac{\text{Amount of LS in LNLs}}{\text{Amount of LNLs obtained}} \times 100$$

$$\% \text{ LS loading efficiency} = \frac{\text{Practical \% LS loading}}{\text{Theoretical \% LS loading}}$$

2. 3. 3. Yield Percentage

To determine the % yield of each formulation batch, the fully dried LNLs obtained after lyophilization was weighed after each batch run.²⁴ The % yield was calculated by applying following equation.

$$\% \text{ Yield} = \frac{\text{Amount of LNLs obtained after lyophilization}}{\text{Total amount of all components used in the formulation batch}} \times 100$$

2. 3. 4. Surface Morphology Study by Field Emission Scanning Electron Microscopy (FESEM)

To obtain surface morphology of the experimental formulation, electron microscope was used (JSM 6100, JEOL, Japan). For the experiment, lyophilized LNLs was spread on a carbon tape, fixed over a stub. Platinum coating was applied on the tested sample for 5 min with a voltage of 10 kV by means of a platinum coater.²² Finally the samples were observed under FESEM under liquid nitrogen conditions.²³

2. 3. 5. Cryo-Transmission Electron Microscopy (Cryo-TEM)

For Cryo-TEM analysis, weighed amount of lyophilized LNLs was dispersed in milli-Q water. The disper-

sion was vortexed in a cyclomixture for 5 min and a minute quantity of the dispersed LNLs (4 μ l) was taken on a clean grid. The sample was then immediately vitrified in liquid ethane followed by storage in liquid nitrogen condition until imaging.^{24,28} Images of the sample was taken with the help of an electron microscope (Tecnai Polara, version 4.6, Netherlands) equipped with an FEI Eagle 4K x 4K charge-coupled device (CCD) camera. During imaging, vitreous grids were transferred into the electron microscope with the help of a cryostage. Throughout the experiment, the temperature of the samples was maintained -170 °C to observe the LNLs in their native form without any damage to the internal structure.

2. 3. 6. In vitro Drug Release Study

For the *in vitro* drug release study of the optimized LNLs, dialysis bag method was employed.^{24,28} The study was conducted at both pH 5 and pH 7.4. For the experiment, a weighed amount of lyophilized sample was dispersed in PBS pH 7.4 containing sodium lauryl sulfate as a solubilizing agent (release medium). The dispersion was put inside a dialysis bag. The two ends of the dialysis bag were tied with the thread and the whole system was immersed in a beaker containing 100 ml of the above release medium. After that, the beaker was placed on a magnetic stirrer at a rotation of 300 rpm using a magnetic bead. At various time intervals for 24 h, 1 ml of sample was withdrawn from the beaker with simultaneous replacement of the fresh release medium to maintain the sink condition. Similar procedure was followed for drug release study at pH 5. Each set was repeated in triplicate. The samples after collection were filtered with the help of membrane filter followed by measurement of the absorbance at 229 nm with the help of High performance liquid chromatography system.

2. 3. 7. Estimation of Drug Release Kinetics

Release kinetics helps to predict the mechanism of drug release from the experimental LNLs. For this, the data obtained from the *in vitro* drug release studies were fitted in various kinetic models. We determined the release pattern of LNLs in five different models such as zero order (cumulative amount of drug released Vs time), first order (logarithmic value of cumulative amount of drug remained to be released Vs time), Higuchi (cumulative amount of drug released Vs square root of time), Korsmeyer–Peppas (logarithmic value of cumulative amount of drug released Vs logarithmic value of time), Hixson–Crowell (cube root of percentage drug remained to be released Vs time).²⁶ The linearity of the plots was assessed from the calculated R^2 values.

2. 3. 8. Assessment of in vitro Cytotoxicity

The *in vitro* cytotoxic effect of the LNLs was tested by MTT assay on C6 rat glioma cells and the effect was

compared to that of free LS suspension at equivalent drug concentrations.²⁹ For the experiment, the tested cell line was cultured in Dulbecco's modified eagle's medium containing 10% fetal bovine serum in a 96 well culture plate and maintained inside a CO_2 -incubator at 37 °C. After attaining required density of cells in the plates (5×10^3 cells per well), the cells were treated with varying concentrations of LNLs, free drug suspension along with blank NLs (without drug). As negative control, few of the wells were treated with equivalent volumes of pure culture medium. After 48 h, media in each well was discarded and about 100 μ l of MTT solution (1 mg/ml) was added to each well. The plate was kept inside CO_2 -incubator for another 4 h. After incubation, MTT solution was removed out of the well followed by addition of dimethyl sulfoxide (100 μ l) in each well. Addition of dimethyl sulfoxide caused solubilization of formazan crystals to produce a purple color. The intensity of the color is related to the number of viable cells present after treatment in the well. The optical density was measured at 560 nm by micro plate reader (Spectra Max, Molecular Devices Corporation, Sunnyvale, USA). Percentage cell viability was evaluated by following formula

$$\% \text{ cell viability} = \frac{\text{Optical density of the sample at 560 nm of treated cells}}{\text{Optical density of the sample at 560 nm of untreated cells}} \times 100$$

2. 3. 9. Assessment of Internalization Efficiency

The internalization capacity of the selected fluorescent lipid nanostructures (FITC-LNLs) was tested on the C6 cells with the help of fluorescence microscopy.^{29,30} For the experiment, the cells were seeded in six-well culture plates and allowed to grow on cover slips at a density of 10^4 cells per well. The volume of cell culture was taken as 3 ml per well and incubated at 37 °C in CO_2 -incubator for 24 h. FITC-LNL was then added to the culture wells at two different subinhibitory concentrations of 50 ng/ml and 100 ng/ml. After 0.5 h, cover slips were taken out and carefully washed with PBS. The treated cells were fixed with 4% paraformaldehyde solution. Following fixation, the cells were washed twice with fresh PBS and stained with DAPI. Cover slips were dried and mounted on glass slide for imaging by a fluorescence microscope (Carl Zeiss, Oberkochen, Germany).

2. 4. In vivo Studies

2. 4. 1. Plasma and Brain Pharmacokinetic Studies

Drug PK profile was studied both in plasma and brain tissue in healthy Swiss albino mice (body weight 20–25 g). For the PK study, animals were divided into three groups.^{22,30} Group I animals were intravenously administered LS suspension as per dose. Group II animals were intravenously (*i.v.*) administered LNLs, containing LS equivalent to 6.5 mg/kg. Group III animals received sa-

line (control group). At each time point of sample collection in Group I and II, 3 animals were taken for both plasma and brain PK studies, whereas for Group III (control group) 2 animals were taken for each time point of the study.

For the plasma PK study, post *i.v.* dosing, blood samples were collected from each set of animals at 0.5, 1, 2, 4, 6, 8, 10, 12, and 20 h intervals by heart puncture in heparinized tubes. A total number of 54 mice (27 each for Group I and II) were used in test groups and 18 mice were used for control groups. The blood samples were centrifuged using cold centrifuge at 5000 rpm for 10 min. Plasma was collected and stored at $-40\text{ }^{\circ}\text{C}$ till analysis.

For brain PK study, similar procedure as described above was followed. After *i.v.* injection, the animals were sacrificed at 0.5, 1, 2, 4, 8, 12 and 24 h intervals. Thus, a total number of 42 mice (21 each for Group I and II) were used in test groups whereas 14 mice were used for the control group. Brains of each animal were removed. The whole brain was homogenized in a tissue homogenizer in PBS (pH 7.4). The homogenates were stored at $-70\text{ }^{\circ}\text{C}$ until further analysis.

For the determination of LS concentration in plasma samples, a Liquid chromatography with tandem mass spectrometry (LCMS/MS) technique was employed. The LCMS/MS Agilent C₁₈ column was used. The mobile phase for the analysis was composed of acetonitrile, milli Q water along with formic acid (0.1%). The flow rate of mobile phase was kept as 0.4 ml/min. Sample volume for injection into chromatographic column was 20 μl . The analyte was monitored using mass spectrometer equipped with a double quadrupole along with electrospray ionization interface, operated in a positive mode (ESI+). To extract LS, samples were extracted with about three volume of methyl-tert-butyl ether. The mixture was then vortexed for 5 minutes followed by centrifugation at 3000 rpm for 10 min. After the process, the extracted LS present in the supernatant was collected. The organic solvent was allowed to dry under nitrogen atmosphere. For LCMS/MS analysis, the dried samples were then mixed in 100 ml of mobile phase (acetonitrile: water: formic acid). From the prepared stock, about 50 ml of reference standard solution was added in each sample. From the mixture, about 20 μl sample was injected into the LCMS/MS column (Agilent 6410, Triple Quad MS-MS, USA). The important PK parameters i.e.

area under the curve (AUC), area under the first moment curve (AUMC), volume of distribution (Vd), mean residence time (MRT), total body clearance (Cl_t) etc. were determined using non-compartmental PK Solver software (Version 2.0).

2. 4. 2. Hemolysis Study

To check the biocompatibility and safety profile of the experimental lipid nanocarriers, hemolysis assay was carried out. For the study, blood samples were collected from Swiss albino mice. The samples were collected in pre-heparinized tubes, followed by cold centrifugation at 5000 rpm for 5–7 min. After that, the red blood cells (RBCs) were washed with PBS (pH 7.4). In a 96 well plate, a measured amount of RBC suspension (190 μl) was taken and treated with varying concentration of LNLs, free LS along with blank NLs (without drug). Double distilled water was used as the positive control. The samples were incubated for 1 h at 37 $^{\circ}\text{C}$ followed by centrifugation for 5 min at 5000 rpm to separate the un-lysed RBCs (as sediments). The supernatant was then taken and absorbance of the sample was measured at 570 nm. Percentage hemolysis was calculated as per the previously reported method.³²

2. 5. Statistical Analysis

All the experiments were carried out triplicate for accuracy and reproducibility. Data was expressed as the mean \pm standard deviation (SD). One-way ANOVA was used to evaluate statistical followed by Tukey *post hoc* test with the help of Origin Pro 8 software. Differences were considered statistically significant when $p < 0.05$ at 95% confidence level.

3. Results

3. 1. In vitro Studies

3. 1. 1. Formulation Optimization

By varying concentration of drug and lipids along with specific manufacturing parameters, we prepared several formulations. All the formulations were characterized

Table 1. Formulation components, % yield, % drug loading and % drug loading efficiency of selected experimental formulations^b

Formulation code	SL:CHL: DSPE	Drug:Lipid ratio (w/w)	% yield ^a ratio (w/w)	Practical % drug loading ^a	% drug loading efficiency ^a
LNL-1	50:50:8	1:2	58.3 \pm 2.2	3.8 \pm 1.4	57.8 \pm 2.9
LNL-2	225:75:8	1:5	76.6 \pm 0.8	8.8 \pm 1.5	87.4 \pm 2.5
LNL-3	250:50:8	1:10	63.5 \pm 1.4	4.7 \pm 0.8	69.3 \pm 1.4

^aData show mean \pm SD (n = 3). ^bAbbreviations: LNL, lomustine loaded lipid nanostructures; SL, soya-L- α -lecithin; CHL, cholesterol; DSPE, 1,2-distearoyl-sn-glycero-3-phosphatidylethanolamine

by different *in vitro* techniques. Out of several formulations, here we report three formulations having desired *in vitro* properties (Table 1). We basically compared the formulations based on their drug loading capacity, % drug loading efficiency, as well as % yield. Out of the three, based on these characteristics, we finally selected LNL-2 as the optimized one for further works.

3. 1. 2. Determination of % Drug Loading, Loading Efficiency and Yield Percentage

The % drug loading for LNL-2 was 8.8 ± 1.5 , whereas for LNL-1 and LNL-3, the values were 3.8 ± 1.4 and 4.7 ± 0.8 respectively. LNL-2 also showed higher loading efficiency (87.4 ± 2.5) and yield percentage (76.6 ± 0.8) than other two formulations (Table 1). Based on these parameters, we selected LNL-2 for all other studies.

3. 1. 3. Determination of Average Vesicle Diameter (Z-average) and Surface Potential

The diffraction light scattering (DLS) data revealed that the experimental formulations were below 100 nm size range. The optimized formulation (LNL-2) showed an average vesicle size of 83.41 ± 1.3 nm (Table 2). The PDI

Table 2. Determination of Z-average, Poly dispersive index (PDI) and zeta potential of the selected formulation

Formulation code	Z-average (dnm.) ^a	PDI ^a	Zeta potential (mV)
LNL-2	83.41 ± 1.3	0.42 ± 0.06	-56.7

^aData show mean \pm SD (n = 3)

value of LNL-2 was 0.42 ± 0.06 . Zeta potential of LNL-2 was found to be -56.7 mV (Table 2). The lower PDI value suggested a narrow size distribution pattern of the experimental formulation. Higher negative value of zeta potential was reported for the optimized formulation, which indicates the formulation would be stable in the suspension stage due to strong repulsive force between individual particles.

3. 1. 4. Surface Morphology Study by FESEM

The FESEM image of the LNL-2 was reported here, which was taken at 60,000x magnification scale (Figure 1A). The FESEM data demonstrated the smooth surface morphology of LNL-2. All vesicles were found spherical in shape and within 30–50 nm size range. Though out the sample, there were no signs of any lumps or formation of big agglomerates, which justifies the good formulation characteristics.

3. 1. 5. Cryo-transmission Electron Microscopy (Cryo-TEM)

Cryo-TEM analysis revealed the internal architecture of the formed vesicles. Image showed formation of unilamellar vesicles with intact lamellarity. Though, experimental NLs sample was found as polydisperse, i.e. both larger and smaller size vesicles were found, however all the vesicles were well below 50 nm as we desired. The larger size vesicle was around 40 nm, where as smaller ones were around 25–30 nm as depicted in the photograph (Figure 1B). This was in good agreement with the data obtained from FESEM study. All the vesicles were found distinctively spread throughout the diluted sample without any damage to their native internal structure.

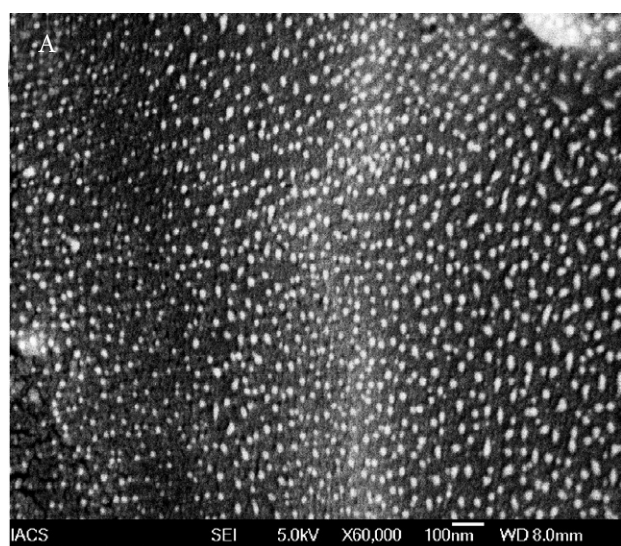


Fig. 1. (A) Field emission scanning electron microscopy (FESEM) image of optimized lomustine incorporated lipid nanostructures (LNL-2). (B) Cryo-transmission electron microscopy (Cryo-TEM) image of LNL-2

3. 1. 6. In vitro Drug Release Study and Analysis of Drug Release Kinetics

For the *in vitro* drug release study of the optimized formulation (LNL-2) at pH 5 and pH 7.4, dialysis method was employed. Result showed a pH dependent sustained drug release pattern over 48 h experimental time period at pH 5 and 7.4 (Fig. 2). Initially, though the drug release increased with time, but after 10 h, a more sustained release pattern was observed for the experimental formulation. However, amount of drug release was higher at pH 5 (endocytotic vesicular pH). A cumulative amount of $82.34 \pm 2.71\%$ LS was released from LNL-2 at pH 5 over the experimental study period. To determine the nature of drug release from the experimental formulation, release data was fitted in different kinetic equations. From the respective graphs, corresponding R^2 values were calculated (Table 3). For LNL-2, among all the tested models, Koresmeyer–Peppas model demonstrated good linearity than other models ($R^2 = 0.988$).

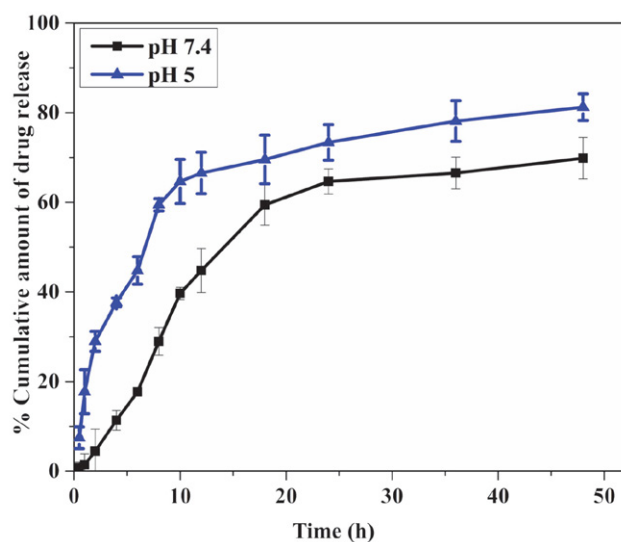


Fig. 2. *In vitro* drug release study of lomustine incorporated lipid nanostructures (LNL-2) at pH 7.4 and pH 5 respectively.

Table 3. *In vitro* drug release kinetics with R^2 values of selected formulation

Kinetic Model	LNL-2
Zero Order Kinetics	$y = 2.430x + 7.537$ $R^2 = 0.786$
First Order Kinetics	$y = -0.014x + 1.221$ $R^2 = 0.923$
Koresmeyer Peppas	$y = 0.915x + 0.224$ $R^2 = 0.977$
Higuchi	$y = 19.68x - 12.46$ $R^2 = 0.944$
Hixon Crowell Kinetics	$y = -0.063x + 2.532$ $R^2 = 0.864$

3. 1. 7. Assessment of *in vitro* Cytotoxicity

In vitro cytotoxic or anti-proliferative effect of LNL-2 was evaluated in C6 rat glioma cells. MTT assay demonstrated a lower IC_{50} (inhibitory concentration causing 50% of cell death) for LNL-2 as compared to free LS (Fig. 3). The plot of % cell viability against the tested dose ($\mu\text{g/ml}$) showed that with increase in concentration of both LNL-2 and free drug, the death rate of C6 cells increased. However, LNL-2 was found more effective ($IC_{50} 9.4 \pm 0.8 \mu\text{g/ml}$) as compared to free LS ($IC_{50} 23.8 \pm 1.3 \mu\text{g/ml}$) at equivalent drug concentration. The results further showed that blank LNLs (without drug) were almost non-toxic to the experimental C6 cell line even at the highest tested concentration (Fig. 3). Percentage of viable cells treated with blank LNLs was much higher compared to free LS, LNL-2, justifying non-toxic nature of ingredients used for the formulation.

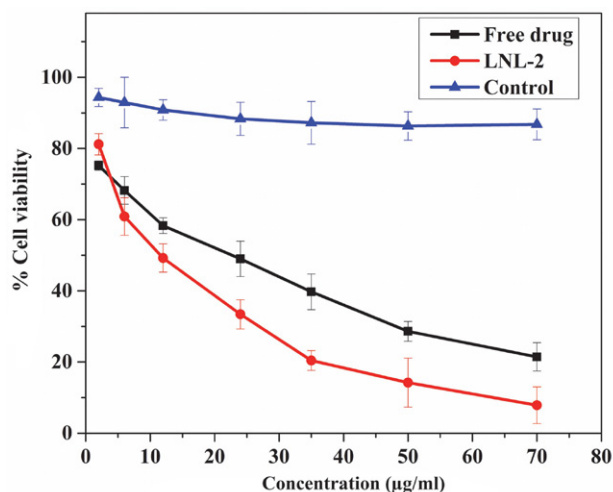


Fig. 3. Comparison of percentage C6 cell viability upon treatment with optimized lomustine loaded lipid nanostructures (LNL-2), free drug, and blank lipid nanostructures (LNLs).

3. 1. 8. Assessment of internalization Efficiency

To estimate whether the optimized formulation possesses the ability to permeate into the cancer cells or not, we tested *in vitro* internalization capacity of the fluorescent optimized formulation (FITC-LNL-2) at two different sub-inhibitory concentrations in C6 cells by fluorescence microscopy (Fig. 4). Fluorescent images of the cell line clearly showed preferential internalization of FITC-LNL-2 into the cells. The fluorescent formulation could successfully penetrate into cell and distributed throughout the cytoplasm. However, no nuclear permeation by the formulation was visualized. The nuclei of the cells were stained by DAPI, which distinctively visualized in the image and thus confirmed that FITC-LNL-2 could not cross the nucleus. A higher amount of internalization was observed in C6 cells at 100 ng/ml than the cells treated with 50 ng/ml during 0.5 h study period. Thus, a concentration dependent uptake was clearly noticed for the experimental formulation.

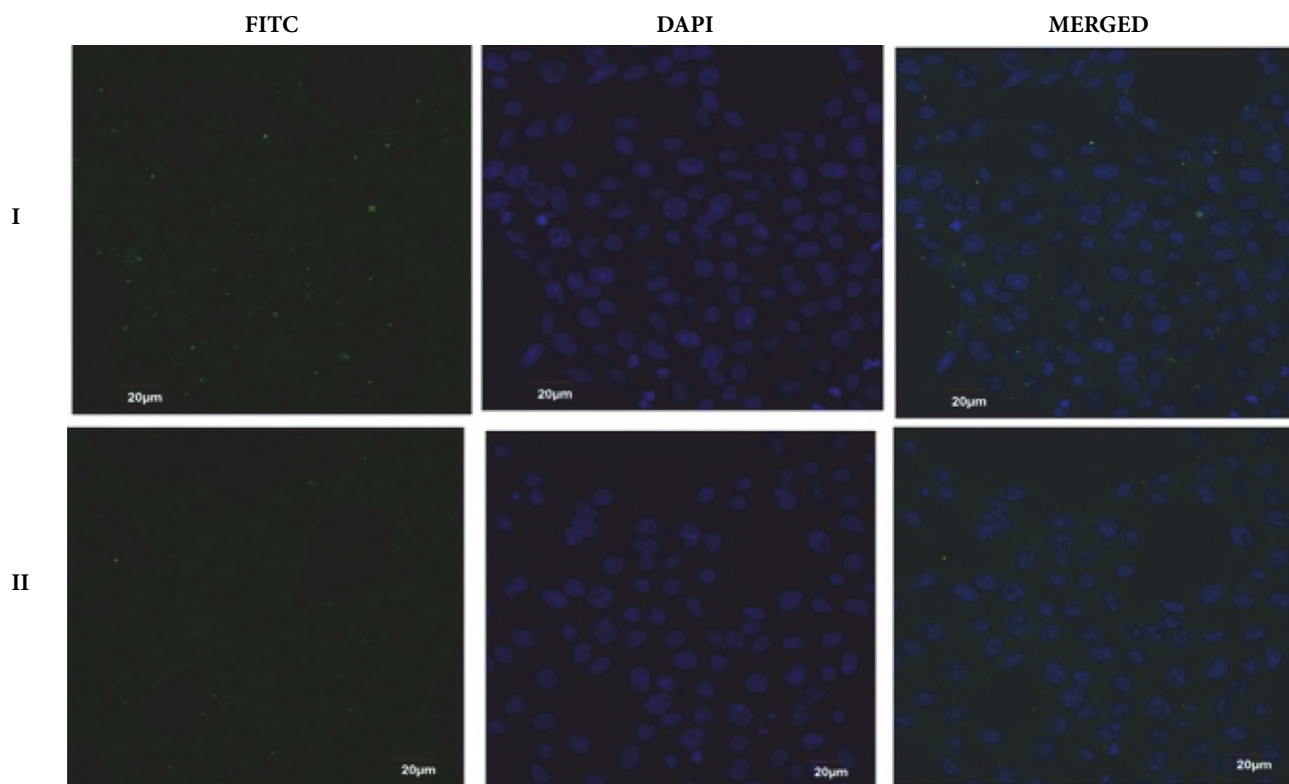


Fig. 4. Cellular internalization study of fluorescein isothiocyanate labelled lomustine loaded lipid nanostructures (FITC-LNL-2) in C6 rat glioma cells (0.5 h incubation) by confocal laser scanning microscopy at I) 50 ng/ml; II) 100 ng/ml. The nucleus was stained with 4',6-diamidino-2-phenylindole (DAPI).

3. 2. In vivo Studies

3. 2. 1. Plasma Pharmacokinetics Study

PK study was carried out to detect LS at different time points in blood of the experimental mice. From plasma PK study, a reasonable difference was observed in the important PK parameters between LNL-2 and free LS treatments (Table 4). From the graph between plasma drug concentration Vs time, a prolonged blood residence time for LNL-2 was clearly observed than free LS (Fig. 5A). After 8 h, the concentration of LS from conventional suspension was not detectable; but LS encapsulated in LNLs showed a much sustained release of the drug and even detectable at 20 h (21.33 ng/ml \pm 1.41). However, at 24h, the LS concentration

dropped beyond threshold identification limit of LCMS/MS, and thus was non-identifiable. $AUC_{0-\infty}$ value was 7214.32 ± 311.41 ng h ml⁻¹ for free LS administration, whereas it was 12451.1 ± 234.16 ng h ml⁻¹ for LNL-2 administration. Similarly other important parameters like AUMC, MRT also showed preferential enhancements for LNL-2 as compared to free LS injection. MRT was increased almost three fold for LNL-2 treated animals (9.31 h) than the animals treated with free LS (3.64 h).

3. 2. 2. Brain Pharmacokinetics Study

Brain PK data showed increased brain availability of LS from LNL-2 than LS suspension (Fig. 5B). The $AUC_{0-\infty}$

Table 4. Estimation of plasma and brain pharmacokinetic parameters of lomustine (LS) after intravenous bolus administration of free lomustine (LS) and lomustine loaded lipid nanostructures (LNL-2) suspensions

Pharmacokinetic parameters	Plasma ^a		Brain ^a	
	free LS	LNL-2	free LS	LNL-2
$AUC_{0-\infty}$ (ng h ml ⁻¹)	7214.32 \pm 311.41	12451.1 \pm 234.16*	3302.635 \pm 138.6	15113.77 \pm 221.4*
$AUMC_{0-\infty}$ (ng h ² ml ⁻¹)	31541.11 \pm 1541.15	91322.42 \pm 6561.25*	41505 \pm 231.66	87657 \pm 172.62*
Cl (L h ⁻¹)	0.072 \pm 0.04	0.211 \pm 0.31	0.013 \pm 0.06	0.531 \pm 0.32*
$MRT_{0-\infty}$ (h)	3.64 \pm 0.32	9.31 \pm 0.22*	5.61 \pm 1.21	12.49 \pm 3.21*
V_{ss} (ml)	0.039 \pm 2.31	0.151 \pm 0.13	2.431 \pm 0.03	4.311 \pm 1.76*

^a Data show mean \pm SD (n = 6). AUC: area under the plasma concentration time curve; AUMC: area under the first moment curve; Cl: clearance; MRT: mean residence time; $t_{1/2}$: plasma half life; V_{ss} : steady state volume of distribution * Data were significantly different (p < 0.05) where free LS and LNL-2 were compared. It was assessed by one-way analysis of variance (ANOVA) through Tukey-Kramer's multiple comparisons test.

value of LS from selected formulation (LNL-2) ($15113.77 \pm 221.4 \text{ ng h ml}^{-1}$) was significantly higher than that from LS suspension ($3302.635 \pm 138.6 \text{ ng h ml}^{-1}$). A significant difference was also found in $AUMC_{0-\infty}$ values in between LNL-2 and LS suspension treated groups (87657 ± 172.62 Vs 41505 ± 231.66). Data showed a higher volume of distribution and a lower rate of clearance (Cl) of drug from LNL-2 than that from LS suspension (Table 4). A 2.5 fold enhancement in the mean residence time of the drug in LNL-2 treated group was reported as compared to free LS treated group. Higher value of AUC, MRT, V_{ss} along with lower value of Cl signifies higher bioavailability and prolonged retention of drug from LNL-2 in the brain tissue. Brain PK data further provided quantitative assessment of the superiority of the experimental formulation in crossing BBB than conventional free LS.

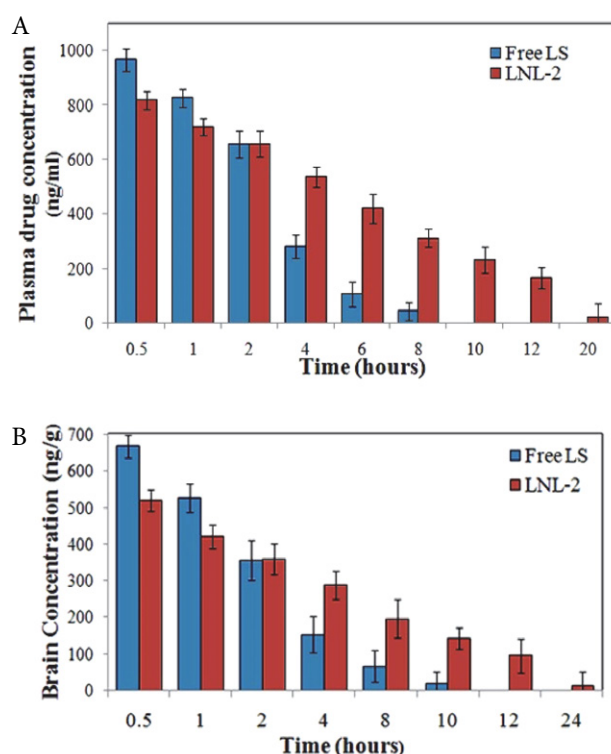


Fig. 5. A) Plasma concentration–time profiles of lomustine (LS) in Swiss albino mice after *i.v.* administration of lomustine loaded lipid nanostructures (LNL-2) and free lomustine (LS) suspension. ^aData show mean \pm SD (n = 6); B) Brain concentration–time profiles of LS in Swiss albino mice after *i.v.* administration of LNL-2 and free LS suspension. ^aData show mean \pm SD.

3. 2. 3. Hemolysis Study

Hemolytic assay was carried out in mice RBCs in order to estimate the blood-compatibility of the optimized formulation (LNL-2) and drug-free NLs along with free drug at different concentrations (0.25–50 $\mu\text{g/ml}$). As depicted in Fig. 6, RBCs up on treatment with LNL-2 showed negligible toxicity (hemolysis up to \sim 7.1%) even at highest tested drug concentration. A comparatively lower toxic ef-

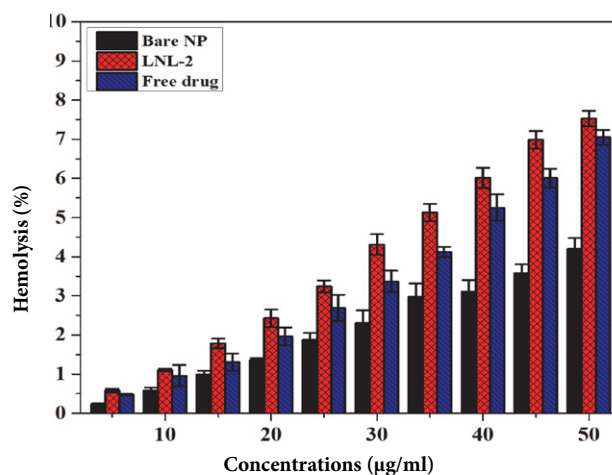


Fig. 6. Comparison of the hemolysis percentage of mice red blood cells (RBCs) treated with lomustine loaded lipid nanostructures (LNL-2), free lomustine (LS) and bare nanocarriers. Data shown for mean \pm SD (n = 3).

fect on RBCs was observed for the free drug, where as the drug-free NLs were also found almost non toxic at all tested concentrations. The haemolytic values were observed up to 7.1% for LNL-2, where as 4.2% for blank NLs. For free LS, up to 6.8% haemolytic effect was detected. Over all, the haemolytic effect follows the order as blank NLs < free LS < LNL-2. Lower haemolytic activity of the tested formulation suggested its safety and compatibility nature for *in vivo* applications.

4. Discussion

The present study was intended to develop an optimized method for formulation of LS loaded NLs and to evaluate its potentiality in glioma cells. LS is a FDA approved established anticancer drug used for the treatment of different types of cancers including glioma. However it is associated with severe side effects like bone marrow depression along with shorter plasma half life. Thus, it is hypothesized that phospholipid based nanostructures may improve the delivery of LS to glioma cells and maintain desired therapeutic concentration in brain tissue over a period of time due to sustained drug release. Further, it would reduce the dose related severe toxicity of the conventional dosage forms. During product development, we found that specific formulation composition and critical in-process parameters have significant impact on the formation of nanosize LNLs and to produce desired *in vitro* properties. Initially we varied amount of SL, CHL (at a fixed LS concentration) to develop different batches of formulations and tested *in vitro* drug loading, loading efficiency, yield percentage etc. in each batch. However, amount of DSPE was kept constant. DSPE is the type of sphingo lipid, which is present abundantly in brain tissue. Thus, brain tissue-mimicking nature of DSPE is expected

to increase the accumulation and retention the experimental formulation in brain tissue. Reports from our previous work also justified this hypothesis.²⁴

In the present work, percentage drug loading was initially increased with increase in the amount of drug. However, beyond certain amounts, percentage loading was not increased in direct proportion with the amount of drug. That indicates % drug loading was independent on amount of drug in the formulation. Thus, higher amount of drug does not guarantee higher drug loading in NLS. This was also in good agreement with the previous reports.^{24,28} Further, different process parameters, such as duration of hydration, temperature, sonication time, speed and time of centrifugation etc. affected the morphology, average vesicle size as well as drug loading capacity of the formulations. In our work, we have therefore standardized critical in-process parameters to obtain LNLs with desired physicochemical properties. At a fixed ratio of 1:5 drug:lipid (w/w) along with specific manufacturing parameters such as 45 min hydration in PBS at 140 rpm, 40 min sonication in a bath type sonicator, 45 min ultra centrifugation at 15,000 rpm etc. the obtained formulation showed satisfactory characteristics in terms of % yield, % drug loading and loading efficiency and thus taken for further studies throughout the work.

The selected formulation (LNL-2) showed a satisfactory percentage of drug loading. For nanosize vesicular carriers, it has always been a problem to achieve higher drug loading. However, in our case, a reasonable drug loading of 8.8% was reported, which may be attributed to the standardized formulation composition and in-process parameters selected in our study.

The experimental lipid nanostructures (LNL-2) had a nanosize range as depicted from DLS study with a narrow distribution pattern. A lower PDI value of LNL-2 (0.42 ± 0.06) signifies homogenous distribution pattern of nanostructures in the formulation. It is known that smaller size nanodrug carriers remain suspended for a longer period of time as compared to larger size carriers, since the rate of sedimentation of suspended particles is mostly governed by Stoke's law. According to Stoke's law, rate of sedimentation of suspended particles are directly proportional to the diameter of the suspended particles. Again, a higher value of zeta potential on the experimental formulations (-56.7 mV) would help them to remain separated from each other due to higher repulsive force between individual vesicles. It has been reported that a zeta potential of more negative than -30 mV or more positive than $+30$ mV is taken as critical to form stable suspensions.^{24,27} Thus, in our case, ultra micron size (below 100 nm) and higher negative surface charge of selected formulation would help to form stable suspension.

FESEM images demonstrated smooth surface morphology, nanosize range (30–40 nm) and a clear homogenous nature of the experimental lipid nanostructures. It was observed that size of lyophilized LNL-2 found in the FE-

SEM image was less than those detected by DLS method. It is because the DLS method mostly measures average hydrodynamic diameter of the vesicles in aqueous phase, whereas in FESEM dried powdered samples (lyophilized) are analysed. The formed vesicles while dispersed for a reasonable time period in milli Q water during sample preparation for DLS measurement might swell and increase in size than their native form. We found similar observations in some of the previous reports also.^{24,25,31} However, size of the sample observed by cryo-TEM was in good agreement with that of FESEM. Cryo-TEM method actually maintains the LNLs in their native form where they are observed under liquid nitrogen environment. Thus, the delicate nature of lipid vesicles is well maintained in cryo-TEM method than normal TEM. In our study, cryo-TEM images showed intact bilayer of the formed vesicles without any damage to their native structure. We have taken experimental LNLs at a diluted state so that the vesicles could be distinctively visualized. Cryo-TEM thus confirmed satisfactory production of LNLs by the standardized process as well as maintenance of their internal architecture.

In vitro drug release study was carried out at physiological pH of blood (i.e. pH 7.4) as well as endocytotic vesicular pH (pH 5) to simulate different *in vivo* environments. Drug release though found to be sustained nature for both the pH, however, a higher cumulative percentage of drug was released at pH 5, than at pH 7.4. For both cases, initially, the amount of drug release was increased with time, but after 10 h, a more sustained release pattern was observed. A comparatively lower cumulative drug release at pH 7.4 signifies reduced loss of the drug at physiological condition and more specific to targeted site. As tumor microenvironment has reduced pH (pH 5–5.5) due to anaerobic respiration of malignant cells, higher drug release from the optimized formulation at pH 5 would enhance its therapeutic action at tumor area. Further, the sustained release behavior of the formulation would reduce dose, dosing frequency as well as associated toxic effects of LS. The pattern of drug release when fitted to different kinetics models, the formulation was best fitted with the Korsmeyer–Peppas kinetics model. Adherent to this model signifies that the drug release pattern from LNL-2 might follow complex mechanisms and include both diffusion and erosion. In case of the Korsmeyer–Peppas model, the fraction of drug release with time is generally represented as $M_t/M_\infty = Kt^n$, where the release mechanism is governed by 'n'. The drug release is said to follow Fickian diffusion mechanism, when $n \leq 0.45$. Similarly, when value of 'n' lies in between 0.45–0.89, the drug release is said to follow non-Fickian diffusion mechanism and when n remains ≥ 0.89 , it is considered Case II (relaxational) transport.²⁸ In our case, 'n' value was found as 0.724, which suggests that the drug release from LNL-2 might follow non-Fickian diffusion mechanism.

The *in vitro* cytotoxicity data demonstrated higher death rate of C6 cells treated with LNL-2 as compared to

free LS suspension at equivalent drug concentration. Data clearly revealed better antitumor efficacy of the tested formulation than free drug. LS delivered through LNLs was more cytotoxic to the glioma cells with lower IC_{50} value (9.4 $\mu\text{g}/\text{ml}$) as compared to free LS (23.8 $\mu\text{g}/\text{ml}$). The blank formulation (without drug) showed no significant impact on the cell death rate even at highest tested concentrations. Clearly, it suggests the biocompatible and non-toxic nature of excipients used in the formulation development, which is a good sign for *in vivo* applications.

In order to visualize the internalization of LNL-2 by C6 cells, FITC was used as a fluorescent marker. The FITC-LNL-2 produced green fluorescence while visualized under fluorescence microscope. Further, DAPI was used as coloring agent to stain nucleus, which produces blue fluorescence. In the study, we have chosen two different concentrations of the LNL-2, which are subinhibitory concentrations, i.e. quite less than the reported IC_{50} value. Thus, at these concentrations, no damage to the normal cellular architecture could be there and the cells were visualized in their native form. Confocal images depicted a preferential uptake of FITC-LNL-2 by C6 cells. The formulation was predominantly spread throughout the cytoplasm, around the nucleus. Higher cellular internalization of the optimized formulation could be attributed to the ultra micron size range. It may be possible that due to much smaller size as well as higher lipophilic property, the experimental LNLs could sufficiently permeate through the cancer cells, which is again a good finding towards successful application of the experimental formulation for the treatment of glioma.

The PK parameters of LNL-2 treated mice demonstrated a higher value of AUC, AUMC, V_{ss} , and MRT in comparison to animals treated with free LS suspension. The plasma drug concentration for LNL-2 treated group at 24 h was reasonably higher than that of LS treated groups. The drug concentration for free LS treated groups was not detectable after 10 h, since it dropped beyond the minimum detectable limit (10ng/ml) of our LCMS/MS system, whereas LS from LNL-2 showed its presence up to 20 h study period. The data justified the potential of the optimized formulation to remain circulated for prolonged period of time in blood. Further, due to longer blood residence profile, the formulation would get sufficient time to reach into brain tissue by crossing BBB. Owing to its extreme small size, and higher negative surface charge, the experimental LNLs might escape from the trap of reticulo-endothelial cells successfully and could maintain a longer presence in blood.

A similar observation was found in case of brain PK parameters in mice treated with LNLV-2/free LS. The LS incorporated in lipid nanostructures showed a much sustained release up to 24 h than LS suspension. Initially, LS concentration was higher in case of plain suspension than LNL-2. Interestingly, at 2 h post *i.v.* injection, drug concentration was almost similar for both LNL-2 and free LS

suspension. However, after 4 h, drug level was drastically reduced in case of free LS, whereas it dropped in a much controlled manner for LSNL-2 till 24 h of study period. After 10h, the drug level from free LS reduced beyond the threshold limit of detection of LCMS/MS and thus could not be detected. Even at 24 h, 13.76 ng/ml of drug was detected from LNL-2, which signifies the sustained release and prolonged residence time of LNL-2 in brain tissue. The significant enhancements in AUC and AUMC in the LNL-2 treated group signified higher bioavailability of the drug from LNL-2 than free LS. Brain PK results further confirmed the potentiality of optimized lipid nanostructures to cross BBB and enter into brain for a reasonable time period, which is very crucial data for successful *in vivo* applications in glioma.

Though application of LS for the treatment of brain and intracranial tumors are not new, but development of novel strategies to enhance its efficacy and to reduce the associated toxic effects have been tried in recent times only. Funmilola A. F. et al., 2016 reported the development of LS loaded nanoparticles for improved brain delivery and to check the dose-related myelosuppression. The *in vivo* efficacy of the selected LS loaded nanoparticles was assessed in orthotopic U87 MG glioblastoma animal model. Results showed that LS delivered through nanoparticulate system improved the survival of intracranial tumour bearing mice and also did not produce no additional myelosuppressive effects.²¹ Another work reported by Salman J. et al showed efficacy of LS loaded superparamagnetic iron oxide nanoparticles on U87 MG cancer cell line.³³ The encapsulation efficiency for the LS loaded nanoformulation was $46 \pm 6.8\%$. The experimental nanostructures were found cytotoxic on U87 MG cancer cells at concentration above 100 $\mu\text{g}/\text{mL}$. Further, they did not report PK studies or any other related animal experiments to justify the suitability of the experimental nanoparticle formulations for *in vivo* applications.

We must say that the present work will be quite different from all such reported works, since till now LS loaded LNLs have not been evaluated for their *in vitro* efficacy on C6 glioma cells. Further, no study has been reported so far both the plasma and brain PK profile of LS encapsulated in LNLs. Hemolysis assay further adds novelty to the work. The simple formulation technique used for the study along with clear optimization of critical manufacturing parameters would be beneficial for furthering its research towards technology transfer. Higher encapsulation efficiency of the optimized formulation adds value to the work. Overall the data presented in FESEM, cryo-TEM, confocal microscopy, PK profile etc. stands unique in their parts.

For the desired *in vivo* applications, blood compatibility of the nanodrug formulations is an essential criterion. Hemolysis assay of the selected formulation in the experimental mice RBCs depicted an excellent blood compatibility nature of LNL-2 since a very low hemolysis (up to 7.1%) was observed for the optimized formulation even

at highest tested concentration. The haemolytic effect for the free LS was also less than LNL-2. From the negligible hemolysis activity, it may be concluded that LNL-2 could be employed as a safe, non-toxic and effective nanocarrier platform for its future clinical investigations.

5. Conclusion

The study reported an optimized and easily controllable method for the development of lipid based nanostructures for sustained delivery of LS for the treatment of glioma. The selected formulation (LNL-2) showed a preferable nanosize (within 50 nm) as depicted from FESEM and cryo-TEM study. A reasonable drug loading (8.8%) was reported for LNL-2 along with a sustained *in vitro* drug release profile during a 48 h study period. Owing to its ultra small size and high lipophilic nature, LNL-2 showed preferential internalization in C6 glioma cells. MTT assay showed a higher toxicity of LNL-2 on the tested cancer cells than free LS. The formulation showed improved PK profile both in blood and brain in experimental mice models than free drug suspension. A higher mean residence time of LNL-2 in blood signifies its higher *in vivo* stability. Significant increase in important brain PK parameters like AUC and MRT for LNL-2 justified its higher bioavailability and prolonged retention in brain tissue. Further negligible hemolysis in mice RBCs justified the non-toxic and biocompatible nature of LNL-2 for safe *in vivo* application. The formulation development steps were simple and well standardized, which would be helpful during technology transfer. Results of the study overall suggest the potential application of LNL-2 for sustained delivery of LS for glioma treatment. However, further *in vivo* testing on various pharmacological and toxicological aspects of LNL-2 is warranted for its future clinical application.

Declaration of interest

The authors of this article have no conflict of interest to declare.

Acknowledgement

The authors are very much grateful to Prof. Manoj Ranjan Nayak, President, Siksha 'O' Anusandhan (Deemed to be University) for providing necessary research facilities and encouragement.

Data Availability Statement

The authors hereby state that all data available in the article can be shared for scientific search as there are no ethical issues. Neither, these data violate the protection of human subjects, nor any other valid ethical, privacy, or security concerns.

6. References

1. D. Giakoumettis, A. Kritis, and N. Foroglou, *Hippokratia*. **2018**, *22*, 105–112.
2. S. Kesari, in *Seminars in Oncology*. **2011**, *38*, 2–10. DOI:10.1053/j.seminoncol.2011.09.005
3. D. N. Louis, *Acta Neuropathol*, **2016**, *3*, 803–820. DOI:10.1007/s00401-016-1545-1
4. S. Stamatovic, R. Keep, and A. Andjelkovic, *Curr. Neuropharmacol*. **2018**, *6*, 179–192. DOI:10.2174/157015908785777210
5. J. Guo *et al.*, *Biomaterials*. **2011**, *26*, 8010–8020. DOI:10.1016/j.biomaterials.2011.07.004
6. A. Bhowmik, R. Khan, and M. K. Ghosh, *BioMed Research International*, **2015**, *2015*, 1–20. DOI:10.1155/2015/320941
7. K. K. Jain, *Nanomedicine*. **2012**, *7*, 1225–1233. DOI:10.2217/nmm.12.86
8. H. Athmakur and A. K. Kondapi, *Int. J. Appl. Pharm*. **2018**, *10*, 234–241. DOI:10.22159/ijap.2018v10i6.28004
9. M. C. Chamberlain, *Expert Review of Neurotherapeutics*, **2010**, *10*, 1537–1544. DOI:10.1586/ern.10.32
10. Y. Hao, L. Wang, Y. Zhao, D. Merg, D. Li, H. Li, B. Zhang, *Macromol. Biosci*. **2015**, *15*, 1571–1585. DOI:10.1002/mabi.201500091
11. X. Li *et al.*, *Journal of Drug Targeting*, **2017**, *25*, 17–28. DOI:10.1080/1061186X.2016.1184272
12. X. Hu, F. Yang, Y. Liao, L. Li, and L. Zhang, *Drug Deliv*. **2017**, *24*, 121–132. DOI:10.1080/10717544.2016.1233590
13. M. L. Bondi, R. Di Gesù, and E. F. Craparo, *Methods in Enzymology*. **2012**, *508*, 229–251. DOI:10.1016/B978-0-12-391860-4.00012-4
14. A. Laouini, C. Jaafar-Maalej, I. Limayem-Blouza, S. Sfar, C. Charcosset, and H. Fessi, *J. Colloid Sci. Biotechnol*, **2012**, *1*, 147–168. DOI:10.1166/jcsb.2012.1020
15. A. Akbarzadeh *et al.*, *Nanoscale Res. Lett*, **2013**, *8*, 102–110. DOI:10.1186/1556-276X-8-102
16. N. M. Shamhari, B. S. Wee, S. F. Chin, and K. Y. Kok, *Acta Chim. Slov*. **2018**, *65*, 578–585. DOI:10.17344/acsi.2018.4213
17. Sonali, Rahul.S, Nitesh.S, Gunjan.S, Biplob.S, *Drug Deliv*. **2016**, *23*, 1261–1271. DOI:10.3109/10717544.2016.1162878
18. S. Yi, F. Yang, C. Jie, and G. Zhang, *Artif. Cells, Nanomedicine Biotechnol*. **2019**, *47*, 3438–3447. DOI:10.1080/21691401.2019.1652628
19. K. A. Harvey, Zhidong. X, Haiyan.W, Karen. P, *J. Neurosurg*. **2015**, *122*, 547–556. DOI:10.3171/2014.10.JNS14759
20. S. Lonardi, A. Tosoni, and A. A. Brandes, *Cancer Treat. Rev*. **2005**, *31*, 79–89. DOI:10.1016/j.ctrv.2004.12.005
21. F. A. Fisusi *et al.*, *Pharm. Res*. **2016**, *33*, 1289–1303. DOI:10.1007/s11095-016-1872-x
22. A. Mehrotra and J. K. Pandit, *J. Nanomed. Nanotechnol*. **2015**, *6*, 328–341. DOI:10.4172/2157-7439.1000328
23. O. Arjmand, M. Ardjmand, A. M. Amani, and M. H. Eikani, *Acta Chim. Slov*. **2020**, *67*, 496–506. DOI:10.17344/acsi.2019.5513
24. B. S. Satapathy, B. Mukherjee, R. Baishya, M. C. Debnath, N. S. Dey, and R. Maji, *RSC Adv*. **2016**, *6*, 85261–85274. DOI:10.1039/C6RA16426A

25. B. Sinha, B. Mukherjee, and G. Pattnaik, *Nanomedicine Nanotechnology, Biol. Med.* **2013**, *9*, 94–104.
DOI:10.1016/j.nano.2012.04.005
26. N. Shekhar Dey, B. Mukherjee, R. Maji, and B. Sankar Satapathy, *Curr. Cancer Drug Targets.* **2015**, *16*, 357–372.
DOI:10.2174/1568009616666151106120606
27. A. Rudra, R. M. Deepa, M. K. Ghosh, S. Ghosh, and B. Mukherjee, *Int. J. Nanomedicine.* **2010**, *5*, 811–823.
DOI:10.2147/IJN.S13031
28. T. K. Shaw *et al.*, *Drug Deliv.* **2017**, *24*, 346–357.
DOI:10.1080/10717544.2016.1253798
29. R. Maji, N. S. Dey, B. S. Satapathy, B. Mukherjee, and S. Mondal, *Int. J. Nanomedicine.* **2015**, *9*, 3107–3118.
DOI:10.2147/IJN.S63535
30. J. Panda, B. S. Satapathy, S. Majumder, R. Sarkar, B. Mukherjee, and B. Tudu, *J. Magn. Magn. Mater.* **2019**, *485*, 165–173.
DOI:10.1016/j.jmmm.2019.04.058
31. L. Dutta, B. Mukherjee, T. Chakraborty, M. Das, L. Mondal, S. Bhattacharya, R. H. Gaonka, *Drug Deliv.* **2018**, *25*, 504–516.
DOI:10.1080/10717544.2018.1435749
32. M. Zamani, E. Naderi, M. Aghajanzadeh, M. Naseri, A. Sharafi, and H. Danafar, *J. Mol. Liq.* **2019**, *274*, 60–67.
DOI:10.1016/j.molliq.2018.10.083
33. S. Jafari, M. B. Tavakoli, A. Zarrabi, *Iran J Pharm. Res.* **2020**, *19*, 134–144. DOI:10.22037/IJPR.2020.1101032

Povzetek

Učinkovito zdravljenje gliomov v medicini še vedno predstavlja izziv. Namen dela je izdelati in ovrednotiti nanostrukture na osnovi lipidov za izboljšano dostavo lomustina v možganske tumorske celice. Poskusne formulacije (LNL) so bile razvite s spremenjeno tehniko hidracije lipidne plasti in njihove značilnosti ovrednotene z *in vitro* metodami, ki vključujejo analizo velikosti delcev, površinskega naboja, površinske morfologije, notranje strukture, *in vitro* nalaganja učinkovine, profil sproščanja učinkovine itd. Protirakavi potencial je bil testiran *in vitro* na glioma celični liniji C6. Elektronsko-mikroskopska študija je prikazala velikost manj kot 50 nm za izbrane LNL pri 8.8 % vključitvi učinkovine s težnjo po podaljšanem sproščanju učinkovine v obdobju 48 h. Konfokalna mikroskopija je pokazala obsežno internalizacijo izbranih LNL v celice C6. S testom MTT je bilo ugotovljeno, da so LNL bolj citotoksični kot prosta učinkovina in prazni nanonosilci. Izbrani LNL so izkazovali izboljšan farmakokinetični profil v krvi in možganih pri poskusnih modelih miši skupaj z zanemarljivo hemolizo mišjih krvnih celic. Za prenos LNL v klinično uporabo so v prihodnosti upravičene nadaljnje študije.



Except when otherwise noted, articles in this journal are published under the terms and conditions of the Creative Commons Attribution 4.0 International License

Scientific paper

Synthesis, Characterization, X-Ray Crystal Structures and Antibacterial Activity of Cobalt(III) Complexes Derived from 5-Bromo-2-((2-(phenylamino)ethylimino)methyl)phenol

Cheng Liu

School of Medicine, Huaqiao University, Quanzhou 362021, P. R. China

* Corresponding author: E-mail: liucheng_hqu@163.com

Received: 05-31-2021

Abstract

Two new and similar cobalt(III) complexes, $[\text{CoL}_2] \cdot \text{NO}_3$ (**1**) and $[\text{CoL}_2] \cdot \text{Cl}$ (**2**), where L is 5-bromo-2-((2-(phenylamino)ethylimino)methyl)phenolate, have been synthesized and characterized by IR and UV-Vis spectra. Structures of the complexes were confirmed by single crystal X-ray determination. The Co atoms in the complexes are in octahedral coordination, with the donor atoms come from the two Schiff base ligands, viz. phenolate oxygen, and imino and amino nitrogen. The anions of the cobalt salts crystallized as counteranions in the complexes. The complexes were assayed for antibacterial activities by MTT method.

Keywords: Schiff base; cobalt complex; synthesis; X-ray diffraction; antibacterial activity

1. Introduction

Schiff bases due to their facile synthesis and interesting biological activities, have attracted considerable attention in inorganic and biological chemistry. In the past years, a number of Schiff base compounds have shown antifungal, antibacterial, antiproliferative, and antitumor activities.¹ Schiff base compounds possess N and O donor atoms, are important ligands in coordination chemistry. A huge number of Schiff base complexes have been reported for their structures and interesting properties like magnetism, catalytic application, and biological activities.² It is well known that some drug activities, when administered as metal complexes, are being increased.³ The field of medicine has witnessed an increase in the number of complexes with therapeutic value, for example Schiff base copper, nickel and zinc complexes are biological active agents,⁴ cobalt complexes with Schiff bases have shown effective antibacterial activities.⁵ The coordination chemistry of cobalt is of considerable interest since cobalt(II) and cobalt(III) complexes derived Schiff bases are reported to be biologically active.⁶ In addition, the Schiff bases synthesized from salicylaldehyde derivatives with halo atoms in the aromatic ring, showed effective antibacterial activities.⁷ Herein, we report the

synthesis, characterization, and single crystal structures of two new cobalt(III) complexes, $[\text{CoL}_2] \cdot \text{NO}_3$ (**1**) and $[\text{CoL}_2] \cdot \text{Cl}$ (**2**), where L is 5-bromo-2-((2-(phenylamino)ethylimino)methyl)phenolate. The antibacterial activity of the compounds against Gram-positive bacterial strains (*B. subtilis*, *S. aureus* and *St. faecalis*) and Gram-negative bacterial strains (*E. coli*, *P. aeruginosa* and *E. cloacae*) by MTT method was studied.

2. Experimental

2.1. Materials and Physical Methods

4-Bromosalicylaldehyde, *N*-phenylethane-1,2-diamine, cobalt nitrate and cobalt chloride were purchased from Aldrich. The solvents used in the synthesis and biological assay were commercial obtained and used as received. Elemental analyses for C, H and N were performed on a Perkin-Elmer 2400 II analyzer. FT-IR spectra were recorded as KBr pellets on Bruker Tensor-27. UV-Vis spectra were recorded on Lambda 35 spectrophotometer. Single crystal X-ray diffraction was carried out with a Bruker Apex II CCD diffractometer. Molar conductivity was measured in methanol with a DDS-11A molar conductivity meter.

2. 2. Synthesis of [CoL₂] · NO₃ (1)

4-Bromosalicylaldehyde (0.20 g, 1.0 mmol) and *N*-phenylethane-1,2-diamine (0.14 g, 1.0 mmol) were reacted in methanol (30 mL). The mixture was stirred at reflux for 30 min, and cobalt nitrate hexahydrate (0.29 g, 1.0 mmol) was added. After one hour stirring, the solution was cooled to room temperature, filtered, and with the filtrate kept still for slow evaporation. The diffraction quality block like brown single crystals that deposited over a period of 8 days were collected by filtration and washed with methanol. The yield was 0.16 g (42%). Anal. Calc. (%) for C₃₀H₂₈Br₂CoN₅O₅: C, 47.58; H, 3.73; N, 9.25. Found (%): C, 47.39; H, 3.82; N, 9.13. IR data (KBr, cm⁻¹): 3155w, 3054w, 2971w, 2933w, 2853w, 1650s, 1586s, 1520m, 1490w, 1427s, 1382s, 1325w, 1310w, 1291m, 1196w, 1130m, 1077w, 1055w, 1038w, 943w, 913m, 852w, 800w, 777w, 770w, 755w, 693w, 604w, 561w, 470w. UV–Vis data [methanol, λ/nm (ε/L·mol⁻¹·cm⁻¹): 245 (16,630), 263 (15,820), 302 (9,870), 385 (2,450), 495 (243). Λ_M (10⁻³ mol L⁻¹ in methanol): 128 Ω⁻¹ cm² mol⁻¹.

2. 3. Synthesis of [CoL₂] · Cl (2)

This complex was prepared with the similar method as described for complex 1, with cobalt nitrate hexahydrate replaced by cobalt chloride hexahydrate (0.24 g, 1.0 mmol). The diffraction quality block like brown single crystals that

deposited over a period of 5 days were collected by filtration and washed with methanol. The yield was 0.21 g (58%). Anal. Calc. (%) for C₃₀H₂₈Br₂ClCoN₄O₂: C, 49.31; H, 3.86; N, 7.67. Found (%): C, 49.43; H, 3.81; N, 7.58. IR data (KBr, cm⁻¹): 3167w, 3047w, 2962w, 2891w, 2849w, 1648s, 1586s, 1519m, 1489w, 1427s, 1327w, 1291m, 1202w, 1189m, 1124m, 1079w, 1058w, 1040w, 943w, 913m, 853w, 787w, 770w, 757w, 701w, 693w, 600w, 561w, 466w. UV–Vis data [methanol, λ/nm (ε/L·mol⁻¹·cm⁻¹): 230 (16,120), 248 (16,530), 260 (16,400), 304 (9,720), 385 (1,810), 497 (225). Λ_M (10⁻³ mol L⁻¹ in methanol): 135 Ω⁻¹ cm² mol⁻¹.

2. 4. X-Ray Structure Determination

Intensity data of the complexes were collected at 298(2) K on a Bruker Apex II CCD diffractometer using graphite-monochromated MoK_α radiation (λ = 0.71073 Å). For data processing and absorption correction the packages SAINT and SADABS were used.⁸ Structures of the complexes were solved by direct and Fourier methods and refined by full-matrix least-squares based on *F*² using SHELXL.⁹ The non-hydrogen atoms were refined anisotropically. The amino hydrogen atom were located from electronic density maps, and refined with N–H distances restrained to 0.90(1) Å. The remaining hydrogen atoms have been placed at geometrical positions with fixed thermal parameters. Crystallographic data of the complexes are summarized in Table 1. Selected bond lengths and angles are listed in Table 2.

Table 1. Crystallographic data and refinement details for the complexes

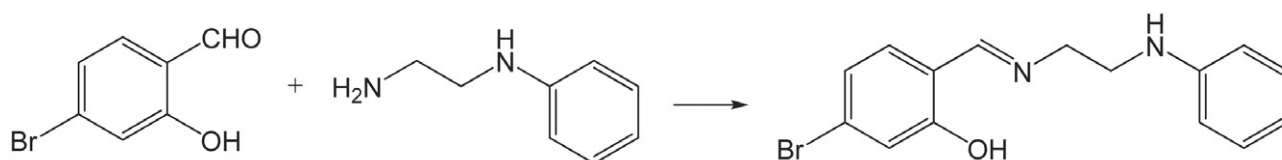
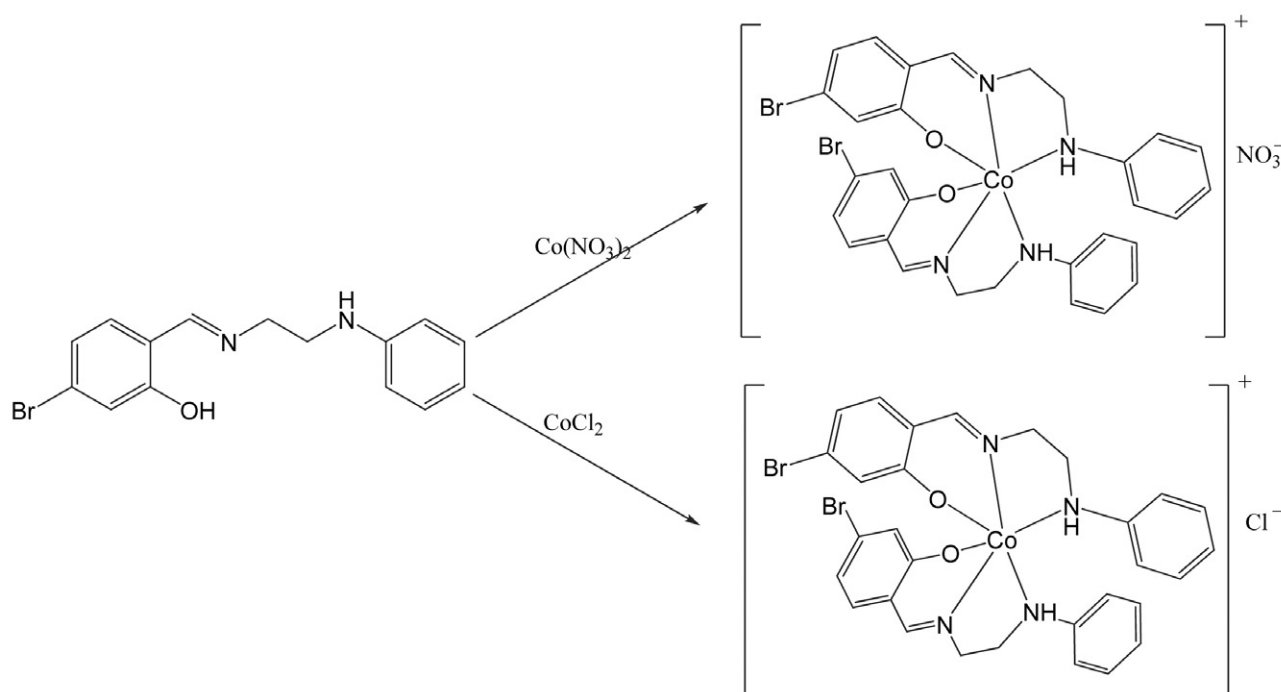
	1	2
Chemical Formula	C ₃₀ H ₂₈ Br ₂ CoN ₅ O ₅	C ₃₀ H ₂₈ Br ₂ ClCoN ₄ O ₂
Molecular weight	757.32	730.76
Crystal color, habit	Brown, block	Brown, block
Crystal size, mm	0.23 × 0.22 × 0.20	0.26 × 0.23 × 0.23
Crystal system	Monoclinic	Monoclinic
Space group	Cc	Cc
Unit cell dimensions:		
<i>a</i> , Å	10.667(2)	10.4703(11)
<i>b</i> , Å	19.0095(16)	19.0897(13)
<i>c</i> , Å	15.1924(11)	15.1449(12)
β, °	100.151(1)	103.973(1)
<i>V</i> , Å ³	3032.5(7)	2937.5(4)
<i>Z</i>	4	4
ρ _{calcd} , g cm ⁻³	1.659	1.652
μ, mm ⁻¹	3.249	3.431
θ Range collected, deg	2.143–25.493	2.134–25.496
<i>T</i> _{min} and <i>T</i> _{max}	0.522 and 0.563	0.469 and 0.506
Reflections collected/unique	7800/4645	7793/4102
Observed reflections (<i>I</i> ≥ 2σ(<i>I</i>))	3526	3496
Data/restraints/parameters	4645/4/394	4102/4/370
GOOF on <i>F</i> ²	0.983	0.970
<i>R</i> ₁ , <i>wR</i> ₂ (<i>I</i> ≥ 2σ(<i>I</i>))	0.0556, 0.1445	0.0328, 0.0603
<i>R</i> ₁ , <i>wR</i> ₂ (all data)	0.0740, 0.1558	0.0435, 0.0644

Table 2. Selected bond distances (Å) and angles (°) for the complexes

	1	2
Co1-O1	1.866(8)	1.884(4)
Co1-O2	1.881(8)	1.875(4)
Co1-N1	1.888(8)	1.909(5)
Co1-N2	2.021(9)	2.049(5)
Co1-N3	1.908(9)	1.899(5)
Co1-N4	2.021(10)	2.027(5)
O1-Co1-O2	90.7(4)	89.79(18)
O1-Co1-N1	94.1(4)	93.88(19)
O2-Co1-N1	86.6(3)	86.12(18)
O1-Co1-N3	85.7(4)	85.63(18)
O2-Co1-N3	95.3(4)	95.34(19)
N1-Co1-N3	178.0(4)	178.5(2)
O1-Co1-N2	177.7(4)	176.9(2)
O2-Co1-N2	87.2(4)	87.2(2)
N1-Co1-N2	84.9(4)	85.3(2)
N3-Co1-N2	95.3(4)	95.24(19)
O1-Co1-N4	88.4(4)	89.39(19)
O2-Co1-N4	179.0(4)	179.1(2)
N1-Co1-N4	93.9(4)	93.6(2)
N3-Co1-N4	84.2(4)	84.9(2)
N2-Co1-N4	93.7(4)	93.6(2)

2. 5. Antibacterial Activity

Antibacterial activity of the complexes was tested against *B. subtilis*, *S. aureus*, *S. faecalis*, *P. aeruginosa*, *E. coli*, and *E. cloacae* using MTT medium. The minimum inhibitory concentrations (MICs) of the compounds were determined by a colorimetric method using MTT dye.¹⁰ A stock solution of the compounds ($50 \mu\text{g mL}^{-1}$) in DMSO was prepared and quantities of the compounds were incorporated in specified quantity of sterilized liquid medium. A specified quantity of the medium containing the compounds was poured into micro-titration plates. Suspension of the microorganism was prepared to contain approximately 10^5 cfu mL^{-1} and applied to micro-titration plates with serially diluted compounds in DMSO to be tested, and incubated at 37°C for 24 h for bacteria. After the MICs were visually determined on each micro-titration plate, $50 \mu\text{L}$ of phosphate buffered saline (PBS 0.01 mol L^{-1} , pH 7.4: $\text{Na}_2\text{HPO}_4 \cdot 12\text{H}_2\text{O}$ 2.9 g, KH_2PO_4 0.2 g, NaCl 8.0 g, KCl 0.2 g, distilled water 1000 mL) containing 2 mg mL^{-1} of MTT was added to each well. Incubation was continued at room temperature for 4–5 h. The content of each well was removed, and $100 \mu\text{L}$ of isopropanol containing 5% 1 mol L^{-1} HCl was added to extract the dye. After 12 h of in-

**Scheme 1.** The synthetic procedure for HL.**Scheme 2.** The synthetic procedure for the complexes.

cupation at room temperature, the optical density (OD) was measured with a microplate reader at 570 nm.

3. Results and Discussion

3.1. Chemistry

The Schiff base HL was readily prepared by the reaction of 4-bromosalicylaldehyde and *N*-phenylethane-1,2-diamine in methanol (Scheme 1). The complexes were prepared in a similar method, by the reaction of the Schiff base ligand with cobalt nitrate and cobalt chloride, respectively (Scheme 2). The conductivity values of the complexes (128–135 $\Omega^{-1} \text{ cm}^2 \text{ mol}^{-1}$) indicated that they are 1:1 electrolytes in methanol solution.¹¹

3.2. IR and UV-Vis Spectra Study

The weak absorptions at 3155 and 3167 cm^{-1} for the infrared spectra of complexes **1** and **2** are assigned to $\nu_{\text{N-H}}$. The characteristic imine stretching for the complexes are observed at 1650 cm^{-1} for **1** and 1648 cm^{-1} for **2**.¹² The Schiff base ligand coordination through the phenolate oxygen is indicated by the absorption bands of the Ar–O bonds at about 1190 cm^{-1} in the complexes.¹³ In general, the infrared spectra of complexes **1** and **2** are similar to each other, except the absorption at 1382 cm^{-1} for the nitrate anion of complex **1**.¹⁴

The absorption spectral data of the complexes were measured in methanol solution. In both complexes, peaks between 240–250 nm, 260–310 nm and 380–390 nm are assigned to $\pi \rightarrow \pi^*$, $n \rightarrow \pi^*$ and ligand to metal charge transfer transitions, respectively.¹² In the visible spectra of both complexes, weak bands are observed at 495–497 nm.

3.3. Structure Description of the Complexes

Molecular structures of complexes **1** and **2** are shown in Figs. 1 and 2, respectively. Complex **1** contains a $[\text{CoL}_2]^+$ cation and a nitrate anion. Complex **2** contains a $[\text{CoL}_2]^+$ cation and a chloride anion. In the cation, the Co atom is coordinated by two phenolate oxygen (O1, O2), two imino nitrogen (N1, N3) and two amino nitrogen (N2, N4) from two Schiff base ligands, forming octahedral geometry. In general, the coordination geometry around the Co atom in each complex displays only slight distortion. In both complexes, the bond lengths of Co–O and Co–N are similar and range from 1.866(8) to 2.021(10) Å for complex **1**, and range from 1.875(4) to 2.049(5) Å for complex **2**. The greatest deviations of the bond angles from those expected for an ideal octahedral geometry are 84.2(4)° for N3–Co1–N4 and 95.3(4)° for O2–Co1–N3 for complex **1**, and 84.9(2)° for N3–Co1–N4 and 95.3(2)° for O2–Co1–N3 for complex **2**. The remaining bond angles around the Co atoms are nearly close to the ideal values for octahedral geometry. Moreover, the coordinate bond values are comparable to those ob-

served in similar Schiff base cobalt(III) complexes with octahedral geometry.¹⁵ The average deviation (0.033(4) Å for complex **1**, 0.037(3) Å for complex **2**) of the four donor atoms (O1, N1, N2, N3) and the displacement (0.001(2) Å for Co1 and 0.013(3) Å for Co2) of the Co atoms from the least-squares planes defined by the four donor atoms indicate that the ON₃ cavities afford almost perfect planes to the Co centers. The Schiff base ligands are twisted with dihedral angles between the benzene rings of 85.8(5) and 84.9(5)° for complex **1**, and 89.1(5) and 85.8(5)° for complex **2**.

In the crystal structure of complex **1** (Fig. 3), the nitrate anions are linked to the complex cations through N–H...O and C–H...O hydrogen bonds. In the crystal structure of complex **2** (Fig. 4), the chloride anions are linked to the complex cations through N–H...Cl and C–H...Cl hydrogen bonds. In addition, the molecules in both complexes are stack along the *a* axis via $\pi \cdots \pi$ interactions among the rings Co1–N1–C8–C9–N2, C1–C2–C3–C4–C5–C6, C10–C11–C12–C13–C14–C15 and C16–C17–C18–C19–C20–C21.

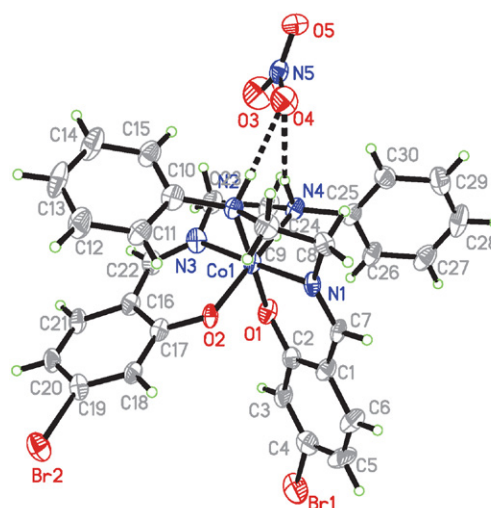


Fig. 1. Molecular structure of complex **1**.

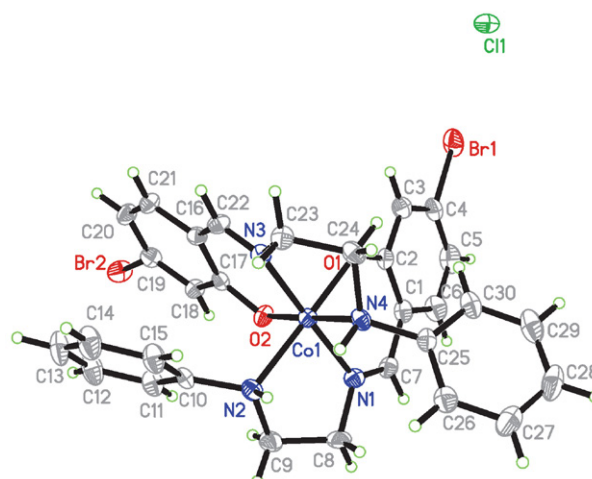


Fig. 2. Molecular structure of complex **2**.

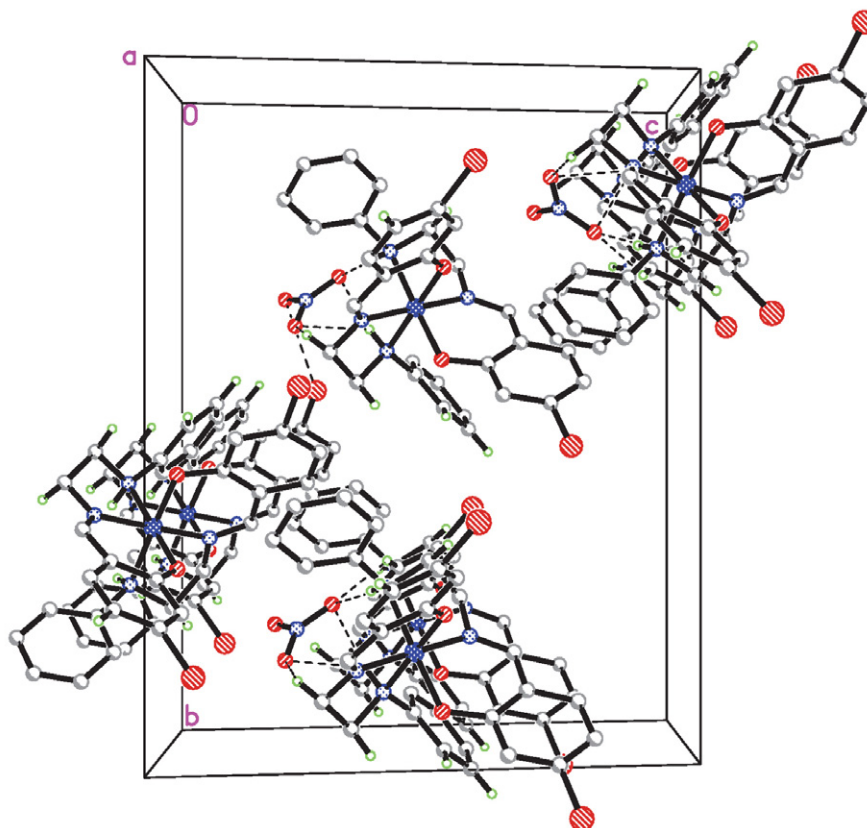


Fig. 3. Molecular packing diagram of complex 1, viewed along the *a* axis. Hydrogen bonds are drawn as dashed lines.

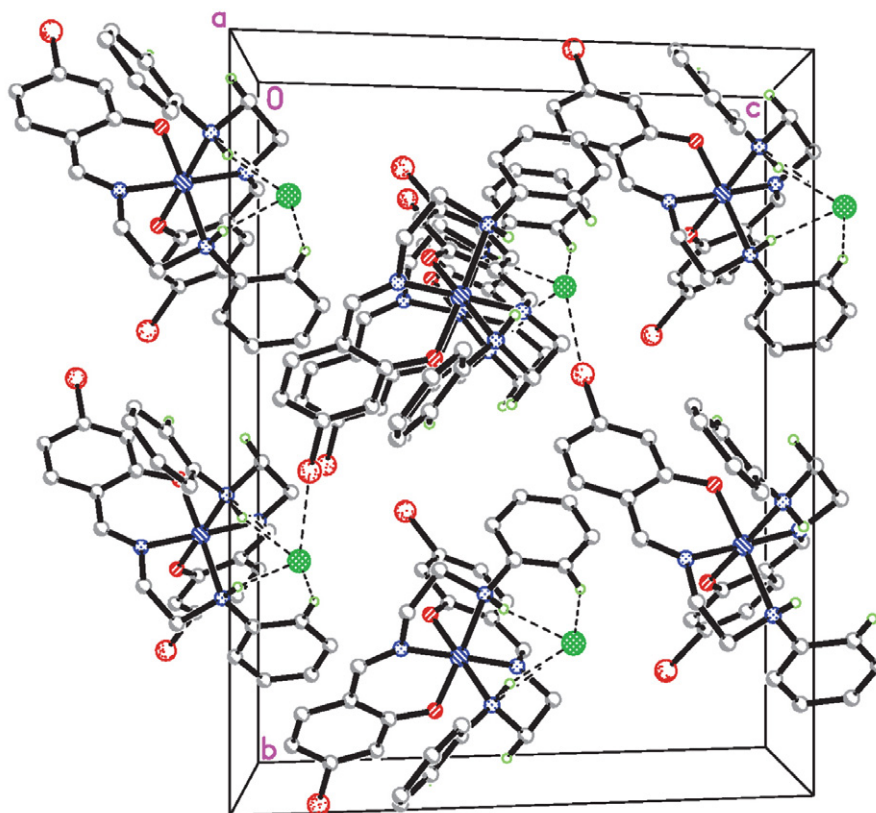


Fig. 4. Molecular packing diagram of complex 2, viewed along the *a* axis. Hydrogen bonds are drawn as dashed lines.

3. 4. Antibacterial Activity of the Compounds

The cobalt complexes were screened for antibacterial activities against three Gram-positive bacterial strains (*B. subtilis*, *S. aureus*, and *St. faecalis*) and three Gram-negative bacterial strains (*E. coli*, *P. aeruginosa*, and *E. cloacae*) by MTT method. The MICs of the compounds against the bacteria are presented in Table 3. Penicillin and Kanamycin were tested as reference drugs. The cobalt complexes have equal activities against all the bacterial strains. Both complexes showed strong activity against *B. subtilis*, *S. aureus* and *E. coli* (MICs = 0.39–3.12 $\mu\text{g mL}^{-1}$), weak activity against *St. faecalis* (MIC = 25 $\mu\text{g mL}^{-1}$), and no activity against *P. aeruginosa* and *E. cloacae*. Notably, both complexes have similar or better activity against *B. subtilis*, *S. aureus* and *E. coli* than the reference drugs.

Both complexes have stronger activities against *S. aureus* and *P. aeruginosa* than the cobalt(II) complexes with the Schiff bases, (4-X-2-[[2-(2-pyridine-2-yl-ethylsulfanyl)ethylimino]methyl]phenol (X = methoxy (OMe), phenylazo (N_2Ph), bromo (Br), nitro (NO_2)),¹⁶ and against *B. subtilis*, *S. aureus* and *E. coli* than the oxidovanadium(V) complexes with hydrazone ligands.¹⁷ The complexes have similar activities against *B. subtilis*, *S. aureus* and *E. coli*, but weak activities against *St. faecalis*, *P. aeruginosa* and *E. cloacae* when compared with the manganese complex with the Schiff base *N,N'*-bis(3,5-dichlorosalicylidene)-1,4-butanediamine.¹⁸

4. Conclusion

Two new cobalt(III) complexes with the Schiff base 5-bromo-2-((2-(phenylamino)ethylimino)methyl)phenol have been synthesized and characterized. Crystal structures of the complexes are determined and described. Both complexes are mononuclear cobalt species with octahedral coordination. The anions of the cobalt salts used in the preparation of the complexes act as the counteranions of the final structures. Both complexes have effective antibacterial activities against *B. subtilis*, *S. aureus* and *E. coli*.

Supplementary Materials

The crystal data for the complexes have been deposited with the Cambridge Crystallographic Data Centre

(CCDC nos. 2086791 (1) and 2086793 (2); deposit@ccdc.cam.ac.uk or <http://www.ccdc.cam.ac.uk>).

Acknowledgment

The author acknowledges Huaqiao University for supporting this work.

7. References

- (a) E. A. Fayed, R. R. E. Eldin, A. B. M. Mehany, A. H. Bayoumi, Y. A. Ammar, *J. Mol. Struct.* **2021**, *1234*, 130159; DOI:10.1016/j.molstruc.2021.130159
(b) K. C. Gan, K. M. Sim, T. M. Lim, K. C. Teo, *Lett. Org. Chem.* **2020**, *17*, 191–198; DOI:10.2174/1570178616666190724114741
(c) A. S. Hassan, H. M. Awad, A. A. Magd-El-Din, T. S. Hafez, *Med. Chem. Res.* **2018**, *27*, 915–927. DOI:10.1007/s00044-017-2113-5
- (a) N. Kordestani, H. A. Rudbari, A. R. Fernandes, L. R. Raposo, A. Luz, P. V. Baptista, G. Bruno, R. Scopelliti, Z. Fatemina, N. Micale, N. Tumanov, J. Wouters, A. A. Kajani, A. K. Bordbar, *Dalton Trans.* **2021**, *50*, 3990–4007; DOI:10.1039/D0DT03962D
(b) A. Patra, H. Puschmann, S. C. Manna, *Polyhedron* **2021**, *201*, 115146; DOI:10.1016/j.poly.2021.115146
(c) H. Kargar, A. A. Ardakani, M. N. Tahir, M. Ashfaq, K. S. Munawar, *J. Mol. Struct.* **2021**, *1233*, 130112; DOI:10.1016/j.molstruc.2021.130112
(d) B. Cristovao, D. Osypiuk, B. Miroslaw, A. Bartyzel, *Polyhedron* **2020**, *188*, 114703; DOI:10.1016/j.poly.2020.114703
(e) H. Mahmoudi, M. Bagherzadeh, S. Ataie, R. Kia, S. H. Moravej, M. Zare, P. R. Raithby, F. Ferlin, L. Vaccaro, *Inorg. Chim. Acta* **2020**, *511*, 119775. DOI:10.1016/j.ica.2020.119775
- L. A. Saghatforoush, F. Chalabian, A. Aminkhani, G. Karimnezhad, S. Ershad, *Eur. J. Med. Chem.* **2009**, *44*, 4490–4495. DOI:10.1016/j.ejmech.2009.06.015
- (a) E. Lodyga-Chruscinska, M. Symonowicz, A. Sykula, A. Bujacz, E. Garribba, M. Rowinska-Zyrek, S. Oldziej, E. Klewicka, M. Janicka, K. Krolewska, M. Cieslak, K. Brodowska, L. Chruscinski, *J. Inorg. Biochem.* **2015**, *143*, 34–47; DOI:10.1016/j.jinorgbio.2014.11.005

Table 3. MICs ($\mu\text{g mL}^{-1}$) of the compounds and related materials

Tested material	Gram positive			Gram negative		
	<i>B. subtilis</i>	<i>S. aureus</i>	<i>St. faecalis</i>	<i>P. aeruginosa</i>	<i>E. coli</i>	<i>E. cloacae</i>
HL	12.5	6.25	> 50	> 50	12.5	> 50
1	1.56	0.39	25	> 50	3.12	> 50
2	1.56	0.39	25	> 50	3.12	> 50
Penicillin	1.56	1.56	1.56	6.25	6.25	3.12
Kanamycin	0.39	1.56	3.12	3.12	3.12	1.56

- (b) Y.-F. Chen, L. Wei, J.-L. Bai, H. Zhou, Q.-M. Huang, J.-B. Li, Z.-Q. Pan, *J. Coord. Chem.* **2011**, *64*, 1153–1164; DOI:10.1080/00958972.2011.563846
- (c) W. A. Zoubi, A. A. S. Al-Hamdani, S. D. Ahmed, Y. G. Ko, *J. Phys. Org. Chem.* **2018**, *31*, e3752; DOI:10.1002/poc.3752
- (d) J. McGinley, M. McCann, K. J. Ni, T. Tallon, K. Kavanagh, M. Devereux, X. M. Ma, V. McKee, *Polyhedron* **2013**, *55*, 169–178; DOI:10.1016/j.poly.2013.03.023
- (e) P. S. Mane, S. M. Salunke, B. S. More, T. K. Chondhekar, *Asian J. Chem.* **2012**, *24*, 2235–2238.
5. (a) M. Salehi, M. Amirnasr, S. Meghdadi, K. Mereiter, H. R. Bijanzadeh, A. Khaleghian, *Polyhedron* **2014**, *81*, 90–97; DOI:10.1016/j.poly.2014.05.049
- (b) M. Ghosh, M. Layek, M. Fleck, R. Saha, D. Bandyopadhyay, *Polyhedron* **2015**, *85*, 312–319; DOI:10.1016/j.poly.2014.08.014
- (c) S. Mandal, T. Sen, U. Mandal, D. Bhunia, C. Rizzoli, D. Bandyopadhyay, *J. Coord. Chem.* **2019**, *72*, 3614–3624; DOI:10.1080/00958972.2019.1704275
- (d) G. Kalaiarasi, S. Dharani, S. R. J. Rajkumar, M. Ranjani, V. M. Lynch, R. Prabhakaran, *Inorg. Chim. Acta* **2021**, *515*, 120060. DOI:10.1016/j.ica.2020.120060
6. S. Esmailzadeh, Z. Zare, L. Azimian, *Bull. Chem. Soc. Ethiop.* **2016**, *30*, 209–220. DOI:10.4314/bcse.v30i2.5
7. (a) B. K. Mallandur, G. Rangaiah, N. V. Harohally, *Synth. Commun.* **2017**, *47*, 1065–1070; DOI:10.1080/00397911.2017.1309668
- (b) L. Shi, H.-M. Ge, S.-H. Tan, H.-Q. Li, Y.-C. Song, H.-L. Zhu, R.-X. Tan, *Eur. J. Med. Chem.* **2007**, *42*, 558–564. DOI:10.1016/j.ejmech.2006.11.010
8. G. M. Sheldrick, SAINT (version 6.02), SADABS (version 2.03), Madison (WI, USA): Bruker AXS Inc, **2002**.
9. G. M. Sheldrick, *Acta Crystallogr.* **2008**, *A64*, 112–122. DOI:10.1107/S0108767307043930
10. J. Meletiadis, J. Meis, J. W. Mouton, J. P. Donnelly, P. E. Verweij, *J. Clin. Microbiol.* **2000**, *38*, 2949–2956.
11. W. J. Geary, *Coord. Chem. Rev.* **1971**, *7*, 81–122. DOI:10.1016/S0010-8545(00)80009-0
12. L. Pogány, J. Moncol, M. Gál, I. Šalitroš, R. Boča, *Inorg. Chim. Acta* **2017**, *462*, 23–29. DOI:10.1016/j.ica.2017.03.001
13. Y.-M. Zhou, X.-R. Ye, F.-B. Xin, X.-Q. Xin, *Trans. Met. Chem.* **1999**, *24*, 118–120. DOI:10.1023/A:1006989707001
14. M. F. Iskander, T. E. Khalil, R. Werner, W. Haase, I. Svoboda, H. Fuess, *Polyhedron* **2000**, *19*, 1181–1191. DOI:10.1016/S0277-5387(00)00366-1
15. (a) D. Bandyopadhyay, M. Layek, M. Fleck, R. Saha, C. Rizzoli, *Inorg. Chim. Acta* **2017**, *461*, 174–182; DOI:10.1016/j.ica.2017.02.018
- (b) M. Ghosh, S. Mandal, M. Fleck, R. Saha, C. Rizzoli, D. Bandyopadhyay, *J. Coord. Chem.* **2018**, *71*, 4180–4193; DOI:10.1080/00958972.2018.1532080
- (c) M. Hasanzadeh, M. Salehi, M. Kubicki, S. M. Shahcheragh, G. Dutkiewicz, M. Pyziak, A. Khaleghian, *Trans. Met. Chem.* **2014**, *39*, 623–632. DOI:10.1007/s11243-014-9841-x
16. L. A. Saghatforoush, F. Chalabian, A. Aminkhani, G. Karimnezhad, S. Ershad, *Eur. J. Med. Chem.* **2009**, *44*, 4490–4495. DOI:10.1016/j.ejmech.2009.06.015
17. H.-Y. Qian, *Acta Chim. Slov.* **2019**, *66*, 995–1001. DOI:10.4149/neo_2019_190112N36
18. H.-Y. Qian, N. Sun, *Transition Met. Chem.* **2019**, *44*, 501–506. DOI:10.1007/s11243-018-00296-x

Povzetek

Sintetizirali smo dva strukturno podobna kompleksa Co(III), $[\text{CoL}_2] \cdot \text{NO}_3$ (**1**) in $[\text{CoL}_2] \cdot \text{Cl}$ (**2**), kjer je L = 5-bromo-2-((2-(fenilamino)etilimino)metil)fenolat, ter produkta karakterizirali z IR in UV-Vis spektroskopijo. Strukture kompleksov smo določili z monokristalno rentgensko difrakcijo. Kobaltovi atomi v kompleksih so oktaedrično koordinirani, pri čemer so donorski atomi iz dveh ligandov: kisik iz fenolne skupine ter dušikova atoma iz imino in amino skupine. Anioni kobaltovih soli kristalizirajo kot protiioni. Antibakterijsko učinkovitost kompleksov smo preverili z metodo MTT.



Except when otherwise noted, articles in this journal are published under the terms and conditions of the Creative Commons Attribution 4.0 International License

Scientific paper

Novel Structural Hybrids of Pyrrole and Thiazole Moieties: Synthesis and Evaluation of Antibacterial and Antifungal Activities

Mohamed A. Salem,¹ Samir Y. Abbas,^{2,*} Marwa A. M. Sh. El-Sharief,^{1,3}
Mohamed H. Helal,⁴ Moustafa A. Gouda,⁵ Mohammed A. Assiri,⁶
and Tarik E. Ali^{6,7}

¹ Department of Chemistry, Faculty of Science and Arts, King Khalid University, Mohail, Assir, Saudi Arabia

² Organometallic and Organometalloid Chemistry Department, National Research Centre, Cairo, Egypt

³ Applied Organic Chemistry Department, National Research Centre, Cairo, Egypt

⁴ Department of Chemistry, Faculty of Arts and Science, Northern Border University, Rafha, KSA

⁵ Department of Chemistry, Faculty of Science and Arts, Ulla, Taibah University, Medina, Saudi Arabia

⁶ Department of Chemistry, Faculty of Science, King Khalid University, Abha, Saudi Arabia

⁷ Department of Chemistry, Faculty of Education, Ain Shams University, Cairo, Egypt

* Corresponding author: E-mail: samiryoussef98@yahoo.com; sy.abbas@nrc.sci.eg

Received: 06-01-2021

Abstract

One of the best ways to design new biocidal agents is synthesizing hybrid molecules by combining two or more bioactive moieties in a single molecular scaffold. So, new series of pyrroles bearing a thiazole moiety were synthesized using 1-methyl-1*H*-pyrrole-2-carbaldehyde thiosemicarbazones **1a–c**. Cyclization of thiosemicarbazone derivatives **1a–c** with ethyl chloroacetate, ethyl 2-chloropropanoate, chloroacetone and phenacyl bromide afforded the corresponding thiazolidin-4-ones **2a–c**, 5-methylthiazolidin-4-ones **3a–c**, 4-methyl-2,3-dihydrothiazoles **4a–c**, and 4-phenyl-2,3-dihydrothiazoles **5a–c**, respectively. The antimicrobial activity of the new thiazole derivatives was evaluated.

Keywords: Pyrroles; Thiosemicarbazones; Thiazoles; Antibacterial activity; Antifungal activity

1. Introduction

One of the most serious future challenges to health care professionals is the emergence of multi-drug resistance pathogenic bacteria that rapidly develop resistance to currently used antibiotics. These medical problems can be reduced by the discovery of novel antibacterial and antifungal agents.^{1–10}

Pyrrole is widely known as a biologically active scaffold which possesses a diverse nature of activities.^{11,12} The combination of different pharmacophores in a pyrrole ring system has led to the formation of more active compounds.¹² The marketed drugs containing a pyrrole ring system are known to have many biological properties such

as antipsychotic, β -adrenergic antagonist, anxiolytic, anticancer (leukemia, lymphoma and myelofibrosis etc.), antibacterial, antifungal, antiprotozoal, antimalarial and many more.^{13–15} Pyrrolomycins and *N*-alkylated derivatives of pyrrolomycin are natural antibiotics and contain nitropyrrole nucleus which is stable and chemically reactive for antifungal activity.¹⁶ Verrucarine E and fenpiclonil are therapeutically useful antibacterial compounds. A naturally occurring pyoluteorin was found to possess antibacterial activity. Sortase A is a transpeptidase responsible for covalently anchoring many surface proteins in Gram-positive peptidoglycan, thus encouraging adhesion and biofilm formation. The inhibition of SrtA is related to the at-

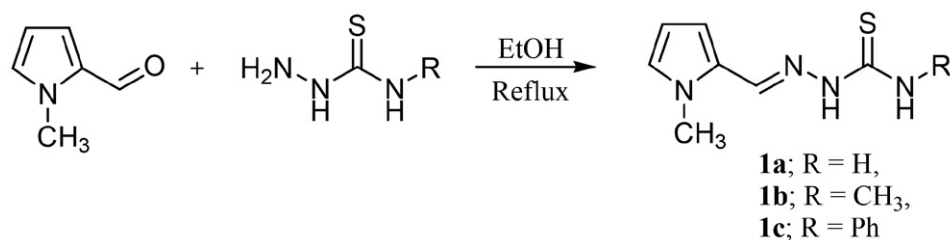
tenuation of virulence in *Staphylococcus aureus* and also in other important Gram-positive pathogens, such as *Listeria monocytogenes*, *S. pneumoniae*, and *S. smutans*.^{17,18}

Thiazole moiety frequently appears in the structure of many natural products as well as biologically active compounds. Thiazole moiety displayed crucial role in the medicinal chemistry research, where they have therapeutic effects against several diseases. Thiazoles showed the broad variety of biological activities, such as anti-inflammatory,¹⁹ analgesic,²⁰ allergies,²¹ hypertension,²² hypnotics,²³ schizophrenia,²⁴ anti-cancer,²⁵ antibacterial, antifungal¹ and anti-HIV²⁶ activities. Thiazole moiety represented the integral scaffold of the all penicillin derivatives. Penicillins are the first effective antibiotics used to treat microbes that played critical roles in the therapy of the bacterial diseases.²⁷ Abafungin is a broad-spectrum antifungal agent. Thiabendazole is a fungicide and parasiticide where it represented a new bacterial DNA gyrase B inhibitors.²⁸ Furthermore, most of fused thiazoles are attractive scaffolds for obtaining high potential drug candidates.^{29,30} Fused thiazoles, such as purine and their analogs possess significant biological activities.³¹

The synthesized compounds design was based on three points. First point is the many reports validation of pyrrole as antimicrobial agents. Second point, thiazole moiety has been already reported for its antimicrobial activity, thiazoles have occupied a prominent role in the design of biologically active agents. Thirdly, one of the main strategies for the discovery of new drugs is to modify the structure of a known drug or to unite two or more pharmacophoric moieties that being combined in one molecular scaffold to obtain the synergistic effect or developing newly affordable antibacterial activity having a new mode of action. To assemble novel biologically active compounds with potent antimicrobial effect, it is aimed to synthesize and evaluate the antimicrobial activity of series of 2-substituted pyrroles containing thiazole nucleus separated by a hydrophobic linker.

2. Results and Discussion

The starting 1-methyl-1*H*-pyrrole-2-carbaldehyde thiosemicarbazones **1a–c** were synthesized through the condensation reaction between 1-methyl-1*H*-pyrrole-2-carbaldehyde and thiosemicarbazide derivatives in ethanol

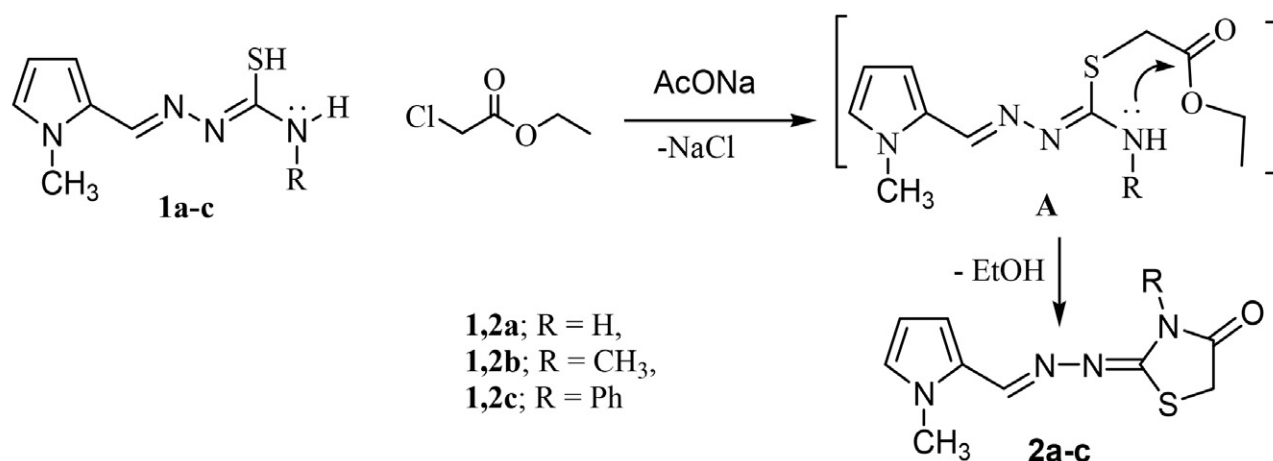


Scheme 1: Synthesis of 1-methyl-1*H*-pyrrole-2-carbaldehyde thiosemicarbazones **1a–c**

under reflux (Scheme 1). ¹H NMR spectrum of **1b** indicated doublet and singlet signals at δ 3.01 and 3.80 ppm for NH-CH₃ and NCH₃ protons, two signals at δ 7.88 and 11.14 ppm assignable for two NH protons, in addition to three multiplet signals at δ 6.08, 6.51 and 6.94 ppm for pyrrole protons with singlet signal at δ 8.04 ppm corresponding to CH=N proton. Also, ¹³C NMR indicated signals at δ 31.3 (CH₃), 36.51 (CH₃), 108.73, 114.85, 127.34, 128.28, 136.32 (CH=N) and 177.49 (C=S) ppm.

Thiosemicarbazones **1a–c** were subjected to cycloalkylation with different halogenated compounds in the hope of obtaining biologically activity thiazoles. Thus, when thiosemicarbazones **1a–c** were left to react with ethyl chloroacetate in refluxing ethanol containing a catalytic amount of fused sodium acetate resulted in the formation of the corresponding thiazolidines **2a–c** that were obtained in good yields. Evidence for assigned structures is provided by analytical and spectroscopic data. For example, ¹H NMR spectrum of **2a**, as an example, exhibited two singlet signals at δ 3.86 and 3.87 ppm assignable to CH₃ and CH₂ protons. The three protons of pyrrole ring were displayed at δ 6.12, 6.56 and 7.01 ppm as multiplet, singlet and singlet signals, respectively. A singlet signal at δ 8.25 ppm appeared for azomethine proton and a broad signal at δ 11.84 ppm due to imino proton. The formation of thiazolidone **2** may be assumed to proceed through initial alkylation for thiosemicarbazones **1** to afford the non-isolable intermediate **A** followed by intramolecular cyclization with elimination of ethanol (Scheme 2).

Similarly, 5-methyl-thiazolidin-4-one derivatives **3a–c** were obtained *via* cycloalkylation of thiosemicarbazones **1a–c** with ethyl 2-chloropropanoate in ethanol in the presence of sodium acetate under reflux condition. ¹H NMR spectrum of **3a** showed three diagnostic aliphatic signals for CH₃-CH, NCH₃ and CH-CH₃ protons at δ 1.49 (doublet), 3.87 (singlet) and 4.17 (quartet) ppm, respectively. The protons of pyrrole were displayed at δ 6.12, 6.55 and 7.10 ppm. Beside the last aromatic protons, ¹H NMR spectrum displayed signals for azomethine at δ 8.25 ppm together with NH broad signals at δ 11.80 ppm. In addition, under the same reaction conditions, cyclocondensation of thiosemicarbazones **1a–c** with chloroacetone furnished the corresponding 4-methyl-2,3-dihydrothiazole derivatives **4a–c**. ¹H NMR spectrum of **4a** exhibited two characteristic singlet signals for two methyl protons at δ 2.14 and 3.83 ppm. The H-5 of thiazole appeared at δ 6.06

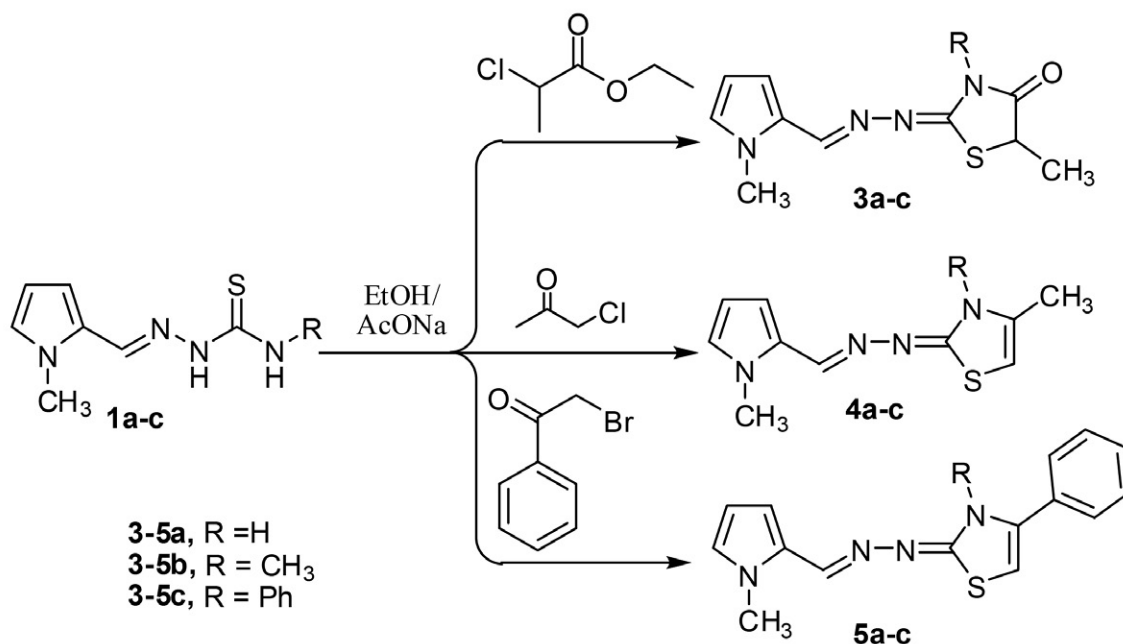


Scheme 2: Synthesis of thiazolidines 2a–c

ppm. The pyrrole protons were displayed at δ 6.28, 6.37 and 6.90 ppm, azomethine at δ 7.94 ppm. A broad signal at δ 11.39 ppm appeared for NH proton. Moreover, cyclocondensation of thiosemicarbazones **1a–c** with phenacyl bromide furnished the corresponding 4-phenyl-2,3-dihydrothiazole derivatives **5a–c**. ¹H NMR spectrum of **5a** showed singlet signal at δ 3.87 ppm assignable to NCH₃. The protons of phenyl group were displayed at δ 6.08, 7.40 and 7.85 ppm as triplet (one proton), triplet (two protons), and doublet (two protons), respectively. The protons of pyrrole were displayed at δ 6.93, 7.25 and 7.30 ppm. Signals at 6.41 and 7.98 ppm were characteristics for CH-thiazole and CH=N, respectively and a broad signal at δ 11.77 ppm due to NH proton (Scheme 3).

The newly synthesized compounds were screened for their expected antifungal and antibacterial activities.

Three different microbial groups were used. Group 1: Gram-positive bacteria: *Bacillus subtilis* (RCMB 015 (1) NRRL B-543) and *Staphylococcus aureus* (ATCC 25923). Group 2: Gram-negative bacteria: *Proteus vulgaris* (RCMB 004 (1) ATCC 13315) and *Escherichia coli* (ATCC 25922). Group 3: Fungi: *Candida albicans* (RCMB 005003 (1) ATCC 10231) and *Aspergillus fumigatus* (RCMB 002008). For the screening of antibacterial activity, diffusion agar technique¹ was applied at 10 mg/mL concentration, well diameter 6.0 mm (100 μ L was tested). For comparison, Gentamycin and Ketoconazole were used as antibacterial and antifungal agents, respectively. The inhibition zone diameters are depicted in Table 1. Regarding the antimicrobial activity of thiazole derivatives, they displayed good effects towards *P. vulgaris* only. Few compounds displayed weak effects towards some of the tested organisms. The



Scheme 3: Synthesis of thiazole derivatives 3a–c, 4a–c and 5a–c.

Table 1: The mean results of inhibition zone in mm produced on a range of pathogenic microorganisms

Compd. No.	Gram positive bacteria		Gram negative bacteria		Fungi	
	<i>B. subtilis</i>	<i>S. aureus</i>	<i>P. vulgaris</i>	<i>E. coli</i>	<i>C. albicans</i>	<i>A. fumigatus</i>
2a	NA	NA	21	10	NA	NA
2b	NA	NA	23	9	NA	NA
2c	NA	NA	10	NA	NA	NA
3a	NA	NA	16	NA	NA	NA
3b	9	NA	15	10	8	NA
3c	8	8	16	9	NA	9
4a	12	NA	13	NA	9	8
4b	NA	NA	24	12	NA	NA
4c	8	9	18	10	8	8
5a	9	NA	15	13	NA	NA
5b	NA	NA	18	8	NA	NA
5c	9	NA	17	9	9	8
Gentamycin	26	24	25	30	—	—
Ketoconazole	—	—	—	—	20	17

major compounds displayed no effects towards most of the tested organisms.

3. Conclusion

New series of pyrroles bearing a thiazole moiety were synthesized through cyclization of 1-methyl-1*H*-pyrrole-2-carbaldehyde thiosemicarbazone derivatives with ethyl chloroacetate, ethyl 2-chloropropanoate, chloroacetone and phenacyl bromide. The thiazole derivatives displayed good effects towards *P. vulgaris* only. Few compounds displayed weak effects towards some of the tested organisms. The major compounds displayed no effects towards most of the tested organisms.

3.1. Experimental Section

Nuclear magnetic resonance spectra were carried out in deuterated dimethylsulfoxide (DMSO-*d*₆) by using Bruker spectrometers (¹H NMR 400 MHz; ¹³C NMR 101 MHz) with chemical shift in δ from internal TMS. Mass spectra were recorded on GC/MS Finnigan SSQ 7000 spectrophotometer and GC Ms-QP 1000 EX mass spectrometer at 70 eV. Elemental analyses were carried out on a EuroVector instrument C, H, N analyzer EA3000 Series.

Synthesis of *N*-Substituted-2-((1-methyl-1*H*-pyrrol-2-yl)methylene)hydrazinecarbothioamides 1a–c³²

The mixture of 0.01 mol of 1-methyl-1*H*-pyrrole-2-carbaldehyde and 0.01 mol of the selected thiosemicarbazides (thiosemicarbazide, *N*-methylthiosemicarbazide, *N*-phenylthiosemicarbazide) was heated in 50 mL ethanol under reflux for 0.5 h., left to cool, the resultant solid product was collected by filtration. The solid products were crystallized from ethanol.

***N*-Methyl-2-((1-methyl-1*H*-pyrrol-2-yl)methylene)hydrazinecarbothioamide (1b).** Yield 1.76 g (90%); m.p. 180–182 °C; ¹H NMR δ 3.01 (d, 3H, *J* = 4.6 Hz, NHCH₃), 3.80 (s, 3H, NCH₃), 6.08 (m, 1H, pyrrole-H), 6.51 (m, 1H, pyrrole-H), 6.94 (m, 1H, pyrrole-H), 7.88 (br, 1H, NH), 8.04 (s, 1H, CH=N), 11.14 (s, 1H, NH); ¹³C NMR: δ 31.3 (CH₃), 36.51 (CH₃), 108.73, 114.85, 127.34, 128.28, 136.32 (CH=N), 177.49 (C=S); MS *m/z* (%): 196 (M⁺; 67.4). Anal. Calcd. for C₈H₁₂N₄S (196.27): C, 48.96; H, 6.16; N, 28.55. Found: C, 48.87; H, 6.14; N, 28.47%.

***N*-Methyl-2-((1-methyl-1*H*-pyrrol-2-yl)methylene)hydrazinecarbothioamide (1c).** Yield 2.45 g (95%); m.p. 140–142 °C; ¹H NMR: δ 3.86 (s, 3H, NCH₃), 6.12 (m, 1H, pyrrole-H), 6.64 (m, 1H, pyrrole-H), 6.99 (m, 1H, pyrrole-H), 7.18 (t, 1H, *J* = 7.4 Hz, Ph-H), 7.35 (t, 2H, *J* = 7.8 Hz, Ph-H), 7.64 (d, 2H, *J* = 7.7 Hz, Ph-H), 8.15 (s, 1H, CH=N), 9.55 (s, 1H, NH), 11.55 (s, 1H, NH); MS *m/z* (%): 258 (M⁺; 46.0). Anal. Calcd. for C₁₃H₁₄N₄S (258.34): C, 60.44; H, 5.46; N, 21.69. Found: C, 60.38; H, 5.45; N, 21.73%.

Synthesis of Thiazolidin-4-one Derivatives 2a–c

The mixture of 0.01 mol of the thiosemicarbazide derivatives 1a–c, 0.01 mol of ethyl chloroacetate and 0.02 mol of fused sodium acetate was dissolved 50 mL ethanol. The solution was heated under reflux for 3 hours, then left to cool. The obtained products were collected by filtration. The solid products were recrystallized from ethanol.

2-(((1-Methyl-1*H*-pyrrol-2-yl)methylene)hydrazono)thiazolidin-4-one (2a). Yield 1.89 g (85%); m.p. 248–250 °C; ¹H NMR: δ 3.86, 3.87 (2s, 5H, CH₂ and CH₃), 6.12 (m, 1H, pyrrole-H), 6.56 (s, 1H, pyrrole-H), 7.01 (s, 1H, pyrrole-H), 8.25 (s, 1H, CH=N), 11.84 (s, 1H, NH); MS *m/z* (%): 222 (M⁺; 33.8). Anal. Calcd. for C₉H₁₀N₄OS (222.27): C, 48.63; H, 4.53; N, 25.21. Found: C, 48.57; H, 4.55; N, 25.17%.

3-Methyl-2-(((1-methyl-1*H*-pyrrol-2-yl)methylene)hydrazono)thiazolidin-4-one (2b). Yield 1.88 g (80%); m.p. 183–184 °C; ¹H NMR: δ 3.16 (s, 3H, CH₃), 3.88 (s, 3H, CH₃), 3.92 (s, 2H, CH₂-thiazole), 6.13 (s, 1H, pyrrole-H), 6.59 (s, 1H, pyrrole-H), 7.03 (s, 1H, pyrrole-H), 8.35 (s, 1H, CH=N); ¹³C NMR: δ 29.77 (CH₃), 32.54 (CH₃), 37.02 (CH₂), 109.00, 117.49, 127.55, 129.74, 150.00 (CH=N), 162.69 (CH=N), 172.61 (C=O); MS *m/z* (%): 236 (M⁺; 62.2). Anal. Calcd. for C₁₀H₁₂N₄OS (236.29): C, 50.83; H, 5.12; N, 23.71. Found: C, 50.86; H, 5.10; N, 23.67%.

2-(((1-Methyl-1*H*-pyrrol-2-yl)methylene)hydrazono)-3-phenylthiazolidin-4-one (2c). Yield 2.53 g (85%); m.p. 256–258 °C; ¹H NMR: δ 3.88 (s, 3H, CH₃), 4.07 (s, 2H, CH₂-thiazole), 6.10 (m, 1H, pyrrole-H), 6.53 (m, 1H, pyrrole-H), 7.02 (s, 1H, pyrrole-H), 7.38 (d, 2H, *J* = 7.2 Hz, Ph-H), 7.46 (d, 1H, *J* = 7.3 Hz, Ph-H), 7.52 (t, 2H, *J* = 7.4 Hz, Ph-H), 8.15 (s, 1H, CH=N); MS *m/z* (%): 298 (M⁺; 22.3). Anal. Calcd. for C₁₅H₁₄N₄OS (298.36): C, 60.38; H, 4.73; N, 18.78. Found: C, 60.43; H, 4.75; N, 18.82%.

Synthesis of 5-Methyl-thiazolidin-4-one Derivatives 3a–c

The mixture of 0.01 mol of the thiosemicarbazide derivatives **1a–c**, 0.01 mol of ethyl 2-chloropropanoate and 0.02 mol of fused sodium acetate was dissolved 50 mL ethanol. The solution was heated under reflux for 5 hours. After cooling, precipitated solid were obtained which were collected by filtration and recrystallized from ethanol.

5-Methyl-2-(((1-methyl-1*H*-pyrrol-2-yl)methylene)hydrazono)thiazolidin-4-one (3a). Yield 1.65 g (70%); m.p. 210–212 °C; ¹H NMR: δ 1.49 (d, 3H, *J* = 7.2 Hz, CH₃), 3.87 (s, 3H, NCH₃), 4.17 (q, 1H, *J* = 7.2 Hz, thiazole-H), 6.12 (m, 1H, pyrrole-H), 6.55 (m, 1H, pyrrole-H), 7.10 (s, 1H, pyrrole-H), 8.25 (s, 1H, CH=N), 11.80 (br, 1H, NH); MS *m/z* (%): 236 (M⁺; 49.0). Anal. Calcd. for C₁₀H₁₂N₄OS (236.29): C, 50.83; H, 5.12; N, 23.71. Found: C, 50.86; H, 5.11; N, 23.67%.

3,5-Dimethyl-2-(((1-methyl-1*H*-pyrrol-2-yl)methylene)hydrazono)thiazolidin-4-one (3b). Yield 1.68 g (67%); ¹H NMR: δ 1.50 (d, 3H, *J* = 7.2 Hz, CH₃), 3.27 (s, 3H, CH₃), 3.89 (s, 3H, CH₃), 4.20 (m, 1H, thiazole-H), 6.14 (m, 1H, pyrrole-H), 6.55 (m, 1H, pyrrole-H), 7.13 (s, 1H, pyrrole-H), 8.25 (s, 1H, CH=N); MS *m/z* (%): 250 (M⁺; 18.7). Anal. Calcd. for C₁₁H₁₄N₄OS (250.32): C, 52.78; H, 5.64; N, 22.38. Found: C, 52.73; H, 5.61; N, 22.42%.

5-Methyl-2-(((1-methyl-1*H*-pyrrol-2-yl)methylene)hydrazono)-3-phenylthiazolidin-4-one (3c). Yield 2.34 g (75%); ¹H NMR: δ 1.51 (d, 3H, *J* = 7.2 Hz, CH₃), 3.86 (s, 3H, NCH₃), 4.22 (m, 1H, thiazole-H), 6.10–7.10 (m, 8H, Ph-H and pyrrole-H), 8.32 (s, 1H, CH=N); MS *m/z* (%): 312 (M⁺; 27.0). Anal. Calcd. for C₁₆H₁₆N₄OS (312.39): C, 61.52; H, 5.16; N, 17.93. Found: C, 61.48; H, 5.14; N, 17.96%.

Synthesis of 4-Methyl-2,3-dihydrothiazole Derivatives 4a–c

The mixture of 0.01 mol of the thiosemicarbazide derivatives **1a–c**, 0.01 mol of chloroacetone and 0.02 mol of fused sodium acetate was dissolved 50 mL ethanol. The solution was heated under reflux for 6 h and left to cool. The obtained product was collected by filtration. The solid products were recrystallized from ethanol.

4-Methyl-2-(((1-methyl-1*H*-pyrrol-2-yl)methylene)hydrazono)-2,3-dihydrothiazole (4a). Yield 1.65 g (75%); m.p. 177–179 °C; ¹H NMR: δ 2.14 (s, 3H, CH₃), 3.83 (s, 3H, NCH₃), 6.06 (m, 1H, pyrrole-H), 6.28 (s, 1H, thiazole-H), 6.37 (m, 1H, pyrrole-H), 6.90 (s, 1H, pyrrole-H), 7.94 (s, 1H, CH=N), 11.39 (s, 1H, NH); MS *m/z* (%): 220 (M⁺; 46.6). Anal. Calcd. for C₁₀H₁₂N₄S (220.29): C, 54.52; H, 5.49; N, 25.43. Found: C, 54.48; H, 5.50; N, 25.38%.

3,4-Dimethyl-2-(((1-methyl-1*H*-pyrrol-2-yl)methylene)hydrazono)-2,3-dihydro-thiazole (4b). Yield 1.64 g (70%); m.p. 196–198 °C; ¹H NMR: δ 2.12 (s, 3H, CH₃), 3.31 (s, 3H, NCH₃), 3.86 (s, 3H, NCH₃), 5.95 (m, 1H, Ar-H), 6.06 (m, 1H, Ar-H), 6.39 (m, 1H, thiazole-H), 6.89 (s, 1H, Ar-H), 8.17 (s, 1H, CH=N); ¹³C NMR: δ 14.21 (CH₃), 31.48 (CH₃), 36.86 (CH₃), 95.69, 108.40, 114.34, 127.78, 128.77, 136.52, 143.22, 168.37 (CH=N); MS *m/z* (%): 234 (M⁺; 45.7). Anal. Calcd. for C₁₁H₁₄N₄S (234.32): C, 56.38; H, 6.02; N, 23.91; S, 17.34. Found: C, 56.34; H, 6.04; N, 23.87%.

4-Methyl-2-(((1-methyl-1*H*-pyrrol-2-yl)methylene)hydrazono)-3-phenyl-2,3-dihydrothiazole (4c). Yield 2.22 g (75%); ¹H NMR: δ 2.15 (s, 3H, CH₃), 3.85 (s, 3H, NCH₃), 5.95 (m, 1H, Ar-H), 6.10–6.90 (m, 8H, pyrrole-H and Ph-H), 8.26 (s, 1H, CH=N); MS *m/z* (%): 296 (M⁺; 24.8). Anal. Calcd. for C₁₆H₁₆N₄S (296.39): C, 64.84; H, 5.44; N, 18.90. Found: C, 64.86; H, 5.42; N, 18.86%.

Synthesis of 4-Phenyl-2,3-dihydrothiazole Derivatives 5a–c

The mixture of 0.01 mol of the thiosemicarbazide derivatives **1a–c**, 0.01 mol of phenacyl bromide and 0.02 mol of fused sodium acetate was dissolved 50 mL ethanol. The solution was heated under reflux for 6 h and left to cool. The obtained product was collected by filtration. The solid products were recrystallized from ethanol.

2-(((1-Methyl-1*H*-pyrrol-2-yl)methylene)hydrazono)-4-phenyl-2,3-dihydrothiazole (5a).^[33] Yield 2.40 g (85%); m.p. 180–182 °C; ¹H NMR: δ 3.87 (s, 3H, CH₃), 6.08 (m, 1H, pyrrole-H), 6.41 (m, 1H, pyrrole-H), 6.93 (s, 1H, pyrrole-H), 7.25 (s, 1H, thiazole-H), 7.30 (d, 1H, *J* = 7.3 Hz, Ph-H), 7.40 (t, 2H, *J* = 7.6 Hz, Ph-H), 7.85 (d, 2H, *J* = 7.4 Hz, Ph-H), 7.98 (s, 1H, CH=N); 11.77 (br, 1H, NH); MS *m/z* (%): 282 (M⁺; 43.1). Anal. Calcd. for C₁₅H₁₄N₄S (282.36): C, 63.80; H, 5.00; N, 19.84. Found: C, 63.77; H, 4.98; N, 19.78%.

3-Methyl-2-(((1-methyl-1H-pyrrol-2-yl)methylene)hydrazono)-4-phenyl-2,3-dihydrothiazole (5b). Yield 2.37 g (80%); m.p. 127–128 °C; ¹H NMR: δ 3.27 (s, 3H, CH₃), 3.89 (s, 3H, CH₃), 6.06 (m, 1H, pyrrole-H), 6.32 (s, 1H, thiazole-H), 6.43 (m, 1H, pyrrole-H), 6.93 (s, 1H, pyrrole-H), 7.50 (m, 5H, Ar-H), 8.23 (s, 1H, CH=N); MS *m/z* (%): 296 (M⁺; 23.2). Anal. Calcd. for C₁₆H₁₆N₄S (296.39): C, 64.84; H, 5.44; N, 18.90. Found: C, 64.79; H, 5.46; N, 18.87%.

2-(((1-Methyl-1H-pyrrol-2-yl)methylene)hydrazono)-3,4-diphenyl-2,3-dihydro-thiazole (5c). Yield 3.04 g (85%); ¹H NMR: δ 3.92 (s, 3H, CH₃), 6.06 (m, 14H, thiazole-H, pyrrole-H, 2Ph-H), 8.34 (s, 1H, CH=N); MS *m/z* (%): 358 (M⁺; 49.0). Anal. Calcd. for C₂₁H₁₈N₄S (358.46): C, 70.36; H, 5.06; N, 15.63. Found: C, 70.41; H, 5.08; N, 15.57%.

Acknowledgment

The authors extend their appreciation to the Deanship of Scientific Research at King Khalid University for funding this work through General Research Project under grant number (RGP. 2/88/42).

4. References

- S. I. Eissa, A. M. Farrag, S. Y. Abbas, M. F. El Shehry, A. Ragab, E. A. Fayed, Y. A. Ammar, *Bioorg. Chem.*, **2021**, *110*, 104803 DOI:10.1016/j.bioorg.2021.104803
- M. F. El Shehry, S. Y. Abbas, A. M. Farrag, S. I. Eissa, S. A. Fouad, Y. A. Ammar, *Med. Chem. Res.*, **2018**, *27*, 2287–2296. DOI:10.1007/s00044-018-2235-4
- M. A. Salem, A. Ragab, A. A. Askar, A. El-Khalafawy, A. H. Makhoulf, *Eur. J. Med. Chem.*, **2020**, *188*, 111977. DOI:10.1016/j.ejmech.2019.111977
- M. A. Salem, A. Ragab, A. El-Khalafawy, A. H. Makhoulf, A. A. Askar, Y. A. Ammar, *Bioorg. Chem.* **2020**, *96*, 103619. DOI:10.1016/j.bioorg.2020.103619
- S. A. Fouad, S. A. Hessein, S. Y. Abbas, A. M. Farrag, Y. Ammar, *Croat. Chem. Acta*, **2018**, *91*, 99–107.
- M. F. El Shehry, M. M. Ghorab, S. Y. Abbas, E. A. Fayed, S. A. Shedid, Y. A. Ammar, *Eur. J. Med. Chem.*, **2018**, *143*, 1463–1473. DOI:10.1016/j.ejmech.2017.10.046
- M. A. M. S. El-Sharief, S. Y. Abbas, Z. Moussa, E. W. El-Gammal, A. M. S. El-Sharief, *Croat. Chem. Acta*, **2018**, *91*, 335–340. DOI:10.5562/cca3354
- M. A. M. S. El-Sharief, S. Y. Abbas, K. A. M. El-Bayouki, E. W. El-Gammal, *Eur. J. Med. Chem.* **2013**, *67*, 263–268. DOI:10.1016/j.ejmech.2013.06.031
- S. Y. Abbas, M. A. M. S. El-Sharief, W. M. Basyouni, I. M. I. Fakhr, E. W. El-Gammal, *Eur. J. Med. Chem.*, **2013**, *64*, 111–120. DOI:10.1016/j.ejmech.2013.04.002
- M. H. Helal, S. Y. Abbas, M. A. Salem, A. A. Farag, Y. A. Ammar, *Med. Chem. Res.* **2013**, *22*, 5598–5609. DOI:10.1007/s00044-013-0524-5
- G. L. Petri, V. Spano, R. Spatola, R. Holl, M. V. Raimondi, P. Barraja, A. Montalbano, *Eur. J. Med. Chem.*, **2020**, *208*, 112783. DOI:10.1016/j.ejmech.2020.112783
- V. Bhardwaj, D. Gumber, V. Abbot, S. Dhimana, P. Sharma, *RSC Adv.*, **2015**, *5*, 15233–15266. DOI:10.1039/C4RA15710A
- R. P. Wurz, A. B. Charette, *Org. Lett.*, **2005**, *7*, 2313–2316. DOI:10.1021/ol050442l
- H. Lee, J. Lee, S. Lee, Y. Shin, W. Jung, J.-H. Kim, K. Park, K. Kim, H. S. Cho, S. Ro, *Bioorg. Med. Chem. Lett.*, **2001**, *11*, 3069–3072. DOI:10.1016/S0960-894X(01)00624-2
- W. W. Wilkerson, R. A. Copeland, M. Covington, J. M. Trzaskos, *J. Med. Chem.*, **1995**, *38*, 3895–3901. DOI:10.1021/jm00020a002
- M. Koyama, N. Ohtani, F. Kai, I. Moriguchi, S. Inouye, *J. Med. Chem.*, **1987**, *30*, 552–562. DOI:10.1021/jm00386a019
- S. Cascioferro, D. Raffa, B. Maggio, M. V. Raimondi, D. Schillaci, G. Daidone, *J. Med. Chem.* **2015**, *58*, 9108–9123. DOI:10.1021/acs.jmedchem.5b00779
- S. Cascioferro, B. Maggio, D. Raffa, M. V. Raimondi, M. G. Cusimano, D. Schillaci, B. Manachini, F. Plescia, G. Daidone, *Eur. J. Med. Chem.* **2016**, *123*, 58–68. DOI:10.1016/j.ejmech.2016.07.030
- S. Sinha, M. Doble, S. L. Manju, *Eur. J. Med. Chem.* **2018**, *158*, 34–50. DOI:10.1016/j.ejmech.2018.08.098
- S. O. Pember, G. L. Mejia, T. J. Price, R. J. Pasteris, *Bioorg. Med. Chem. Lett.* **2016**, *26*, 2965–2973. DOI:10.1016/j.bmcl.2016.02.061
- K. D. Hargrave, F. K. Hess, J. T. Oliver, *J. Med. Chem.* **1983**, *26*, 1158–1163. DOI:10.1021/jm00362a014
- W. C. Patt, H. W. Hamilton, M. D. Taylor, M. J. Ryan, D. G. Taylor Jr., C. J. C. Connolly, A. M. Doherty, S. R. Klutchko, I. Sircar, B. A. Steinbaugh, B. L. Batley, C. A. Painchaud, S. T. Rapundalo, B. M. Michniewicz, S. C. J. Olso, *J. Med. Chem.* **1992**, *35*, 2562–2572. DOI:10.1021/jm00092a006
- N. Ergenc, G. Capan, N.S. Gunay, S. Ozkirimli, M. Gungor, S. Ozbey, E. Kendi, *Arch. Pharm. Pharm. Med. Chem.* **1999**, *332*, 343–347. DOI:10.1002/(SICI)1521-4184(199910)332:10<343::AID-ARDP343>3.0.CO;2-0
- J. C. Jaen, L. D. Wise, B. W. Caprathe, H. Tecle, S. Bergmeier, C. C. Humblet, T. G. Heffner, L. T. Meltzner, T. A. Pugsley, *J. Med. Chem.* **1990**, *33*, 311–317. DOI:10.1021/jm00163a051
- Y. Wang, C. Wu, Q. Zhang, Y. Shan, W. Gu, S. Wang, *Bioorg. Chem.* **2019**, *84*, 468–477. DOI:10.1016/j.bioorg.2018.12.010
- F. W. Bell, A. S. Cantrell, M. Hogberg, S. R. Jaskunas, N. G. Johansson, C. L. Jordon, M. D. Kinnick, P. Lind, J. M. Morin Jr., R. Noreen, B. Oberg, J. A. Palkowitz, C. A. Parrish, P. Pranc, C. Sahlberg, R. J. Ternansky, R. T. Vasileff, L. Vrang, S. J. West, H. Zhang, X. X. Zhou, *J. Med. Chem.* **1995**, *38*, 4929–4936.
- S. Oncu, M. Punar, H. Erakosy, *Chemotherapy* **2004**, *50*, 98–100. DOI:10.1159/000077810
- J. Rudolph, H. Theis, R. Hanke, R. Endermann, L. Johannsen, F. U. Geschke, *J. Med. Chem.*, **2001**, *44*, 619–626. DOI:10.1021/jm0010623
- A. Srinivas, M. Sunitha, S. Shamili, *Acta Chimica Slovenica*, **2020**, *67*, 1061–1071. DOI:10.17344/acsi.2019.5752

- 30 M. A. Salem, M. Helal, M. El-Gaby, Y. Ammar, M. Gouda, S. Y. Abbas, *To Chem. J.*, **2018**, *1*, 114–144.
- 31 W. M. Basyouni, S. Y. Abbas, R. M. Dawood, K. A. M. El-Bayouki, M. K. El Awady, T. H. Abdelhafez, *J. Heterocycl. Chem.*, **2021**, *58*, 1766–1774. DOI:10.1002/jhet.4307
- 32 F. E. Anderson, C. J. Duca, J. V. Scudi *J. Am. Chem. Soc.*, **1951**, *73*, 4967–4968. DOI:10.1021/ja01154a501
- 33 L. Yurttaş, Y. Özkay, Z. A. Kaplancikli, Y. Tunalı, H. Karaca, *J. Enz. Inhib. Med. Chem.*, **2013**, *28*, 830–835. DOI:10.3109/14756366.2012.688043

Povzetek

Eden izmed najboljših načinov za načrtovanje novih biocidnih spojin je sinteza hibridnih molekul, do katerih pridemo s povezavo dveh ali več bioaktivnih fragmentov v eno samo molekulsko ogrodje. Tako smo iz serije 1-metil-1*H*-pirol-2-karbaldehid tiosemikarbazonov **1a–c** pripravili nov set pirolov, ki so vsebovali tiazolni fragment. Ciklizacija tiosemikarbazonskih derivatov **1a–c** z etil kloroacetatom, etil 2-kloropropanoatom, kloroacetonom ali fenacil bromidom je vodila do ustreznih tiazolidin-4-onov **2a–c**, 5-metiltiazolidin-4-onov **3a–c**, 4-metil-2,3-dihidrotiazolov **4a–c** in 4-fenil-2,3-dihidrotiazolov **5a–c**. Določili smo tudi antimikrobne aktivnosti novih tiazolskih derivatov.



Except when otherwise noted, articles in this journal are published under the terms and conditions of the Creative Commons Attribution 4.0 International License

Scientific paper

Statistical Optimization of As(V) Adsorption Parameters onto Epichlorohydrin/Fe₃O₄ Crosslinked Chitosan Derivative Nanocomposite using Box-Behnken Design

Vijayanand Nagarajan,^{1,*} Raja Ganesan,¹ Srinivasan Govindan²
and Prabha Govind³

¹ Anna University, Faculty of Chemistry, Paavai Engineering College, Namakkal 637018, TN, INDIA

² Anna University, Faculty of Chemical Engineering, Paavai Engineering College, Namakkal 637018, TN, INDIA

³ Anna University, Department of Applied Science and Technology, Alagappa College of Technology, Chennai 600005 INDIA

* Corresponding author: E-mail: vijayanandnagarajanpec@paavai.edu.in
Phone: +91 8344488356

Received: 06-07-2021

Abstract

In this study, Box-Behnken design (BBD) in response surface methodology (RSM) was employed to optimize As(V) removal from an aqueous solution onto synthesized crosslinked carboxymethylchitosan-epichlorohydrin/Fe₃O₄ nanocomposite. The factors like solution pH, adsorbent dose, contact time and temperature were optimized by the method which shows high correlation coefficient ($R^2 = 0.9406$), and a predictive quadratic polynomial model equation. The adequacy of the model and parameters were evaluated by analysis of variance (ANOVA) with their significant factors of Fischer's *F*-test ($p < 0.05$). Seven significant parameters with interaction effects in the experiment with p -value < 0.0001 was observed, having a maximum removal efficiency of As(V) is 95.1%. Optimal conditions of dosage, pH, temperature, initial ion concentration and contact time in the process were found to be 0.7 g, pH 6.5, 308K, 10 mg/L and 60 min respectively. Langmuir isotherm model fitted better than the Freundlich model having a maximum adsorption capacity of 28.99 mg/g, a high regression value of 0.9988, least chi-square value of 0.1781. The process was found to follow monolayer adsorption and pseudo-second-order kinetics. Thermodynamic parameters indicate the process is spontaneous, endothermic and physisorption in nature. Successful regeneration of the adsorbent implies its applicability to the removal of arsenic from real life wastewater.

Keywords: Biosorption; isotherm; kinetics; thermodynamic; optimization; response surface methodology.

1. Introduction

Arsenic is a pervasive element in the environment and has been known as a notorious toxic substance to man and living organisms for centuries.¹ Groundwater Arsenic is primarily associated with oxidative weathering and geochemical reaction of reactive carbon induce mobilization of arsenic in the sediments.² Arsenic contaminated groundwater affects over 100 million people in Bangladesh, West Bengal, China, Mexico, Chile, Myanmar, and United states.³ Long term exposure to arsenic in drinking water causes skin diseases (pigmentation, dermal hyperkeratosis, skin cancer), cardiovascular, neurological, renal, respiratory and black foot diseases, as well as lung, liver, kidney and prostate cancers.⁴ To protect public health, the

World Health Organization has set a provisional guideline limits of 10 µg/L for arsenic in drinking water which was afterward adopted by the European Union and India.⁵ The removal of Arsenic by Co-precipitation, flotation, ion-exchange, ultra-filtration, and reverse osmosis⁶ have been received more attention due to its high concentration efficiency.⁶ Several adsorbents have been found suitable for arsenic removal counting activated carbon,⁷ activated alumina,⁸ red mud,⁹ etc., In the last decade developments in the knowledge of biosorption exposed high adsorption capacities, low costs and regenerability of natural biosorption materials.¹⁰ However, challenges encountered for biosorbents with high uptake, low cost and as well as in understanding the mechanism of reaction. Chitosan is produced from N-deacetylation of chitin, available from

seafood processing wastes, having hydroxyl and amine group promises good sorption capacity for heavy metal ions through complexation reaction.¹¹ However, in practical applications it requires a chemical modification to improve the nature of hydrophilic property and adsorption capacity. Carboxymethyl chitosan (CMC) is an amphiprotic chitosan derivative, having hydroxyl (-OH), carboxyl(-COOH) and amine (-NH₂) groups in the molecule can be a substitute for chitosan. But, its poor chemical stability¹² can be overcome by crosslinking reaction with the agents like, glutaraldehyde, glyoxal, and ethylene glycol diglycidyl ether(EDGE), but these cross-linking agents block the amino (NH₂) functional group in CMC backbone.¹³ Therefore, epichlorohydrin (EPC) as a mono functional cross linking agent was an effective substitute that will not bind to amino groups in CMC biopolymer and improve the hydrophilic property of CMC and provide enough adsorption sites for increasing adsorption capacity.¹⁴ However, the fact of high desirability exist between inorganic arsenic species and iron¹⁵ tends to advance the utility of Fe (III)-bearing materials like hematite,¹⁶ ferrihydrite,¹⁷ and iron-doped activated carbons for arsenic adsorption.¹⁸ Thus, the objective of the present study is to prepare and evaluate a hybrid composite biopolymer of crosslinked epichlorohydrin/Fe₃O₄ nanocomposite (CMC-EPC/INC) for removal of As(V). RSM is a multivariate technique employed to reduce the number of experimental runs required to provide sufficient information for statistically acceptable results.¹⁹ Hence the parameters such as adsorbent dosage, initial metal ion concentration, solution pH, working temperature were optimized through Box-Behnken design model (BBM), which provide an insight of parameters level for maximum performances.²⁰ The Langmuir and Freundlich isotherm models were applied to evaluate the adsorption equilibrium. Kinetic studies, thermodynamic property and desorption experiments were carried and discussed.

2. Experimental

2.1. Material

Carboxymethylchitosan (CMC, MW = 2.65 × 10⁵), Epichlorohydrin (EPC), Ferric chloride hexahydrate (FeCl₃·6H₂O), Ferrous chloride tetrahydrate (FeCl₂·4H₂O), Sodium hydrogen arsenate (Na₂HAsO₄·7H₂O), 1-ethyl-3-carbodiimide hydrochloride (EDC), N-hydroxyl succinimide (NHS), Sodium hydroxide and acetic acid were of analytical grade, acquired from Sigma Aldrich. Stock As(V) solution (1000mg/L) were prepared from sodium hydrogen arsenate. All the reagents and glassware were prepared with de-ionized water.

2.2. Preparation of Fe₃O₄ Nanoparticles

Fe₃O₄ nanoparticles synthesized,²¹ by taking 0.02 moles of FeCl₃·6H₂O and 0.01moles of FeCl₂·4H₂O dis-

solved in 100 mL of deionized water at 30 °C, under vigorous stirring precipitation occurs by the addition of 1M NaOH after 60min. Then it was heated to 60 °C for 3h under the pH ± 12. After cooled the solution to room temperature, the precipitate was collected by a magnet and washed with deionized water until the pH reached neutral. Finally, it was washed with acetone and dried in an oven at 60 °C for 24h.

2.3. Synthesis of CMC-EPC/Fe₃O₄ Nanocomposite

1g of CMC was dissolved in acetic acid (50 mL, 5% v/v), and the mixture was sonicated at room temperature for 3 h. Then 0.6 g of magnetic nanosized ferroferric oxide was added and left it for 24 h at room temperature with vigorous stirring to ensure complete mixing. Beads of CMC-Fe₃O₄ (MCMC) formed when the resultant solution was injected into a 100 mL sodium hydroxide (0.5 M) by syringe needle (10 mL) as drops, and washed with distilled water plenty for the removal of excess sodium hydroxide solution. The crosslinking steps were carried out by dissolving 1 g of MCMC beads in 60 mL of ultrapure water followed by adding 0.6 g of EDC and 0.8 g of NHS at pH 5–6 in order to activate the carboxyl groups of MCMC. After 1 h, 1% epichlorohydrin (100 mL) was added to the beads with gentle stirring in water bath at 40 °C for 24 h. Then the crosslinked (CMC-EPC/INC) beads were washed many times by distilled water, air dried and grinded using mortar and dried constantly in the oven. Finally, the prepared adsorbent was sieved to a particle size < 250µm for study.

2.4. Batch Adsorption Experiments

Batch experiments were carried out with 50mL of As(V) solution having an initial concentration of 10 mg/L. The investigation of parameters are temperature (20–50 °C), pH (2–10), reaction time (5 min–5 h), and adsorbent dosage (0.1–2g/50 mL) in order to find the maximum uptake of arsenic ions. Samples were collected at fixed intervals and the adsorbent was removed by centrifugation at 6000 rpm for 6 min. The supernatant was analyzed for As(V) removal by AAS. Blanks were used for control in all the experiments. The amount of arsenic adsorbed (mg/g) was determined by the following equation.

$$qe = (C_0 - C_e) \times v / m \quad (1)$$

Where C₀ and C_e are the initial and equilibrium concentrations of the metal ion (mg/L), *m* is the dry mass of iron-doped chitosan (g) and *v* is the volume of the solution (L). The % removal of As(V) from aqueous solution was calculated by the following equation;

$$\text{Removal (\%)} = [(C_0 - C_e) / C_0] \times 100 \quad (2)$$

2. 5. Experimental Design

Response surface methodology (RSM) with Box–Behnken design (BBD) was employed to determine the effect of four independent variables. The effect of parameters including temperature (x_1), pH (x_2), reaction time (x_3), and adsorbent dosage (x_4) were analysed. For data analysis, design expert software (Stat Ease, Inc., Version 11, USA) was used. By batch experiments. The following equation explain the coded values of the process variables.

$$X_i = \frac{(x_i - x_{oi})}{\Delta x_i}, i = 1, 2, 3 \dots \dots k \quad (3)$$

Where X_i and x_i are the coded and uncoded values of the i_{th} variables, x_{oi} denotes the uncoded values of the i_{th} variable at the center point, and Δx_i is the step change value. The process parameters were optimized by 29 experimental runs and the levels of parameters used in the adsorption process were summarized in Table 1. The % removal of As(v) was determined by the following second order polynomial equation.

$$Y = \beta_0 + \sum_{i=1}^4 \beta_i x_i + \sum_{i=1}^4 \beta_{ii} x_i^2 + \sum_{i,j=1(i \neq j)}^4 \beta_{ij} x_i x_j + \varepsilon \quad (4)$$

Where Y is the response variable, β_0 , β_i , β_{ij} , and β_{ii} , are the regression coefficients for intercept, linear effect, double interaction, and quadratic effects, respectively, x_i , x_j are the independent variables, and ε is a random error. Statistical analysis system software was used for the study of Analysis of variance (ANOVA), response surface studies and 3D surface plot generation.

Table 1. Factors and level of various parameters of BBD design for As(V) adsorption

Parameters	Level of factors			
Variables	Code	-1	0	1
Temperature (°C)	x_1	30	35	40
pH	x_2	5	6.5	8
Contact time(min)	x_3	45	60	75
Adsorbent dosage(mg L ⁻¹)	x_4	600	700	800

2. 6. Analytical Measurements

Micromeritics ASAP 202 analyzer, pH-potentiometric titration method, reported by Vieira and Beppu,²² was carried out to determine the porosity and amino group content in the biosorbent respectively. Shimadzu AA 7000 model atomic absorption spectrometer (AAS) was used to find the concentration of adsorbed arsenic at 193.7nm with an air-acetylene flame type.²³

3. Results and Discussion

3. 1. Porosity and Potentiometric Analysis

The adsorbent has BET analysis surface area of 2.85 (m²/g). Surface morphology of the composite indicates, Fig. S1 (a), that the adsorbent is porosity with more white patches, Fig.S1(b), indicates that the adsorbent complexes with arsenic ions after the adsorption. The cross-linking of EPI,²⁴ reacts with the primary alcoholic group (-CH₂OH) at position C-5 of CMC's pyranose ring thus indicated that the amino (-NH₂) group plays a major role in the adsorption of arsenic anion by electrostatic attraction.²⁵

3. 2. FTIR Analysis

The FTIR spectra of the pure CMC, CMC-EPI/INC before and after As(V) adsorption were displayed in Fig. 1.

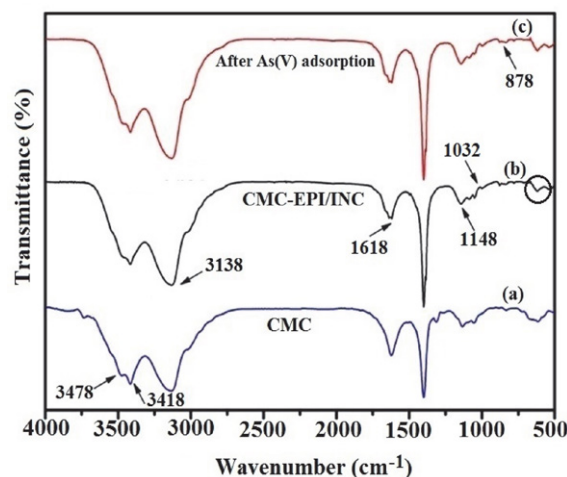


Fig. 1. FT-IR spectra of a) CMC b) CMC-EPI/INC before and c) after As(V) adsorption

The IR spectrum of CMC in Fig.1 (a), show peaks at 3478 cm⁻¹, 3418 cm⁻¹, 3138 cm⁻¹ and 1618 cm⁻¹ were attributed to the symmetrical, asymmetric stretching vibration of and -NH₂ group and stretching vibration of O-H, with the effect of hydrogen bonds, and C = O in amide respectively. The peaks at ~1148 cm⁻¹ and ~1032 cm⁻¹ in Fig.1(b), corresponds to stretching of C-O-C and C-O bonds respectively, resulted in the formation of covalent bonds due to reaction between EPI with the carbon atoms in CMC, which causes the opening of the epoxide ring of EPI and the releasing of a chlorine atom.²⁶ The bands around 600–700 cm⁻¹ is assigned to the bending vibration of Fe-O-Fe bond. The appearance of new band ~878 cm⁻¹ shown in Fig.1 (c), corresponds to the existence of arsenic anion.

3. 3. Equilibrium Isotherm

The equilibrium parameters of adsorbent dosage, pH, temperature, initial ion concentration and contact

time were found to be 0.7 g, pH 6.5, 308 K, 10 mg/L and 60 min, respectively and found that the reaction takes place by diffusion and complexation process.²⁷

3. 4 Quadratic Model for As(v) Adsorption

The BBM technique were employed for the optimization of As(v) adsorption capacity. Table 2, displays the 29 runs of experimental design, along with corresponding

adsorption results. The removal efficiency as functions parameters was correlated with the developed second-order polynomial equation. The empirical model in terms of process variables, is expressed by the following equation.

The effect of independent variables on the adsorption efficiency of As(V) was described by the equation shown above. The amount of maximum As(V) adsorption was found to be 95.1%. Experimental curve fitting was evaluated to govern the apparent model by calculating

$$\begin{aligned} \% \text{ removal of As(v)} = & -203.02898 + 8.97600 + 22.29704 + 0.188444 + 0.153967 - 0.023333 \\ & - 0.001333 + 0.000150 + 0.038889 - 0.005167 + 0.000233 - 0.122133 - 1.55148 - 0.004293 - 0.000095 \end{aligned} \quad (5)$$

Table 2. Experimental design of variables with adsorption results

Std	Run	Coded levels				Removal of As(v)%
		x_1	x_2	x_3	x_4	
21	1	35	3	60	600	88.1
1	2	30	3	60	700	86.3
12	3	40	4.5	60	800	93.1
26	4	35	4.5	60	700	95.1
17	5	30	4.5	45	700	87.8
14	6	35	6	45	700	88.4
27	7	35	4.5	60	700	95.1
29	8	35	4.5	60	700	95.1
6	9	35	4.5	75	600	92.6
25	10	35	4.5	60	700	93.8
4	11	40	6	60	700	90.2
24	12	35	6	60	800	90.4
15	13	35	3	75	700	91.1
8	14	35	4.5	75	800	93.4
9	15	30	4.5	60	600	89.2
20	16	40	4.5	75	700	92.9
22	17	35	6	60	600	89.5
23	18	35	3	60	800	92.1
2	19	40	3	60	700	89.6
19	20	30	4.5	75	700	89.8
10	21	40	4.5	60	600	91.8
5	22	35	4.5	45	600	93.4
11	23	30	4.5	60	800	90.2
18	24	40	4.5	45	700	91.3
13	25	35	3	45	700	90.7
28	26	35	4.5	60	700	95.1
16	27	35	6	75	700	92.3
3	28	30	6	60	700	87.6
7	29	35	6.5	45	800	92.8

larger F - and lower probability values (p -values) with significant terms were chosen. From the data given in Table 3, a quadratic model was suggested for higher F -value (40.7) and lower p -value (<0.0001) with significant terms for this experimental design. The cubic model was found to be insignificant. The significance of the quadratic model was justified by ANOVA by correlating with the response variables such as the main effects, the interaction effects, and the error terms. The F and p values represented the enormosity of these variables. BBD was adopted to design 29 experiments (Table 4) for investigate the individual and interactive effects of the four independent variables on removal of As(V). The experimental data of As(V) removal, were statistically analyzed by analysis of variance (ANOVA) and the results are presented in Table 4.

From the Table 4, the F -value of 15.84 indicated that the model was statistically significant and there is only a 0.01% chance that an F -value this large could occur due to noise. The model suggested was highly significant due to its p -value of <0.0001 . The Table 4, shows the seven significant terms with low p -values were x_1 , x_3 , x_4 , x_1^2 , x_1^2 , x_2^2 , x_3^2 , and x_4^2 . Other significant terms were not discussed because of their high p -values. The above model accuracy could be assessed by the fortitude of regression coefficient R^2 value 0.9406, indicated that only 6% of the total variables were not explained by the model.

The adjusted coefficient value ($R^2_{\text{adj}} = 0.8813$) was not in realistic arrangement with observed R^2 . The model has undesirable lack of fit by the indication of lack of fit p -value (>0.05) suggested that it is not significantly relative to the pure error and, thus, above quadratic equation and the model were accurate for the experiment.²⁸ The

Table 3. Experimental curve fitting of optimization

Model	Sum of Source	DF	Mean Squares	F -Square	p -value	Remarks value
Linear vs Mean	36.53	4	9.13	1.64	0.1976	–
2FI vs Linear	6.14	6	1.02	0.15	0.9879	–
Quadratic vs 2FI	117.65	4	29.41	40.70	<0.0001	Suggested
Cubic vs Quadratic	7.06	8	0.89	1.74	0.2589	Aliased

Table 4. Analysis of variance for the model by BBM optimization for As(v) adsorption

Source	DF	Mean Square	F-value	p-value	Remarks
Model	14	11.45	15.84	< 0.0001	significant
x_1 (°C)	1	27.00	37.36	< 0.0001	significant
x_2 (pH)	1	0.0208	0.0288	0.8676	–
x_3 (min)	1	4.94	6.84	0.0204	significant
x_4 (mg)	1	4.56	6.31	0.0248	significant
x_1x_2	1	0.1225	0.1695	0.6868	–
x_1x_3	1	0.0400	0.0553	0.8174	–
x_1x_{24}	1	0.0225	0.0311	0.8625	–
x_2x_3	1	3.06	4.24	0.0587	–
x_2x_4	1	2.40	3.32	0.0897	–
x_3x_4	1	0.4900	0.6780	0.4241	–
x_1^2	1	60.47	83.68	< 0.0001	significant
x_2^2	1	79.04	109.37	< 0.0001	significant
x_3^2	1	6.05	8.37	0.0118	significant
x_4^2	1	5.90	8.16	0.0127	significant
Residual	14	0.7227	–	–	–
Lack of Fit	10	0.8766	2.59	0.1858	not significant
Pure Error	4	0.3380	–	–	–

value of signal to noise ratio is 13.511, ratio >4 is desirable, indicated an adequate signal to navigate the design space.²⁹ The Fig. 2a graph, plotted between actual and predicted values shows no apparent violation from the assumptions underlying of the analyses,³⁰ indicated that the distribution of actual values were relatively close to the straight line, specify the accuracy of the assumptions, as well as the independence of the residuals. The plot between studentized residuals and run number, in Fig. 2b, showed that the random distribution of residuals around

± 3.9 (limit is $< \pm 4.00$) was a good sign of well fitted experimental data with the model.³¹

3. 5. Effect of Process Variables on Removal of As(v)

The optimization process parameters and the interaction between the variables were studied by a plot of three-dimensional curves for the efficient adsorption of As(V). Fig. 3a, represents the effect of temperature and pH

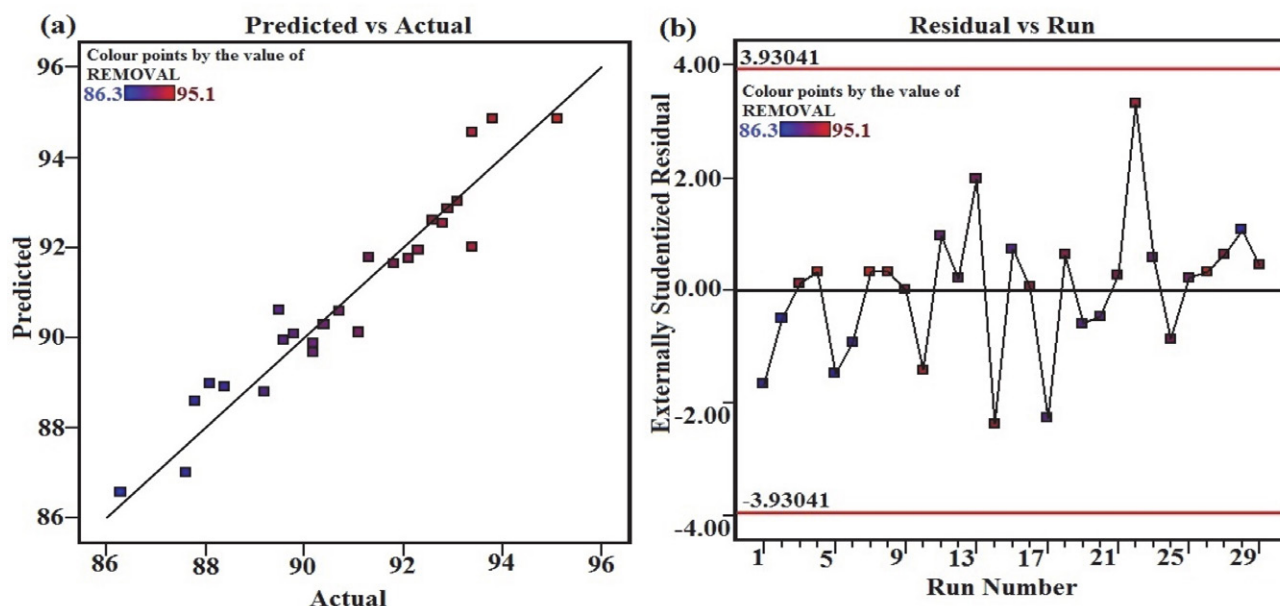


Fig. 2. RSM model graphs of a) Predicted vs Actual values b) Studentized residuals vs experimental run number on optimized parameters of As(V) removal

indicated that the adsorption reaches maximum at 35 °C on pH 6.5 beyond that desorption process start and continues due to complexation. Fig. 3b represents the correlation of temperature and reaction time having optimal adsorption efficiency of 95.1% was reached within 60 min at temperature of 35 °C, beyond that contact time (>60 min) and temperature (>35 °C), the adsorption rate decreased. The plot of temperature versus adsorbent dosage in Fig. 3c, shows that the degree of adsorption increases with increasing adsorbent dosage, upto 700 mg on 35 °C, due to high surface availability, beyond 800 mg dosage and 35 °C it has equilibrium and decreasing trend continues infers, that the process is controlled by temperature.³² Fig. 3d, shows the effect of time and pH and the adsorption capacity was almost constant in the pH range 5–6, and then increases and reaches maximum at pH 6.5, which matches

with the pKa value of chitosan.³³ From the above it was evident that the adsorption rate mainly depends on temperature and pH, while the contact time had fringe effect only. The above fact is supported by the contour plot,³⁴ in Fig. S2, between pH and temperature had a difference minimum 0.5% between experimental and predicted removal efficiency shows that the adsorption is endothermic took place by the increasing diffusion rate and the growing rate of complexation between adsorbent and adsorbate.³⁵

3. 6. Langmuir Isotherms

The isotherm models employed describes the sorption data, sorption mechanism, the surface properties and the affinity between sorbent and sorbate.³⁶ The Langmuir isotherm model represents the monolayer sorption on an

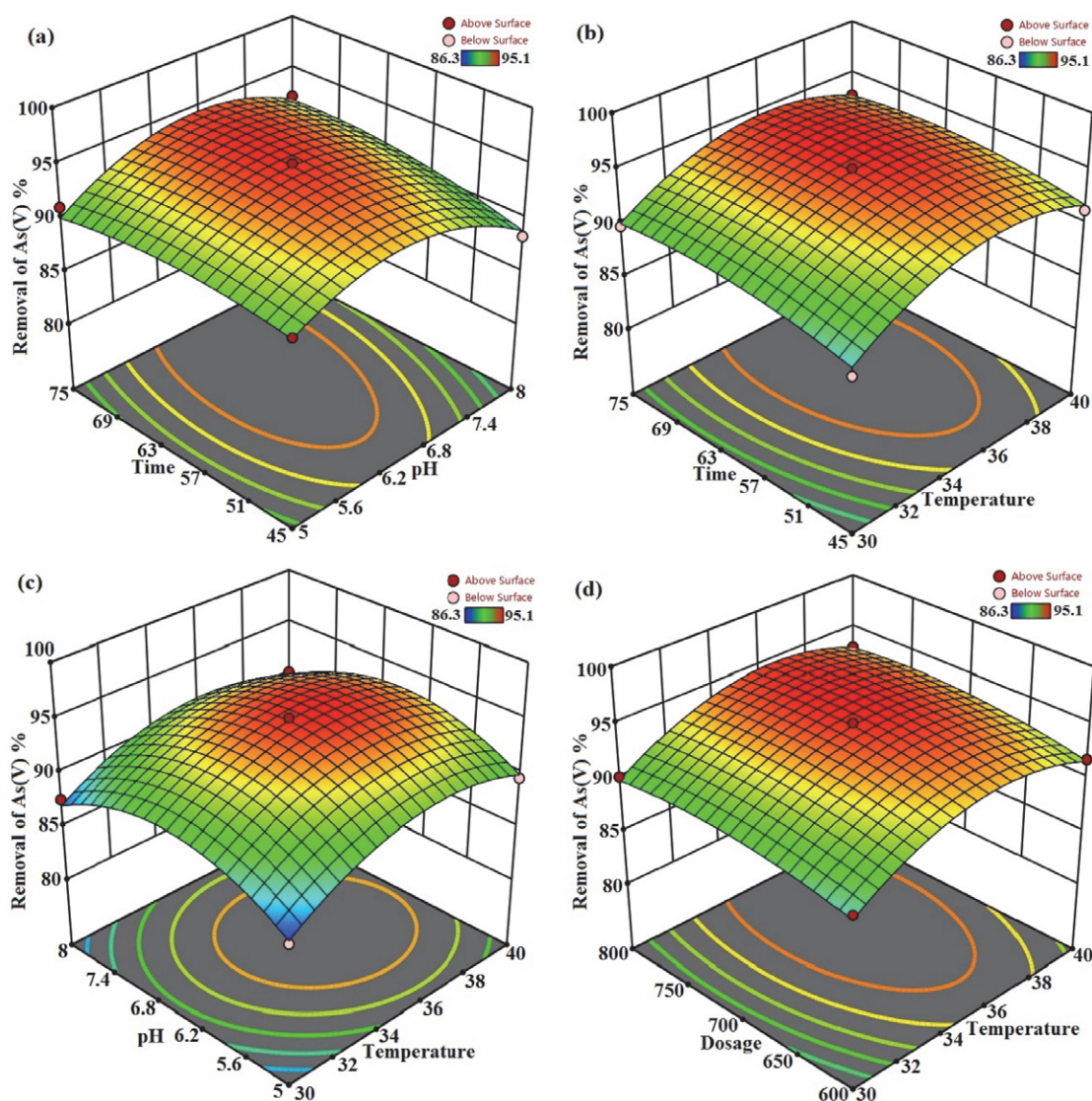


Fig. 3. 3D surface plot of interaction effects between variables of a) time vs pH b) time vs temperature c) pH vs temperature and d) adsorbent dosage vs temperature on As(V) removal

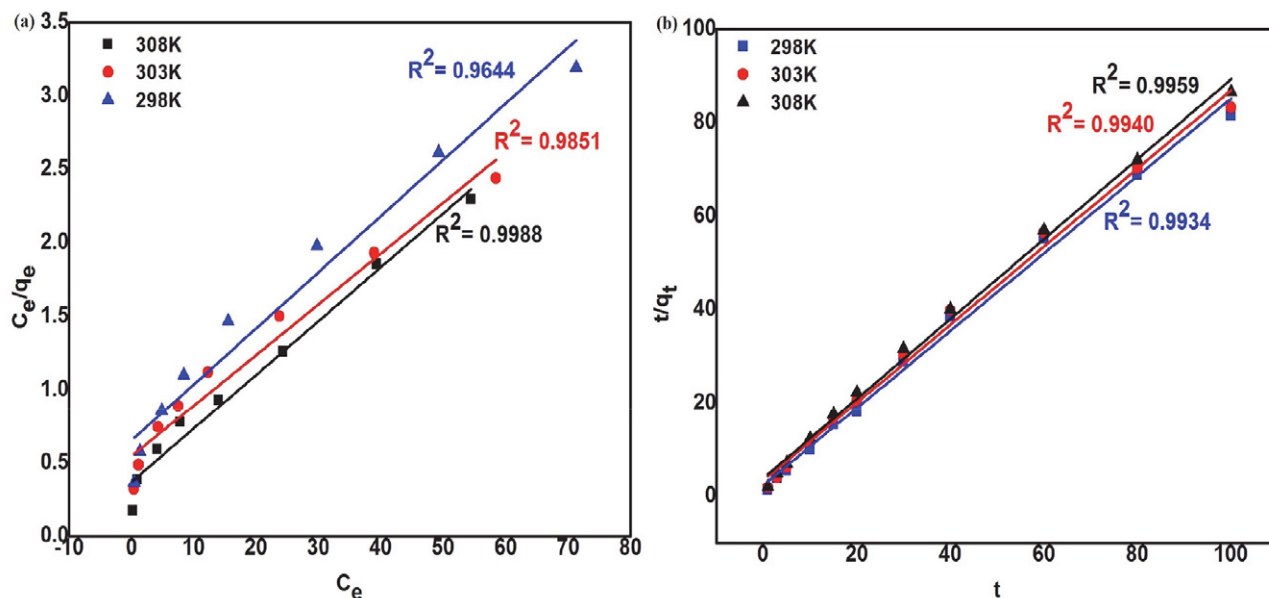


Fig. 4. 3D surface plot of interaction effects between variables of a) time vs pH b) time vs temperature c) pH vs temperature and d) adsorbent dosage vs temperature on As(V) removal

energetically uniform surface having maximum adsorption capacity, $q_m = 26.11\text{--}28.99\text{ mg g}^{-1}$, and higher regression coefficient, $R^2 = 0.9988$ obtained from the relevant plots, Fig. 4a, and Table 5, suggesting that the surface of the sorbent was homogenous. The dimensionless factor ($R_L = 1/(1 + bC_0)$) was calculated as <1 , indicates favourable and monolayer adsorption process. The certainty of the isotherm were committed by the least RMSE and χ^2 values for Langmuir model than Freundlich model.

3. 7. Freundlich Isotherm

The isotherm describes the sorption on an energetically heterogeneous surface and the exponential distribution of active sites and their energies.³⁷ The value of n (adsorption intensity) obtained by the Table 5, from the plot (Fig.S3) in the range 1–10 signifies the good performance of Fe_3O_4 doped CMC-EPI adsorbent towards As(V) adsorption.

3. 8. Residual Mean Square Error (RMSE) and Chi-square (χ^2) statistical test

To represent the errors in the isotherm curves the RMSE and *Chi-square* (χ^2) statistical analysis is employed.

$$\text{RMSE} = \frac{1}{n-2} \sum_{i=1}^n (q_{e,\text{exp}} - q_{e,\text{cal}})^2 \quad (6)$$

$q_{e,\text{exp}}$, $q_{e,\text{cal}}$ and n are the experimental, calculated values and number of observations respectively.³⁸ The χ^2 test confirms the suitability of a particular isotherm model given by the equaton,³⁹

$$\chi^2 = \sum \frac{(q_{e,\text{exp}} - q_{e,\text{cal}})^2}{q_{e,\text{cal}}} \quad (7)$$

The RMSE and χ^2 value would be less if the adsorption data correlated concurs with experimental values. By

Table 5. Isotherm parameters for As(v) adsorption on pH = 6.5, adsorbent dosage = 700mg/L, contact time = 60 min at different temperatures onto the CMC-EPI/INC composite

Parameters	Langmuir			Parameters	Freundlich		
	Temperature (K)				Temperature (K)		
	298	303	308		298	303	308
$q_m(\text{mg} \cdot \text{g}^{-1})$	26.11	27.38	28.99	$k_f(\text{mg} \cdot \text{g}^{-1})$	1.4027	1.4276	1.5327
$k_1(\text{L} \cdot \text{mg}^{-1})$	0.0594	0.0668	0.0941	η	1.9592	1.6489	1.8221
R^2	0.9644	0.9851	0.9988	R^2	0.9623	0.9821	0.9898
R_L	0.6274	0.5995	0.5152	RMSE	2.9651	3.1475	3.2541
RMSE	0.3852	0.3526	0.2978	χ^2	5.9621	5.6254	4.9632
χ^2	0.2943	0.2896	0.1781				

which, from Table V, the adsorption suitability more correlate with the Langmuir model than other models.

3. 9. Kinetic Study

The kinetics,⁴⁰ effective adsorption capacity, initial adsorption rate and the rate constant of As(v) adsorption without any parameter in advance were evaluated using the pseudo First order and Second order equation.⁴¹ The linear form of pseudo-first-order Lagergren equation and pseudo-second-order equation is given as equation 8 and 9.

$$\log (q_e - q_t) = \log q_e - \frac{k_1 t}{2.303} \quad (8)$$

$$\frac{t}{q_t} = \frac{1}{k_2 q_e^2} + \frac{t}{q_e} \quad (9)$$

The initial adsorption rate, h (mg/(g min)), as $t \rightarrow 0$, can be defined as:

$$h = k_2 q_e^2 \quad (10)$$

Where, k_1 and k_2 are the rate constant of Pseudo first order and second order equation respectively. The kinetic parameters were obtained through the Pseudo first order plot (Fig.S4), and second order plot (Fig. 4b) shows higher regression coefficient value of 0.996, (Table 6) for the second order model, exposed its applicability in fitting the experimental kinetic data. From the Table 6, it shows that the h value of As(V) adsorption at 35 °C was higher than at 25 °C.

3. 10. Intraparticle diffusion

The Weber-Morris model for intraparticle diffusion, explored the nature of the 'rate-controlling step, which is given by the equation as,⁴²

$$q_{id} = k_{id} t^{0.5} + c \quad (11)$$

Where k_{id} is the intraparticle diffusion rate constant ((mg/g min^{0.5})). From the plots q_e versus $t^{0.5}$, Fig. S5, the relationship is not linear and follows rate-limiting step. The first sharper portion being rapid external surface ad-

sorption, the second portion being gradual adsorption and the final phase being final equilibrium stage due to the low concentration of As(V) in the solution phase as well as less number of available adsorption sites.

3. 11. Adsorption Thermodynamics

The thermodynamic parameters were utilized to elucidate the feasibility of adsorption.⁴³ The Van't Hoff plot, Fig. 5 (ln K_c against 1/T) relates the parameters as

$$\ln K_c = \frac{-\Delta H}{RT} + \frac{\Delta S}{R} \quad (12)$$

$$\Delta G = - RT \ln K_c \quad (13)$$

Where K_c is the equilibrium constant, T the absolute temperature (K), and R is the universal gas constant (8.314 J mol⁻¹). The calculated values of the energy parameters ΔG (change in free energy), ΔH (change in enthalpy), and ΔS (change in entropy) are given in the Table 7. The negative ΔG values observed at various temperatures suggested the feasibility and spontaneous adsorption process.

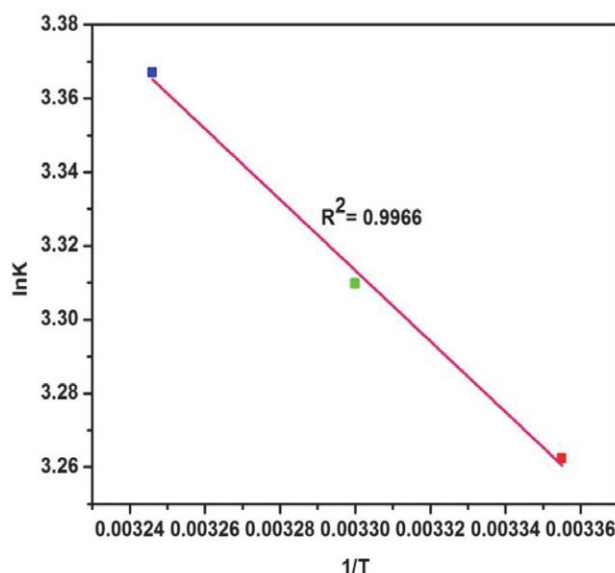


Fig. 5. Van't Hoff plot of As(V) adsorption at different temperatures

Table 6. Kinetic parameters for As(V) adsorption on pH = 6.5, adsorbent dosage = 700 mg/L, contact time = 60 min at different temperatures onto the CMC-EPI/INC composite

Temp (K)	Pseudo first order				Pseudo Second order				Intra particle diffusion
	$q_{e,exp}$ mg/g	$q_{e,cal}$ mg/g	k_1 (min ⁻¹)	R^2	h (mg . min ⁻¹)	$q_{e,cal}$ mg/g	k_1 (min ⁻¹)	R^2	K_{id} (mg/g . min ^{1/2})
298	1.1954	1.169	0.019	0.980	0.1957	1.019	0.2326	0.993	0.045
303	1.2015	1.198	0.021	0.987	0.2142	1.128	0.2432	0.994	0.043
308	1.2235	1.035	0.025	0.992	0.2583	1.175	0.1885	0.996	0.040

Table 7. Thermodynamic results of As(V) adsorption at different temperatures

Temp (kJ/mol)	Van't Hoff plot		ΔS
	ΔG (kJ/mol)	ΔH (J/mol/k)	
289K	-8.0787	7.9835	0.0539
303K	-8.3482		
308K	-8.6177		

The positive nature and the value of $\Delta H = 7.9835!!!!$ ($< 80 \text{ kJ} \cdot \text{mol}^{-1}$) suggesting that the reaction follows endothermic physisorption. The positive value of ΔS reflects the affinity and some structural changes in adsorbent and adsorbate during adsorption process.⁴⁴

3. 12. Desorption Experiments

Desorption studies carried out with 0.1M NaOH, in a batch reactor. The desorption result (Table S1), revealed that after four cycles around 81–87% of loaded As(V) were found to be desorbed during desorption cycles. The desorption ratio was calculated by:

$$R(\%) = \frac{C_2}{C_0 - C_1} \times 100\% \quad (14)$$

Where C_0 , C_1 , and C_2 are the initial, equilibrium concentration of adsorbed and desorbed solution in mg/L respectively.

4. Conclusions

The removal of As(V) were successfully carried out in this study by the prepared novel hybrid crosslinked magnetite enhanced carboxymethylchitosan biosorbent. The optimization results of main variables by Box-Behnken Design of RSM model ($R^2 = 0.9406$) shows the process were good in agreement with arsenic adsorption. This factorial experimental design approach developed an empirical equation for the prediction and understanding of As(V) adsorption efficiency. The model outcome with seven significant figures, maximum removal efficiency of 95.1%, with 0.5% difference between actual and predicted values. The interaction effect results infers the most influencing parameters are pH and temperature while contact time and adsorbent dosage are the least influencing parameters. The maximum sorption capacity for As(V) was calculated to be 28.99 mg g^{-1} from the Langmuir isotherm, correlate with low RMSE and chi square value, and follows pseudo-second-order kinetics. Thermodynamic studies revealed the process is spontaneous, endothermic and physisorption in nature. Interfering ions had minimal ef-

fects on adsorption. The adsorbent was successfully recycled for four cycles and efficiently treated with As (V) contaminated wastewater. Thus, it could be concluded that the CMC-EPI/INC biosorbent would be a prospective candidate for arsenic filtering units, due to its biocongenial nature.

Acknowledgment

The authors also would like to thank Department of Chemistry, IIT Madras and Center for Environment, CLRI Chennai for providing the analytical instrumentation facility. One of the authors Dr.G.Prabha would like to thank University Grant Commission (UGC), Government of India, for providing the fund under the scheme of UGC – Dr. D.S. Kothari Postdoctoral Fellowship (Award No:F.4-2/2006(BSR)/CH/18-19/0110).

Conflict of interest

As the author(s), we declare that there is no conflict of interest regarding the publication of this article.

5. References

1. A. K. Sharma, J. C. Tjell J. C, J. J. Sloth, P. E. Holm, *Appl. Geochem.*, (2014), 41:11–33.
DOI:10.1016/j.apgeochem.2013.11.012
2. S. Fendorf, H. A. Michael, A. Geen, *Science Mag.*, (2010), 328 (5928), 1123–1127.
DOI:10.1126/science.1172974
3. P. L. Smedley, D. G. Kinniburgh, *Appl. Geochem.*, (2002), 17, 517–568. DOI:10.1016/S0883-2927(02)00018-5
4. W. E. Morton, D. A. Dunette, *Arsenic in the Environment, Part II, Wiley and sons*, New York (1994), 17–34.
DOI:10.1002/jat.2550150320
5. Drinking water Quality Information, *World Health Organization*, Vol 2, WHO, Geneva (1984), 940–949.
DOI:10.1002/food.19860300121
6. V. M. Boddu, K. Abburi, J. L. Talbott, E. D. Smith, R. Haasch, *Water. Res.*, (2008), 42, 633–642.
DOI:10.1016/j.watres.2007.08.014
7. A. Dabrowski, Z. Hubicki, P. Podkościelny, E. Robens, *Chemosphere.*, (2004), 56(2), 91–106.
DOI:10.1016/j.chemosphere.2004.03.006
8. T. F. Lin, J. K. Wu, *Water Res.*, (2001), 35(8), 2049–2057.
DOI:10.1016/S0043-1354(00)00467-X
9. H. Genc-Fuhrman, J. C. Tjell, D. McConhie, *J. Colloid Interface Sci.*, (2004), 27(2) 313–320.
DOI:10.1016/j.jcis.2003.10.011
10. F. Fu, Q. Wang, *J. Environ. Mgmt.*, (2011), 92(3), 407–418.
DOI:10.1016/j.jenvman.2010.11.011
11. R. S. Juang, F. C. Wu, R. L. Tseng, *Water Res.*, (1999), 33(10), 2403–2409. DOI:10.1016/S0043-1354(98)00469-2
12. P. Pillewan, S. Mukherjee, T. Roychowdhury, S. Das, A. Ban-

- siwal, S. Rayalu, *J. Hazard. Mater.*, (2011), 186 (1), 367–375.
DOI:10.1016/j.jhazmat.2010.11.008
13. M. Bilal, Z. Jing, Y. Zhao, H. M. Iqbal, *Biocatal. Agric. Biotechnol.*, (2019), 19, 101174–101184.
DOI:10.1016/j.bcab.2019.101174
14. Y. Gutha, Y. Zhang, W. Zhang, X. Jiao, *Int. J. Biol. Macromol.*, (2017), 97, 85–98. DOI:10.1016/j.ijbiomac.2017.01.004
15. F. Marrakchi, W. A. Khanday, M. Asif, B. H. Hameed, *Int. J. Biol. Macrol.*, (2016), 93(pt A), 1231–1239.
DOI:10.1016/j.ijbiomac.2016.09.069
16. K. P. Raven, A. Jain, R. H. Leoppert, *Environ. Sci. Technol.*, (1998), 32(3), 344–349. DOI:10.1021/es970421p
17. V. Fierro, G. Muniz, M. L. Ballinas, *J. Hazard. Mater.*, (2009), 168(1), 430–437. DOI:10.1016/j.jhazmat.2009.02.055
18. H. Genc-Fuhrman, J. C. Tjell, D. McConchie, *Environ. Sci. Technol.*, (2004), 38(8), 2428–2439.
DOI:10.1021/es035207h
19. A. H. Jawad, N. N. Abd Malek, A. S. Abdulhameed, R. Razuan, *J. of Polymers and the Environ.*, (2020), 28, 1068–1082.
DOI:10.1007/s10924-020-01669-z
20. A. Reghioia, D. Barkat, Ali H. Jawad, A. S. Abdulhameed, A. A. Al-Kahtani, Z. A. AlOthman, *J. of Environ. Chem. Eng.*, (2021) 9(3), 105166. DOI:10.1016/j.jece.2021.105166
21. T. S. Anirudhan, L. Divya, J. Parvathy, *Journal of Chemical Technology & Biotechnology*, (2013), 88(5), 878–886.
DOI:10.1002/jctb.3916
22. R. S. Vieira, M. M. Beppu, *Coll. Surf. A*, (2006), 279(1–3), 196–207. DOI:10.1016/j.colsurfa.2006.01.026
23. E. Guibal, T. Vincent, R. Navarro, *J. Mater. Sci.*, (2014), 49, 5505–5518. DOI:10.1007/s10853-014-8301-5
24. Y. Haldorai, T. Rengaraj, Y. S. Huh, Y. K. Han, *Mater. Sci. and Eng B*, (2015), 136921, 01–10.
DOI:10.1016/j.mseb.2015.01.006
25. A. T. Mohammad, A. S. Abdulhameed, A. H. Jawad, *Int. J. Macromol.*, (2019), 129, 98–109.
DOI:10.1016/j.ijbiomac.2019.02.025
26. K. Manzoor, M. Ahmad, S. Ahad, S. Ikram, *RSC Adv.*, (2019), 9, 7890–7902. DOI:10.1039/C9RA00356H
27. M. Monier, D. A. Abdel-Latif, *Int. J. Biol. Macromol.*, (2017), 105(1), 777–787. DOI:10.1016/j.ijbiomac.2017.07.098
28. J. L. Wang, C. Chen, *Biotechnol Adv.*, (2009), 27, 195–226.
DOI:10.1016/j.biotechadv.2008.11.002
29. E. Guibal, *Purif. Technol.*, (2004), 38(1), 43–74.
DOI:10.1016/j.seppur.2003.10.004
30. Ali H. Jawad, I. A. Mohammed, A. S. Abdulhameed, *J of Poly and the Environ.*, (2020), 28, 2720–2733.
DOI:10.1007/s10924-020-01804-w
31. N. Ayawei, A. T. Ekubo, D. Wankasi, E. D. Dikio, *Oriental. J. of Chem.*, (2015), 5(03), 56–70.
DOI:10.4236/ojpc.2015.53007
32. S. Sharma, M. Bharathi, and N. Rajesh, *Chemical Eng. J.*, (2015), 59, 457–466. DOI:10.1016/j.cej.2014.08.002
33. C. Chia-Pin, L. Ming-Chao, L. Chung-Min, *J. of Hazard. Mater.*, (2009), 171(1–3), 859–864.
DOI:10.1016/j.jhazmat.2009.06.086
34. Ali H. Jawad, Ahmed Saud Abdulhameed, Nurul Najwa Abd Malek, Zeid A. AlOthman, M. *Inter. J. of Bio. Macromol.*, (2020), 164(020) 4218–4230.
DOI:10.1016/j.ijbiomac.2020.08.201
35. H. Guo H. Y. Li, K. Zhao, *J. of Hazard Mater.*, (2010), 176(1–3), 174–180. DOI:10.1016/j.jhazmat.2009.11.009
36. C. Yuwei, W. Jianlong, *Chemical Eng. J.*, (2011), 168(1), 286–292. DOI:10.1016/j.cej.2011.01.006
37. G. E. J. Poinern, D. Parsonage, B. Touma B, M. K. Issa Ghosh, E. Paling, P. Singh, *Inter. J. of Eng Sci. and Technol.*, (2010), 2(8), 13–24. DOI:10.4314/ijest.v2i8.63776
38. A. S. Krishna Kumar, C. Uday Kumar, R. Vidhya, N. Rajesh, *Inter. J. of Biological macromol.*, (2014), 66, 135–143.
DOI:10.1016/j.ijbiomac.2014.02.007
39. G. Anjali, M. Yunus, S. Nalini, *Chemosphere.* (2012), 86(2), 150–155. DOI:10.1016/j.chemosphere.2011.10.003
40. B. Choudhary, D. Paul, *J. Environ. Chem. Eng.* (2018), 6(2), 2335–2343. DOI:10.1016/j.jece.2018.03.028
41. K. Y. Foo, B. H. Hameed, *Chem. Eng. J.*, (2010), 156(1), 2–10.
DOI:10.1016/j.cej.2009.09.013
42. W. J. Weber Jr, J. C. Morris, *J. Saint. Eng Div.*, (1963), 89, 31–42.
DOI:10.1061/JSEDAI.0000430
43. Ali H. Jawad, Ahmed Saud Abdulhameed, M. A. K. M. Hanafiah, Zeid A. AlOthman, Mohammad Rizwan Khan, S. N. Surip, *Korean J of Chem Eng* (2021), 38, 1499–1509.
DOI:10.1007/s11814-021-0801-9
44. H. M. Guo, D. Stuben, Z. Berner, *Appl Geochem.*, (2007), 22(5), 1039–1051.
DOI:10.1016/j.apgeochem.2007.01.004

Povzetek

V tej študiji smo z uporabo metode odzivnih površin (RSM) z zasnovno Box-Behnkenovega načrtovanja optimizirali odstranjevanje As(V) iz vodnih raztopin s pripravljenim zamreženim ciklometilhitozanskim-epiklorhidrinskim/ Fe₃O₄ nanokompozitom. Optimizacijo pH vrednost raztopine, količine adsorbenta, kontaktnega časa in temperature smo izvedli s kvadratno polinomsko funkcijo z visokim korelacijskim koeficientom ($R^2 = 0.9406$). Ustreznost modela in izbranih členov smo preverili z analizo variance (ANOVA) in pokazali njihovo pomembnost z F – testom ($p < 0.05$). Izbrali smo sedem pomembnih členov s p -vrednostjo < 0.0001 , na osnovi katerih smo določili optimum pri katerem je bila učinkovitost odstranjevanja As(V) 95.1 %, dosežena pri količini adsorbenta 0.7g, pH vrednosti 6.5, temperaturi 308K, koncentraciji arzena 10 mg/ml in kontaktnem času 60 min. Langmuirjev model, ki je z R^2 0.9988 in χ^2 0.1781 opisal eksperimentalne podatke bolje od Freundlichovega, kaže na maksimalno kapaciteto adsorpcije 28.99 mg/g. Proces kaže na enoplastno adsorpcijo in kinetiko psevdo-drugega reda. Termodinamski parametri kažejo, da je proces spontan in endotermen ter poteka fizikalna adsorpcija. Uspešna regeneracija adsorbenta kaže na njegov praktičen potencial pri odstranjevanju arzena iz onesnaženih voda.



Except when otherwise noted, articles in this journal are published under the terms and conditions of the Creative Commons Attribution 4.0 International License

Scientific paper

Syntheses, Characterization, Crystal Structures and Antimicrobial Activity of Schiff Base Copper(II) Complexes Derived from 2-Bromo-6-((2-(isopropylamino)ethylimino)methyl)phenol

Yong Yuan,^{1,*} Xi-Kun Lu,¹ Gao-Qi Zhou² and Xiao-Yang Qiu^{2,*}¹ Institute of Automotive & Mechanical and Electronic Engineering, ZhouKou Vocational and Technical College, ZhouKou 466000, P. R. China¹ College of Science & Technology, Ningbo University, Ningbo 315315, P. R. China

* Corresponding author: E-mail: xiaoyang_qiu@126.com (Xiao-Yang Qiu), 2060349461@qq.com (Yong Yuan)

Received: 07-24-2021

Abstract

Three new copper(II) complexes, [Cu(LH)₂]Br₂ (**1**), [Cu(LH)₂]NCS₂ (**2**), and [Cu(LH)₂](NO₃)₂ (**3**), where LH is the zwitterionic form of 2-bromo-6-((2-(isopropylamino)ethylimino)methyl)phenol (HL), were synthesized and characterized by elemental analysis, IR and UV-vis spectroscopy. The structures of the complexes were further confirmed by single crystal X-ray structure determination. All compounds are mononuclear copper(II) complexes. The Cu atoms in the complexes are coordinated by two imino N and two phenolate O atoms from two LH ligands, forming square planar coordination. The compounds were assayed for their antimicrobial activities.

Keywords: Schiff base; copper complex; crystal structure; antimicrobial activity

1. Introduction

The design and preparation of metal complexes with specific applications has been the subject of extensive research. The complexes with transition metals have been used in various chemical and biological applications. Among the complexes, those with Schiff base ligands have interesting structural diversity, and the possibility of the presence of various electron-donating or electron-withdrawing substituents.¹ Schiff base copper complexes have been extensively studied and are considered as excellent alternatives for classic organic antibacterial, antifungal and antitumor.² Despite the presence of a large number of studies on the antibacterial activities of such complexes, it is still necessary to explore new complexes with more effective activities. It has been proven that the compounds with electron-withdrawing substituent groups can improve their antimicrobial ability.³ Rai *et al.* reported some compounds with fluoro, chloro, bromo, and iodo-substituted groups, and their remarkable antimicrobial property.⁴ Schiff base complexes of copper have potential antibacterial property.⁵ Recently, our research group has re-

ported some Schiff base complexes with biological properties.⁶ In pursuit of new Schiff base complexes with potential antimicrobial property, in this work, three new copper(II) complexes, [Cu(LH)₂]Br₂ (**1**), [Cu(LH)₂]NCS₂ (**2**), and [Cu(LH)₂](NO₃)₂ (**3**), where LH is the zwitterionic form of 2-bromo-6-((2-(isopropylamino)ethylimino)methyl)phenol (HL), and their antimicrobial activities are present.

2. Experimental

2.1. Materials and Methods

3-Bromosalicylaldehyde, *N*-isopropylethane-1,2-diamine, copper bromide, copper nitrate, and ammonium thiocyanate were obtained from Sigma-Aldrich. All other chemicals were commercial obtained from Xiya Chemical Co. Ltd. Elemental analyses of C, H and N were carried out in a Perkin-Elmer automated model 2400 Series II CHNS/O analyzer. FT-IR spectra were obtained on a Perkin-Elmer 377 FT-IR spectrometer with samples prepared as KBr pellets. UV-Vis spectra were obtained on a Lambda

35 spectrometer. Single crystal structural X-ray diffraction was carried out on a Bruker APEX II CCD diffractometer.

2. 2. Synthesis of HL

3-Bromosalicylaldehyde (1.0 mmol, 0.20 g) and *N*-isopropylethane-1,2-diamine (1.0 mmol, 0.10 g) were mixed and stirred in methanol (30 mL). The mixture was refluxed for 30 min, and with the solvent removed by distillation. The solid product was recrystallized from methanol to give yellow product. Yield 87%. Anal. calc. for $C_{12}H_{17}BrN_2O$: C, 50.54; H, 6.01; N, 9.82; found: C, 50.38; H, 6.12; N, 9.73%. IR data (cm^{-1}): 1634, 1468, 1381, 1242, 1098, 928, 915, 457. UV-Vis data (MeOH, λ_{max} , nm): 230, 275, 332, 417.

2. 3. Synthesis of Complex 1

3-Bromosalicylaldehyde (0.10 mmol, 20 mg), *N*-isopropylethane-1,2-diamine (0.10 mmol, 10 mg), and copper bromide (0.10 mmol, 22 mg) were mixed in methanol (15 mL) to give a clear blue solution. Block blue single crystals of the complex, suitable for X-ray diffraction, were grown from the solution upon slowly evaporation within 6 days. The crystals were isolated by filtration. Yield 32%. Anal. calc. for $C_{24}H_{34}Br_4CuN_4O_2$: C, 36.32; H, 4.32; N, 7.06; found: C, 36.13; H, 4.41; N, 9.91%. IR data (cm^{-1}): 2971, 2933, 2816, 2782, 1618, 1592, 1530, 1438, 1391, 1329, 1228, 1186, 1132, 1073, 1035, 905, 843, 738, 671, 612, 550. UV-Vis data (MeOH, λ_{max} , nm): 222, 247, 267, 372.

2. 4. Synthesis of Complex 2

3-Bromosalicylaldehyde (0.10 mmol, 20 mg), *N*-isopropylethane-1,2-diamine (0.10 mmol, 10 mg), copper bromide (0.10 mmol, 22 mg) and ammonium thiocyanate (0.10 mmol, 7.6 mg) were mixed in methanol (15 mL) to give a clear blue solution. Block blue single crystals of the complex, suitable for X-ray diffraction, were grown from the solution upon slowly evaporation within 4 days. The crystals were isolated by filtration. Yield 41%. Anal. calc. for $C_{26}H_{34}Br_2CuN_6O_2S_2$: C, 41.63; H, 4.57; N, 11.20; found: C, 41.45; H, 4.50; N, 11.31%. IR data (cm^{-1}): 2969, 2939, 2038, 1619, 1592, 1530, 1441, 1412, 1319, 1230, 1183, 1132, 1073, 1031, 905, 850, 781, 739, 663, 617, 549, 473. UV-Vis data (MeOH, λ_{max} , nm): 220, 255, 265, 370.

2. 5. Synthesis of Complex 3

3-Bromosalicylaldehyde (0.10 mmol, 20 mg), *N*-isopropylethane-1,2-diamine (0.10 mmol, 10 mg) and copper nitrate trihydrate (0.10 mmol, 24 mg) were mixed in methanol (15 mL) to give a clear blue solution. Block blue single crystals of the complex, suitable for X-ray diffraction, were grown from the solution upon slowly evaporation within 7

days. The crystals were isolated by filtration. Yield 27%. Anal. calc. for $C_{24}H_{34}Br_2CuN_6O_8$: C, 38.03; H, 4.52; N, 11.09; found: C, 38.22; H, 4.61; N, 10.93%. IR data (cm^{-1}): 2971, 2937, 1619, 1590, 1530, 1443, 1413, 1382, 1323, 1230, 1177, 1146, 1070, 1033, 905, 846, 753, 654, 632, 546, 461. UV-Vis data (MeOH, λ_{max} , nm): 220, 250, 265, 373.

2. 6. X-ray Crystallography

X-ray diffraction was carried out at a Bruker APEX II CCD area diffractometer equipped with MoK α radiation ($\lambda = 0.71073 \text{ \AA}$). The collected data were reduced with SAINT,⁷ and multi-scan absorption correction was performed using SADABS.⁸ The structures of the complexes were solved by direct method, and refined against F^2 by full-matrix least-squares method using SHELXTL.⁹ All of the non-hydrogen atoms were refined anisotropically. The hydrogen atoms including those on nitrogen atoms were placed in calculated positions and constrained to ride on their parent atoms. The isopropyl group N4-C22-C23-C24 is disordered over two sites, with occupancies of 0.48(3) and 0.52(3), respectively. The crystallographic data and refinement parameters for the complexes are listed in Table 1. Selected bond lengths and angles are listed in Table 2.

2. 7. Antimicrobial Assay

The antibacterial property of the complexes was tested against *Bacillus subtilis*, *Staphylococcus aureus*, *Escherichia coli*, and *Pseudomonas fluorescens* using MH (Mueller–Hinton) medium.¹⁰ The antifungal activities of the compounds were tested against *Candida albicans* and *Aspergillus niger* using RPMI-1640 medium. The MIC values of the tested compounds were determined by a colorimetric method using the dye MTT.¹¹ A stock solution of the compound ($150 \mu\text{g mL}^{-1}$) in DMSO was prepared and graded quantities ($75 \mu\text{g mL}^{-1}$, $37.5 \mu\text{g mL}^{-1}$, $18.8 \mu\text{g mL}^{-1}$, $9.4 \mu\text{g mL}^{-1}$, $4.7 \mu\text{g mL}^{-1}$, $2.3 \mu\text{g mL}^{-1}$, $1.2 \mu\text{g mL}^{-1}$, $0.59 \mu\text{g mL}^{-1}$) were incorporated in specified quantity of the corresponding sterilized liquid medium. A specified quantity of the medium containing the compound was poured into micro-titration plates. Suspension of the microorganism was prepared to contain approximately $1.0 \times 10^5 \text{ cfu mL}^{-1}$ and applied to microtitration plates with serially diluted compounds in DMSO to be tested and incubated at $37 \text{ }^\circ\text{C}$ for 24 h and 48 h for bacteria and fungi, respectively. Then the MIC values were visually determined on each of the microtitration plates, $50 \mu\text{L}$ of PBS (phosphate buffered saline 0.01 mol L^{-1} , $\text{pH} = 7.4$) containing 2 mg mL^{-1} of MTT was added to each well. Incubation was continued at room temperature for 4–5 h. The content of each well was removed and $100 \mu\text{L}$ solution of isopropanol (95%) and 1 mol L^{-1} HCl (5%) was added to extract the dye. After 12 h of incubation at room temperature, the optical density was measured with a microplate reader at 550 nm.

Table 1. Crystallographic and refinement data for the complexes

Complex	1	2	3
Formula	C ₂₄ H ₃₄ Br ₄ CuN ₄ O ₂	C ₂₆ H ₃₄ Br ₂ CuN ₆ O ₂ S ₂	C ₂₄ H ₃₄ Br ₂ CuN ₆ O ₈
Formula weight	793.73	750.07	757.93
T (K)	298(2)	298(2)	298(2)
Crystal system	Monoclinic	Orthorhombic	Triclinic
Space group	<i>P2₁/n</i>	<i>Pbca</i>	<i>P-1</i>
<i>a</i> (Å)	12.5850(13)	13.6410(18)	5.8585(11)
<i>b</i> (Å)	17.8439(10)	9.7930(16)	10.4956(12)
<i>c</i> (Å)	14.2664(12)	23.2285(16)	12.5848(13)
α (°)	90	90	86.090(1)
β (°)	109.717(1)	90	82.966(1)
γ (°)	90	90	84.240(1)
<i>V</i> (Å ³)	3015.9(4)	3103.0(7)	762.9(2)
<i>Z</i>	4	4	1
<i>D</i> _{calc} (g cm ⁻³)	1.748	1.606	1.650
μ (Mo K α) (mm ⁻¹)	6.051	3.448	3.389
<i>F</i> (000)	1564	1516	383
Measured reflections	16027	15250	4017
Unique reflections	5617	2891	2806
Observed reflections (<i>I</i> \geq 2 σ (<i>I</i>))	2929	2047	2076
Parameters	344	180	189
Restraints	42	0	0
GOOF	1.005	1.102	1.129
<i>R</i> ₁ , <i>wR</i> ₂ [<i>I</i> ³ 2 <i>s</i> (<i>I</i>)] ^a	0.0480, 0.1064	0.0654, 0.1633	0.0492, 0.1544
<i>R</i> ₁ , <i>wR</i> ₂ (all data) ^a	0.1176, 0.1342	0.0936, 0.1780	0.0693, 0.1701

$$^a R_1 = \frac{\sum ||F_o| - |F_c||}{\sum |F_o|}, wR_2 = \left\{ \frac{\sum [w(F_o^2 - F_c^2)^2]}{\sum [w(F_o^2)^2]} \right\}^{1/2}$$

Table 2. Selected bond distances (Å) and angles (°) for the complexes

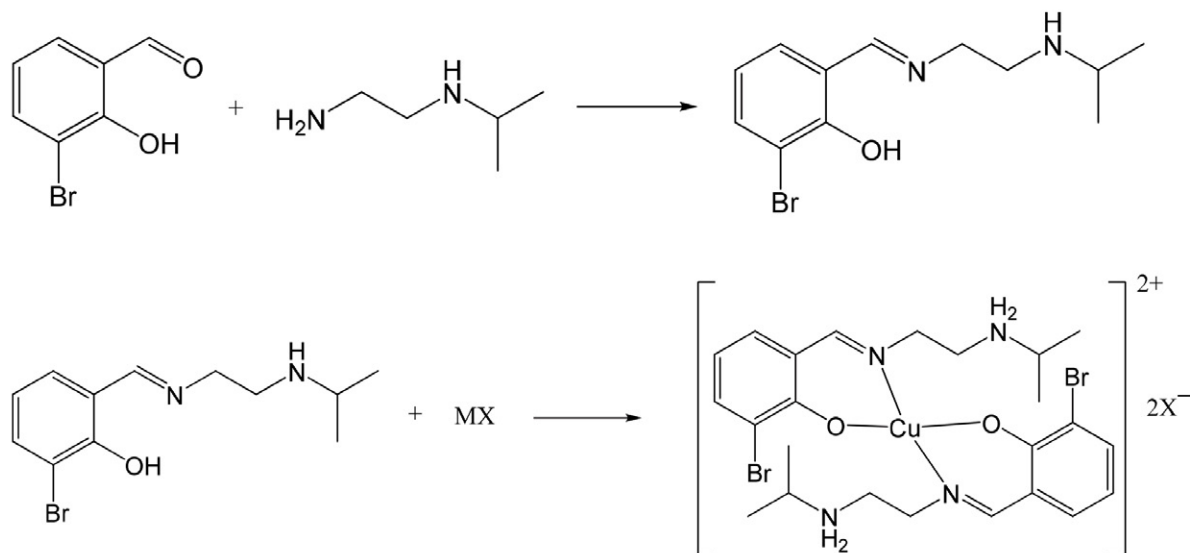
1			
Cu1–O1	1.907(4)	Cu1–O2	1.908(4)
Cu1–N1	1.985(5)	Cu1–N3	1.983(5)
O2–Cu1–O1	165.1(2)	O2–Cu1–N3	92.6(2)
O1–Cu1–N3	88.3(2)	O2–Cu1–N1	88.1(2)
O1–Cu1–N1	91.8(2)	N3–Cu1–N1	177.1(2)
2			
Cu1–O1	1.954(4)	Cu1–N1	2.014(5)
O1–Cu1–O1A	180	O1–Cu1–N1	90.22(19)
O1–Cu1–N1A	89.78(19)	N1–Cu1–N1A	180
Symmetry code for A: 1 - <i>x</i> , - <i>y</i> , - <i>z</i> .			
3			
Cu1–O1	1.913(3)	Cu1–N1	2.009(4)
O1–Cu1–O1A	180	O1–Cu1–N1A	88.58(16)
O1–Cu1–N1	91.42(16)	N1–Cu1–N1A	180
Symmetry code for A: 1 - <i>x</i> , 1 - <i>y</i> , 1 - <i>z</i> .			

3. Results and Discussion

3. 1. Synthesis and Characterization

The Schiff base HL was readily prepared by the reaction of equimolar quantities of 3-bromosalicylaldehyde and *N*-isopropylethane-1,2-diamine in methanol. Complex 1 was prepared by the reaction of HL with copper bromide in methanol. Complex 2 was prepared by the similar

method as complex 1, followed by the addition of ammonium thiocyanate. Complex 3 was prepared by the similar method as complex 1, but with copper bromide replaced with copper nitrate (Scheme 1). Single crystals of the complexes were obtained by slow evaporation of their methanolic solution. From the preparation of complexes 1 and 2, it can be seen that the bromide anions can be replaced by thiocyanate anions. Elemental analyses of the complexes



Scheme 1. The synthetic procedure for HL and the complexes. MX = CuBr₂ for 1, CuBr₂ and NH₄NCS for 2, and Cu(NO₃)₂ for 3.

are in accordance with the molecular structures determined by the single crystal X-ray analysis.

3. 2. Spectroscopic Studies

The typical and strong absorptions at 1618–1619 cm⁻¹ of the complexes are generated by the vibrations of the C=N bonds, indicating the formation of the Schiff bases from the condensation reaction of the 3-bromosalicylaldehyde and *N*-isopropylethane-1,2-diamine during the coordination.¹¹ The intense absorption at 2038 cm⁻¹ for complex 2 is attributed to the stretching vibration of the thiocyanate anions.¹² The spectrum of complex 3

shows an intense band at 1382 cm⁻¹ characteristic of ionic nitrate.¹³

In the UV-Vis spectra of the complexes, the bands at 370–373 nm are attributed to the azomethine chromophore $\pi \rightarrow \pi^*$ transition.¹⁴ The bands at higher energies (220–222 and 247–267 nm) are associated with the benzene $\pi \rightarrow \pi^*$ transition.¹⁴

3. 3. Structure Description of the Complexes

Molecular structures of complexes 1–3 are shown in Figures 1–3, respectively. All the complexes contain

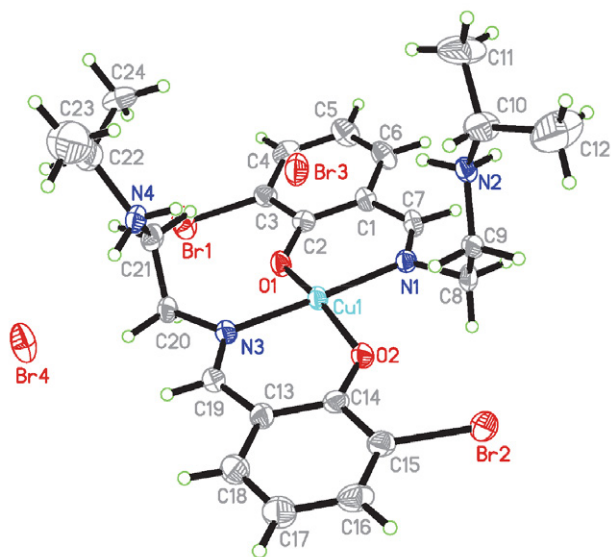


Figure 1. A perspective view of complex 1 with the atom labeling scheme. Thermal ellipsoids are drawn at the 30% probability level.

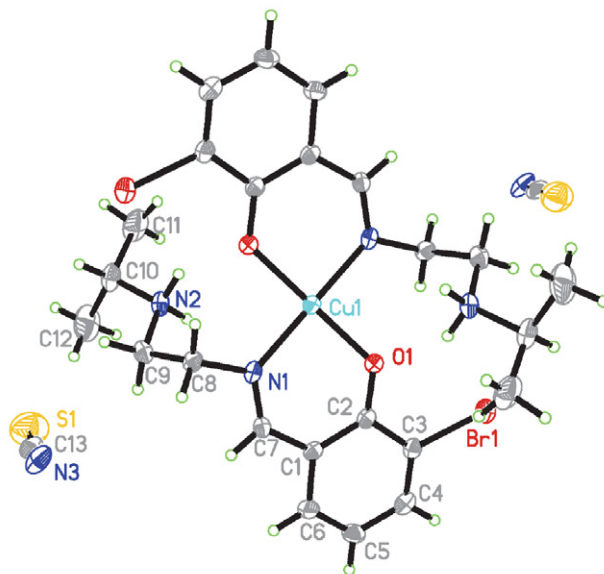


Figure 2. A perspective view of complex 2 with the atom labeling scheme. Thermal ellipsoids are drawn at the 30% probability level. The unlabeled atoms are related to the symmetry operation $1 - x, -y, -z$.

$[\text{Cu}(\text{LH})_2]^{2+}$ cations, and two anions, viz. Br^- for **1**, SCN^- for **2**, and NO_3^- for **3**. The Cu atoms in the cations are coordinated in square planar geometry, with the phenolate O and imino N atoms of the Schiff base ligand LH. The Schiff base ligand, acts as a bidentate ligand, chelate the Cu atoms by generating one six-membered ring with bite angles of $88.1(2)^\circ$ and $92.6(2)^\circ$ for **1**, $89.78(19)^\circ$ and $90.22(19)^\circ$ for **2**, and $88.58(16)^\circ$ and $91.42(16)^\circ$ for **3**, respectively. The *trans* angles in the complexes are $1651(2)^\circ$ and $177.11(2)^\circ$ for **1**, and 180° for **2** and **3**. Thus, the bond lengths and angles in the square planar coordination are similar to each other, and comparable to those in the reported Schiff base copper complexes.¹⁵

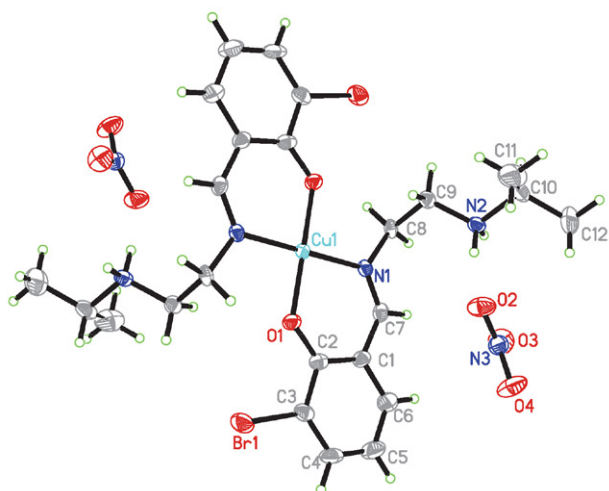


Figure 3. A perspective view of complex **3** with the atom labeling scheme. Thermal ellipsoids are drawn at the 30% probability level. The unlabeled atoms are related to the symmetry operation $1 - x, 1 - y, 1 - z$.

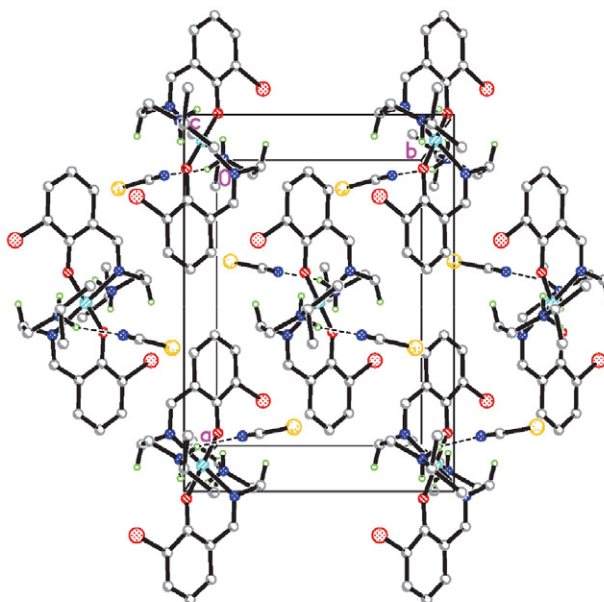


Figure 5. Molecular packing structure of complex **2**, viewed along the *c* axis. Hydrogen bonds are shown as dashed lines.

In the crystal structure of complex **1**, the $[\text{Cu}(\text{LH})_2]^{2+}$ cations and the Br^- anions are linked through hydrogen bonds of $\text{N-H}\cdots\text{Br}$ and $\text{C-H}\cdots\text{Br}$, to form two-dimensional sheets parallel to the *bc* plane (Figure 4). In the crystal structure of complex **2**, the $[\text{Cu}(\text{LH})_2]^{2+}$ cations and the SCN^- anions are linked through hydrogen bonds of $\text{N-H}\cdots\text{N}$ (Figure 5). In the crystal structure of complex **3**, the $[\text{Cu}(\text{LH})_2]^{2+}$ cations and the NO_3^- anions are linked through hydrogen bonds of $\text{C-H}\cdots\text{O}$ and $\text{N-H}\cdots\text{O}$, to form one-dimensional chains running along the *c* axis (Figure 6).

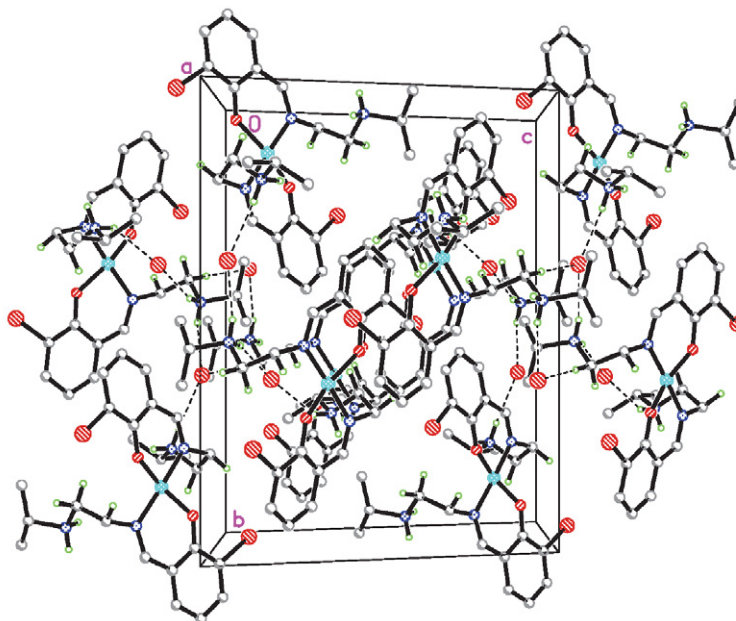


Figure 4. Molecular packing structure of complex **1**, viewed along the *a* axis. Hydrogen bonds are shown as dashed lines.

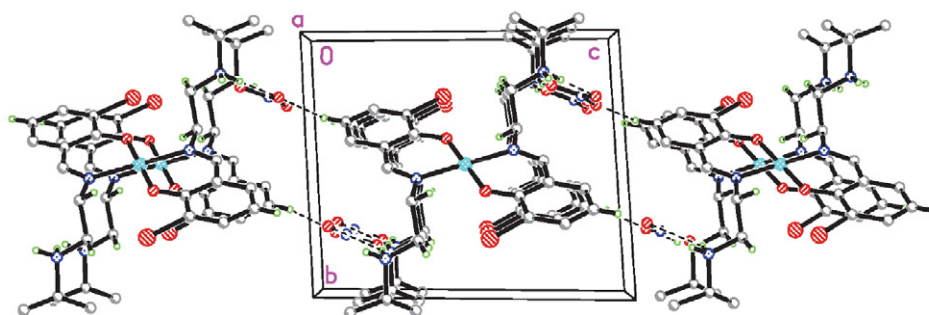


Figure 6. Molecular packing structure of complex 3, viewed along the *a* axis. Hydrogen bonds are shown as dashed lines.

Table 3. Distances (Å) and angles (°) involving hydrogen bonding of the complexes

D-H...A	d(D-H)	d(H...A)	d(D...A)	Angle(D-H...A)
1				
N4-H4B...Br4	0.89	2.45	3.313(6)	164(5)
N4-H4A...Br3	0.89	2.41	3.238(5)	155(5)
N2-H2B...Br4 ⁱ	0.89	2.42	3.309(5)	175(5)
N2-H2A...Br3	0.89	2.46	3.216(5)	143(5)
C21-H21B...Br4 ⁱⁱ	0.97	2.89	3.848(8)	171(5)
2				
N2-H2B...N3 ⁱⁱⁱ	0.90	2.15	3.000(8)	156(7)
3				
N2-H2A...O2 ^{iv}	0.89	2.59	3.130(6)	120(6)
N2-H2A...O4 ^{iv}	0.89	2.01	2.898(7)	174(6)
N2-H2B...O3	0.89	2.52	3.169(6)	131(6)
C8-H8A...O1 ^v	0.97	2.30	2.752(6)	107(6)

Symmetry codes: i: $1\frac{1}{2} - x, \frac{1}{2} + y, \frac{1}{2} - z$; ii: $2 - x, 1 - y, -z$; iii: $x, -1 + y, z$; iv: $-1 + x, y, z$; v: $1 - x, 1 - y, 1 - z$.

3. 4. Antimicrobial Activity

The three complexes were screened for antibacterial activities against two Gram (+) bacterial strains (*Bacillus subtilis* and *Staphylococcus aureus*) and two Gram (-) bacterial strains (*Escherichia coli* and *Pseudomonas fluorescens*) by MTT method. The MIC (minimum inhibitory concentration, $\mu\text{g mL}^{-1}$) values of the compounds against four bacteria are listed in Table 4. Penicillin G was used as the standard drug. As expected, the three complexes have the same activities against all the bacteria within the standard uncertainty. Since the difference of the three complexes is the anions, it is easy to conclude that the anions like bromide, thiocyanate and nitrate do not have obvious

influence on the antibacterial activity. All the complexes show strong activity against *B. subtilis* and *S. aureus*, and medium activity against *E. coli*, while weak activity against *P. fluorescens*. For the bacteria *B. subtilis*, *S. aureus* and *E. coli*, the complexes have stronger activities than copper bromide and Penicillin G. However, for the bacteria *P. fluorescens*, the complexes have weaker activities than copper bromide, while stronger activities than Penicillin G. However, all the complexes have no activity on the fungal strains *Candida albicans* and *Aspergillus niger*. The present complexes have higher activities against *B. subtilis*, *S. aureus* and *E. coli*, when compared with the vanadium complex with hydrazone ligands,¹⁶ and the copper complexes with Schiff bases.¹⁷

Table 4. Antibacterial activities of the complexes with minimum inhibitory concentrations ($\mu\text{g mL}^{-1}$)

Tested material	<i>B. subtilis</i>	<i>S. aureus</i>	<i>E. coli</i>	<i>P. fluorescens</i>
1	1.2	2.3	9.4	37.5
2	1.2	2.3	9.4	37.5
3	1.2	2.3	9.4	37.5
Copper bromide	4.7	9.4	37.5	9.4
Penicillin G	2.3	4.7	>150	>150

4. Conclusion

Three new structurally similar mononuclear Schiff base copper(II) complexes with the cation $[\text{Cu}(\text{LH})_2]^{2+}$ and different anions were synthesized from the Schiff base 2-bromo-6-((2-(isopropylamino)ethylimino)methyl)phenol. The complexes have been characterized by physico-chemical method, and their structures have been confirmed by single crystal X-ray structure determination. The Cu atoms in the complexes are in square planar coordination. The complexes have strong activities against the bacteria *B. subtilis*, *S. aureus* and *E. coli*.

Supplementary Data

CCDC 2095686 (1), 2095687 (2) and 2095688 (3) contain the supplementary crystallographic data for the compounds. These data can be obtained free of charge via <http://www.ccdc.cam.ac.uk/conts/retrieving.html>, or from the Cambridge Crystallographic Data Centre, 12 Union Road, Cambridge CB2 1EZ, UK; fax: (+44) 1223-336-033; or e-mail: deposit@ccdc.cam.ac.uk.

Acknowledgments

This work was financially supported by K. C. Wong Magna Fund in Ningbo University, Ningbo Public Fund (Project No. 202002N3056), the State Key Laboratory Development Fund of Structural Chemistry (Project No. 20190028), and the Ningbo Public Welfare Funds (Project Nos. 202002N3056 and 2021S142).

5. References

1. M. H. Esfahani, H. Iranmanesh, J. E. Beves, M. Kaur, J. P. Jasiniski, M. Behzad, *J. Coord. Chem.* **2019**, *72*, 2326–2336. DOI:10.1080/00958972.2019.1643846
2. (a) S. Mandal, M. Layek, R. Saha, C. Rizzoli, D. Bandyopadhyay, *Transition Met. Chem.* **2020**, *46*, 9–16; DOI:10.1007/s11243-020-00416-6
(b) M. H. Esfahani, M. Behzad, *J. Coord. Chem.* **2020**, *73*, 154–163; DOI:10.1080/00958972.2020.1725492
(c) N. Caliskan, A. Usta, F. S. Beris, N. Baltas, E. Celik, *Lett. Org. Chem.* **2020**, *17*, 631–638; DOI:10.2174/1570178617666200108111211
(d) S. Mandal, T. Sen, U. Mandal, D. Bhunia, C. Rizzoli, D. Bandyopadhyay, *J. Coord. Chem.* **2019**, *72*, 3614–3624; DOI:10.1080/00958972.2019.1704275
(e) A. Frei, A. P. King, G. J. Lowe, A. K. Cain, F. L. Short, H. Dinh, A. G. Elliott, J. Zuegg, J. J. Wilson, M. A. T. Blaskovich, *Chem. Eur. J.* **2020**, *27*, 2021–2029; DOI:10.1002/chem.202003545
(f) P.-L. Lam, K. K.-H. Lee, S. H.-L. Kok, R. Gambari, K.-H. Lam, C.-L. Ho, X. Ma, Y.-H. Lo, W.-Y. Wong, D.-C. Dong, Z.-X. Bian, C.-H. Chui, *RSC Advances* **2016**, *6*, 104575–104581;

- DOI:10.1039/C6RA20186E
(g) K. Venkateswarlu, N. Ganji, S. Daravath, K. Kanneboina, K. Rangan, Shivaraj, *Polyhedron* **2019**, *171*, 86–97; DOI:10.1016/j.poly.2019.06.048
(h) N. R. Palepu, S. L. Nongbri, J. R. Premkumar, A. K. Verma, K. Bhattacharjee, S. R. Joshi, S. Forbes, Y. Mozharivskiy, R. Thounaojam, K. Aguan, M. R. Kollipara, *J. Biol. Inorg. Chem.* **2015**, *20*, 619–638. DOI:10.1007/s00775-015-1249-3
3. (a) G. Paraskevopoulos, S. Monteiro, R. Vosatka, M. Kratky, L. Navratilova, F. Trejtnar, J. Stolarikova, J. Vinsova, *Bioorg. Med. Chem.* **2017**, *25*, 1524–1532; DOI:10.1016/j.bmc.2017.01.016
(b) M. Zhang, D.-M. Xian, H.-H. Li, J.-C. Zhang, Z.-L. You, *Aust. J. Chem.* **2012**, *65*, 343–350; DOI:10.1071/CH11424
(c) H.-F. Guo, Y. Pan, D.-Y. Ma, P. Yan, *Chinese J. Inorg. Chem.* **2013**, *29*, 1447–1453.
 4. N. P. Rai, V. K. Narayanaswamy, T. Govender, B. K. Manuprasad, S. Shashikanth, P. N. Arunachalam, *Eur. J. Med. Chem.* **2010**, *45*, 2677–2682. DOI:10.1016/j.ejmech.2010.02.021
 5. A. Bhattacharjee, S. Das, B. Das, P. Roy, *Inorg. Chim. Acta* **2021**, *514*, 119961; DOI:10.1016/j.ica.2020.119961
(b) S. Mandal, M. Layek, R. Saha, C. Rizzoli, D. Bandyopadhyay, *Transition Met. Chem.* **2020**, *46*, 9–16; DOI:10.1007/s11243-020-00416-6
(c) M. H. Esfahani, M. Behzad, *J. Coord. Chem.* **2020**, *73*, 154–163; DOI:10.1080/00958972.2020.1725492
(d) N. Rajendran, A. Periyasamy, N. Kamatchi, V. Solomon, *J. Coord. Chem.* **2019**, *72*, 1937–1956. DOI:10.1080/00958972.2019.1634806
 6. C.-L. Zhang, X.-Y. Qiu, S.-J. Liu, *Acta Chim. Slov.* **2019**, *66*, 719–725; DOI:10.17344/acsi.2019.5241
(b) L.-Y. He, X.-Y. Qiu, J.-Y. Cheng, S.-J. Liu, S.-M. Wu, *Polyhedron* **2018**, *156*, 105–110; DOI:10.1016/j.poly.2018.09.017
(c) S. M. Wu, X. Y. Qiu, J. C. Wang, S. J. Liu, L. Y. He, *Russ. J. Coord. Chem.* **2019**, *45*, 384–390.
 7. Bruker, SMART (Version 5.625) and SAINT (Version 6.01). Bruker AXS Inc., Madison, Wisconsin, USA, 2007.
 8. G. M. Sheldrick, SADABS. Program for Empirical Absorption Correction of Area Detector, University of Göttingen, Germany, 1996.
 9. G. M. Sheldrick, SHELXTL V5.1 Software Reference Manual, Bruker AXS, Inc., Madison, Wisconsin, USA, 1997.
 10. J. Meletiadis, J. F. G. M. Meis, J. W. Mouton, J. P. Donnelly, P. E. Verweij, *J. Clin. Microbiol.* **2000**, *38*, 2949–2954. DOI:10.1128/JCM.38.8.2949-2954.2000
 11. (a) S. Manna, E. Zangrando, H. Puschmann, S. C. Manna, *Polyhedron* **2019**, *162*, 285–292; DOI:10.1016/j.poly.2019.01.057
(b) P. Chakraborty, S. Majumder, A. Jana, S. Mohanta, *Inorg. Chim. Acta* **2014**, *410*, 65–75. DOI:10.1016/j.ica.2013.10.013
 12. (a) M. Sarwar, A. M. Madalan, F. Lloret, M. Julve, M. Andruh, *Polyhedron* **2011**, *30*, 2414–2420; DOI:10.1016/j.poly.2011.06.011
(b) J. Nishijo, T. Yoshida, M. Enomoto, *Polyhedron* **2015**, *87*, 233–236. DOI:10.1016/j.poly.2014.11.015
 13. (a) M. F. Iskander, T. E. Khalil, R. Werner, W. Haase, I. Svoboda, H. Fuess, *Polyhedron* **2000**, *19*, 949–958;

- DOI:10.1016/S0277-5387(00)00340-5
(b) S. Chandra, A. K. Sharma, J. Coord. Chem. 2009, 62, 3688–3700. DOI:10.1080/00958970903121305
14. L. Pogany, J. Moncol, M. Gal, I. Salitros, R. Boca, *Inorg. Chim. Acta* 2017, 462, 23–29. DOI:10.1016/j.ica.2017.03.001
15. (a) D. Aggoun, M. Fernandez-Garcia, D. Lopez, B. Bouzerafa, Y. Ouennoughi, F. Setifi, A. Ourari, *Polyhedron* 2020, 187, 114640; DOI:10.1016/j.poly.2020.114640
(b) H. Kargar, R. Behjatmanesh-Ardakani, V. Torabi, A. Sarvian, Z. Kazemi, Z. Chavoshpour-Natanzi, V. Mirkhani, A. Sahraei, M. N. Tahir, M. Ashfaq, *Inorg. Chim. Acta* 2021, 514, 120004; DOI:10.1016/j.ica.2020.120004
- (c) T. L. Yusuf, S. D. Oladipo, S. Zamisa, H. M. Kumalo, I. A. Lawal, M. M. Lawal, N. Mabuba, *ACS Omega* 2021, 6, 13704–13718. DOI:10.1021/acsomega.1c00906
16. (a) H.-Y. Qian, *Acta Chim. Slov.* 2019, 66, 995–1001; DOI:10.4149/neo_2019_190112N36
(b) Z.-Q. Sun, S.-F. Yu, X.-L. Xu, X.-Y. Qiu, S.-J. Liu, *Acta Chim. Slov.* 2020, 67, 1281–1289. DOI:10.17344/acsi.2020.6236
17. S.-F. Yu, X.-Y. Qiu, S.-J. Liu, *Acta Chim. Slov.* 2020, 67, 1301–1308. DOI:10.17344/acsi.2020.6321

Povzetek

Sintetizirali smo tri nove bakrove(II) komplekse, $[\text{Cu}(\text{LH})_2]\text{Br}_2$ (**1**), $[\text{Cu}(\text{LH})_2]\text{NCS}_2$ (**2**) in $[\text{Cu}(\text{LH})_2](\text{NO}_3)_2$ (**3**), kjer je LH ion-dvojček 2-bromo-6-((2-(izopropilamino)etilimino)metil)fenola (HL), in jih okarakterizirali z elementarno analizo, IR in UV-vis spektroskopijo. Strukture kompleksov so bile dodatno potrjene z določitvijo monokristalne rentgenske strukture. Vse spojine so enojedrni bakrovi(II) kompleksi. Cu atomi v kompleksih so koordinirani z dvema imino N in dvema fenolato O atomoma iz dveh LH ligandov, kar tvori kvadratno planarno koordinacijo. Pri spojinah smo ugotavljali njihovo protimikrobno delovanje.



Except when otherwise noted, articles in this journal are published under the terms and conditions of the Creative Commons Attribution 4.0 International License

Scientific paper

Developing Students' Problem-Solving Skills Using Learning Tasks: an Action Research Project in Secondary School

Martina Tóthová and Martin Rusek*

Charles University, Faculty of Education, Department of Chemistry and Chemistry Education, Magdalény Rettigové 4, 116 39 Praha

* Corresponding author: E-mail: martin.rusek@pedf.cuni.cz

Received: 07-29-2021

Abstract

Studies on students' problem-solving skills worldwide suggest there is a room for improvement. This study aimed at improving upper-secondary school students' problem-solving skills in chemistry lessons. They were given a problem tasks pre-test focused on their conceptual knowledge regarding the periodic table, ability to apply knowledge on the factors affecting chemistry reaction rate and compounds' properties. Most students (72 out of 112) did not succeed to solve the tasks. For this reason, an intervention was designed based on a study using eye-tracking combined with think-aloud. It consisted of students' working on (PISA-like) context-based chemistry problem tasks with a special scaffolding. A teacher provided formative assessment promoting students' expansive strategies. The intervention's effect was again assessed using problem tasks in two post-tests. The results showed the action plan was successful in helping the majority of students reach above-average test score. The ratio of successful solvers also rose and unsuccessful significantly declined.

Keywords: Chemistry education; action research; problem solving; students' skills development

1. Introduction

There is a significant gap between research (researchers) and school practice (teachers' understanding of the research).^{1,2} Teachers consider research and theory to be something remotely related to their actual practice.³ In action research, a teacher becomes an observer (e.g. in order to maintain objectivity).⁴ In this respect, action research seems to be one of the possible remedies as it combines academic research with practice, e.g.^{5,6} The teacher plans and systematically verifies the learning process, the teacher is a part of the research process and not only subject to investigation or a non-participating observer.^{3,4,7}

The presented action research was guided by a definition by Cohen, et al.,⁸ who point it out as an on-the-spot procedure which focuses on a specific problem located in a current situation. The process is ideally supposed to be monitored step-by-step using different tools (questionnaires, diaries, interviews, and case studies, for example).

Research on chemistry education mostly focuses either on lower-secondary or upper-secondary education, namely grammar schools, or at university level. There is, however, a numerous group of non-chemical vocational

school students who have been neglected by researchers so far.⁹ They follow a curriculum which contains chemistry as a school subject of general education at schools oriented in various fields but science. Teaching chemistry at this level is influenced by several factors, such as students' attitudes to this subject - which is not the part of the school-leaving exam nor their study profile.¹⁰ Also, their school is considered lower success grammar school students.⁹ The curriculum for these schools is exempt from some of the content objectives in the field of chemistry. Nevertheless, the key competencies remain the same for different types of upper-secondary schools: Framework Educational Programme for Grammar school,¹¹ Framework Educational Programme for Economic lyceum.¹² With the students' focus in mind, the goal of chemistry education at this type of school remains mostly in skills (competences) development via the chemistry subject matter, however, the curricular objectives have the potential to stimulate the higher-order cognitive operations which should be included in the tasks students solve.¹³ This action research was therefore motivated by one of the 21st century skills cf.¹⁴ - problem solving. As an integral aspect strongly linked with science education, problem solving belongs among widely

studied phenomena.^{15–17} Its aim was to identify the state of students' problem-solving skills and to improve the strategies and skills necessary for problem solving. These can be, unlike problem solving itself, cultivated in schools.¹⁸

Problems in chemistry were elaborated by Johnstone.¹⁹ He classified eight types of problems according to the three variables: data, methods, goals. Type 1 (where data and goals are given, used methods are familiar) is the most used type of problem in chemistry and can be considered as "exercise" or algorithmic problems.²⁰ Problems are not hierarchical and related to their difficulty. They can be also well-structured or ill structured.^{21,22} Some authors e.g.²³ consider any chemical situation that students are not familiar with *conceptual problems*. This approach is taken in this paper.

When making international comparisons, Czech students achieve average results in surveys based on problem tasks.^{24,25} Other evidence of their skills can be drawn from the use of problem (indicator) tasks verifying the expected objectives' achievement. These tasks were verified²⁶ and used to research the steps students used while solving these tasks.²⁷ Even the results in this area do not show the success of these students. Moreover, they indicate so-called false-positive results when mere paper-testing is executed.

2. Goals

The aim of the action research was to increase non-chemical vocational school students' (age 15–16) ability to solve chemistry problem tasks. The research followed this research question (RQ):

How does the practice of general problem-solving strategies translate into students' ability to solve chemistry problem-tasks?

Successful task solution determines the student's ability to read and understand the assignment correctly. It requires a direct relationship with reading literacy²⁸ and subsequently identifying the problem and choosing an appropriate strategy to solve it.^{29,30} It is therefore desirable to lead activities which develop both the students' skills and this ability in view of the level of the specific students' strategies.

The RQ is closely associated with the results from a qualitative study using eye-tracking and retrospective think-aloud to find students' strategies and problems.³¹ Eye-tracking has found a broad use in (science) education³² including chemistry education.^{33–35} The action plan developed according to these research findings was subsequently tested.

3. Methods

3.1. The Research Team

The action research was attended not only by a teacher (the first author) as it is usual see ref.,³⁶ but was support-

ed by a researcher (the second author). He helped the teacher choose appropriate research methods (namely eye-tracking and think-aloud), analyzed the data and was present at the realization of an intervention – teaching approach emphasizing problem solving strategies - as an observer and when needed, as a teaching assistant. This combination allows the researcher to use the teacher's practical knowledge, which is reflected in theory and analyzed based on the acquired data cf.⁴

3.2. Eye-Tracking and Think aloud Methods

Eye-tracking is a method based on eye movement recording. Its analysis reveals cognitive processes and mechanisms involved in visual perception.³² It basically enables researchers observe what a subject fixates with their eyes, therefore processes in their mind.³⁷ To understand the subject's cognitive processes in more detail, the *think-aloud* method is being used.³¹ Participants are asked to describe out loud their thought process when solving the task with no interruption of researcher.³⁸ Combination of these methods thus enables researchers to explain the results in more detail, including reasons of failure, applied strategies etc.

3.3. The Action Plan

The action research was organized in typical steps³⁹ (see Figure 1).

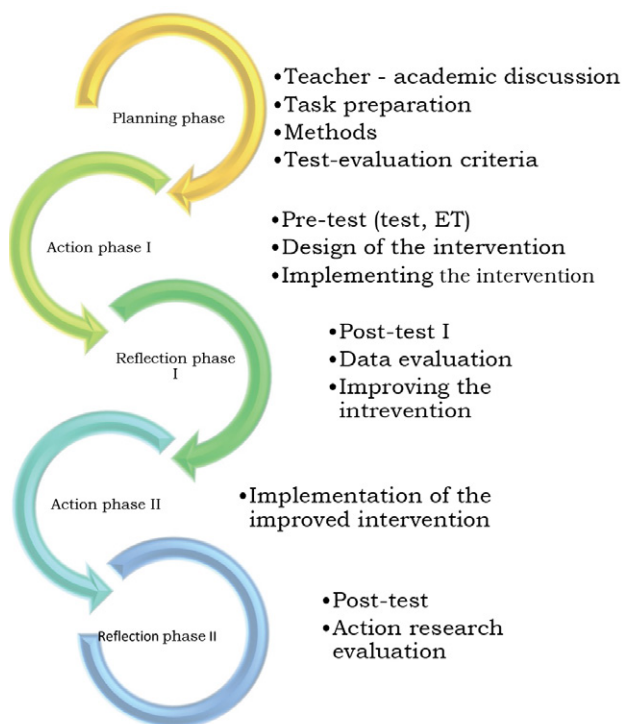


Figure 1. The action plan

I. Planning phase (June 2018)

In the planning phase, the problems the teacher observed during chemistry lessons were discussed with the researcher (chemistry education expert/teacher trainer). Based on the literature, a possible method to intervene was proposed, and research questions were set (see Goals).

The methods to verify the students' skills initial status and the criterion to evaluate the success of the teaching approach emphasizing problem solving strategies were developed (see Action phase I).

Altogether, three tests of comparable difficulty containing three tasks each were developed. To prevent the negative effect of students' possible task recollection, different tasks were used. They were taken from *Methodical commentary and tasks from the Standards for Basic Education – Chemistry*⁴⁰ – a publication adjacent to the Czech national curriculum. The tasks target the expected outcomes, i.e. lower-secondary curricular objectives. These tasks were complex task, formulated in a non-standard way for students. During solving, they can learn some information from the text, therefore are considered as problem-tasks, in accordance with other authors.^{19,23} To ensure the pre- and post-tests comparability, task-difficulty scores derived from an expert panel evaluation²⁶ and further piloting^{26,27,41} were used to select the tasks for the test. The tasks were evaluated in a manner similar to PISA tasks, i.e. successful, partially successful and successful. Each task in the test was assigned a maximum of two points (2 – completely successful, 1 – partially successful 0 – unsuccessful).

II. Action phase I (September - December 2018)

Pre-tests

This action research was planned in reaction to previous research results which showed deficiencies both in students' knowledge problem solving skills.³¹ Therefore, the prior study served as a pre-test. The students' knowledge and skills which they acquired in lower-secondary education, i.e. the starting point for chemistry teaching at secondary school was assessed using a set of three tasks. Also, as described in the prior study,³¹ based on the pre-test out of 139 tested, eight students' problem-solving skills (strategies they employed and problems they faced when solving tasks) were further investigated using eye-tracking and retrospective think-aloud (RTA) method.

The pre-test consisted of three tasks. In the first task, the students worked with the periodic table of elements. Knowledge of the: proton number, oxidation number, conductivity (heat and electric), non-conductors, metals, metalloids, semi-metals as well as basic orientation in the periodic table (group, period) was tested. The task was to identify a certain group of elements based on their characteristics' description, i.e. all non-metal elements from the second period etc. A periodic table including a legend with the element groups was provided.

In the second task, students were supposed to apply their knowledge of the factors influencing chemistry reaction rate and work with a graph. They were provided a context which introduced them to a new hypothetical battery production. It contained an equation of manganese's reaction with hydrochloric acid and a graph of the reaction rate's dependency on time (see Figure 2). Their task was to match the following steps to the particular phases in the graph: adding Mn, adding 25% HCl, adding 10% HCl and heating. The students were also asked to justify their answer.

The third task concerned the physical properties of organic chemistry substances. It focused on the students' understanding of the properties and their application. The students were provided a table of melting and boiling points and the density of five substances (methane, toluene, benzene, isooctane, naphthalene), and were supposed to decide on particular statements (true or false) under laboratory conditions (temperature and atmospheric pressure): benzene is gas, isooctane is solid, naphthalene is solid, toluene is gas.

Pre-test evaluation

The pre-tests were evaluated according to the Authors' key see.⁴⁰ As the mere test evaluation can be insufficient to fully understand the reasons behind students' problems, 8 students at different levels of success were selected for a qualitative (ET) part of the study. This part of study used eye-tracking and think-aloud method and the methods – procedure of this qualitative part were already published elsewhere see.³¹ For action research's and mainly for the understanding's sake, the important results are summarized in this article. Students used following expansive and limiting strategies and faced these problems:

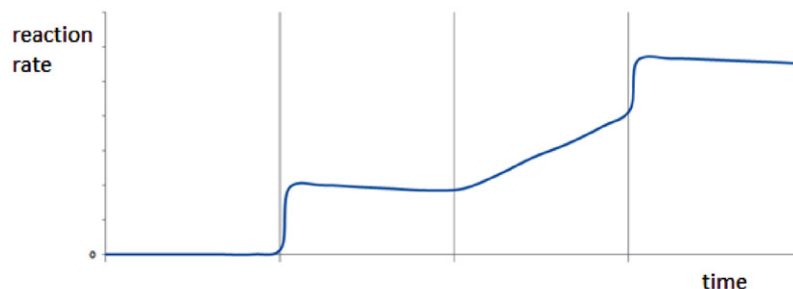


Figure 2. Graph from the second task

Expansive strategies:

- Gradual chaining,⁴²
- logical justification,⁴³
- working with the information in the assignment,²⁷
- self-reflection (working with error),⁴⁴
- finding a pattern – the principle of function.⁴³

Limiting strategies:

- Guessing the result,⁴⁵
- drawing conclusions from the assignment structure,²⁷
- memorization-based solutions.⁴⁶

Problems:

- Problem identification (misunderstanding of input, inattentive reading, editing the assignment),
- motivation (giving up, not solving a task),
- inability to use knowledge,
- lack of knowledge.

The students struggled with reading (multiple cases). For example, in the task where the students were supposed to write a code consisting of proton numbers, they wrote the elements' symbols. The ability to read proved to be crucial.⁴⁷ The students also struggled with motivation. This phenomenon most often occurred in a task in which they had to perform simple mathematical operations. Some students tended to answer by guessing when a task was more demanding – requiring several steps. There were students who had no idea about the term 'proton number' or who could not use the periodic table. This shows the curricular objectives of basic education in the field of chemistry were not reached with these students.

Intervention preparation (January 2019)

With respect to the identified strategies and problems, the action plan was designed to strengthen the use of expansive strategies and eliminate limiting strategies as well as target the missing functional knowledge regarding lower-secondary chemistry subject matter.⁴⁸ The teaching approach emphasizing problem solving strategies was based on students working with tasks released from the PISA project, enriched by chemistry-oriented tasks of a similar nature.

Action I (February – March 2019)

The intervention took place one lesson (out of two in total) per week for two months. Students in groups (2–3 students) were given a set of released PISA tasks. These contextual, science-oriented tasks were used without any changes and were chosen due to students' problems ascertained in the above-mentioned eye-tracking/think-aloud study.³¹ They were mostly related to reading - finding the main problem to solve as well as the provided hints and variables. Added instructions led students to understanding the assignment better. Under the teachers' guidance, the following steps were taken: 1. What is the task (what they have to answer, what will be the form of the answer), 2. Schedule the procedure, 3. What data is provided (data

needed). Students were also supposed to identify the causes of their mistakes (self-reflection strategy). Later during the action phase, the teacher performed them only with groups who did not express their willingness to try solving the tasks on their own first.

III. Refslection phase

Post-test I (March 2019)

After two months, in the end of *action phase I*, a post-test I was given to the students in order to measure the intervention's effect. The post-test I tasks contained tasks of a similar nature and difficulty to the pre-test. The tasks included student choice of an appropriate procedure (including quantity of individual substances, heating, cooling, etc.) that would be suitable for preparing a solution (food for bees). The second task was directed towards the students' scientific text reading skills. They were supposed to use information from a disinfectant label to decide which type of disinfection is suitable for a specific given situation and which method of preparation to choose from methods mentioned on the product's label. In the third task, the students were supposed to determine a proportion of particular elements in different given fertilizers and compare which fertilizer of a given mass is richer in nitrogen - $\text{Ca}(\text{NO}_3)_2$ or NaNO_3 .

Improving the intervention plan

Although the results were promising (see below), changes in the procedure were made (see below).

IV. Action phase II (April – May 2019)

The teacher's role (especially the students' guidance through the particular steps) was diminished so the learning tasks were targeted at the students. The tasks were completed with scaffolding in the form of a description of each groups' solution procedure for the teacher to control each group's work easier. Formative feedback methods were introduced. It was above all the "traffic light method" in which students are given cards or cups of three (traffic light) colours to signal their progress or state to the teacher. Green shows they think they know what they are doing, orange shows they feel insecure but resume working, red shows they are either stuck, do not understand the task or face another problem. This method is supposed to develop students' metacognition as well as helping the teacher to orientate in numerous classes (more than 30 students) focusing their attention to those who seem to need it the most at times.⁴⁹ The intervention continued for another two months. After the intervention, the post-test II was realised.

V. Reflection phase II (June – September 2019)

Post-test II (June 2019)

After another two months of the intervention's application, a post-test II was given to the students in order to measure the effectiveness of the teaching approach emphasizing problem solving strategies.

Action research evaluation (June – September 2019)

To evaluate the test results, the students were divided into three categories according to the score they achieved. The category of *unsuccessful* students includes those with a score ≤ 2 . *Partially successful* students reached 3 or 4 points, the *successful* students reached ≥ 5 points. Based on the results, changes to the future plan were made.

3. 4. Data Analysis

With respect to the data (test scores), a non-parametric test - Friedman's ANOVA was used to evaluate differences between students' test scores in each of the three tests. They were followed by the Wilcoxon's post-hoc test using IBM SPSS Statistics 26. To measure the effect-sizes, r was calculated. Levels of 0.10 are considered a small effect, 0.10–0.30 a medium and over 0.50 a large effect.⁵⁰ The level of significance was set to 0.01.

The statistical methods were applied only to the results of the students who took part in all three test phases ($N = 112$). The rest, such as the comparison of relative improvement in a test, the rate of improvement, etc. were calculated for all the students who took part in two compared tests ($N = 136$).

4. Results and Discussion

4. 1. Information About Respondents

Altogether, 144 students from the first grade of a non-chemical vocational school took part in the action research. All data about students were anonymized. As the action research was conducted without disturbing the normal course of the school year, naturally, not all the students were present in all the lessons during the research. These students were not included in the total sample for the statistics (see Tab. 1).

With an exception of two students who graduated from lower-secondary in 2017, all the rest graduated in 2018. Therefore, they were tested with only a summer break pause from graduating. The presumption of them having mastered the lower-secondary education objectives was therefore valid. The information about the students is shown in Table 1.

Table 1. The number of students in the action research

	N	Girls	Boys	Schools
Students in total	144	94	50	87
Selected students*	112	75	37	74

* The students who took all three tests, therefore are included in the statistical analysis.

The number of schools the students came from to the upper-secondary school showed the variety of teaching approaches these students underwent. Also, the pre-test re-

sults, in a way, reflect lower-secondary chemistry teaching's effectiveness at a considerable number of schools. As far as the students' school success at the beginning of the action research (the first mid-term) was concerned, the overall ($N = 144$) mean of the students' school grade was 2.03 (grades from 1 – the best and 5 – the least successful). When only selected students (students who took all three tests; $N = 112$) were taken into account, the mean of school grades was 2.01. The grade distribution is shown in Figure 3.

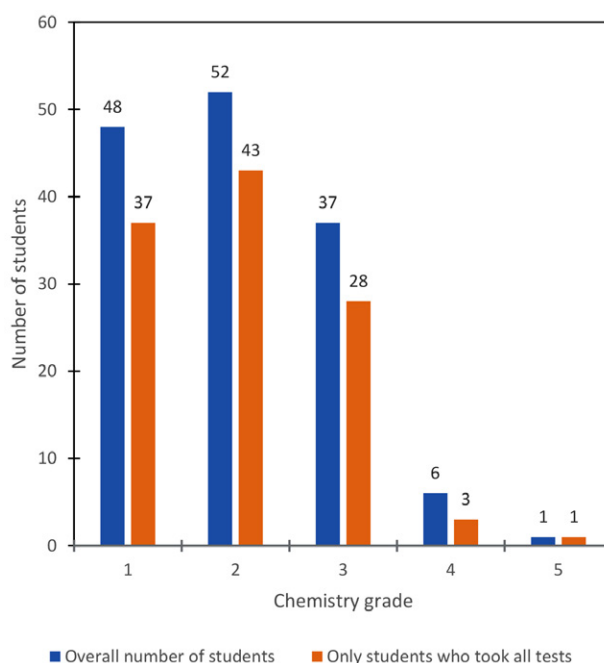


Figure 3. Student distribution according to the school grades

In the whole group of included students there were about 5% of students with a low school-success (judging by their grades). About 30% of the students were considered partially-successful and the rest successful. Given the fact non-chemical vocational school chemistry follows only a slightly advanced chemistry curriculum to lower-secondary school,⁹ it was possible to assume the students with better grades will be more successful in the pre-test than those with worse grades.

4. 2. Action Research Results in Total

Figure 4 shows the development of students' test score during the action research. Only results of the stu-

Table 2. The overall test results

	N	Med	Min.	Max.
Pre-test	112	1	0	4
Post-test I	112	2	0	6
Post-test II	112	3	0	6

dents' participating in all three tests were included to give a more accurate picture of their performance shifts (see Table 2).

The results showed the unsuccessful students' improvement as an effect of the action research. The scores, as expressed by the students' mean points in the tests, improved from the pre-test to the post-test I and from the post-test I to the post-test II. The Friedman's ANOVA test showed the difference among the three tests is statistically significant ($p < 0.001$). Kendall's W test result ($W = 0.54$) suggests a strong effect of the difference. Particular differences will be described in more detail below test-by-test.

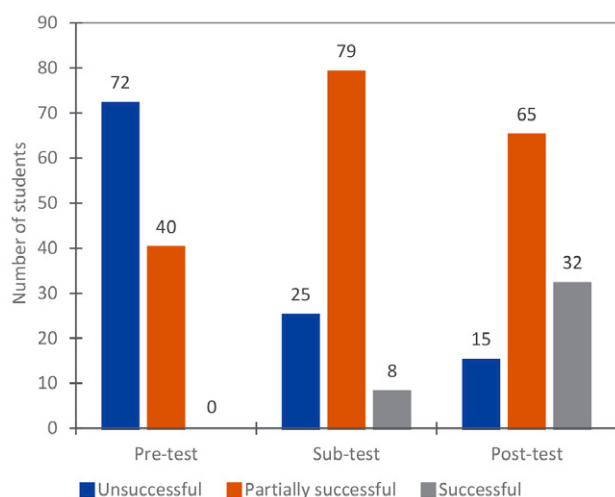


Figure 4. Students' scores in the three tests according to the success group ($N = 112$)

Despite the teaching approach emphasizing problem solving strategies proved successful, there were still a considerable number of students who reached the level only partially or did not reach it at all see Figure 4.

Pre-test results

The students' results in the pre-test are shown in Figure 5. Almost half of them did not receive a single point and were considered unsuccessful. This is in con-



Figure 5. Students' success in the pre-test ($N = 139$)

trast with their school grade (see Figure 3), as these suggest more than a half of the students were successful in chemistry.

The pre-test results showed that the lower-secondary chemistry objectives were not met by most of the students. 85% of the students did not manage to identify correct elements according to their description in the text. They did not prove their understanding of the element groups within the table, their ability to identify metals, non-metals and metalloids and only 14% proved their knowledge and skills in this respect. Considering the students knowledge regarding factors influencing chemistry reaction rate was concerned (task 2), 65,5% failed to match a particular procedure to the graph of the reaction rate, 28,5% managed partially (matched the procedures correctly without any or correct explanation) and only 5% solved the task correctly. As far as the third task – applying compounds' physical property data in the tables – was concerned, 83% of the students failed to infer the properties, i.e. apply two sources of information to identify the state of the given compounds. Only 16% of the students managed this task.

This was an important finding for the teacher's attitude towards grading. The fact no student was considered successful (reached 5 or 6 points) in the test, suggests that the tested students had not reached the curricular objective for lower-secondary chemistry education. This result supports the findings by the Czech School Inspectorate:⁵¹ the students do not possess the knowledge and skills required in this tasks (oriented at the end of compulsory education). The research shows that these results are similar in other school subjects too. Also, these students' low motivation to handle unfamiliar, more complex and challenging tasks proved to be an intervening factor as many of them gave up solving the task when they first encountered a problem. Nevertheless, this form of teaching, when some information is given and students need to apply it to a new situation, meets the contemporary (chemistry) teaching paradigm.^{48,52}

There are several possible explanations for this result. First, the curricular objectives as translated to the tasks are too demanding. This would mean the piloting²⁶ was not performed thoroughly enough. Second,

non-chemical vocational school students' attitudes are already formed during lower-secondary school attendance with chemistry being not a popular subject *cf.*,⁵³ which is reflected not only in their choice of study program, but also in the effort they are willing to put into learning chemistry.⁹ If proven true, this would put PISA and other international tests into serious question. Third, the tested curricular objectives are usually tested right after a topic is finished. In this case, it has been more than half a year (for some topics even longer) since the students covered the topics, therefore the students could have forgotten most of it and failed because of the lack of the necessary content knowledge.

Post-test I results

After two months of the action (intervention), a post-test I was carried out. Again, three problem tasks of comparable difficulty *see*⁴⁰ to the pre-test were used. The students could achieve a maximum of six points (see Figure 6).

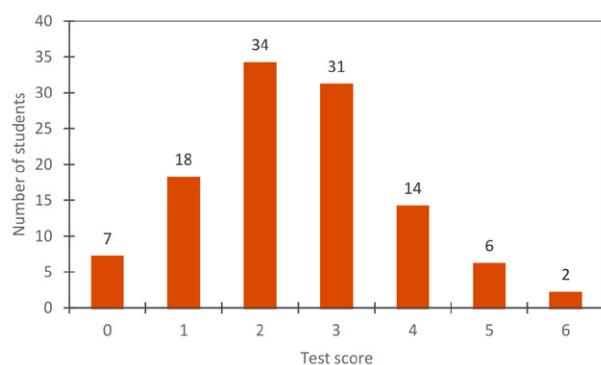


Figure 6. Students' success in the post-test I ($N = 136$)

The teaching approach emphasizing problem solving strategies seems to have a positive effect on the students' results. The number of students with 0 or 1 point diminished rapidly, causing the 33% of students from the unsuccessful to move into partially successful group. There were also 6 students in the successful group (two students who solved the tasks completely correctly (6 points) and another six with five points in total. A statistically significant difference ($p < .001$) was found between the pre- and post-test I results. The comparative analysis results are presented in the Table 2. The effect of the difference ($r = .501$) is large.

The students' skills seem to have developed, especially in the transfer of the students unsuccessful to successful in the test. More detailed information was received after performing a post-hoc test. The Wilcoxon signed ranks test results show that 82 students improved, 23 achieved the same score and 7 received less points. This shift was mainly caused by 30 (27%) students improving only by 1 and 2 points (mostly from 0 to 1 or 2 points). In the group of students successful in the post-test I, with an ex-

ception of two students who improved from an original 3 to 5 or 6 points, the rest improved from 0, 1 or 2 points. Therefore, it is possible to assume the intervention plan targeted all groups of students.

Most of the students whose results worsened in the post-test I received 3 or 4 points in the pre-test and only 2 in the post-test I. With the comparable difficulty of the tasks in mind, this result can be explained by false positive pre-test results.^{31,41}

The students who did not score differently in the post-test I or the pre-test mostly remained with 0, 1 or 3 points. In the first two groups, the intervention seems not to have affected these students. In case of the latter group, a limited number of these students seems to have been reached and remain in the middle of the point scale.

In spite of the positive shift after the first intervention, 58% of the students still did not reach at least 3 points (50% of the points) and are therefore considered unsuccessful. Seven of the eight students from the qualitative (eye-tracking) study were in the unsuccessful group of students after the post-test I. The strategies and problems as identified by apply more to the unsuccessful students.⁴¹ This is in favour of the action plan with these particular students.

Post-test II results

Evaluating the second intervention phase was conducted with the use of a post-test II. Again, it consisted of 3 problem tasks very similar to the pre-test. Figure 7 shows an increase in the group of partially successful (3–4 points) and successful (5–6 points) students, together with a decrease in the number of unsuccessful students compared to Figure 6.

There were 25% unsuccessful, 63% partially successful, and 27% successful task 1 solvers. In the second task, 27% failed, 22% solved it partially successfully and 51% successfully. 48% failed and 48% succeeded in solving the third task after the intervention.

The Table 2 again shows an overall increase in the students' results. The value of the Friedman's ANOVA test

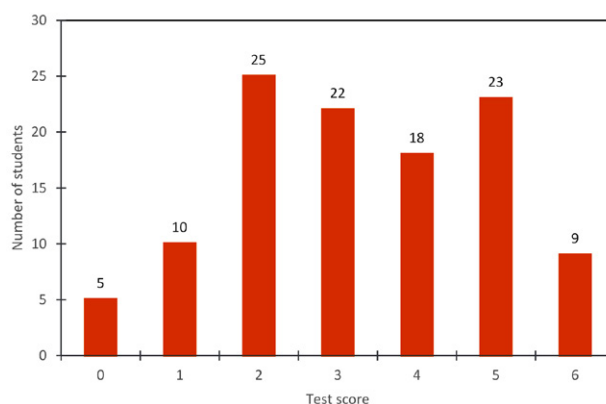


Figure 7. Students' success in the post-test: number of points received ($N = 115$)

($p < .001$) shows the difference is statistically significant. The effect of the difference ($r = 0.284$) was medium.

The post-hoc test's results showed that 67 students improved, 25 received the same number of points and 20 scored worse comparing to the post-test I.

The students who received 5 or six points (61 resp. 39%) mostly improved from 3 resp. 4 points in the post-test I. Surprisingly, only three students who received 5 or 6 points in the post-test I confirmed their result by reaching the same score in the final test. Two of them even sank into the unsuccessful category with 2 or 1 point in the post-test II.

As far as the group with no shift in their score was concerned, the majority received 2 resp. 3 points (33 resp. 21%). This, again, could be caused by these students' limits. For most of the students in the group with a negative shift, the decline in score was relatively small. 16 students (47%) scored 2 points lower and 12 students (35%) 1 point lower. Several students who succeeded in the post-test I got a lower score in the post-test II (7 from 4 points, 5 from 3 points and 4 from 5 points). Only several students sank more dramatically – 3 students to 0 and for 4 students to 1 point.

The overall success of the teaching approach emphasizing problem solving strategies was assessed using the pre-test - post-test II comparison. Table 2 shows the overall difference in the students' score. The p value ($p < 0.001$) showed a statistically significant difference between the two test results. The r-value ($r = 0.545$) showed a large effect. 93 students' results improved, 13 remained unchanged and 6 worsened.

The approach seems have effect on the students with some fundamental knowledge and skills which could be further developed. 56% of the students whose results did not change received 0 points. Also, most students whose result worsened from the pre- to post-test II (63% out of all students whose results worsened; $N = 16$) received no points in the post-test II. As these students achieved only 1 or 2 points in the pre-test, therefore still unsuccessful, the situation is similar to the students who did not score any point in the pre-test. There are two possible explanations of this result. First, a certain indifference towards the influence of school, i.e. the intervention steps is presumed. Apart from aforementioned reading skills, students' misconceptions had been blamed to prevent them from learning chemistry.⁵⁴ Second, The intervention built upon certain basic skills. The unsuccessful students might have been below this level. Considering the fact, the research was performed on upper-secondary students, this was not anticipated. The qualitative part of the study revealed that many problems lie, apart from lack of knowledge, in reading and the inability to identify the problem.³¹ For many students, this was corrected by the described intervention. The students' ability to read chemistry texts⁴¹ seems to have increased by the practice, so did their ability to identify the problem, as well as indicia given in the task for the

problem to be solved.^{55–56} As observed in the lessons, experiencing success motivated the students to stay on a task, even if it seemed difficult at the beginning.

The intervention showed that problem-solving skills can be promoted when systematically worked upon.¹⁸ Focusing on relevant⁵⁷ problems seems more important than just on knowledge that students are often unable to apply.^{52,58}

Nevertheless, the results showed there was still a group of students whose abilities could not be improved in the above-described manner. This points to a new, necessary line of research – identification of appropriate intervention underachieving students would benefit from.

5. Conclusions

The presented action plan can be considered effective as it helped improve the students' problem-solving skills. At the beginning, only 15% of the students received at least half of the test points. In the pre-test, the maximal reached score was four points out of six, with almost half of the students receiving no points and another 38% only one or two points (unsuccessful). The results show the students entering upper-secondary schools mostly did not reach the lower-secondary chemistry curricular objectives with the students' chemistry knowledge and skills on a rather low level. This could be a result of their school choice – vocational schools are usually not chosen by students with the highest academic achievement. The school this research was conducted in, however, belongs among prestigious schools using a student selection process which places the school among the top of its kind in the country. The results showed the students did not understand the basic concepts, e.g. a proton number, electronegativity or conductivity. Also, the students struggled with chemical processes used in real life, such as a chemical reaction or how to prepare a solution. This may serve as an argument for undergoing curricular reform.

The intervention focused on the students' ability to apply the basic knowledge gained from the text and break up the presented problem into partial steps. After the intervention, 65% of the students achieved more than half points (shift from 15%), with 30% students considered successful (from 0% at the beginning). This shift applied especially to students who proved at least an elementary background (knowledge, strategies, skills). A considerable number of students without this background proven in the pre-test showed no progress after the intervention, which suggests alternative approach is needed for these students' improvement.

The overall positive effect of the intervention could be caused by the foundation received from the earlier performed eye-tracking study completed with retrospective think-aloud. It helped identify reading problems in particular, but also other limiting strategies and helped to shape

the intervention to fit the students' needs as well as possible.

Another favorable aspect of the intervention was the combination of using problem tasks, expertly evaluated (and if needed altered) groupwork, gradually phased problem-solving steps and formative assessment, which seems to have led to the positive results. This approach led to error retrieval in quite a short period of time (2 months, 1 lesson a week).

Based on the experience with the tasks, their more frequent use can be recommended by the teacher. The question of the task results' evaluation can be solved either by using open-ended questions or multiple-tier tasks to limit the false-positive results.

With enough data about students' problem-solving skills gathered from several studies like this, the qualitative phase (think aloud supported with eye-tracking study) could be omitted. Students could be tested only to find their actual state of knowledge and skills based on a pre-test. Later, a set of "bespoke" tasks (different versions of the tasks based on the pre-test) could be used in a similar way.

Limitations

Several limitations in this study were caused by the research method used. The typical limit of action research is that the teacher is the only researcher.⁵⁸ The effect was eased by a researcher's participation. Another limitation is related to the results' vigor. They are limited by a low number of respondents. It exceeds usual action research samples; however, it does not enable a full generalization of the results. Also, the respondent choice – students from one vocational school – may influence the results because the students' focus may divert from science cf.⁹ On the other hand, the sample represents students from various lower-secondary schools (87) and therefore has the potential to reflect reality. Another limit of the study is the lack of repeatability and rigour as the feedback the teacher gave students reflected their actual problems. Nevertheless, there are certain steps which can be repeated with other students with no changes. By repeating the process, the range of problem-solving skills is expected to become clear enough so the pre-test's qualitative part could be omitted, and the procedure run universally.

In addition, the results could be limited by using only two points to score students' results in each task. Despite following the same approach used by PISA, assigning more points to each task could help distinguish the students more.

Last but not least, a limit of the intervention needs to be discussed. Despite teachers cannot always attract and have influence on all the students, this considerably high number of students seemingly unaffected by the intervention is a group which requires more attention in the future. Apart from a typical sample for qualitative eye-tracking study (successful vs. unsuccessful, novice vs. experts), these could be given a special attention. A follow up inter-

vention which would target these students better would complete the results.

Implications

For educators

As the problem-solving ability is one of 21st century competencies,¹⁴ teachers should build their lessons around problem tasks which on one hand contain subject-matter of a corresponding topic, and, on the other hand, develop students' problem-solving skills. Having students work in groups further adds to other skills such as groupwork and communication. Moreover, using the traffic-light method of formative feedback proved to be an effective tool in classroom instruction.

For researchers

A cooperation of a teacher with a researcher proved to fill the gap between educational research and the implemented curriculum. The research results relevant to the lesson instruction had their value for the teacher. In addition, the researcher could experience an unusually instant effect of the offered evidence-based improvements.

The action research proved to be an effective tool bringing teaching and research together. Being able to analyze students' results in more detail and literally dissect their problem and focus on it in ordinary teaching enabled the teacher to look beyond everyday practice. On the other hand, the researcher gained more insight into the classroom's dynamics as well as other intervening factors which would remain hidden in ordinary research.

The next steps in this direction will target the very problem of the students' performance on the tasks. They need to be divided into smaller parts and studied separately to provide more information not only about the already studied strategies students use, but also their reading performance, the effect of visual representations and even used text (cf.⁵⁹).

Acknowledgments

This work has been supported by the Charles University Research Centre program No. UNCE/HUM/024.

Declaration of interest

As it was action research, the first author was teaching the students. No other conflict is to declare.

6. Reference

1. N. Costa, L. Marques, R. Kempa. *Res. Sci. Tech. Educ.* **2000**, *18*, 37–44. DOI:10.1080/713694955
2. R. Vanderlinde, J. van Braak. *Brit. Educ. Res. J.* **2010**, *36*, 299–316. DOI:10.1080/01411920902919257
3. W. Carr, *Becoming critical: Knowing through action research*. Deakin University: Geelong, **1983**.

4. M. Souto-Manning. *Childhood Educ.* **2012**, 88, 54–56. DOI:10.1080/00094056.2012.643726
5. M. Stuckey, I. Eilks. *Chemistry under Your Skin? Experiments with Tattoo Inks for Secondary School Chemistry Students* **2015**, 92, 129–134. DOI:10.1021/ed400804s
6. M. Stuckey, I. Eilks. *J. Chem. Res. Pract.* **2014**, 15, 156–167. DOI:10.1039/C3RP00146F
7. C. A. Mertler, *Action research: Teachers as researchers in the classroom*. Sage: **2009**.
8. L. Cohen, L. Manion, K. Morrison, *Educational research methodology*. Metaixmio: Athens, **1994**.
9. M. Rusek. Výzkum postojů žáků středních škol k výuce chemie na základní škole. [Vocational school students' attitudes towards chemistry education at lower-secondary schools research]. Doctoral thesis, Univerzita Karlova, Praha, **2013**.
10. M. Rusek. *Scientia Educ.* **2014**, 5, 13–29. DOI:10.14712/18047106.113
11. *Rámcový vzdělávací program pro gymnázia*. [Framework educational programme for grammar schools]; Výzkumný ústav pedagogický v Praze: Praha, **2007**, p 100.
12. *Rámcový vzdělávací program pro obor vzdělání 78-42-M/02 Ekonomické lyceum*. [Framework educational programme for educational field 78-42-M/02 Economic lyceum]; NÚOV: Praha, **2007**.
13. R. Elmas, M. Rusek, A. Lindell, P. Nieminen, K. Kasapoglu, M. Bílek. *Chem. Educ. Res. Pract.* **2020**, 21, 839–851. DOI:10.1039/D0RP00058B
14. J. A. Bellanca, *21st century skills: Rethinking how students learn*. Solution Tree Press: **2010**.
15. B. Sket, S. A. Glazar, J. Vogrinc. *Acta Chim. Slov.* **2015**, 62, 462–472. DOI:10.17344/acsi.2014.1148
16. R. F. Angawi. *J. Chem. Educ.* **2014**, 91, 823–829. DOI:10.1021/ed4004436
17. E. Hejnová, M. Kekule. *Scientia Educ.* **2018**, 9, 102–116. DOI:10.14712/18047106.1018
18. A. H. Johnstone. *Uni. Chem. Educ.* **2001**, 5, 12–18. DOI:10.7748/mhp.4.5.18.s16
19. A. H. Johnstone, Introduction. In *Creative Problem Solving in Chemistry*, Wood, C.; Sleet, R., Eds. The Royal Society of Chemistry: London, **1993**.
20. N. Reid, M.-J. Yang. *Res. Sci. Technol. Educ.* **2002**, 20, 83–98. DOI:10.1080/02635140220130948
21. S. K. Reed. *Educ. Psychol. Rev.* **2016**, 28, 691–716. DOI:10.1007/s10648-015-9343-1
22. D. H. Jonassen. *Eudc. Tech. Res.* **1997**, 45, 65–94. DOI:10.1007/BF02299613
23. Z. Haláková, M. Prokša. *Two Kinds of Conceptual Problems in Chemistry Teaching* **2007**, 84, 172. DOI:10.1021/ed084p172
24. OECD, *PISA 2015 Results (Volume I)*. **2016**.
25. OECD, *PISA 2018 Results (Volume I)*. **2019**.
26. K. Vojíš, J. Holec, M. Rusek In: Rusek, M., Stárková, D., Bílková, I. (Eds.) *Přírodopisné a chemické úlohy pro základní vzdělávání a jejich metodické komentáře: Projektové vyučování v přírodovědných předmětech XIV.*, Praha, **2017**, pp 221–228.
27. K. Koreneková. Výzkum strategií uplatňovaných žáky při řešení problémových úloh z chemie. [Research of strategies applied by students during chemistry problem-tasks' solving]. Master thesis, Praha, **2018**.
28. I. V. Mullis, A. M. Kennedy, M. O. Martin, M. Sainsbury, *PIRLS 2006 Assessment Framework and Specifications: Progress in International Reading Literacy Study*. ERIC: **2004**.
29. S. Greiff, S. Wüstenberg, B. Csapó, A. Demetriou, J. Hautamäki, A. C. Graesser, R. Martin. *Educ. Res. Rev.* **2014**, 74–83. DOI:10.1016/j.edurev.2014.10.002
30. G. Polya, *How to solve it: A new aspect of mathematical method*. Princeton university press: New Jersey, **2004**.
31. M. Tóthová, M. Rusek, V. Chytrý. *J. Chem. Educ.* **2021**, 98, 1831–1840. DOI:10.1021/acs.jchemed.1c00167
32. M. L. Lai, M. J. Tsai, F. Y. Yang, C. Y. Hsu, T. C. Liu, S. W. Y. Lee, M. H. Lee, G. L. Chiou, J. C. Liang, C. C. Tsai. *Educ. Res. Rev.* **2013**, 10, 90–115. DOI:10.1016/j.edurev.2013.10.001
33. M. Slapničar, V. Tompa, I. Devetak, S. A. Glazar, J. Pavlin, Using an Eye-Tracker to Study Students' Attention Allocation When Solving a Context-Based Problem on the Sublimation of Water. In *Applying Bio-Measurements Methodologies in Science Education Research*, Devetak, I., Glazar, S. A., Eds. Springer International Publishing: Cham, **2021**, pp 107–127. DOI:10.1007/978-3-030-71535-9_6
34. M. Slapničar, V. Tompa, S. A. Glazar, I. Devetak, J. Pavlin. *Acta Chim. Slov.* **2020**, 67, 904–915. DOI:10.17344/acsi.2020.5908
35. M. Rodemer, J. Eckhard, N. Graulich, S. Bernholt. *J. Chem. Educ.* **2020**, 97, 3530–3539. DOI:10.1021/acs.jchemed.0c00418
36. R. Evans, *The Human Side of School Change: Reform, Resistance, and the Real-Life Problems of Innovation. The Jossey-Bass Education Series* ERIC: **1996**.
37. M. A. Just, P. A. Carpenter. *Psychol. Rev.* **1980**, 87, 329–354. DOI:10.1037/0033-295X.87.4.329
38. M. Van Someren, Y. Barnard, J. Sandberg, *The think aloud method: a practical approach to modelling cognitive*. London Academic Press: London, **1994**.
39. G. W. Kuhne, B. A. Quigley. *New Dir. Adult Cont. Educ.* **1997**, 73, 23–40. DOI:10.1002/ace.7302
40. J. Holec, M. Rusek, *Metodické komentáře a úlohy ke Standardům pro základní vzdělávání - chemie*. [Methodological comments and tasks to Standards for lower-secondary education - chemistry], NÚV: Praha, **2016**, p 105.
41. M. Rusek, K. Koreneková, M. Tóthová In: Rusek, M., Vojíš, K. (Eds.) *How Much Do We Know about the Way Students Solve Problem-tasks: Project-based Education and Other Activating Strategies in Science Education XVI.*, Prague, **2019**, pp 98–104.
42. A. S. Dhillon. *Sci. Educ.* **1998**, 82, 379–405. DOI:10.1002/(SICI)1098-237X(199806)82:3<379::AID-SCE5>3.0.CO;2-9
43. A. S. Posamentier, S. Krulik, *Problem-solving strategies for efficient and elegant solutions, grades 6-12: a resource for the mathematics teacher*. Corwin press: **2008**.
44. M. D. Lew, H. G. Schmidt. *Adv. Health Sci. Educ.* **2011**, 16, 529. DOI:10.1007/s10459-011-9298-z

45. J. Skalková, *Obecná didaktika*. [General didactics], Grada: Praha, 2007.
46. A. Chupáč. *Ped. Or.* **2008**, 18, 73–82.
DOI:10.3233/BME-2008-0510
47. J. T. Wilson, I. Chalmers Neubauer. *J. Chem. Educ.* **1988**, 65, 996. DOI:10.1021/ed065p996
48. V. Talanquer, J. Pollard. *Chem. Educ. Res. Pract.* **2010**, 11, 74–83. DOI:10.1039/C005349J
49. P. Black, D. Wiliam, Changing teaching through formative assessment: Research and practice. In *Formative assessment: Improving learning in secondary classrooms*, Looney, J., Ed. OECD: Paris, **2005**, pp 223–240.
50. J. Cohen. *Psych. bul.* **1992**, 112, 155.
DOI:10.1037//0033-2909.112.1.155
51. *Kvalita a efektivita vzdělávání a vzdělávací soustavy ve školním roce 2017/2018*. [Quality and effectivity of education and educational system in 2017/2018]; Česká školní inspekce: Prague, **2018**.
52. A. H. Johnstone. *J. Chem. Educ.* **2010**, 87, 22–29.
DOI:10.1021/ed800026d
53. T. Jarvis, A. Pell. *J. Res. Sci. Teach.* **2002**, 39, 979–1000.
DOI:10.1002/tea.10055
54. M. B. Nakhleh. *J. Chem. Educ.* **1992**, 69, 191–196.
DOI:10.1021/ed069p191
55. P. S. Steif, J. M. Lobue, L. B. Kara, A. L. Fay. *J. Eng. Educ.* **2010**, 99, 135–142.
DOI:10.1002/j.2168-9830.2010.tb01050.x
56. A.-M. Hoskinson, M. D. Caballero, J. K. Knight. *CBE—Life Sci. Educ.* **2013**, 12, 153–161.
DOI:10.1187/cbe.12-09-0149
57. M. Stuckey, A. Hofstein, R. Mamlok-Naaman, I. Eilks. *Stud. Sci. Educ.* **2013**, 49, 1–34.
DOI:10.1080/03057267.2013.802463
58. P. Gibbs, P. Cartney, K. Wilkinson, J. Parkinson, S. Cunningham, C. James-Reynolds, T. Zoubir, V. Brown, P. Barter, P. Sumner. *Educ. Act. Res.* **2017**, 25, 3–22.
DOI:10.1080/09650792.2015.1124046
59. M. Rusek, K. Vojíš. *Chem Educ Res Pract* **2019**, 20, 85–94.
DOI:10.1039/C8RP00141C

Povzetek

Raziskave o spretnostih problemskega reševanja po vsem svetu kažejo, da je še veliko možnosti za izboljšave. Namen te študije je bil izboljšati spretnosti problemskega reševanja pri urah kemije pri srednješolcih. Dijaki so opravili predtest s problemskimi nalogami, ki je bil osredotočen na njihovo konceptualno znanje o periodnem sistemu, sposobnost uporabe znanja o dejavnikih, ki vplivajo na hitrost kemijske reakcije, in lastnostih spojin. Večina učencev (72 od 112) nalog ni uspela rešiti. Zato je bila zasnovana intervencija, ki je temeljila na študiji z uporabo sledenja očem v kombinaciji z glasnim razmišljanjem. Vključevala je delo učencev pri reševanju kemijskih problemskih nalog (podobnih PISA nalogam), ki temeljijo na kontekstu, s posebnimi podpornimi ukrepi. Učitelj je zagotovil formativno ocenjevanje, ki je spodbujalo učenčeve strategije. Učinek intervencije je bil ponovno ocenjen z uporabo problemskih nalog v dveh naknadnih testih. Rezultati so pokazali, da je akcijski načrt uspešno pomagal večini učencev pri doseganju nadpovprečnih rezultatov na testu. Povečalo se je tudi razmerje uspešnih reševalcev, delež neuspešnih pa se je občutno zmanjšal.



Except when otherwise noted, articles in this journal are published under the terms and conditions of the Creative Commons Attribution 4.0 International License

Scientific paper

Square-Wave Voltammetric Sensing of Lawsone (2-Hydroxy-1,4-Naphthoquinone) Based on the Enhancement Effect of Cationic Surfactant on Anodically Pretreated Boron-Doped Diamond Electrode

Pınar Talay Pınar,^{1*} Yavuz Yardım¹ and Zühre Şentürk²¹ Yuzuncu Yil University, Faculty of Pharmacy, Department of Analytical Chemistry, 65080 Van, Turkey² Yuzuncu Yil University, Faculty of Science, Department of Analytical Chemistry, 65080 Van, Turkey

* Corresponding author: E-mail: ptalay@gmail.com

Tel: 5057649740

Received: 12-08-2020

Abstract

In this reported work, an anodically pretreated boron-doped diamond (BDD) electrode was used for the inexpensive, simple and quick detection of a natural dye, lawsone. Lawsone had a well-defined, irreversible and diffusion-controlled oxidation peak at approximately +0.19 V in phosphate buffer solution (PBS, 0.1 M, pH 2.5) using cyclic voltammetry (CV). The oxidation peak heights of lawsone were significantly increased in PBS using the cationic surfactant cetyltrimethylammonium bromide (CTAB). Under optimized experimental conditions, the calibration curve was linear over a concentration range of 0.1–5.0 μM with detection limit of 0.029 μM in 0.1 M PBS (pH 2.5) containing 0.1 mM CTAB by using square-wave voltammetry (SWV). To evaluate the practical applicability of the BDD electrode, it was used for the quantification of lawsone in commercial henna, a natural dye made from the leaves of the henna plant.

Keywords: Lawsone; boron-doped diamond electrode; square-wave voltammetry; cetyltrimethylammonium bromide; henna samples

1. Introduction

Lawsone (2-hydroxy-1,4-naphthoquinone) (Figure 1.), known as hennotannic acid, is a red-orange dye found in the leaves of the henna plant (*Lawsonia inermis*) and water hyacinth flower.^{1–3} Henna extract or its purified compounds exhibit a variety of biological activities such as antimicrobial, cytotoxic, anti-inflammatory, antioxidant, anticancer and analgesic activities. Henna leaves have been used as a cosmetic colorant for centuries and contain a high proportion of lawsone (1.0–1.4%).^{4–7} Lawsone is also used as a corrosion inhibitor for metals such as aluminum (Al), iron (Fe), zinc (Zn) and nickel (Ni) in both acidic and alkaline solutions. A survey of the literature revealed that chromatographic methods such as high-performance liquid chromatography with ultraviolet detection (HPLC–UV) and liquid chromatography-tandem mass spectrometry (LC/MS–MS) were used for determination of lawsone content in plant extracts prepared from leaves, shoots and fruits.^{8–12} Voltammetric techniques were also applied for lawsone analyses.^{13,14}

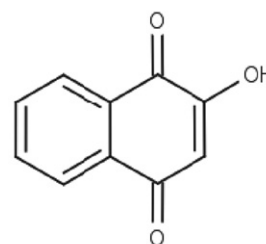


Figure 1. Structure of lawsone

Boron-doped diamond (BDD) electrode, a specific form of carbon, is widely used in both aqueous and non-aqueous media. It has important properties such as wide electrochemical potential window, low and stable background current, relative insensitivity to dissolved oxygen, low adsorption of pollutants, mechanical stability and high repeatability.^{15–19} Therefore, this electrode, used in many different application areas, is very important in terms of electroanalytical chemistry.

However, it should be noted that for many electroactive substances the BDD electrode is highly dependent on surface termination, which can be replaced by appropriate electrochemical pretreatment (anodic or cathodic)²⁰ or mechanical treatment.²¹ To our knowledge, no study related to the determination of lawsone using a BDD electrode has appeared in the literature.

In this paper, the electrochemical oxidation and detection of lawsone using BDD electrode is explained for the first time. Lawsone is an electroactive compound and it is possible to measure its amount in real samples through oxidation. Determination of lawsone in commercial henna samples was carried out using square wave voltammetry.

2. Experimental

2.1. Chemicals

Lawsone (2-Hydroxy-1,4-naphthoquinone), acetic acid, hydrochloric acid, phosphoric acid, boric acid, monobasic sodium phosphate and sodium hydroxide were obtained from Sigma-Aldrich, Turkey. Henna samples were obtained from a commercial local herbalist. All chemicals used were at least analytical grade and their solutions were prepared with deionized water further purified with a Milli-Q unit (Millipore). Because of lawsone's low solubility in aqueous solution, stock standard solutions (0.01 M) were prepared in methanol. It was stored at +4 °C when not in use and protected from daylight during use in the laboratory. Phosphate (0.1 M, pH 2.5 and 7.4), Britton-Robinson (BR, 0.1 M, pH 2–8), and acetate (0.1 M, pH 4.7) buffers were used as supporting electrolyte solutions.

2.2. Apparatus and Analytical Procedure

All electrochemical experiments were carried out at room temperature using an Autolab PGSTAT128N (Metrohm Autolab B.V., The Netherlands) which was managed by the software GPES 4.9. The counter electrode was platinum wire, the reference electrode was Ag/AgCl electrode and the working electrode was a BDD electrode (3 mm diameter, geometric surface area of 0.07 cm² and declared boron doping level of 1000 ppm). Before experiments, the BDD electrode was electrochemically pretreated in an independent electrochemical cell. At the start of each experiment day, anodic pretreatment was completed by applying +1.8 V (unless otherwise stated) for 180 seconds in 0.5 M H₂SO₄ solution.^{16,23} An activation program was used with 30 seconds duration in the same experimental conditions between individual measurements. Later, the BDD electrode surface was used directly for voltammetric measurements with repeatable signals.

The analytical performance and practical applicability were assessed using SWV, with the optimized operating parameters (frequency (*f*) 75 Hz; step potential (ΔE_s), 14 mV; pulse amplitude (ΔE_{sw}), 14 mV). All voltammetric

measurements were carried out in triplicate at room temperature.

SW voltammograms were recorded after each addition of the study compound. Validation parameters like precision, accuracy, linearity, LOD (detection limit) and LOQ (quantification limit) were calculated. LOD and LOQ values were found using the following equations.

$$\text{LOD} = 3 s/m; \text{LOQ} = 10 s/m,$$

where, *s* is the standard deviation of the peak current at minimum concentration in the relevant linear interval (preliminary study) and *m* is the slope of the relevant calibration curve.

About 0.1 g of commercial henna sample was dissolved in 5 mL of ethanol and diluted to 20 mL with pH 2.5 phosphate buffer solution, stirred at room temperature for 90 minutes and filtered. The obtained filtrate had SW voltammetric studies completed with cationic surfactant, CTAB, using 0.1 M PBS in pH 2.5 solution. An aliquot volume (20 μ L) of these solutions was transferred to the voltammetric cell containing the same solution, and analyzed on the day of preparation according to the procedure developed for the pure electrolyte using the calibration curve for the related regression equation.

3. Results and Discussion

3.1. Investigation of the Electrochemical Behavior at the Boron Doped Diamond Electrode

The electrochemical behavior of lawsone was examined by the CV method on the anodic pre-treated (APT) BDD electrode (see below for pre-treatment studies) surface. With 0.2 mM lawsone, 0.1 M PBS, pH 2.5 in the interval –0.5 to +0.6 V at 100 mV s⁻¹ scanning rate, CV was studied in three cycles. In the oxidation step, a well-defined anodic peak was obtained at nearly +0.19 V for lawsone on the first scan. In the reverse scan (return), a reduction peak was obtained at nearly –0.20 V (Figure 2A).

The effects of the scan rate for 0.2 mM lawsone on the peak current was assessed with cyclic voltammetry at different scan rates from 10 to 600 mV s⁻¹ at pH 2.5 in 0.1 M PBS. As can be seen in Figure 2B, the oxidation peak shifted toward more positive potential as the scan rate increased. The results show that the lawsone oxidation peak current (*I_a*) increased linearly with the square root of increasing scan rate ($v^{1/2}$) and can be expressed as follows:

$$I_a \text{ (nA)} = 258.98 v^{1/2} \text{ (mV s}^{-1}\text{)}^{1/2} - 306.96, \\ (r = 0.999, n = 7).$$

In addition, the linearities of plots of log *i_p* versus log *v* are expressed as follows:

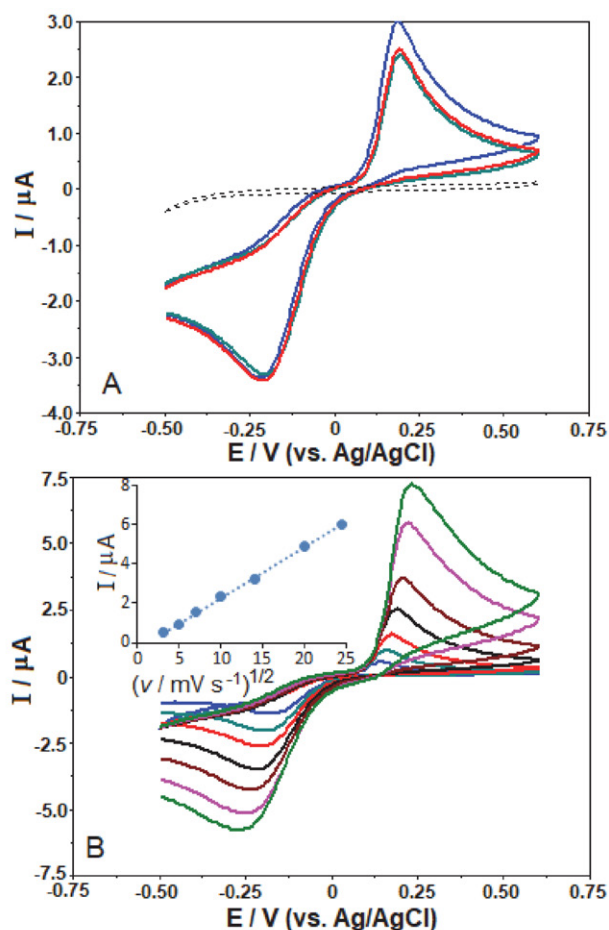


Figure 2. The repetitive cyclic voltammograms at scan rate of 100 mV s^{-1} (A), and the cyclic voltammograms at different scan rates (10, 25, 50, 100, 200, 400 and 600 mV s^{-1}) (B) of 0.2 mM lawsone solutions in 0.1 M phosphate buffer (pH 2.5) solution. A; Dashed lines represent background current. B; Inset depicts the plot of peak current (I_a) vs. square root of the scan rate ($v^{1/2}$).

$$\log I_a \text{ (nA)} = 0.588 \log v \text{ (mV s}^{-1}\text{)} + 2.169$$

($r = 0.999$, $n = 7$)

According to the findings above, the theoretical value of the slope is close to 0.5, showing that lawsone electrooxidation on the APT-BDD electrode is basically diffusion controlled. It is known that the electrochemical response of electroactive molecules on BDD electrodes depends on the type of pre-treatment. When the BDD electrode is pre-treated anodically, its surface changes to predominantly oxygen-terminated; in the case of cathodic pre-treatment, the ratio of surface BDD electrodes predominantly changes to hydrogen-terminated.²² The electrode was treated both anodically (+1.8 V for 180 s in 0.5 M H_2SO_4) and cathodically (−1.8 V for 180 s in 0.5 M H_2SO_4) in this work. Figure 3 shows the voltammetric response obtained for the determination of 0.1 mM lawsone in a 0.1 M PBS (pH 2.5) on an untreated or electrochemically (anodic and cathodic) pre-treated BDD electrode. As can be inferred from this figure, anodic pre-treatment of the BDD elec-

trode leads to a higher oxidation peak current value than untreated or cathodic pre-treatment. Therefore, all the following experiments were carried out using an anodic pre-treated BDD electrode at +1.8 V for 180 seconds. This electrochemical pretreatment procedure was repeated daily before starting the voltammetric measurements. It is worth mentioning that this anodic pretreatment (at +1.8 V for 30 s) procedure was carried out before each measurement in order to obtain reproducible and reliable results.

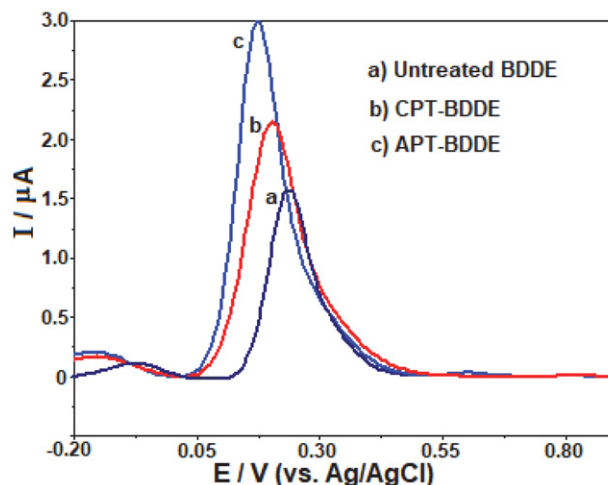


Figure 3. SW voltammograms of 0.1 mM lawsone solutions obtained at untreated (a) and cathodically (b) or anodically (c) pre-treated BDD electrode in 0.1 M phosphate buffer (pH 2.5) solution. SWV parameters: frequency, 50 Hz; step potential, 8 mV; pulse amplitude, 30 mV.

Further work was dedicated to analyzing the dependence of the voltammetric performance for the compound on the solution pH using APT-BDD electrode. In Figure 4A, this parameter was established in a series of BR buffers with pH 2.0–8.0 by carrying out voltammetric measurements on 0.1 mM lawsone solutions. For the peak potential (E_p) of lawsone, the pH value from 2.0 to 4.0 has little influence on the peak potential ($E_p \text{ (mV)} = -20.0 \text{ pH} + 219.2$, $r = 0.995$), whereas no important shift of E_p was observed between pH 4.0 and 8.0. SW voltammograms of the different supporting electrolytes are shown in Figure 4B. Using pH 2.5 and 7.4 of 0.1 M phosphate buffer solutions, pH 4.7 of acetate buffer solution had E_p of 0.18, 0.14 and 0.09 V, respectively. As can be seen from Figure 4, 0.1 M phosphate buffer pH 2.5 was chosen as the most suitable medium because the maximum peak current of lawsone obtained with this solution.

To increase the sensitivity of the electrochemical process, the effect of cationic surfactant (positive charge) on the lawsone oxidation signal was assessed. Lawsone concentration was fixed to 0.1 mM within 0.1 M PBS (pH 2.5) and the concentration of 0.1 mM CTAB was investigated in the electrochemical cell. As can be seen on Figure 5, the addition of CTAB to the electrochemical cell caused

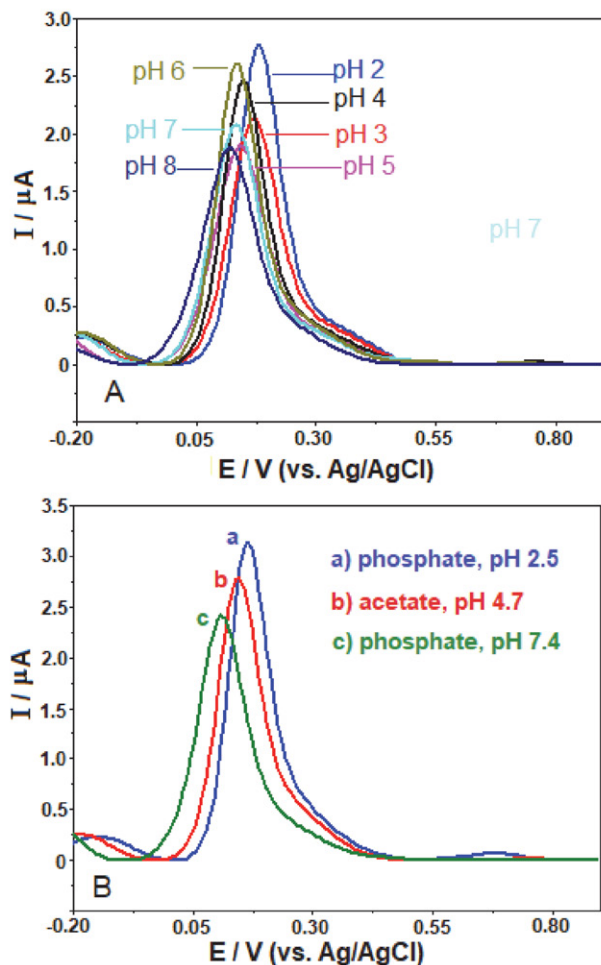


Figure 4. SW voltammograms of 0.1 mM lawsone solutions in Britton-Robinson buffer pH 2.0–8.0 (A), and in various supporting electrolytes (B). Other operating conditions as indicated in Figure 3.

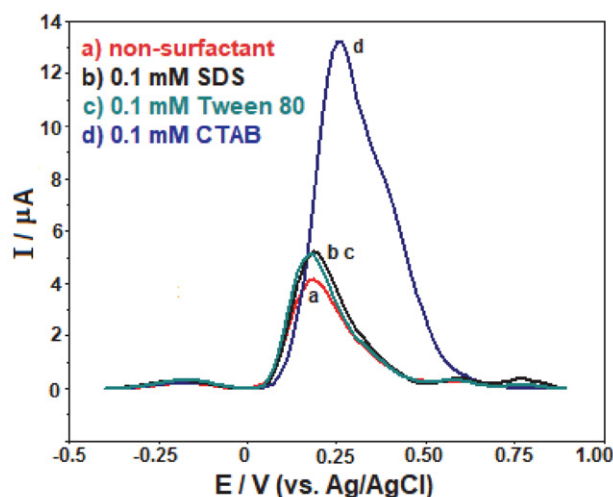


Figure 5. The SW voltammograms of 0.1 mM lawsone solutions in phosphate buffer (pH 2.5) at the different surfactants' media on APT-BDD electrode. SWV parameters: frequency, 50 Hz; step potential, 8 mV; pulse amplitude, 30 mV.

the lawsone peak potential to shift to more positive potential. When the peak currents are compared in the presence and absence of CTAB, the electrochemical cell containing CTAB was observed to have peak current increased by 4 times. Later, in order to choose the most appropriate surfactant for analytic purposes, the electrochemical reactions with the anionic surfactant of sodium dodecylsulfate (SDS) and non-ionic surfactant of Tween 80 on lawsone were researched. Figure 5 gives the SW voltammograms for different surfactants with 0.1 mM concentration. As can be seen on the figure, the cationic surfactant increased the peak current intensity by a significant degree compared to other surfactants, and at the same time caused a shift in peak potential.

The peak current obtained from SW voltammetry is linked to a variety of method parameters like frequency (f), step potential (ΔE_s) and pulse amplitude (ΔE_{sw}). Optimizing the method parameters is important in terms of sensitivity. When the frequency changed between 15 and 125 Hz ($\Delta E_s = 8$ mV, $\Delta E_{sw} = 30$ mV, fixed), the peak current increased linearly; however, the background current and noise increase at frequency values higher than 75 Hz. When the step potential is changed from 4 to 16 mV ($f = 75$ Hz, $\Delta E_{sw} = 30$ mV), the recorded signal increased up to 14 mV and then slowly increased from 14 to 16 mV. Examining the form of the peak and current, the most appropriate step potential was evaluated as 14 mV. The effect of amplitude was investigated from 10 to 70 mV ($\Delta E_s = 14$ mV, $f = 75$ Hz). The peak current of the molecule rapidly increased up to 70 mV. However, when assessed in terms of peak morphology, the sharper form of the peak and peak current, the most appropriate value was determined to be 60 mV. In conclusion, the generally optimized parameters for all experiments below can be summarized as $f = 75$ Hz, ΔE_s of 14 mV and $\Delta E_{sw} = 60$ mV.

3. 2. Analytical Applications

Using the APT-BDD electrode, the most appropriate chemical conditions and instrumental parameters were created to record the analytic curve for the lawsone molecule in 0.1 M PBS (pH 2.5) containing 0.1 mM CTAB. Figure 6 shows the SWV curves obtained by successive addition of lawsone in the concentration interval from 0.1 to 5.0 μM . At +0.19 V potential peak current, the lawsone concentration (Figure 6, inset) proportionally increased to give a very linear calibration graph: $i_p (\mu A) = 0.278 C (\mu M) + 0.065$ ($r = 0.999$, $n = 10$). Here, i_p is peak current, C is lawsone concentration, r is the correlation coefficient and n is the number of experiments.

The LOD and LOQ values, calculated by using data for the calibration curve, were found to be 0.029 μM and 0.097 μM , respectively. The comparison between lawsone estimation with the analytic parameters in the proposed method with some voltammetric methods previously reported in the literature is given in Table 1.

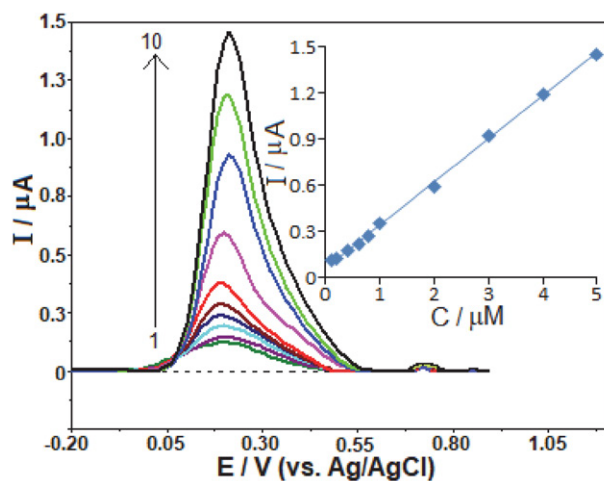


Figure 6. SW voltammograms for lawsone levels of (1) 0.1, (2) 0.2, (3) 0.4, (4) 0.6, (5) 0.8, (6) 1.0, (7) 2.0, (8) 3.0, (9) 4.0 and (10) 5.0 μM in 0.1 M phosphate buffer (pH 2.5) solution with 0.1 mM CTAB. Inset depicts a corresponding calibration plot for the quantitation of lawsone on APT-BDD electrode. SWV parameters: frequency, 75 Hz; step potential, 14 mV; pulse amplitude, 60 mV.

Table 1. Comparison of the efficiency of the anodically pretreated boron-doped diamond electrode (APT-BDDE), hanging mercury drop electrode (HMDE) and glassy carbon electrode (GCE), APT-BDDE, used for lawsone determination.

Electrode	Detection Limit (M)	Reference
HMDE	1.1×10^{-7}	[13]
GCE	6.0×10^{-9}	[14]
APT-BDD	2.9×10^{-8}	This work

The intraday and interday repeatability at the BDD electrode was evaluated under optimum experimental conditions. The intraday repeatability of peak current magnitude was determined with successive measurements of 0.1 μM lawsone solution. The results of ten repeated measurements provide a relative standard deviation (RSD) of 5.43% showing repeatability of results. Additionally, interday repeatability was done by measuring the magnitude of the peak current response for the same lawsone concentration at the BDD electrode on three consecutive days and the RSD was 6.87%.

The practical usability of the proposed electroanalytical methodology was tested for a commercial henna sample by using the interlay corresponding regression equation in the calibration graph obtained for standard lawsone solutions. Sample preparation procedures are described in the relevant section in detail. The mean value of lawsone was found to be 0.59 μM in the measurement cell. Taking into account the successive dilutions of the sample, 1.03% of lawsone was determined in the henna sample. The recovery experiments were completed with standard lawsone solutions (0.1, 0.6 and 1.0 μM) added to 10 mL sample solution within the voltammetric cell and voltammetric reactions were evaluated (Figure 7). Recov-

ery of lawsone was calculated in comparison with pure lawsone at the obtained concentration of the supplemented mixtures. The recovery varied from 91.8% to 103.7% and this shows no interaction effects of these matrices (Table 2). Lawsone can be quantitatively recovered with the proposed method, so there is a guarantee for the accuracy of lawsone voltammetric detection in commercial henna samples.

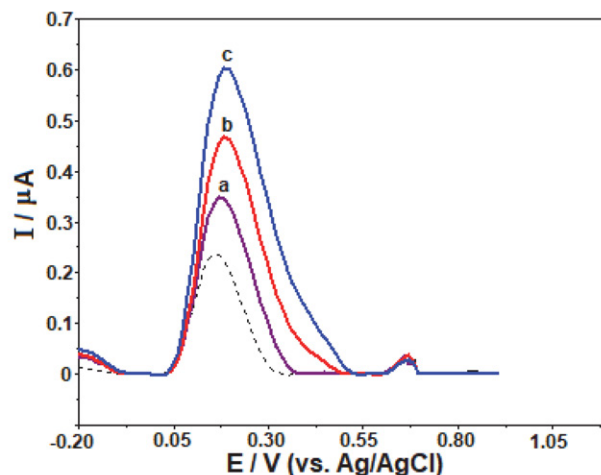


Figure 7. SW voltammograms of the diluted henna sample (dashed line) and after standard additions of 0.1 (a), 0.6 (b) and 1.0 (c) μM lawsone in 0.1 M phosphate buffer (pH 2.5) solution with 0.1 mM CTAB on BDD electrode. Other operating conditions as indicated in Figure 6.

Table 2 Results of the recovery analysis of lawsone (the average of three independent analysis of each spiked sample) in the sample of the commercial henna samples.

Lawsone added (μM)	Level determined (μM)	Recovery (%) \pm RSD (%)
0	0.59	–
0.1	0.63	91.8 ± 5.05
0.6	1.26	105.9 ± 4.43
1.0	1.65	103.7 ± 3.31

4. Conclusions

This article represents the first successful attempt to investigate the electrochemical behavior of lawsone using APT-BDDE (without any modification of the electrode surface) coupled with the SW voltammetric method. Contributions to the sensitivity of the developed method were provided by a cationic surfactant (CTAB). The results indicated that one irreversible and diffusion-controlled anodic peak of lawsone was observed using CV at potential of about +0.19 V in the presence of 0.1 M in pH 2.5 PBS as supporting electrolyte.

Acknowledgements

The authors gratefully acknowledge financial support from the Van Yuzuncu Yil University Scientific Research Foundation (Project number: FBA-2017-5537).

5. References

1. A. K. Jordão, M. D. Vargas, A. C. Pinto, F. d. C. da Silva and V. F. Ferreira, *RSC Adv.* **2015**, *5*, 67909–67943. DOI:10.1039/C5RA12785H
2. M. Monroy-Cárdenas, D. Méndez, A. Trostchansky, M. Martínez-Cifuentes, R. Araya-Maturana, and E. Fuentes, *Front. Chem.* **2020**, *8*, 533. DOI:10.3389/fchem.2020.00533
3. K. V. Krishnamurthy, R. Siva, and T. K. Senthil, In Proceedings of National Seminar on the Conservation of the Eastern Ghats, Environment Protection Training and Research Institute, Hyderabad, 24–26 March **2002**, pp. 151–153.
4. N. M. Rahmoun, Z. Boucherit-Otmami, K. Boucherit, M. Benabdallah, D. Villemin, and N. Choukchou-Braham, *Méd. et Mal. Infec.* **2012**, *42*, 270–275. DOI:10.1016/j.medmal.2012.05.002
5. M. Barani, M. Mirzaei, M. Torkzadeh-Mahani, and M. H. Nematollahi, *Daru* **2018**, *26*, 11–17. DOI:10.1007/s40199-018-0207-3
6. I. Al Nasr, J. Jentzsch, I. Winter, R. Schobert, K. Ersfeld, and W. S. Koko, *Archiv. Pharm.* **2019**, *352*, 1900128. DOI:10.1002/ardp.201900128
7. S. B. Zaware, R. G. Gonnade, D. Srinivas, A. Khan, S. Y. Rane, *New J. Chem.* **2011**, *8*, 1615–1623. DOI:10.1039/c1nj20176j
8. F. Z. Alem, S. A. Gita, L. Cougnaud, C. Affnar, I. Nounah, B. Youssef, and B. Rhourri-Frih, *Indus. Crops and Pro.* **2020**, *158*, 112960–112960. DOI:10.1016/j.indcrop.2020.112960
9. H. Arkaban, M. Mirzaei, M. Behzadi, *Preprints* **2020**, 2020090668 DOI: 10.20944/preprints202009.0668.v1).
10. Y. Oda, S. Nakashima, E. Kondo, S. Nakamura, M. Yano, C. Kubota, and H. Matsuda, *J. Nat. Med.* **2018**, *72*, 890–896. DOI:10.1007/s11418-018-1221-y
11. P. Babula, R. Mikelova, D. Potesil, V. Adam, R. Kizek, L. Hav-el, and Z. Sladky, *Biomed. Papers* **2005**, *149*, 25–28.
12. N. S. El-Shaer, J. M. Badr, M. A. Aboul-Ela, and Y. M. Gohar, *J. Sep. Sci.* **2017**, *30*, 3311–3315. DOI:10.1002/jssc.200700223
13. P. Babula, J. Vanco, L. Krejcova, D. Hynek, J. Sochor, V. Adam, and R. Kizek, *Int. J. Electrochem. Sci.* **2012**, *7*, 7349–7366.
14. B. K. Chethana, S. Basavanna, Y. A. Naik, *J. Anal. Chem.* **2014**, *69*, 887–891. DOI:10.1134/S1061934814090044
15. S. Baluchova, A. Danhel, H. Dejmkova, V. Ostatna, M. Fojta, K. Schwarzova-Peckova, *Anal. Chim. Acta* **2019**, *1077*, 30–66.
16. F. Karahan, Z. Baş, E. Keskin, P. Talay Pınar, Y. Yardım, and Z. Şentürk, *ChemistrySelect* **2020**, *5*, 12862–12868. DOI:10.1002/slct.202002921
17. B. C. Lourencao, R. F. Brocenschi, R. A. Medeiros, O. Fatibello-Filho, and R. C. Rocha-Filho, *ChemElectroChem*, **2020**, *7*, 1291–1311. DOI:10.1002/celec.202000050
18. S. O. Ganiyu, M. G. El-Din, *Appl. Catal. B-Environ.* **2020**, *279*, 119366. DOI:10.1016/j.apcatb.2020.119366
19. O. Sarakhman, L. Dubenska, L. Švorc, *J. Electroanal. Chem.* **2020**, *858*, 113759–113759. DOI:10.1016/j.jelechem.2019.113759
20. P. Talay Pınar, S. Allahverdiyeva, Y. Yardım, and Z. Şentürk, *Microchem. J.* **2020**, 104772–104772.
21. A. Yigit, Y. Yardım, and Z. Şentürk, *J. Anal. Chem.* **2020**, *75*, 653–661. DOI:10.1134/S1061934820050184
22. M. Yence, A. Cetinkaya, G. Ozcelikay, S. I. Kaya, and Sibel A. Ozkan, *Crit. Rev. Anal. Chem.* DOI:10.1080/10408347.2020.1863769
23. H. S. Ali, A. A. Abdullah, P. T. Pınar, Y. Yardım, and Z. Şentürk, *Talanta*, **2017**, *170*, 384–391. DOI:10.1016/j.talanta.2017.04.037

Povzetek

Z borom dopirano diamantno elektrodo smo anodno obdelali in jo uporabili za preprosto, hitro in cenovno ugodno določanje naravnega barvila lavsona. Z uporabo ciklične voltmetrije smo za lavson v raztopini fosfatnega pufru (PBS, 0,1 M, pH 2,5) dobili dobro opredeljen, ireverzibilen in difuzijsko nadzorovan oksidacijski vrh pri približno + 0,19 V. Z dodatkom kationske površinsko aktivne snovi – cetiltrimetilamonijevega bromida (CTAB) smo dosegli značilno povečanje višin oksidacijskih vrhov. Z uporabo voltmetrije s kvadratnim spreminjanjem potenciala («square wave voltammetry») je bila pri optimiziranih eksperimentalnih pogojih umeritvena krivulja za lavson linearna v koncentracijskem območju 0,1–5,0 µM, meja zaznave pa je bila 0,029 µM (v 0,1 M PBS (pH 2,5) z dodatkom 0,1 mM CTAB). Uporabnost elektrode smo preverili z določanjem vsebnosti lavsona v komercialni kani, naravnem barvilu iz kaninih listov.



Except when otherwise noted, articles in this journal are published under the terms and conditions of the Creative Commons Attribution 4.0 International License

AUTHOR INDEX

Acta Chimica Slovenica
Year 2021, Vol. 68 No. 1–4

Abbas Samir Y.	990	Cai Ya-Jun	804
Abdallah Amira E. M.	604	Chakraborty Tanmoy	178
Abi Masoome Nazar	374	Chen Qiao	693
Afroz Mubashra	617	Chen Wei	441
Agrahari Saumya	617	Choudhury Chirantan Roy	212
Ahmad Masood	667	Chtita Samir	289
Ajani Emmanuel Oladipo	118	Chua Lee Suan	765
Akay M. Abdulkadir	930	Çitlakoğlu Meryem	466
Alabi Mutiu Adewunmi	118	Čavić Anže	193
Ali Shujat	667	Čelan Korošin Nataša	229
Ali Tarik E.	990	Čolnik Maja	433
Aliyev Akif Shikhan	185	Dashtifard Hani	791
Al-Qaim Fouad F.	811	Debeljak Maruša	683
Alqaim Zahraa H.	811	Deng Tong-Tong	541
Al-Ta'ani Mohammad R.	589	Devseren Esra	25
Al-Taweel Samir A.	589	Ding Jin-Yan	693
Al-Trawneh Salah A.	589	Djeghaba Zeineddine	575
Alwan Ensaf Sultan	51	Djobbi Boutheina	548
Amin Asif	667	Do Nascimento Patrícia Aleixa	313
Ardiles Paula	629	Dolinar Marko	545
Asiltürk Erol	645	Dun Li-Nan	239
Assiri Mohammed A.	990	Eddike Driss	718
Atakol Orhan	930	El Taweel Yehia	304
Babanly Dunya Mahammad	185	El-Abadelah Mustafa M.	589
Bagherzade Ghodsieh	109	El-Husseiny Adel	304
Balantič Katja	753	El-rouby Mahmoud	185
Barik Binapani	970	El-Sharief Marwa A. M. Sh.	990
Bashir Nadeem	667	Esmaili Hossein	363, 791
Battelino Tadej	683	Faganeli Jadran	587
Baysal Omur	781	Farag Hassan	304
Behrouz Somayeh	374	Farahi Mahnaz	332
Belaidi Houmam	289	Farouq Rania	304
Belaidi Salah	289, 882	Frontera Antonio	212
Belferdi Fatiha	355	Fu Xu	17
Belghith Hafedh	575	Furlani Borut	268
Belhaj Inès	575	Gabersček Simona	488
Benamia Fatiha	575	Gadetskaya Anastassiya V.	589
Bertok Sara	683	Gan Xiang	693
Beyzaei Hamid	109	Ganesan Raja	997
Bhadoria Vivek	341	Gao Ruoxuan	205
Biček Ajda	488	Gao Yuan-Yuan	205
Biswas Niladri	212	Gargouri Ali	575
Blagojević Bojana	896	Gavazov Kiril Blazhev	37
Bouabdallah Ibrahim	718	Geetha Reshma	955
Boudergua Samia	882	Genç Fatma	320
Bounour Selma	575		
Bouremmad Farida	355		
Bren Urban	773		

Glamočlija Una	144	Komsari Parisa Fallah	945
Gouda Moustafa A.	990	Kouter Katarina	268
Govind Prabha	997	Kovač Nives.....	S87
Govindan Srinivasan	997	Kovalenko Serhii Ivanovych	395
Gulgun Mehmet Ali	355	Krajnc Bor	S87
Gupta Arijit Dutta	341	Kramar Peter	753
Gupta Mahesh Kumar.....	617	Krasovska Nataliia.....	395
Gurpinar Kubra	930	Kravanja Gregor	494
Habiddin Habiddin	736	Križaj Igor	753
Hajare Ashok	861	Kulkarni Naveen V.	955
Han Li-Min	205	Kumar John Elisa	833
Han Shuang	961	Kumar Ladi Alik	970
Hao Yu-Mei.....	102	Kumar Meenu	955
Harit Tarik.....	718	Ladjama Ali	575
Hassen Rached Ben.....	548	Lanez Touhami	882
He Guo-Xu	567	Latip Jalifah	811
Helal Maher H. E.....	604	Lei Yan.....	44
Helal Mohamed H.	990	Li Chuan-Bi.....	239
Hong Chao	791	Li Li-Jie.....	541
Hovnik Tinka.....	683	Li Qiao	562
Hristov Danail Georgiev.....	37	Li Qing-Bin	17
Htare Thet T.....	667	Li Zhi-Tao.....	693
Hu Jing	804	Liang Ji-Hong	921
Humelnicu Doina	821	Liang Min	441
Humelnicu Ionel	821	Liang Wei.....	239
Ibrahim Latifat Bolanle.....	118	Liu Cheng	983
Ibrahim Rehab Ali.....	51	Liu Huan-Yu.....	693
Idowu Patience Funmilayo.....	118	Liu Xiu-Rui	804
Ignat Maria	821	Lone Mohsin Yousuf	667
Ilic Marija D.	709	Lu Xi-Kun	1008
İnal Emine Kubra	930	Lubej Samo.....	494
Isleroglu Hilal.....	658	Maciejewski Hieronim	849
Ivanič Andrej.....	494	Majidzade Vusala Asim	185
Jaiswal Vivek	341	Malej Alenka	S87
Jarag Ravindra	861	Malek Fouad.....	718
Jones William D.	955	Mallick Subrata	159
Kandemirli Fatma.....	320	Marković Marija S.	709
Kandemirli Sedat Giray	320	Masoud Ayat Ali	72
Karakoyun Gülen Önal.....	645	Mavri Janez.....	426
Karami Bahador.....	332	Mazela Bartłomiej	849
Karataş Haluk.....	25	Meglič Vladimir	913
Karimi Mozghan.....	279	Miklavčič Damijan	753
Karpenko Oleksandr.....	395	Milad Yara Raafat	72
Kavčič Hana	426	Milanov Dubravka	896
Kaymak-Ertekin Figen.....	25	Miled Ghofrane Lassoued Ben	548
Kello Martin	151	Mitić Violeta D.....	709
Kerouaz Bilal.....	575	Mofeed Germeen J.....	604
Keshavarz Raziye.....	332	Mohamadi Hediye.....	128
Khamouli Saida.....	289	Mohareb Rafat M.....	51, 72, 604
Khan Shafi U.	667	Moradi Ashraf.....	109
Kharmawphlang Wanshanlang	833	Moradian Mohsen	594
Kitanovski Nives.....	475, 532	Moses Opemipo Adekanye	118
Kljun Jakob.....	144	Mostaghni Fatemeh.....	170
Knez Željko.....	433	Motiee Fereshteh	128
Koç Mehmet.....	25	Muarifin Muarifin	736
Kogawa Ana Carolina	313	Mulai Tsungom	833
		Mussa Zainab H.	811

Nabavi-Amri Sayyed Ahmad.....	279	Saber-Tehrani Mandana	128
Nadeem Said	781	Saha Sandeepta	212
Nagarajan Vijayanand	997	Sahoo Mihir Kumar	833
Nanda Ashirbad.....	159	Sahoo Rudra Narayan	159
Nandi Souvik.....	159	Salahshour Roya	363
Nangare Sopan	861	Salem Mohamed A.	990
Naqvi Tahira.....	667	Salihović Mirsada	144
Nazarabi Masoomeh	594	Sargazi Soheila	109
Nazir Hasan	930	Sarıkaya Aslı Göçenoğlu.....	587
Nečemer Marijan	913	Sarlah David.....	247
Nivas Avula Sri.....	404	Satapathy Bhabani Sankar	970
Nosulenko Inna	395	Sayan Perviz	414
Nunes Salgado Hérica Regina	313	Segaran Abirame	765
Oblak Adrijana	488	Semache Noura.....	575
Ocak Özgül Özdestan	25	Şener Burak	781
Ogrinc Nives	887	Şentur Zuhre	1026
Okut Dilara.....	25	Seo Ean-Jeong.....	589
Órdenes Daniel.....	629	Sert Sema	483
Ouassaf Mebarka	289	Shakya Pawan Raj	904
Öz Özden Barım.....	521	Shanbedi Mehdi.....	363
Ozalp-Sendur Tuba Nur.....	414	Sharan Rajeshwar Nath	833
Özkaya Ahmet	222	Shawuti Shalima	355
Palma Jenifer	629	Shojaei Abdollah Fallah	945
Pattnaik Gurudutta	970	Shrestha Prem Kumar	904
Pavlica Damjan Jan.....	728	Silme Ragıp Soner	781
Pavlović Aleksandra N.....	709	Singh Harinder	341
Pavlović Ksenija	896	Sinkovič Lovro	913
Peng Qi-An	804	Slemnik Mojca	447
Perdih Franc.....	193	Solár Peter.....	151
Perdih Anton.....	137	Solárová Zuzana.....	151
Petrovič Jan.....	247	Soleymanpour Ahmad.....	279
Pietras Przemysław	849	Sopacı Ş. Betül	930
Piltan Mohammad Amin	374	Soualmia Fatima	882
Pınar Pınar Talay	1026	Stankov Jovanović Vesna P.	709
Pipan Barbara	913	Stavytskyi Viktor.....	395
Pirnat Edvard	488	Stirn Kranjc Brabka.....	683
Počkaj Marta	475, 532	Stojanović Gordana S.....	709
Podlipnik Črtomir.....	728	Suhag Vandana	178
Polat Sevgi	414	Svoboda Ingrid	930
Pompe Matevž.....	728	Škerget Mojca.....	433
Popović Boris M.	896	Špirtović-Halilović Selma.....	144
Powar Trupti	861	Štajner Dubravka	896
Pramanik Arunima	159	Štukovnik Zala	773
Pregeljc Domen	426	Taghvaei-Ganjali Saeed.....	128
Qian Heng-Yu.....	638, 700	Tagiyev Dilgam Babir.....	185
Qiu Xiao-Yang	1008	Tamše Samo.....	887
Racheva Petya Vassileva	37	Tan Yao.....	44
Raddadi Hatem.....	548	Tandon Hiteshi	178
Rahal Mahmoud.....	718	Tandon Praveen Kumar	617
Rao Enugala Kalyan	404	Tanemura Kiyoshi	387
Rohand Taoufik	387	Tarawneh Amer H.....	589
Rozman Damjana.....	268	Tchouar Nouredine	822
Rozman Martin	773	Tekavčič Pompe Manca	683
Ruiz-Dominguez Mari Carmen	629	Thayban Thayban	736
Rusek Martin	1016	Tillard Monique.....	718
		Toledo Constanza.....	629
		Toncheva Galya Konstantinova	37
		Topal Tufan.....	88

Tošič Snežana B.....	709	Wang Zhong-Hui.....	239
Tothova Martina	1016	Wong Hoi Jin	765
Trebušak Podkrajšek Katarina.....	683	Xue Ling-Wei	17, 567
Tuncer Yaprak Gursoy	930	Yao Lei	791
Turel Iztok	144	Yardıı Yavuz	1026
Türk Valentina	S87	Yarmohammadi Elahe	109
Türkan Kenan	222	Yolcu Zuhall	466
Turker İzzet	658	Yolođlu Ertan	521
Uçkun Aysel Alkan.....	521	You Zhong-Lu.....	541
Uçkun Miraç	521	Yuan Yong	1008
Umek Nejc.....	426	Yurtcan Sinem.....	466
Ungarean Chad Nicholas.....	247	Zaletel Katja.....	488
Urbič Tomaž.....	505	Zang Guo-Wei	541
Utomo Yudhi.....	736	Zangrando Ennio	212
Veljović Elma	144	Završnik Davorka	144
Verdnik Aleksandra	433	Zhang Bao-Sheng	239
Videtič Paska Alja.....	268	Zhang Wei-Guang	921
Vilchez Carlos	629	Zhao Gan-Qing.....	17
Vintar Neli.....	426	Zhao Hui	804
Vončina Ernest.....	744	Zhao Yang.....	562
Voskoboinik Oleksii.....	395	Zhou Gao-Qi	1008
Vranješ Dejan	896	Zhu Hai-Yun	65
Vranješ Marijana	896	Zhu Ning.....	205
Wang Enju	562	Zinicovscaia Inga	821
Wang Fu-Ming.....	541	Zou Dong-Hui	441
Wang He	239	Zukić Selma.....	144
Wang Jia-Jun	239	Zupančič Marija.....	229
Wang Xue	804	Žnidaršič-Plazl Polona.....	1
Wang Yuan	961		

DRUŠTVENE VESTI IN DRUGE AKTIVNOSTI
SOCIETY NEWS, ANNOUNCEMENTS, ACTIVITIES

Vsebina

Navodila za avtorje S110

Contents

Instructions for authors S110

Acta Chimica Slovenica

Author Guidelines

Submissions

Submission to ACSi is made with the implicit understanding that neither the manuscript nor the essence of its content has been published in whole or in part and that it is not being considered for publication elsewhere. All the listed authors should have agreed on the content and the corresponding (submitting) author is responsible for having ensured that this agreement has been reached. The acceptance of an article is based entirely on its scientific merit, as judged by peer review. There are no page charges for publishing articles in ACSi. The authors are asked to read the Author Guidelines carefully to gain an overview and assess if their manuscript is suitable for ACSi.

Additional information

- Citing spectral and analytical data
- Depositing X-ray data

Submission material

Typical submission consists of:

- full manuscript (PDF file, with title, authors, abstract, keywords, figures and tables embedded, and references)
- supplementary files
 - **Full manuscript** (original Word file)
 - **Statement of novelty** (Word file)
 - **List of suggested reviewers** (Word file)
 - **ZIP file containing graphics** (figures, illustrations, images, photographs)
 - **Graphical abstract** (single graphics file)
 - **Proposed cover picture** (optional, single graphics file)
 - **Appendices** (optional, Word files, graphics files)

Incomplete or not properly prepared submissions will be rejected.

Submission process

Before submission, authors should go through the checklist at the bottom of the page and prepare for submission.

Submission process consists of 5 steps.

Step 1: Starting the submission

- Choose one of the journal sections.
- Confirm all the requirements of the **checklist**.
- Additional plain text comments for the editor can be provided in the relevant text field.

Step 2: Upload submission

- Upload full manuscript in the form of a Word file (with title, authors, abstract, keywords, figures and tables embedded, and references).

Step 3: Enter metadata

- First name, last name, contact email and affiliation for all authors, in relevant order, must be provided. Corresponding author has to be selected. Full postal address and phone number of the corresponding author has to be provided.

- **Title and abstract** must be provided in plain text.
- Keywords must be provided (max. 6, separated by semicolons).
- Data about contributors and supporting agencies may be entered.
- **References** in plain text must be provided in the relevant text field.

Step 4: Upload supplementary files

- Original Word file (original of the PDF uploaded in the step 2)
- **List of suggested reviewers** with at least five reviewers with two recent references from the field of submitted manuscript must be uploaded as a Word file. At the same time, authors should declare (i) that they have no conflict of interest with suggested reviewers and (ii) that suggested reviewers are experts in the field of the submitted manuscript.
- All **graphics** have to be uploaded in a single ZIP file. Graphics should be named Figure 1.jpg, Figure 2.eps, etc.
- **Graphical abstract image** must be uploaded separately
- **Proposed cover picture** (optional) should be uploaded separately.
- Any additional **appendices** (optional) to the paper may be uploaded. Appendices may be published as a supplementary material to the paper, if accepted.
- For each uploaded file the author is asked for additional metadata which may be provided. Depending of the type of the file please provide the relevant title (Statement of novelty, List of suggested reviewers, Figures, Graphical abstract, Proposed cover picture, Appendix).

Step 5: Confirmation

- Final confirmation is required.

Article Types

Feature Articles are contributions that are written on editor's invitation. They should be clear and concise summaries of the most recent activity of the author and his/her research group written with the broad scope of ACSi in mind. They are intended to be general overviews of the authors' subfield of research but should be written in a way that engages and informs scientists in other areas. They should contain the following (see also general directions for article structure in ACSi below): (1) an introduction that acquaints readers with the authors' research field and outlines the important questions to which answers are being sought; (2) interesting, new, and recent contributions of the author(s) to the field; and (3) a summary that presents possible future directions. Manuscripts normally should not exceed 40 pages of one column format (letter size 12, 33 lines per page). Generally, experts in a field who have made important contribution to a specific topic in recent years will be invited by an editor to contribute such an **Invited Feature Article**. Individuals may, however, send a proposal (one-page

maximum) for an Invited Feature Article to the Editor-in-Chief for consideration.

Scientific articles should report significant and innovative achievements in chemistry and related sciences and should exhibit a high level of originality. They should have the following structure:

1. Title (max. 150 characters),
2. Authors and affiliations,
3. Abstract (max. 1000 characters),
4. Keywords (max. 6),
5. Introduction,
6. Experimental,
7. Results and Discussion,
8. Conclusions,
9. Acknowledgements,
10. References.

The sections should be arranged in the sequence generally accepted for publications in the respective fields and should be successively numbered.

Short communications generally follow the same order of sections as Scientific articles, but should be short (max. 2500 words) and report a significant aspect of research work meriting separate publication. Editors may decide that a Scientific paper is categorized as a Short Communication if its length is short.

Technical articles report applications of an already described innovation. Typically, technical articles are not based on new experiments.

Preparation of Submissions

Text of the submitted articles must be prepared with Microsoft Word. Normal style set to single column, 1.5 line spacing, and 12 pt Times New Roman font is recommended. Line numbering (continuous, for the whole document) must be enabled to simplify the reviewing process. For any other format, please consult the editor. Articles should be written in English. Correct spelling and grammar are the sole responsibility of the author(s). Papers should be written in a concise and succinct manner. The authors shall respect the ISO 80000 standard [1], and IUPAC Green Book [2] rules on the names and symbols of quantities and units. The Système International d'Unités (SI) must be used for all dimensional quantities.

Graphics (figures, graphs, illustrations, digital images, photographs) should be inserted in the text where appropriate. The captions should be self-explanatory. Lettering should be readable (suggested 8 point Arial font) with equal size in all figures. Use common programs such as MS Excel or similar to prepare figures (graphs) and ChemDraw to prepare structures in their final size. Width of graphs in the manuscript should be 8 cm. Only in special cases (in case of numerous data, visibility issues) graphs can be 17 cm wide. All graphs in the manuscript should be inserted in relevant places and **aligned left**. The same graphs should be provided separately as images of appropriate resolution (see below) and submitted together in a ZIP file (Graphics ZIP). Please do not submit figures as a Word file. In **graphs**, only the graph area determined by both axes should be in the frame, while a frame around the whole graph should be omitted. The graph area should be white. The legend should be inside the graph area. The style of all graphs should be the same. **Figures and illustrations** should be of sufficient quality for the

printed version, i.e. 300 dpi minimum. **Digital images and photographs** should be of high quality (minimum 250 dpi resolution). On submission, figures should be of good enough resolution to be assessed by the referees, ideally as JPEGs. High-resolution figures (in JPEG, TIFF, or EPS format) might be required if the paper is accepted for publication.

Tables should be prepared in the Word file of the paper as usual Word tables. The captions should appear above the table and should be self-explanatory.

References should be numbered and ordered sequentially as they appear in the text, likewise methods, tables, figure captions. When cited in the text, reference numbers should be superscripted, following punctuation marks. It is the sole responsibility of authors to cite articles that have been submitted to a journal or were in print at the time of submission to ACSi. Formatting of references to published work should follow the journal style; please also consult a recent issue:

1. J. W. Smith, A. G. White, *Acta Chim. Slov.* **2008**, *55*, 1055–1059.
2. M. F. Kemmere, T. F. Keurentjes, in: S. P. Nunes, K. V. Peinemann (Ed.): *Membrane Technology in the Chemical Industry*, Wiley-VCH, Weinheim, Germany, **2008**, pp. 229–255.
3. J. Levec, Arrangement and process for oxidizing an aqueous medium, US Patent Number 5,928,521, date of patent July 27, **1999**.
4. L. A. Bursill, J. M. Thomas, in: R. Sersale, C. Collela, R. Aiello (Eds.), *Recent Progress Report and Discussions: 5th International Zeolite Conference*, Naples, Italy, 1980, Gianini, Naples, **1981**, pp. 25–30.
5. J. Szegezdi, F. Csizmadia, Prediction of dissociation constant using microconstants, http://www.chemaxon.com/conf/Prediction_of_dissociation_constant_using_microconstants.pdf, (assessed: March 31, 2008)

Titles of journals should be abbreviated according to Chemical Abstracts Service Source Index (CASSI).

Special Notes

- Complete characterization, **including crystal structure**, should be given when the synthesis of new compounds in crystal form is reported.
- Numerical **data should be reported with the number of significant digits corresponding to the magnitude** of experimental uncertainty.
- **The SI system of units and IUPAC recommendations** for nomenclature, symbols and abbreviations should be followed closely. Additionally, the authors should follow the general guidelines when citing spectral and analytical data, and depositing crystallographic data.
- **Characters** should be correctly represented throughout the manuscript: for example, 1 (one) and l (ell), 0 (zero) and O (oh), x (ex), D7 (times sign), B0 (degree sign). Use Symbol font for all Greek letters and mathematical symbols.
- The rules and recommendations of the **IUBMB** and the **International Union of Pure and Applied Chemistry (IUPAC)** should be used for abbreviation of chemical names, nomenclature of chemical compounds, enzyme nomenclature, isotopic compounds, optically active isomers, and spectroscopic data.

- **A conflict of interest** occurs when an individual (author, reviewer, editor) or its organization is involved in multiple interests, one of which could possibly corrupt the motivation for an act in the other. Financial relationships are the most easily identifiable conflicts of interest, while conflicts can occur also as personal relationships, academic competition, etc. **The Editors** will make effort to ensure that conflicts of interest will not compromise the evaluation process; potential editors and reviewers will be asked to exempt themselves from review process when such conflict of interest exists. When the manuscript is submitted for publication, **the authors** are expected to disclose any relationships that might pose potential conflict of interest with respect to results reported in that manuscript. In the Acknowledgement section the source of funding support should be mentioned. The statement of disclosure must be provided as Comments to Editor during the submission process.
- **Published statement of Informed Consent.** Research described in papers submitted to ACSi must adhere to the principles of the Declaration of Helsinki (<http://www.wma.net/e/policy/b3.htm>). These studies must be approved by an appropriate institutional review board or committee, and informed consent must be obtained from subjects. The Methods section of the paper must include: 1) a statement of protocol approval from an institutional review board or committee and 2), a statement that informed consent was obtained from the human subjects or their representatives.
- **Published Statement of Human and Animal Rights.** When reporting experiments on human subjects, authors should indicate whether the procedures followed were in accordance with the ethical standards of the responsible committee on human experimentation (institutional and national) and with the Helsinki Declaration of 1975, as revised in 2008. If doubt exists whether the research was conducted in accordance with the Helsinki Declaration, the authors must explain the rationale for their approach and demonstrate that the institutional review body explicitly approved the doubtful aspects of the study. When reporting experiments on animals, authors should indicate whether the institutional and national guide for the care and use of laboratory animals was followed.
- To avoid conflict of interest between authors and referees we expect that not more than one referee is from the same country as the corresponding author(s), however, not from the same institution.
- Contributions authored by **Slovenian scientists** are evaluated by non-Slovenian referees.
- Papers describing **microwave-assisted reactions** performed in domestic microwave ovens are not considered for publication in *Acta Chimica Slovenica*.
- *Manuscripts that are not prepared and submitted in accord with the instructions for authors are not considered for publication.*

Appendices

Authors are encouraged to make use of supporting information for publication, which is supplementary ma-

terial (appendices) that is submitted at the same time as the manuscript. It is made available on the Journal's web site and is linked to the article in the Journal's Web edition. The use of supporting information is particularly appropriate for presenting additional graphs, spectra, tables and discussion and is more likely to be of interest to specialists than to general readers. When preparing supporting information, authors should keep in mind that the supporting information files will not be edited by the editorial staff. In addition, the files should be not too large (upper limit 10 MB) and should be provided in common widely known file formats to be accessible to readers without difficulty. All files of supplementary materials are loaded separately during the submission process as supplementary files.

Proposed Cover Picture and Graphical Abstract Image

Graphical content: an ideally full-colour illustration of resolution 300 dpi from the manuscript must be proposed with the submission. Graphical abstract pictures are printed in size 6.5 x 4 cm (hence minimal resolution of 770 x 470 pixels). Cover picture is printed in size 11 x 9.5 cm (hence minimal resolution of 1300 x 1130 pixels)

Authors are encouraged to submit illustrations as candidates for the journal Cover Picture*. The illustration must be related to the subject matter of the paper. Usually both proposed cover picture and graphical abstract are the same, but authors may provide different pictures as well.

* The authors will be asked to contribute to the costs of the cover picture production.

Statement of novelty

Statement of novelty is provided in a Word file and submitted as a supplementary file in step 4 of submission process. Authors should in no more than 100 words emphasize the scientific novelty of the presented research. Do not repeat for this purpose the content of your abstract.

List of suggested reviewers

List of suggested reviewers is a Word file submitted as a supplementary file in step 4 of submission process. Authors should propose the names, full affiliation (department, institution, city and country) and e-mail addresses of five potential referees. Field of expertise and at least two references relevant to the scientific field of the submitted manuscript must be provided for each of the suggested reviewers. The referees should be knowledgeable about the subject but have no close connection with any of the authors. In addition, referees should be from institutions other than (and countries other than) those of any of the authors. Authors declare no conflict of interest with suggested reviewers. Authors declare that suggested reviewers are experts in the field of submitted manuscript.

How to Submit

Users registered in the role of author can start submission by choosing USER HOME link on the top of the page, then choosing the role of the Author and follow the relevant link for starting the submission process. Prior to submission we strongly recommend that you familiarize yourself with the ACSi style by browsing the journal, particularly if you have not submitted to the ACSi before or recently.

Correspondence

All correspondence with the ACSi editor regarding the paper goes through this web site and emails. Emails are sent and recorded in the web site database. In the correspondence with the editorial office please provide ID number of your manuscript. All emails you receive from the system contain relevant links. **Please do not answer the emails directly but use the embedded links in the emails for carrying out relevant actions.** Alternatively, you can carry out all the actions and correspondence through the online system by logging in and selecting relevant options.

Proofs

Proofs will be dispatched via e-mail and corrections should be returned to the editor by e-mail as quickly as possible, normally within 48 hours of receipt. Typing errors should be corrected; other changes of contents will be treated as new submissions.

Submission Preparation Checklist

As part of the submission process, authors are required to check off their submission's compliance with all of the following items, and submissions may be returned to authors that do not adhere to these guidelines.

1. The submission has not been previously published, nor is it under consideration for publication in any other journal (or an explanation has been provided in Comments to the Editor).
2. All the listed authors have agreed on the content and the corresponding (submitting) author is responsible for having ensured that this agreement has been reached.
3. The submission files are in the correct format: manuscript is created in MS Word but will be **submitted in PDF** (for reviewers) as well as in original MS Word format (as a supplementary file for technical editing); diagrams and graphs are created in Excel and saved in one of the file formats: TIFF, EPS or JPG; illustrations are also saved in one of these formats. The preferred position of graphic files in a document is to embed them close to the place where they are mentioned in the text (See **Author guidelines** for details).
4. The manuscript has been examined for spelling and grammar (spell checked).
5. The **title** (maximum 150 characters) briefly explains the contents of the manuscript.
6. Full names (first and last) of all authors together with the affiliation address are provided. Name of author(s) denoted as the corresponding author(s), together with their e-mail address, full postal address and telephone/fax numbers are given.
7. The **abstract** states the objective and conclusions of the research concisely in no more than 150 words.
8. Keywords (minimum three, maximum six) are provided.
9. **Statement of novelty** (maximum 100 words) clearly explaining new findings reported in the manuscript should be prepared as a separate Word file.
10. The text adheres to the stylistic and bibliographic requirements outlined in the **Author guidelines**.
11. Text in normal style is set to single column, 1.5 line spacing, and 12 pt. Times New Roman font is

recommended. All tables, figures and illustrations have appropriate captions and are placed within the text at the appropriate points.

12. Mathematical and chemical equations are provided in separate lines and numbered (Arabic numbers) consecutively in parenthesis at the end of the line. All equation numbers are (if necessary) appropriately included in the text. Corresponding numbers are checked.
13. Tables, Figures, illustrations, are prepared in correct format and resolution (see **Author guidelines**).
14. The lettering used in the figures and graphs do not vary greatly in size. The recommended lettering size is 8 point Arial.
15. Separate files for each figure and illustration are prepared. The names (numbers) of the separate files are the same as they appear in the text. All the figure files are packed for uploading in a single ZIP file.
16. Authors have read **special notes** and have accordingly prepared their manuscript (if necessary).
17. References in the text and in the References are correctly cited. (see **Author guidelines**). All references mentioned in the Reference list are cited in the text, and vice versa.
18. Permission has been obtained for use of copyrighted material from other sources (including the Web).
19. The names, full affiliation (department, institution, city and country), e-mail addresses and references of five potential referees from institutions other than (and countries other than) those of any of the authors are prepared in the word file. At least two relevant references (important recent papers with high impact factor, head positions of departments, labs, research groups, etc.) for each suggested reviewer must be provided. Authors declare no conflict of interest with suggested reviewers. Authors declare that suggested reviewers are experts in the field of submitted manuscript.
20. Full-colour illustration or graph from the manuscript is proposed for graphical abstract.
21. **Appendices** (if appropriate) as supplementary material are prepared and will be submitted at the same time as the manuscript.

Privacy Statement

The names and email addresses entered in this journal site will be used exclusively for the stated purposes of this journal and will not be made available for any other purpose or to any other party.

ISSN: 1580-3155

Koristni naslovi

Slovensko kemijsko društvo
Slovenian Chemical Society



Slovensko kemijsko društvo

www.chem-soc.si

e-mail: chem.soc@ki.si



Wessex Institute of Technology

www.wessex.ac.uk



SETAC

www.setac.org



European Water Association

<http://www.ewa-online.eu/>



European Science Foundation

www.esf.org



European Federation of Chemical Engineering

<https://efce.info/>



I U P A C

INTERNATIONAL UNION OF
PURE AND APPLIED CHEMISTRY

International Union of Pure and Applied Chemistry

<https://iupac.org/>

Novice evropske zveze kemijskih društev EuChemS najdete na:

 **EuChemS**
European Chemical Society

Brussels News Updates

<http://www.euchems.eu/newsletters/>



DONAU LAB Ljubljana
Member of LPPgroup

 **BINDER**

Best conditions for your success



Komore za testiranje baterij

Vakuumski sušilniki

Klimatske komore



Donau Lab d.o.o., Ljubljana
Tbilisjska 85
SI-1000 Ljubljana
www.donaulab.si
office-si@donaulab.com

Lek d. d.



Prejemniki Novartisovih nagrad za izjemne dosežke na področju raziskav in razvoja (z leve):
dr. Drago Kuzman, mag. Nejc Golob, dr. Biljana Jankovič, dr. Andrej Kocijan in dr. Rok Grahek

Naša skupna strast. Prebojne inovacije.

Ekipe naših znanstvenikov in strokovnjakov uvajajo pionirske pristope v razvoj in proizvodnjo zdravil za dostopno zdravljenje.

Novartis je vodilni ponudnik zdravil v Sloveniji, kjer delujejo Lek, Novartis Pharma Services in Sandoz. Z vrhunskimi odkritji in odličnimi proizvodnimi procesi nam vsak dan uspeva, da so bolnikom doma in po vsem svetu na voljo najnovejša inovativna in zahtevna generična zdravila.

**Smo Novartis.
Soustvarjamo medicino.**



 **NOVARTIS** | Reimagining Medicine

VITAMIN D3 Krka

ZAGOTOVITE SI SONCE.
PREPROSTO.

- ✓ **EDINI** kot zdravilo brez recepta.
- ✓ **ZAGOTOVI** priporočeni dnevni odmerki vitamina D.
- ✓ **BREZ** konzervansov, barvil in glutena.



www.vitamind3krka.si

 KRKA

PRED UPORABO NATANČNO PREBERITE NAVODILO!
O TVEGANJU IN NEŽELENIH UČINKIH SE POSVETUJTE Z ZDRAVNIKOM ALI S FARMACEVTOM.



NATIONAL INSTITUTE OF CHEMISTRY **75**^{years}

Hajdrihova 19,
1000 Ljubljana
Slovenia
www.ki.si



research
EXCELENCE

Basic and applied research in materials, life sciences, biotechnology, chemical engineering, structural and theoretical chemistry, analytical chemistry and environmental protection.

In line with EU research and innovation priorities: nanotechnology, genomics and biotechnology for health, sustainable development, climate change, energy efficiency and food quality and safety.

We expand knowledge and technology transfer to domestic and foreign chemical, automotive and nanobiotechnology industries.

We are aware of the power of youth, so we transfer our knowledge to younger generations and offer many opportunities for cooperation.



contact: mladi@ki.si

ActaChimicaSlovenica

ActaChimicaSlovenica

Electroporation is the method to increase the permeability of the cell membrane by high-voltage electric pulses. Electroporation is progressively used for internalization of various molecules into the cells in oncology and gene therapy, or extraction of molecules in biotechnology. It is also used as tissue ablation method and in food technology. (page 753)



Year 2021, Vol. 68, No. 4

